The copyright of this thesis vests in the author. No quotation from it or information derived from it is to be published without full acknowledgement of the source. The thesis is to be used for private study or non-commercial research purposes only.

Published by the University of Cape Town (UCT) in terms of the non-exclusive license granted to UCT by the author.

University of Cape Town

For my late father, Peter Milburn Atkinson,

and my late step-father, Denis Harold Daykin

Numerical Modelling of Explosively Loaded Steel V-Plates Using the Jones-Wilkins-Lee Equation of State

Leigh Milburn Atkinson Daykin

Department of Mechanical Engineering
University of Cape Town
South Africa

September 2002

Thesis submitted in partial fulfillment of the requirements for a Masters in Engineering

Declaration

I, Leigh Milburn Atkinson Daykin, declare that this thesis is essentially my own work and has not been submitted in this or any other form for a degree at any other university.

Synopsis

Mine warfare is a very effective method of warfare as it has the element of surprise, it doesn't require interaction with the enemy, and it has a high percentage of fatalities. Because of this, mine warfare has been used extensively across the world during conflicts and therefore there is a need for mine-detecting and mine-protected vehicles. The systems of protection of these vehicles need to be investigated so that they can be optimized.

The study in this document investigates the effect of a disc of high explosive on a steel V-shaped plate through numerical modelling. This system is a simplified simulation of a mine detonating beneath the V-shaped hull of a mine-protected vehicle.

Parameters of the numerical model which will be varied are:

- position of the explosive relative to the V-plate.
- mass of the explosive disc (keeping the disc diameter constant).
- included angle of the V-plate.

One of the objectives of this thesis is to determine if finite element method modelling is capable of accurately predicting the response of exploded V-plates using the Jones-Wilkins-Lee (JWL) Equation of State. Another objective is to determine any trends and thresholds of the exploded V-plates that are dependent on the above-mentioned parameters. In particular, the plastic strain energy and impulse absorbed and deflected by the different V-plates should be determined, as they indicate the level of protection the V-plate would offer.

Two versions of the system involving shaped explosive charges exploding V-plates, had to be modelled:

1) A V-plate with a round rod of explosive positioned slightly above the mid-point of the ridge of the V formed by the joining of the two halves of the V-plate.

2) A V-plate with a disc of explosive positioned slightly above the mid-point of the ridge of the V-plate.

Verification of a numerical model is very important as the results could appear to be accurate but actually be completely incorrect. This is why two versions of the system have to be modelled even though the second system involving the disc of explosive is the only version of interest as it simulates a landmine detonation.

Experimentation has already been conducted on the first system containing the explosive rod by Lockley [43] but not on the second system containing the explosive disc. The processed results of these experiments can be compared with the results obtained from the numerical model of the rod explosive system. The results will be comparable because the geometry, boundary conditions, and material properties of the rod explosive version of the system will be modelled to be identical to those used in the experiments.

If the results are similar, the ABAQUS model will be verified as it produces realistic results. This then indicates that similar numerical models, such as the model involving the explosive disc, should also produce realistic results.

The models created were quarter models owing to planes of symmetry. These models consisted of flanged steel V-plates modeled with hexahedral continuum elements with mesh bias, and disc or rod explosives above the V-plates, modelled with hexahedral and tetrahedral continuum elements. The detonation and reaction of the explosives are governed by the JWL equation of state. The material model of the steel V-plates included strain sensitivity, strain rate sensitivity, and temperature dependency

The JWL EOS models of the systems involving rod explosives were unacceptably inaccurate with their predictions as the mid-point deflections and degrees of deformation were greatly underpredicted. Because of this the models

containing rod explosives were not verified and therefore the accuracy of the models containing disc explosives could not be determined. The reason for the inaccuracies is thought to be because of an incorrect transfer of impulse from the explosives to the V-plates. The reason for this incorrect impulse transfer is not known. The results of the models containing disc explosives appear promising but they will have to be verified with experiments.

Because of the problems encountered in this study, certain objectives of this study could not be achieved. It is believed, however, that if the problem causing the inaccuracies is found and rectified, the JWL EOS method of modelling explosives has the potential to produce suitably accurate results.

Acknowledgements

I would like to appreciate and acknowledge the assistance received from my supervisor Professor G. N. Nurick and the CERECAM staff, especially Mr. V. Balden.

I especially wish to thank my mother, Pat, for her support.

Table of Contents

Chapter	Page
1. Introduction	1
1.1 Background	1
1.2 Objectives of this Thesis	6
1.3 Procedure of this Thesis	6
1.4 Scope of this Thesis	8
1.5 Plan of Development	8
2. Literature Review	10
2.1 Mine-Protected Vehicle Study	11
2.2 Explosives in General	14
2.3 Interaction of Explosives with Metal Plates	29
2.3.1 Experimental Studies	29
2.3.2 Theoretical Studies	34
2.3.3 Numerical Studies	42
2.4 Finite Element Methods	57
2.4.1 Numerical Methods	57
2.4.1.1 Numerical Solution of a Governing Equation	58
2.4.1.2 Energy Methods	58
2.4.1.3 Finite Element Methods	59
2.4.1.3.1 Finite Element Methods Fundamentals	60
2.4.1.3.1 a) Structural Idealisation	60
2.4.1.3.1 b) Evaluation of the Element Properties	61
2.4.1.3.1 c) Structural Analysis of the Element Assemblage	62
2.4.1.3.2 Dynamic and Non-Linear Systems	63
2.4.1.3.2 a) Dynamic Linear Systems	63
2.4.1.3.2 b) Static Non-Linear Systems	64
2.4.1.3.2 c) Dynamic and Non-Linear Systems	65
2.4.1.3.3 Programming	65

3. ABAQUS Overview 67
3.1 Aspects of ABAQUS Relevant to this Study 67
3.1.1 The Analysis Procedure 68
3.1.2 Modelling of Mechanical Properties 70
3.1.2.1 Modelling of Elastic-Plastic Behaviour 70
3.1.2.2 Yield Hardening 71
3.1.2.2.1 Perfect Plasticity 72
3.1.2.2.2 Isotropic Hardening 72
3.1.2.2.3 Johnson-Cook Hardening 72
3.1.2.3 Rate Dependence 72
3.1.2.3.1 Direct Tabular Data 73
3.1.2.3.2 Yield Stress Ratios 73
3.1.2.3.2 a) The Overstress Power Law 73
3.1.2.3.2 b) The Tabular Method 74
3.1.2.3.2 c) Johnson-Cook Rate Dependence 74
3.1.2.4 Temperature Dependence 74
3.1.2.4.1 Adiabatic Heating 74
3.1.2.5 The Modelling of Failure 75
3.1.2.5.1 Shear Failure Model 75
3.1.2.5.2 Tensile Failure Model 76
3.1.2.6 Equations of State 76
3.1.2.6.1 The Energy Equation 76
3.1.2.6.2 The Equation of State 77
3.1.2.6.2 a) The Mie-Gruniesen Equations of State 78
3.1.2.6.2 a) i) The Linear U_s - U_p Hugoniot Form 79
3.1.2.6.2 a) ii) The Jones-Wilkins-Lee Equation of State 79
3.1.2.6.2 b) The Ideal Gas Equation of State 81
3.1.3 Modelling of Contact Interaction 82
3.1.3.1 Pure and Balanced Master-Slave Contact Surfaces 82

3.1.3.1.1 Pure Master-Slave Contact 82
3.1.3.1.2 Balanced Master-Slave Contact 83
3.1.3.2 Kinematic and Penalty Contact Algorithms 83
3.1.3.2.1 Kinematic Contact Algorithm 83
3.1.3.2.2 Penalty Contact Algorithm 84
3.1.3.3 Hard and Soft Contact 86
3.1.3.3.1 Hard Contact 86
3.1.3.3.2 Soft Contact 86
3.1.3.4 Separation and No Separation of Surfaces 88

4. The Finite Element Model 89
4.1 Selection of Model 89
4.1.1 Modelling the Explosive 91
4.1.2 Planes of Symmetry 91
4.1.3 Including the Explosive Fuse 92
4.2 Variations of the Model and the Resulting Dimensions 94
4.3 Elements and Meshing 99
4.3.1 The V-Plate 99
4.3.1.1 Element Type 99
4.3.1.2 Mesh Bias 101
4.3.1.3 Number and Size of Elements 102
4.3.2 The Explosive Charge 103
4.3.2.1 Element Type 103
4.3.2.2 Number and Size of Elements 106
4.3.2.2.1 Element Distortion 107
4.4 Duration of Model Analysis and Time Steps 110
4.5 Boundary Conditions 111
4.6 The Mechanical and Material Properties 114
4.6.1 The V-Plate 114
4.6.1.1 Yield Hardening 115
4.6.1.2 Strain Rate Sensitivity 116
4.6.1.3 Temperature Dependence 118
4.6.1.4 The Modelling of Failure 121
4.6.2 The Explosive 121
4.7 The Contact Interaction 124
4.7.1 Pure or Balanced Master-Slave Contact Surfaces 124

4.7.2 Kinematic or Penalty Contact Algorithm 124
4.7.3 Hard or Soft Contact 125
4.7.4 Separation or No Separation of Surfaces 126

5. Previous Experimental and Numerical Results 127
5.1 Previous Experimental Results 127
5.2 Previous Numerical Results 130

6. Results and Discussion 135
6.1 The Flat Circular Plate and Explosive Disc Model 135
6.2 The V-Plate and Explosive Rod and Explosive Disc Models 137
6.2.1 General Observations 137
6.2.1.1 Detonation of the Explosives 138
6.2.1.2 Interaction of the Explosives with the V-Plates 143
6.2.1.3 Displacement and Time Response of V-Plates 147
6.2.2 The Results of the Models Containing an Explosive Rod 148
6.2.2.1 Comparison Between the JWL Equation of State Model Predictions of the V-Plate Mid-Point Displacements, the Pressure Profile Model Mid-Point Displacements, and the Experimental Mid-Point Displacements 148
6.2.2.1.1 Comparison of the V-Plate Mid-Point Displacements Versus the Explosive Rod Masses 149
6.2.2.1.2 Comparison of the V-Plate Mid-Point Displacements Versus the V-Plate Angles 157
6.2.2.2 Comparison Between the JWL Equation of State Model Predictions of the V-Plate Profiles, the Pressure Profile Model Profiles, and the Experimental Profiles 165
6.2.2.2.1 Comparison of the V-Plate Profiles 165
6.2.2.2.2 Tearing of the V-Plates 171
6.2.2.3 Comparison Between the Effectiveness of the V-Plates determined by the JWL Equation of State Model, the Pressure Profile Model, and the Experiments 172
6.2.2.4 Attempts to Determine What Causes the Inaccuracies in the Models Containing Rod Explosives and How to

Improve the Results 176
6.2.2.4.1 The Soft Contact Algorithm Option 176
6.2.2.4.2 Other Attempts 177
6.2.3 The Results of the Models Containing an Explosive Disc 183
6.2.3.1 Model Predictions of the V-Plate Mid-Point Displacements 184
6.2.3.1.1 V-Plate Mid-Point Displacements Versus the Explosive Disc Masses 184
6.2.3.1.2 V-Plate Mid-Point Displacements Versus the V-Plate Angles 185
6.2.3.2 Model Predictions of the V-Plate Profiles 187
6.2.3.2.1 Predictions of the V-Plate Profiles for the Systems with Varying Explosive Masses and V-Plate Angles 187
6.2.3.2.2 Predictions of the V-Plate Profiles for the Systems with the Explosive Discs Horizontally Offset 191
6.2.3.2.3 Tearing of the V-Plates 195
6.2.4 Comparison of the Results of the Models Containing Rod Explosives and the Models Containing Disc Explosives 196

7. Conclusions 202
7.1 The Finite Element Modelling Technique 202
7.1.1 Element Selection 202
7.1.2 Mesh Selection 203
7.1.3 Boundary Conditions 203
7.1.4 Contact Interaction 204
7.2 Results of the Models 205
7.2.1 Results of the Models Containing Explosive Rods 206
7.2.1.1 Comparison Between the JWL Equation of State Model Predictions of the V-Plate Mid-point Displacements, the Pressure Profile Model Displacements, and the Experimental Displacements 206
7.2.1.1.1 Comparison of the V-Plate Mid-Point Displacements Versus the Explosive Rod Masses 207

7.2.1.1.2 Comparison of the V-Plate Mid-Point Displacements Versus the V-Plate Angles 207
7.2.1.2 Comparison Between the JWL Equation of State Model Predictions of the V-Plate Profiles, the Pressure Profile Model Profiles, and the Experimental Profiles 208
7.2.1.3 Comparison Between the Effectiveness of the V-Plates Determined by the JWL Equation of State Model, the Pressure Profile Model, and the Experiments 209
7.2.1.4 Attempts to Determine What Causes the Inaccuracies in the Models Containing Rod Explosives and How to Improve the Results 210
7.2.1.5 Tearing of the V-Plates 210
7.2.2 Results of the Models Containing Explosive Discs 211
7.2.2.1 Model Predictions of the V-Plate Mid-Point Displacements 211
7.2.2.1.1 V-Plate Mid-Point Displacements Versus the Explosive Disc Masses 212
7.2.2.1.2 V-Plate Mid-Point Displacements Versus the V-Plate Angles 212
7.2.2.2 Model Predictions of the V-Plate Profiles 212
7.2.2.3 Tearing of the V-Plates 213
7.2.3 Comparison of the Results of the Models Containing Rod Explosives and the Models Containing Disc Explosives 214
7.3 Concluding Remarks 214

8. Recommendations 216
8.1 The Finite Element Model 216
8.2 The Results of the Models 217

9. Appendices A.1
9.1 Appendix A: Photographs of Experimentally Deformed V-Plates Exploded by PE4 Rod Explosives A.1
9.2 Appendix B: Pictures of Pressure Profile Method Numerically Predicted Deformed V-Plates Exploded by PE4 Rod Explosives B.1

9.3 Appendix C: Graphs of JWL Equation of State Method Numerically Predicted Deformed V-Plate Profiles Exploded by PE4 Rod Explosives, Compared with the Corresponding Experimental and Pressure Profile Method Numerically Predicted V-Plate Profiles C.1

9.3.1 Comparison of the Experimental and Numerically Predicted Deformed V-Plate Profiles for the 60^0 V-Plates C.2

9.3.2 Comparison of the Experimental and Numerically Predicted Deformed V-Plate Profiles for the 90^0 V-Plates C.13

9.3.3 Comparison of the Experimental and Numerically Predicted Deformed V-Plate Profiles for the 120^0 V-Plates C.24

9.3.4 Comparison of the Experimental and Numerically Predicted Deformed V-Plate Profiles for the 150^0 V-Plates C.35

9.4 Appendix D: Graphs of JWL Equation of State Method Numerically Predicted Deformed V-Plate Profiles Exploded by PE4 Disc Explosives D.1

9.4.1 JWL Equation of State Method Numerically Predicted Deformed V-Plate Profiles for the 60^0 V-Plates D.2

9.4.2 JWL Equation of State Method Numerically Predicted Deformed V-Plate Profiles for the 90^0 V-Plates D.8

9.4.3 JWL Equation of State Method Numerically Predicted Deformed V-Plate Profiles for the 120^0 V-Plates D.18

9.4.4 JWL Equation of State Method Numerically Predicted Deformed V-Plate Profiles for the 150^0 V-Plates D.24

9.5 Appendix E: Co-Ordinates of the Deformed V-Plate Profiles Exploded by PE4 Rod Explosives for the Experimental and Numerically Predicted Profiles (Both the JWL Equation of State Method and Pressure Profile Method) E.1

9.5.1 Co-Ordinates of the Deformed V-Plate Profiles for the 60^0 V-Plates E.2
9.5.2 Co-Ordinates of the Deformed V-Plate Profiles for the 90^0 V-Plates E.20
9.5.3 Co-Ordinates of the Deformed V-Plate Profiles for the 120^0 V-Plates E.32
9.5.4 Co-Ordinates of the Deformed V-Plate Profiles for the 150^0 V-Plates E.42
9.6 Appendix F: Co-Ordinates of the JWL Equation of State Method Numerically Predicted Deformed V-Plate Profiles Exploded by PE4 Disc Explosives F.1
9.6.1 Co-Ordinates of the Deformed V-Plate Profiles for the 60^0 V-Plates F.2
9.6.2 Co-Ordinates of the Deformed V-Plate Profiles for the 90^0 V-Plates F.5
9.6.3 Co-Ordinates of the Deformed V-Plate Profiles for the 90^0 V-Plates Exploded by Offset Disc Explosives F.8
9.6.4 Co-Ordinates of the Deformed V-Plate Profiles for the 120^0 V-Plates F.11
9.6.5 Co-Ordinates of the Deformed V-Plate Profiles for the 150^0 V-Plates F.13
9.7 Appendix G: Mid-Point Displacements and their Error Percentages, of the Deformed V-Plates Exploded by PE4 Rod Explosives, Obtained from the Experiments and from the Pressure Profile Method Numerical Predictions and the JWL Equation of State Method Numerical Predictions G.1
9.7.1 Mid-Point Displacements of the Deformed V-Plates G.2
9.7.2 Error Percentages of the Mid-Point Displacements of the Deformed V-Plates G.4
9.8 Appendix H: Mid-Point Displacements of the Deformed V-Plates Exploded by PE4 Disc Explosives, Obtained from the JWL Equation of State Method Numerical Predictions H.1

9.9 Appendix I: An Example of the Input Decks Used to Model V-Plates Being Exploded by PE4 Disc Explosives I.1

9.10 Appendix J: Experimentally Obtained Impulses Transferred to the V-Plates Exploded by Rod Explosives J.1

10. References R.1

List of Figures

Figure		Page
Figure 1.1:	A vehicle which detonted an anti-tank mine. The front of the vehicle was destroyed and the driver seriously injured.	1
Figure 1.2:	A mine-detecting vehicle with trailers to detonate mines.	2
Figure 1.3:	A Kudu MK10 mine-protected vehicle.	3
Figure 1.4:	A mine-protected mortar carrier.	4
Figure 1.5:	The Mamba.	4
Figure 1.6:	The Caspar II.	5
Figure 2.1:	Detonation process in explosive of infinite extent.	17
Figure 2.2:	Temperature, pressure, density, and composition distributions within the reaction zone.	18
Figure 2.3:	Detonation front arising from a point explosion.	21
Figure 2.4:	Detonation of explosive and expansion of explosion products from a finite bounded charge.	22
Figure 2.5:	Overpressure in shock as a function of distance from source at several subsequent times.	23
Figure 2.6:	Shock wave front which develops around a line charge.	24
Figure 2.7:	Detonation of explosive and expansion of explosion products from an explosive layer of varying thickness.	24
Figure 2.8:	Pressure-time profiles at three positions, A, B, and C on metal plate in system of Figure 1.13	25
Figure 2.9:	Pressure distribution set up by reflection at a rigid boundary of exponentially decaying shock in water.	26
Figure 2.10:	Reflection from rigid boundaries of (a) weak oblique shocks; (b) medium strong oblique shocks; (c) strong oblique shocks.	27
Figure 2.11:	Schematic of typical experimental set-up of an explosive and flat plate.	29
Figure 2.12:	Diagrams illustrating the three failure modes; (a) mode 1; (b) model II; (c) mode III.	31
Figure 2.13:	Initial velocity profiles simulating explosive loading; (a) uniform velocity over entire plate; (b) trapezoidal velocity over central area of plate.	34
Figure 2.14:	Pressure profiles simulating explosive loading; (a) uniform pressure over entire plate; (b) uniform pressure over central area of plate.	34
Figure 2.15:	Pressure pulses over which pressure profiles are applied; (a) square pulse; (b) triangular pulse.	34
Figure 2.16:	Schematic of metal-working set-up to which the energy transfer approximations reported by Ezra [16] apply.	36

Figure 2.17: Schematic representation of the different boundary conditions of blast loaded plates modelled by Gelman [30]. 45

Figure 2.18: Diagrams illustrating; (a) the experimental set-up; (b) the geometry; of a ballistic Pendulum 48

Figure 2.19: A schematic representation of the experimental set-up that Bimha [26] modelled and the pressure profile used in the model. 50

Figure 2.20: A Diagram of the plate model, modelled with axisymmetric elements (CAX4R) by Wiehahn [34]. 54

Figure 2.21: The half model of the explosive and flat circular plate modelled with axisymmetric elements (CAX4R), used by Grobbelaar [35]. 56

Figure 2.22: Numerical methods used for structural analysis 58

Figure 2.23: Finite element one-dimensional idealisation of a framed structure. 59

Figure 2.24: Finite element two-dimensional idealisation of a dam. 59

Figure 3.1: A schematic representation of a typical Hugoniot curve. 78

Figure 3.2: Diagrams of the three pressure-overclosure relationships; (a) linear relationship; (b) exponential relationship; (c) piecewise linear relationship. 87

Figure 4.1: Diagram of V-Plate with Explosive Rod and Fuse 89

Figure 4.2: Diagram of V-Plate with Explosive Disc 90

Figure 4.3: Diagrams of the two different rod explosive models; (a) with a fuse; (b) without a fuse 92

Figure 4.4: A magnified section of the comparison of the profiles obtained from two models where one model has an explosive rod with a fuse (9g) and the other model has a rod without a fuse (8g). A 90 degree V-plate was used in both the models. 93

Figure 4.5: Diagrams showing the expansion of the detonation front from the detonation point through the rod explosive; (a) with a fuse; (b) without a fuse. 94

Figure 4.6: Diagram showing how parametric changes alter the; (a) rod explosive model; (b) the disc explosive model. 96

Figure 4.7: The dimensions of the; (a) disc explosive; (b) rod explosive. 97

Figure 4.8: The dimensions of the V-plates. 98

Figure 4.9: A comparison between results of an exploded flat circular steel plate model obtained using shell elements, and results obtained from the model using continuum elements, as conducted by Grobbelaar [35]. 100

Figure 4.10: The element mesh of the 150^0 V-plate models. 103

Figure 4.11: The mesh generated by ABAQUS/CAE for a quarter disc explosive. 104

Figure 4.12: A picture showing how tetrahedral explosive elements form 'spikes' which impact with the V-plate. 105

Figure 4.13: Meshing the explosive rod; (a) with a fuse; (b) without a fuse. 106

Figure 4.14: Pictures showing distorted explosive elements resulting from the flow of the explosive down the sides of the V-plate. 107

Figure 4.15: An explosive disc meshed; (a) manually; (b) with ABAQUS/CAE. 109

Figure 4.16: Diagram of timeline showing the model analysis duration and its subdivision into steps. 111

Figure 4.17: A diagram indicating the translational degrees of freedom which are constrained on the axes of symmetry of a quarter model of a disc. The translational degrees of freedom are constrained in the directions of the arrows for the entire surface which the arrows are touching. 112

Figure 4.18: Diagrams indicating, with arrows, the top and bottom surfaces of the V-plate flange which have all their degrees of freedom constrained to simulate clamping. 113

Figure 4.19: The yield stress versus plastic strain curve of the steel used for the V-plate, at room temperature. 116

Figure 4.20: A graph of the yield stress versus the plastic strain percentage of the V-plate steel at different strain rates according to the Cowper Symonds relationship with D=40.4 s^{-1} and n=5. 117

Figure 4.21: A graph showing the relationship between the Young's modulus and the temperature of the V-plate steel according to equation 4.1. 119

Figure 4.22: A graph showing the relationship between the yield stress and the temperature of the V-plate steel according to equation 4.2. 120

Figure 4.23: Diagram indicating the explosive detonation points of; (a) the rod explosive; (b) the disc explosive. 123

Figure 5.1: A picture of the experimental set-up of the experiments conducted by Lockley [43] 128

Figure 5.2: The experimentally exploded 120^0 V-plates obtained by Lockley [43]. 129

Figure 5.3: The results of the numerical models for the 120^0 V-plates modelled by Nannucci [44]. 131

Figure 5.4: Numerical instability resulting from modelling the explosive as a pressure load over a localised area of the V-plate for a short duration. 133

Figure 6.1: A Comparison Between the Flat Plate Profiles of Grobbelaar's Axisymmetric JWL EOS Model, the Three-Dimensional JWL EOS Model from this Study, and the Experiment. 136

Figure 6.2: The pressure distribution during the detonation of a 9g rod and fuse explosive. The units are Mbar. 139

Figure 6.3: The pressure distribution during the detonation of a 8g disc explosive. The units are Mbar. 141

Figure 6.4: Rod explosive velocity distribution after detonation (cm. μs^{-1}) 142

Figure 6.5: Disc explosive velocity distribution after detonation (cm. μs^{-1}) 142

Figure 6.6: Interaction between an 8g explosive disc and a 150^0 V-plate (represented by a quarter model). The stress distributions are shown. The units are Mbar. 144

Figure 6.7: Displacement versus time for the ridge of a V-plate profile from a model containing an 8g explosive disc and a 90 degree V-plate 147

Figure 6.8: 60^0 V-Plate Mid-Point Displacement Versus Explosive Rod Mass Obtained from

the Experiments, the ABAQUS Pressure Profile Analyses, and the ABAQUS Equation of State Analyses. 150

Figure 6.9: 90^0 V-Plate Mid-Point Displacement Versus Explosive Rod Mass Obtained From the Experiments, the ABAQUS Pressure Profile Analyses, and the ABAQUS Equation of State Analyses. 150

Figure 6.10: 120^0 V-Plate Mid-Point Displacement Versus Explosive Rod Mass Obtained From the Experiments, the ABAQUS Pressure Profile Analyses, and the ABAQUS Equation of State Analyses. 151

Figure 6.11: 150^0 V-Plate Mid-Point Displacement Versus Explosive Rod Mass Obtained From the Experiments, the ABAQUS Pressure Profile Analyses, and the ABAQUS Equation of State Analyses. 151

Figure 6.12: All the V-Plate Mid-Point Displacements Versus Explosive Rod Masses Obtained From the Experiments and the ABAQUS Equation of State Analyses. 157

Figure 6.13: V-Plate Mid-Point Displacement From 3g Explosive Rod Versus V-Plate Angle Obtained From the Experiments, the ABAQUS Pressure Profile Analyses, and the ABAQUS Equation of State Analyses. 158

Figure 6.14: V-Plate Mid-Point Displacement From 5g Explosive Rod Versus V-Plate Angle Obtained From the Experiments, the ABAQUS Pressure Profile Analyses, and the ABAQUS Equation of State Analyses. 158

Figure 6.15: V-Plate Mid-Point Displacement From 7g Explosive Rod Versus V-Plate Angle Obtained From the Experiments, the ABAQUS Pressure Profile Analyses, and the ABAQUS Equation of State Analyses. 159

Figure 6.16: V-Plate Mid-Point Displacement From 9g Explosive Rod Versus V-Plate Angle Obtained From the Experiments, the ABAQUS Pressure Profile Analyses, and the ABAQUS Equation of State Analyses. 159

Figure 6.17: All the V-Plate Mid-Point Displacements Versus the V-Plate Angles Obtained From the Experiments and the ABAQUS Equation of State Analyses. 165

Figure 6.18: Comparison of a Magnified Section of the Experimental Deformed Profile of a V-Plate (90 degrees) Exploded by a PE4 Rod (5g), With the ABAQUS Deformed Profile Obtained Using a Pressure Profile, and With the ABAQUS Deformed Profile Obtained Using the EOS 166

Figure 6.19: Comparison of a Magnified Section of the Experimental Deformed Profile of a V-Plate (90 degrees) Exploded by a PE4 Rod (7g), With the ABAQUS Deformed Profile Obtained Using a Pressure Profile, and With the ABAQUS Deformed Profile Obtained Using the EOS 167

Figure 6.20: Comparison of a Magnified Section of the Experimental Deformed Profile of a V-Plate (90 degrees) Exploded by a PE4 Rod (9g), With the ABAQUS Deformed Profile Obtained Using a Pressure Profile, and With the ABAQUS Deformed Profile Obtained Using the EOS 167

Figure 6.21: Comparison of a Magnified Section of the Experimental Deformed Profile of a

V-Plate (90 degrees) Exploded by a PE4 Rod (11g), With the ABAQUS Deformed Profile Obtained Using a Pressure Profile, and With the ABAQUS Deformed Profile Obtained Using the EOS 168

Figure 6.22: Comparison of a Magnified Section of the Experimental Deformed Profile of a V-Plate (90 degrees) Exploded by a PE4 Rod (13g), With the ABAQUS Deformed Profile Obtained Using a Pressure Profile, and With the ABAQUS Deformed Profile Obtained Using the EOS 168

Figure 6.23: Comparison of a Magnified Section of the Experimental Deformed Profile of a V-Plate (120 degrees) Exploded by a PE4 Rod (9g), With the ABAQUS Deformed Profile Obtained Using a Pressure Profile, and With the ABAQUS Deformed Profile Obtained Using the EOS 169

Figure 6.24: The temperature distribution (in C^0) of a deformed 150^0 V-plate as predicted by the model containing an 11g explosive rod 171

Figure 6.25: A diagram of the forces exerted on the V-plate in the models. 174

Figure 6.26: Comparison of a Magnified Section of the Experimental Deformed Profile of a V-Plate (60 degrees) Exploded by a PE4 Rod (13g), With the ABAQUS Deformed Profile Obtained Using a Pressure Profile, and With the ABAQUS Deformed Profile Obtained Using the EOS 179

Figure 6.27: An explosive element 'see-sawing' on a V-plate ridge 180

Figure 6.28: Diagrams indicating ridges of V-plates which are; (a) rounded; (b) flat-topped. 180

Figure 6.29: V-Plate Mid-Point Displacement Versus Explosive Disc Mass Obtained From the ABAQUS Equation of State Analyses for Different Angles. 184

Figure 6.30: V-Plate Mid-Point Displacement Versus V-Plate Angle for the Models Containing Explosive Discs, Obtained From the ABAQUS Equation of State Analyses for Different Masses. 186

Figure 6.31: The Deformed Profile of a V-Plate (120 degrees) Exploded by a PE4 Disc (4g) As Predicted By ABAQUS Using the JWL Equation of State 188

Figure 6.32: The Deformed Profile of a V-Plate (120 degrees) Exploded by a PE4 Disc (6g) As Predicted By ABAQUS Using the JWL Equation of State 188

Figure 6.33: The Deformed Profile of a V-Plate (120 degrees) Exploded by a PE4 Disc (8g) As Predicted By ABAQUS Using the JWL Equation of State 189

Figure 6.34: The Deformed Profile of a V-Plate (120 degrees) Exploded by a PE4 Disc (10g) As Predicted By ABAQUS Using the JWL Equation of State 189

Figure 6.35: The Deformed Profile of a V-Plate (120 degrees) Exploded by a PE4 Disc (12g) As Predicted By ABAQUS Using the JWL Equation of State 190

Figure 6.36: The Deformed Profile of a V-Plate (90 degrees) Exploded by a PE4 Disc (8g) As Predicted By ABAQUS Using the JWL Equation of State 191

Figure 6.37: The Deformed Profile of a V-Plate (90 degrees) Exploded by a PE4 Disc (8g; 5mm Offset) As Predicted By ABAQUS Using the JWL Equation of State 192

Figure 6.38: The Deformed Profile of a V-Plate (90 degrees) Exploded by a PE4 Disc

(8g; 10mm Offset) As Predicted By ABAQUS Using the JWL Equation of State 192

Figure 6.39: The Deformed Profile of a V-Plate (90 degrees) Exploded by a PE4 Disc (8g; 15mm Offset) As Predicted By ABAQUS Using the JWL Equation of State 193

Figure 6.40: The Deformed Profile of a V-Plate (90 degrees) Exploded by a PE4 Disc (8g; 20mm Offset) As Predicted By ABAQUS Using the JWL Equation of State 193

Figure 6.41: The temperature distribution of a deformed 150^0 V-plate as predicted by the model containing a 12g explosive disc 196

Figure 6.42: Comparison Between the 150 Degree V-Plate Profiles of an Experiment Containing a 9g Explosive Rod, the JWL EOS Model Containing a 9g Explosive Rod, and the JWL EOS Model Containing an 8g Explosive Disc. 197

Figure 6.43: Comparison Between the 150 Degree V-Plate Mid-Point Displacement Versus Explosive Mass Relationships of the Rod Explosive Experiments, the Models Containing Rod Explosives, and the Models Containing Disc Explosives 198

Figure 6.44: Comparison Between the 150 Degree V-Plate Mid-Point Displacement Versus V-Plate Angle Relationships of the 9g Rod Explosive Experiments, the Models Containing 9g Rod Explosives, and the Models Containing 8g Disc Explosives 199

Figure A.1: Photographs of Lockley's [43] experimentally deformed V-plates exploded by PE4 rod explosives with the V-plates grouped together according to the V-plate angles of; (a) 60^0; (b) 90^0; (c) 120^0; (d) 150^0. Appendix A

Figure B.1: Pictures of Nannucci's [44] pressure profile method numerically predicted deformed V-plates exploded by PE4 rod explosives with the V-plates grouped together according to the V-plate angles of; (a) 60^0; (b) 90^0; (c) 120^0; (d) 150^0. Appendix B

Figure C.1: Comparison of the Experimental Deformed Profile of a V-Plate (60 degrees) Exploded by a PE4 Rod (5g), With the ABAQUS Deformed Profile Obtained Using a Pressure Profile, and With the ABAQUS Deformed Profile Obtained Using the EOS Appendix C

Figure C.2: Comparison of a Magnified Section of the Experimental Deformed Profile of a V-Plate (60 degrees) Exploded by an PE4 Rod (5g), With the ABAQUS Deformed Profile Obtained Using a Pressure Profile, and With the ABAQUS Deformed Profile Obtained Using the EOS Appendix C

Figure C.3: Comparison of the Experimental Deformed Profile of a V-Plate (60 degrees) Exploded by a PE4 Rod (7g), With the ABAQUS Deformed Profile Obtained Using a Pressure Profile, and With the ABAQUS Deformed Profile Obtained Using the EOS Appendix C

Figure C.4: Comparison of a Magnified Section of the Experimental Deformed Profile of a V-Plate (60 degrees) Exploded by an PE4 Rod (7g), With the ABAQUS Deformed Profile Obtained Using a Pressure Profile, and With the ABAQUS Deformed Profile Obtained Using the EOS Appendix C

Figure C.5: Comparison of the Experimental Deformed Profile of a V-Plate (60 degrees) Exploded by a PE4 Rod (9g), With the ABAQUS Deformed Profile Obtained

Using a Pressure Profile, and With the ABAQUS Deformed Profile Obtained Using the EOS Appendix C

Figure C.6: Comparison of a Magnified Section of the Experimental Deformed Profile of a V-Plate (60 degrees) Exploded by an PE4 Rod (9g), With the ABAQUS Deformed Profile Obtained Using a Pressure Profile, and With the ABAQUS Deformed Profile Obtained Using the EOS Appendix C

Figure C.7: Comparison of the Experimental Deformed Profile of a V-Plate (60 degrees) Exploded by a PE4 Rod (11g), With the ABAQUS Deformed Profile Obtained Using a Pressure Profile, and With the ABAQUS Deformed Profile Obtained Using the EOS Appendix C

Figure C.8: Comparison of a Magnified Section of the Experimental Deformed Profile of a V-Plate (60 degrees) Exploded by a PE4 Rod (11g), With the ABAQUS Deformed Profile Obtained Using a Pressure Profile, and With the ABAQUS Deformed Profile Obtained Using the EOS Appendix C

Figure C.9: Comparison of the Experimental Deformed Profile of a V-Plate (60 degrees) Exploded by a PE4 Rod (13g), With the ABAQUS Deformed Profile Obtained Using a Pressure Profile, and With the ABAQUS Deformed Profile Obtained Using the EOS Appendix C

Figure C.10: Comparison of a Magnified Section of the Experimental Deformed Profile of a V-Plate (60 degrees) Exploded by a PE4 Rod (13g), With the ABAQUS Deformed Profile Obtained Using a Pressure Profile, and With the ABAQUS Deformed Profile Obtained Using the EOS Appendix C

Figure C.11: Comparison of the Experimental Deformed Profile of a V-Plate (90 degrees) Exploded by a PE4 Rod (5g), With the ABAQUS Deformed Profile Obtained Using a Pressure Profile, and With the ABAQUS Deformed Profile Obtained Using the EOS Appendix C

Figure C.12: Comparison of a Magnified Section of the Experimental Deformed Profile of a V-Plate (90 degrees) Exploded by a PE4 Rod (5g), With the ABAQUS Deformed Profile Obtained Using a Pressure Profile, and With the ABAQUS Deformed Profile Obtained Using the EOS Appendix C

Figure C.13: Comparison of the Experimental Deformed Profile of a V-Plate (90 degrees) Exploded by a PE4 Rod (7g), With the ABAQUS Deformed Profile Obtained Using a Pressure Profile, and With the ABAQUS Deformed Profile Obtained Using the EOS Appendix C

Figure C.14: Comparison of a Magnified Section of the Experimental Deformed Profile of a V-Plate (90 degrees) Exploded by a PE4 Rod (7g), With the ABAQUS Deformed Profile Obtained Using a Pressure Profile, and With the ABAQUS Deformed Profile Obtained Using the EOS Appendix C

Figure C.15: Comparison of the Experimental Deformed Profile of a V-Plate (90 degrees) Exploded by a PE4 Rod (9g), With the ABAQUS Deformed Profile Obtained

Using a Pressure Profile, and With the ABAQUS Deformed Profile Obtained Using the EOS Appendix C

Figure C.16: Comparison of a Magnified Section of the Experimental Deformed Profile of a V-Plate (90 degrees) Exploded by a PE4 Rod (9g), With the ABAQUS Deformed Profile Obtained Using a Pressure Profile, and With the ABAQUS Deformed Profile Obtained Using the EOS Appendix C

Figure C.17: Comparison of the Experimental Deformed Profile of a V-Plate (90 degrees) Exploded by a PE4 Rod (11g), With the ABAQUS Deformed Profile Obtained Using a Pressure Profile, and With the ABAQUS Deformed Profile Obtained Using the EOS Appendix C

Figure C.18: Comparison of a Magnified Section of the Experimental Deformed Profile of a V-Plate (90 degrees) Exploded by a PE4 Rod (11g), With the ABAQUS Deformed Profile Obtained Using a Pressure Profile, and With the ABAQUS Deformed Profile Obtained Using the EOS Appendix C

Figure C.19: Comparison of the Experimental Deformed Profile of a V-Plate (90 degrees) Exploded by a PE4 Rod (13g), With the ABAQUS Deformed Profile Obtained Using a Pressure Profile, and With the ABAQUS Deformed Profile Obtained Using the EOS Appendix C

Figure C.20: Comparison of a Magnified Section of the Experimental Deformed Profile of a V-Plate (90 degrees) Exploded by a PE4 Rod (13g), With the ABAQUS Deformed Profile Obtained Using a Pressure Profile, and With the ABAQUS Deformed Profile Obtained Using the EOS Appendix C

Figure C.21: Comparison of the Experimental Deformed Profile of a V-Plate (120 degrees) Exploded by a PE4 Rod (3g), With the ABAQUS Deformed Profile Obtained Using a Pressure Profile, and With the ABAQUS Deformed Profile Obtained Using the EOS Appendix C

Figure C.22: Comparison of a Magnified Section of the Experimental Deformed Profile of a V-Plate (120 degrees) Exploded by a PE4 Rod (3g), With the ABAQUS Deformed Profile Obtained Using a Pressure Profile, and With the ABAQUS Deformed Profile Obtained Using the EOS Appendix C

Figure C.23: Comparison of the Experimental Deformed Profile of a V-Plate (120 degrees) Exploded by a PE4 Rod (5g), With the ABAQUS Deformed Profile Obtained Using a Pressure Profile, and With the ABAQUS Deformed Profile Obtained Using the EOS Appendix C

Figure C.24: Comparison of a Magnified Section of the Experimental Deformed Profile of a V-Plate (120 degrees) Exploded by a PE4 Rod (5g), With the ABAQUS Deformed Profile Obtained Using a Pressure Profile, and With the ABAQUS Deformed Profile Obtained Using the EOS Appendix C

Figure C.25: Comparison of the Experimental Deformed Profile of a V-Plate (120 degrees) Exploded by a PE4 Rod (7g), With the ABAQUS Deformed Profile Obtained

Using a Pressure Profile, and With the ABAQUS Deformed Profile Obtained Using the EOS Appendix C

Figure C.26: Comparison of a Magnified Section of the Experimental Deformed Profile of a V-Plate (120 degrees) Exploded by a PE4 Rod (7g), With the ABAQUS Deformed Profile Obtained Using a Pressure Profile, and With the ABAQUS Deformed Profile Obtained Using the EOS Appendix C

Figure C.27: Comparison of the Experimental Deformed Profile of a V-Plate (120 degrees) Exploded by a PE4 Rod (9g), With the ABAQUS Deformed Profile Obtained Using a Pressure Profile, and With the ABAQUS Deformed Profile Obtained Using the EOS Appendix C

Figure C.28: Comparison of a Magnified Section of the Experimental Deformed Profile of a V-Plate (120 degrees) Exploded by a PE4 Rod (9g), With the ABAQUS Deformed Profile Obtained Using a Pressure Profile, and With the ABAQUS Deformed Profile Obtained Using the EOS Appendix C

Figure C.29: Comparison of the Experimental Deformed Profile of a V-Plate (120 degrees) Exploded by a PE4 Rod (11g), with the ABAQUS Deformed Profile Appendix C

Figure C.30: Comparison of a Magnified Section of the Experimental Deformed Profile of a V-Plate (120 degrees) Exploded by a PE4 Rod (11g), with the ABAQUS Deformed Profile Appendix C

Figure C.31: Comparison of the Experimental Deformed Profile of a V-Plate (150 degrees) Exploded by a PE4 Rod (3g), With an ABAQUS Deformed Profile Obtained Using a Pressure Profile, and With an ABAQUS Deformed Profile Obtained Using the EOS Appendix C

Figure C.32: Comparison of a Magnified Section of the Experimental Deformed Profile of a V-Plate (150 degrees) Exploded by a PE4 Rod (3g), With an ABAQUS Deformed Profile Obtained Using a Pressure Profile, and With an ABAQUS Deformed Profile Obtained Using the EOS Appendix C

Figure C.33: Comparison of the Experimental Deformed Profile of a V-Plate (150 degrees) Exploded by a PE4 Rod (5g), With an ABAQUS Deformed Profile Obtained Using a Pressure Profile, and With an ABAQUS Deformed Profile Obtained Using the EOS Appendix C

Figure C.34: Comparison of a Magnified Section of the Experimental Deformed Profile of a V-Plate (150 degrees) Exploded by a PE4 Rod (5g), With an ABAQUS Deformed Profile Obtained Using a Pressure Profile, and With an ABAQUS Deformed Profile Obtained Using the EOS Appendix C

Figure C.35: Comparison of the Experimental Deformed Profile of a V-Plate (150 degrees) Exploded by a PE4 Rod (7g), With the ABAQUS Deformed Profile Obtained Using a Pressure Profile, and With the ABAQUS Deformed Profile Obtained Using the EOS Appendix C

Figure C.36: Comparison of a Magnified Section of the Experimental Deformed Profile of a

V-Plate (150 degrees) Exploded by a PE4 Rod (7g), With the ABAQUS Deformed Profile Obtained Using a Pressure Profile, and With the ABAQUS Deformed Profile Obtained Using the EOS Appendix C

Figure C.37: Comparison of the Experimental Deformed Profile of a V-Plate (150 degrees) Exploded by a PE4 Rod (9g), With the ABAQUS Deformed Profile Obtained Using a Pressure Profile, and With the ABAQUS Deformed Profile Obtained Using the EOS Appendix C

Figure C.38: Comparison of a Magnified Section of the Experimental Deformed Profile of a V-Plate (150 degrees) Exploded by a PE4 Rod (9g), With the ABAQUS Deformed Profile Obtained Using a Pressure Profile, and With the ABAQUS Deformed Profile Obtained Using the EOS Appendix C

Figure C.39: Comparison of the Experimental Deformed Profile of a V-Plate (150 degrees) Exploded by a PE4 Rod (11g), with the ABAQUS Deformed Profile Appendix C

Figure C.40: Comparison of a Magnified Section of the Experimental Deformed Profile of a V-Plate (150 degrees) Exploded by a PE4 Rod (11g), with the ABAQUS Deformed Profile Appendix C

Figure D.1: The Deformed Profile of a V-Plate (60 degrees) Exploded by a PE4 Disc (4g) As Predicted By ABAQUS Using the JWL Equation of State Appendix D

Figure D.2: The Deformed Profile of a V-Plate (60 degrees) Exploded by a PE4 Disc (6g) As Predicted By ABAQUS Using the JWL Equation of State Appendix D

Figure D.3: The Deformed Profile of a V-Plate (60 degrees) Exploded by a PE4 Disc (8g) As Predicted By ABAQUS Using the JWL Equation of State Appendix D

Figure D.4: The Deformed Profile of a V-Plate (60 degrees) Exploded by a PE4 Disc (10g) As Predicted By ABAQUS Using the JWL Equation of State Appendix D

Figure D.5: The Deformed Profile of a V-Plate (60 degrees) Exploded by a PE4 Disc (12g) As Predicted By ABAQUS Using the JWL Equation of State Appendix D

Figure D.6: The Deformed Profile of a V-Plate (90 degrees) Exploded by a PE4 Disc (4g) As Predicted By ABAQUS Using the JWL Equation of State Appendix D

Figure D.7: The Deformed Profile of a V-Plate (90 degrees) Exploded by a PE4 Disc (6g) As Predicted By ABAQUS Using the JWL Equation of State Appendix D

Figure D.8: The Deformed Profile of a V-Plate (90 degrees) Exploded by a PE4 Disc (8g) As Predicted By ABAQUS Using the JWL Equation of State Appendix D

Figure D.9: The Deformed Profile of a V-Plate (90 degrees) Exploded by a PE4 Disc (8g; 5mm Offset) As Predicted By ABAQUS Using the JWL Equation of State Appendix D

Figure D.10: The Deformed Profile of a V-Plate (90 degrees) Exploded by a PE4 Disc (8g; 10mm Offset) As Predicted By ABAQUS Using the JWL Equation of State Appendix D

Figure D.11: The Deformed Profile of a V-Plate (90 degrees) Exploded by a PE4 Disc (8g; 15mm Offset) As Predicted By ABAQUS Using the JWL Equation of State Appendix D

Figure D.12: The Deformed Profile of a V-Plate (90 degrees) Exploded by a PE4 Disc (8g; 20mm Offset) As Predicted By ABAQUS Using the JWL Equation of State Appendix D

Figure D.13: The Deformed Profile of a V-Plate (90 degrees) Exploded by a PE4 Disc (10g) As Predicted By ABAQUS Using the JWL Equation of State Appendix D
Figure D.14: The Deformed Profile of a V-Plate (90 degrees) Exploded by a PE4 Disc (12g) As Predicted By ABAQUS Using the JWL Equation of State Appendix D
Figure D.15: The Deformed Profile of a V-Plate (120 degrees) Exploded by a PE4 Disc (4g) As Predicted By ABAQUS Using the JWL Equation of State Appendix D
Figure D.16: The Deformed Profile of a V-Plate (120 degrees) Exploded by a PE4 Disc (6g) As Predicted By ABAQUS Using the JWL Equation of State Appendix D
Figure D.17: The Deformed Profile of a V-Plate (120 degrees) Exploded by a PE4 Disc (8g) As Predicted By ABAQUS Using the JWL Equation of State Appendix D
Figure D.18: The Deformed Profile of a V-Plate (120 degrees) Exploded by a PE4 Disc (10g) As Predicted By ABAQUS Using the JWL Equation of State Appendix D
Figure D.19: The Deformed Profile of a V-Plate (120 degrees) Exploded by a PE4 Disc (12g) As Predicted By ABAQUS Using the JWL Equation of State Appendix D
Figure D.20: The Deformed Profile of a V-Plate (150 degrees) Exploded by a PE4 Disc (4g) As Predicted By ABAQUS Using the JWL Equation of State Appendix D
Figure D.21: The Deformed Profile of a V-Plate (150 degrees) Exploded by a PE4 Disc (6g) As Predicted By ABAQUS Using the JWL Equation of State Appendix D
Figure D.22: The Deformed Profile of a V-Plate (150 degrees) Exploded by a PE4 Disc (8g) As Predicted By ABAQUS Using the JWL Equation of State Appendix D
Figure D.23: The Deformed Profile of a V-Plate (150 degrees) Exploded by a PE4 Disc (10g) As Predicted By ABAQUS Using the JWL Equation of State Appendix D
Figure D.24: The Deformed Profile of a V-Plate (150 degrees) Exploded by a PE4 Disc (12g) As Predicted By ABAQUS Using the JWL Equation of State Appendix D

List of Tables

Table 4.1: General material properties for steel V-plates 114
Table 4.2: The material constants required by ABAQUS to model the explosive (PE4). 122
Table 6.1: The slopes and slope errors of the trend-lines of the displacement versus explosive mass relationships from the Rod Explosive Systems 155
Table 6.2: The average error of the displacement points for each displacement versus explosive mass relationship, and the overall error of the displacement points from the Rod Explosive Systems 155
Table 6.3: The slopes and slope errors of the trend-lines of the displacement versus V-plate angle relationships for the Rod Explosive Systems 163
Table 6.4: The average error of the displacement points for each displacement versus the V-plate angle relationship, and the overall error of the displacement points from the rod explosive systems 163
Table E.1: Co-Ordinates of the Deformed V-Plate Profiles for the 60^0 V-Plates and 3g Rod Explosive Appendix E
Table E.2: Co-Ordinates of the Deformed V-Plate Profiles for the 60^0 V-Plates and 5g Rod Explosive Appendix E
Table E.3: Co-Ordinates of the Deformed V-Plate Profiles for the 60^0 V-Plates and 7g Rod Explosive Appendix E
Table E.4: Co-Ordinates of the Deformed V-Plate Profiles for the 60^0 V-Plates and 9g Rod Explosive Appendix E
Table E.5: Co-Ordinates of the Deformed V-Plate Profiles for the 60^0 V-Plates and 11g Rod Explosive Appendix E
Table E.6: Co-Ordinates of the Deformed V-Plate Profiles for the 60^0 V-Plates and 13g Rod Explosive Appendix E
Table E.7: Co-Ordinates of the Deformed V-Plate Profiles for the 90^0 V-Plates and 3g Rod Explosive Appendix E
Table E.8: Co-Ordinates of the Deformed V-Plate Profiles for the 90^0 V-Plates and 5g Rod Explosive Appendix E
Table E.9: Co-Ordinates of the Deformed V-Plate Profiles for the 90^0 V-Plates and 7g Rod Explosive Appendix E
Table E.10: Co-Ordinates of the Deformed V-Plate Profiles for the 90^0 V-Plates and 9g Rod Explosive Appendix E
Table E.11: Co-Ordinates of the Deformed V-Plate Profiles for the 90^0 V-Plates and 11g Rod Explosive Appendix E
Table E.12: Co-Ordinates of the Deformed V-Plate Profiles for the 90^0 V-Plates and 13g Rod Explosive Appendix E
Table E.13: Co-Ordinates of the Deformed V-Plate Profiles for the 120^0 V-Plates and 3g Rod

Explosive
Table E.14: Co-Ordinates of the Deformed V-Plate Profiles for the 120^0 V-Plates and 5g Rod Explosive Appendix E
Table E.15: Co-Ordinates of the Deformed V-Plate Profiles for the 120^0 V-Plates and 7g Rod Explosive Appendix E
Table E.16: Co-Ordinates of the Deformed V-Plate Profiles for the 120^0 V-Plates and 9g Rod Explosive Appendix E
Table E.17: Co-Ordinates of the Deformed V-Plate Profiles for the 120^0 V-Plates and 11g Rod Explosive Appendix E
Table E.18: Co-Ordinates of the Deformed V-Plate Profiles for the 150^0 V-Plates and 3g Rod Explosive Appendix E
Table E.19: Co-Ordinates of the Deformed V-Plate Profiles for the 150^0 V-Plates and 5g Rod Explosive Appendix E
Table E.20: Co-Ordinates of the Deformed V-Plate Profiles for the 150^0 V-Plates and 7g Rod Explosive Appendix E
Table E.21: Co-Ordinates of the Deformed V-Plate Profiles for the 150^0 V-Plates and 9g Rod Explosive Appendix E
Table E.22: Co-Ordinates of the Deformed V-Plate Profiles for the 150^0 V-Plates and 11g Rod Explosive Appendix E
Table F.1: Co-Ordinates of the Deformed V-Plate Profiles for the 60^0 V-Plates Appendix F
Table F.2: Co-Ordinates of the Deformed V-Plate Profiles for the 90^0 V-Plates Appendix F
Table F.3: Co-Ordinates of the Deformed V-Plate Profiles for the 90^0 V-Plates exploded by offset disc explosives Appendix F
Table F.4: Co-Ordinates of the Deformed V-Plate Profiles for the 120^0 V-Plates Appendix F
Table F.5: Co-Ordinates of the Deformed V-Plate Profiles for the 150^0 V-Plates Appendix F
Table G.1: Mid-point deflection predictions of 60^0 V-plates exploded by rod explosives Appendix G
Table G.2: Mid-point deflection predictions of 90^0 V-plates exploded by rod explosives Appendix G
Table G.3: Mid-point deflection predictions of 120^0 V-plates exploded by rod explosives Appendix G
Table G.4: Mid-point deflection predictions of 150^0 V-plates exploded by rod explosives Appendix G
Table G.5: Error Percentages of the mid-point deflection predictions of 60^0 V-plates exploded by rod explosives Appendix G
Table G.6: Error Percentages of the mid-point deflection predictions of 90^0 V-plates exploded by rod explosives Appendix G
Table G.7: Error percentages of the mid-point deflection predictions of 120^0 V-plates exploded by rod explosives Appendix G
Table G.8: Error percentages of the mid-point deflection predictions of 150^0 V-plates exploded by rod explosives Appendix G
Table H.1: Mid-Point displacements of the deformed V-plates exploded by PE4 disc explosives, obtained from the JWL EOS method numerical predictions Appendix H
Table J.1: Experimentally obtained impulses transferred to the V-plates exploded by rod explosives Appendix J

List of Symbols

D = velocity of detonation

P_0 = original inert explosive pressure

P = reacted explosive pressure

u_0 = original inert explosive velocity

u = reacted explosive streaming velocity

$t_1, t_2, t_3, t_4, t_5, t_6$ = points in time

Φ = dimensionless damage number

M = mass of plate

d = diameter of plate

t = thickness of plate

ρ = density of plate

a = radius of explosive sheet

V_b = velocity of detonation

M = mass of entire ballistic pendulum

$\dot{x}_0$ = initial velocity of ballistic pendulum

T = period of ballistic pendulum

β = damping constant

x_1, x_2 = pendulum displacement functions

$P(r)$ = pressure distribution as a function of radius

R = radius of plate

k = exponential decay constant

e_0 = internal energy per unit volume of explosive

A = impulsive load application area

V_0 = peak initial velocity of plate

P_0 = peak pressure applied to plate

I = impulse transferred to plate

τ = pressure pulse duration

$[K^e]$ = local stiffness matrix

$[K]$ = global stiffness matrix

$\{F\}$ = applied nodal force vector

$\{\delta\}$ = nodal displacement vector

t = point in time

$\dot{u}^N$ = velocities during dynamic analysis

$\ddot{u}^N$ = accelerations during dynamic analysis

M^{NJ} = mass matrix

P^J = applied load vector

I^J = internal force vector

u^N = a degree of freedom

i = time increment number in a step

Δt = time increment

$\omega_{\max}$ = highest frequency of system

$\xi_{\max}$ = fraction of critical damping in highest frequency mode

$L_{\min}$ = smallest element dimension

c_d = dilatational wave speed

$\dot{\bar{\varepsilon}}^{pl}$ = equivalent plastic strain

σ_0 = static yield stress

σ = dynamic yield stress

σ_y = temperature dependent static yield stress

σ_{y0} = static yield stress at reference temperature of tensile test

D,n = material parameters

$\dot{\varepsilon}_0, C$ = material constants

r^{pl} = heat flux

η = inelastic heat fraction

σ = stress

ρ = material density

$c(T)$ = specific heat as a function of temperature

T = temperature

p = pressure stress

p_{bv} = pressure stress due to bulk viscosity

S = deviatoric stress tensor

$\dot{e}$ = deviatoric part of strain rate

$\dot{Q}$ = heat rate per unit mass

E_m = internal energy per unit mass

ρ = current density

p_H = Hugonoit pressure

Γ_0 = material constant

ρ_0 = reference density

c_0, s = constants defining relationship between shock velocity and particle velocity

U_s = linear shock velocity

U_p = particle velocity

E_{m_0} = initial energy per unit mass

A, B, R_1, R_2, ω = material constants

t_d^{mp} = arrival time of detonation wave at material point

x_d^N = vector position of Nth detonation point

t_d^N = detonation delay time of Nth detonation point

C_d = detonation wave speed of explosive material

F_b = detonation burn fraction

B_s = constant that controls width of burn wave

l_e = characteristic length of element

K_{pd} = predetonation bulk modulus

p_A = ambient pressure

R = gas constant

θ = current gas temperature

θ^Z = absolute zero on temperature scale being used

θ_0 = initial gas temperature

c_v = specific heat at constant volume

v = specific volume

E = Young's modulus

υ = Poisson's ratio

F = force applied to object

I_2 = impulse applied in the 2 direction

$F_{reaction_2}$ = reaction force in the 2 direction

n = constraining node number

P_0 = ambient pressure

P_1 = pressure behind incident shock wave

P_2 = pressure behind reflected shock wave

α = angle of incidence of incident shock wave

α' = angle of reflection of reflected shock wave

1. Introduction

1.1 Background

Mine warfare is used in conflicts all over the world.
Over 110 million mines which have been planted since World War 2 litter 68 countries [1]. Mine warfare is a very effective method of warfare as it has the element of surprise, it doesn't require interaction with the enemy, and it has a high percentage of fatalities.

Mine warfare dates back to the American Civil War when soldiers adapted artillery shells and buried them in the ground with a fuse or trip wire to explode on contact. Mines as we know them today, were first designed in the 1930's. There are two main types of mines: anti-personnel mines and anti-tank mines. People who detonate anti-personnel mines are either maimed or killed [1]. Vehicles which detonate anti-tank mines are usually damaged beyond repair, and the vehicle crew are often injured or killed. A vehicle that detonated an anti-tank mine can be seen in Figure 1.1.

Figure 1.1: A vehicle which detonated an anti-tank mine. The front of the vehicle was destroyed and the driver seriously injured.

Mines are a long term danger as many of them remain undetected long after the conflict is over (e.g. Mozambique, Cambodia, and Afghanistan) rendering farmland useless and killing livestock and humans. Each year, 10 000 to 20 000 people are killed by mines, and as many are disabled. Mine-clearing is a laborious, dangerous, and expensive process. The United Nations estimates it will take more than 1000 years and nearly $33 billion to safely clear the world's minefields [1]. South Africa is regarded to be among the world's leaders in landmine clearance technology. The Denel subsidiary, Mechem, has been involved in clearing landmines in Angola, Mozambique, Croatia, Bosnia, and Kosovo and is currently undertaking a large mine clearance project in Iraq [2] Because so many landmines are so widely dispersed around the world, there is a need for mine-detecting and mine-protected vehicles.

The main purpose of mine-detecting vehicles is to detect and clear laid mines. These vehicles often have sacrificial components which are used to detonate mines and which can easily be replaced. The operator of the mine-detecting vehicle is usually at a safe distance from the blast. A mine detection vehicle can be seen in Figure 1.2.

Figure 1.2: A mine-detecting vehicle with trailers to detonate mines.

The main purpose of mine-protected vehicles is not mine detection. Instead, they are usually used for personnel transport, to provide anti-tank or support fire, or as a general purpose utility vehicle. These vehicles are mine-protected as a precaution against accidentally detonated mines, and the sole purpose of the protection is to preserve human life. Mine-protected vehicles are the vehicles of interest in this study.

Some examples of where mine-protected vehicles have been used are Rhodesia (now Zimbabwe), South Africa, and for United Nations (UN) missions all over the world.

Mine warfare was used extensively in the civil war in Rhodesia (1965-1980). The colonial community there, designed and built mine-protected vehicles ranging from small farm vehicles to large military vehicles. Examples of these vehicles can be seen in Figures 1.3 and Figure 1.4.

Figure 1.3: A Kudu MK10 mine-protected vehicle.

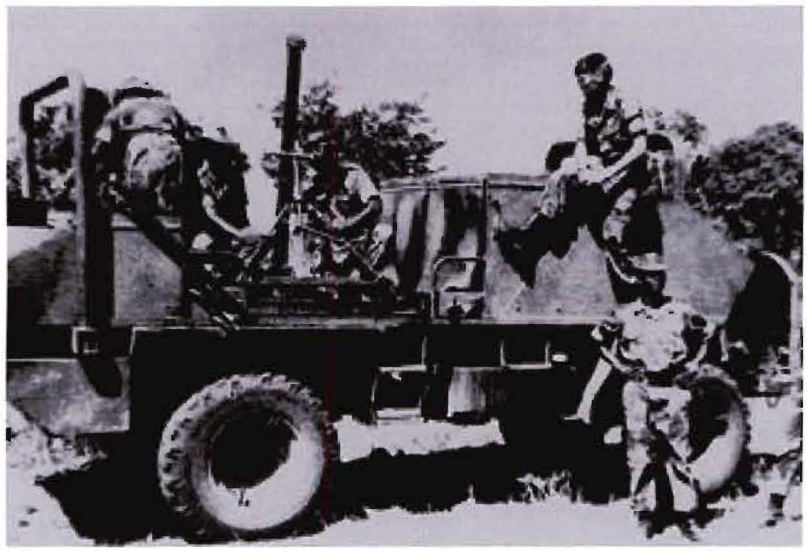

Figure 1.4: A mine-protected mortar carrier.

South Africa is a major manufacturer of mine-protected vehicles. Many of the vehicles were used extensively in the local border wars. The United Kingdom and the UN have been among some of South Africa's customers. Examples of South African mine-protected vehicles can be seen in Figure 1.5 and Figure 1.6.

Figure 1.5: The Mamba

Figure 1.6: The Caspir II

In the past few years, soldiers operating in UN missions have been exposed to an increasing mine threat. Since the task of the UN is often to reduce hostility between opposing factions, the vehicles used in support, command and liaison roles by UN troops are often at risk and need to be mine-protected [3].

Most mine-protected vehicles share a common method of protection - a V-shaped hull or undercarriage which is meant to deflect the mine blast away from the vehicles cab and its occupants. The deflection capabilities of these V-shaped hulls are improved the steeper the angle of the V is (the smaller the included angle is). Unfortunately, the steeper the angle of the hull, the higher the vehicle must be raised off the ground to allow for ground clearance. This reduces the toppling stability of the vehicle and the steeper V-plate angle increases the mass of the hull as more material is required to form the steeper angle. Clearly this means that the interaction of the mine blast with the V-shaped hull should be studied so that the angle of the V can be optimised.

There have been many studies on impulsively loaded flat metal plates in the past. Experiments have been conducted involving explosively loaded circular and square stiffened and unstiffened plates to determine the trends and

thresholds of the systems and to verify any theoretical approaches at predicting the plate response. Attempts at formulating analytical solutions for characteristics such as the mid-point deflection and deformed plate profile, have been conducted with varying levels of success. More recently, these explosively loaded plates have been numerically modelled and the predictions have been reasonably accurate. Many of these investigations will be discussed in more detail in the literature review.

1.2 Objectives of this Thesis

The study in this document investigates the effect of a disc of high explosive on a steel V-shaped plate through numerical modelling. This system is a simplified simulation of a mine detonating beneath the V-shaped hull of a mine-protected vehicle.

Parameters of the numerical model which will be varied are:

- position of the explosive relative to the V-plate.
- mass of the explosive disc (keeping the disc diameter constant).
- included angle of the V-plate.

One of the objectives of this thesis is to determine if finite element method modelling is capable of accurately predicting the response of exploded V-plates using the Jones-Wilkins-Lee (JWL) Equation of State. Another objective is to determine any trends and thresholds of the exploded V-plates that are dependent on the above-mentioned parameters. In particular, the plastic work and impulse absorbed and deflected by the different V-plates should be determined, as they indicate the level of protection the V-plate would offer.

1.3 Procedure of this Thesis

This thesis progressed as follows:

1. Review literature on mine-protected vehicles, explosives, previous studies of exploded flat/V-shaped plates (theoretical, experimental, and numerical), and finite element methods.

2. Develop a simple numerical model, using ABAQUS Explicit, containing a round rod of explosive and a V-plate. The geometries and properties of the model will match that of previously conducted experiments. The purpose of this model containing the round rod of explosive, is to verify the capabilities of the numerical modelling as there are experimental results to which these numerical results can be compared.
3. Process the experimental data from the previously conducted experiments of round rods of explosive exploding V-plates so that it is comparable to the numerical results of the model containing the round rod of explosive and V-plate.
4. Compare the simple numerical model results to the experimental data for model verification.
5. Create variations of the model involving a range of explosive masses and V-plate angles which correspond with the previously conducted experiments.
6. Compare the results of all the models to the experimental data to further verify the capabilities of the numerical modelling of this system.
7. Develop a simple numerical model containing a flat disc of explosive and a V-plate. There are no previously conducted experiments on which this model can be based, but the properties and geometries of this model will be similar to the first set of models containing the round rod of explosive.
8. Create variations of the model involving a range of explosive masses, explosive positions, explosive dimensions, and V-plate angles. The models in this set all have similar characteristics to those of the first set of models.
9. Examine the numerical results and determine any trends or thresholds exhibited by the exploded V-plates.
10. Draw conclusions and make recommendations.

1.4 Scope of this Thesis

The scope of this study involves numerically modelling a range of explosively loaded V-plates and verifying the numerical models. Verification of the numerical models involves comparing the numerical predictions of a system similar to the one of interest, with the results obtained from experiments performed on identical systems. Characteristics of the deformed V-plates which will be used for comparison are mid-point deflection, the deformed plate profile, and impulse transferred to the V-plates. The experiments corresponding to the numerical models created in this study, were conducted by previous investigators but the literature has been lost. However, some of the experimental results were available but had to be processed before they were suitable for comparison with the numerical predictions. The numerical results of the system of interest will be studied to determine any trends or thresholds the system may have. The impulse transferred to the V-plates and the plastic strain energy of deformation of the V-plates will be extracted from the numerical results as they indicate how much of the blast was absorbed and how much was deflected. This is a measure of the level of protection the V-plate has to offer.

1.5 Plan of Development

This thesis has the following plan of development:

- *Literature Review* – this chapter discusses explosives, a study on mine-protected vehicles, and many of the experimental, theoretical, and numerical studies which have been conducted on impulsively loaded metal plates. Numerical methods, with the focus on finite element methods, are also briefly reviewed.
- *ABAQUS Overview* - the method of analysis of the finite element package is reviewed, and aspects of the package which are relevant to the models in this study, are focused on.
- *The Finite Element Model* – the selection of the model representing the explosively loaded V-plate systems, the element and meshing choices,

the boundary conditions, the material properties, the modelling of the explosive reaction using the JWL Equation of State and models, and the duration and steps of the analysis, are all discussed in this chapter.

- *Previous Experimental and Numerical Results* – some of the available results from previous experimental studies which are used to attempt to verify the models in this study, are shown here. The results of a previous numerical study, which will be compared to the numerical results of this study to compare the performance of the different numerical methods, are also presented here. The processing of these previous experimental and numerical results, so that they are suitable for comparison with the numerical predictions from this study, is then discussed.
- *Results and Discussion* – the results and observations of the range of models are presented and discussed.
- *Conclusions* – conclusions are drawn in this chapter from the numerical models and their results, and the literature review. The success of the study is also discussed.
- *Recommendations* – aspects of modelling that should be considered, and further investigations relative to this study, are suggested.

2. Literature Review

A wide range of literature was reviewed on mine-protected vehicles, explosives, previous studies of exploded flat/V-shaped plates (theoretical, experimental, and numerical), and finite element methods.

Literature on mines and mine-protected vehicles established a general background on the field by outlining the use and need for mine-protected vehicles (covered in the introduction). The literature also allowed the kill mechanisms of a detonated mine to be identified.

The characteristics, physics, and use of explosives are also covered in the literature review. This gave an understanding into the dependency of deformed steel plate profiles on the size, shape, and position of the explosive. The practical methods of setting up and detonating explosives are also covered.

There is a vast amount of literature on studies of impulsively loaded flat plates (circular and square) and stiffened plates (circular and square).
Impulsive loading was defined by Jones [4] as being when the external pressure loadings have a finite impulse with an infinitely large magnitude and an infinitesimally short duration. Explosive loading falls into this category.

The studies of impulsively loaded plates include experiments where a range of plates have been exploded. They also include theoretical approaches where attempts were made to determine empirical equations for the maximum deflections and profiles of the exploded plates and also the energy transferred to them. Numerical modelling was also conducted in these studies where various attempts were made to simulate the flat plate being exploded. Experimental results were often compared to numerical results to verify the numerical methods. The literature on experimental and theoretical exploded flat plates and stiffened plates will only be discussed briefly as it isn't directly relevant to this study. The numerical studies are of greater

relevance as they were a guide in setting up the numerical model for this study, and therefore, these studies will be covered in more detail.

Little literature on exploded V-plates could be found. Two of the main studies have been lost, but the necessary results were available. The results of an experimental study where V-plates were exploded will be used to verify the numerical modelling in this study.

Literature on finite element methods and the related software packages was also reviewed so that a suitable numerical model would be developed in this study.

2.1 Mine-Protected Vehicle Study

Lafrance [3] conducted experiments on military support vehicles (Chevrolet 5/4 ton pick-up truck) by detonating anti-tank blast mines underneath them. The purpose of the study was to develop an optimal protection system for the crew of such vehicles. The different kill mechanisms which occur during and after a mine strike were characterised, and a vulnerability study based on the experimental results and real accident information were performed to understand the human body's reactions. Finally, blast deflectors and attenuation systems were developed and tested. Computer modelling and simulation were used in the development phase.

Lafrance [3] reported that Bergeron and Watkins [47] and Bergeron, Watkins, and Walker [48] established the threat to be a 7.5 kg medium size blast mine of TNT and that tests had been conducted on unprotected wheeled vehicles. These tests indicated that severe injuries and death could occur when a mine is detonated under such vehicles. From these trials, principles of protection were developed, followed by prototypes which were derived and tested.

It was reported by Lafrance [3] that the principle mine injury mechanisms that have been identified are: fragmentation, shock, acceleration and deceleration,

over-pressure (blast), hot combustion gases and other mechanisms independent of the mine.

Fragmentation

Two types of fragments result from a mine blast: primary and secondary fragments. Primary fragments are the numerous particles of the mine casing which travel at high velocities. Secondary fragments originate from the ground and road material and from vehicle parts sheared off by the mine detonation. Protection from mine-generated fragments is similar to that against ballistic projectiles (small calibre weapons and artillery fragments). It is important that the ballistic protection and its supporting structure are able to resist the deformation and stresses produced by the mine blast. If this condition is not met, the protection itself becomes a secondary fragment resulting in lethal injuries.

Shock

Explosive detonation results in a rapidly advancing shock wave, which precedes any fragment, pressure wave or accelerating forces. The shock is transmitted to the occupants through the vehicle structure. the rapid deflection causes multiple fractures of feet, ankles or legs that are in contact with the floor.

Acceleration and Deceleration

When a mine is detonated, the vehicle is accelerated upward rapidly, and if the mine is off centre, the vehicle will also be accelerated horizontally. These rapid accelerations can cause injuries to the crew ranging from incapacitating to lethal. The vehicle will fall back to the ground after rising to its maximum height. The impact with the ground will produce a deceleration that can sometimes be higher than the initial acceleration produced by the detonation. The deceleration thus compounds the injuries produced by the acceleration.

Over-Pressure

The detonation of explosives is accompanied by a rapidly expanding pressure wave. The pressure levels decrease with distance from the mine as the surface area increases. Blast pressures entering the crew compartment through apertures or torn floors will enter the body air cavities (eardrums and lungs) of the crew and cause injuries such as eardrum rupture and haemorrhaging of the lungs. The confinement of the crew compartment concentrates the pressure wave and causes complex wave reflections which may result in increased injuries.

Hot Combustion Gases

The initial detonation produces a flash of hot gases which could ignite flammable material or burn exposed flesh. The flash is short lived but is recognised as a fire hazard. If an opening is created in the floor of the vehicle, there is a probability of leg burn injuries.

Other Mechanisms Independent of the Mine

When the mine is detonated, the vehicle is in motion. The blast will disorientate or incapacitate the driver, change the trajectory of the vehicle, and destroy the wheel suspension and steering linkages. If the vehicle crashes, the damages are likely to be more severe than ordinary accidents because the structural integrity of the vehicle is affected prior to the crash. Other possible kill mechanisms are when the detonated mine causes other nearby mines to detonate, or when munitions and explosives carried in the vehicles detonate. The flammable components or cargo of a vehicle can produce fires. Corrosive spills from batteries or spills from hazardous cargo can also cause injury.

Lafrance's [3] experiments included a mine-protected vehicle.
The protection system comprised of right and left wheel well deflectors, a centreline deflector under the cab and wing deflectors to protect both sides of the cab floor. The purpose of these deflectors was to deflect the blast, gasses and ejecta away from the crew compartment and prevent the

penetration of primary or secondary fragments. This protection system was tested using a 5 kg charge of C4 explosive and it was found that the deflectors were effective in keeping the integrity of the vehicle cab.

Computer simulations were performed to compare deflector geometry effects. The Interactive Fluid-Structure Analysis Software (IFSAS) was used to study the fluid flow and the local structure response to the blast and shock threats. Results of these simulations were not presented as the software was still in the developmental phase.

An interesting observation from these tests was that the soil conditions have a major effect on the results. Saturated, hard or frozen ground caused much more severe damage. This agreed well with the theory that a more confined explosive produces more damage. It was also concluded that the energy of the blast that can be absorbed through various mechanical means, is negligible. Instead, focus should be put on deflecting the blast away from the vehicle cab.

2.2 Explosives in General

Gregory [5] and Rinehart [6] discuss explosives in general. Rinehart [6] gives a good review of the physics involved during detonation of an explosive.

The exothermic decomposition of an explosive produces exceedingly high gas pressures at the prevailing high temperatures of the reaction. Therefore the effectiveness of an explosive depends upon the amount of heat liberated. Although the explosive energy is equi-directional, its rupturing effect is greatest in the path of least resistance. If the explosive decomposition reaction moves through the charge faster than the speed of sound, it is termed *detonation*. If slower, it is termed *deflagration*. All high explosives and blasting agents detonate when properly initiated, whereas low explosives (black powder) deflagrate [5]. Detonation occurs in a stable manner progressing through the explosive at a constant and reproducible rate. The

constancy of the detonation rate is an important and characteristic physical attribute of an explosive permitting its effective use [6].

There are 5 main types of modern commercial explosive:

1. Initiating Explosives

The ease with which an explosive charge can be detonated is known as the initiation sensitivity. Initiating explosives have a high initiation sensitivity and can therefore be detonated by means of thermal ignition. High explosives have a lower initiation sensitivity, and if thermally ignited they will burn or deflagrate and then, maybe, detonate. However, for proper and effective control, detonation of high explosives is rather initiated with the use of initiating explosives. Because of their high cost initiating explosives are only suitable for initiating high explosive charges as detonating agents in small quantities. Upon initiation (thermal ignition) of the initiating explosives, they produce an intense shock capable of initiating a detonating wave in a charge of high explosive. These initiating explosives are loaded as small pressed charges into copper or aluminium tubes to form detonators, or as a core load in detonating cord.

2. High Explosives

According to their composition, these explosives detonate at very high velocities of 1600 - 7500m/s and produce large volumes of gases and considerable heat at extremely high pressure. The performance of such an explosive depends chiefly on the volume and temperature of the gases produced and on the velocity of detonation. The velocity of detonation (VOD) refers to the speed at which a one-dimensional detonation wave representing a shock front, travels through a charge of explosive. The VOD of an explosive depends upon various other factors, such as the density, the constituents, their particle size, the diameter of the charge, the degree of confinement, the coupling ratio, and the size of the primer. The coupling ratio relates to the efficiency

with which the chemical energy of the explosive is transferred to the item being exploded (e.g. steel plate or rock). With good coupling, there is little energy lost (e.g. through air space between the charge and the item to be exploded). A primer is a cartridge of high explosive which incorporates a detonator. When the detonator is thermally ignited by a safety fuse or an electrical impulse, a detonation wave (shock wave) is produced. This shock wave then proceeds along the high explosive charge with a transient VOD until it reaches the main charge and the main charge is initiated. High explosives usually contain chemical components with a more or less unstable molecular structure, capable, on detonation, of molecular rearrangement into more stable forms of potential energy. All the products of the explosion are usually gaseous. High explosives are used in this study.

3. Deflagrating or Low Explosives

These were the earliest types of explosives developed.
This type of explosion is really a rapid form of combustion in which the particles burn at their surfaces and expose more and more of the bulk until all has been consumed. Typical of these low explosives is Blasting Powder or gunpowder which is a mixture of substances having an affinity for oxygen with others which are rich in oxygen. Propellants in ammunition are low explosives. The slow gradual development of pressure in the chamber of a gun allows the projectile to issue with a high muzzle velocity without shattering the gun barrel. Since about half the products of combustion are solids, much smoke is formed.

4. Blasting Agents

These are mixtures consisting of a fuel and an oxidiser, intended for blasting. These blasting agents are actually not classified as explosives, provided that the finished product cannot be detonated by a No. 8 blasting cap in a specific test prescribed by the Bureau of Mines. Blasting agents are extensively used for both surface and underground blasts.

5. Binary Explosives

These explosives consist of two separate components, each intrinsically safe, but which can develop a high explosive power when mixed and detonated [5].

Ideal detonation of an explosive, seen in Figure 2.1, can be viewed relatively simply as a sharp discontinuity moving through the explosive at a constant velocity of detonation, D.

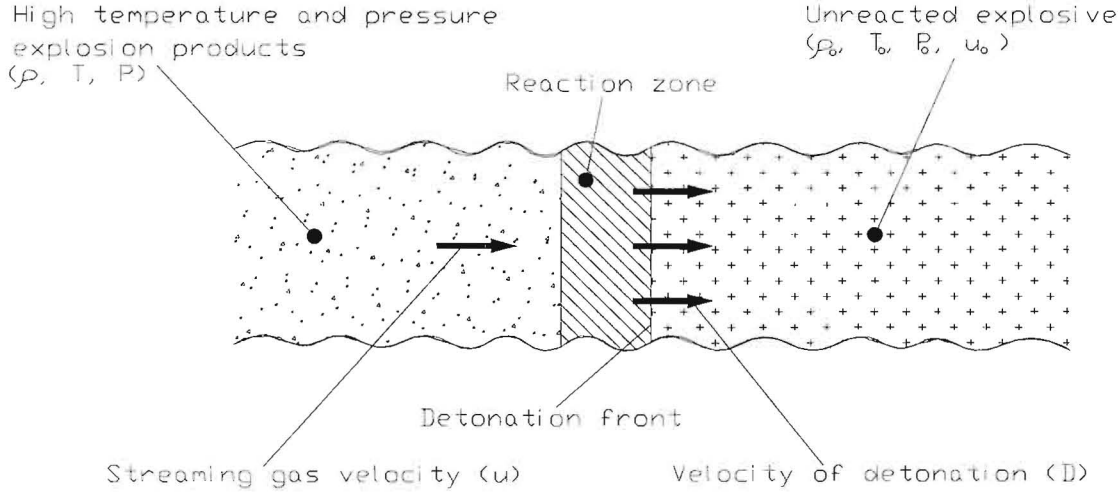

Figure 2.1: Detonation process in explosive of infinite extent.

To the right of the detonation front, the condition of the original inert explosive can be specified by its density, ρ_0, and by its temperature, T_0.

To the far left of the detonation front is the region where the explosive has completely reacted, filling the volume with gases at high temperatures, T, and at high pressure, P, compressing the gases to a higher density, ρ, than the density of the inert explosive and imparting to them a streaming velocity, u, to the right. Between this region of explosion products and the region of unreacted explosive lies the reaction zone where the conversion from solid explosive to gaseous products occurs. During stable detonation, this region

of finite thickness remains geometrically unchanged when viewed from a co-ordinate system moving with the detonation front. Since the energy which sustains the propagation of detonation originates in this zone, the nature of the reaction zone is an important attribute of an explosive, influencing greatly the detonation velocities and the dimensions and performance of usable charges. Chemical reactions take a finite time to come to completion so the distribution of temperature, pressure, density, and degree of decomposition of the explosive are not uniform through the reaction zone. The dependence of each parameter on location within the reaction zone can be seen in Figure 2.2. The abrupt rise of pressure to its maximum value immediately before reaction begins, continually initiates the reaction.

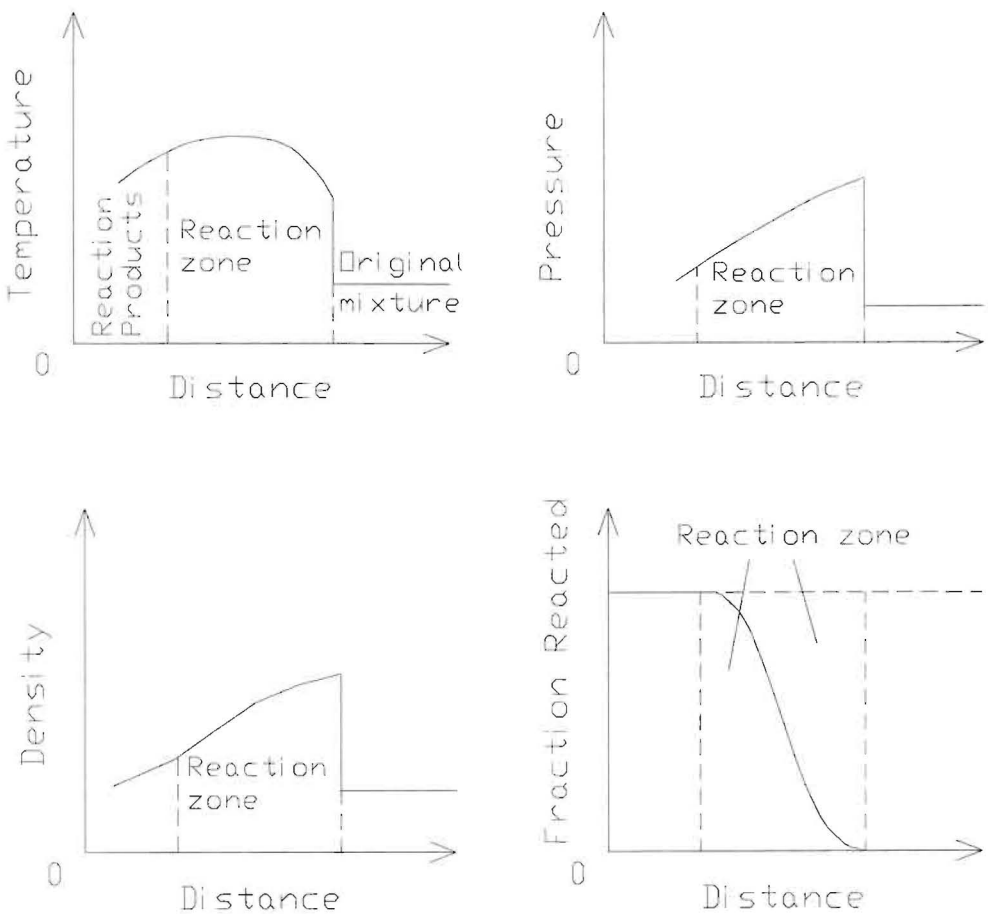

Figure 2.2: Temperature, pressure, density, and composition distributions within the reaction zone.

In the ideal situation which involves an explosive of infinite extent, no lateral dispersion of the hot gases is assumed possible. The dimensions of the reaction zone are not particularly important and have little influence on the velocity of propagation of the detonation front as the density and amount of energy released during the reaction are the controlling parameters. The situation is quite different for charges of finite extent. The dimensions of the reaction zone are particularly important when they are significant relative to the dimensions of the explosive charge. Under these circumstances the explosion products can expand laterally, allowing the explosive to be literally blown apart before the reaction is complete, thereby preventing full utilisation of the internal energy of the explosive. In the extreme case where the dimensions of the charge are small, as for thin sheets and narrow rods, the detonation may not propagate at all because of dissipation of energy through the mechanical dispersion of substantial quantities of unreacted explosive substances [6]. This phenomenon falls under the explosive characteristic known as propagation sensitivity. The measure of the ability of an explosive to support or reinforce a detonation that has already been created is known as the propagation sensitivity. Since the tendency for the detonation wave to fail or fade increases as the diameter of a round rod of explosive charge is reduced, it has become customary to measure propagation sensitivity by the (minimum) critical diameter of a rod charge at least six diameters long that will support the detonation process once created. At a point below this value, a detonation wave cannot be consistently propagated, and a misfire or an incomplete reaction may occur [5]. The critical diameter depends on the physical nature of the explosive, density, grain size, and packing, as well as its chemical nature, reaction rate, energy release, and composition. But in general, for stable chemical substances, those having the higher energy content per unit volume have the smallest critical diameter for detonation. A useful guide is that detonation will propagate in a charge whose diameter is no smaller than the thickness of its reaction zone.

The ability of thin sheets and narrow rods of explosive to support detonation are often improved by confining the charge. This can be done with a sheath of lead or steel around the charge which restricts lateral expansion of the explosion products, permitting the reaction to go more nearly to completion with consequent release of more energy and hence the development of the higher detonation velocity.

In spite of very extensive experimental investigations, the details of the initiation and burning processes are not completely understood.
It appears that two types of reactions take place but there is the possibility of a third type of reaction:

- In the first type, the surface of an individual grain of explosive is ignited by the hot, high pressure gases adjacent to it, with burning then proceeding from the surface inward. This is supported by experimental observations that large grain explosives have, in general, relatively thick reaction zones.
- In the second type, adiabatic compression from the detonation shock heats the explosive internally to such a degree that it begins to react at internal points.
- There is strong experimental indication that a third type of reaction initiation takes place. This initiation seems to occur at localised "hot spots" which are created by the sudden and intense adiabatic compression of voids or gas bubbles within the explosive.

Whatever the process, detonation proceeds in an amazingly orderly and stable fashion, making possible the practical use of explosives.

Generally, detonation of an explosive is initiated at a point. The detonation wave proceeds outward from this point at a constant rate, making the detonation front spherical, as can be seen in Figure 2.3 for the case of an infinite medium.

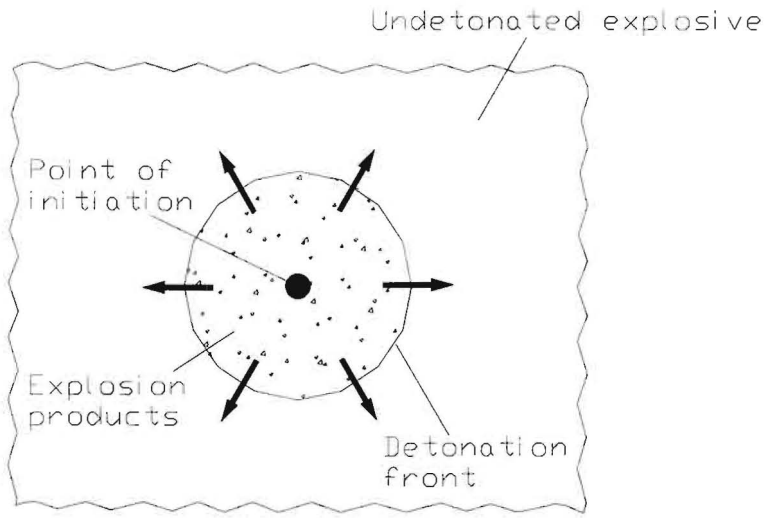

Figure 2.3: Detonation front arising from a point explosion.

As the wave spreads out, the curvature of the front becomes less so that at large distances the wave front can be considered plane. The development of such a front in a finite bounded charge is illustrated in Figure 2.4. A cylindrical stick of dynamite is a common example of such a charge. The constancy of detonation velocity which explosives have, allows explosive charges to be designed to accomplish particular tasks. It is possible to achieve a preselected, temporal distribution of pressure by using the appropriately shaped charge.

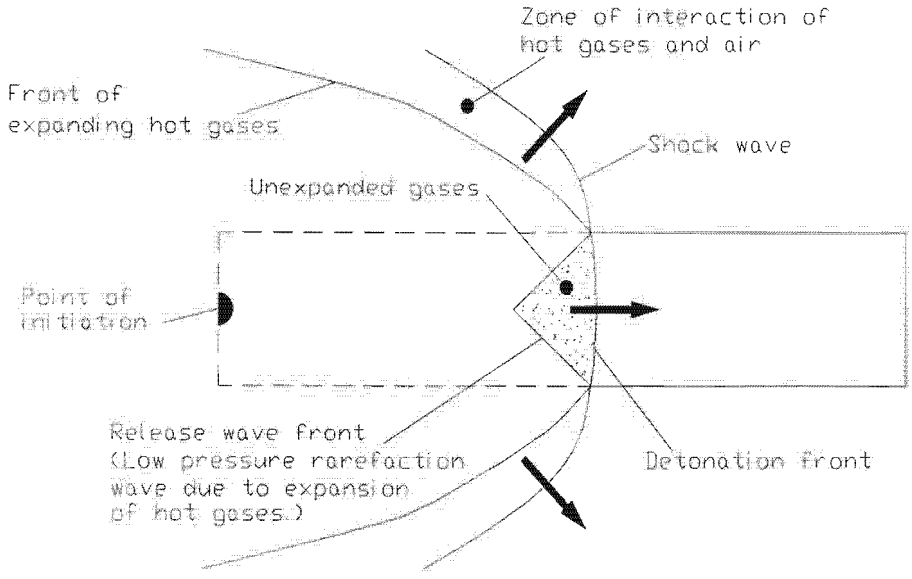

Figure 2.4: Detonation of explosive and expansion of explosion products from a finite bounded charge.

When the hot gaseous explosion products of a detonated explosive expand outwards, the surrounding fluid (e.g. air, water) is compressed ahead of them. A major part of the impulse developed is then transmitted as a shock wave through the surrounding fluid at a velocity greatly in excess of the gaseous products themselves. This shock wave manifests itself as a sharp discontinuity in pressure. The velocity of sound in a fluid plays a vital and determining role in the transfer of pressure, impulse, and energy as it is the characteristic velocity with which a sudden change in pressure will propagate through the fluid. Water has a much higher density and capacity for absorbing momentum than air, so the pressure in the initial shock wave will be much higher. The peak pressure of the shock occurs at the shock wave front and decays in an exponential manner behind it. The magnitude of the impulse and peak pressure of the shock wave decays with respect to distance travelled. These effects are illustrated in Figure 2.5.

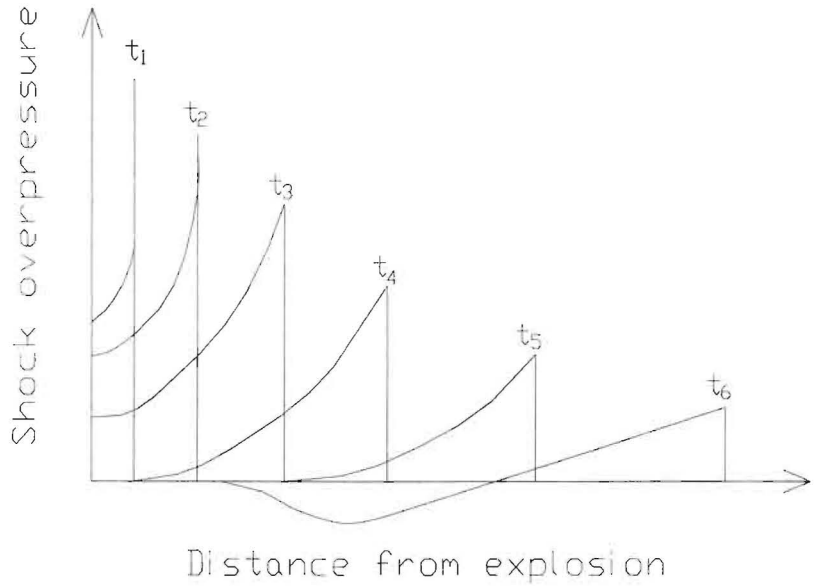

Figure 2.5: Overpressure in shock as a function of distance from source at several subsequent times.

With a decay of peak pressure with distance, the velocity of propagation of the shock front decays until it finally approaches the velocity of sound in the medium. The decay in peak pressure occurs for two reasons: there is an irreversible absorption of energy by the fluid through which the wave is passing; and if the shock wave is expanding, it distributes its energy over an ever increasing area. The shape of the explosive charge therefore affects the decay of pressure in the shock wave front. The influence of the charge shape can be seen in Figure 2.6 where a line charge (long, small diameter cylindrical charge) is detonated from one end. The shock waves generated at the ends of the charge are roughly hemispherical and expand greatly over a certain time duration, while the cylindrical shock waves generated from the sides of the line charge expand far less over the same time duration. The pressure of the hemispherical waves decay significantly while the pressure of the cylindrical waves decay far less.

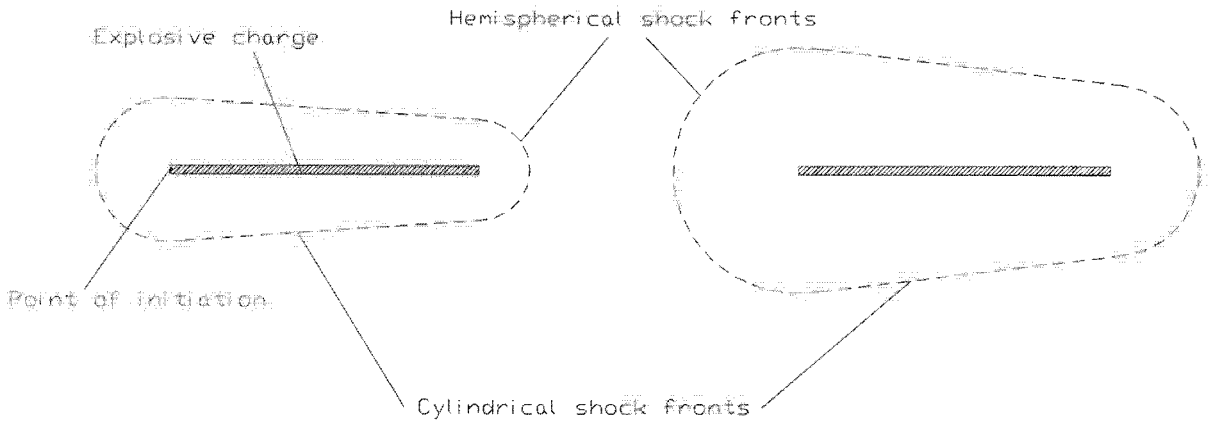

Figure 2.6: Shock wave front which develops around a line charge

The intensity of a shock wave depends upon the mass of the explosive charge with heavier charges producing stronger shocks. The thickness of the explosive charge affects the pressure duration of the shock wave but not the initial peak pressure. The thicker the layer of explosive, the longer the pressure will be sustained. Figure 2.7 And Figure 2.8 illustrate this phenomenon, where a layer of explosive of varying thickness is detonated on a metal plate.

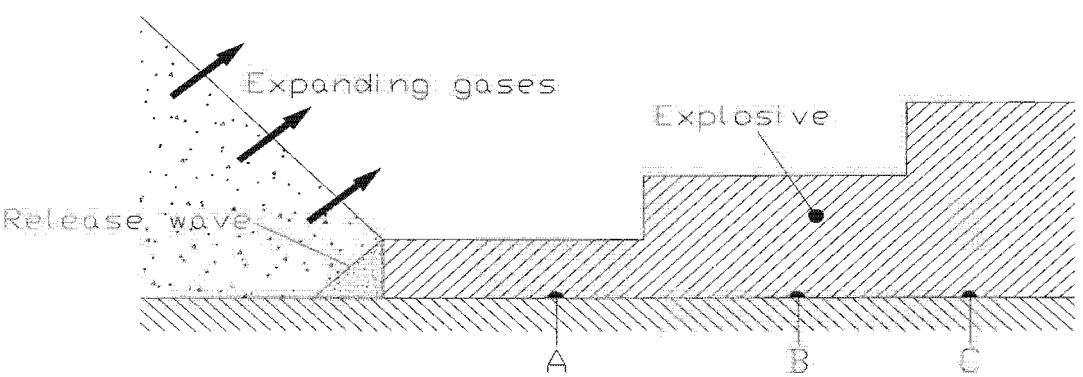

Figure 2.7: Detonation of explosive and expansion of explosion products from an explosive layer of varying thickness.

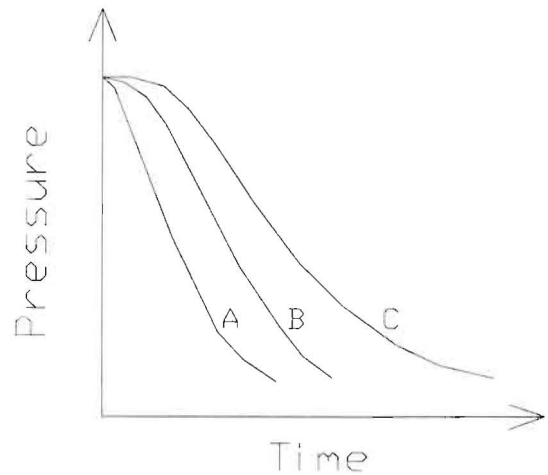

Figure 2.8: Pressure-time profiles at three positions, A, B, and C on metal plate in system of Figure 2.7.

The pressure experienced by an object which a shock wave strikes may be more than the pressure of the incident shock wave. When a shock wave strikes a rigid or fixed boundary, it is reflected, the reflected wave moves back into the incident wave, and the pressure therefore becomes redistributed. A shock wave may strike the surface of the object obliquely or it may hit it normally (head on). A shock wave in water striking a rigid boundary normally can be seen in Figure 2.9. It can be seen that simple acoustic doubling of the pressure can be assumed at the boundary.

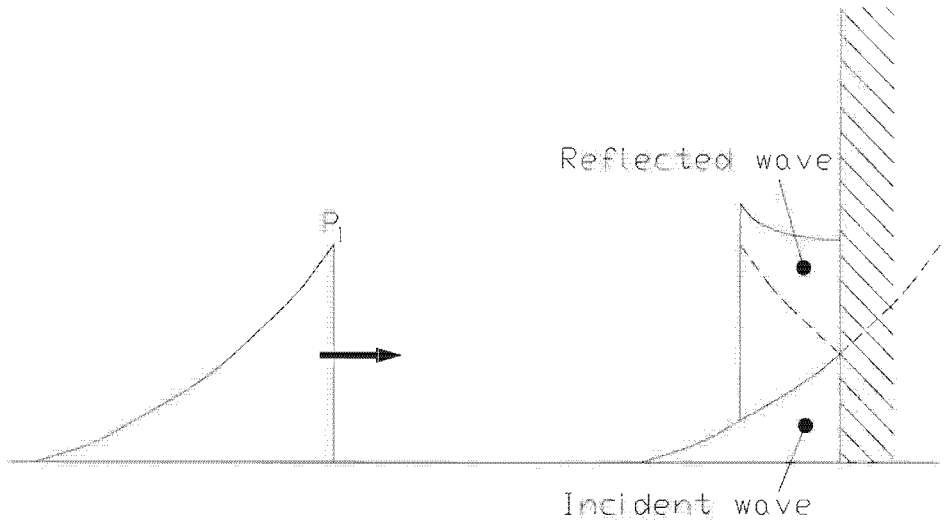

Figure 2.9: Pressure distribution set up by reflection at a rigid boundary of exponentially decaying shock in water.

When a similar incident occurs in air, a pressure multiplication of up to eight can occur for very strong shocks. This is because the strong pressure of the shock alters the air through which it has passed so that the pressure of the reflected wave is greater than the pressure within the incident wave. The physical properties of water can only be significantly altered in this way for shocks of extremely high intensity. When a shock wave strikes a surface obliquely, one of three distinctly different situations may develop depending on the angle of incidence of the shock and its intensity. These three situations are illustrated, respectively, in Figure 2.10(a) for a weak shock, Figure 2.10(b) for a fairly strong and not very oblique shock, and Figure 2.10(c) for a very strong shock.

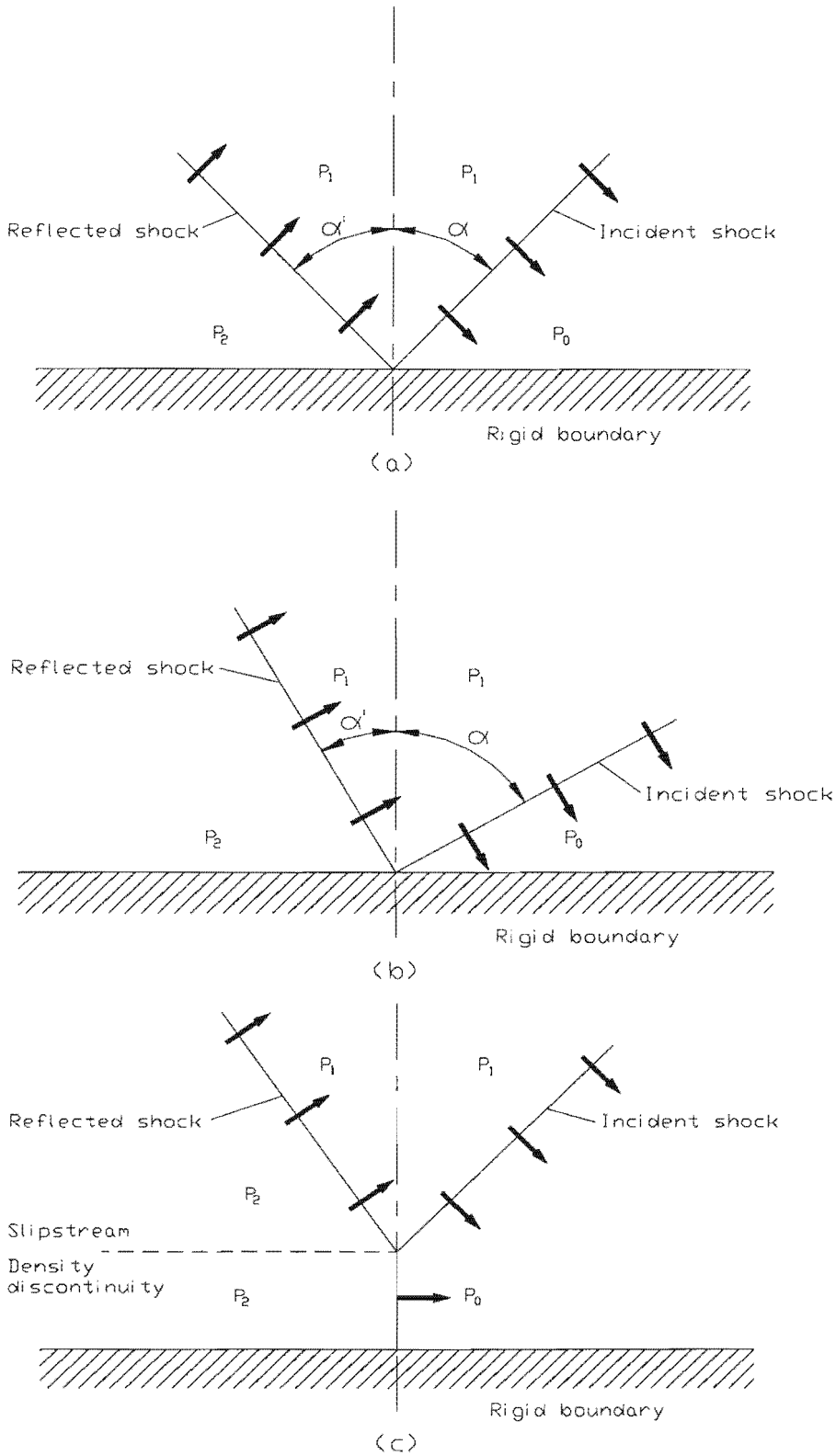

Figure 2.10: Reflection from rigid boundaries of (a) weak oblique shocks; (b) medium strong oblique shocks; (c) strong oblique shocks.

For weak shocks, the angle at which the wave is reflected is equal to the angle of incidence of the incident wave and the pressure behind the reflected wave, P_2, is just twice the pressure behind the incident wave, P_1. For a step pressure function, the distribution of pressure within the fluid would, at any instant, appear as illustrated in Figure 2.10(a), with pressure discontinuities moving in the directions indicated. There exists three well-defined pressure regions, that region in which the ambient pressure, P_0, has been unaffected by the incident wave, that in which the pressure of the incident wave, P_1, and that in which the pressure is P_2, P_2 being just twice P_1.

As the intensity of the incident shock increases, two changes take place in the pressure fields: the angle of reflection, α', no longer remains equal to the angle of incidence (Figure 2.10(b)), becoming progressively greater as the intensity of the shock increases; and the pressure, P_2, within the region affected by both the incident and reflected waves is no longer equal to $2P_1$, being always greater.

Finally, for very strong shocks and quite oblique incidence, a new condition known as irregular reflection develops with a Mach stem evolving. The pressure distributions then become as illustrated in Figure 2.10(c). Slippage of fluid occurs along the surface and the incident and reflected waves do not intercept at the surface within the fluid but at some distance from it. A third shock front then extends from this point to the surface. Whether Mach reflection will occur depends on both shock intensity and how oblique the angle of incidence is. For a given intensity shock there is a critical angle of obliquity above which Mach reflection occurs. The non-acoustic behaviour of air begins at relatively low shock pressures, so that the effects just mentioned can be quite pronounced [6].

2.3 Interaction of Explosives with Metal Plates

2.3.1 Experimental Studies

Experimental studies are conducted to explore any trends or thresholds that may exist for the response of the exploded plates. The experimental data is also often used to verify analytical and numerical prediction methods.

A typical experimental set-up of the studies to be discussed would consist of a clamped flat plate. Placed on top of the plate would be a sheet of polystyrene which prevents spallation of the plate. A sheet of explosive would then be placed on top of the polystyrene. This set-up can be seen in Figure 2.11. The explosive sheet, in most of the experimental studies, is placed over the entire exposed area of the plate and therefore the whole plate is subjected to blast loading (as in Figure 2.11). Other experimental studies place a small disc of explosive over the central area of the plate creating centralised loading.

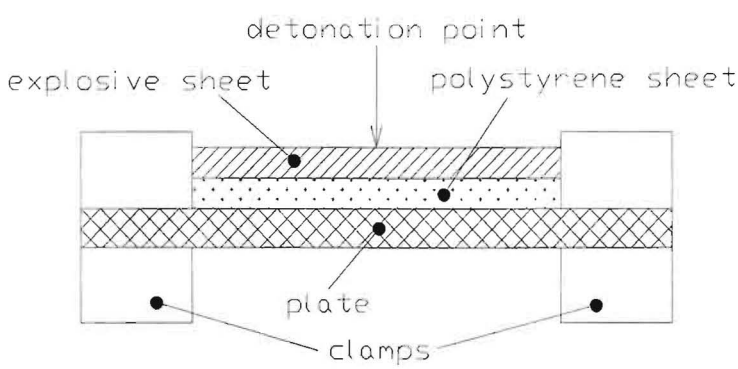

Figure 2.11: Schematic of typical experimental set-up of an explosive and flat plate.

Wierzbicki and Florence [7] studied the dynamic response of a circular plate subjected to explosive loading. The circular plates were clamped only to prevent rotation but not radial displacements at the outside diameter. Uniform loading was applied over the entire plate using sheet explosive which was

separated from the specimen by a layer of Neoprene. The impulse generated by the explosive was estimated by calibration of the actual explosive.

Bodner and Symonds [8] dealt with plates that were centrally loaded instead of plates loaded over their entire surface. The deflection-time history was measured by placing a condenser microphone near the centre of the plate. The impulse transferred to the plates was measured using a ballistic pendulum. The theory and usage of a ballistic pendulum will be discussed further on.

Menkes and Opat [10] identified three major modes of failure in their experimental study on impulsively loaded clamped aluminium beams. These modes were:

- large inelastic transverse deformation (mode I)
- tensile tearing failure in outer fibres, at the support (mode II)
- transverse shear failure at the support (mode III)

These three failure modes can be seen in Figure 2.12. Many future studies (experimental, theoretical, and numerical) made use of these failure modes.

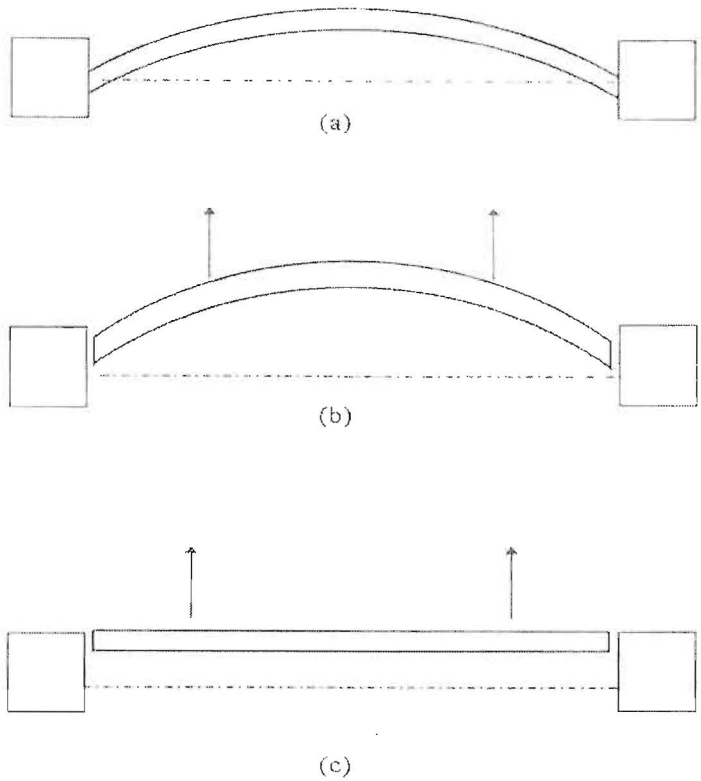

Figure 2.12: Diagrams illustrating the three failure modes; (a) mode I; (b) mode II; (c) mode III

Nurick and Martin [11] reviewed the experimental work that had been previously conducted on the deformation of thin plates subjected to impulsive loading. Most of the studies involved uniform loading over the entire plate. The experimental techniques listed by Nurick and Martin [11] included information such as the plate dimensions, specimen type and material, deflection to thickness ratio and response time. The experimental results were compared by means of a dimensionless damage number, Φ, and the displacement-thickness ratio. The dimensionless number is a function of impulse, plate geometry, plate dimensions, and material properties. This method of comparison gave good correlation between the experimental data of the different studies.

Teeling-Smith and Nurick [12] also presented experimental results using the dimensionless damage number, Φ. The experiments, conducted on thin circular plates subjected to uniform impulsive loading over the entire plate, exhibited the three major failure modes defined by Menkes and Opat [10]. In this study, the impulse required for the different failure modes, the velocity of the circular metal disc after complete tearing, and the final mid-point deflection were measured. The impulse values, obtained with the aid of a ballistic pendulum, allowed the input energy to be calculated. From the experimental data, the relationship between the deflection-thickness ratio and Φ for mode I and mode II, was developed.

Nurick and Teeling-Smith [13] considered the failure of circular fully clamped plates. The experimental data was used to predict the onset of necking and failure in plates loaded over the entire surface. It was found in some cases that failure would occur at a particular impulse while at slightly higher impulses no failure would occur. This made predictions of the impulse at failure difficult. It was found that plate failure occurred in the range of plate deflections of 17-18 plate thicknesses, and a global stiffness reduction was observed for plate deflections greater than ten plate thicknesses.

Nurick and Shave [14] conducted impulsive loading experiments on clamped square plates. For comparison purposes, specimens of similar area and thickness and a similar experimental set-up to the circular plate experiments by Teeling-Smith and Nurick [12] was used for the experiments on thin square plates. All three failure modes were exhibited. Mode II was divided into three subcategories: mode II* (tensile tearing at outer fibres over part of the support), mode IIa (complete tearing of sides and mid-point deflection of plate increases with increasing impulse), mode IIb (complete tearing of sides but mid-point deflection decreases with increasing impulse). Comparison of these experimental results with those of Teeling-Smith and Nurick [12] showed that, although the responses of the two geometries differed, a similar maximum mid-point deflection-thickness ratio was obtained. There were significant differences in mode II and mode III failure owing to the different geometries.

Wierzbicki and Florence [7] presented an experimental study of final deflection profiles of thin circular plates subjected to centralised explosive loading. The experimental procedure used is similar to that used by Bodner and Symonds [8] and Teeling-Smith and Nurick [12]. The total impulse, mid-point deflection and plate profile were measured. Tests with different loading radii were conducted. It was observed that smaller loading radii led to a more localised bulging near the plate centre and failure took the form of a disc, whereas the larger loading radii failure occurred as tearing at the clamped boundary.

Schleyer, Hsu and White [15] presented the results of a series of pressure pulse loading tests on square, stiffened steel plates with and without in-plane restraint. A new test facility that had been recently developed, was used to provide the blast loading. Instead of using hydrocarbons or explosives to create the pressure pulse, the pulse is generated by a transient differential pressure created by the timed blow-down of two pressure loading chambers on either side of the test plate. A large flanged nozzle in each of the chambers allows the pressure in the chambers to be released quickly by means of a bursting diaphragm. The test results showed that in-plane restraint is responsible for reducing the maximum transient deflections by almost 50% and permanent deformations by more than a factor of 4. It was also found that the ribs in the stiffened plates reduced the maximum deflections.

Blast loading experiments were conducted on steel V-plates by Lockley [43]. Unfortunately, this literature has been lost, but photographs of the exploded plates were available along with the values of impulse transferred to the V-plates and the mid-point permanent deflections of the V-plates. The results of these experiments will be used in this study to attempt to verify the finite element models developed.

2.3.2 Theoretical Studies

The many different theoretical approaches try to predict the way the plates will respond under explosive loading. Predictions have been made of, for example, energy transferred to the plate, the mid-point deflection, the deformed profile, and the onset of tearing. Some of the main blast loading simulation methods used in both the theoretical and numerical methods are depicted in Figure 2.13, Figure 2.14, and Figure 2.15. The blast loading is usually simulated by means of either an initial velocity over the entire plate or localised load area, or by a short duration pressure over the entire plate or localised load area.

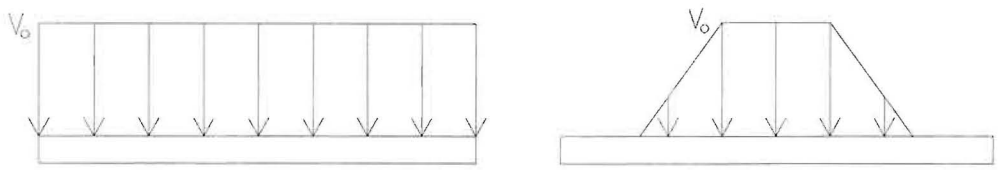

(a) (b)

Figure 2.13: Initial velocity profiles simulating explosive loading; (a) uniform velocity over entire plate; (b) trapezoidal velocity over central area of plate.

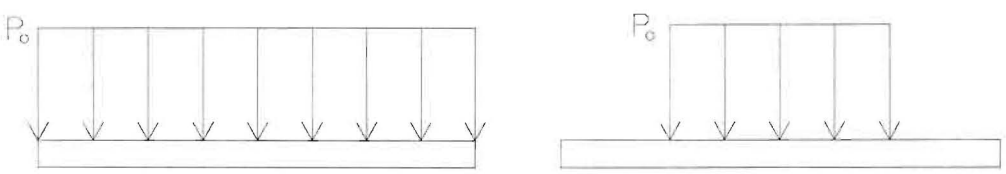

(a) (b)

Figure 2.14: Pressure profiles simulating explosive loading; (a) uniform pressure over entire plate; (b) uniform pressure over central area of plate.

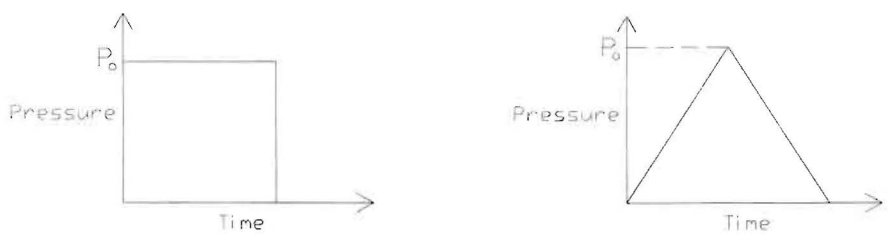

(a) (b)

Figure 2.15: Pressure pulses over which pressure profiles are applied; (a) square pulse; (b) triangular pulse.

Ezra [16] discusses explosives in general but the literature mainly focuses on the use of explosives in metalworking. Three methods of estimating the amount of energy delivered by an explosive charge to a metal work-piece (blank), are also documented.

For a given type and size of charge, the efficiency of energy transfer depends to a great extent on the configuration of the work-piece relative to the charge. For example, if the charge were exploded at the centre of a spherical work-piece which completely surrounds the charge, the energy transfer would be maximised. A flat plate with the same surface area as the sphere would receive far less energy if its centre were at a perpendicular distance from the charge equal to the radius of the sphere.

The properties of the energy transfer medium between the charge and the metal blank also have a significant effect on the efficiency of energy transfer. If the charge is exploded in a vacuum, very little energy will be delivered. If the charge is exploded in air, a substantial amount of energy is transferred. If water is the energy transfer medium, it will be even more efficient. Water is a very popular medium for metalworking for many reasons. Its efficiency is much higher than that for air, it is readily available, and the sound is muffled. Because of this, this literature mainly focuses on underwater explosions.

Three methods of approximating the total energy transmitted to the metal blank are discussed. The second and third methods can only be applied to underwater explosions. The first method can be applied to transfer mediums other than water, but only the equations for water explosion are given in the literature. All the methods consider the charge to be a point charge and do not take the shape of the charge into account. The system to which these methods apply can be seen in Figure 2.16.

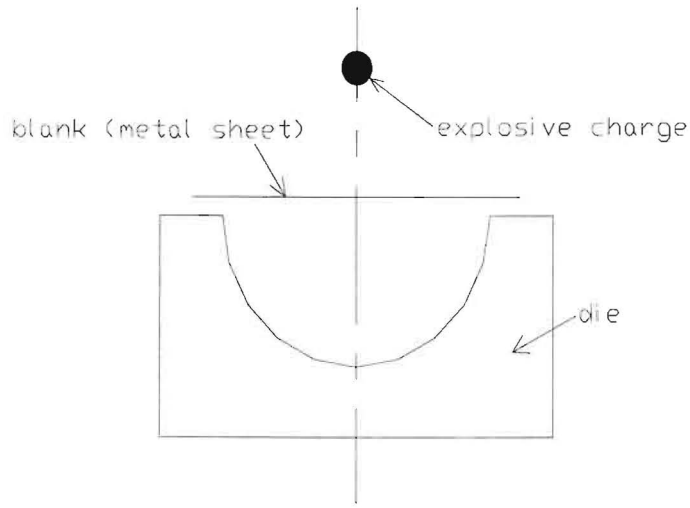

Figure 2.16: Schematic of metal-working set-up to which the energy transfer approximations reported by Ezra [16] apply.

The first method (Geometrical Method) is based primarily on the specific energy of the explosive (i.e. the energy per unit mass), and the configuration of the work-piece relative to the charge. The work-piece configuration is expressed in terms of the ratio of the solid angle subtended by the metal work-piece at the charge centre to the solid angle subtended by a sphere surrounding the charge. The influence of the energy transfer medium is expressed by an empirical factor.

The second method (Energy Method) is based on the empirical energy density formulae derived from measurements of underwater explosions with diaphragm gauges which thus include the reloading effects.
The reloading phenomenon delivers even more energy to the blank than the primary shock wave. It occurs when the primary shock wave impacts with the metal blank and imparts an initial velocity. The motion of the blank then sends a rarefaction wave back into the water which lowers the pressure in the water adjacent to the blank until cavitation occurs. The blank then slows down due to its restraints and the separated water then catches up with it. The resulting impact is referred to as the reloading phenomenon. The energy densities from the empirical energy density formulae are integrated over the

area of the work-piece. The use of this method is limited to those explosives for which the appropriate empirical energy constants have been determined.

Both the first and second methods provide upper bound estimates of the explosive energy delivered to the work-piece from both the primary shock wave and the reloading phenomenon. The third method gives lower bound estimates based on empirical pressure and impulse formulae, and does not include the energy delivered in the reloading phase. The third method should only be used when the reloading phenomenon is absent.

For the third method (Impulse Method), the impulse is considered to act radially outwards from the expanding spherical shock wave. The method uses the theory that when the shock wave from a concentrated charge impinges on the metal blank, only the resolved component of the impulse acting normal to the blank will determine the resulting normal velocity of the blank.

Duffey [17] developed a simplified energy method for rigid-plastic material behaviour which equates the dissipated strain energy to the initial kinetic energy imparted to a clamped circular plate. Several deformed shape profiles are assumed, including sinusoidal and various polynomial forms to find the best fit to the experimental results. This method provides good correlation with experimental results.

A theoretical analysis was presented by Wierzbicki and Florence [7] for predicting the response of impulsively loaded clamped circular plates. For small applied impulses the resulting plate deflections are small and the plate response is governed by bending and/or shear resistance. The response of plates subjected to large impulses and undergoing large deflections is dominated by a membrane stretching resistance [9]. The theoretical analysis of Wierzbicki and Florence [7] combines the influences of the membrane forces and the bending moments and considers the influence of material strain rate sensitivity modelled by a linear visco-plastic constitutive equation. When the results were compared with experimental data, it was found that

this theoretical analysis gives better predictions for the final transverse deflections of the plate near the transition from bending dominant to membrane dominant behaviour than those provided by theories which retain either membrane forces or bending moments alone.

Lippman [18] used an energy approximation method to predict impulsively loaded circular plate deformations. This method includes both bending and membrane effects in a model that assumes a deformed shape with a radial thickness variation to predict the mid-point deflection. By starting from Tresca's yield condition and the associated flow, it is possible to reduce the problem to one single-order differential equation which can be solved numerically. Lippman [18] used this to derive an approximate analytical solution by assuming that the material of the membrane moves vertically downwards only. The results correlated well with experimental data.

Jones [19] conducted a theoretical investigation to predict the threshold velocities for the onset of the different failure modes in fully clamped beams. This rigid-plastic analysis includes the effects of membrane forces, which are induced by finite displacements for the mode 1 response, and includes transverse shear forces in the yield condition for the mode 3 response.

Symonds and Wierzbicki [20] used the mode approximation technique proposed originally by Martin and Symonds [21] who used the technique for small deflections. Strain rate sensitive mild steel shows a considerable amount of strain hardening and therefore as the strain rate increases, the value of the dynamic yield stress increases. This method allows the calculation of the dynamic stress through an iterative procedure. It was assumed that the explosive imparted a square pressure pulse over the explosive load area of the plate (i.e. the cross-sectional area of the explosive projected onto the plate) and no attempt was made to model the way in which the pressure spread outside the load area. Symonds and Wierzbicki [20] calculated rather than assumed the stationary mode shape by solving a linear eigenvalue problem. This solution did satisfy the field equations and boundary conditions but not the initial condition. This approximate method

gives generally good predictions of the central deflections of the plate, but not of the plate shapes. Because this method only accounted for membrane effects, its predictions tended to underestimate deflections for small deflections. For large deflections, where the energy dissipated in the membrane effect is significant, the predictions are well supported by experimental results which were conducted by Bodner and Symonds [8].

Nurick, Pearce, and Martin [22] used a model in which the mode shape of the plate is computed at each time step. The analysis took into account transverse displacements as well as the effects of lateral displacements in the plane of the plate. This allowed the prediction of in plane strains, and provided good correlation to experimental data.

Duffey [23] used the three major failure modes for predictions of the failure of dynamically loaded cylindrical shells. It was concluded that there was a lack of suitable failure criteria where actual separation occurs for dynamically loaded ductile material shell structures.

Jones [4] developed approximate methods such as the rigid-plastic methods to predict the dynamic, large deformation behaviour of pulse loaded plates. Both membrane and bending effects are included. Two phases of motion are considered for the plate. The first is the response during the loading of a pressure pulse, and the second phase is the inertia response. This method was then simplified for membrane effects only but includes strain rate sensitivity for large deformations of strain hardening materials. It was noted that, for simplicity, impulsive loading is often treated as an instantaneously applied uniform transverse velocity over the entire plate. The deformation values from these methods show satisfactory correlation with experiments.

Nurick and Martin [11] reviewed the theoretical work that had been previously done on the deformation of thin plates subjected to impulsive loading. Most of the studies involved uniform loading over the entire plate. The final mid-point displacement, time response, and sometimes the shape of the plate was predicted using the numerous approximate methods. The earliest studies

predicted only small deformations due to bending effects, but in later work membrane effects were included, and by assuming a deformed shape, such methods were very successful. The dimensionless damage number, Φ , and the deflection-thickness ratio was used to compare the theoretical models. The predictions and experimental results compare favourably for the mid-point displacements and final deformation shapes.

A theoretical analysis was presented by Teeling-Smith and Nurick [12] involving an energy balance. A comparison of previous methods to calculate the energy of deformation of the plate was conducted and it was found that the method used by Duffey [17] gave the best results and was therefore used in the energy balance calculations. Relationships were then developed between the energies and the dimensionless number, Φ.

Shen and Jones [24] presented a theoretical analysis which examines the dynamic plastic response and three failure modes of fully clamped circular plates subjected to uniformly distributed transverse loads. The rigid-plastic analysis caters for the influence of finite transverse displacements. It involves an interaction yield surface which combines the bending moments, membrane force and transverse shear force required for plastic flow, and strain rate sensitivity is also taken into account. The theoretical results compare well with the permanent transverse deflections (mode 1) of Teeling-Smith and Nurick [12] and Bodner and Symonds [8] but the theoretical critical impulse for rupture did not correlate with the experimental results. This was thought to be because the boundary conditions in the experiments were not ideally clamped, as assumed in theory.

Radford [25] considered circular plates fixed at the boundaries subjected to localised loading conditions. A theoretical model was developed in an attempt to predict the plate deformation and resulting strain up to the onset of tearing. The theoretical model is described by two models where the first model uses the mode approximation technique to predict the plate deformation and the second model uses this deformation to predict the strain in the plate. The plates were assumed to be thin enough to be considered as membranes so

no bending effects were taken into account. Strain rate effects were also included. The failure criterion was assumed to be quasi-static uniaxial tensile strain at failure. Generally good correlation between the experimental data, from experiments previously conducted by Radford [25], and the predictions made by the theoretical model, was obtained.

Wierzbicki and Nurick [9] developed a theoretical analytical solution to predict the transient and final deflection profiles for thin circular plates subjected to centralised explosive loading. The fact that the loading is centralised and not spread over the entire plate makes the analytical solution more complex and two new solution techniques based on momentum conservation and an eigenvalue expansion method were developed. It was found that representing the loading of centrally loaded plates by applying a uniform impulse spread over the entire plate does not give correct results. The numerical study by Bimha [26] supports this as it showed that the best agreement with experimental results is obtained with a radially varying impulse. For this reason, the centralised load in the theoretical analysis is applied through a trapezoidal initial velocity distribution. Good correlation was obtained between the predicted and experimental normalised deflection profiles.

A simplified pseudo elastic-plastic analysis was used by Schleyer, Hsu, and White [15] to predict the transient and final permanent deflections of square, stiffened steel plates with and without in-plane restraint, subjected to pressure pulse loading. This method approximates the structural behaviour of the stiffened plates by means of an appropriate shape function and was considered suitable for the study due to the significance of the elastic membrane effects and large geometry change of the plates during deformation. The results of this analysis compared to experimental results revealed mixed successes. It was stated, however, that the analysis needed further development with respect to the yield and plastic flow mechanisms.

2.3.3 Numerical Studies

Olson, Nurick, and Fagnan [27] used finite element computations to investigate the different failure modes of blast loaded square plates. The in-house code NAPSSE (non-linear analysis of plate structures using super elements) was used. It is sufficient to model the entire plate with only one of the specially designed super elements which utilise displacement fields represented by analytical as well as polynomial functions. The code uses Kirchhoff thin plate theory, and includes geometrical and material non-linearity, finite element equations obtained by virtual work principles, as well as strain rate sensitivity. For mode II predictions, the high local strains at the boundary were modelled using hinge lines, and failure was defined as the instant when the maximum strain reaches the rupture strain in the static uniaxial test. Good correlation with experimental results for mode I failure was obtained, while correlation for mode II failure was not as satisfactory. The predictions were limited to the onset of tearing only and mode III was not considered.

Rudrapatna, Vaziri, and Olson [28] used NAPSSE to develop a similar model of clamped, square, thin steel plates subjected to blast loading to predict the tearing and rupture. An interactive failure criterion comprising bending, tensile tearing, and transverse shear was proposed to predict the various modes of failure. In previous work done by Rudrapatna, Olson, and Vaziri [45], the shear stress required for determining the interactive failure function was considered to be uniformly distributed over the plate boundary with the magnitude equal to the dynamic reaction force divided by the remaining cross-sectional area. Unfortunately, this technique masks the peaks and troughs of the shear stresses which are vital in the evaluation of the failure functions and detection of critical points in the structure. To overcome this, the plate was modelled to rest on a continuous bed of very stiff elastic springs around the boundary so that the vertical reaction force (shear force) was no longer constant and its magnitude would change with the amount of vertical deflection from point to point in the structure. The model was then more capable of predicting partial failure. A node release algorithm was developed

to simulate the progression of rupture. The numerical predictions of the impulse required for mode II and mode III failure compared reasonably well with experimental results.

Farrow, Nurick, and Mitchell [29] used the ABAQUS finite element code to predict the large inelastic deformation (mode I) of circular plates under uniform impulsive loads over the entire plate. A short-duration uniform pressure was applied to the plate to simulate the impulsive loading. The plate was modelled using 2-noded axisymmetric shell elements governed by Kirchhoff thin shell theory, and which take thinning and finite strain behaviour into account. The model incorporated strain rate sensitivity, non-linear geometry, and material effects. The plate displacements, deformation shapes, residual strains, dynamic yield stress, and thinning predictions show satisfactory correlation with experimental and analytical results.

Radford [25] generated a finite element model of circular plates fixed at the boundaries subjected to localised loading conditions. These predictions were generated for comparison with the theoretical and experimental results generated by Radford [25]. The finite element model criteria used are the same as those used by Farrow, Nurick, and Mitchell [29] in which strain rate sensitivity, non-linear geometry, and material effects are incorporated. The plate was modelled using 2-noded axisymmetric shell elements. The impulsive load was locally applied in the form of a short-duration triangular pressure pulse of uniform pressure over the explosive load area only, instead of over the entire plate. The finite element model did not give satisfactory results. This was because even for small impulses, the pressure applied to the plate over the small load area was so extreme, that numerical instabilities occurred in the finite element solution.

Gelman [30] also used the ABAQUS finite element code to investigate the response of thin circular plates subjected to impulsive loads. Previous analytical and numerical predictions of the plate response have assumed a fully constrained boundary condition for the plate, while experiments have involved the use of both clamped and integral (fully built-in) boundary

conditions. This investigation studied the effects that the boundary conditions could have on the plate results by modelling a variety of more realistic boundary conditions. Fully built-in plates were modelled by the inclusion of a material boundary, and clamped plates by the use of rigid clamping elements and a simple friction condition between the surfaces of the clamps and plate. The inclusion of a fillet radius at the integral boundary of the plate, and a clamp edge with a radius at the clamped boundary, were also modelled. Figure 2.17 shows these different boundary conditions.

The plates were modelled using 4-noded axisymmetric continuum elements instead of simpler shell elements because localised detail at the boundaries needed to be observed. The impulsive loading was applied through short duration square pressure pulses over the entire plate. The model incorporated geometric and material non-linearity, and strain rate sensitivity. The failure criterion was maximum equivalent strain. It was concluded that the large inelastic deformation (mode I) was not highly dependent on the type of boundary fixation, although small variations were noted. It was also reported that the permanent deflection of the plate was not dependent on the selected pressure-time history of the pressure pulse, provided that the time selected is short compared to the overall response time of the plate. The mode I results Gelman [30] obtained correlated well with experimental results, while the mode II results (tearing at supports) did not correlate well as ABAQUS predicted tearing at about 60% of the actual tearing threshold impulses. It was also reported that there was a lack of suitable failure criteria in numerical modelling of dynamically loaded structures. Failure criteria such as maximum equivalent plastic strain or maximum equivalent stress were inadequate, and a reliable method needed to be found.

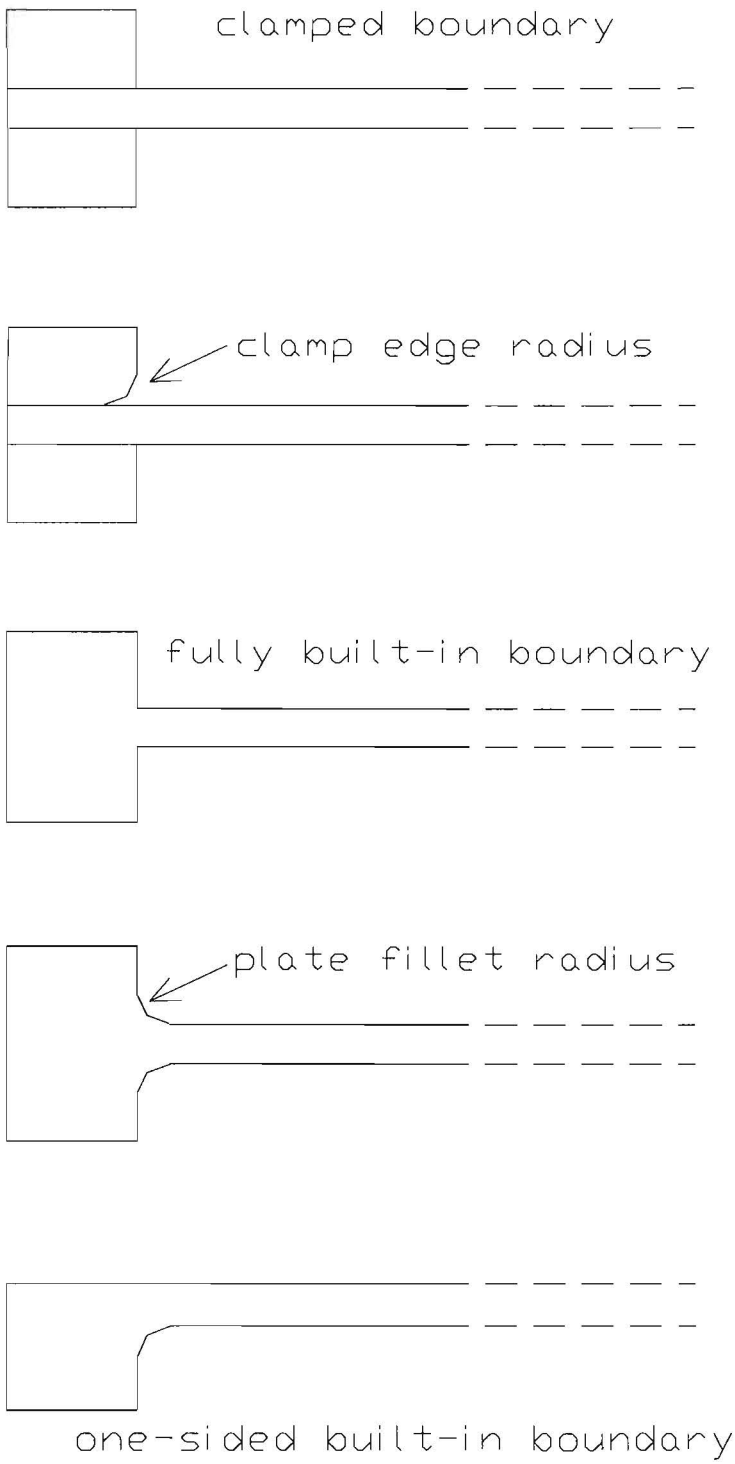

Figure 2.17: Schematic representation of the different boundary conditions of blast loaded plates modelled by Gelman [30].

Most of the finite element models discussed above represented the impulsive loading by means of either an initial velocity over the entire plate or localised load area, or a pressure pulse of short duration over the entire plate or localised load area (refer to Figure 2.13, Figure 2.14, and figure 2.15). To use these methods, the initial velocity magnitude or the pressure pulse peak magnitude and duration has to be calculated. The magnitude of the uniform initial velocity is calculated from the relationship

$$V_o = \frac{I}{M} \qquad where \qquad M = \frac{\pi d^2 t \rho}{4}$$

where

$I = impulse\ transferred\ to\ plate$

$M = mass\ of\ plate$

$d = diameter\ of\ plate$

$t = thickness\ of\ plate$

$\rho = density\ of\ plate$

The peak magnitude of the uniform or localised pressure pulse is calculated from the relationship

$$P_o = \frac{I}{A\tau} \qquad for\ a\ square\ pulse$$

and

$$P_o = \frac{2I}{A\tau} \qquad for\ a\ triangular\ pulse$$

where

$A = load\ application\ area$

$\tau = pressure\ pulse\ duration$

The assumption that the duration of the pressure pulse τ is equal to the approximate explosive burn time has often been used in explosively loaded plate analysis problems Jones [4], Olson, Nurick, and Fagnan [27], Shen and

Jones [24], Gelman [30], Radford [25], Bimha [26]. The time duration of the pressure pulse is calculated from the relationship

$$\tau = \frac{a}{V_b}$$

where

$a = radius\ of\ \text{explosive sheet}$

$V_b = velocity\ of\ \text{detonation}$

The impulse transferred to the plate, I, is obtained from experimental data. A ballistic pendulum, as used by Nurick [31], was used to determine the magnitude of the impulse.

The ballistic pendulum consists of an I-beam suspended by four wires from a rigid ceiling. The plate specimen is mounted onto the pendulum, and known masses are applied to ensure a balance of load through the suspending wires so that the impulse is applied through the centroid of the pendulum. A pen is also attached to the pendulum to record the pendulum oscillation. The experimental set-up and geometry of the ballistic pendulum can be seen in Figure 2.18.

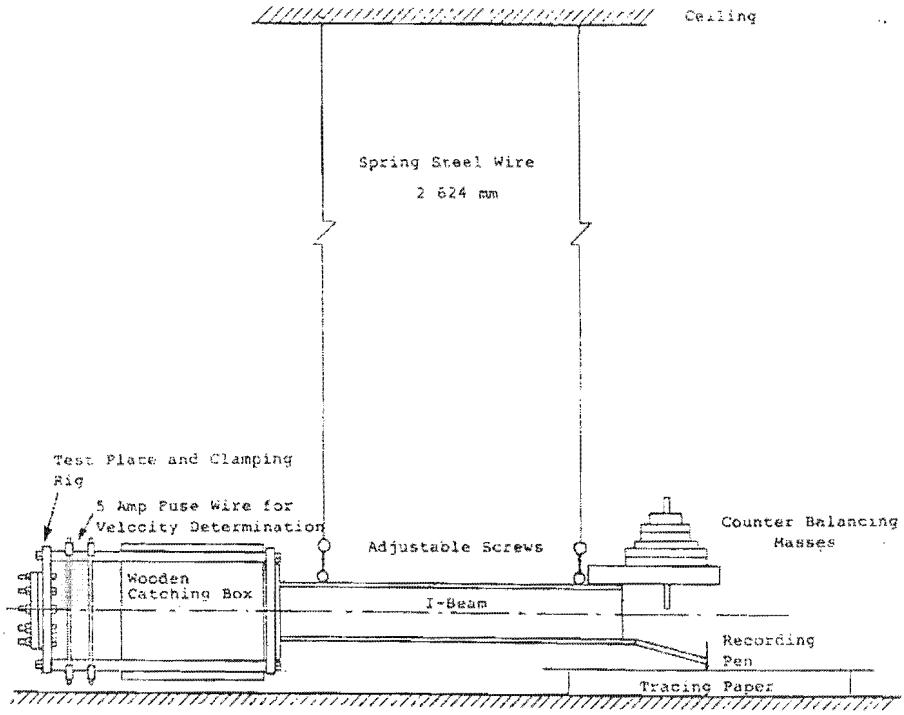

(a)

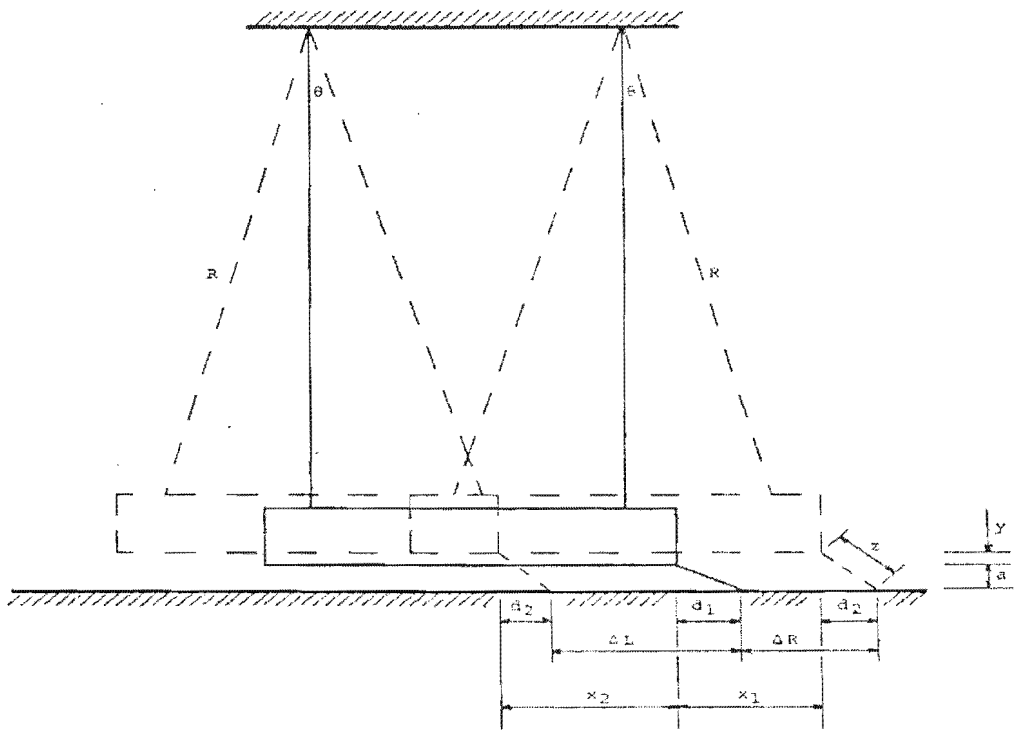

(b)

Figure 2.18: Diagrams illustrating; (a) the experimental set-up; (b) the geometry; of a ballistic pendulum

The impulse transferred to the pendulum can be calculated, as reported by Nurick [31], from

$$I = M\dot{x}_o$$

where

M = *mass of entire pendulum*

$\dot{x}_0$ = *initial velocity of pendulum*

The initial velocity of the pendulum is calculated from

$$\dot{x}_o = \frac{2\pi}{T} x_1 e^{(1/4)\beta t}$$

where

T = *period of pendulum*

β = *damping constant*

x_1 = *displacement function* (*Figure* 2.18 (*b*))

The damping constant β takes the form

$$\beta = \frac{2}{T} \ln\left(\frac{x_1}{x_2}\right)$$

where

x_2 = *displacement function* (*see Figure* 2.18 (*b*))

Bimha [26] attempted to model explosive loading more realistically by refining the pressure pulse loading method. Previously, as discussed, either a uniform pressure pulse was applied over the entire plate, or over the localised explosive load area. Bimha's [26] method applies a uniform pressure over the localised load area in conjunction with an exponentially decaying pressure starting at the perimeter of the localised load area and decaying to zero at the perimeter of the plate. The pressure is still applied in the form of a square pulse. Figure 2.19 illustrates this method.

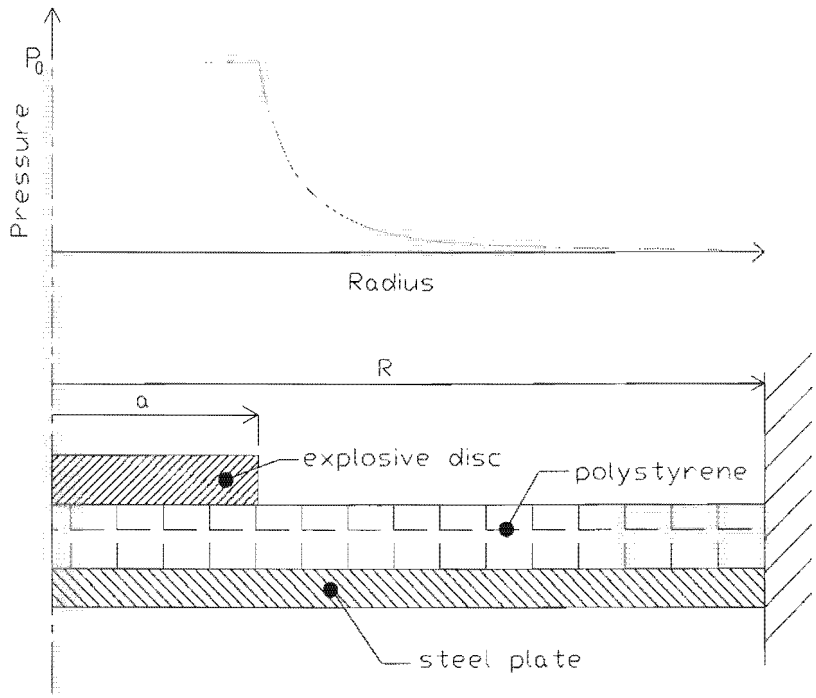

Figure 2.19: A schematic representation of the experimental set-up that Bimha [26] modelled and the pressure profile used in the model.

This method makes calculating the peak pressure more complex.
The relationship between measured impulse and the pressure load is

$$I = t_h \int_0^R P(r)dA \qquad (2.1)$$

where

$P(r) = pressure\ distribution\ as\ a\ function\ of\ radius$

$R = radius\ of\ plate$

The pressure distribution function is

$$P_a = constant \qquad for\ r \le a$$

and

$$P(r) = P_o e^{-k(r-a)} \qquad for\ a \le r \le R$$

where

$$k = \text{exponential decay constant}$$

Equation 2.1 can be written as

$$I = \tau\int_0^a P_o dA + \tau\int_a^R P_o e^{-k(r-a)} dA \qquad \text{where} \qquad dA = 2\pi r dr$$

which becomes

$$I = \tau\int_0^a 2\pi r P_o dr + \tau\int_a^R 2\pi r P_o e^{-k(r-a)} dr$$

After integration, the result is

$$I = \pi\tau P_o\left[a^2 + 2\left\{\left(\frac{a}{k}+\frac{1}{k^2}\right) - \left(\frac{R}{k}+\frac{1}{k^2}\right)e^{k(a-R)}\right\}\right]$$

Changing the subject of the formula to peak pressure

$$P_o = \frac{I}{\pi\tau\left[a^2 + 2\left\{\left(\frac{a}{k}+\frac{1}{k^2}\right) - \left(\frac{R}{k}+\frac{1}{k^2}\right)e^{k(a-R)}\right\}\right]}$$

The relationship determining the exponential decay constant, k, generated from experimental results, is

$$k = 130 - 261\left(\frac{a}{R}\right) + 948\left(\frac{a}{R}\right)^2$$

and is applicable over the range

$$0.15 < \left(\frac{a}{R}\right) < 0.6$$

The plate was modelled using 2-noded axisymmetric shell elements. Two boundary conditions were considered; a plate clamped to its support by bolts and a plate fully built-in. The mid-plate permanent deflections, deformed profiles, strain rate dependence, strain predictions, response time and rupture were compared to experimental data, analytical solutions, and other numerical results. It was found that the predicted responses compared reasonably well.

Raftenberg [32] used the EPIC Lagrangian wavecode to simulate experiments in which a circular plate of rolled homogeneous armour (RHA) was loaded by the detonation of a nearby cylindrical charge. The material model of the plate took strain hardening, strain-rate hardening, and thermal softening into account. A failure model was also incorporated. The plate and explosive mesh were both made up of three-noded triangular elements. The detonation of the explosive was modelled by a programmed burn algorithm. This algorithm is governed by two material constants, detonation speed, D, and the internal energy per unit volume, e_0. The algorithm propagates a spherically symmetrical detonation wave from the point of initiation by dumping the appropriate energy into each finite element at the time steps during which the wavefront passes through the element. Another material constant is the initial density of the solid explosive which was assumed to be equal to the initial density of the gaseous explosive products. The motion of the gaseous products was represented by the Jones-Wilkins-Lee (JWL) Equation of State. It was observed that during the analysis the explosive elements became greatly distorted while interacting with the plate, but the effect this had on the results was thought to be insignificant. Failure of the plate did not occur in any of the models. Reasonable agreement with experimental results was found for the steady-state centre-of-mass velocity and the swept-back volume of the plate.

The finite element method package, ABAQUS, was also used by Schleyer, Hsu, and White [15] to predict the transient and final permanent deflections of square, stiffened steel plates with and without in-plane restraint, subjected to pressure pulse loading. The boundary conditions of the plate were simulated

by restraining the out-of plane rotation and using non-linear springs for the in-plane translation. The plate was modelled with thick shell elements which take account of finite membrane strain and transverse shear, and which are capable of modelling buckling. Strain rate sensitivity was taken into account for the steel plates. The pressure was applied in the form of a short duration triangular pulse of a uniform pressure over the entire plate. The overall profiles of the displacement-time histories agreed reasonably well with the experimental results. There was a good correlation between the predicted results and the test results for the maximum transient deflections, however, the final deflections of the unrestrained plates were under-estimated.

Tollner and Nurick [33] used the finite element code, ABAQUS, to model clamped, stiffened circular plates subjected to a uniform load distributed over the entire plate. Continuum elements were used to model the stiffened plate and the clamped boundary condition was simulated by modelling a clamp using rigid body elements and then applying a pressure to the clamp. A coefficient of friction between the clamp and the plate surfaces was then specified. The blast load was modelled by exerting a square pressure pulse of a uniform pressure over the entire plate. Strain hardening and strain rate sensitivity were incorporated in the model. The finite element method results were compared to the experimental results reported by Nurick and Lumpp [46] and satisfactory correlation with the experimental results for mode I failure was found. No predictions for tearing were attempted.

Wiehahn [34] studied the method of fracture and the energy of tearing of circular plates subjected to blast impulses, using the finite element code, ABAQUS. The material model incorporated temperature, strain, and strain rate dependency, and a strain based shear failure predictor was also used. The plate was modelled axisymmetrically and the built-in boundary conditions of the plate were simulated by actually modelling the thicker edge support into which the plates were built. The edges of the support were then encastered. The impulsive loading was applied using the same method Bimha [26] developed where a short duration pressure pulse is applied using a uniform pressure over the explosive load area and an exponentially decaying pressure

over the rest of the plate. A plate model to which the pressure pulse was applied can be seen in Figure 2.20.

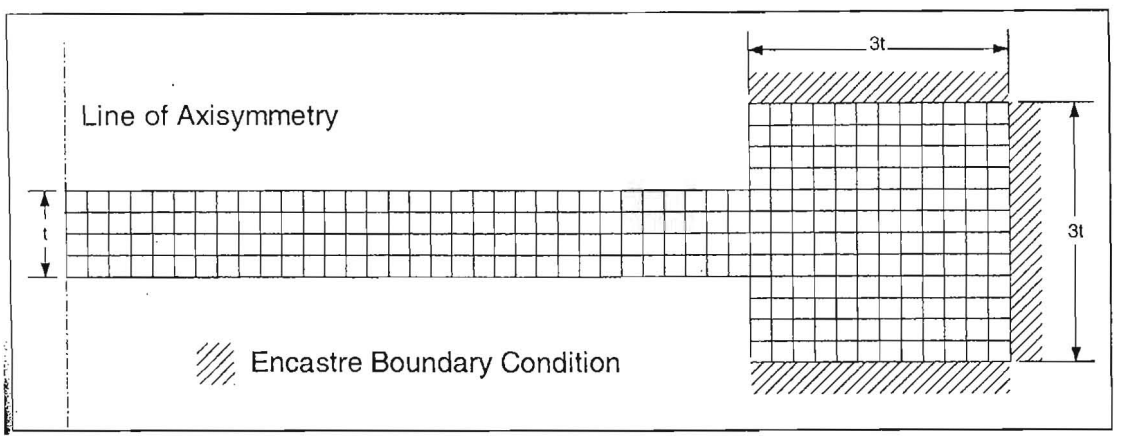

Figure 2.20: A Diagram of the plate model, modelled with axisymmetric elements (CAX4R) by Wiehahn [34].

Wiehahn [34] also attempted to use the JWL Equation of State to model the explosive but found that the computational run times greatly increased and the impulse values obtained did not compare well to the experimental values despite the fact that the displacement profiles of the plates were acceptable, so this approach was abandoned. The numerical results of the pressure loading models were compared to experimental results. It was found that coarse meshes in the model resulted in good overall modelling in terms of the radius of the resulting cap (circular metal disc fragment), cap velocity, and the prediction of the critical impulse required to cause failure. Fine meshes yielded poor results for these properties, but were able to predict the localised phenomenon of shear band formation which is thought to be the cause of fracture.

Nannucci [44] modelled the blast loading of steel V-plates using the ABAQUS finite element code. Unfortunately, this work was lost and only the images of the deformed profiles were available. Without the literature, the method of simulating the blast loading is not certain, but it is thought to be either the

method of uniform pressure loading over the load area, or the method that Bimha [26] developed involving uniform pressure loading over the load area in conjunction with a exponentially decaying pressure over the rest of the plate. It is known that the short duration pressure pulse was square. These numerical results will be compared with the results of the finite element models developed in this study.

Grobbelaar [35] modelled circular plates subjected to blast loads using the finite element code ABAQUS. This study focused on modelling more realistic loading conditions as previous loading methods were based on assumptions that produced the desired plate deformations, but could not successfully model other loading phenomena. The plates were modelled with 4-noded axisymmetric elements and the clamped boundary conditions simulated by fixing most of the nodes on the surface of the plate where the clamps would be in contact. Part of the clamp contact surface of the plate was not fixed to allow for the plate to bend away from the clamp. The material model of the plate took strain and strain rate dependency into account. The explosive loading was simulated by actually modelling the explosive disc. The explosive disc was modelled with 4-noded axisymmetric elements and its actions governed by the JWL Equation of State. The JWL Equation of State requires the material constants, density, and internal energy per unit volume, for the specific explosive (PE4), as well as the point of detonation. The modelled system can be seen in Figure 2.21. The models developed were verified using experimental data reported by Radford [25]. It was found that the numerical predictions compared well with the experimental results with respect to the mid-point displacement, displacement profiles, and the inflection diameters. The inflection diameter is the diameter of a deformed circular plate where the curvature of the deformed profile changes direction.

An ABAQUS model incorporating the JWL Equation of State for modelling of an explosive was found in the ABAQUS Example Problems Manual [49]. In this model, two concentric steel pipes have the annulus between them filled with high explosive. This system does not directly relate to this study, but the

example clearly demonstrates the usage of the JWL Equation of State for explosives in an ABAQUS model.

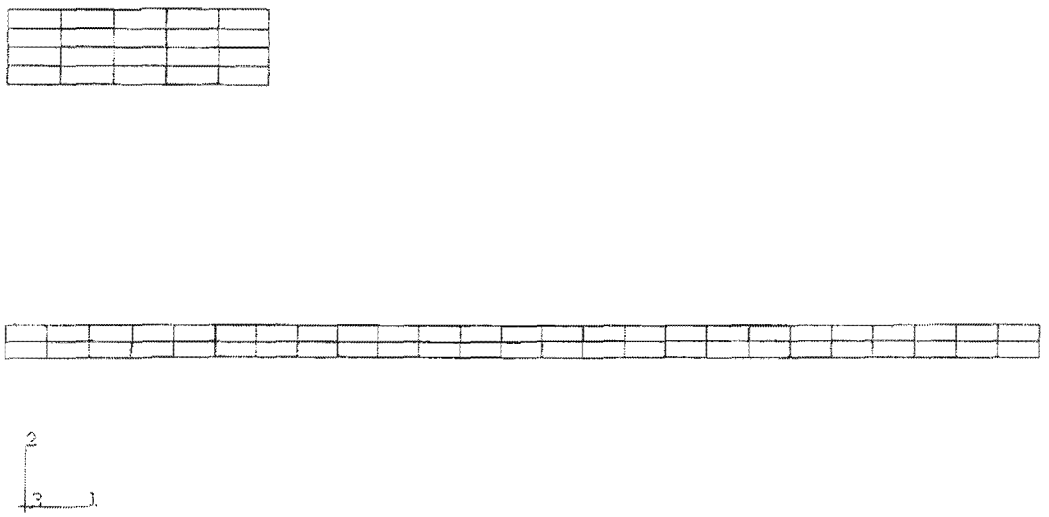

Figure 2.21: The half model of the explosive and flat circular plate modelled with axisymmetric elements (CAX4R), used by Grobbelaar [35].

2.4 Finite Element Methods

Methods of stress and structural analysis can be divided into two main classes - analytical and numerical methods. A brief overview of numerical methods and a more in-depth review of finite element methods was presented by British Gas Research and Technology [36].

2.4.1 Numerical Methods

Numerical methods are employed when:

- the system is too complex to be evaluated with simple calculations and more complex analytical solutions are not available.
- obtaining the results through experimentation would be time consuming and costly.

Numerical methods are frequently used to optimise the design of components and to predict the reactions of these components to different scenarios.

British Gas Research and Technology [36] listed three main categories of numerical methods:

- Numerical solution of the governing equation, e.g. Finite Difference Methods.
- Energy methods, e.g. Rayleigh-Ritz Method.
- Finite element methods (also known as discrete element methods) using matrix algebra.

Figure 2.22 shows the different numerical methods used for structural analysis as presented by British Gas Research and Technology [36].

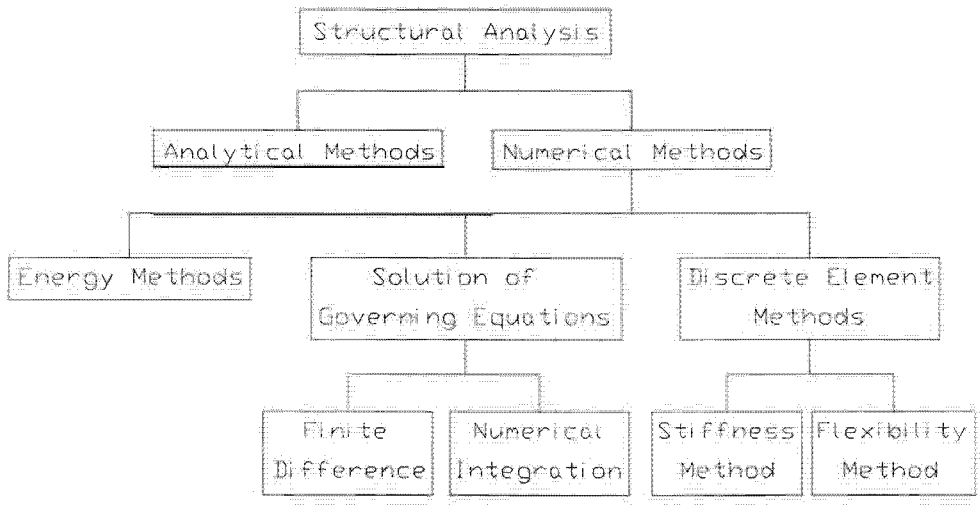

Figure 2.22: Numerical methods used for structural analysis

2.4.1.1 Numerical Solution of a Governing Equation

In the first category an approximate solution of the governing equation is sought by means of a finite difference or numerical integration technique. The problem must be such that these equations can be determined and it is this feature which limits the use of this method.

2.4.1.2 Energy Methods

Energy methods are based on the concept that the work done to a system must be equal to the energy absorbed by the system. The work done is the product of the force applied to the system and the distance through which the force moves. The energy absorbed is calculated from the strain from within the structure. The advantage of the energy methods is that they result in upper bound displacements and are effective in the post-yield region. Their disadvantage is that they give little information concerning dynamic response, are less easy to model in the post-yield region and will generally result in conservative solutions.

2.4.1.3 Finite Element Methods

This study uses finite element methods and therefore these methods will be discussed in more detail.

With the finite element methods the component or structure is assumed to consist of a number of segments or elements joined only at points called nodes. This concept can be applied to an ordinary framed structure where the elements are one-dimensional simple beams such as in Figure 2.23, or it can be applied to an elastic continuum where the elements are two- or three-dimensional structural elements such as in Figure 2.24.

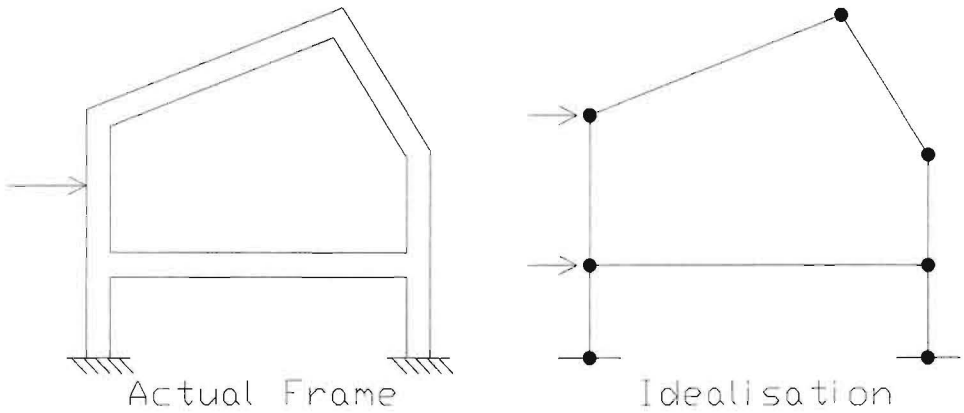

Figure 2.23: Finite element one-dimensional idealisation of a framed structure.

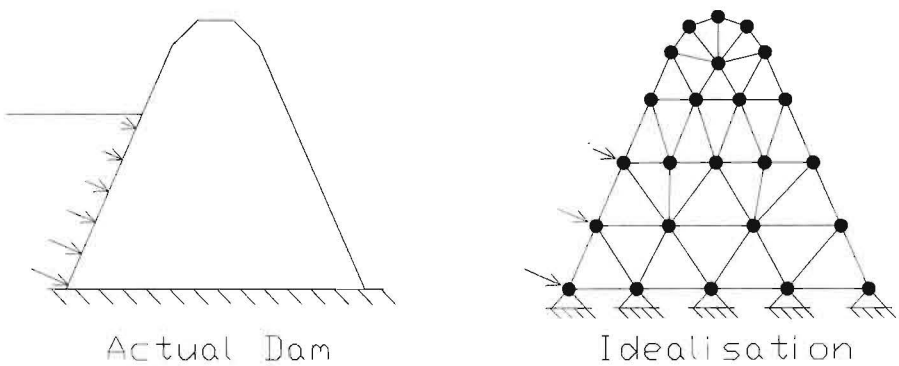

Figure 2.24: Finite element two-dimensional idealisation of a dam.

An advantage of finite element methods is that they have the capacity to incorporate complex material properties into the analysis such as non-linear elasticity or elasto-plasticity.

2.4.1.3.1 Finite Element Methods Fundamentals

The finite element analysis of an elastic continuum may be divided into three phases:

1. Structural idealisation
2. Evaluation of the element properties
3. Structural analysis of the element assemblage

2.4.1.3.1 a) Structural Idealisation

This involves dividing the original system into elements (meshing). It is important that the element division appropriately represents the system because the analysis is performed on this substitute structure and the results will only be valid to the extent that the behaviour of the substitute structure simulates the actual structure. Good results are often obtained with a coarse mesh, and can usually be improved by making use of a finer mesh. However, as the number of elements in the model increase, so the computer time required to obtain a solution also increases.

Regions of the system where there are sharply curved boundaries, detail, or where unknowns are likely to change rapidly, should have a concentration of relatively smaller elements as these are most likely to be the regions of interest and would therefore require a more accurate solution. Where possible, rapid changes in the size of the elements should be avoided and a gradually graded mesh would be better.

The number of elements suitable for a problem cannot be generalised as it is dependent on the particular problem. If possible the meshing should be based on previous reported experience of similar problems. If this is not possible, then a number of analyses involving different mesh sizes should be carried out to test the rate of convergence of a problem.

The loading of the actual system has to also be idealised to suit the idealised structure. The system of loads on the actual structure has to be replaced by an equivalent system of forces at the element nodes. In the case of concentrated loads, the idealisation is made such that a node occurs at the point of application of the load. For distributed loading, the equivalent nodal point loads must be calculated. This can be performed using the principle of virtual work and equating the work done by the actual distributed loads to the work done by the equivalent nodal forces during a virtual displacement.

2.4.1.3.1 b) Evaluation of the Element Properties

The physical property of the element that must be determined is the stiffness or flexibility of the element. The elastic characteristics of an element are represented by the relationship between forces applied to the nodal points and the resulting displacements. This force-displacement relationship is expressed by the flexibility or stiffness matrix of the element. When all the single elements have been separately analysed, the contributions of all the elements are added together and the resulting set of equations solved for the displacements throughout the structure.

Two different approaches are possible within the above system of analysis:

- The Stiffness (displacement) Method.
- The Flexibility (force) Method.

In general it has been found that for highly complex structures of arbitrary form, the displacement method provides the simpler formulation and computer programming task. Therefore this method will be discussed.

Formulation of the stiffness matrix involves:

1. Evaluating the stiffness properties of the individual structural elements, expressing each of them in a convenient local coordinate system, and then formulating a local stiffness matrix, $\left[K^e\right]$, for each element.

2. Transforming the local element stiffness matrices from the local coordinate systems to a global coordinate system.
3. Superpositioning the individual element stiffness contributions to obtain the global stiffness matrix, $[K]$, representing the entire structure. One of the advantages of the Stiffness Method is that the global stiffness matrix is generally sparsely populated and well conditioned. These facts allow efficient solutions to be obtained for large and complex structural systems.

2.4.1.3.1 c) Structural Analysis of the Element Assemblage

Once the global stiffness matrix of the idealised structure has been determined, the equilibrium equations are then assembled expressing the relationship between the applied nodal forces, $\{F\}$, and the resulting nodal displacements, $\{\delta\}$ in the form:

$$\{F\} = [K]\{\delta\}$$

The displacements in the set of simultaneous equations resulting from this relationship cannot yet be solved as there are too many unknowns. To solve this, the boundary conditions of the system are applied by constraining the appropriate displacements, known as degrees of freedom. For example, the nodes at the base of the structures in Figure 2.23 and Figure 2.24, where the structures are fixed to the ground, have all their degrees of freedom constrained. In other words, the degrees of freedom of these nodes are assigned the value zero. Once the boundary conditions have been applied, the unknown displacements can be solved. From the nodal displacements, the element deformations can be computed from kinematic relationships. The element forces can then be determined from the element deformations by means of the element stiffness matrices.

2.4.1.3.2 Dynamic and Non-Linear Systems

The above section on finite element methods fundamentals has outlined the basic building blocks on which the finite element technique is based. If the system being analysed contains any non-linearities or dynamics, the fundamentals discussed so far will be insufficient as they can only cope with static linear problems. A system is considered to be dynamic when the:

- loading varies with time.
- analysis needs to take inertia (acceleration) and damping (velocity) effects into account.

A system is considered to be non-linear when the stiffness matrix or the load vector changes during the analysis. This can occur when there are:

- material properties which are dependent on stress, strain, or temperature.
- large displacements causing additional forces and moments to be introduced to the system.
- geometric non-linearities typically found in tension only or compression only members.
- structural instabilities such as buckling in beam type elements.

The finite element methods fundamentals discussed in the previous section can be expanded to include dynamic and/or non-linear effects.

2.4.1.3.2 a) Dynamic Linear Systems

If a system is dynamic it is necessary to model the system mass via a mass matrix.

The most basic dynamics problems involve modal analysis where the natural frequencies of the system are determined by solving for the system's eigenvalues.

The next level of dynamics problems involve loads which vary sinusoidally against time where the period equals one of the natural modes of the

structure. By factoring and superimposing the results of the different frequencies (using Fourier techniques), it is also possible to model curves of other shapes.

If it is not possible to model the load using a Fourier series, then a time stepping analysis will be necessary. This analysis applies the load in small increments where each increment represents a time step.
Two basic procedures are used:

- Explicit, where the displacements, velocities, and accelerations at time t+1 are calculated purely on the basis of the dynamic equilibrium at the time t. The advantage of this approach is that the calculations to be performed are relatively simple. The disadvantage is that for equilibrium at time t to be representative of that at time t+1, it is necessary to use a small timestep which means the number of calculations are increased.
- Implicit, where the displacements, velocities, and accelerations at time t+1 are calculated on the basis of equilibrium at that time. This requires the solution of sets of equations in order to correctly project forward. Although the solution at each time step is more complex (time consuming), it is possible to use a time step one or two orders of magnitude higher than with the explicit solution.

In both types of analysis it is important to select an appropriate time step if solution accuracy is to be maintained. There are many numerical techniques used to select the appropriate time step.

2.4.1.3.2 b) Static Non-Linear Systems

The main non-linearities encountered are plasticity and large displacements which are both dependent on load levels. They are included in the analysis by ramping up the load in increments. For each increment the stiffness matrix is assumed to be linear and solved using the previously discussed fundamentals. Having solved the linear problem, the stresses are checked. If the yield stress is exceeded then the load vector, stiffness matrix, and

displacements are modified for the next load level to be analysed. In general this requires reformulation and hence solution of the stiffness matrix. As the stiffness matrix is being reformulated it is possible to include modified displacement data.

Non-linear analyses that include plasticity are non-conservative. This results from displacements being locked in as a result of plastic deformation. It is therefore essential that the load increment is kept sufficiently small to prevent "overshoot". This occurs when a particular load step predicts very large plastic deformation when in fact what should be happening is that, at the onset of plasticity, the load effects are redistributed. Load redistribution can only be modelled by modifying the stiffness matrix.

In practice, a large number of numerical techniques have been developed in order to permit the load increment to be as large as possible whilst preventing overshoot. This is necessary in order to minimise the number of matrix solutions.

2.4.1.3.2 c) Dynamic and Non-Linear Systems

Dynamic non-linear systems basically involve a combination of the features discussed under the two headings above. A time stepping procedure is required to solve these problems. These systems can result in further non-linearities which vary against time instead of load level such as strain rate and temperature effects.

2.4.1.3.3 Programming

During the last 30 years many finite element programs have been developed for the use of engineering design offices and research establishments. It is important to realise that a finite element program is a sophisticated analysis tool which has to be mastered in order to be confident in the results.

In the past, the use of finite element methods has been restricted by the unavailability of suitable computers and competent programmers. The last 15 years have seen a dramatic change in this situation because:

- the costs of computers have been lowered so that they are in the budget range of small to medium companies.
- a professional workforce educated in the capabilities of finite element methods and other numerical methods has been built up.
- the speed of computers has greatly improved with advanced technology so that analyses that used to take days or weeks to run can now be run in reasonable times.
- the storage capabilities of computers have greatly improved with advanced technology so that large problems and their results with sizes possibly in the range of 100's of megabytes, can be stored.

It is envisaged that in the near future, computer limitations shall no longer be a restriction on the use of finite element methods, but instead its use will only be limited by the availability of trained and experienced programmers who have sufficient knowledge of the physics of the problems being modelled [36].

3. ABAQUS Overview

The systems to be modelled involve shaped explosive charges exploding V-shaped steel plates. The finite element methods package, ABAQUS, was used as it is a good all-purpose package and can model the dynamics and non-linear aspects of these systems. The investigator alternated between versions 5.8 and 6.2 owing to the advantages (such as improved capabilities) and disadvantages (such as bugs) of the different versions, but version 6.2 was mainly used.

3.1 Aspects of ABAQUS Relevant to this Study

The ABAQUS package includes:

- ABAQUS/Standard - a general-purpose finite element program.
- ABAQUS/Explicit - an explicit dynamics finite element program.
- ABAQUS/CAE - an interactive preprocessor that can be used to create finite element models and the associated input files for ABAQUS.
- ABAQUS/Viewer - a menu-driven interactive postprocessor that provides X-Y plots, animations, contour plots, and tabular outputs of results from ABAQUS/Standard and ABAQUS/Explicit.

The preprocessor, ABAQUS/CAE, is only available in version 6.2 and was used extensively as it allows models to be easily created through a graphic interface. ABAQUS/CAE then compiles an input deck from the model which can be submitted to ABAQUS/Standard or ABAQUS/Explicit for analysis. ABAQUS/CAE greatly saves time and effort as the mesh and input decks do not have to be generated manually and troubleshooting of the input deck is no longer necessary.

ABAQUS/Explicit was the finite element program used for the study as it was best suited to the high-velocity dynamic non-linear systems which had to be modelled. This is because ABAQUS/Explicit is computationally efficient for

the analysis of large models with relatively short dynamic response times and for the analysis of extremely discontinuous events.

3.1.1. The Analysis Procedure

The explicit dynamics analysis procedure is based upon the implementation of an explicit integration rule together with the use of diagonal ("lumped") element mass matrices. This analysis method is considered explicit because the kinematic state is advanced using known values of velocity and acceleration from the previous increment. The method satisfies the dynamic equilibrium equations at the beginning of the increment, t. The accelerations calculated at time t are used to advance the velocity solution to time $t+\frac{\Delta t}{2}$ and the displacement solution to time $t+\Delta t$. The accelerations at the beginning of a time increment are calculated from

$$\ddot{u}^N_{(i)} = \left(M^{NJ}\right)^{-1}\left(P^J_{(i)} - I^J_{(i)}\right) \qquad (3.1)$$

where

$M^{NJ} = mass\ matrix$

$P^J = applied\ load\ vector$

$I^J = the\ \text{int}ernal\ force\ vector$

$u^N = a\ \text{deg}ree\ of\ freedom$

$i = time\ increment\ number\ in\ a\ step$

The accelerations are then substituted into the integrated equations of motion for the body. The equations of motion are integrated using the explicit central difference integration rule

$$\dot{u}^N_{\left(i+\frac{1}{2}\right)} = \dot{u}^N_{\left(i-\frac{1}{2}\right)} + \frac{\Delta t_{(i+1)} + \Delta t_{(i)}}{2}\ddot{u}^N_{(i)}$$

$$u^N_{(i+1)} = u^N_{(i)} + \Delta t_{(i+1)}\dot{u}^N_{\left(i+\frac{1}{2}\right)}$$

Each time increment in this explicit dynamics procedure is relatively inexpensive compared to the direct-integration dynamic analysis procedure available in ABAQUS/Standard because a solution for a set of simultaneous equations is not required. The non-linear dynamic response of ABAQUS/Standard is implicit, meaning that the equilibrium equations must be solved at each time increment, using the iterative Newton's Method.

Even though the explicit integration rule is simple it is not the main reason for the computational efficiency of this explicit dynamic analysis method. The use of diagonal element mass matrices when calculating the increment acceleration in Equation 3.1 provides great computational efficiency as these matrices are easy to invert and because the vector multiplication of the mass inverse by the inertial force requires only n operations, where n is the number of degrees of freedom in the model. The explicit procedure requires no iterations and no tangent stiffness matrix.

The explicit procedure integrates with respect to time by using many small time increments. It is important that these time increments are suitably small to ensure that the solution is stable and accurate, but not too small that the analysis time is excessive. ABAQUS/Explicit automatically selects the time incrementation by default, but incrementation can be also be specified by the user. The stability limit of the time increment is given as

$$\Delta t \leq \frac{2}{\omega_{\max}} \qquad \textit{without damping}$$

$$\Delta t \leq \frac{2}{\omega_{\max}}\left(\sqrt{1+\xi_{\max}^2}-\xi_{\max}\right) \qquad \textit{with damping}$$

where

$\omega_{\max}$ = *highest frequency of system*

$\xi_{\max}$ = *fraction of critical damping in highest frequency* mode

The size of the stable time increment can be estimated as the shortest time it would take a dilatational wave to travel across any element in the mesh

$$\Delta t \approx \frac{L_{\min}}{c_d}$$

where

$L_{\min} = smallest\ element\ \text{dim}ension$
$c_d = dilatational\ wave\ speed$

This estimate is dependent on element size and therefore indicates that the mesh selection will have a significant effect on the number of time increments and therefore the computational run time of an analysis.
In many cases, this estimate is not conservative (safe) and the actual stable time increment chosen by ABAQUS/Explicit will be less than the estimate by a factor between $1/\sqrt{2}$ and 1 in a two-dimensional model, and between $1/\sqrt{3}$ and 1 in a three-dimensional model [37].

3.1.2 Modelling of Mechanical Properties

3.1.2.1 Modelling of Elastic-Plastic Behaviour

Most materials initially respond elastically. Elastic behaviour means that the deformation is fully recoverable when the load is removed so that the specimen returns to its original shape. If the load reaches the magnitude of the yield load of the material, the deformation is no longer fully recoverable and part of the deformation will remain when the load is removed. When deformation is not fully recoverable, plastic behaviour is being exhibited. For ABAQUS to model this plastic behaviour, it still requires an elasticity definition to deal with the recoverable part of the strain.

The plasticity models in ABAQUS/Explicit are "incremental" theories in which the mechanical strain rate is decomposed into an elastic part and a plastic part. Incremental plasticity models are usually formulated in terms of:

- a *yield surface*, which generalises the concept of "yield load" into a test function that can be used to determine if the material responds purely elastically at a particular state of stress, temperature, etc.
- a *flow rule*, which defines the plastic deformation that occurs if the material point is no longer responding purely elastically.
- evolution laws that define the *hardening*. Hardening occurs when the yield/and or flow definitions change as inelastic deformation occurs.

The flow rule uses associated plastic flow. Therefore, as the material yields, the inelastic deformation rate is in the direction of the normal to the yield surface (the plastic deformation is volume invariant). The associated flow models in ABAQUS used with the smooth Mises or Hill yield surface generally predict material behaviour accurately [37].

The V-plates in the models in this study exhibit the elastic-plastic behaviour described above. The elastic behaviour of the steel V-plates is considered to be linear and the only inputs required by ABAQUS for the elasticity is Young's modulus and Poisson's ratio. The plasticity of the steel can be defined in ABAQUS by just the initial yield stress of the steel at 0% plastic strain. These material properties were obtained from uniaxial tensile tests conducted on the steel at a quasi-static rate at room temperature. But there are further factors that have to be considered which could significantly affect the mechanical behaviour of the steel such as yield hardening, strain rate sensitivity, and temperature dependency. These factors affect the Young's modulus and yield stress of the steel.

3.1.2.2 Yield Hardening

ABAQUS offers three types of hardening: perfect plasticity, isotropic hardening, and Johnson-Cook.

3.1.2.2.1 Perfect Plasticity

Perfect plasticity means that no hardening occurs as the yield stress does not change with plastic strain. This plasticity can be defined in tabular form for a range of temperatures and field variables. Only a single yield stress value is required to specify the onset of yield for each temperature and field variable.

3.1.2.2.2 Isotropic Hardening

Isotropic hardening means that the yield surface changes size uniformly in all directions such that the yield stress increases (or decreases) in all stress directions as plastic straining occurs. This is the default type of hardening in ABAQUS and ABAQUS can provide an isotropic hardening model if hardening is not defined. This model is useful in cases involving gross plastic straining or in cases where the straining at each point is essentially in the same direction in strain space throughout the analysis.
If isotropic hardening is defined, the yield stresses and corresponding plastic strain must be given in tabular form. To find a yield stress at a given state, ABAQUS interpolates from the data table, and for plastic strains greater than the last value in the data table, the yield stress remains constant.

3.1.2.2.3 Johnson-Cook Hardening

This is a particular type of isotropic hardening where the yield stress is given as an analytical function of equivalent plastic strain, strain rate, and temperature. This hardening law is suited for modelling high-rate deformation of many materials including most metals [37].

3.1.2.3 Rate Dependence

As strain rate increases, many materials show an increase in their yield strength. When strain rates are high, such as in this study, this effect becomes significant. There are two ways to introduce a strain-rate-dependent yield stress, either by direct tabular data or yield stress ratios.

3.1.2.3.1 Direct Tabular Data

Experimentally determined stress versus strain curves of the material can be provided as tables of yield stress values versus equivalent plastic strain at different equivalent plastic strain rates, $\dot{\bar{\varepsilon}}^{pl}$. A table is required for each different strain rate.

3.1.2.3.2 Yield Stress Ratios

This option requires that the ratio of dynamic yield stress over static yield stress, $\frac{\sigma}{\sigma_0}$, be determined for different equivalent plastic strain rates. The dynamic yield stress, σ, can then be determined for the strain rate present, as the static yield stress of the material has been given by the user. The three methods used to determine the yield stress ratios are: the Overstress Power law, the tabular method, and the Johnson-Cook Method.

3.1.2.3.2 a) The Overstress Power Law

The Overstress Power Law is also known as the Cowper-Symonds equation. This is the default strain rate sensitivity model in ABAQUS.
The Cowper-Symonds relationship is a very popular strain rate sensitivity model as this model can produce reasonably accurate predictions for a wide range of materials and for a wide range of strain rates.
The Cowper-Symonds equation is:

$$\dot{\bar{\varepsilon}}^{pl} = D\left(\frac{\sigma}{\sigma_0} - 1\right)^n \qquad for\ \sigma \geq \sigma_0 \qquad equation\ ?$$

where

$\dot{\bar{\varepsilon}}^{pl} = equivalent\ plastic\ strain\ rate$

$\sigma_0 = static\ yield\ stress$

$\sigma = dynamic\ yield\ stress$

$D = material\ parameter$

$n = material\ parameter$

The material parameters, D and n, can be defined as functions of temperature and possibly other predefined field variables in ABAQUS.

3.1.2.3.2 b) The Tabular Method

The yield stress ratio can be entered in tabular form as a function of the equivalent plastic strain rate, temperature and other field variables.

3.1.2.3.2 c) Johnson-Cook Rate Dependence

The Johnson-Cook rate dependence has the form:

$$\dot{\bar{\varepsilon}}^{pl} = \dot{\varepsilon}_0 \exp\left[\frac{1}{C}\left(\frac{\sigma}{\sigma_0}\right) - 1\right] \qquad for\ \sigma \geq \sigma_0$$

where

$\dot{\varepsilon}_0 = material\ constant$

$C = material\ constant$

The material constants, $\dot{\varepsilon}_0$ and C, do not depend on temperature and are assumed not to depend on predefined field variables [37].

3.1.2.4 Temperature Dependence

Many of the material properties of wide range of materials are dependent on temperature. The systems being modelled in this study are assumed to undergo adiabatic heating and therefore this type of heating will be discussed.

3.1.2.4.1 Adiabatic Heating

Adiabatic heating occurs where plastic deformation causes heating, but the event is so rapid that this heat has no time to diffuse through the material. Because of this, no allowance is made for conduction of heat in an adiabatic analysis.

An adiabatic stress analysis requires that a material's density, specific heat, and inelastic heat fraction (fraction of inelastic dissipation rate that appears as

heat flux) be specified. The temperature increase in an analysis is calculated directly at the material integration points according to the adiabatic thermal energy increases caused by plastic deformation. Temperature is not a degree of freedom in this type of analysis [37]. In an adiabatic analysis plastic straining gives rise to a heat flux per unit volume of:

$$r^{pl} = \eta\sigma:\dot{\varepsilon}^{pl}$$

where

$r^{pl} = heat\ flux$

$\eta = inelastic\ heat\ fraction$

$\sigma = stress$

$\dot{\varepsilon}^{pl} = plastic\ strain\ rate$

The heat equation solved at each integration point is:

$$\rho c(T)\dot{T} = r^{pl}$$

where

$\rho = material\ density$

$c(T) = specific\ heat$

$T = temperature$

3.1.2.5 The Modelling of Failure

Two types of failure models are offered in ABAQUS/Explicit for the Mises and Johnson-Cook plasticity models. One is the shear failure model, the other is the tensile failure model

3.1.2.5.1 Shear Failure Model

This failure model provides a simple failure criterion that is suitable for high-strain-rate deformation of many materials including most metals.

Shear failure is considered to have occurred when a certain amount of equivalent plastic strain is reached as in reality the material will have most likely failed just before reaching this plastic strain. The shear failure model is applicable mainly to high-strain-rate truly dynamic problems.
This failure model offers two choices when the failure criterion is met: one, involves the removal of elements from the mesh as a result of tearing or ripping of the structure, the other does not involve removal of the elements, but allows them to take hydrostatic compressive stress only.

3.1.2.5.2 Tensile Failure Model

This failure model uses the hydrostatic pressure stress as a failure measure to model dynamic spall or a pressure cutoff. It offers a number of failure choices when the failure criterion is met. The failed elements can be deleted from the mesh, or they can remain to allow for brittle or ductile type failure for the deviatoric and hydrostatic parts of stresses. This failure model is also suitable for high-strain-rate deformation of metals and is applicable to truly dynamic problems [37].

3.1.2.6 Equations of State

The equations of states in ABAQUS/Explicit are models of elastic behaviour. They provide a hydrodynamic material model in which the material's volumetric strength is determined by an equation of state.

3.1.2.6.1 The Energy Equation

The equation for conservation of energy equates the increase in internal energy per unit mass to the rate at which work is being done by the stresses and the rate at which heat is being added. In the absence of heat conduction the energy equation can be written as:

$$\rho\frac{\partial E_m}{\partial t} = (p - p_{bv})\frac{1}{\rho}\frac{\partial \rho}{\partial t} + S:\dot{\varepsilon} + \rho\dot{Q} \qquad (3.1)$$

where

p = *pressure stress*

p_{bv} = *pressure stress due to bulk viscosity*

S = *deviatoric stress tensor*

$\dot{e}$ = *deviatoric part of strain rate*

$\dot{Q}$ = *heat rate per unit mass*

E_m = *internal energy per unit mass*

ρ = *current density*

3.1.2.6.2 The Equation of State

The equation of state assumes that the pressure is a function of the current density and the internal energy per unit mass which defines all the equilibrium states that can exist in a material. This relationship is shown in equation 3.2:

$$p = f(\rho, E_m) \tag{3.2}$$

The pressure and internal energy can be solved simultaneously by ABAQUS/Explicit from the equation of state and the energy equation at each material point. When an equation of state is used to model a material, an adiabatic condition is always assumed, unless a dynamic coupled temperature-displacement procedure is used.

The internal energy can be eliminated from the equation of state relationship in Equation 3.2 to obtain a p versus $1/\rho$ relationship that is unique to the material described by the equation of state model. This unique relationship is called the Hugoniot curve and is the locus of pressure-current volume ($p-V$) states achievable behind a shock. Figure 3.1 shows a Hugoniot curve.

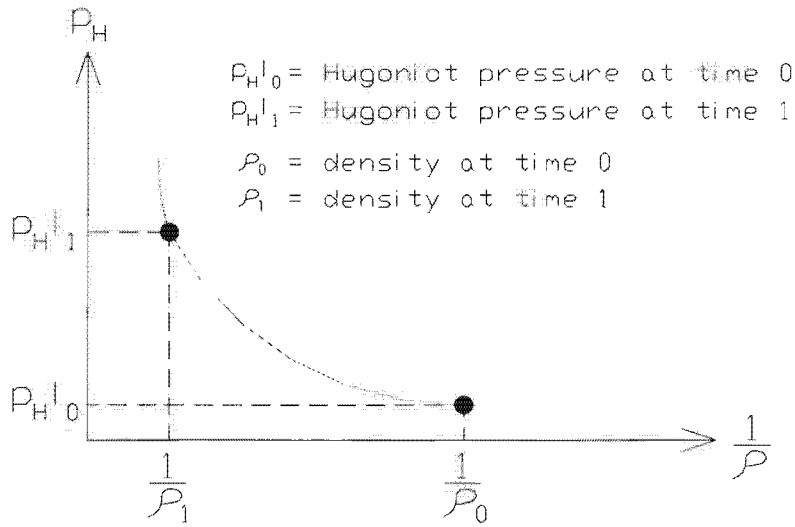

Figure 3.1: A schematic representation of a typical Hugoniot curve.

The Hugoniot pressure, p_H, is a function of density only and can be defined, in general, from fitting experimental data.

3.1.2.6.2 a) The Mie-Gruniesen Equations of State

The Mie-Gruniesen equation of state can be seen in Equation 3.3:

$$p = p_H\left(1-\frac{\Gamma_0\eta}{2}\right)+\Gamma_0\rho_0 E_m \qquad (3.3)$$

where

$$\eta = 1-\frac{\rho_0}{\rho} \qquad (3.4)$$

and where

p_H = *Hugoniot pressure*
Γ_0 = *material constant*
ρ_0 = *reference density*

The derivation of Equation 3.3 can be found in the ABAQUS manual [38].

3.1.2.6.2 a) i) The Linear U_s - U_p Hugoniot Form

A common fit to the Hugoniot data is given by:

$$p_H = \frac{\rho_0 c_0^{\,2} \eta}{(1 - s\eta)^2} \tag{3.5}$$

where c_0 and s define the linear relationship between the linear shock velocity, U_s, and the particle velocity, U_p, as follows:

$$U_s = c_0 + sU_p \tag{3.6}$$

Substituting Equation 3.5 into Equation 3.3 yields the linear U_s - U_p Hugoniot form which is:

$$p = \frac{\rho_0 c_0^{\,2} \eta}{(1 - s\eta)^2}\left(1 - \frac{\Gamma_0 \eta}{2}\right) + \Gamma_0 \rho_0 E_m \tag{3.7}$$

3.1.2.6.2 a) ii) The Jones-Wilkins-Lee Equation of State

The Jones-Wilkins-Lee (JWL) equation of state models the pressure generated by the release chemical energy in an explosive. This model is implemented by using a programmed burn which means that the reaction and initiation of the explosive is not determined by the shock in the material. Instead, the initiation time is determined by a geometric construction using the detonation wave speed and the distance of the material point from the detonation points. The JWL equation of state can be written in terms of the initial energy per unit mass, E_{m_0}, as:

$$p = A\left(1 - \frac{\omega\rho}{R_1\rho_0}\right)e^{-R_1\frac{\rho_0}{\rho}} + B\left(1 - \frac{\omega\rho}{R_2\rho_0}\right)e^{-R_2\frac{\rho_0}{\rho}} + \frac{\omega\rho^2}{\rho_0}E_{m_0} \tag{3.8}$$

where A, B, R_1, R_2, and ω are material constants.

ABAQUS/Explicit calculates the arrival time of the detonation wave at a material point, t_d^{mp}, as the detonation delay time of the nearest detonation point plus the time it takes for the detonation wave to travel from the nearest detonation point to the material point. The time it takes for the detonation wave to travel from the nearest detonation point to the material point is calculated by dividing the distance from the material point to the nearest detonation point by the detonation wave speed. The equation for calculating the arrival time of the detonation wave can be seen in Equation 3.9:

$$t_d^{mp} = \min\left[t_d^N + \sqrt{\left(x^{mp} - x_d^N\right) \cdot \left(x^{mp} - x_d^N\right)} \Big/ C_d \right] \tag{3.9}$$

where

x^{mp} = *vector position of material point*

x_d^N = *vector position of* N^{th} *detonation point*

t_d^N = *detonation delay time of* N^{th} *detonation point*

C_d = *detonation wave speed of explosive material*

Any number of detonation points can be defined for the explosive material. Coordinates of the points must be defined along with any delay time. Each material point responds to the first detonation point it sees. In other words, because there are multiple detonation points, the minimum arrival time of the detonation wave out of all the arrival times of the N detonation points, is selected to be the arrival time.

Another calculation which is necessary to model the detonation, is that of the burn fraction. The burn fraction is computed so that the burn wave is spread over several elements. The equation for the burn fraction is:

$$F_b = \min\left[1, \frac{\left(t - t_d^{mp}\right) C_d}{B_s l_e} \right] \tag{3.10}$$

where

$B_s = constant\ that\ controls\ width\ of\ burn\ wave\ (set\ at\ 2.5)$

$l_e = characterstic\ length\ of\ element$

If the time, t, is less than t_d^{mp}, the pressure is zero in the explosive; otherwise, the pressure is given by the product of F_b and the pressure determined from the JWL equation of state in Equation 3.8.

A further consideration is that explosive materials generally have some nominal volumetric stiffness before detonation. It may be useful to incorporate this stiffness when elements modelled with the JWL equation of state are subjected to stress before initiation of detonation by the arriving detonation wave. To take this into account, the user can define the pre-detonation bulk modulus, K_{pd}. The pressure will be computed from the volumetric strain and bulk modulus until detonation, at which time the pressure will be determined by the JWL equation of state.

3.1.2.6.2 b) The Ideal Gas Equation of State

An ideal gas equation of state can be written in the form of:

$$p + p_A = \rho R(\theta - \theta^Z) \tag{3.11}$$

where

$p_A = ambient\ pressure$

$R = gas\ constant$

$\theta = current\ temperature$

$\theta^Z = absolute\ zero\ on\ temperature\ scale\ being\ used$

This equation of state is an idealisation to real gas behaviour and can be used to model any gases approximately under appropriate conditions (e.g. low pressure and high temperature) and where the value of R is constant.

One of the important features of an ideal gas is that its specific energy depends only on its temperature, therefore, the specific energy can be integrated numerically as:

$$E_m = E_{m_0} + \int_{\theta_0 - \theta^Z}^{\theta - \theta^Z} c_v(T)dT \qquad (3.12)$$

where

E_{m_0} = *initial specific energy at the initial temperature*

θ_0 = *initial temperature*

c_v = *specific heat at constant volume*

When modelling with an ideal gas equation of state ABAQUS/Explicit assumes an adiabatic condition unless otherwise specified where the temperature increase is calculated directly at the material integration points. This is done according to the adiabatic thermal energy increase caused by the work pdv, where v is the specific volume.

3.1.3 Modelling of Contact Interaction

3.1.3.1 Pure and Balanced Master-Slave Contact Surfaces

3.1.3.1.1 Pure Master-Slave Contact

By default, ABAQUS/Explicit strictly enforces contact constraints using a kinematic, predictor/corrector contact algorithm. Alternatively the user can choose a penalty contact algorithm which has a weaker enforcement of contact constraints, but has other advantages. Generally, contact constraints in a finite element model are applied in a discrete manner, meaning that for hard contact a node on one surface is constrained not to penetrate the other surface. In ABAQUS the node with the constraint is on a slave surface, and the surface with which it interacts is called the master surface. The nodes on the master surface can, in principle, penetrate the slave surface unhindered. When a pair of contact surfaces is subjected to these conditions, it is called a pure master-slave contact pair. If these conditions produce undesirable

behaviour, an alternative method for defining contact between two surfaces is to use balanced master-slave contact.

3.1.3.1.2 Balanced Master-Slave Contact

For balanced master-slave contact ABAQUS/Explicit calculates the contact constraints twice for a contact pair, in the form of acceleration corrections for the kinematic contact algorithm or penalty forces for the penalty contact algorithm: once with the first surface acting as the master surface and once with the second surface acting as the master surface. The weighted average of the two corrections (or forces) is applied to the contact pair.

Balanced master-slave contact is more expensive computationally than pure master-slave contact, but for hard contact it minimises the penetration of the contacting bodies, and thus provides more accurate results in most cases.

Care should be taken when selecting the balanced master-slave option if the densities of the two contacting objects are greatly different. This is because contact-induced noise can occur if a surface on the much denser body is at all weighted as a slave surface [38].

3.1.3.2 Kinematic and Penalty Contact Algorithms

3.1.3.2.1 Kinematic Contact Algorithm

This is the default algorithm that ABAQUS/Explicit uses to enforce contact constraints, which doesn't affect the stable time increment as it is a predictor/corrector algorithm.

The models in this study involve pure master-slave contact between two element based surfaces so the kinematic algorithm will be described for these parameter selections.

ABAQUS/Explicit advances the kinematic state of the model for each increment of the analysis, into a predicted configuration without considering the contact conditions. The slave nodes of the predicted configuration which

penetrate the master surface are then determined. The depth of each slave node's penetration, the mass associated with it, and the time increment are used to calculate the resisting force required to oppose penetration. For hard contact, this is the force which, had it been applied during the increment, would have caused the slave node to exactly contact the master surface.

The resisting forces of all the slave nodes are then distributed to the nodes on the master surface. The mass of each contacting slave node is also distributed to the master surface nodes and added to their mass to determine the total inertial mass of the contacting interfaces. ABAQUS/Explicit uses these distributed forces and masses to calculate an acceleration correction for the master surface nodes. Acceleration corrections for the slave nodes are then determined using the predicted penetration for each node, the time increment, and the acceleration corrections for the master surface nodes. These acceleration corrections are then used to obtain a corrected configuration in which the contact constraints are enforced.

The kinematic contact algorithm strictly enforces contact constraints and conserves momentum. To achieve these qualities with a discretised model, some energy is absorbed from the impacting nodes by the contact algorithm upon impact which is plastic, when the hard, kinematic algorithm is used. As the mesh is refined this energy loss is reduced because the mass and kinetic energy of the leading impacting nodes become less significant. Energy losses are insignificant in most models, but can be significant in high-speed impacts, where high mesh refinement near the contact interface is recommended.

3.1.3.2.2 Penalty Contact Algorithm

The penalty contact algorithm results in less stringent enforcement of contact constraints than the kinematic contact algorithm, but the penalty algorithm can model some types of contact that the kinematic contact algorithm cannot, such as contact between rigid surfaces. Since the penalty algorithm introduces additional stiffness behaviour into a model, this stiffness can

influence the stable time increment. ABAQUS/Explicit automatically accounts for the effect of the penalty stiffnesses in the automatic time incrementation, although this effect is usually small. For hard penalty contact, default penalty stiffnesses are chosen such that the stable time increments of the contact surface elements are effectively reduced by 4% for increments in which contact forces are being transmitted. As before, the models in this study involve pure master-slave contact between two element based surfaces so the penalty algorithm will be described for these parameter selections.

The penalty contact algorithm searches for slave node penetrations in the current configuration. Penalty contact and softened kinematic contact introduce numerical softening to the contact enforcement comparable to adding elastic springs to the contact interface, which means that these algorithms do not dissipate energy upon impact (the energy stored in the springs is recoverable).

This numerical softening involves contact forces that are a function of the penetration distance. These forces are applied to the slave nodes to oppose the penetration, while equal and opposite forces act on the master surface at the penetration point. The master surface contact forces are distributed to the nodes of the master face being penetrated. The "spring" stiffness that relates the contact force to the penetration distance is chosen automatically by ABAQUS/Explicit for hard penalty contact, such that the effect on the time increment is minimal yet the allowed penetration is not significant in most analyses. The user can specify a factor by which to scale the default penalty stiffnesses, but if a user-defined softened contact relationship is used, the penalty stiffnesses are not scaled by this parameter. If the default penalty stiffnesses are overridden by a penalty scale factor or softened contact behaviour, the time increment is modified based on the maximum stiffness active in the contact interface. This scaling of the default penalty stiffnesses may affect the automatic time incrementation. Use of a large-scale factor is likely to increase the computational time required for an analysis because of

the reduction in the time increment that is necessary to maintain numerical stability.

If the overall stable time increment is not controlled by elements on the contact interface, the penalty contact algorithm usually will not affect the time increment. As with the pure master-slave kinematic contact algorithm, there is no resistance to master surface nodes penetrating slave surface faces with the pure master-slave penalty contact algorithm. Using a sufficiently refined mesh on the slave surface will help correct the problem [38].

3.1.3.3 Hard and Soft Contact

3.1.3.3.1 Hard Contact

The default contact pressure-overclosure model involves transmitting any contact pressure between surfaces (such as determined by the kinematic or penalty contact algorithm) when the surfaces are in contact. Separated surfaces are considered to come into contact when the clearance between them reduces to zero. The surfaces separate if the contact pressure reduces to zero. With penalty contact enforcement, the "hard" contact model is approximated by automatically determined stiff linear behaviour. This contact minimises penetration of slave nodes into the master surface.

3.1.3.3.2 Soft Contact

Soft contact functions in a similar manner to penalty contact as they both enforce contact constraints using resistance which is a function of distance between the surfaces. This distance comprises of overclosure distance for the penalty contact algorithm, while the distance for soft contact can involve both overclosure and surface separation distance. A difference between the two contact methods is that penalty contact applies a resisting force to the nodes of the contacting surfaces while soft contact applies a resisting pressure to the contacting surfaces. Soft contact can also allow contact pressures to be transmitted between two surfaces when they are still separated. Three types of soft contact relationships are available in ABAQUS/Explicit. The pressure over-closure relationship can be prescribed

by using a linear law, an exponential law, or a piecewise linear law [38]. Figure 3.2 demonstrates these laws.

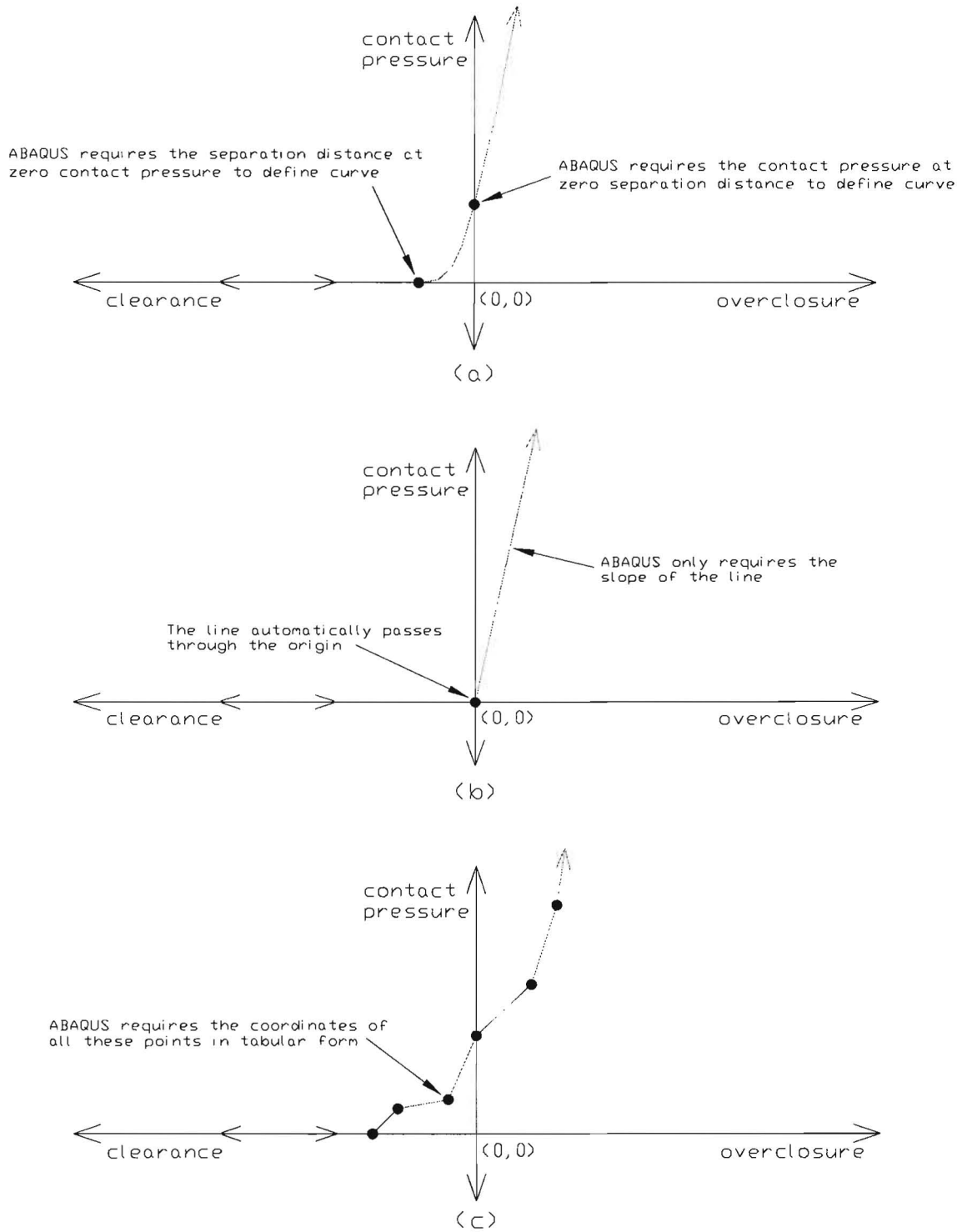

Figure 3.2: Diagrams of the three pressure-overclosure relationships; (a) linear relationship; (b) exponential relationship; (c) piecewise linear relationship.

3.1.3.4 Separation and No Separation of Surfaces

The ABAQUS default selection is for the surfaces to separate after contact. If no separation is chosen, then ABAQUS uses the contact pressure-overclosure model that prevents surfaces from separating once they have come into contact. This option is often used with the rough friction model to model non-intermittent, rough frictional contact. Using this combination of surface interaction models causes surfaces to remain fully bonded together (no separation and no tangential sliding) once they contact, even if the contact pressure between them is tensile. If a softened contact model is specified with no separation, the pressure-overclosure model will include tensile and not purely compressive behaviour as before. The soft contact exponential relationship cannot be used in conjunction with the no separation option [38].

4. The Finite Element Model

4.1 Selection of Model

Two versions of the system involving shaped explosive charges exploding V-plates, had to be modelled:

1. *A V-plate with a round rod of explosive* positioned slightly above the mid-point of the ridge of the V formed by the joining of the two halves of the V-plate. The longitudinal axis of the explosive rod is in line with the ridge. A thin round rod of explosive is also attached to this main rod and acts as a fuse. The V-plate has flanges on the edges of the two tips of the V so that the plate can be clamped. Figure 4.1 shows this system.

2. *A V-plate with a disc of explosive* positioned slightly above the mid-point of the ridge of the V-plate. Figure 4.2 shows this system.

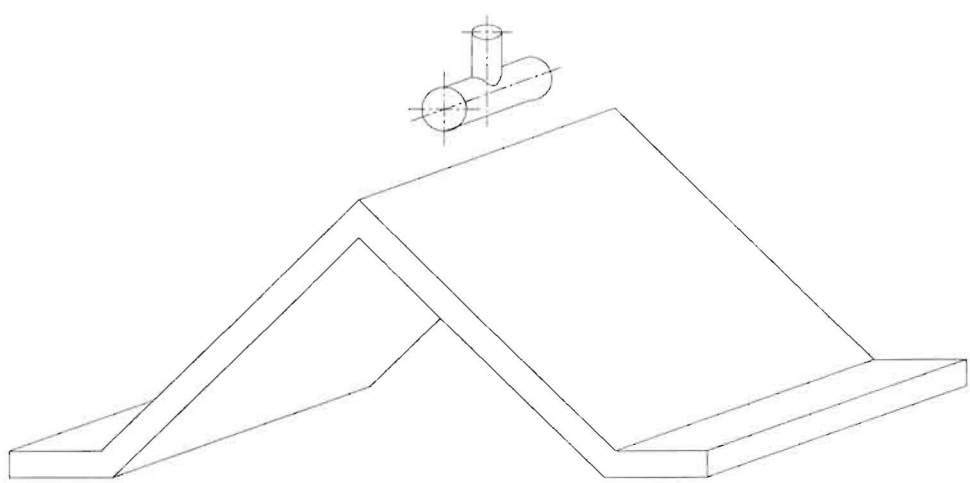

Figure 4.1: Diagram of V-Plate with Explosive Rod and Fuse

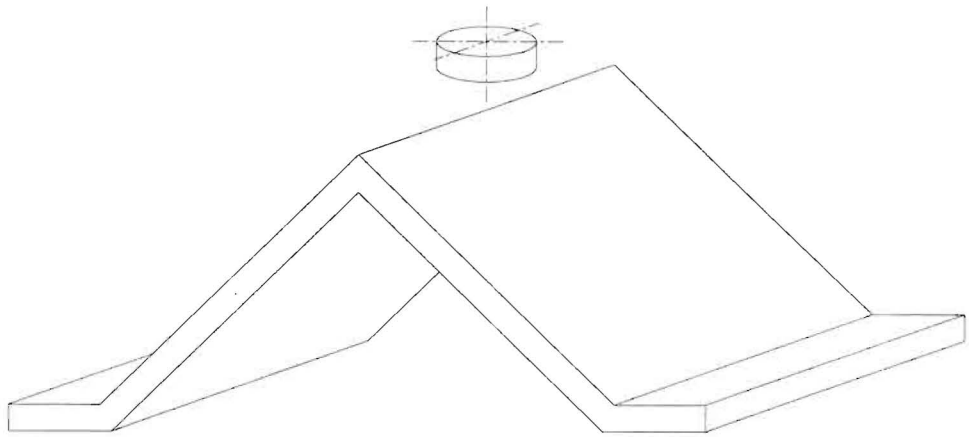

Figure 4.2: Diagram of V-Plate with Explosive Disc

Verification of a numerical model is very important as the results could appear to be accurate but actually be completely incorrect. This is why two versions of the system have to be modelled even though the second system involving the disc of explosive is the only version of interest as it simulates a landmine detonation.

Experimentation has already been conducted on the first system containing the explosive rod by Lockley [43] but not on the second system containing the explosive disc. The processed results of these experiments can be compared with the results obtained from the numerical model of the rod explosive system. The results will be comparable because the geometry, boundary conditions, and material properties of the rod explosive version of the system will be modelled to be identical to those used in the experiments.

If the results are similar, the ABAQUS model will be verified as it produces realistic results. This then indicates that similar numerical models, such as the model involving the explosive disc, should also produce realistic results.

To maximise the likelihood of the disc version producing accurate results if the rod version is verified, the geometry, boundary conditions, and material

properties of the disc explosive version of the system will be modelled to be identical to the rod explosive version.

4.1.1 Modelling the Explosive

In the past, the explosives in systems similar to these were mainly represented in the numerical models by an assumed initial velocity or pressure profile applied to the plates for a pulse duration. This meant that the explosive charge itself was never actually modelled. These loading assumptions have only been formulated for simple explosive shapes such as a disc, so this approach is currently limited to models containing these simply shaped explosives. The loading assumptions are also only capable of producing the desired plate deformations but not other loading phenomena. To use the pressure profile method, experiments have to be conducted to determine the amount of impulse transferred to the object being exploded.

The Jones-Wilkins-Lee Equation of State (JWL EOS) has more recently been used to model the actual explosives [32, 35] and is used to model the explosives in this study. The JWL Equation of State approach is used in the hope of obtaining more realistic results for all the explosive loading phenomena, and to allow systems containing explosives with more complex shapes, to be accurately modelled. This approach also doesn't require any experiments to be conducted as is required for the pressure profile method.

4.1.2 Planes of Symmetry

When a system involves a flat circular plate and a circular disc of explosive it can be modelled axisymmetrically as the section profile of the system does not change when sweeping around a single axis. If a similar system contains a plate or explosive of another shape (such as a square) it has to be modelled in three dimensions. The models in this study had to be created in three dimensions owing to the geometry of the V-plate and the rod explosive. Three dimensional modelling of the systems mean more elements will be present than in an axisymmetric model which causes additional computational expense. It is therefore desirable to reduce the number of elements by

finding planes of symmetry. The system on one side of the plane of symmetry can be completely omitted, and through the application of appropriate boundary conditions to the nodes on the symmetry plane, identical results to that of a complete system will be obtained. Two planes of symmetry are present in both versions of the system, and therefore only a quarter of the systems need to be modelled. An exception to this occurs when the explosive is no longer vertically above the V-plate ridge and is offset. For these systems a half model has to be created with both sides of the V-plate included.

4.1.3 Including the Explosive Fuse

A decision which had to be made for the rod explosive model, was whether the relatively small explosive rod fuse attached to the main charge in the experiments, should be modelled. This fuse makes the explosive geometry more complex and therefore more difficult to model, so it was hoped that the fuse could be excluded from the explosive model without significantly affecting the results. To test this, two models, one with an explosive fuse and one without it, which were identical in every other way, were analysed. These two explosive charges can be seen in Figure 4.3.

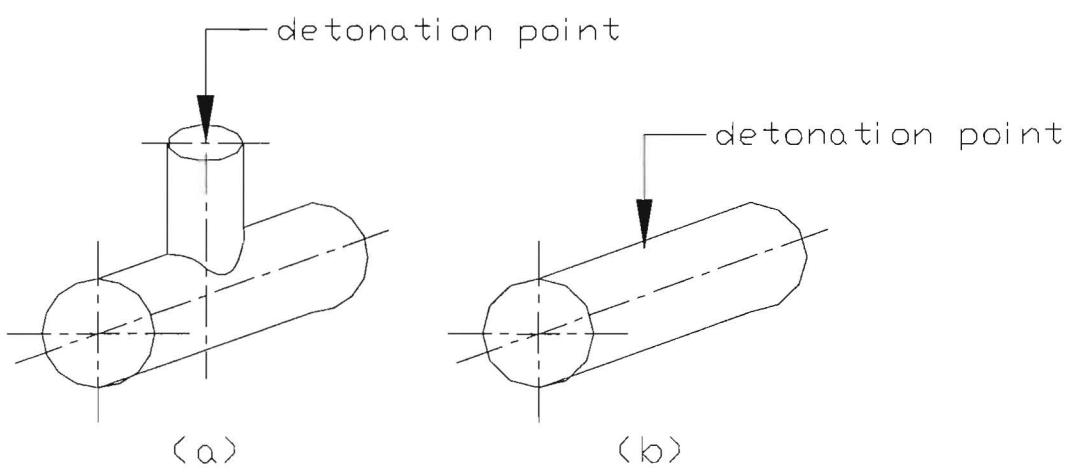

Figure 4.3: Diagrams of the two different rod explosive models; (a) with a fuse; (b) without a fuse

The deformed profiles of the V-plates were compared (see Figure 4.4), and it was found that the profiles were different in shape and that the deflection of the V-plate ridge mid-point was slightly different. This indicated that the fuse had a significant effect on the results, and therefore the explosive fuse was included in the model.

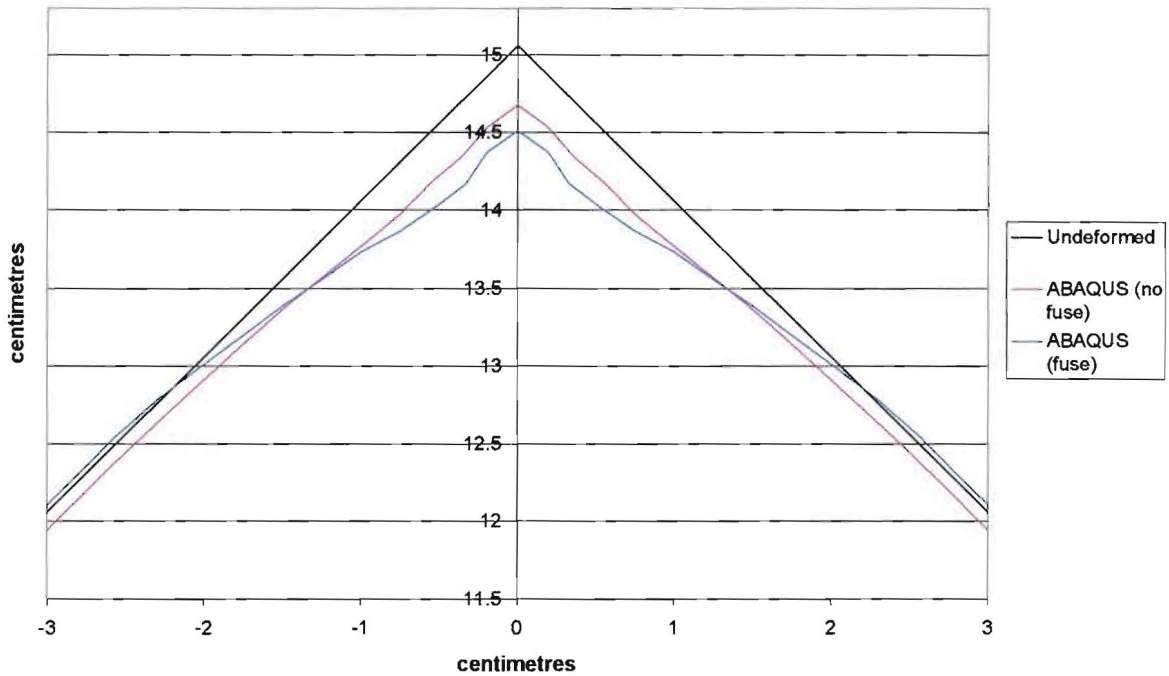

Figure 4.4: A magnified section of the comparison of the profiles obtained from two models where one model has an explosive rod with a fuse (9g) and the other model has a rod without a fuse (8g). A 90 degree V-plate was used in both the models.

The reason the fuse affects the analysis results is thought to be because the fuse affects the shape of the detonation front which travels through the main explosive rod. When a fuse is included, the detonation front is thought to arrive at the main rod in the shape of an almost flat disc, whereas when the fuse is excluded the detonation front begins as a point on the main explosive rod. Therefore the detonation front travels differently through the main explosive charge. Figure 4.5 depicts this theory.

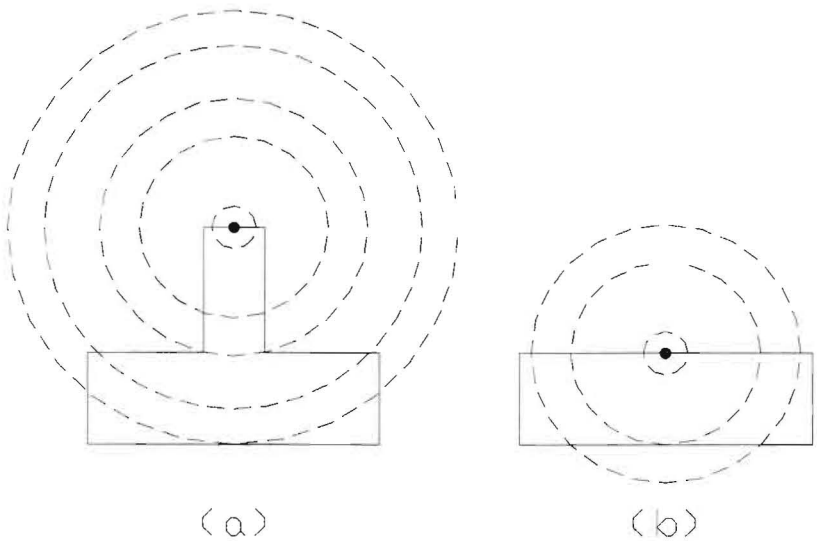

Figure 4.5: Diagrams showing the expansion of the detonation front from the detonation point through the rod explosive; (a) with a fuse; (b) without a fuse.

4.2 Variations of the Model and the Resulting Dimensions

Both the round rod explosive model and the disc explosive model require parameter variation.

The parameters that are varied in the rod explosive model are:

- mass of the explosive (3g, 5g, 7g, 9g, 11g, 13g - where 1g of each of these masses belongs to the fuse) while keeping the rod length constant and the fuse identical.
- included angle of the V-plate (60^0, 90^0, 120^0, 150^0).

Figure 4.6 shows these parametric variations. These parameters are the same as the parameters varied in the experiments and are modelled so that the finite element model can be verified for these parametric changes through comparison with the experimental data.

The parameters that are varied in the disc explosive model are:

- position of the explosive relative to the V-plate (horizontal offset of 0mm, 5mm, 10mm, 15mm, 20mm).
- mass of the explosive disc (3g, 5g, 7g, 9g, 11g, 13g) while keeping the disc diameter constant.
- included angle of the V-plate (60^0, 90^0, 120^0, 150^0).

Figure 4.6 also depicts these parametric variations. Figure 4.7 shows the dimensions of the explosives while Figure 4.8 shows the dimensions of the V-plates. For all the models of both the rod and disc systems, the explosive is situated at a distance of 12mm above the ridge of the V-plate. This distance was selected as a polystyrene block was used in the experiments to position the explosive above the V-plate and to prevent spallation of the V-plate. This polystyrene block separated the explosive and V-plate by 12mm so this distance is used in the numerical models to simulate the systems as accurately as possible.

The parametric variations of the disc explosive models are modelled to determine any trends or thresholds that are dependent on these parameters. These parameters would be of interest in the practical situation of a landmine detonating beneath the V-shaped hull of a mine-protected vehicle.

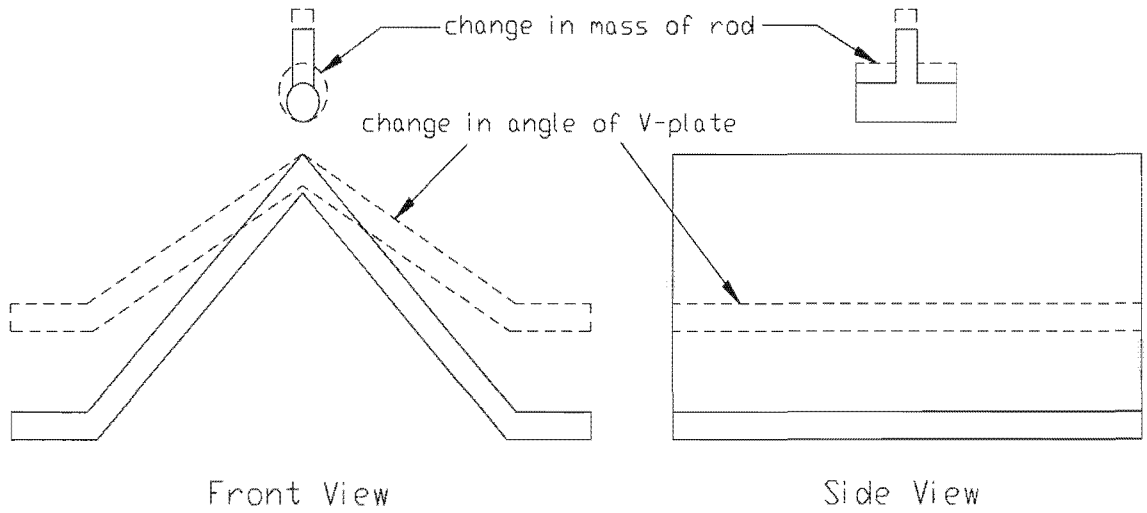

(a)

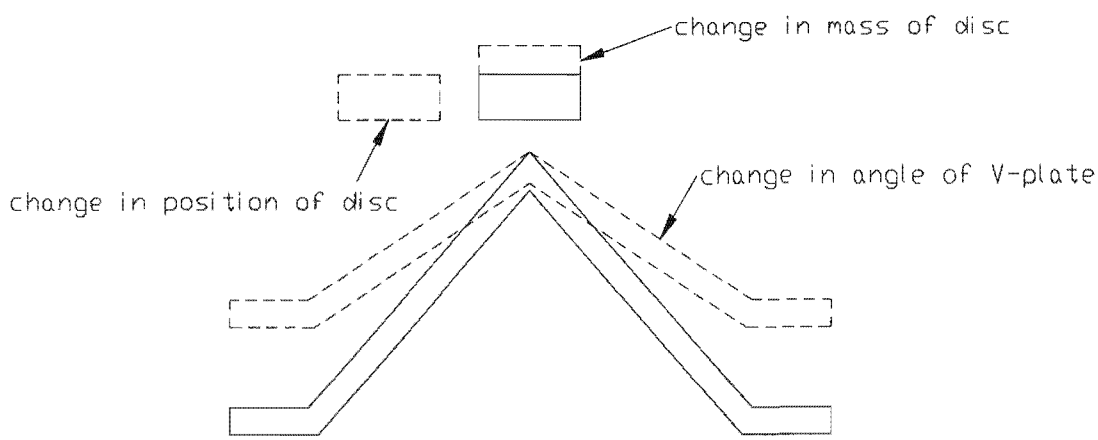

(b)

Figure 4.6: Diagram showing how parametric changes alter the; (a) rod explosive model; (b) the disc explosive model.

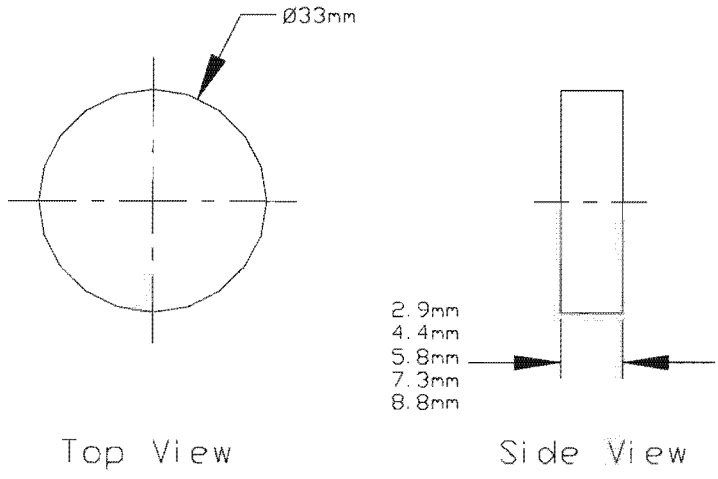

(a)

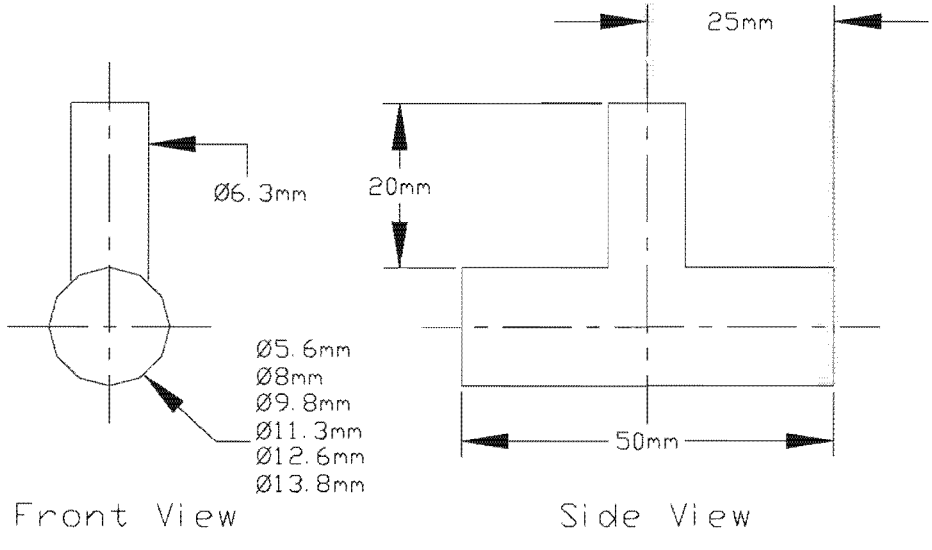

(b)

Figure 4.7: The dimensions of the; (a) disc explosive; (b) rod explosive.

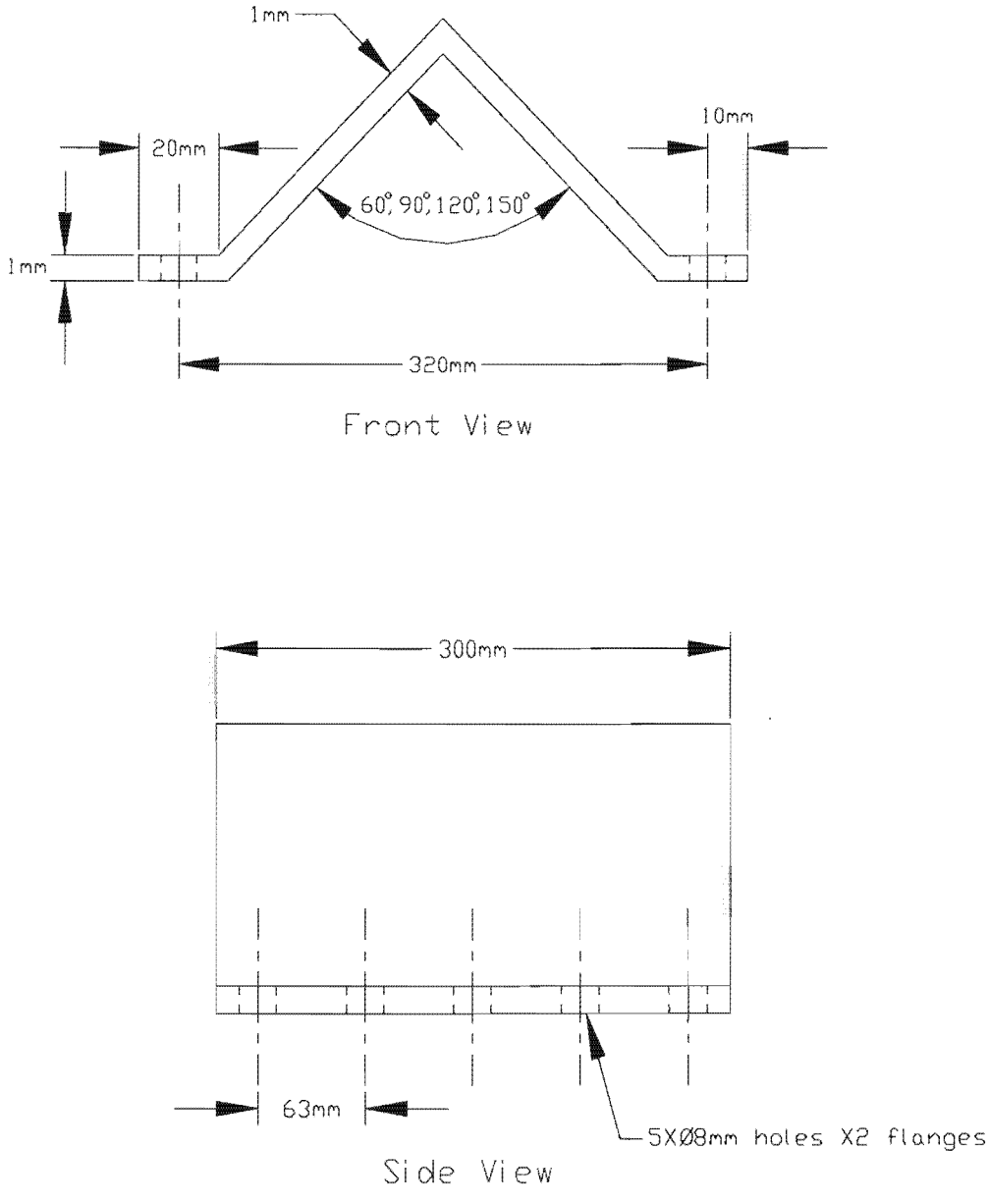

Figure 4.8: The dimensions of the V-plates.

4.3 Elements and Meshing

As previously discussed, the systems in this study are modelled in three dimensions.

4.3.1 The V-Plate

4.3.1.1 Element Type

Both continuum (or solid) and shell elements could be used to model the V-plates as the V-plates are very thin compared to their overall size. It is desirable to use shell elements as they are computationally less expensive, but continuum elements are capable of producing more accurate results.

Grobbelaar [35] reported a comparison between the results of shell elements and continuum elements produced when they were separately used to model the plate in a system similar to the systems in this study. The system discussed by Grobbelaar [35] involved a flat circular steel plate being exploded by a disc of explosive which was slightly offset from the plate above its centre. Two versions of this system were modelled. In one version the flat plate was modelled using shell elements (SAX1) and in the other version it was modelled using continuum elements (CAX4R). The explosive discs were modelled using continuum elements (CAX4R) and all other aspects of the models were identical for both versions. A comparison of the plate profiles resulting from the two versions can be seen in Figure 4.9. Displacement is plotted versus absolute distance. The solid line represents the results obtained using continuum elements, while the dashed line represents the results obtained using shell elements.

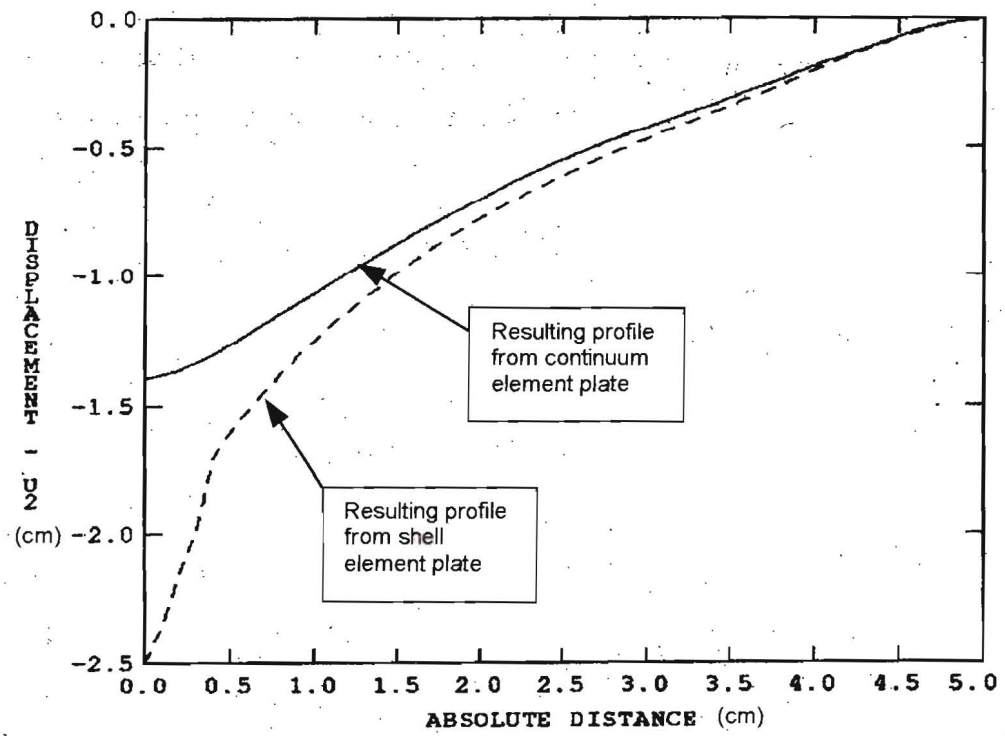

Figure 4.9: A comparison between results of an exploded flat circular steel plate model obtained using shell elements, and results obtained from the model using continuum elements, as conducted by Grobbelaar [35].

The experimentally determined mid-point displacement of the flat plate in the system being discussed, was 15.3mm. From Figure 4.9 it can be seen that the mid-point displacement of the plate for the model using the continuum elements for the plate, is far more accurate. Grobbelaar [35] reported that the inaccuracy of the shell element version was due to lack of sufficient through thickness integration points in the shell elements which limited the rigidity of the shell elements with respect to bending. Because of their superior accuracy, continuum elements are used to model the V-plates in this study.

The next decision involving the elements of the V-plate was which type of continuum element should be used. The three dimensional continuum elements available in ABAQUS/Explicit are:

- C3D4 - 4-node linear tetrahedron.

- C3D6 - 6-node linear triangular prism.
- C3D8R - 8-node linear brick, reduced integration with hourglass control.
- C3D10M - 10-node modified tetrahedron, with hourglass control.

Triangular/tetrahedral elements are geometrically versatile and are capable of meshing complex shapes which the quadrilateral/hexahedral elements cannot always do. However, a good mesh of quadrilateral/hexahedral elements usually provides a solution of equivalent accuracy at less computational cost. Quadrilateral/hexahedral elements have a better convergence rate than triangular/tetrahedral elements, and sensitivity to mesh orientation in regular meshes is not an issue. Triangular/tetrahedral elements, however, are less sensitive to initial element shape, whereas linear quadrilateral/hexahedral elements perform better if their shape is approximately rectangular. The quadrilateral/hexahedral elements become much less accurate when they are initially distorted, whereas the triangular/tetrahedral elements are less sensitive to distortion. Linear triangular/tetrahedral elements are usually overly stiff, and extremely fine meshes are required to obtain accurate results [38].

ABAQUS/CAE which is the preprocessor used to mesh the models in this study, gives the user the choice between hexahedral elements (C3D8R) or tetrahedral (C3D4) elements. After weighing up the advantages and disadvantages of these two types of elements, it was decided that hexahedral elements should be used. ABAQUS/CAE successfully meshed the V-plates as the V-plate geometry easily lends itself to be meshed with these elements.

4.3.1.2 Mesh Bias

Another characteristic introduced to the V-plate mesh is to bias the mesh towards the proximity of the explosive. This means that the distribution of elements in the V-plate mesh is weighted in the direction of the explosive. This is done so that the region where the explosive mostly interacts with the

V-plate has a finer mesh which will produce more accurate and detailed results. This method helps to keep the number of elements to a minimum while still having the desired mesh density at the important regions. Biasing was applied to the V-plate mesh in the direction along the V-plate ridge and in the direction travelling down the sloping side of the V-plate. The bias ratios selected were both 3. The method of selection of this ratio will be discussed below.

4.3.1.3 Number and Size of Elements

A further aspect of this V-plate mesh which has to be determined is the overall number of elements in the mesh. Biasing of the mesh helps with mesh density distribution, but the number of elements in the whole mesh still has to be determined so that the biased mesh contains suitable mesh densities in all regions of the model. Using convergence of results to decide on the coarsest mesh density allowable in the different regions, and computational expense to decide on the finest mesh density allowable in the different regions, a suitable combination of mesh bias and number of elements is arrived at.

For most of the models the smallest element in the mesh is approximately 2mm X 2mm X 1mm and is found at the middle of the V-plate ridge where maximum interaction with the explosive takes place. The largest element in the mesh is approximately 10mm X 6mm X 1mm and is found at the end corners of the flanges which are the furthest points from the explosive interaction and where almost no deformation is likely to take place according to the experimental data. The V-plate mesh can be seen in Figure 4.10. The smallest and largest elements are indicated.

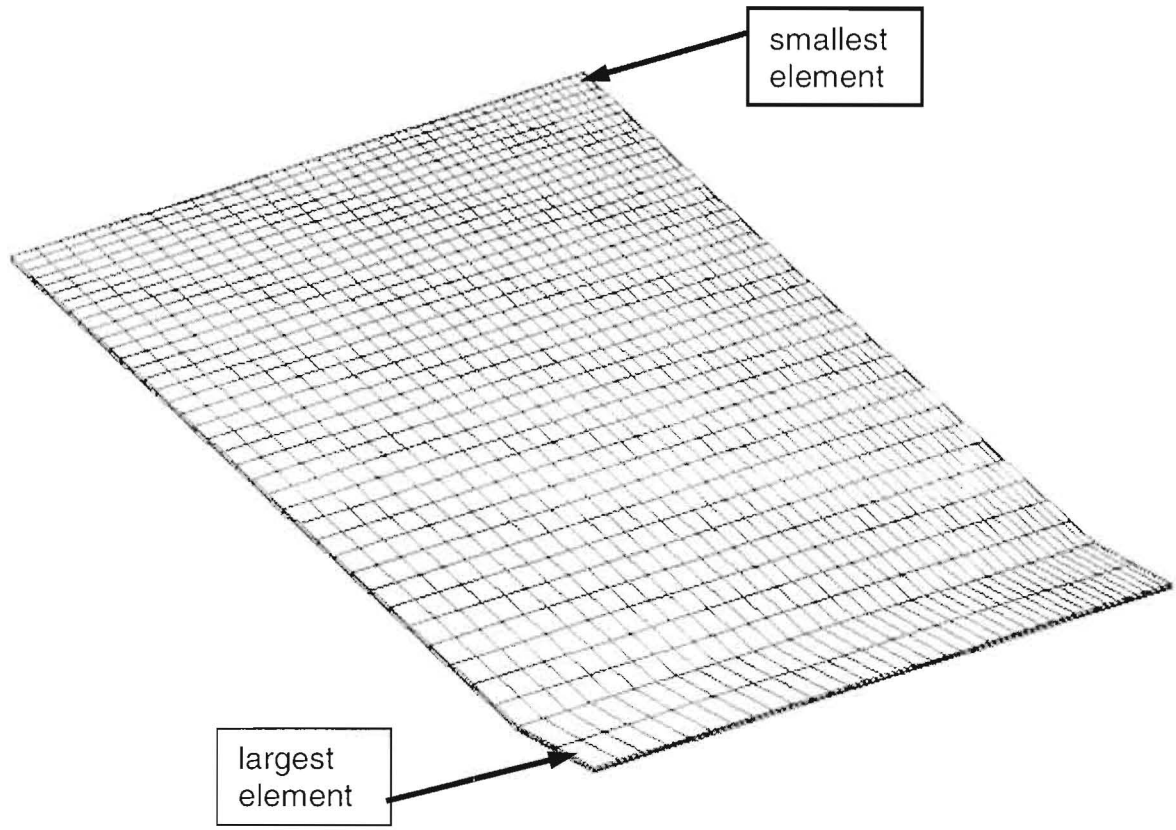

Figure 4.10: The element mesh of the 150^0 V-plate models.

4.3.2 The Explosive Charge

4.3.2.1 Element Type

Continuum (or solid) elements have to be used for the explosives. Hexahedral elements are the preferred choice of element to be used for the same reasons they were chosen for the meshing of the V-plates. The ABAQUS/CAE preprocessor can successfully mesh the explosive discs with these elements. A meshed explosive disc can be seen in Figure 4.11.

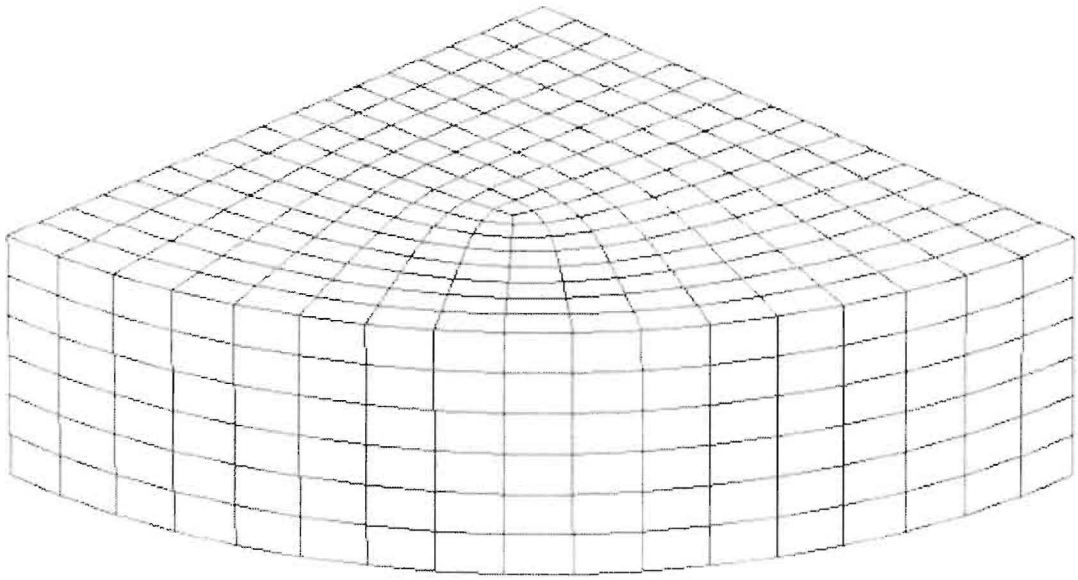

Figure 4.11: The mesh generated by ABAQUS/CAE for a quarter disc explosive.

The preprocessor can also successfully mesh a simple round rod of explosive, but it is unable to mesh the round rod explosive with a fuse attached as the fuse complicates the geometry. To solve this problem, the rod explosive was instead meshed with tetrahedral elements which are capable of meshing almost any geometry. Unfortunately, it was found that the expansion and contact behaviour of the tetrahedral explosive elements after detonation, are very poor. The tetrahedral elements often come into contact with the V-plate in the form of 'spikes' (see Figure 4.12) and the elements soon reach the distortion limit causing the run to terminate before completion very early in the analysis. Element distortion will be discussed later.

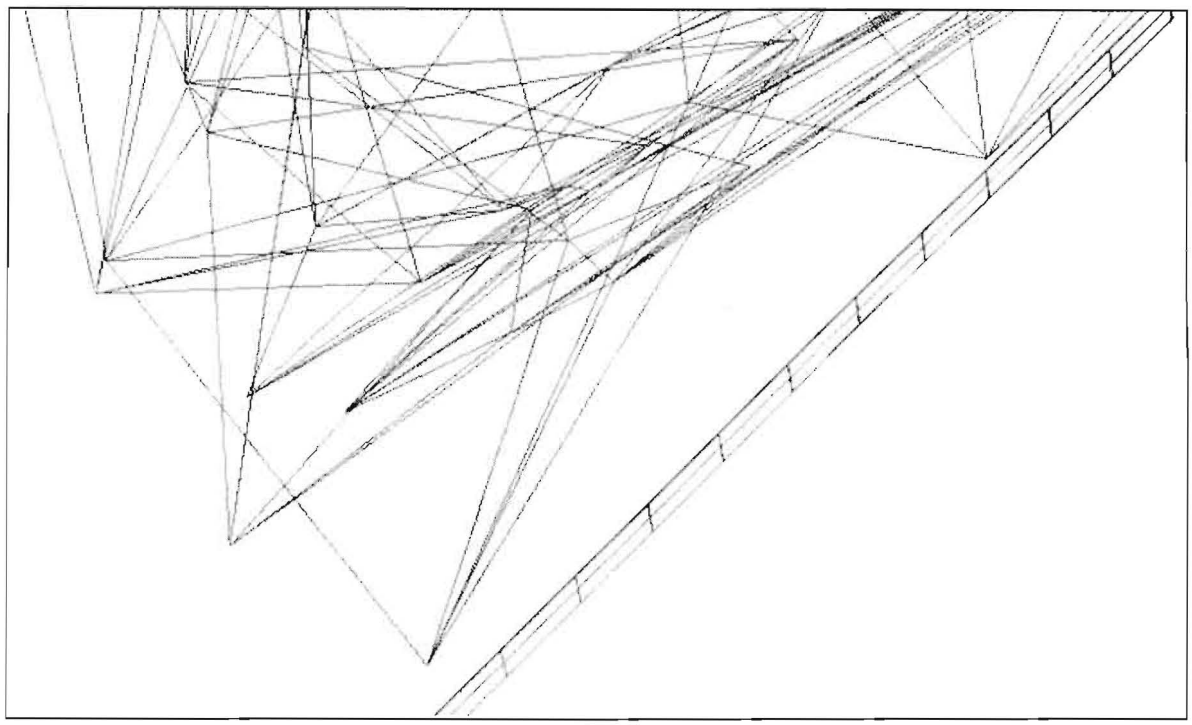

Figure 4.12: A picture showing how tetrahedral explosive elements form 'spikes' which impact with the V-plate.

To overcome this problem, it was decided that a hybrid mesh would have to be created for the rod explosive. This hybrid mesh has a section of hexahedral elements which make up the bottom half of the explosive rod, and another section of tetrahedral elements which make up the fuse and the top half of the explosive rod. The two sections meet at a common face which is a plane cutting through the longitudinal axis of the main explosive rod. To join the two sections, the nodes of the hexahedral and tetrahedral elements which fall on the shared face have identical coordinates so that two nodes exist at each nodal position. The two nodes in each of these two-node sets are then tied together so that they act as one node. Figure 4.13 shows the rod explosive and fuse meshed with this hybrid mesh and a simple rod without a fuse which is easily meshed with hexahedral elements.

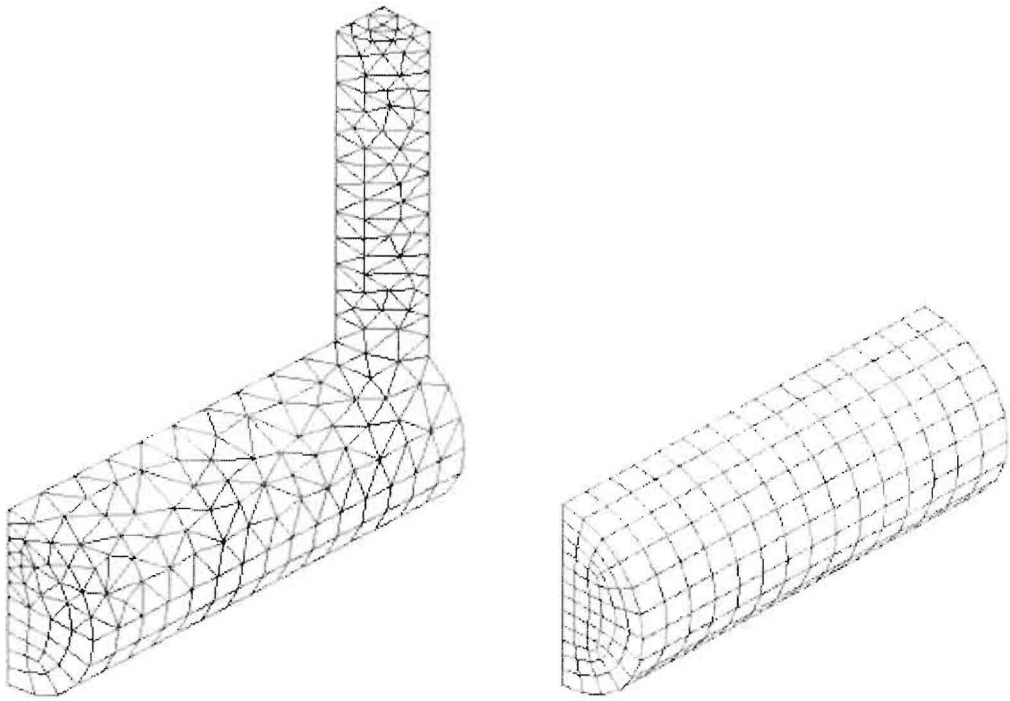

(a) (b)

Figure 4.13: Meshing the explosive rod; (a) with a fuse; (b) without a fuse.

Creating a hybrid mesh is not standard practice but was the last resort in this case. Because the hexahedral elements and the tetrahedral elements are tied together at their interface, the analysis becomes computationally expensive as tying many nodes together significantly increases the computational time. This hybrid mesh is a suitable solution to the problem as the explosive rod and fuse can now be meshed, and the bottom half of the explosive which interacts with the plate after detonation, has good contact behaviour as it is hexahedrally meshed.

4.3.2.2 Number and Size of Elements

An attempt to determine a suitable mesh density for the explosive was made as for the V-plate, using convergence of the results and computational expense as guides. The explosive elements need to be significantly smaller than the elements in the V-plate because when the explosive is detonated

and it expands, the explosive elements rapidly increase in size and when the explosive and V-plate elements interact they will be of similar size which is desirable.

It was found, however, that the minimum size of the explosive elements in this problem is not governed by computational expense but by an error which kept occurring causing the analysis runs of the model to terminate before completion. The error occurs because an element of the explosive distorts excessively. Solving this problem consumed a vast amount of time during the investigation.

4.3.2.2.1 Element Distortion

The cause of the excessive element distortion is the geometry of the V-plate which cannot be altered. When the explosive elements interact with the V-plate, the explosive elements flow down the slopes of the V-plate causing excessive elongation of the elements. When the distortion reaches a limit, ABAQUS terminates the run. Figure 4.14 shows severely distorted explosive elements.

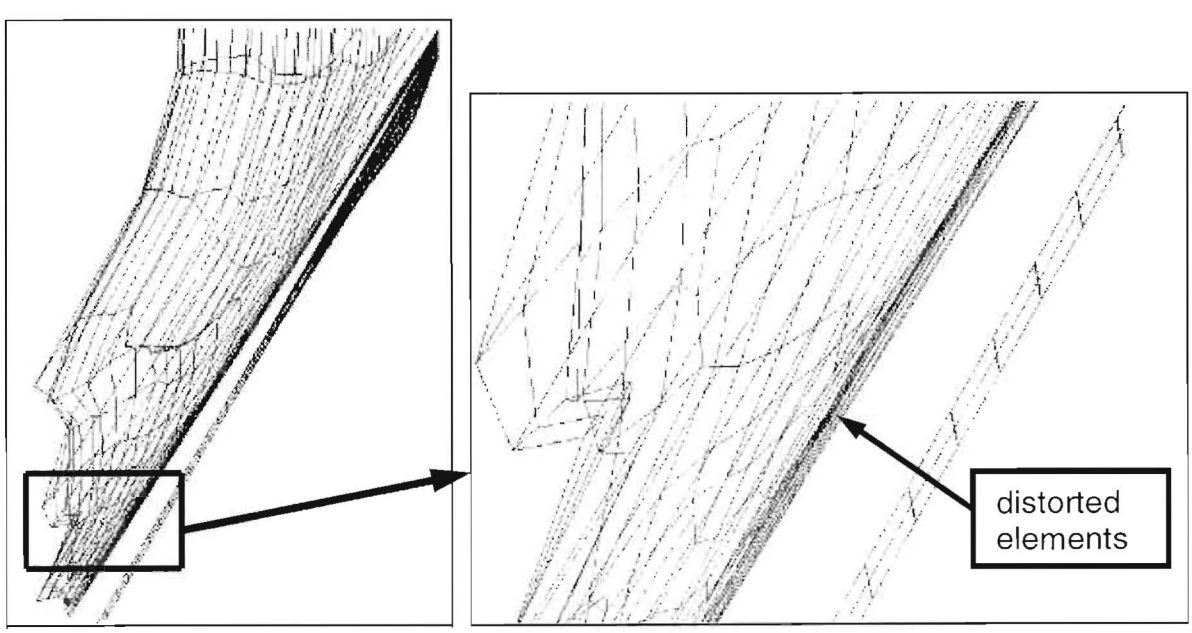

Figure 4.14: Pictures showing distorted explosive elements resulting from the flow of the explosive down the sides of the V-plate.

All aspects of the model were examined and experimented with to try to eliminate the problem.

Firstly, adaptive meshing of the explosive was included in the analysis of the models. Adaptive meshing seemed to be the ideal solution as it repeatedly moves the node positions slightly after a specified number of time increments so that the nodes roughly remain evenly distributed throughout the deforming object. The adaptive meshing option is actually described in the ABAQUS manual [37] as a method for avoiding element distortion. Surprisingly, adaptive meshing caused poorer results as the analysis runs terminated at even earlier times.

The second attempt at solving the problem involved altering the aspect ratios of the elements of the explosive to try and extend the time before the distortion limit was reached. It was found that changing the aspect ratios only made a minimal difference to the run time before termination, and therefore was not a solution.

The third option explored was to alter the mesh density of the explosive. Surprisingly, it was found that the more coarse the mesh (the fewer the elements), the longer the analysis would run before termination. The coarsest mesh that could be considered acceptable still did not allow the analysis to run the full time required. The full time of the analysis is set to be as long as it takes for the explosive and V-plate interaction to be completed and for the motion of the deforming plate to reduce to an insignificant amount. It was noticed, however, that even though the coarsest mesh did not allow the analysis to run the full time, the time the analysis did run was enough to allow the V-plate and explosive to complete their interaction. Once the explosive and V-plate have completed their interaction, the explosive no longer affects the V-plate and is no longer needed in the models. This means that the explosive can be deleted from the models shortly after its interaction with the

V-plate is complete and before one of the explosive elements could distort excessively causing the analysis to terminate.

Through trial and error for each of the models, the meshes were individually refined as much as possible to the point where the analysis would terminate due to distortion just after the explosive/V-plate interaction was complete. The average size of the elements in the explosives varied slightly from model to model, but was on average about 1mm X 1mm X 1mm. The explosive/V-plate interaction was considered to be complete when the contact pressure between the two became zero. Just after the explosive/V-plate interaction and just before the analysis termination due to distortion, the explosive would be deleted from the model so that the analysis would run to completion.

To delete the explosive from the model during the analysis, the analysis had to be imported to ABAQUS/Standard from ABAQUS/Explicit. ABAQUS input decks created by ABAQUS/CAE cannot be imported, so the model was then recreated manually by the investigator. Further complications arose and this option was abandoned. A useful observation from this line of investigation, though, was that the model with the explosive disc ran for a longer time when it was meshed by ABAQUS/CAE than when it was meshed manually by the investigator. Figure 4.15 shows the two different types of meshes.

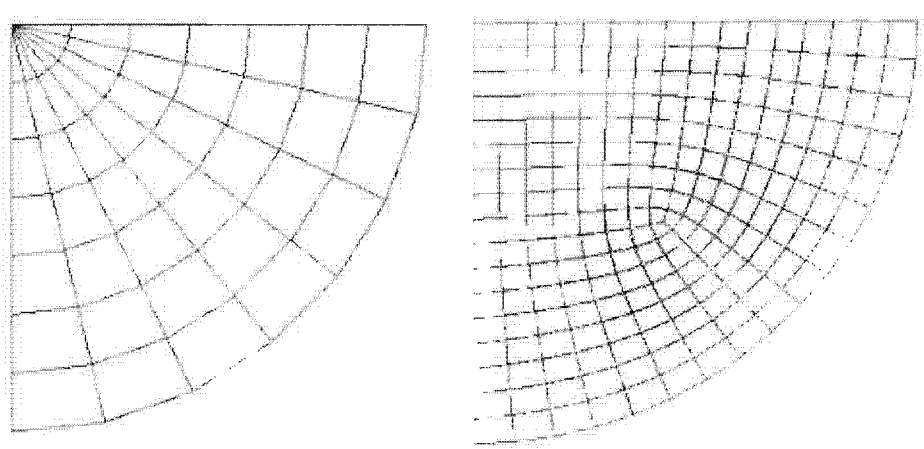

(a) (b)

Figure 4.15: An explosive disc meshed; (a) manually; (b) with ABAQUS/CAE.

The manually created mesh resembles a spider web with elements radiating from the centre of the disc. The elements near the centre of the spider web mesh are excessively slender with large aspect ratios while the elements near the circumference have normal aspect ratios. It is thought that these excessively slender elements quickly reach the distortion limit and are the reason for the early termination of the analysis. The ABAQUS/CAE created mesh is of a different form where most of the elements are of roughly similar size and have normal aspect ratios and therefore the analysis progresses further for this mesh.

Another method of effectively removing the explosive from the models during the analysis, was then attempted. Instead of deleting the explosives from the models after the explosive/V-plate interaction was completed, all the degrees of freedom of the nodes of the explosive were constrained, and the explosives were frozen. This method was successful and allowed all the analyses to run to completion for both the rod and disc versions of the model.

4.4 Duration of Model Analysis and Time Steps

The selection of the time over which the model is analysed is important. This duration has to be as long as it takes for the explosive/V-plate interaction to be completed and for the motion of the deforming plate to reduce to an insignificant amount, but it must also be short enough to avoid unnecessary computational time. The duration selected for the various models ranges around $550\,\mu s$.

The analysis duration of a model can be considered as one long time step, but if any alterations need to be made to the model during the analysis, the analysis duration can be broken up into further steps. In the case of the models in this study, the explosive nodes have to be frozen during the analysis to effectively remove the explosive from the model, so the analysis duration is broken into two time steps. The end of the first time step, involving the reacting explosive, is determined to be when the contact pressure between the V-plate and explosive becomes zero as previously discussed.

The duration of the first time step is determined to be in a range of 30-60 μs for the different models. The explosive is then frozen at the beginning, and for the duration of, the second time step. Together the two steps make up 550 μs. The timeline of the analysis indicating the time steps can be seen in Figure 4.16.

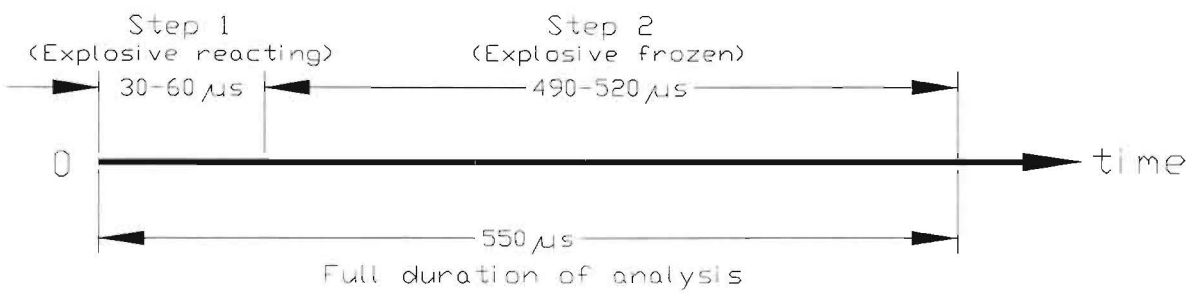

Figure 4.16: Diagram of timeline showing the model analysis duration and its subdivision into steps.

4.5 Boundary Conditions

Boundary conditions are usually applied to a model for two different reasons:

- to allow a model that has been reduced owing to planes of symmetry to produce the same results as that of a complete model.
- to apply the physical constraints present in the actual system.

The first reason for applying boundary conditions - allowing a reduced model to simulate a complete model - is only possible when a plane of symmetry exists in a system. A model need only contain the contents of one side of the plane of symmetry and the contents of the other side can be omitted. For this simplified model to produce the same results as a complete system, suitable boundary conditions have to be applied to the nodes falling on the planes of symmetry.

There are two planes of symmetry in both the rod and disc versions of the system to be modelled. Because of this, a quarter model of the system is created. The boundary conditions applied to the explosive and V-plate nodes falling on the planes of symmetry consist of constraining the translational degree of freedom of the nodes in the direction of the normal of the plane of symmetry. An example of these boundary conditions is demonstrated in Figure 4.17 for the quarter model of a disc explosive.

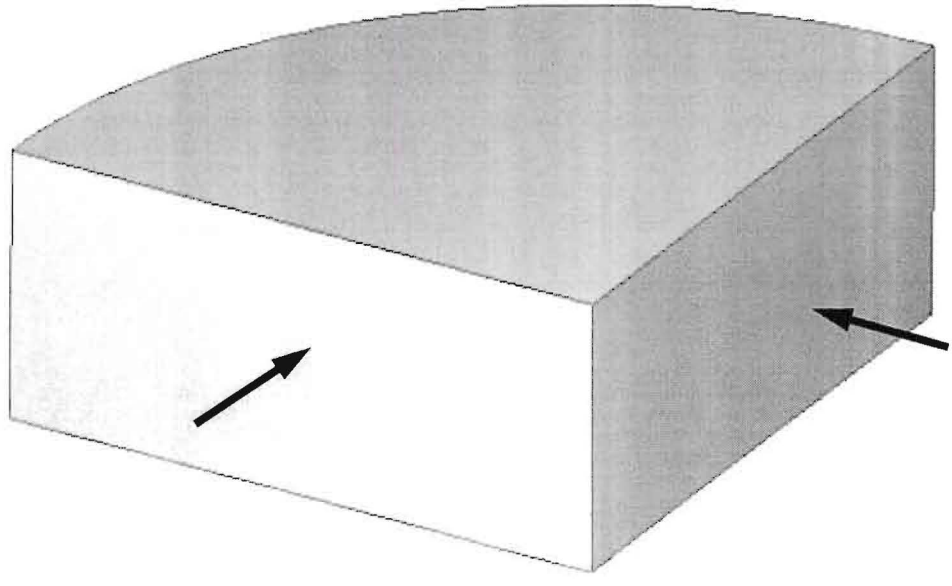

Figure 4.17: A diagram indicating the translational degrees of freedom which are constrained on the axes of symmetry of a quarter model of a disc. The translational degrees of freedom are constrained in the directions of the arrows for the entire surface which the arrows are touching.

The second reason for applying boundary conditions - physical constraint application - is applied to the V-plate in all of the models. All the nodes in the top and bottom surfaces of both flanges of the V-plates have all their degrees of freedom constrained to simulate the flanges being clamped. Figure 4.18 shows these top and bottom surfaces.

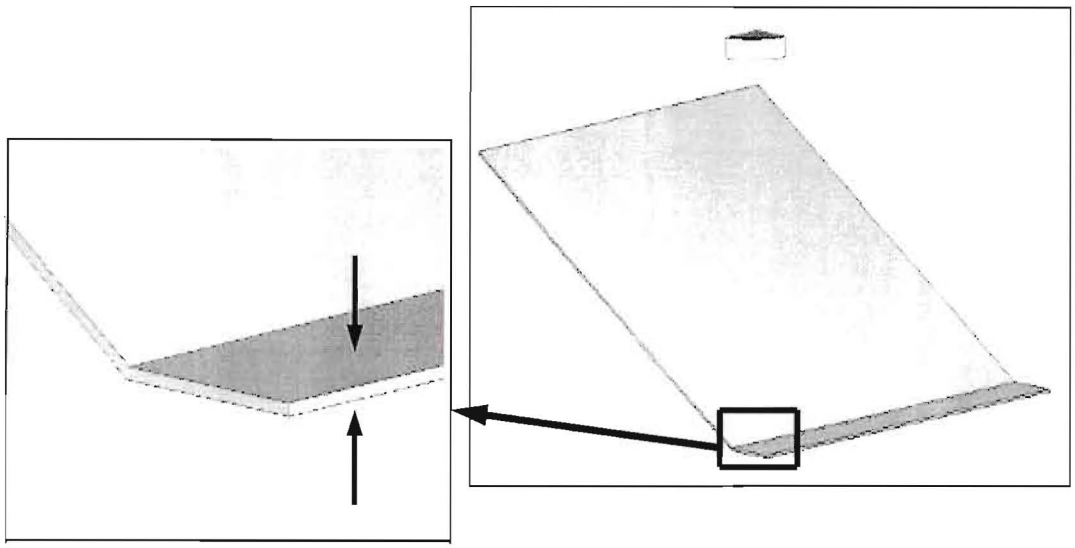

Figure 4.18: Diagrams indicating, with arrows, the top and bottom surfaces of the V-plate flange which have all their degrees of freedom constrained to simulate clamping.

It was thought that perhaps this method of simulation would not accurately represent the clamped conditions. A more realistic representation would be in the form of two rigid bodies on either side of the flange applying a contact pressure to the flange with a friction coefficient between the rigid body and flange surfaces. This method would be computationally slightly more expensive as none of the nodes of the V-plate flanges would be totally constrained and therefore the motion of all the nodes would have to be calculated.

Gelman [30] conducted a study on the different types of boundary conditions that can be applied to simulate the constraint of exploded plates, and it was concluded that the results of the analysis were not significantly dependent on the type of boundary condition applied. Because of this, constraining all the degrees of freedom of the nodes in the top and bottom surfaces of the V-plate flanges, is thought to be an adequate method of simulating clamping.

In this study, boundary conditions are applied to the models for a third unorthodox reason which has been discussed previously. Because the explosive elements distort during the model analysis and cause the run to terminate, the explosive has to be removed from the model. Deleting the explosive during the analysis is not possible so boundary conditions are applied to the nodes of the explosive after its interaction with the V-plate is complete. All the degrees of freedom of the explosive nodes are constrained so that the explosive is frozen and effectively removed from the model.

4.6 The Mechanical and Material Properties

4.6.1 The V-Plate

The material model of the V-plates incorporates yield hardening, strain rate sensitivity, and temperature dependence. A description of these phenomena and their effects can be found in the previous chapter in the "Modelling of Mechanical Properties" section of the "ABAQUS Overview" chapter. The known material properties of the V-plate steel can be seen in Table 4.1. Young's modulus, Poisson's ratio and the uniaxial tensile yield strength of the steel were obtained from quasi-static uniaxial tensile tests, and were also obtained, along with the density, at room temperature.

Young's modulus, E	200 GPa
Poisson's ratio, υ	0.3
Uniaxial Tensile Yield Strength, σ_0	250 MPa
Density, ρ	7850 kg/m^3

Table 4.1: General material properties for steel V-plates

4.6.1.1 Yield Hardening

The material model being used incorporates the von Mises yield criterion with isotropic hardening. Isotropic hardening is the type of hardening selected as the steel displays significant yield hardening and therefore cannot be considered to be perfectly plastic. Johnson-Cook hardening cannot be used as this approach requires the yield stress to be defined analytically as a function of equivalent plastic strain, strain rate, and temperature and this relationship for the steel of the V-plate is not known.

ABAQUS can provide a model for the isotropic hardening or the user can provide a stress versus strain curve of the plastic region of the steel obtained from a quasi-static tensile test. The stress versus strain material curve of the V-plate steel is not available as the report documenting this curve has been lost. A material curve of a steel similar to the V-plate steel is available though and would provide more accurate results than the model provided by ABAQUS, so the option of a user-defined curve was selected.

To define the material curve in ABAQUS, suitable points along this curve are entered in tabular form. Suitable points are selected on the basis that ABAQUS linearly interpolates between given values so appropriate points are selected which would describe the stress versus plastic strain curve to an acceptable level of accuracy. Figure 4.19 shows the plot of stress versus plastic strain for the steel.

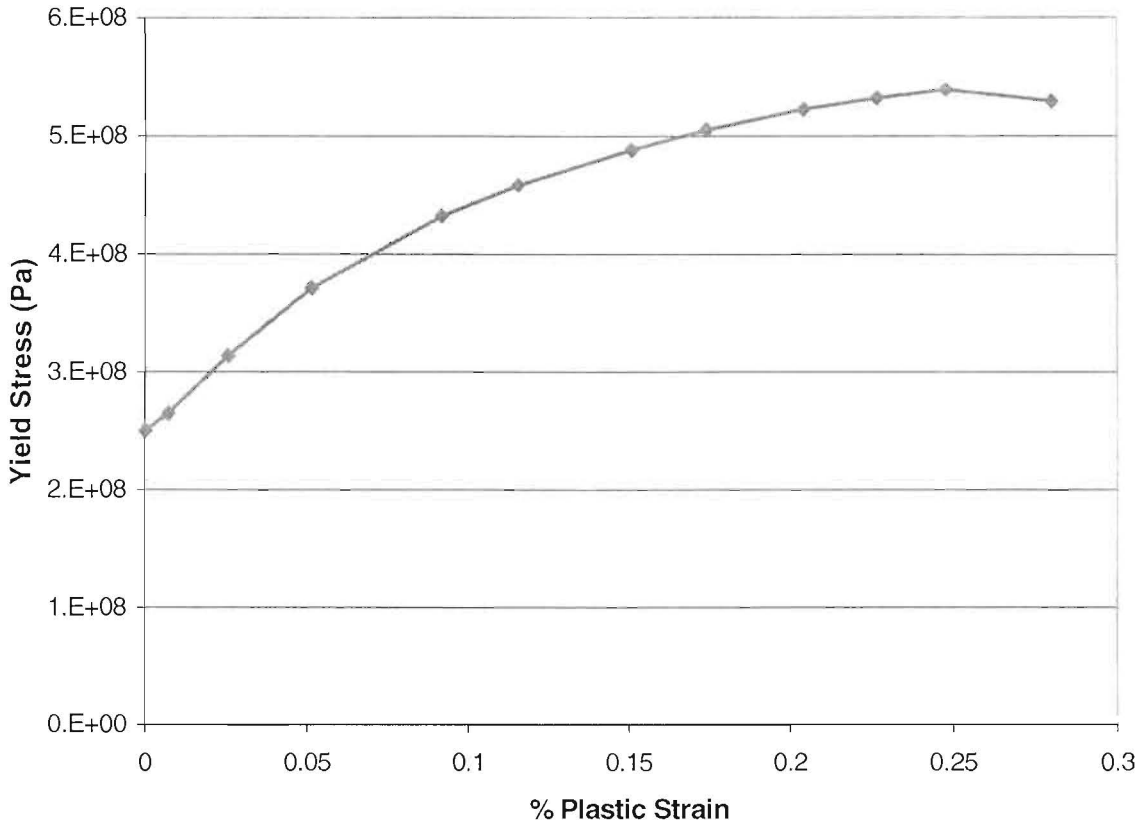

Figure 4.19: The yield stress versus plastic strain curve of the steel used for the V-plate, at room temperature.

4.6.1.2 Strain Rate Sensitivity

Data defining the strain rate sensitivity of the V-plate steel could not be entered in tabular form as the stress vs. strain material curves of the steel at different strain rates required for this are not available. To experimentally obtain these curves would be difficult and would have to be done using apparatus such as the Split Hopkinson Pressure Bar. This means that the methods involving yield stress ratios, $\frac{\sigma}{\sigma_0}$, have to be used. Once again, the tabular method where the yield stress ratios are entered into ABAQUS with the corresponding plastic strain rates, temperature and other field variables, cannot be used as the yield stress ratios at different strain rates are not known. The Johnson-Cook rate dependence method cannot be used to

determine the yield stress ratios as it must be used in conjunction with Johnson-Cook hardening and this hardening model has not been selected. This means that the Overstress Power Law, also known as the Cowper-Symonds equation, has to be used. This relationship can be seen in the "Modelling of Mechanical Properties" section in the "ABAQUS Overview" chapter. The material parameters of this equation, D and n, are considered to not be significantly dependent on temperature or any other field variables, so these parameters remain constant throughout the analysis. The commonly accepted values for steel of D=40.4s^{-1} and n=5 are used in the models [4]. Figure 4.20 demonstrates how the strain rate affects the yield stress of the steel.

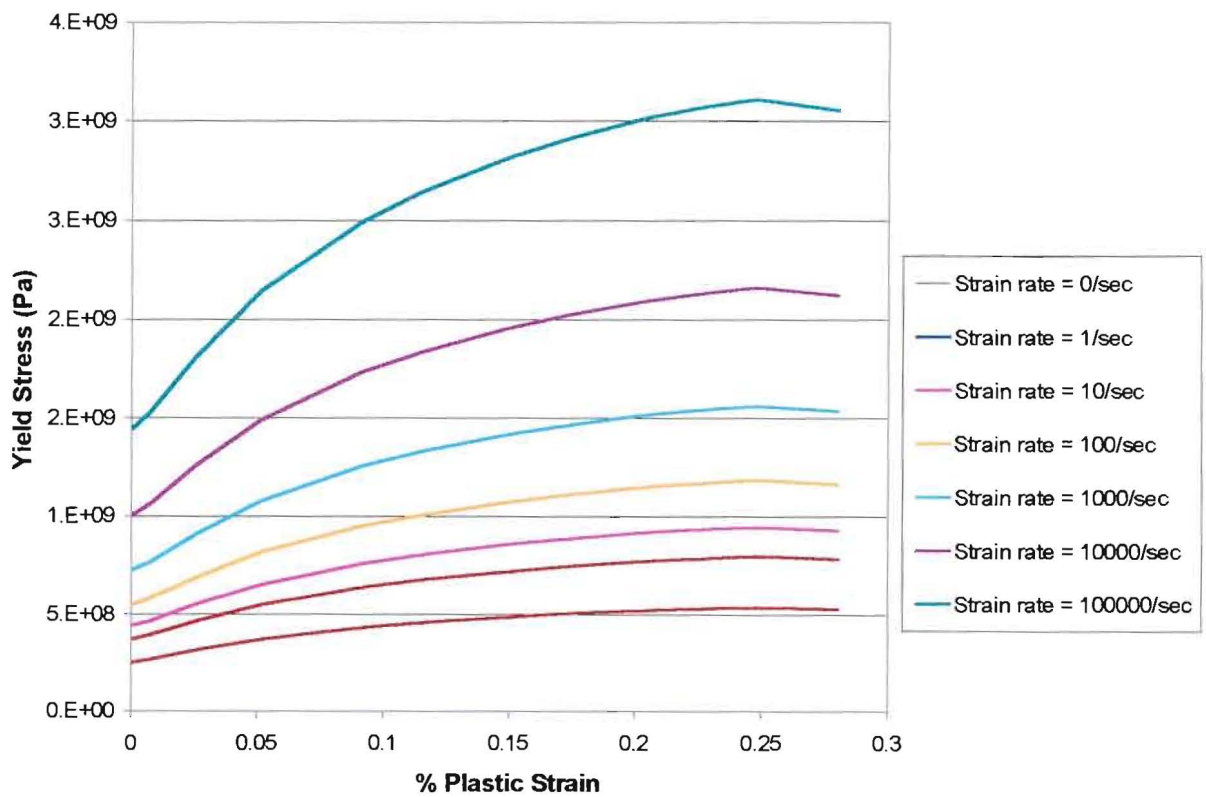

Figure 4.20: A graph of the yield stress versus the plastic strain percentage of the V-plate steel at different strain rates according to the Cowper-Symonds relationship with D=40.4s^{-1} and n=5.

From studying the deforming model of the V-plate, it is seen that the V-plates can undergo strain rates in the order of 10 000/second. From the graph in Figure 4.20 it can be seen that the yield stress of the steel will be significantly affected at this high strain rate.

4.6.1.3 Temperature Dependence

The work done on the V-plates causing plastic deformation is dissipated in the form of heat energy which will affect the material properties of the steel. Almost none of the previous numerical studies on exploded plates incorporated temperature dependency of the material properties, except for Wiehahn [34] and Chung [42]. This is because there is usually a lack of experimental results documenting material temperature dependency as suitable experiments are difficult to perform [30].

To overcome this problem, general equations obtained from Masui [39] for Young's modulus and for the yield stress of steel were used by Wiehahn [34] and Chung [42] and are also used in this study. The equation for the Young's modulus of a steel is a function of temperature. The equation for the yield stress of a steel is a function of both temperature and the static yield stress of the steel at the reference temperature which is usually room temperature. Because the static yield stress is required for the yield stress equation, the static stress versus strain material curve of the steel at the reference temperature is required. These equations obtained from Masui [39] are:

$$\begin{aligned} E &= 210\cdot 10^{9} - 58.34\cdot 10^{6}\cdot T && for \quad T \le 600^{0}C \\ E &= 3.17\cdot 10^{5}(T-1100)^{2} + 97.9\cdot 10^{9} && for \quad 600^{0}C < T \le 1100^{0}C \end{aligned} \tag{4.1}$$

$$\begin{aligned} \sigma_y/\sigma_{y0} &= 1 && for \quad T \le 200^{0}C \\ \sigma_y/\sigma_{y0} &= 1 - 0.00178(T-200) && for \quad 200^{0}C < T < 700^{0}C \\ \sigma_y/\sigma_{y0} &= 0.133 - 0.000388(T-700) && for \quad 700^{0}C \le T \le 1000^{0}C \end{aligned} \tag{4.2}$$

where

σ_y = *temperature dependent static yield stress*

σ_{y0} = *static yield stress at reference temperature of tensile test*

T = *temperature of steel*

E = *Young's* mod*ulus*

The temperature dependency of the Young's modulus and the yield stress of the V-plate steel can be seen in Figure 4.21 and Figure 4.22.

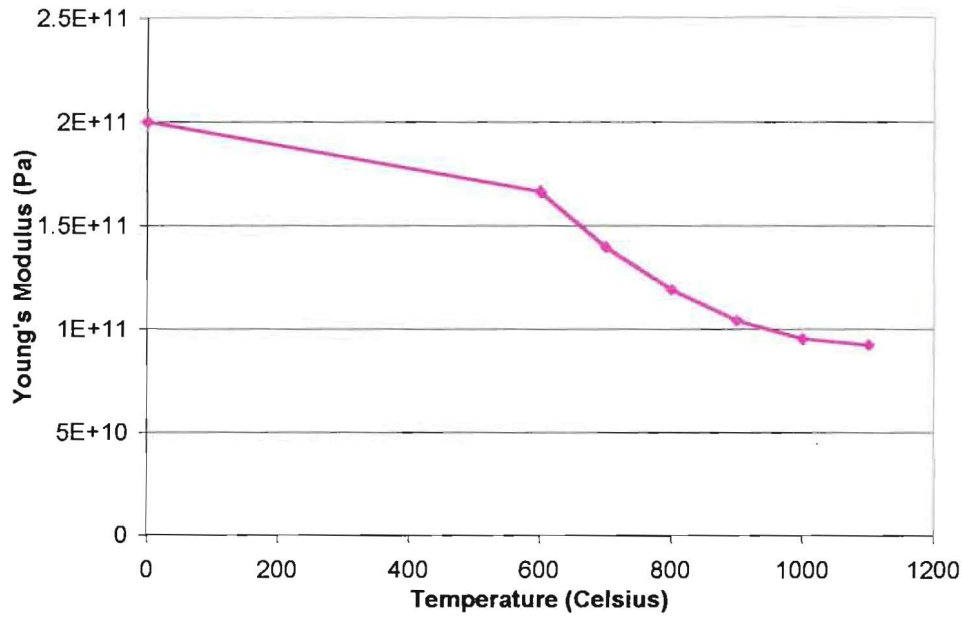

Figure 4.21: A graph showing the relationship between the Young's modulus and the temperature of the V-plate steel according to equation 4.1.

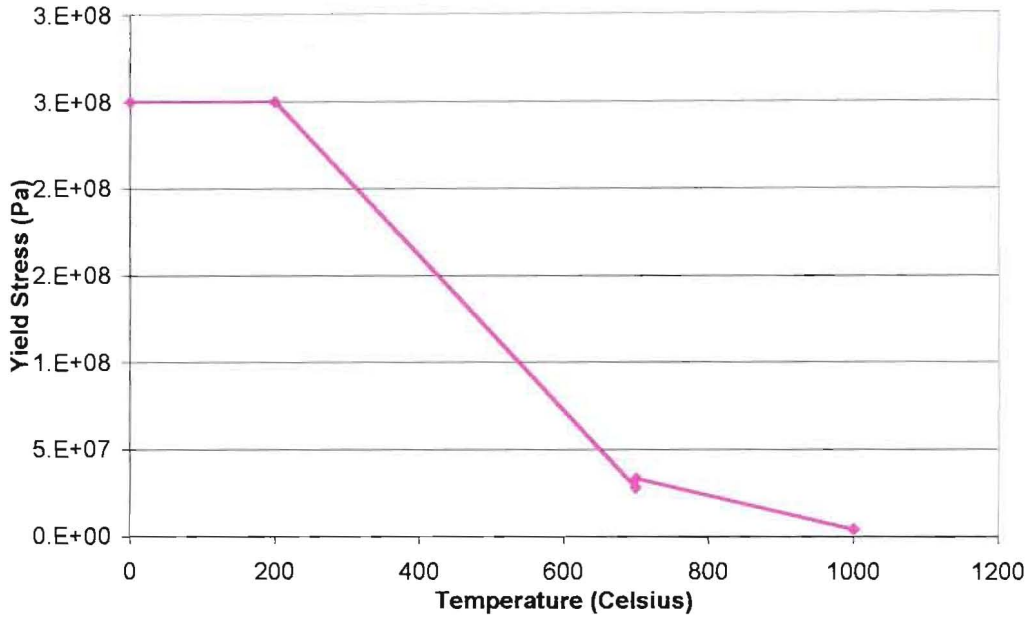

Figure 4.22: A graph showing the relationship between the yield stress and the temperature of the V-plate steel according to equation 4.2.

It can be seen that both the Young's modulus and the yield stress of the V-plate steel are significantly affected by the temperature.

ABAQUS requires stress/strain curves of the steel at different temperatures to incorporate temperature dependency, so stress/strain curves at suitable temperature intervals, determined from equations 4.1 and 4.2, were entered into the input deck in tabular form. As with defining the stress/strain curve of the steel, suitable intervals were selected on the basis that ABAQUS linearly interpolates between given values. This means that only the beginning and end points of the linear relationship are required while the quadratic relationship requires more points to clearly define the relationship.

Heating of the V-plates is considered to be adiabatic as the entire explosion/deformation process is of such a short duration (maximum of 550 μs) that there is no time for the heat to be conducted away. The inelastic heat fraction represents the amount of plastic work which is converted to heat and for this study the fraction is assumed to be 0.9 (i.e. 90% of the plastic work is converted to heat). The specific heat of the steel is assigned the commonly used value of 452 J/kg.K. Experiments that were performed on the systems being modelled were conducted at room temperature. To incorporate this in the model, an initial temperature of 20^{0} C is specified for both the explosive and the V-plate in the model.

4.6.1.4 The Modelling of Failure

It was decided that a failure model would not be incorporated in the models in this study. This is because previous numerical modelling studies of exploded metal plates have shown that these failure models do not predict the tearing failure of the plates accurately. Instead a "rule of thumb" method will be used to predict tearing failure. This method considers tearing failure to have occurred if the equivalent plastic strain of an element exceeds 200% and if the temperature of this element exceeds 600^{0}C [40]. The ABAQUS user will determine if tearing failure should have occurred during the model analysis by inspecting the temperature and strain field variables of the V-plate.

4.6.2 The Explosive

A description of all the equations of state available in ABAQUS/Explicit can be found in the "Modelling of Mechanical Properties" section I the "ABAQUS Overview" chapter. Even though all the equations of state are capable of providing a hydrodynamic material model which could describe the reaction of the gaseous explosive products, the Jones-Wilkins-Lee (JWL) equation of state is chosen. This is because the JWL equation of state has been specifically designed to model the detonation and reaction of high explosives. The other equations of state do not incorporate a detonation model. The JWL equation of state is used to model the reaction of the explosives in all of the models. The JWL equation of state and the modelling of the detonation

process can be found in the previous chapter in "Modelling of Mechanical Properties" section in the "ABAQUS Overview" chapter. To model the detonation and reaction of the explosives, ABAQUS requires certain material constants.

The explosives used in the experiments consisted of PE4 plastic high explosive so the explosives in all the models (both the rod and disc versions) were assigned the material constants of PE4. These material constants can be seen in Table 4.2. The constants are expressed in the unusual units of Mbar, cm, μs^{-1}, and g. This is because these are commonly used units in the field of explosives as resulting pressures are often in the order of 1 Mbar [49]. All properties expressed in this report in units other than these are converted to these units so that the properties are compatible.

Detonation wave speed, C_D	0.819 cm. μs^{-1} (8190 m.s^{-1})
JWL constant, A	6.0977 Mbar (609.77 GPa)
JWL constant, B	0.1295 Mbar (12.95 GPa)
JWL constant, ω	0.25
JWL constant, R_1	4.5
JWL constant, R_2	1.4
Internal energy per unit mass, E_{m0}	0.09 T erg.g^{-1} (9 J.kg^{-1})
Density, ρ	1.6 g.cm^{-3} (1600 kg.m^{-3})

Table 4.2: The material constants required by ABAQUS to model the explosive (PE4).

The point of detonation of an explosive is the co-ordinate point in the model where detonation starts from. The points of detonation of the two different shaped explosives (rod and disc) can be seen in Figure 4.23. The diagram shows the explosive charges in their complete form but it must be

remembered that only a quarter of the explosive charges are being modelled owing to planes of symmetry.

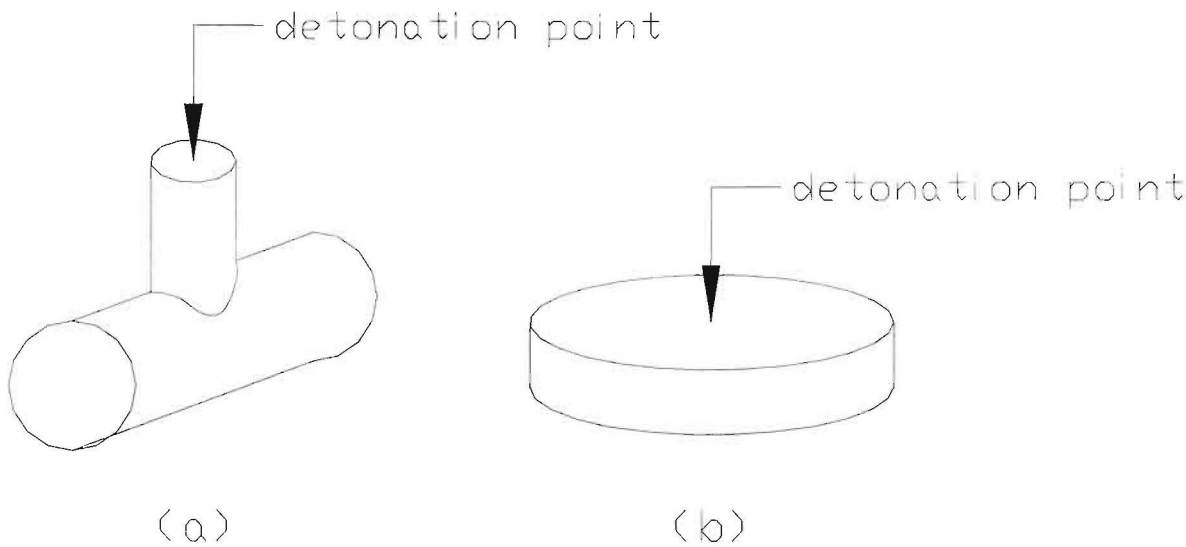

Figure 4.23: Diagram indicating the explosive detonation points of; (a) the rod explosive; (b) the disc explosive.

An example of the incorporation of adiabatic heating for one material and the use of JWL equation of state for another material, in the same model, could not be found in the literature. This combination of parameters is to be used in this study, but the combination caused a 'bug' in ABAQUS/Explicit version 6.2 to surface and the analysis would not run. It was found that to bypass this bug, the *ELASTIC keyword had to be entered for the material being modelled by the equation of state. So even though defining elasticity for the explosive is not necessary, the *ELASTIC keyword has been included in all the input decks purely to overcome the bug. The inclusion of this keyword does not seem to affect the analysis results.

4.7 The Contact Interaction

The interaction of the explosive with the V-plate is an important part of the analysis as this is where the impulse of the explosive is transferred to the V-plate.

There are numerous parameter choices to be made such as the choice between pure or balanced master-slave contact surfaces, kinematic or penalty contact algorithm, hard or soft contact, and separation or no separation of the surfaces after contact. Descriptions of these parameters and their effects can be found in the previous chapter in the "Modelling of Contact Interaction" section in the "ABAQUS Overview" chapter.

4.7.1 Pure or Balanced Master-Slave Contact Surfaces

A choice has to be made between a pure or balanced master surface.

Contact-induced noise can occur in an analysis if a surface on the much denser body is at all weighted as a slave surface [38]. The two contacting objects in the models in this study have densities that differ significantly. The explosive has a density of 1600 kg/m^3, while the V-plate steel has a density of 7850 kg/m^3 . Because of this and the fact that the balanced master-slave contact is computationally more expensive, default pure master-slave contact appears to the superior choice, but Grobbelaar [35] used balanced master-slave with a weighting of 0.5 (i.e. both surfaces are equally weighted). The deformed V-plate profiles of two versions of a model, one with a pure master-slave surface, and one with a balanced master-slave surface, were compared and it was found that there was no significant difference between the two, so pure master-slave contact is selected. The denser V-plate is chosen to be the master surface, and the less dense explosive is the slave surface.

4.7.2 Kinematic or Penalty Contact Algorithm

A choice must be made between the kinematic contact algorithm and the penalty contact algorithm.

Grobbelaar [35] produced sufficiently accurate results using the default kinematic contact algorithm and because this algorithm is computationally less expensive, it was initially chosen.

The rod versions of the models were analysed first using the kinematic algorithm. The results of these models lead to an attempt to use the penalty contact algorithm for the disc versions of the models, on the advice of Dr. Izak Snyman [41]. The reason for this will be discussed in the "Attempts to Determine What Causes the Inaccuracies in the Models Containing Rod Explosives and How to Improve the Results" section in the "Results and Discussion" chapter. Unfortunately, owing to a bug in ABAQUS/Explicit Version 6.2, the penalty algorithm could not be used and the kinematic algorithm had to be settled for. An alternative method of numerical softening of the contact, similar to the penalty algorithm, had to be found to try to solve the problem.

4.7.3 Hard or Soft Contact

Initially, the default hard contact was chosen as Grobbelaar [35] successfully used it and this type of contact minimises penetration of the slave nodes into the master surface. But because the penalty contact algorithm is required, but cannot be used because of an ABAQUS bug, soft contact was then selected as a substitute.

For soft contact, the exponential pressure-overclosure relationship was chosen as it is simple (only requires two points for curve definition) and because it can minimise the penetration of the slave nodes into the master surface. This reduction of penetration is possible because this relationship allows contact pressure to be applied to the surfaces while they are still separate before overclosure occurs. The first input required by ABAQUS is the clearance distance where the exponential curve begins (when the contact pressure is zero). This was selected to be a short distance of 0.5mm so that the explosive and V-plate contact surfaces only experience resistance when

they are close to contact, making the model as realistic as possible. The second input required by ABAQUS is the contact pressure when contact occurs (when the separation distance of the two surfaces is zero). This was determined by trial and error to be 0.01 Mbar as this contact pressure is low enough to allow the surfaces to make contact but high enough to restrict excessive surface penetration.

All the models were analysed using both hard contact and soft contact. From a comparison of the results, hard contact was finally chosen instead of soft contact. The reasons for this will be discussed in the "Attempts to Determine What Causes the Inaccuracies in the Models Containing Rod Explosives and How to Improve the Results" in the "Results and Discussion" chapter.

4.7.4 Separation or No Separation of Surfaces

Initially, it was decided that the contacting surfaces should be allowed to separate in the model as this would occur in the actual system.
But, as before, the results of the rod versions of the models which allowed separation, affected this decision. On the advice of Dr Izak Snyman [41], selecting no separation of the surface was attempted.

The no separation approach was unsuccessful, however, because when the surface of the explosive rebounds from the V-plate surface, the surface of the V-plate moves with the explosive surface as they are bound together. The V-plate is pulled upwards in the opposite direction of its expected deformation and yields completely incorrect results. Because of this, separation of the contacting surfaces is allowed in all of the models.

5. Previous Experimental and Numerical Results

5.1 Previous Experimental Results

To verify the results obtained from the numerical models in this study, these results have to be compared to experimental results.

The first step of verification involves modelling the simple system of a round flat steel plate which is fixed at the boundaries, being exploded by a centrally positioned disc of PE4. Experiments on this system have been conducted by Radford [25] and the experimental results are used to verify this simple model. This system can be modelled using axisymmetric elements, but was instead modelled using three-dimensional continuum elements, and only a quarter model was created owing to planes of symmetry. This was done because the more complex models which are relevant to this study will be modelled in this manner. If this simple model is verified, then the more complex systems relative to this study can be modelled.

Experiments on the V-plate systems containing rod explosives have been previously conducted by Lockley [43]. The numerical models are geometrically identical to these experimental systems so that their results are comparable. The geometry of the rod explosive and the V-plate can be seen in Figure 4.7 and Figure 4.8. The experimental set-up of the rod explosive and V-plate system can be seen in Figure 5.1. The V-plate can be seen to be bolted to the ballistic pendulum, and the pen of the ballistic pendulum can be seen drawing on paper. The polystyrene support which positions the explosive 12mm away from the V-plate and which prevents spallation of the V-plate can be seen on the ridge of the V-plate.

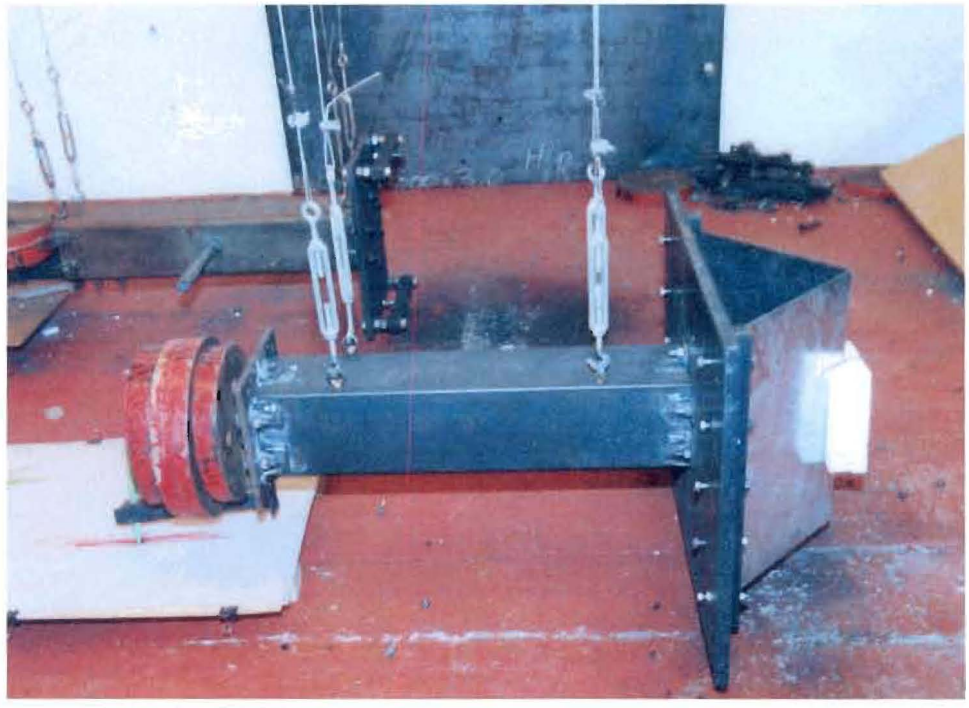

Figure 5.1: A picture of the experimental set-up of the experiments conducted by Lockley [43]

If the models of the rod explosive systems are verified by the experimental results, it indicates that the similar disc explosive systems, which are the models of interest in this study, have a high likelihood of yielding accurate results.

The report compiled by Lockley [43] documenting the experimental study has unfortunately been lost, but the necessary results were available from Nurick [40]. The results consist of the explosive impulse transferred to the V-plates, deflection of the mid-point of the ridge of the V-plates, and photographs of the deformed V-plates. Figure 5.2 shows one of these photographs. The complete set of photographs along with the impulse and deflection values can be found in Appendix A.

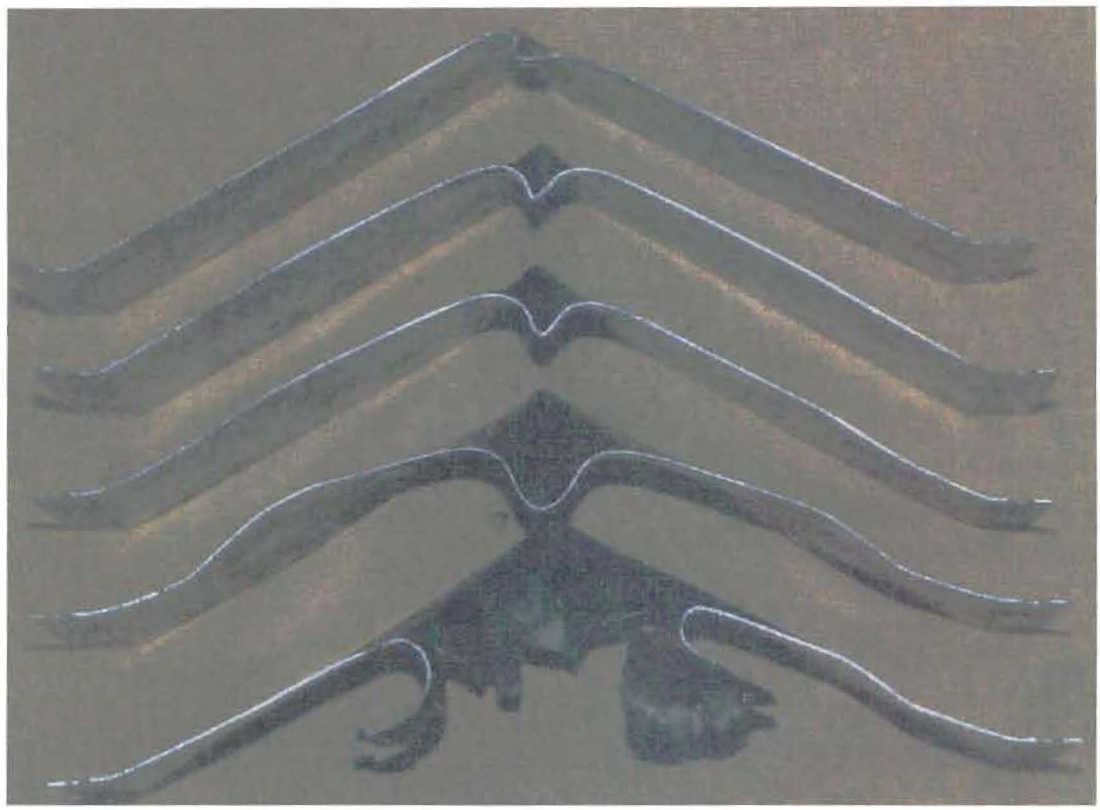

Figure 5.2: The experimentally exploded 120^0 V-plates obtained by Lockley [43].

To verify the models, the mid-point deflections of the V-plates as well as their deformed profiles need to be compared to the deflections and profiles predicted by the ABAQUS models. The only way the deformed profiles of the V-plates could be obtained was to extract them from the photographs. To do this, image-processing had to be performed on the photographs. The computer package, ArcView GIS 3.2, was used to trace the deformed profiles in the photographs onto an arbitrary co-ordinate system. The co-ordinates of points on the traced lines were then extracted and used in Excel to plot the deformed profiles. The profiles, still in the arbitrary co-ordinate system, had to then be scaled to the actual geometry of the V-plates so that they were compatible with the numerically predicted profiles. The profiles could not be scaled with a single factor, but had to be scaled along two perpendicular axes to take into account the perspective in the photographs.

To scale the profiles, the plots, still in the arbitrary co-ordinate system, were rotated until the V-plate profiles were vertical (i.e. the ridge of the V-plate was pointing upwards). The true horizontal widths of the V-plates (which are all identical) was obtained from some experimental specimens found in a display cabinet in the University of Cape Town Mechanical Engineering Department. The true vertical heights of all the deformed V-plates was determined from the true width, the known angle of the plates, and the mid-point deflection of the V-plates obtained from the experimental results. The ratio of the true horizontal width to the horizontal width of a profile in the arbitrary co-ordinate system yields the horizontal scaling factor. Likewise, the ratio of the true vertical height to the vertical height of a profile in the arbitrary co-ordinate system yields the vertical scaling factor.

Once the deformed profile plots had been scaled, they were then translated to a suitable position on the graph. The deformed profiles predicted by ABAQUS will be superimposed over these experimental profiles for comparison.

5.2 Previous Numerical Results

By comparing previous numerical results of a system with numerical results obtained during this study and with the experimental results of this system, the accuracy of the different numerical approaches can be compared to determine the superior approach.

The rod explosive and V-plate systems were numerically modelled by Nannucci [44]. Unfortunately, the report documenting this numerical study has been lost and the only results available were ABAQUS pictures of the meshes of the deformed V-plate profiles, and the predicted deflections of the mid-point of the ridges of the V-plates. These pictures were obtained from Nurick [40]. Figure 5.3 shows some of these pictures. The complete set of pictures along with the deflection values can be found in Appendix B and Appendix G.

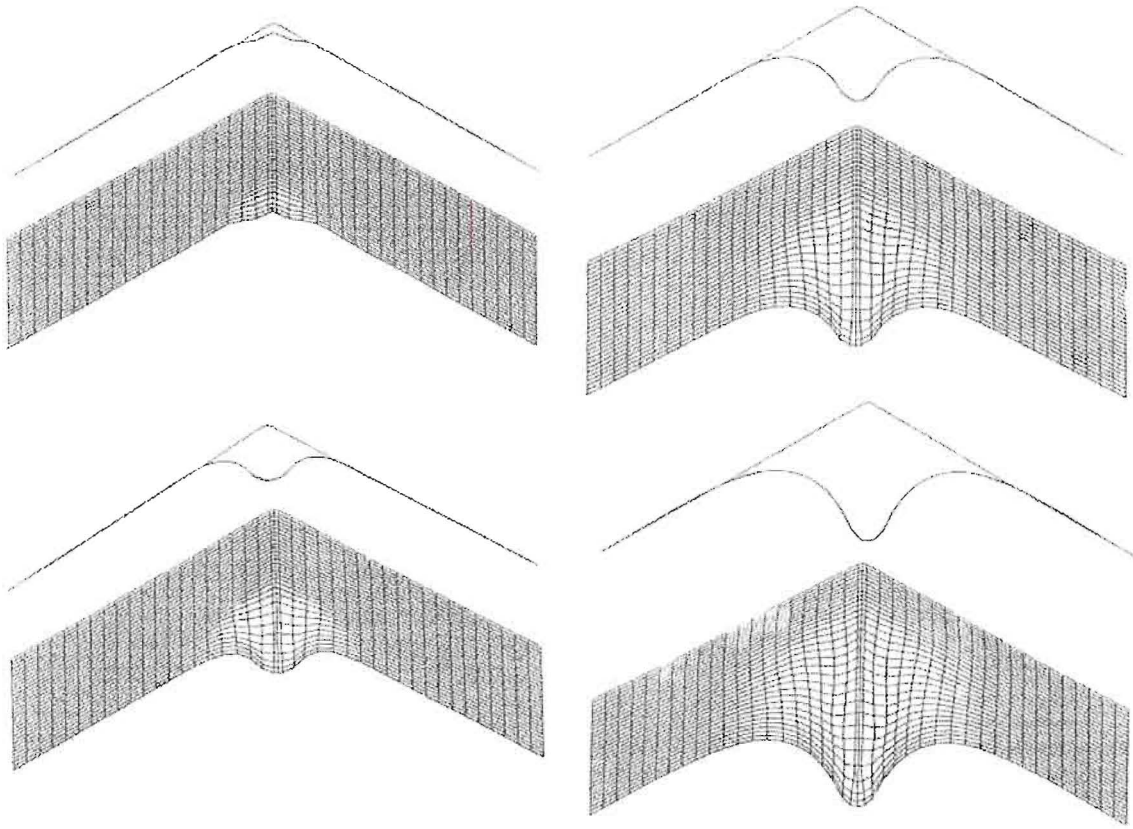

Figure 5.3: The results of the numerical models for the 120^0 V-plates modelled by Nannucci [44].

Points along the deformed profiles in the pictures were extracted and plotted in Excel, as done before when extracting the deformed profiles from the photographs. Because the pictures are two-dimensional a single scaling factor can be applied as distortion due to perspective is not involved. The plots of these numerical results can then have the numerical results obtained during this study and the experimental results superimposed on them for comparison.

The method used by Nannucci [44] of modelling the explosive loading is not certain, but it is known that a pressure profile was used, so the numerical results obtained by Nannucci [44] represent the pressure loading approach.

The numerical results obtained in this study represent the equation of state approach. An attempt was made to determine the pressure loading method used by Nannucci [44]. The method of applying a uniform pressure load over the entire plate surface as used for systems involving flat circular plates, cannot be applied to the V-plate systems.

The most likely method that could have been used is to apply a uniform localised pressure load over the area on the V-plate determined by the projection of the cross-sectional area of the rod explosive. A more complex, but more accurate method that could also have been used, is the pressure loading method developed by Bimha [26]. This method also involves applying a uniform pressure load over the area on the V-plate determined by the projection of the cross-sectional area of the rod explosive. This method goes a step further and also applies an exponentially decaying pressure load as a function of distance from the projected area. These three methods of applying explosive loading in a numerical model by using pressure loading, are discussed in detail in the "Numerical Studies" section in the "Literature Review" chapter.

Attempts were made to recreate the numerical models and results obtained by Nannucci [44] using the two possible methods, so the method used by Nannucci [44] could be found. The first method of applying a uniform pressure load over a localised area did not work as transferring a large impulse to the V-plate over a small area for a very short duration results in an extremely high pressure. This high pressure results in numerical instability of the model and the deforming elements stretch an excessive, unrealistic distance. This numerical instability can be seen in Figure 5.4.

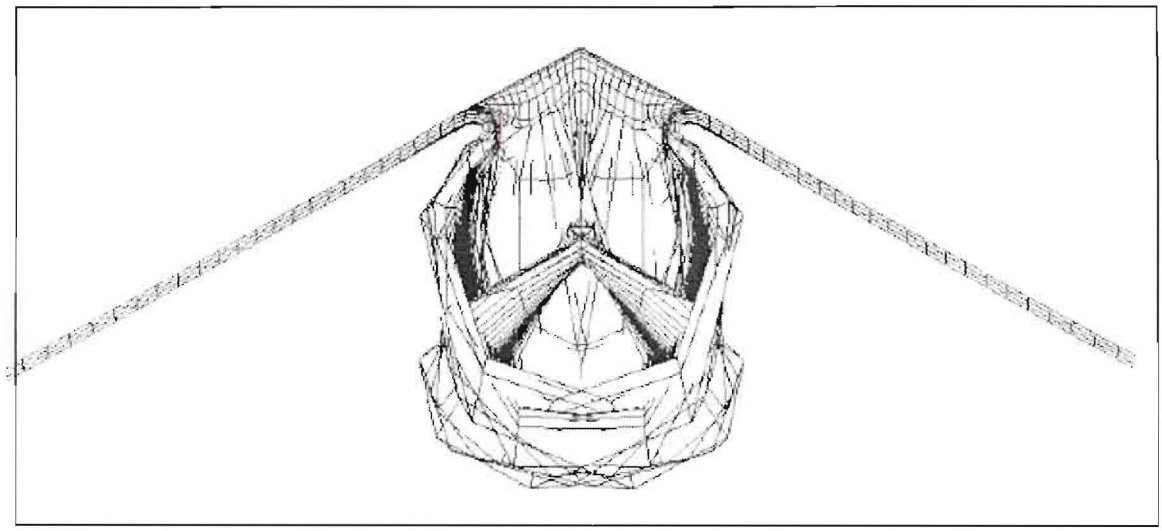

Figure 5.4: Numerical instability resulting from modelling the explosive as a pressure load over a localised area of the V-plate for a short duration.

Extreme mesh refinement and reasonably increasing the duration of the pressure loading did not solve this problem. This numerical instability has also been experienced by previous investigators such as Radford [25] when modelling high impulsive loading over a localised area. Although the localised pressure loading approach is a recognised method, a numerical model successfully using this method for high impulses, could not be found in the literature.

The second possible method used by Nannucci [44] is the method developed by Bimha [26]. Wiehahn [34] used this method to model disc explosives exploding circular flat plates in ABAQUS. To implement this method, Wiehahn [34] used the VDLOAD user subroutine which is written in the FORTRAN programming language, to model the complex pressure profile.

To implement this method for a rod explosive which Nannucci [44] was modelling, would have been complicated and it is unlikely that this was the method used. Nonetheless, this method was attempted.

Unfortunately, a bug in ABAQUS, which was not present in the earlier ABAQUS versions, prevented models containing the VDLOAD user subroutine from running. Because of these obstacles, the models and results obtained by Nannucci [44] could not be recreated.

6. Results and Discussion

The models discussed in the previous chapter ("The Finite Element Model") were created and analysed. The results of these models will be presented and discussed in this chapter.

6.1 The Flat Circular Plate and Explosive Disc Model

The first model to be created and analysed was the simple system of a round flat steel plate which is fixed at the boundaries, being exploded by a centrally positioned disc of PE4 explosive. This system can be modelled using axisymmetric elements, but was instead modelled using three-dimensional continuum elements, and only a quarter model was created owing to planes of symmetry. This was done because the more complex models which are relevant to this study will be modelled in this manner. Experiments on this system have been conducted by Radford [25] and the experimental results are used to verify this simple model as the geometries of the model are identical to those in the experiments. If this simple model is verified, then the more complex systems relative to this study can be modelled with a certain degree of confidence. Figure 6.1 shows the comparison between the results of this simple system obtained from the three-dimensional continuum element quarter model, the results obtained from Grobbelaar's axisymmetric model [35], and the experimental results obtained from the experiments conducted by Radford [25].

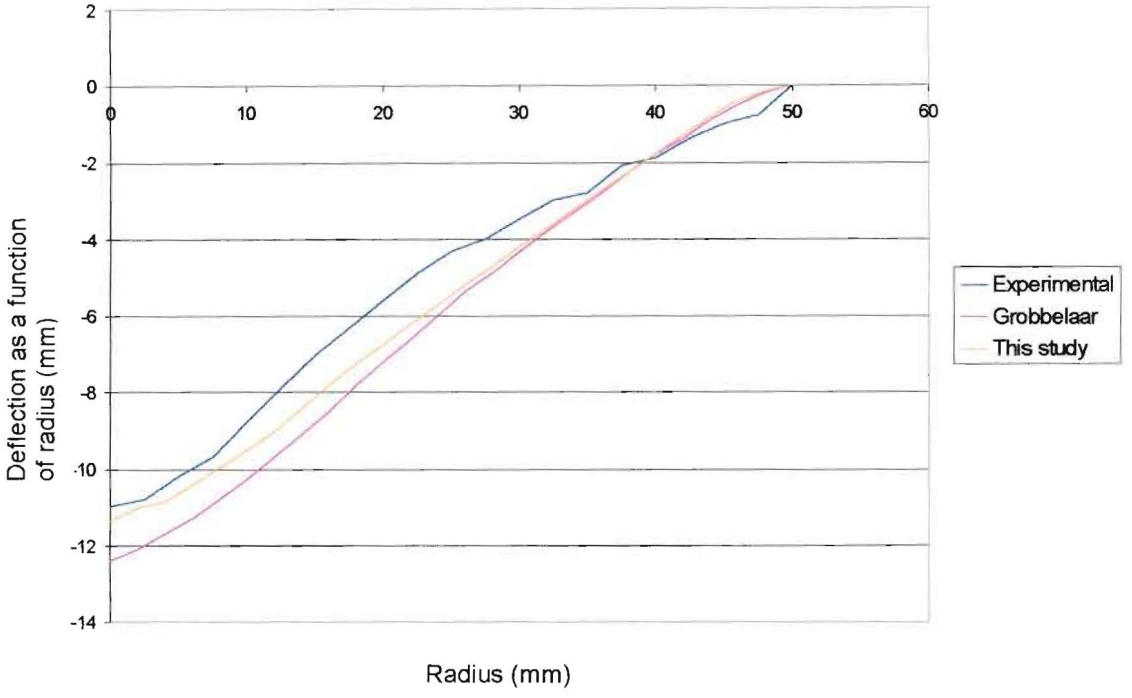

Figure 6.1: A Comparison Between the Flat Plate Profiles of Grobbelaar's Axisymmetric JWL EOS Model, the Three-Dimensional JWL EOS Model from this Study, and the Experiment.

From Figure 6.1 it is clear that the three-dimensional continuum element quarter model analysed in this study gives comparably acceptable results. The results of this model are even slightly superior to those obtained from Grobbelaar's axisymmetric model [35]. The model created by Grobbelaar [35] predicts the mid-point displacement to be 12.4mm while the model analysed in this study predicts a displacement of 11.4mm which is closer to the experimental displacement of 11mm. The numerically predicted deformed profile of the flat circular plate obtained from the model in this study is also very similar to the experimental deformed profile - more so than the deformed profile obtained from Grobbelaar's model [35].

The successful results of the model analysed in this study indicate that the material properties and meshes, the boundary conditions on the plate boundaries, the boundary conditions on the planes of symmetry, and all other aspects of the model are suitable. They also indicate that ABAQUS has successfully modelled the detonation, expansion, and interaction of the explosive with the plate. This means that the simple model has been verified and that all the aspects of this model can be used, where applicable, with a certain degree of confidence in the more complex models of this study.

6.2 The V-Plate and Explosive Rod and Explosive Disc Models

These models contain steel V-plates with either an explosive rod and fuse, or an explosive disc, positioned centrally above the V-plate ridge. Only a quarter model of the system is created owing to planes of symmetry.
The upper and lower surfaces of the V-plate flanges are fixed to simulate clamping. (See the "The Finite Element Model" chapter for in-depth details of this model).

6.2.1 General Observations

When all the models had been analysed, the results were examined.
ABAQUS/CAE allows the user to view many different requested outputs at the intervals that were requested in the input deck of the model.
The requested outputs can be operated on to form new outputs.
All the outputs can be reported in tabular form in report files, they can be plotted on graphs, and they can be viewed graphically. When viewing the results graphically, the deforming model can be viewed at the intervals in the form of 'snapshots'. These snapshots can be automatically sequenced so that the model appears animated and resembles a 'movie clip'.

From examining the results of all the different models using these methods, general observations can be made. Later, observations, results, and trends of specific sets of models will be reported and discussed.

All general observations discussed, apply to both the models containing rod explosives and the models containing disc explosives unless otherwise specified.

6.2.1.1 Detonation of the Explosives

The first part of the models to react is the explosive, so the detonation of the explosive was examined first. Typical snapshot sequences of detonating explosives can be seen in Figure 6.2 and Figure 6.3. Figure 6.2 shows a detonating explosive rod and fuse and Figure 6.3 shows a detonating explosive disc. Both these figures show the pressure distribution throughout the explosives.

It can be seen that in both Figure 6.2 and Figure 6.3 the explosives start to detonate at the designated detonation points. The detonation point for the rod and fuse explosive is at the centre of the top surface of the fuse, and the detonation point for the explosive disc is at the centre of the top surface of the explosive disc (see Figure 4.23). The detonation fronts of the explosives spread out from the detonation points at the detonation speed of the explosive, $C_D = 8190$ m.s^{-1}. When the detonation fronts pass a point in the explosive, this point begins to expand. In order to avoid discontinuities, the burn wave is spread over several elements. These elements are subjected to a pressure which is determined by using the burn fraction. The use of the burn fraction can be reviewed in the "Jones-Wilkins-Lee Equation of State" section in the "ABAQUS Overview" chapter and allows for a 'smooth' distribution of the pressure which can be seen in both Figure 6.2 and Figure 6.3. Application of the burn fraction means that the peak pressures of the explosives slightly trail the detonation fronts. The peak pressures range from about 0.15 Mbar to 0.2 Mbar for the rod and fuse explosive, and from about 0.13 Mbar to 0.16 Mbar for the disc explosive. Once the explosives have completely detonated it can be seen that the pressure distributions do not vary much across the explosives.

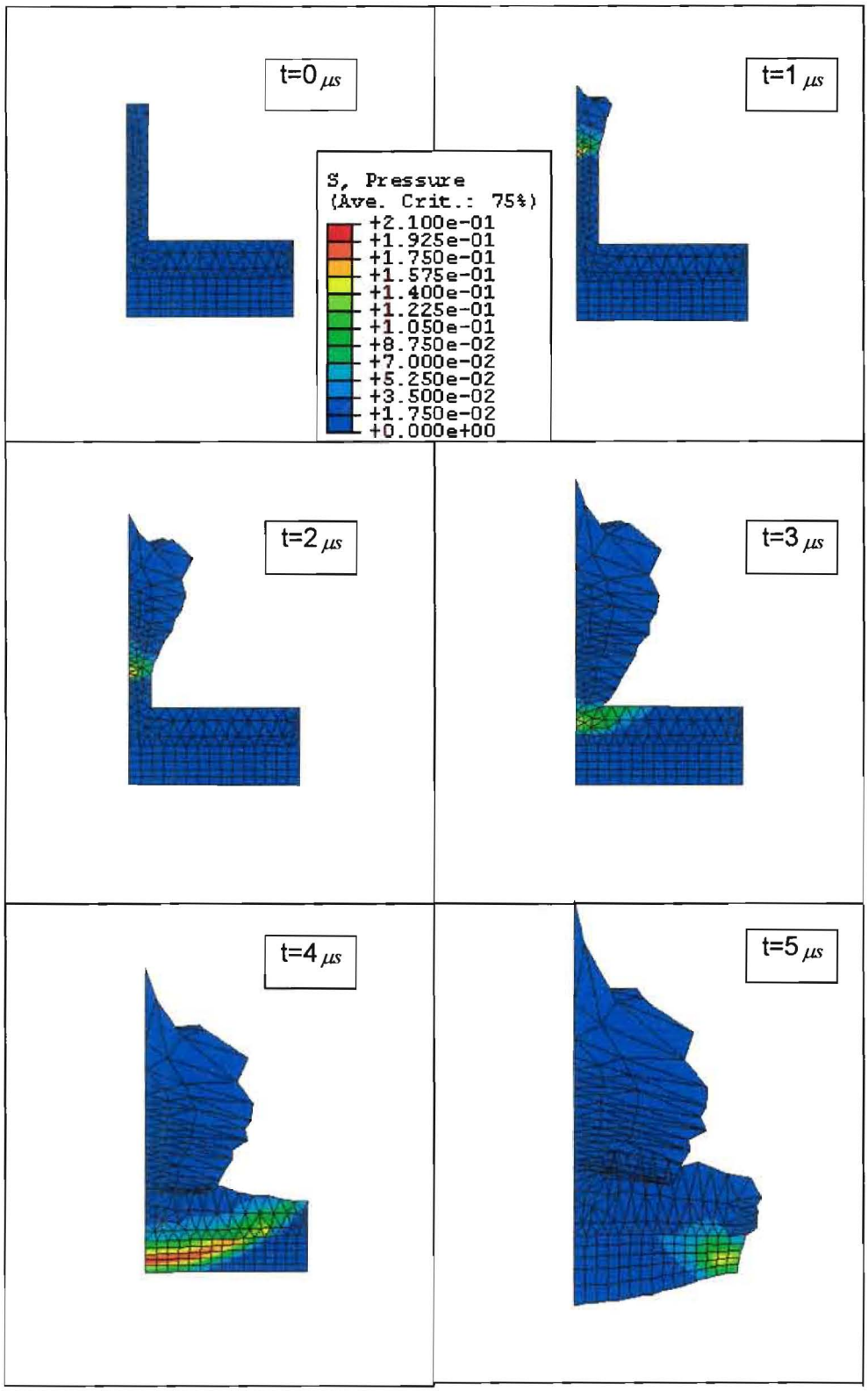

Figure 6.2: The pressure distribution during the detonation of a 9g rod and fuse explosive. The units are Mbar.

The expansion of the explosives occur at extremely high velocities. The highest velocities occur at the expanding boundaries of the explosives and are in the region of 4500 $m.s^{-1}$ for both the rod and fuse explosive and the disc explosive. The explosives strike the V-plates at approximately this velocity. Figure 6.4 and Figure 6.5 show the velocity distributions of an expanding rod explosive and an expanding disc explosive respectively.

Grobbelaar [35] summarised the three parameters which define the expansion of an explosive. They are:

- Position of the detonation point.
- Burn speed (detonation speed) of the explosive.
- Geometry of the explosive.

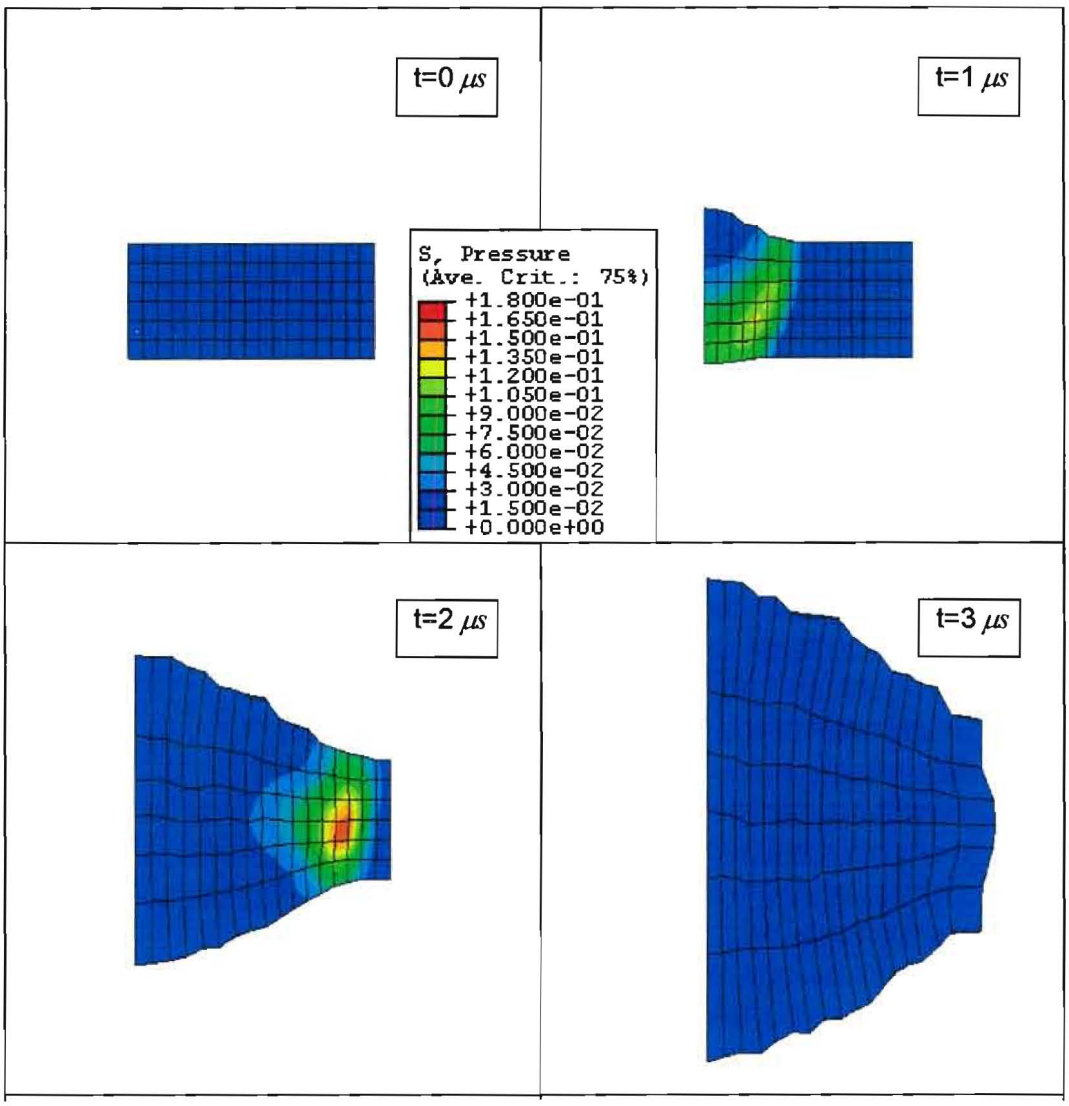

Figure 6.3: The pressure distribution during the detonation of a 8g disc explosive. The units are Mbar.

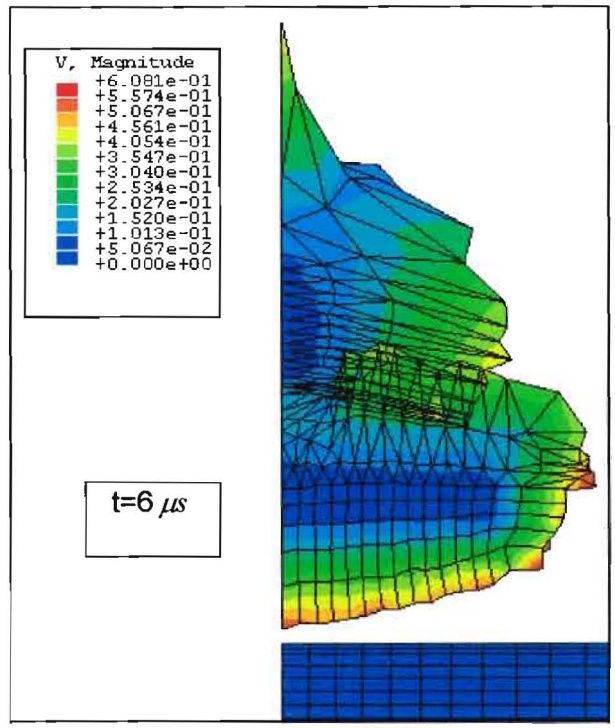

Figure 6.4: Rod explosive velocity distribution after detonation (cm. μs^{-1})

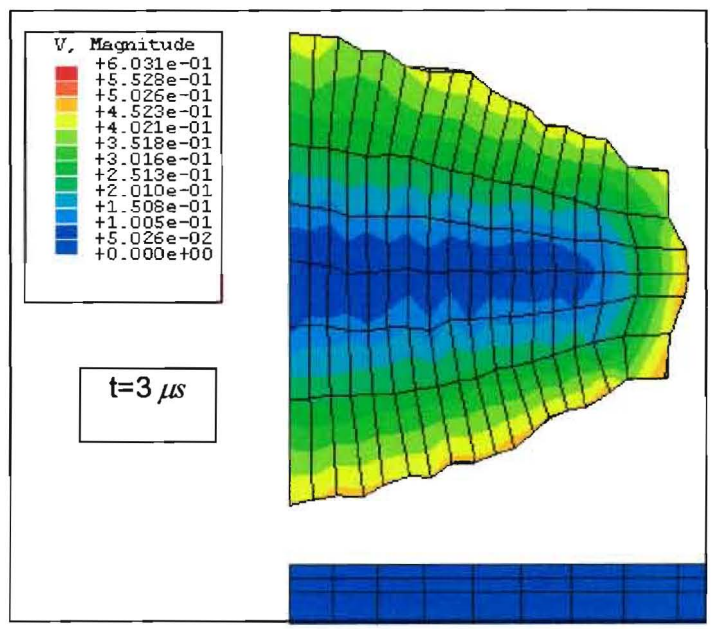

Figure 6.5: Disc explosive velocity distribution after detonation (cm. μs^{-1})

6.2.1.2 Interaction of the Explosives with the V-Plates

A typical snapshot sequence of an entire model (i.e. explosive and V-plate) can be seen in Figure 6.6. This model contains an explosive disc.

As the explosive disc detonates, the explosive elements expand and elongate in the direction of the plate. It takes approximately 4 μs from the time of detonation (0 μs) until the nodes of the disc explosive make contact with the V-plate, and 7 μs for the rod explosive nodes to make contact with the plate after detonation. The rod explosive takes longer to make contact with the V-plate because of the fuse, as the detonation front has to travel a further distance before the explosive has completely detonated.

For both the rod and disc explosives, when the nodes of the explosive come into contact with the plate, the plate immediately starts deforming in the direction away from the impacting nodes. The strain rate of the V-plate reaches the order of 10 000 s^{-1}. The explosive nodes then begin to slide down the sides of the deforming V-plate. Because of this the explosive elements in contact with, and near the V-plate, become extremely elongated and flattened. This distortion is what led to the errors discussed previously in the "Element Distortion" section in the "The Finite Element Model Chapter". Both the rod and disc explosives interact with approximately 3-6cm of the side of the V-plate from the ridge. The explosives then slowly rebound from the V-plate, eventually separating from the V-plate completely.

After separation, the nodes of the explosives are frozen to prevent termination of the analysis, and the V-plate continues deforming under its own inertia. Both the rod and disc explosives are frozen at between 30-60 μs after detonation. This means that complete separation of the explosives from the V-plates occurs just before these times.

Figure 6.6: Interaction between an 8g explosive disc and a 150^0 V-plate (represented by a quarter model). The stress distributions are shown. The units are Mbar.

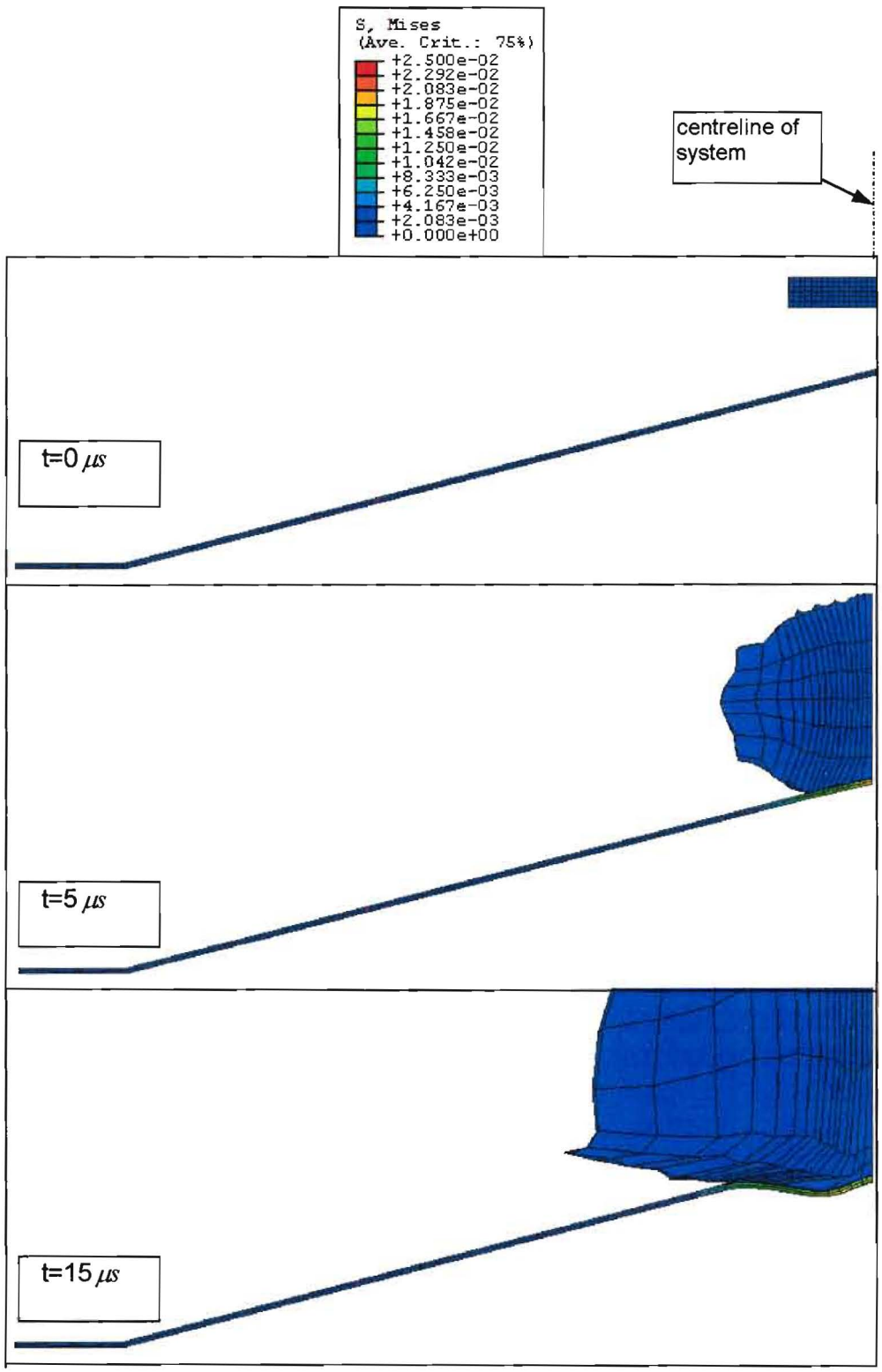

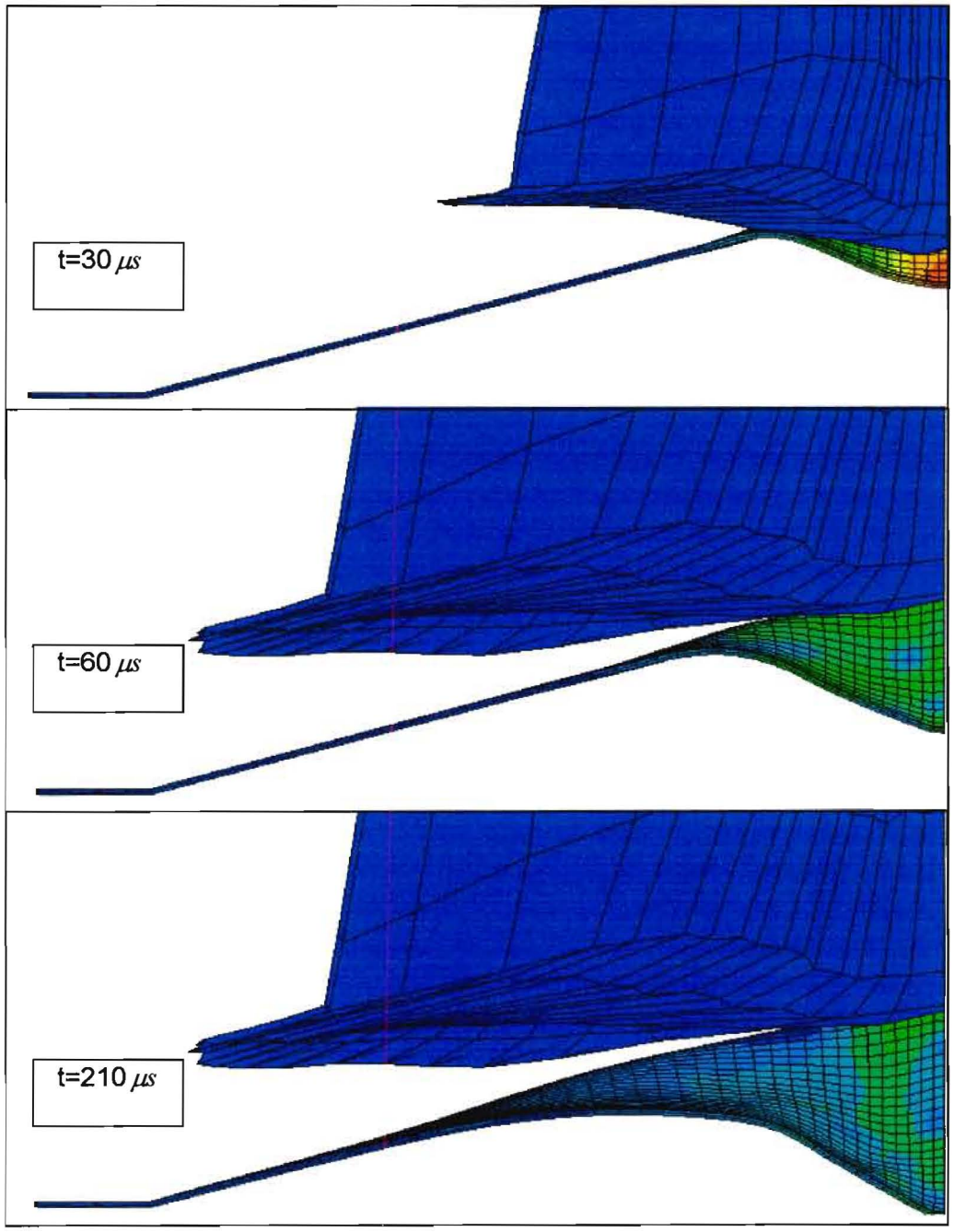
t=30 μs
t=60 μs
t=210 μs

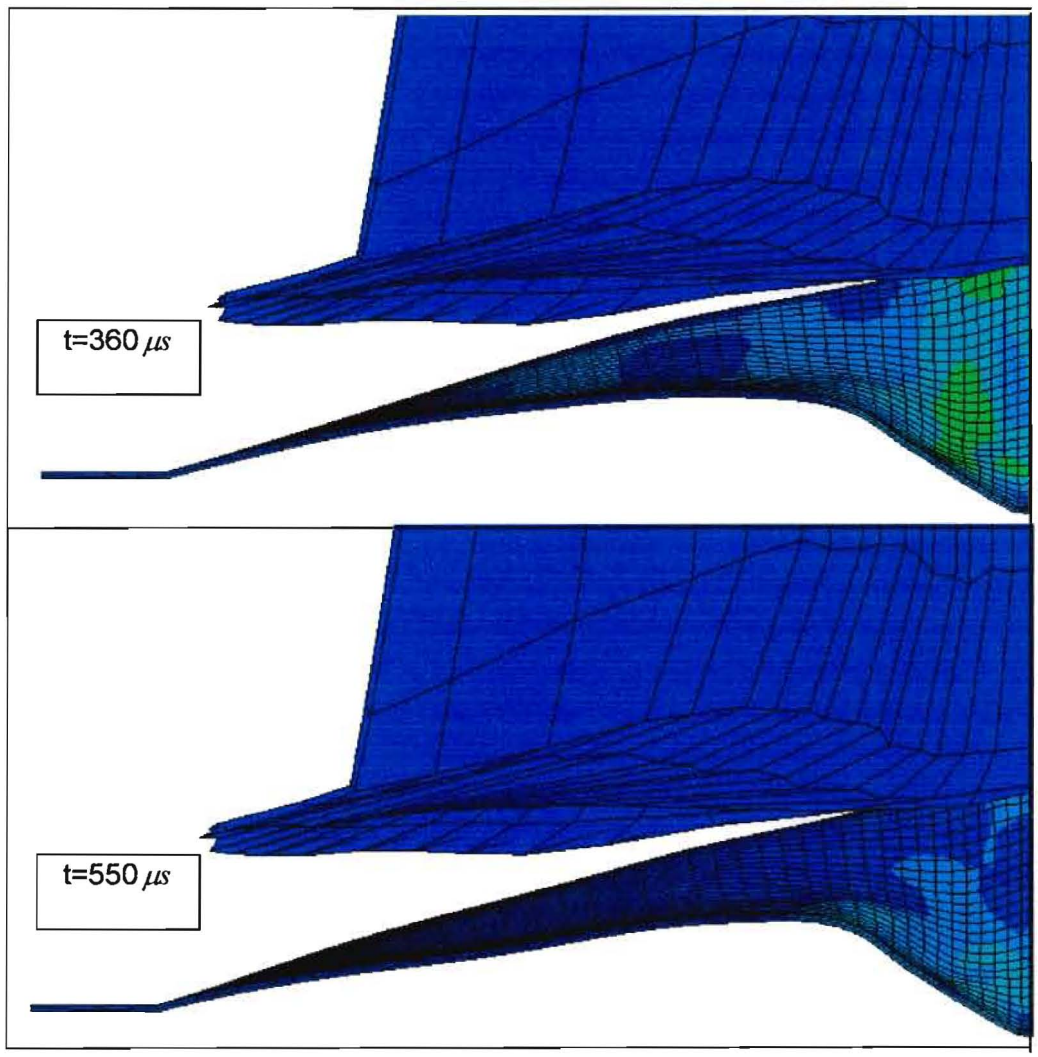
t=360 μs
t=550 μs

6.2.1.3 Displacement and Time Response of V-Plates

Both the rod and disc explosives first make contact with the ridge of the V-plate which instantly starts deforming. The explosives then slide and spread down the V-plate side. As the explosives reach a part of the V-plate, that part begins to deform. Once the explosives separate from the V-plate the V-plate continues deforming under its own momentum. The deformation 'hinge' which is the boundary between the deformed area and the undeformed area of the V-plate, appears to generally remain at the position of the outer limits of the explosive interaction with the V-plate.

The analysis ends at 550 μs when it is assumed that the motion of the V-plate has reached a steady state. To check if the motion has reached steady state, the displacement history of the node on the ridge of a V-plate profile, is plotted. This node undergoes the greatest displacement. Figure 6.7 shows the displacement versus time plot of this node from a model containing a 90 degree V-plate and an 8g explosive disc.

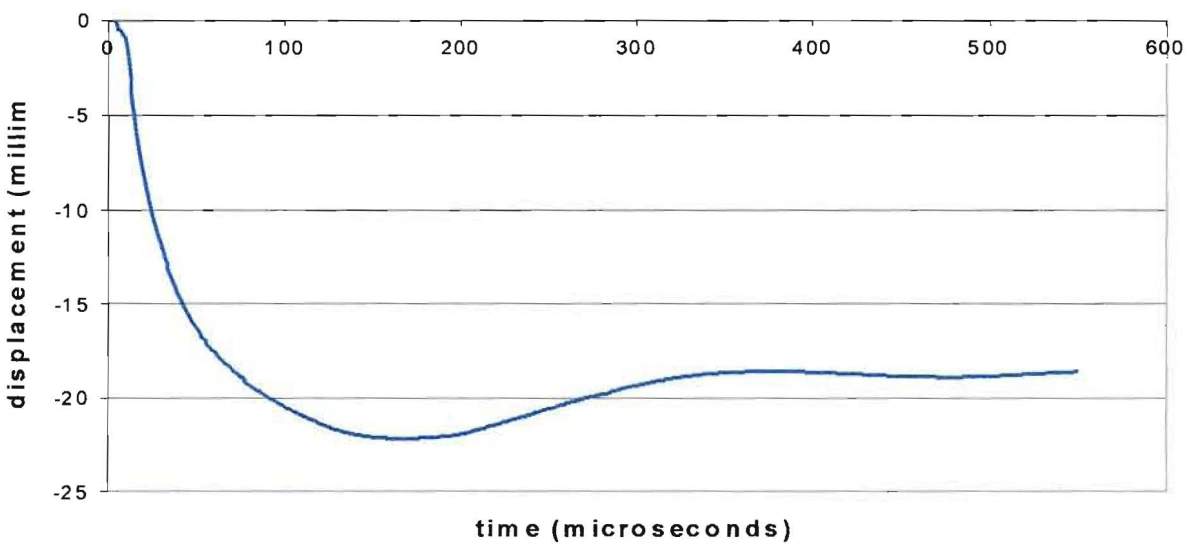

Figure 6.7: Displacement versus time for the ridge of a V-plate profile from a model containing an 8g explosive disc and a 90 degree V-plate

Figure 6.7 illustrates that the node reaches a reasonable equilibrium at approximately 350 μs so the analysis duration of 550 μs is considered suitable. Similar tests were conducted on the other models containing different V-plates, and explosives of different masses and diameters. It was found that 550 μs was suitable for all the models.

6.2.2 The Results of the Models Containing an Explosive Rod

The results of the models containing an explosive rod will be presented and discussed here. The results from these JWL Equation of State models in this study will be compared to results from previous pressure profile models created by Nannucci [44] and experimental results obtained by Lockley [43]. Characteristics of the V-plates such as the mid-point displacements and the profiles will be compared. The impulses transferred to the V-plates, as calculated by the models in this study, will also be compared to the experimental results. All the results obtained from the models will be examined for trends to determine the dependency of the displacements and profiles of the V-plates on parametric variations.

6.2.2.1 Comparison Between the JWL Equation of State Model Predictions of the V-Plate Mid-Point Displacements, the Pressure Profile Model Mid-Point Displacements, and the Experimental Mid-Point Displacements

The relationships that the V-plate mid-point displacements have with the explosive rod masses and the V-plate angles are investigated.

It must be mentioned that some (not many) of the experimental mid-point displacements used for comparison in these investigations were altered. This is because the original displacements were clearly not correct according to

the V-plate profiles obtained from the image processing results so the displacements obtained from the image processing were used instead.

Some (not many) of the experimental mid-point displacements used for comparison in these investigations had to be estimated. This is because the displacements did not originally have displacement values from the experimental results as the V-plates in these experiments tore along the ridge, so there were no specific mid-point displacements of these V-plate profiles. For the V-plates which had only slight tearing, the V-plate profiles were used to calculate the average of the displacements of the ends of the torn sides for the mid-point displacements. For the V-plates which had extreme tearing, no estimates were made as the estimates may be highly inaccurate. The reason for estimating mid-point displacements is that there were not sufficient experimental displacements for comparison with the model results or to determine trends.

All the mid-point displacements can be seen in Appendix G. The altered and estimated displacements are indicated in this Appendix.

6.2.2.1.1 Comparison of the V-Plate Mid-Point Displacements Versus the Explosive Rod Masses

The first relationship examined was between the displacement of the mid-point of the V-plate and the explosive mass used. Graphs displaying this relationship for V-plates of different angles can be seen in Figure 6.8 to Figure 6.11.

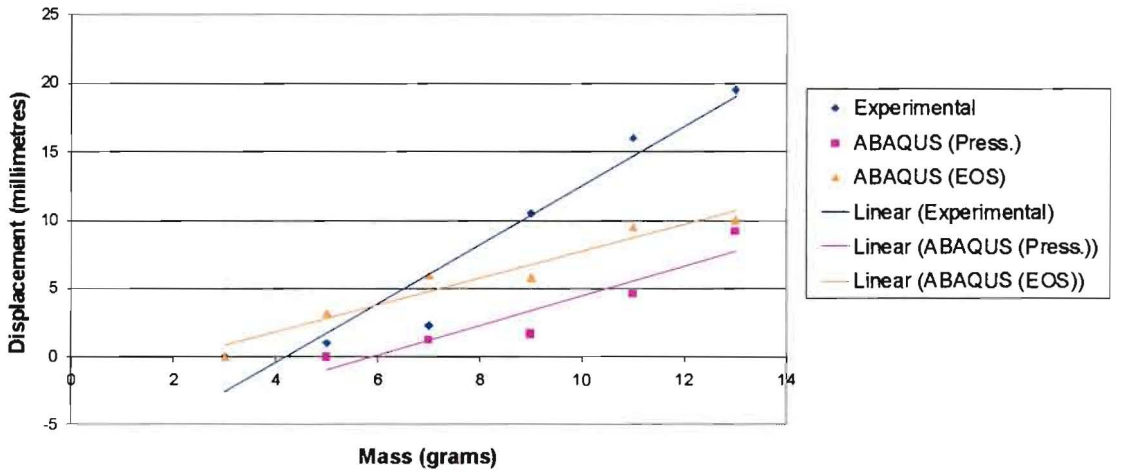

Figure 6.8: 60^0 V-Plate Mid-Point Displacement Versus Explosive Rod Mass Obtained from the Experiments, the ABAQUS Pressure Profile Analyses, and the ABAQUS Equation of State Analyses.

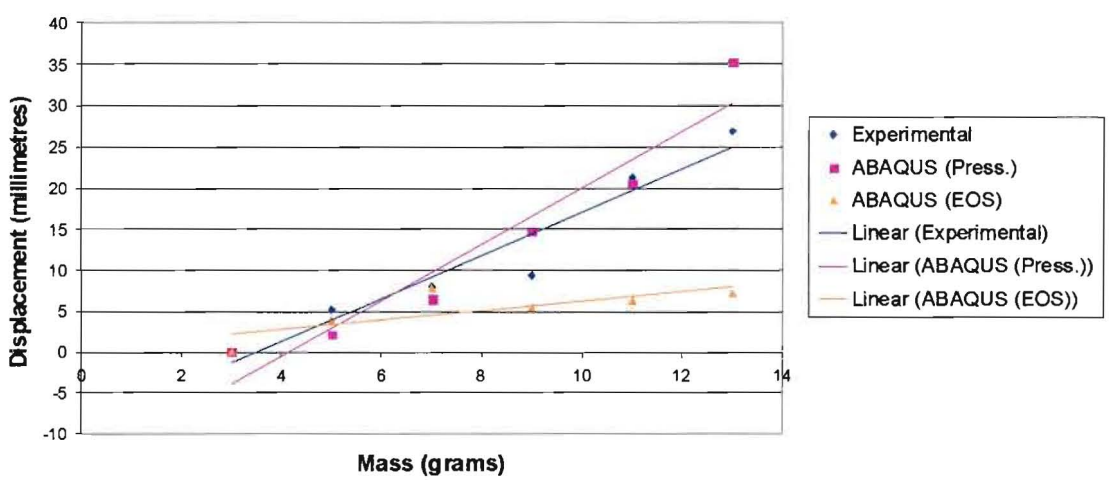

Figure 6.9: 90^0 V-Plate Mid-Point Displacement Versus Explosive Rod Mass Obtained From the Experiments, the ABAQUS Pressure Profile Analyses, and the ABAQUS Equation of State Analyses.

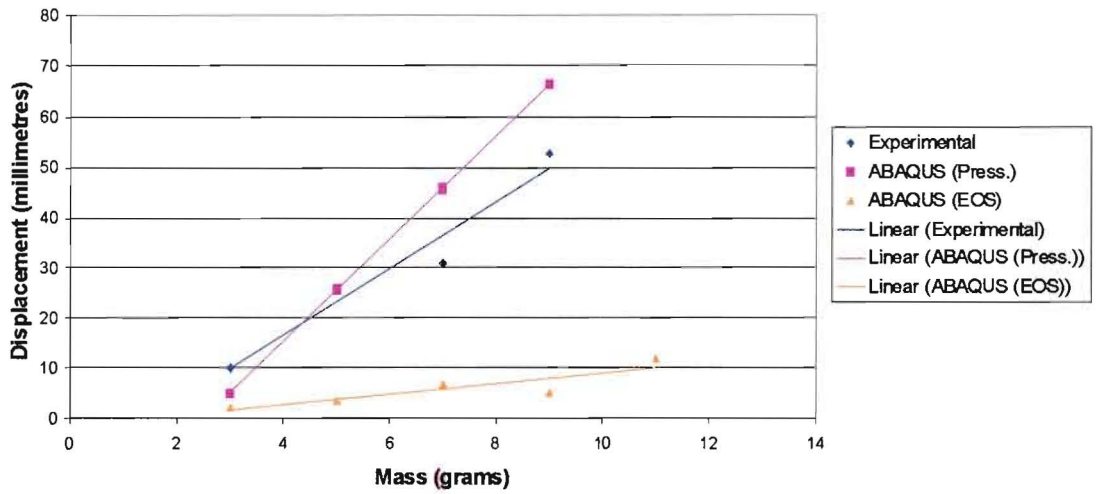

Figure 6.10: 120^0 V-Plate Mid-Point Displacement Versus Explosive Rod Mass Obtained From the Experiments, the ABAQUS Pressure Profile Analyses, and the ABAQUS Equation of State Analyses.

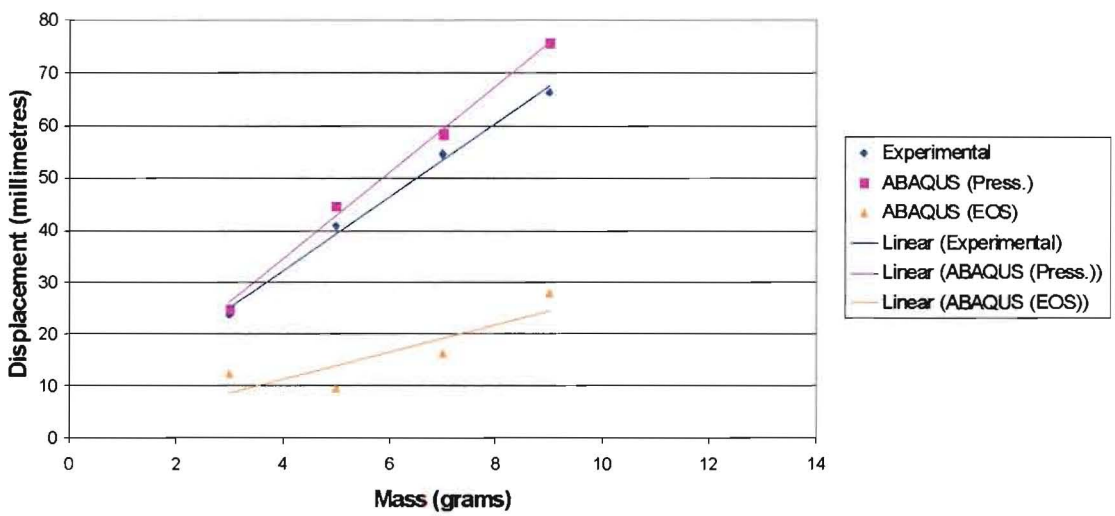

Figure 6.11: 150^0 V-Plate Mid-Point Displacement Versus Explosive Rod Mass Obtained From the Experiments, the ABAQUS Pressure Profile Analyses, and the ABAQUS Equation of State Analyses.

It is clear from the graphs that the relationship between the permanent mid-point displacement and the explosive mass is linear. This is reflected by both the model predictions and the experimental results. Linear trend-lines were inserted on the graphs to demonstrate this linearity and it can be seen that the points of each series do not deviate greatly from their trend-line. As expected, the mid-point displacement increases with increasing explosive mass for both the model predictions and the experiments, therefore the 3g explosive rods produced the smallest displacements. This indicates that the 3g explosives cause the least damage to the V-plates. The slopes of the JWL EOS model trend-lines, which is the rate of increase of the displacement with respect to explosive mass, is significantly less than the slopes of the experimental trend-lines in all of the graphs in Figure 6.8 to Figure 6.11.

In Figure 6.8, which shows the displacement versus mass for 60^0 V-plates, the magnitudes of the JWL EOS model displacements are higher than the corresponding experimental displacements for the 5g, and 7g explosives, but are lower for the 9g, 11g, and 13g explosives. The JWL EOS model displacement for 3g is the same as the experimental displacement as both are zero. The largest difference in the displacement results is for the 13g explosive rod where the experimental displacement is 19.5mm while the JWL EOS model displacement is 10.1mm - a difference of 9.4mm, which is a 48% error. The pressure profile model displacements trend-line slope is similar but slightly greater than the JWL EOS model trend-line. The pressure profile model displacements are all less than their corresponding JWL EOS model displacements, and all significantly less than their corresponding experimental displacements, except for the 3g explosive displacements which are all the same as they are zero. It must be mentioned that the 3g explosive displacement obtained from the ABAQUS pressure profile models, has been excluded from the graph in Figure 6.8. The 5g explosive displacement is also zero and including the 3g explosive displacement would adversely affect the related trend-line. From Figure 6.8 it can be seen that , for the 60^0 V-plates, the JWL EOS models yield slightly better displacement predictions than the predictions obtained from the pressure profile models for the 9g, 11g, 13g

explosive masses, but poorer results for the 5g and 7g masses. Both models produce the same displacement prediction of zero for the 3g explosive mass.

In Figure 6.9, which shows the displacement versus mass for 90^0 V-plates, the magnitudes of the JWL EOS model displacements are all lower than their corresponding experimental displacements, except for the 3g explosive mass, where the two displacements are the same as both are zero. The largest difference in the displacement results is for the 13g explosive rod where the experimental displacement is 26.9mm while the JWL EOS model displacement is 7.2mm - a difference of 19.7mm, which is a 74% error. The pressure profile model displacements trend-line slope is higher than the JWL EOS model trend-line, and is similar, but a little higher than the experimental displacements trend-line. The pressure profile model displacements are lower than the JWL EOS model displacements for the 5g, and 7g explosives, but are higher for the 9g, 11g, and 13g explosives, except for the 3g explosive displacements which are all the same as they are zero. The pressure profile model displacements are lower than the experimental displacements for the 5g, 7g, and 11g explosives, but are higher for the 9g, and 13g explosives. The 3g explosive displacements are the same as they are both zero. From Figure 6.9 it can be seen that the pressure profile models yield better displacement predictions than the predictions obtained from the JWL EOS models, for 90^0 V-plates.

In Figure 6.10, which shows the displacement versus mass for 120^0 V-plates, the magnitudes of the JWL EOS model displacements are all significantly lower than their corresponding experimental displacements. The largest difference in the displacement results is for the 9g explosive rod (experimental results for 11g and 13g explosives were not available) where the experimental displacement is 52.7mm while the JWL EOS model displacement is 5.3mm - a difference of 47.4mm, which is a 90% error. The pressure profile model displacements trend-line slope is significantly higher than the JWL EOS model trend-line, and is also a little higher than the experimental displacements trend-line. The pressure profile model

displacements are all higher than their corresponding JWL EOS model displacements. The pressure profile model displacements are lower than the experimental displacements for the 3g explosive, but are higher for the 5g, 7g, and 9g explosives. From Figure 6.10 it can be seen that the pressure profile models yield significantly better displacement predictions than the predictions obtained from the JWL EOS models, for 120^0 V-plates.

In Figure 6.11, which shows the displacement versus mass for 150^0 V-plates, the magnitudes of the JWL EOS model displacements are all significantly lower than their corresponding experimental displacements. The largest difference in the displacement results is for the 9g explosive rod (experimental results for 11g and 13g explosives were not available) where the experimental displacement is 66.3mm while the JWL EOS model displacement is 28mm - a difference of 38.3mm, which is a 58% error. The pressure profile model displacements trend-line slope is significantly higher than the JWL EOS model trend-line, and is also a little higher than the experimental displacements trend-line. The pressure profile model displacements are all significantly higher than their corresponding JWL EOS model displacements, and are all slightly higher than their corresponding experimental displacements. From Figure 6.11 it can be seen that the pressure profile models yield significantly better displacement predictions than the predictions obtained from the JWL EOS models, for 150^0 V-plates.

From the mid-point displacement results seen in Figure 6.8 to Figure 6.11, the slopes of the pressure profile model trend-lines, and the JWL EOS trend-lines were calculated. The percentage error was determined for each of the slopes for the two model types and then the overall average error percentages of the slopes were found. These results can be seen in Table 6.1.

The percentage error for each displacement point of the pressure profile models and JWL EOS models was also calculated. The average error percentages for each series of these displacement points were calculated and then the overall average percentage error was found. The average error

percentages for each series of the displacement points and the overall average percentage error can be seen in Table 6.2. The error percentages for all the individual displacement points can be found in Appendix G.

	Experimental	ABAQUS (Press.)	% Error	ABAQUS (EOS)	% Error
Angle	**$mm.g^{-1}$**	**$mm.g^{-1}$**	**%**	**$mm.g^{-1}$**	**%**
60^0	2.16	0.81	62	1	54
90^0	2.7	3.5	37	0.4	85
120^0	6.6	10.3	56	1.3	80
150^0	7	8.3	19	2.8	60
		Overall % Error	**44**	**Overall % Error**	**70**

Table 6.1: The slopes and slope errors of the trend-lines of the displacement versus explosive mass relationships from the Rod Explosive Systems

	ABAQUS (Press.) Ave. % Error	ABAQUS (EOS) Ave. % Error
Angle	**%**	**%**
60^0	59	84
90^0	28	36
120^0	31	83
150^0	9	63
Overall % Error	**32**	**67**

Table 6.2: The average error of the displacement points for each displacement versus explosive mass relationship, and the overall error of the displacement points from the Rod Explosive Systems

The overall average percentage error of the slopes of the trend-lines of the mid-point displacement versus the explosive mass relationship is 44% for the pressure profile models and 70% for the JWL EOS models. These errors represent how inaccurate the sensitivity to explosive mass is for the two different ABAQUS model types. The pressure profile models are overall 44% too sensitive and the JWL EOS models are overall 70% too insensitive.

The overall average percentage error of the mid-point displacement is 31.7% for the pressure profile models and 66.5% for the JWL EOS models. These percentages indicate the overall accuracy of the two model types. Clearly the pressure profile models produce more accurate displacement results.

It can be seen from Figure 6.8 to Figure 6.11 that the differences between the mid-point displacements of the JWL EOS models and the experimental mid-point displacements increase with an increase in explosive mass. However, the error percentages of these mid-point displacements, exhibit no particular trend.

The large errors of the JWL EOS models are depicted in Figure 6.12 where the displacement versus mass results for all the V-plate angles are graphed along with the experimental results. The insensitivity to explosive mass of the JWL EOS models can also be seen from the small slopes of the mid-point displacements versus explosive masses trend-lines.

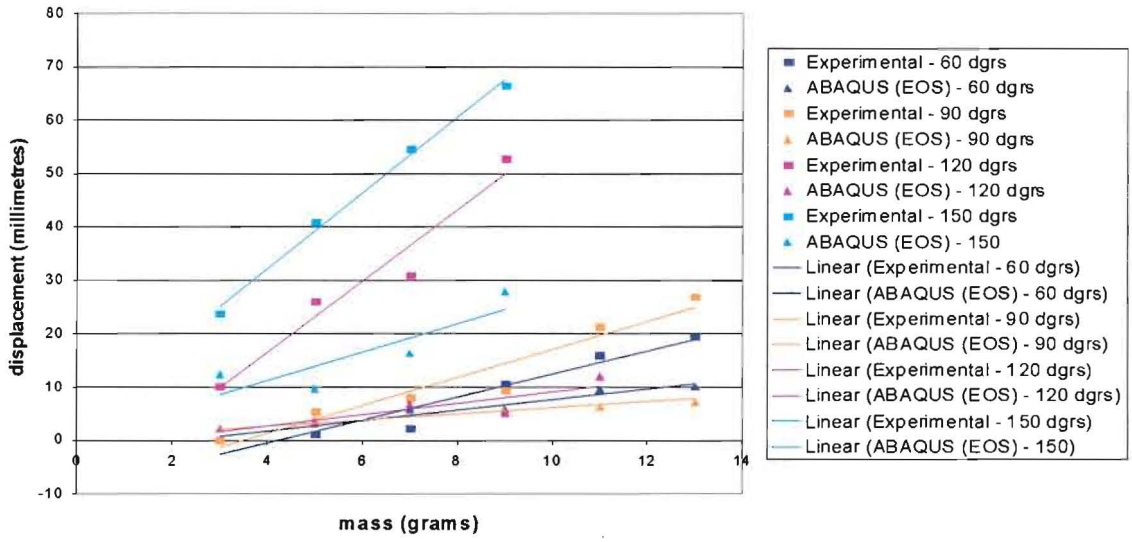

Figure 6.12: All the V-Plate Mid-Point Displacements Versus Explosive Rod Masses Obtained From the Experiments and the ABAQUS Equation of State Analyses.

In summary, from the results discussed, it is clear that the pressure profile models produce more accurate results than the JWL EOS models for the relationship between the mid-point displacements of the V-plates and the masses of the rod explosives.

6.2.2.1.2 Comparison of the V-Plate Mid-Point Displacements Versus the V-Plate Angles

The next relationship examined was between the displacement of the mid-point of the V-plate and the V-plate angle. Graphs displaying this relationship for rod explosives of different masses can be seen in Figure 6.13 to Figure 6.16.

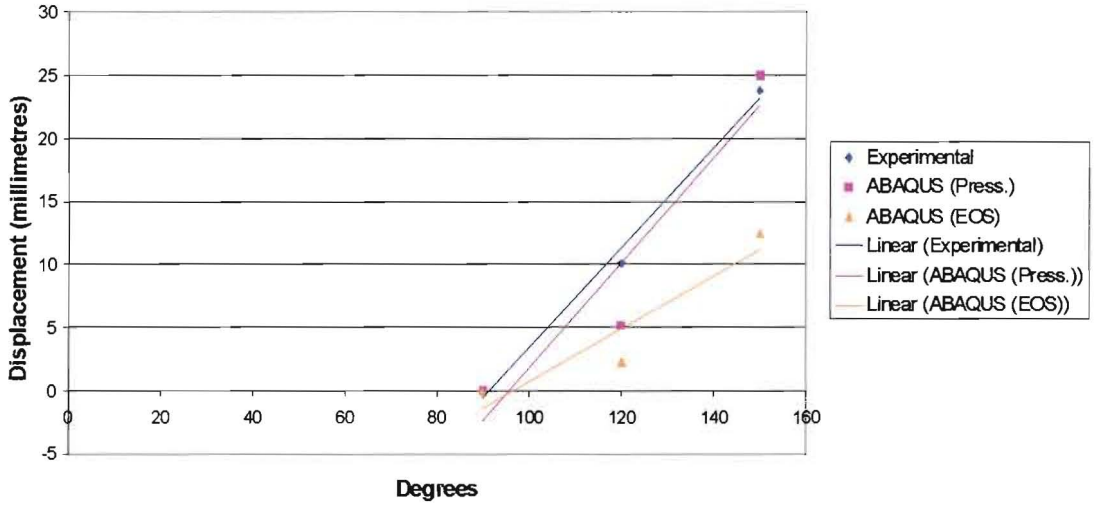

Figure 6.13: V-Plate Mid-Point Displacement From 3g Explosive Rod Versus V-Plate Angle Obtained From the Experiments, the ABAQUS Pressure Profile Analyses, and the ABAQUS Equation of State Analyses.

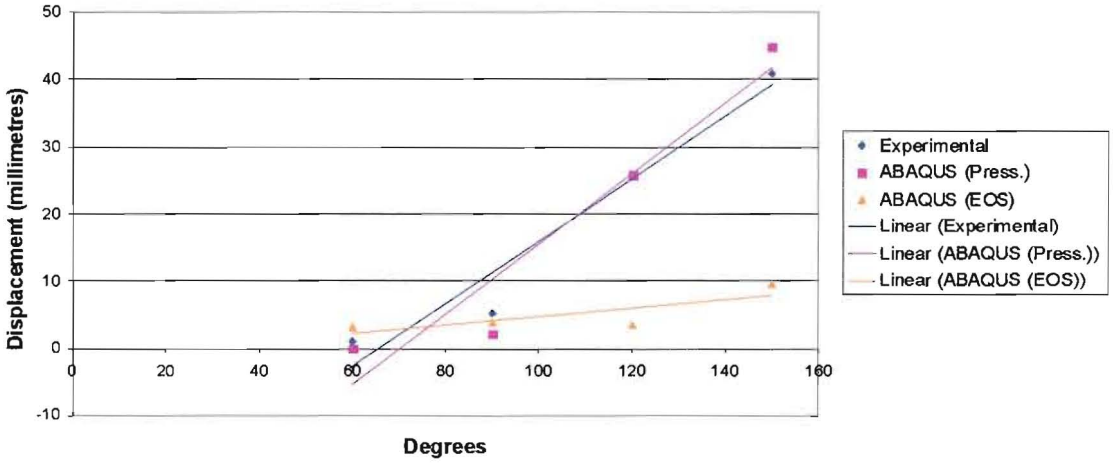

Figure 6.14: V-Plate Mid-Point Displacement From 5g Explosive Rod Versus V-Plate Angle Obtained From the Experiments, the ABAQUS Pressure Profile Analyses, and the ABAQUS Equation of State Analyses.

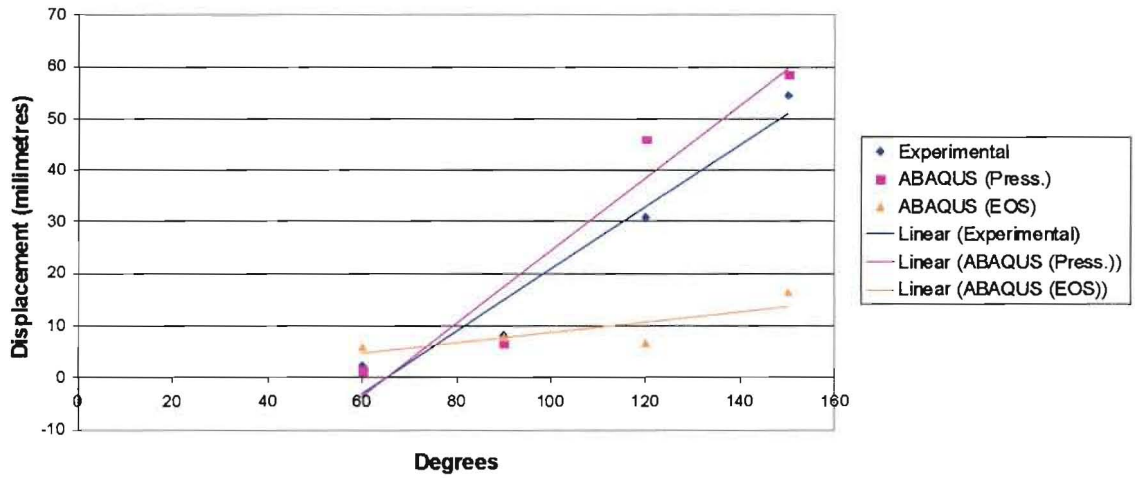

Figure 6.15: V-Plate Mid-Point Displacement From 7g Explosive Rod Versus V-Plate Angle Obtained From the Experiments, the ABAQUS Pressure Profile Analyses, and the ABAQUS Equation of State Analyses.

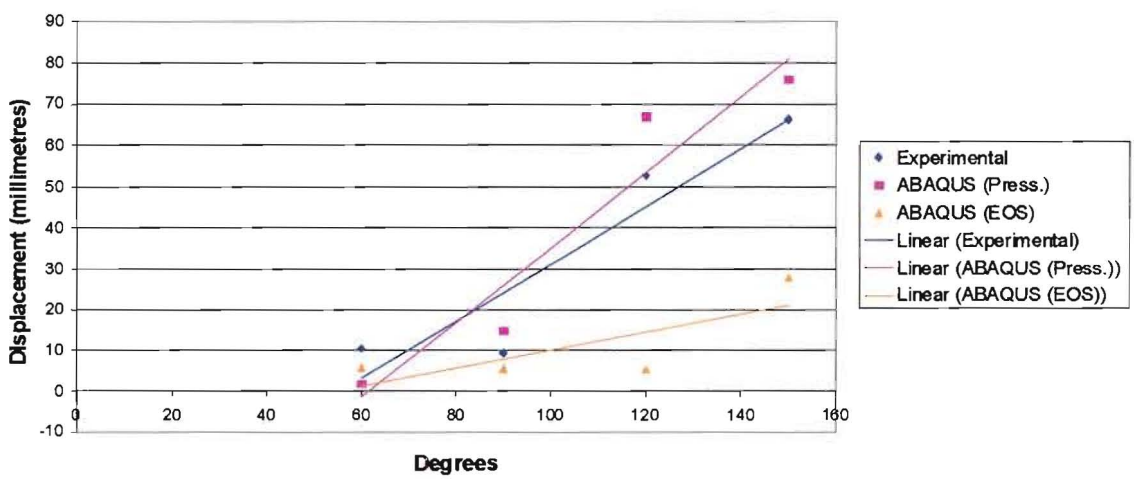

Figure 6.16: V-Plate Mid-Point Displacement From 9g Explosive Rod Versus V-Plate Angle Obtained From the Experiments, the ABAQUS Pressure Profile Analyses, and the ABAQUS Equation of State Analyses.

It is clear from the graphs that the relationship between the mid-point displacement and the V-plate angle is linear. This is reflected by both the model predictions and the experimental results. Linear trend-lines were inserted on the graphs to demonstrate this linearity and it can be seen that the points of each series do not deviate greatly from their trend-line, although they deviate more than for the displacement versus explosive mass relationships. As expected, the mid-point displacement increases with increasing V-plate angle for both the model predictions and the experiments, therefore the 60^0 V-plates have the smallest displacements. This indicates that the 60^0 V-plates sustain the least damage. The slopes of the JWL EOS model trend-lines, which is the rate of increase of the V-plate mid-point displacement with respect to the V-plate angle, is significantly less than the slopes of the experimental trend-lines in all of the graphs in Figure 6.13 to Figure 6.16.

In Figure 6.13, which shows the displacement versus V-plate angle for 3g explosive rods, the magnitudes of the JWL EOS model displacements are all lower than the corresponding experimental displacements. The JWL EOS model displacement for 3g is the same as the experimental displacement as both are zero. The largest difference in the displacement results is for the 150^0 V-plate where the experimental displacement is 23.8mm while the JWL EOS model displacement is 12.5mm - a difference of 11.3mm, which is a 47.5% error. The pressure profile model displacements trend-line slope is significantly greater than the JWL EOS model trend-line, and is similar but slightly higher than the experimental displacements trend-line. The pressure profile model displacements are all greater than their corresponding JWL EOS model displacements. The pressure profile model displacements are less than their corresponding experimental displacements for the120^0 V-plate, but are greater for the 150^0 . The 60^0 and 90^0 V-plate displacements are all the same as they are zero. It must be mentioned that the 60^0 V-plate displacements obtained from both the ABAQUS models and the experiment, have been excluded from the graph in Figure 6.13 as all the 90^0 V-plate displacements are also zero and including the 60^0 V-plate displacement

would adversely affect the related trend-line. From Figure 6.13 it can be seen that the pressure profile models yield significantly better displacement predictions than the predictions obtained from the JWL EOS models, for the 3g explosive rods.

In Figure 6.14, which shows the displacement versus mass for the 5g explosive rods, the magnitudes of the JWL EOS model displacements are higher than the corresponding experimental displacements for the 60^0 V-plate, but are lower for the 90^0, 120^0, and 150^0 V-plates. The largest difference in the displacement results is for the 150^0 V-plate where the experimental displacement is 40.9mm while the JWL EOS model displacement is 9.7mm - a difference of 31.2mm, which is a 76.3% error. The pressure profile model displacements trend-line slope is significantly greater than the JWL EOS model trend-line, and is similar, but slightly higher than the experimental displacements trend-line. The pressure profile model displacements are less than the corresponding JWL EOS model displacements for the 60^0 and 90^0 V-plates, but are greater for the 120^0 and 150^0 V-plates. The pressure profile model displacements are less than their corresponding experimental displacements for the 60^0 and 90^0 V-plates, are almost the same for the 120^0 V-plate, and are greater for the 150^0 V-plate. From Figure 6.14 it can be seen that the pressure profile models yield significantly better displacement predictions than the predictions obtained from the JWL EOS models, for the 5g explosive rods.

In Figure 6.15, which shows the displacement versus mass for the 7g explosive rods, the magnitudes of the JWL EOS model displacements are higher than the corresponding experimental displacements for the 60^0 V-plate, are almost the same for the 90^0 V-plate, but are lower for the 120^0 and 150^0 V-plates. The largest difference in the displacement results is for the 150^0 V-plate where the experimental displacement is 54.6mm while the JWL EOS model displacement is 16.4mm - a difference of 38.2mm, which is a 70% error. The pressure profile model displacements trend-line slope is significantly greater than the JWL EOS model trend-line, and is similar but a

little higher than the experimental displacements trend-line. The pressure profile model displacements are less than the corresponding JWL EOS model displacements for the 60^0 and 90^0 V-plates, but are greater for the 120^0 and 150^0 V-plates. The pressure profile model displacements are less than their corresponding experimental displacements for the 60^0 and 90^0 V-plates, and are greater for the 120^0 and 150^0 V-plates. From Figure 6.15 it can be seen that the pressure profile models yield significantly better displacement predictions than the predictions obtained from the JWL EOS models, for the 7g explosive rods.

In Figure 6.16, which shows the displacement versus mass for the 9g explosive rods, the magnitudes of the JWL EOS model displacements are lower than the corresponding experimental displacements for all the V-plates. The largest difference in the displacement results is for the 120^0 V-plate where the experimental displacement is 52.7mm while the JWL EOS model displacement is 5.3mm - a difference of 47.4mm, which is a 89.9% error. The pressure profile model displacements trend-line slope is significantly greater than the JWL EOS model trend-line, and is similar but a little higher than the experimental displacements trend-line. The pressure profile model displacements are less than the corresponding JWL EOS model displacements for the 60^0 V-plate, but are greater for the 90^0, 120^0 and 150^0 V-plates. The pressure profile model displacements are less than their corresponding experimental displacements for the 60^0 V-plate, and are greater for the 90^0, 120^0 and 150^0 V-plates. From Figure 6.16 it can be seen that the pressure profile models yield better displacement predictions than the predictions obtained from the JWL EOS models, for the 9g explosive rods.

From the displacement results seen in Figure 6.13 to Figure 6.16 the slopes of the pressure profile model trend-lines, and the JWL EOS trend-lines were calculated. The percentage error was determined for each of the slopes for the two model types and then the overall average error percentages of the slopes were found. These results can be seen in Table 6.3.

The percentage error for each displacement point of the pressure profile models and JWL EOS models was also calculated. The average error percentages for each series of these displacement points were calculated and then the overall average percentage error was found. The average error percentages for each series of the displacement points and the overall average percentage error can be seen in Table 6.4. The error percentages for all the individual displacement points can be found in Appendix G.

	Experimental	ABAQUS (Press.)	% Error	ABAQUS (EOS)	% Error
Mass	**mm.degree^{-1}**	**mm.degree^{-1}**	**%**	**mm.degree^{-1}**	**%**
3g	0.39	0.41	5	0.21	46
5g	0.46	0.52	13	0.06	87
7g	0.6	0.7	17	0.1	83
9g	0.71	0.92	30	0.22	69
		Overall % Error	**16**	**Overall % Error**	**71**

Table 6.3: The slopes and slope errors of the trend-lines of the displacement versus V-plate angle relationships for the rod explosive systems

	ABAQUS (Press.) Ave. % Error	ABAQUS (EOS) Ave. % Error
Mass	**%**	**%**
3g	13	31
5g	42	101
7g	30	77
9g	46	59
Overall % Error	**33**	**67**

Table 6.4: The average error of the displacement points for each displacement versus the V-plate angle relationship, and the overall error of the displacement points from the rod explosive systems

The overall average percentage error of the slopes of the trend-lines of the mid-point displacement versus the explosive angle relationship is 16% for the pressure profile models and 71% for the JWL EOS models. These errors represent how inaccurate the sensitivity to the V-plate angle is for the two different ABAQUS model types. The pressure profile models are overall 16% too sensitive and the JWL EOS models are overall 71% too insensitive.

The overall average percentage error of the mid-point displacement is 33% for the pressure profile models and 67% for the JWL EOS models. These percentages indicate the overall accuracy of the two model types. Clearly the pressure profile models produce more accurate displacements.

It can be seen from Figure 6.13 to Figure 6.16 that the differences between the mid-point displacements of the JWL EOS models and the experimental mid-point displacements increase with an increase in the V-plate angle. However, the error percentages of these mid-point displacements, exhibit no particular trend.

The large errors of the JWL EOS models are depicted in Figure 6.17 where the displacement versus the V-plate angle results for all the V-plate angles are graphed along with the experimental results. The insensitivity to the V-plate angles of the JWL EOS models can also be seen from the small slopes of the mid-point displacements versus explosive masses trend-lines.

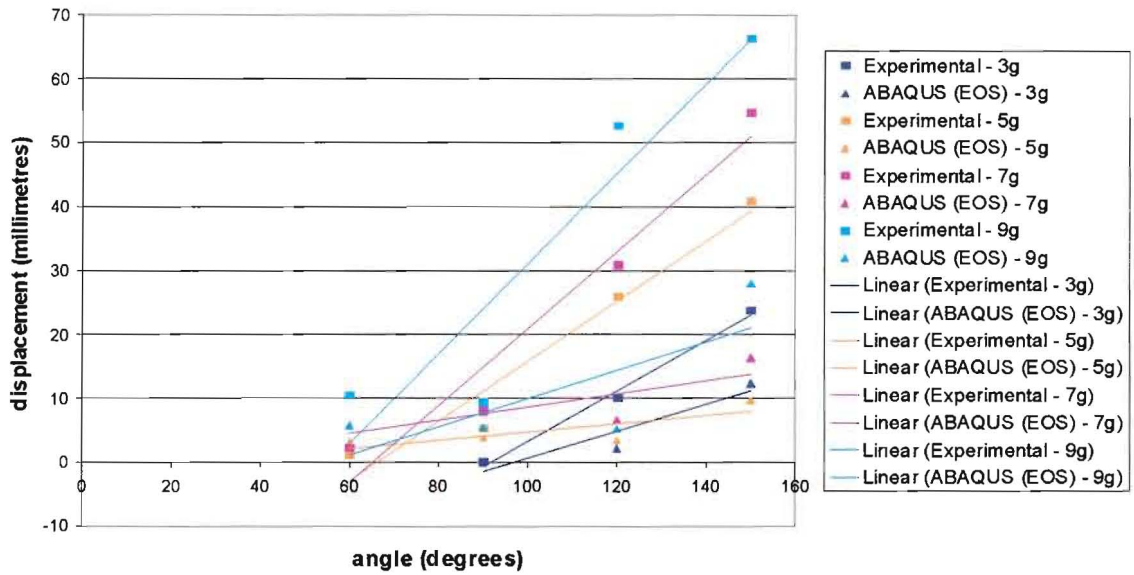

Figure 6.17: All the V-Plate Mid-Point Displacements Versus the V-Plate Angles Obtained From the Experiments and the ABAQUS Equation of State Analyses.

In summary, from the results discussed, it is clear that the pressure profile models produce more accurate results than the JWL EOS models for the relationship between the mid-point displacements of the V-plates and the angles of the V-plates.

6.2.2.2 Comparison Between the JWL Equation of State Model Predictions of the V-Plate Profiles, the Pressure Profile Model Profiles, and the Experimental Profiles

6.2.2.2.1 Comparison of the V-Plate Profiles

Comparing the V-plate mid-point displacements of the model profiles and the experimental profiles is a quantitive way of determining the accuracy of the model predictions. But it is also necessary to compare the shapes of the V-plate profiles from the models and experiments to determine the accuracy of

the model predictions. This is because the mid-point displacements of the models could be similar to the experimental displacements, but the profile shapes could be completely different.

The deformed V-plate profiles obtained from the JWL EOS models, the pressure profile models, and the experiments are compared in Figure 6.18 to Figure 6.22 for the 90^0 V-plates exploded by different explosive rod masses. The deformed profiles of all the other V-plate and explosive rod models and experiments can be seen in Appendix C.

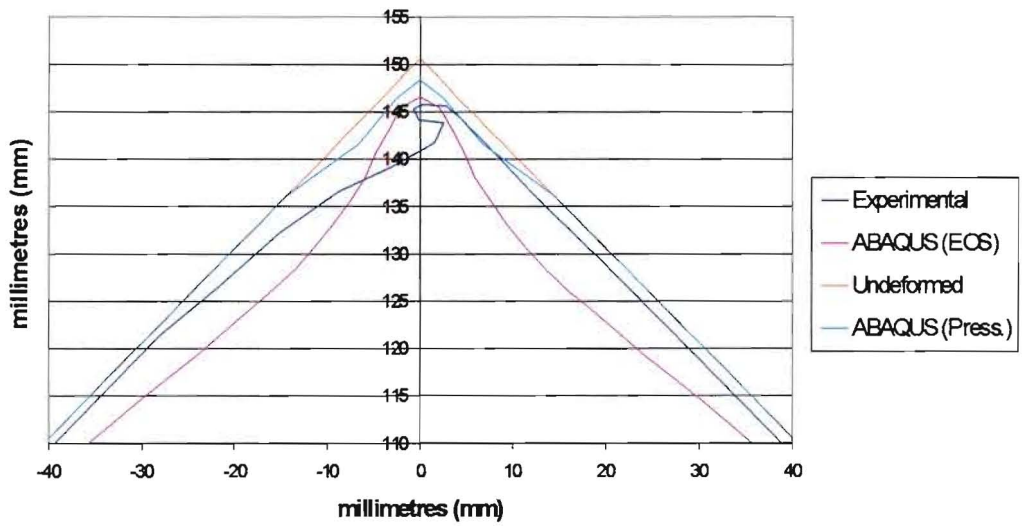

Figure 6.18: Comparison of a Magnified Section of the Experimental Deformed Profile of a V-Plate (90 degrees) Exploded by a PE4 Rod (5g), With the ABAQUS Deformed Profile Obtained Using a Pressure Profile, and With the ABAQUS Deformed Profile Obtained Using the EOS

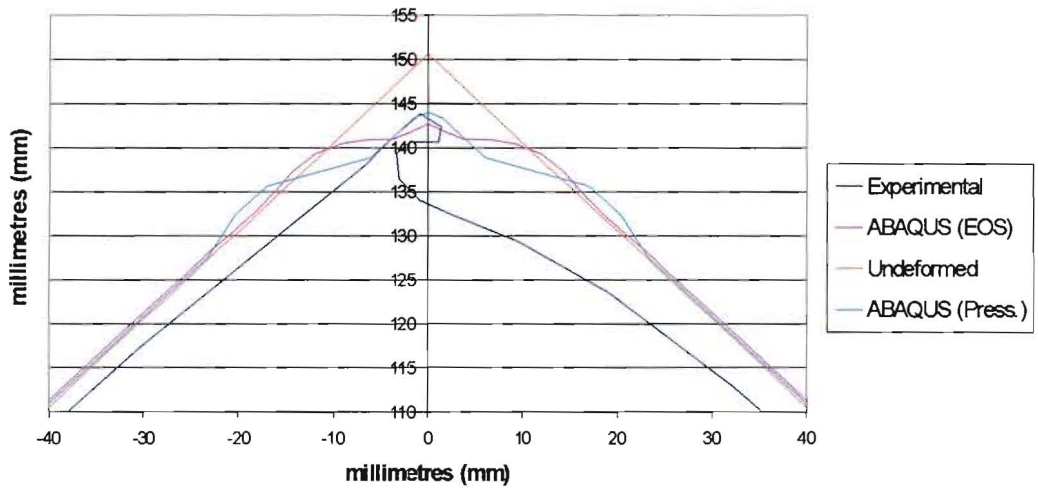

Figure 6.19: Comparison of a Magnified Section of the Experimental Deformed Profile of a V-Plate (90 degrees) Exploded by a PE4 Rod (7g), With the ABAQUS Deformed Profile Obtained Using a Pressure Profile, and With the ABAQUS Deformed Profile Obtained Using the EOS

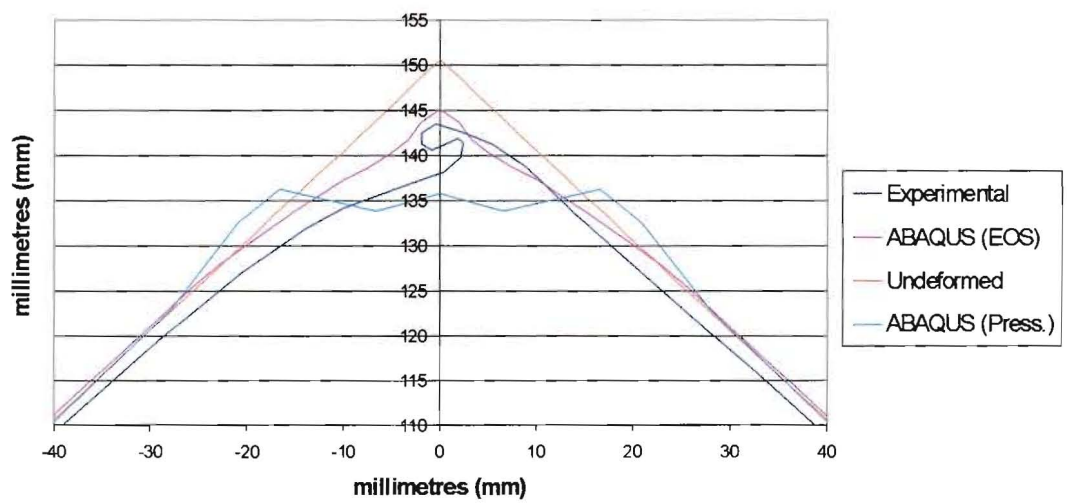

Figure 6.20: Comparison of a Magnified Section of the Experimental Deformed Profile of a V-Plate (90 degrees) Exploded by a PE4 Rod (9g), With the ABAQUS Deformed Profile Obtained Using a Pressure Profile, and With the ABAQUS Deformed Profile Obtained Using the EOS

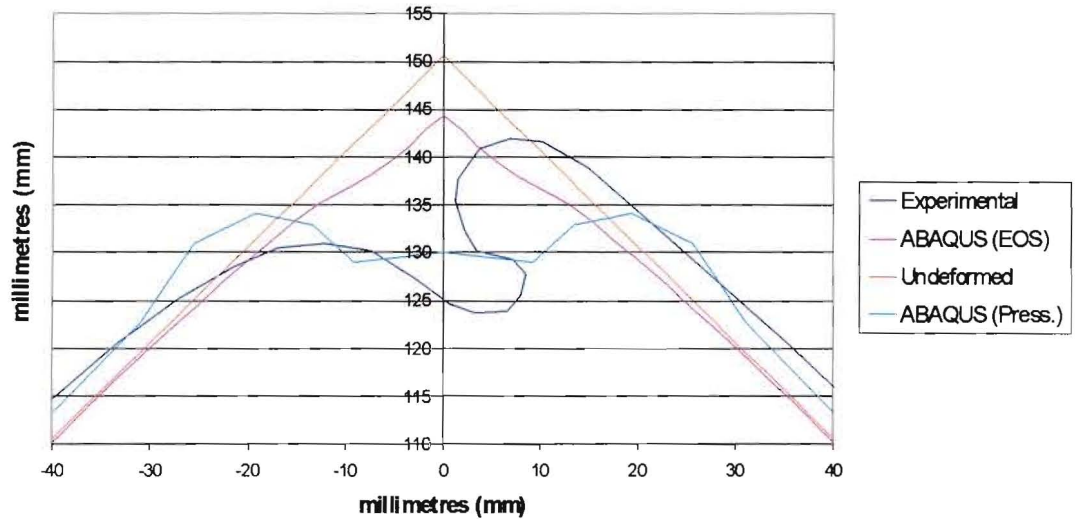

Figure 6.21: Comparison of a Magnified Section of the Experimental Deformed Profile of a V-Plate (90 degrees) Exploded by a PE4 Rod (11g), With the ABAQUS Deformed Profile Obtained Using a Pressure Profile, and With the ABAQUS Deformed Profile Obtained Using the EOS

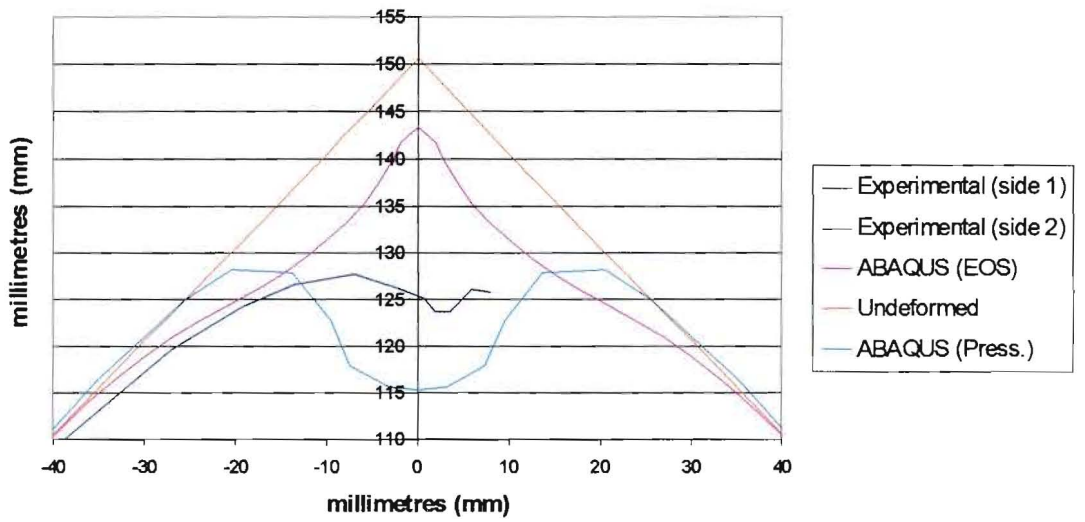

Figure 6.22: Comparison of a Magnified Section of the Experimental Deformed Profile of a V-Plate (90 degrees) Exploded by a PE4 Rod (13g), With the ABAQUS Deformed Profile Obtained Using a Pressure Profile, and With the ABAQUS Deformed Profile Obtained Using the EOS

It is noticed that the experimental V-plate profiles in the series seen in Figure 6.18 to Figure 6.22 all exhibit significantly asymmetric profiles while the models have been created to simulate symmetric behaviour. The degree of experimental profile asymmetry seems to decrease as the V-plate angles of the models increase as can be seen from the model profiles in Appendix C. However, the predictions of the JWL EOS models of the V-plate profiles remain inaccurate for these higher V-plate angles as the degree to which the profiles are deformed are highly under-predicted. The profile predictions of the lower angle plates, but which are exploded by the larger explosive masses, are also significantly under-predicted. So whenever there is a large degree of deformation according to the experimental V-plate profiles, the JWL EOS greatly under-predicts the profiles. A V-plate profile which was greatly under-predicted by the JWL EOS model can be seen in Figure 6.23.

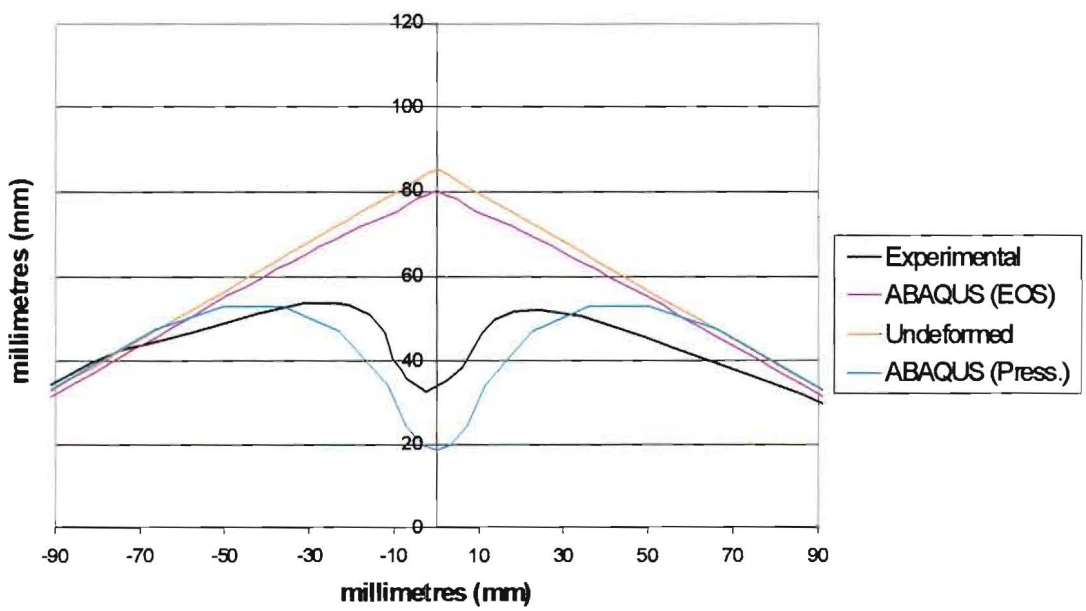

Figure 6.23: Comparison of a Magnified Section of the Experimental Deformed Profile of a V-Plate (120 degrees) Exploded by a PE4 Rod (9g), With the ABAQUS Deformed Profile Obtained Using a Pressure Profile, and With the ABAQUS Deformed Profile Obtained Using the EOS

In Figure 6.23 the JWL EOS predicted V-plate profile has hardly been deformed while the experimental profile has deformed greatly and the V-plate tip has actually inverted completely. From examining the profiles of all the JWL EOS models analysed, it appears that the V-plates 'resist' inversion of the tip. When large deformation such as tip inversion should take place, such as for the series of 120^0 V-plates exploded by different explosive masses, the sides of the predicted V-plate profile appear to compress and shorten instead. When extreme deformation takes place such as in the series of 150^0 V-plates exploded by different explosive masses, the JWL EOS does eventually show tip inversion, but the degree of deformation and inversion is greatly under-predicted.

The pressure profile models manage to exhibit inverted profiles when expected and therefore they more accurately represent the V-plate profiles at higher V-plate angles (120^0 and 150^0). This superior profile prediction can be seen in Figure 6.23. The displacement profiles predicted by the pressure profile models for the lower V-plate angles (60^0 and 90^0) are equally as inaccurate as the JWL EOS model predictions, as they too cannot exhibit asymmetric profiles.

From the V-plate profiles obtained from the experiments and predicted by the models, it can be seen that V-plate displacement profiles predicted by the JWL EOS models are not suitably accurate. The pressure profile models predict equally inaccurate displacement profiles for the lower V-plate angles, but predict more accurate profiles for the higher V-plate angles than the JWL EOS models. This means that the pressure profile models produce superior displacement profile predictions to the predictions of the JWL EOS models. It is speculated though, that if the problem involving the insufficient impulse transfer is corrected, the profiles predicted will be reasonably similar to the corresponding experimental profiles for the 120^0 and 150^0 V-plates. This will not necessarily be the case for the 60^0 and 90^0 V-plates as asymmetry is the main reason for the differences between the predicted profiles and the corresponding experimental profiles.

6.2.2.2.2 Tearing of the V-Plates

An ABAQUS tearing model has not been incorporated into the JWL EOS models as the tearing models have not yielded accurate results in the past [30]. The rule of thumb of 200% strain and 600^{0}C temperature [40] is used to predict tearing of the V-plates from the results of the models. The tearing predictions can then be compared to the experimental profiles to see if tearing took place in the experiments. Tearing of the experimental V-plates occurred for V-plates with large angles and which were exploded by rod explosives of large masses. One of the experiments which exhibited definite tearing was the experiment containing a 150^0 V-plate and an 11g explosive rod. A picture of this experimentally exploded V-plate can be seen in Appendix A. The tearing appears to have initially occurred along the V-plate ridge and then strips of the V-plate sides were 'peeled' away. The results of the model corresponding to this experiment were examined for tearing. Figure 6.24 shows the temperature distribution for the deformed V-plate predicted by this model.

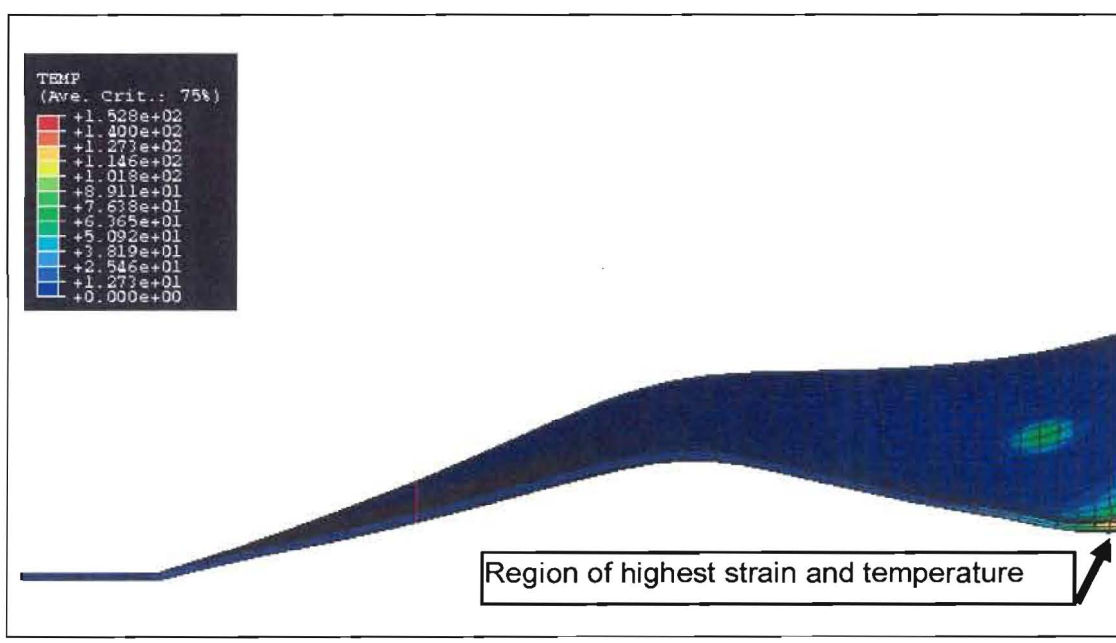

Figure 6.24: The temperature distribution (in C^0) of a deformed 150^0 V-plate as predicted by the model containing an 11g explosive rod

The region with the highest strain and temperature was found to be midway along the V-plate ridge, as expected. The strain in this region in the JWL EOS model reached approximately 40% and the temperature reached about 150°C. This indicates that this region has not torn. According to the ABAQUS results, tearing does not occur in any of the rod explosive models. This was expected because the deformation of the V-plate profiles are greatly under-predicted by the JWL EOS models so it is unlikely that the V-plates in these models would have reached the point of tearing.

It is speculated, though, that even if the predictions of the V-plate deformations were accurate, the models results might not always exhibit tearing conditions when the corresponding experiments exhibit tearing. This would be because of the residual stresses present in the ridges of the experimental V-plates resulting from the sharp bending of the flat sheets of steel into the V-plates.

6.2.2.3 Comparison Between the Effectiveness of the V-Plates Determined by the JWL Equation of State Model and the Experiments

A method to determine the effectiveness of the different V-plates as protection from explosive blasts, is required, so that the characteristics of this V-plate can be applied to the undercarriage of mine-protected vehicles. One way to do this is to determine the impulse transferred from the explosive to the V-plate. From this impulse, the percentage of the total explosive impulse deflected by the V-plate can be calculated. This percentage is considered to indicate the effectiveness of the V-plate and can be plotted against parameters, such as the explosive mass, to determine the most effective combinations of explosive masses and V-plate angles.

Comparing the transferred impulses obtained from the numerical models to the impulses obtained from the experiments will further test the accuracy of

the numerical models. The impulses transferred to the V-plates in the experiments were determined using a ballistic pendulum. This method measures the impulse transferred in one direction only.

Impulse transferred to an object is defined by the equation:

$$I = \int_0^T F dt \tag{6.1}$$

where

F = *force applied to object*

t = *time*

T = *total time force is applied to object*

To obtain the impulse transferred from the explosive to the V-plate from a numerical model so that it can be compared to the experimentally determined transferred impulse, the reaction forces of the V-plates are required. The reaction forces are used as they will be equal in magnitude to the component forces in the direction of the reaction force, applied to the V-plates by the explosives. Figure 6.25 demonstrates the forces which are relative to the impulse calculations.

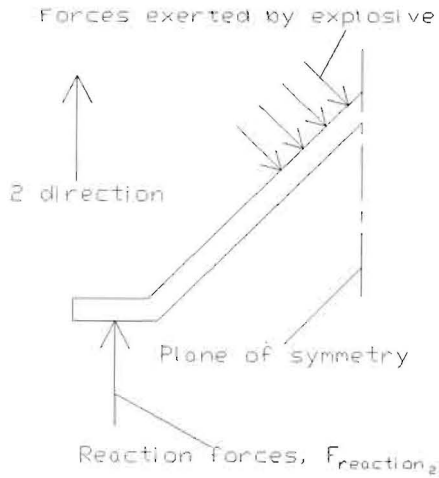

Figure 6.25 : A diagram of the forces exerted on the V-plate in the models.

To calculate the impulse transferred to the V-plate in the 2 direction, the total reaction force, $F_{reaction_2}$, is substituted into Equation 6.1:

$$I_2 = \int_0^T F_{reaction_2}(t)dt \tag{6.2}$$

To obtain the total reaction force of the V-plate, the reaction force (reaction force history as a function of time, compiled from each time step) of each of the nodes constraining the V-plate is extracted from ABAQUS and summed:

$$F_{reaction_2}(t) = \sum_{n=1}^{n=no.\ constraining\ nodes} F_{reaction_{2_n}}(t) \tag{6.3}$$

Substituting this relationship into Equation 6.2 yields:

$$I = \int_0^T \sum_{n=1}^{n=no.\ constraining\ nodes} F_{reaction_{2_n}}(t)dt \tag{6.4}$$

The reaction forces of the nodes extracted from ABAQUS were operated on according to Equation 6.4 to obtain the impulses transferred to the V-plates. The impulse transferred to a 120^0 V-plate by a 9g explosive rod was

calculated to be 4.48 N.s with the aid of the JWL EOS model results, while the transferred impulse obtained from the corresponding experiment was 11.93 N.s. This meant that the results from the JWL EOS had produced a large transferred impulse error of 62%. This great under-prediction of the transferred impulse is probably responsible for the fact that the deformation of the V-plate profile is greatly under-predicted by the model. It is thought that the detonated explosives in ABAQUS, governed by the JWL EOS, may not be correctly transferring their impulses to the V-plates, and hence the predicted deformations of the V-plates are far less than they should be.

It was found that Wiehahn [34] had encountered similar large errors when attempting to determine the transferred impulse from a JWL EOS model using the above method. Wiehahn [34] calculated the transferred impulse from the model predictions for a 3.8g explosive disc blasting a flat steel plate to be 3.5 N.s while the experimental transferred impulse was 7.13 N.s. This yields a large error of 50.9%. When modelling the same system using the pressure profile method instead of the JWL EOS method, a transferred impulse of 6.89 N.s was obtained. This yields a small error of 3.4%. These results obtained by Wiehahn [34] seem to support the theory that the error lies in the transfer of impulse from the explosive governed by the JWL EOS. However, it must be noted that according to Wiehahn [34], the JWL EOS models produced reasonable displacement profiles, and only slightly under-predicted certain models displacements, which casts some doubt on the theory that the impulse is not correctly transferred to the V-plate. Instead, according to Wiehahn's [34] statement, it appears that the reaction forces are incorrectly calculated by ABAQUS and therefore affect the impulse calculations. Results to support Wiehahn's [34] statement could not be found though.

Because the transferred impulse is greatly under-predicted, the effectiveness of the V-plates could not be accurately determined from the numerical models.

Seeing that the mid-point displacement of the V-plate profiles, the displacement profiles, and the transferred impulses of the systems containing the rod explosives were not accurately predicted by the JWL EOS models, the JWL EOS models have not been verified.

6.2.2.4 Attempts to Determine What Causes the Inaccuracies in the Models Containing Rod Explosives and How to Improve the Results

Because the JWL EOS models produced large unacceptable errors, attempts were made to determine what causes these inaccuracies and to improve the results. The obvious error would be that the material properties of the explosive or V-plate, or the geometry of the system had been specified incorrectly in the model. But the geometry was checked repeatedly and the material properties were actually copied from the successful simple model of the disc explosive and flat circular plate, so a simple input error is unlikely. This meant that other possibilities responsible for the JWL EOS inaccuracies had to be explored.

6.2.2.4.1 The Soft Contact Algorithm Option

In the "Hard or Soft" section in the "The Finite Element Model" chapter it was mentioned that the results of the models containing rod explosives led to an attempt to use the penalty contact algorithm instead of the kinematic algorithm and to stop the contacting surfaces of the V-plate and explosive from separating. This attempt was conducted on the advice of Dr. Izak Snyman [41]. The mid-point displacements of the V-plates are severely under-predicted by the JWL EOS models, and it was suggested that the use of the penalty contact algorithm in conjunction with stopping surface separation would lead to larger mid-point displacements. It was thought that by fixing the explosive surface nodes which come into contact with the V-plate, to the V-plate nodes, the explosive nodes behind the contact surface nodes would 'follow up' and transfer more impulse to the V-plate, instead of bouncing away. But it was found that the explosive surface nodes fixed to the

V-plate surface still rebounded after impact and dragged the V-plate up with them, yielding totally incorrect results. So this option was not used. Owing to a bug in ABAQUS, the penalty algorithm could not be used either and the option of using the soft contact algorithm had to be considered as a substitute.

All the models containing rod explosives were analysed with the hard contact algorithm and the soft contact algorithm, and the results were compared. It was found that the use of the soft contact algorithm did affect the mid-point displacement results of the V-plates, but not to a great enough extent and not always as desired. When the soft contact increased the displacements of the mid-points, it was only by a small distance and the error percentage remained unacceptably high. It was found that the use of soft contact often did not increase the mid-point displacements as desired, but actually reduced them. So it was decided that the soft contact algorithm would not be used.

6.2.2.4.2 Other Attempts

Because the displacement profiles of the V-plates were greatly under-predicted it was thought that the impulse of the explosive governed by the JWL EOS was not being correctly transferred to the V-plate. Another possible explanation though, is that the V-plate is more rigid in the model than in reality. A triangle is a very rigid structure so in reality the deformation of the V-plate is often influenced by a material or structural imperfection, or slight asymmetry of the V-plate or its loading. This means that the V-plate will often undergo deformation at a lower load and to a larger extent than theory would predict.

When the V-plate is created in ABAQUS, it is modelled as being structurally perfect with perfectly homogenous material properties. The model assumes perfect symmetry of the V-plate and explosive and the explosive positioning relative to the V-plate, hence the planes of symmetry. This means that the explosive symmetrically expands and impacts with the V-plate and the forces are considered to be exactly equally distributed down the two arms of the V-

plate. Because the arms of the V-plate are perfectly straight ABAQUS will find it difficult to predict bulging or buckling. Because of all these factors making the model mathematically perfect the V-plate will appear very rigid compared to reality. To compensate for this mathematical perfection in the ABAQUS models, slight alterations were made to the models to try to simulate a more realistic situation.

A slight curvature was introduced to the arms of the V-plates so that ABAQUS could easily determine any buckling. This alteration made no significant difference to the results.

Another attempt to 'weaken' the V-plate involved meshing the explosive asymmetrically so the explosive nodes would impact with the V-plate slightly asymmetrically. This alteration also made no significant difference to the results.

To exaggerate the asymmetry of the explosive loading, the explosive was horizontally offset from its central position by 4mm. This was thought to be the maximum offset that would occur realistically. This alteration also made no significant difference. Many of the experimental results show asymmetric deformation locally at the V-plate mid-point. Before the mid-point of the V-plate could be forced down by the explosive causing it to flatten or invert, it appears that the explosive punched in the sides of the V-plate tip. This gives the V-plate tip a 'pinched' look. It appears that this pinched tip then sometimes folded over slightly to one side or tore along the ridge. An asymmetric deformed V-plate shape can be seen in Figure 6.26.

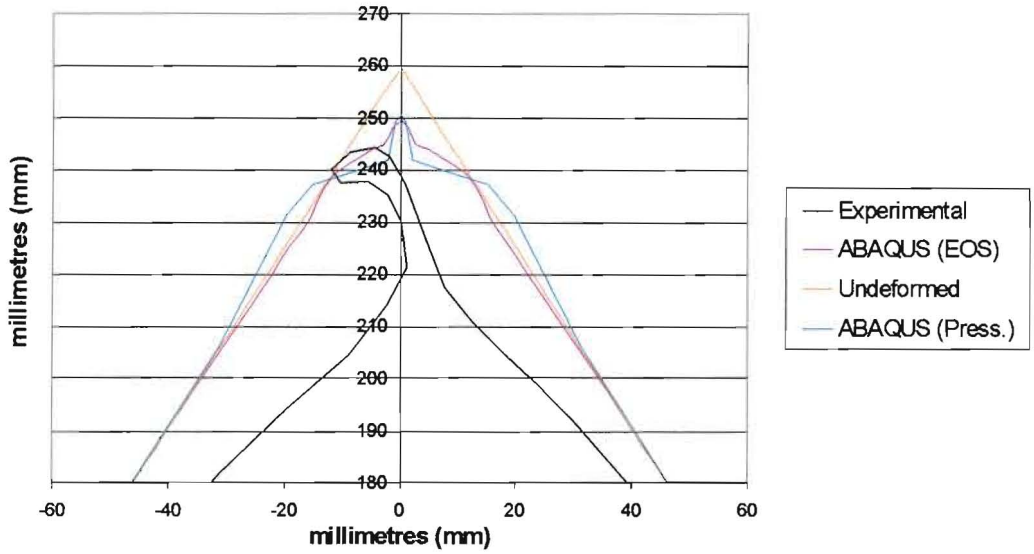

Figure 6.26: Comparison of a Magnified Section of the Experimental Deformed Profile of a V-Plate (60 degrees) Exploded by a PE4 Rod (13g), With the ABAQUS Deformed Profile Obtained Using a Pressure Profile, and With the ABAQUS Deformed Profile Obtained Using the EOS

It was hoped that the models with the offset explosives would be able to simulate this asymmetric behaviour and produce more accurate displacements. Unfortunately, it was found that the expansion of the explosive elements prevented these models from producing any significant asymmetric results or improvements to the displacement profiles. When the expanding explosive elements reach the V-plate they are relatively large and the element which strikes the V-plate first strikes the ridge of the V-plate. This element 'see-saws' on the V-plate ridge causing a large force to be applied to this ridge making the V-plate tip flatten or invert first. This see-sawing element can be seen in Figure 6.27. This see-sawing behaviour does not occur in perfectly symmetric models as the element nodes are directly above the V-plate ridge. This means that when the explosive impacts with the V-plate the nodes will rest on the V-plate ridge and the elements comprising of these nodes are free to pivot down to the sides of the V-plate.

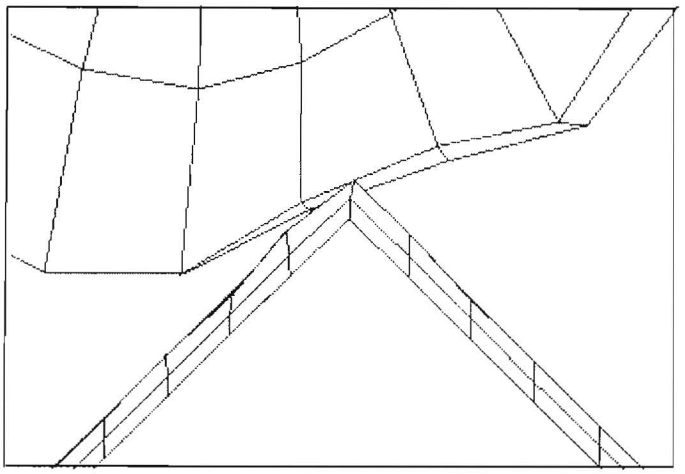

Figure 6.27: An explosive element 'see-sawing' on a V-plate ridge

A force applied to the ridge is perfectly central. The see-sawing element also makes it difficult for the elements around it to make contact with the sides of the tip of the V-plate so that the elements can asymmetrically impact with the V-plate and perhaps punch in the sides of the tip. Because of these behaviour patterns, the models with the offset explosives didn't produce significantly asymmetric results and the displacement profiles of the V-plates were not significantly improved.

Another attempt to improve the results of the models was to give the V-plates a small rounded or flat-topped ridge instead of a ridge with a perfect edge. Figure 6.28 demonstrates these alterations.

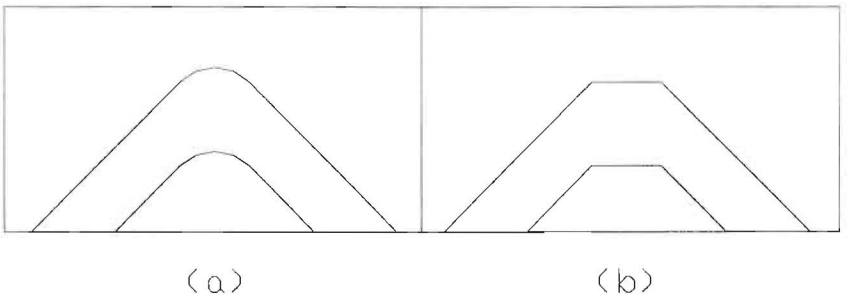

Figure 6.28: Diagrams indicating ridges of V-plates which are; (a) rounded; (b) flat-topped.

The rounded or flat-topped ridge occurs in reality as the metal sheet was bent into a V-plate for the experiments. The rounded or flat-topped ridge provides a surface which the explosive nodes can impact with more directly (not obliquely) and hopefully transfer more impulse to the V-plate tip to improve the displacement profiles. It was found that these alterations made no significant differences to the displacement profiles of the V-plates.

None of the attempts to weaken the V-plate or to increase the momentum transfer to the V-plate in the models made any significant differences to the displacement profiles of the V-plates. A fact which casts doubt on the theory that the exaggerated rigidity of the V-plates in ABAQUS causes the great under-prediction of the V-plate displacement profiles by the JWL EOS models, is that Nannucci [44] obtained reasonably successful results. Nannucci [44] also modelled the explosively loaded V-plates in ABAQUS but used the pressure profile method to model the explosives instead of the JWL EOS. Reasonably accurate displacement profiles were obtained from these models, leading to the belief that the original theory explaining the under-predictions involving an incorrect transfer of impulse to the V-plates, is more likely.

The reason for the incorrect transfer of impulse to the V-plates is unknown, but because models using the JWL EOS to model the explosives, created by Grobbelaar [35], yielded reasonable results, all differences between the models in this study and Grobbelaar's [35] models are examined.

The explosives in the models created by Grobbelaar [35] impact with flat plates meaning that the explosive nodes strike the plates very directly (not obliquely). The explosives in this study impact with V-plates meaning that the explosive nodes strike the V-plate obliquely. It is thought that ABAQUS may have difficulty with this oblique impact, but an observation which contradicts this theory is that the errors in the model results increase with increasing V-plate angle. In other words, as the V-plate gets flatter and the explosive node

impacts get more direct, the error increases. So it is unlikely that the angle of explosive node impact is the problem.

The models created by Grobbelaar [35] contain an explosive disc as do most of the numerical models created in previous studies. The models created by Grobbelaar [35] yielded results of acceptable accuracy as did the model created in this study which modelled one of Grobbelaar's [35] systems and therefore contained a disc explosive. The models yielding inaccurate results so far in this study, contain round rods of explosives with a thin long fuse attached to it. This indicates that the accuracy of the results may be dependent on the shape of the explosives. It is thought that ABAQUS may have difficulty working with the complex shape of a rod and fuse, but there is no logical explanation for this theory.

A consequence of the complex shape of the explosive though, was that the explosives had to be meshed with a hybrid mesh of two different types of elements because of the explosive fuse. The "Element Type" section in the "The Finite Element Model" chapter discusses this hybrid mesh. ABAQUS may experience difficulty with this hybrid mesh, although there is no logical explanation for this theory. When deciding whether to use an explosive fuse in the model or not, a system without a fuse and an identical system with a fuse and with a hybrid mesh was modelled. The results of the two models were compared and can be seen in Figure 4.4. From these results it can be seen that the model including an explosive fuse, and hence a hybrid explosive mesh, had a larger V-plate mid-point displacement and therefore yielded slightly improved results. This contradicts the theory that the hybrid explosive mesh results in a poor impulse transfer to the V-plate.

To further test this theory, the system containing a 150^0 V-plate was modelled with a rod explosive without a fuse, and with a rod explosive with a fuse and a hybrid mesh. This system was chosen as, when it is modelled, the mid-point prediction is largely under-predicted in comparison to the model predictions of the other systems. A comparison between the V-plate mid-point

displacements of the two versions of the model was then made. The model containing the explosive rod with a fuse and hybrid mesh produced a mid-point displacement of 28mm. The model containing the explosive rod without a fuse and with a homogenous mesh produced a mid-point displacement of 19.5mm. The experimental mid-point displacement is 66.3mm, so both predictions are still very inaccurate. Once again the model containing the hybrid mesh and explosive fuse had a larger V-plate mid-point displacement and therefore yielded improved results. It must be taken into account that the explosive models including a fuse have an extra gram of explosive owing to this fuse. Removing this extra one gram, however, will not reduce the mid-point displacement significantly and the mid-point displacement of this model will still be larger than the model without a fuse. This result clearly shows that the theory stating that the hybrid explosive mesh results in a poor impulse transfer to the V-plate, is not the reason for the inaccurate results of the models containing explosive rods.

6.2.3 The Results of the Models Containing an Explosive Disc

The results of the models containing an explosive disc will be presented and discussed here. Because there are no experimental results or pressure profile model results for the system containing explosive discs, the V-plate deformation predicted by the JWL EOS models could not be compared with any other results. Because of this the accuracy of the JWL EOS models for these systems could not be determined.

Characteristics of the V-plates such as the predicted mid-point displacements and the predicted profiles will be examined for trends to determine the dependency of the displacements and profiles of the V-plates on parametric variations.

6.2.3.1 Model Predictions of the V-Plate Mid-Point Displacements

The relationships that the V-plate mid-point displacements have with the explosive disc masses and the V-plate angles are investigated.

6.2.3.1.1 V-Plate Mid-Point Displacements Versus the Explosive Disc Masses

The first relationship examined was between the displacement of the mid-point of the V-plate predicted by the JWL EOS models, and the explosive mass used. A graph displaying this relationship for V-plates of different angles can be seen in Figure 6.29.

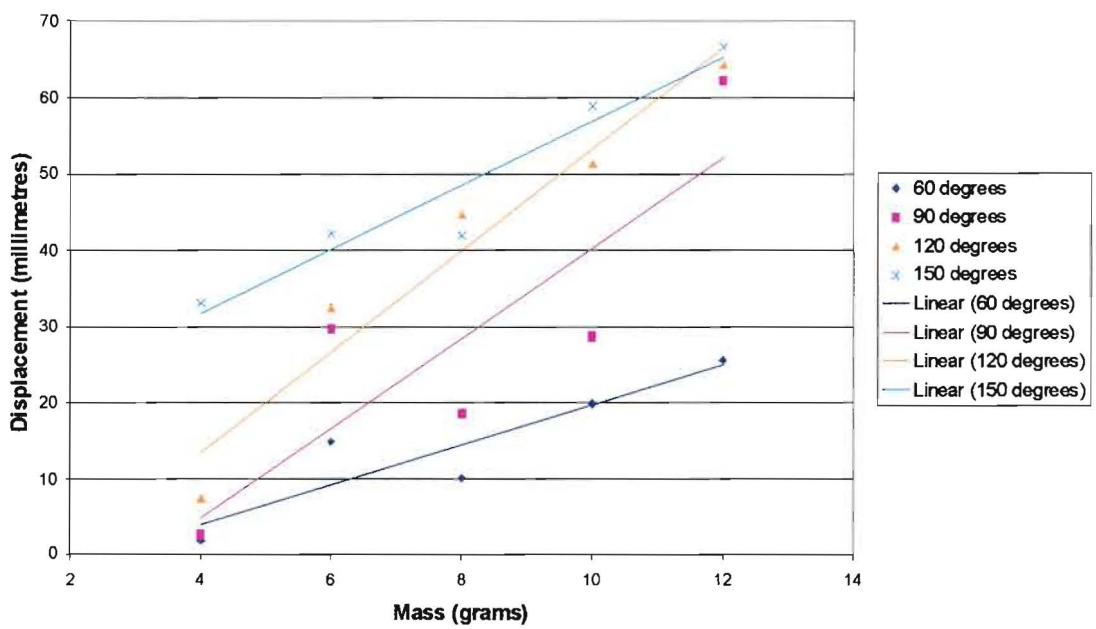

Figure 6.29: V-Plate Mid-Point Displacement Versus Explosive Disc Mass Obtained From the ABAQUS Equation of State Analyses for Different Angles.

It is clear from the graphs that the relationship between the mid-point displacement and the explosive mass is also linear. Linear trend-lines were inserted on the graph to demonstrate this linearity. It can be seen that

generally the points on the graph do not deviate greatly from their respective trend-lines except for the 90^0 V-plate.

As expected, the mid-point displacement increases with increasing explosive mass. The slopes of the trend-lines, which is the rate of increase of the displacement with respect to explosive mass, vary. The slopes of the trend-lines of the 60^0 and 150^0 V-plate mid-point displacements are 2.7 $mm.g^{-1}$ and 4.1 $mm.g^{-1}$ respectively, with a small difference of 1.4$mm.g^{-1}$. The trend-line slopes of the 90^0 and 120^0 V-plates are considerably steeper than the 60^0 and 150^0 slopes at 5.9 $mm.g^{-1}$ and 6.6 $mm.g^{-1}$ respectively, with an even smaller difference of 0.7 $mm.g^{-1}$. The steeper slopes indicate that the mid-point displacements of the 90^0 and 120^0 V-plates are more sensitive to the mass of the explosives. Each V-plate mid-point displacement trend-line is noticeably offset from the others. This indicates that the mid-point displacements are significantly sensitive to the angle of the V-plates, and that as the angles of the V-plates increase, the V-plate mid-point displacements also significantly increase.

6.2.3.1.2 V-Plate Mid-Point Displacements Versus the V-Plate Angles

The next relationship examined was between the displacement of the mid-point of the V-plate predicted by the JWL EOS models, and the V-plate angle used. A graph displaying this relationship for explosives of different masses can be seen in Figure 6.30.

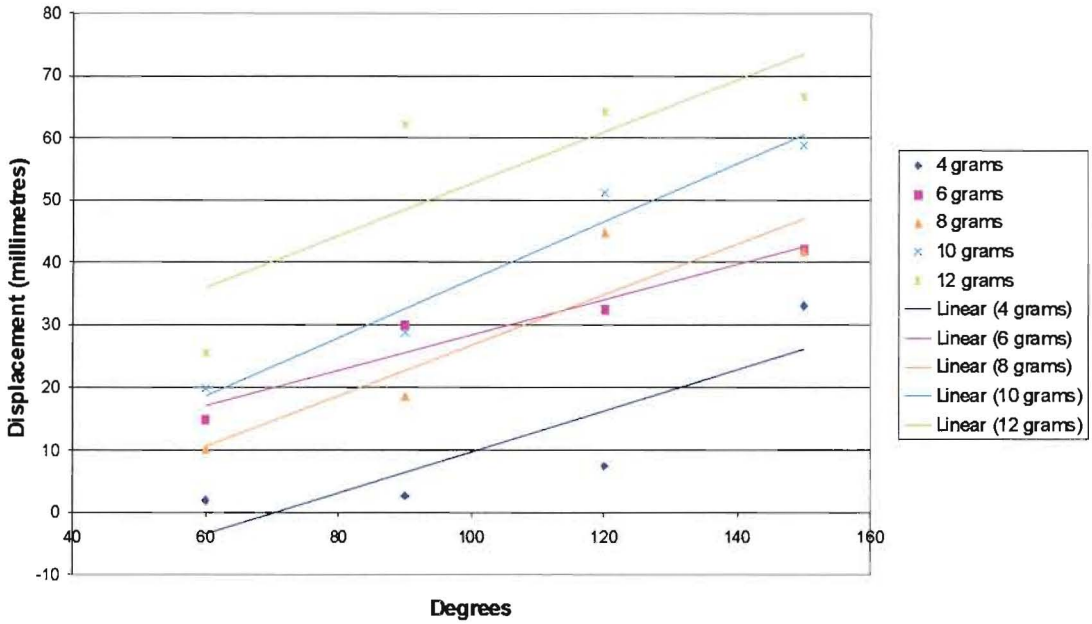

Figure 6.30: V-Plate Mid-Point Displacement Versus V-Plate Angle for the Models Containing Explosive Discs, Obtained From the ABAQUS Equation of State Analyses for Different Masses.

It is clear from the graphs that the relationship between the mid-point displacement and the V-plate angle is also linear. Linear trend-lines were inserted on the graph to demonstrate this linearity. It can be seen that generally the points on the graph do not deviate greatly from their respective trend-lines. As expected, the mid-point displacement increases with increasing V-plate angle. The slopes of the trend-lines, which are the rates of increase of the displacement with respect to V-plate angle, are similar and are $0.33mm.degree^{-1}$, $0.28mm.degree^{-1}$, $0.4mm.degree^{-1}$, $0.46mm.degree^{-1}$, and $0.41mm.degree^{-1}$ for the 4g, 6g, 8g, 10g, and 12g masses respectively. The similar trend-line slopes mean that the JWL EOS models have almost the same level of mid-point displacement sensitivity to the V-plate angle, for all the explosive masses. Each V-plate mid-point displacement trend-line is noticeably offset from the others, except for the 6g and 8g explosive trend-lines which are close together and overlap. These offsets indicate that the

mid-point displacements are significantly sensitive to the explosive masses, except in the 6g and 8g region. The offsets also display that the V-plate mid-point displacements generally increase with increasing explosive mass which has already been observed in the displacement versus explosive mass relationships.

From the mid-point displacement results, the accuracy of the JWL EOS models containing disc explosives appears promising. This is because the displacement results are of a far higher magnitude and there is greater variation than the greatly under-predicted displacement results of the models containing rod explosives.

6.2.3.2 Model Predictions of the V-Plate Profiles

Once again, the mid-point displacements of the V-plates are not solely a sufficient representation of the deformed V-plates, so the V-plate profiles were also examined.

6.2.3.2.1 Predictions of the V-Plate Profiles for the Systems with Varying Explosive Masses and V-Plate Angles

The series of 120^0 V-plate displacement profiles exploded by varying explosive disc masses, predicted by the JWL EOS models, can be seen in Figure 6.31 to Figure 6.35. The deformed profiles of all the other V-plates predicted by the JWL EOS models can be seen in Appendix D.

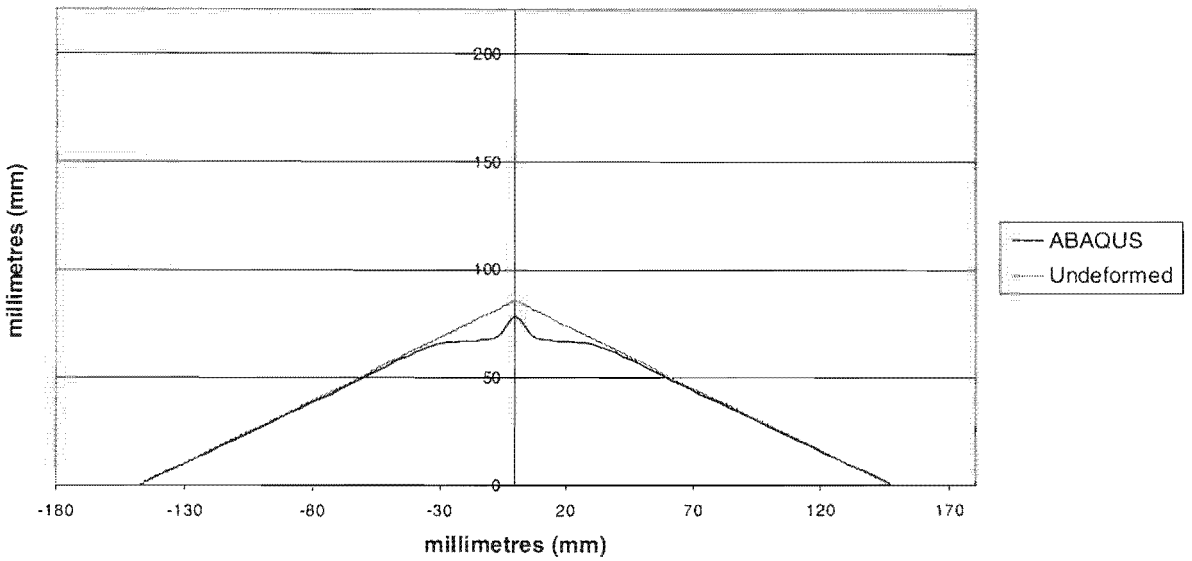

Figure 6.31: The Deformed Profile of a V-Plate (120 degrees) Exploded by a PE4 Disc (4g) As Predicted By ABAQUS Using the JWL Equation of State

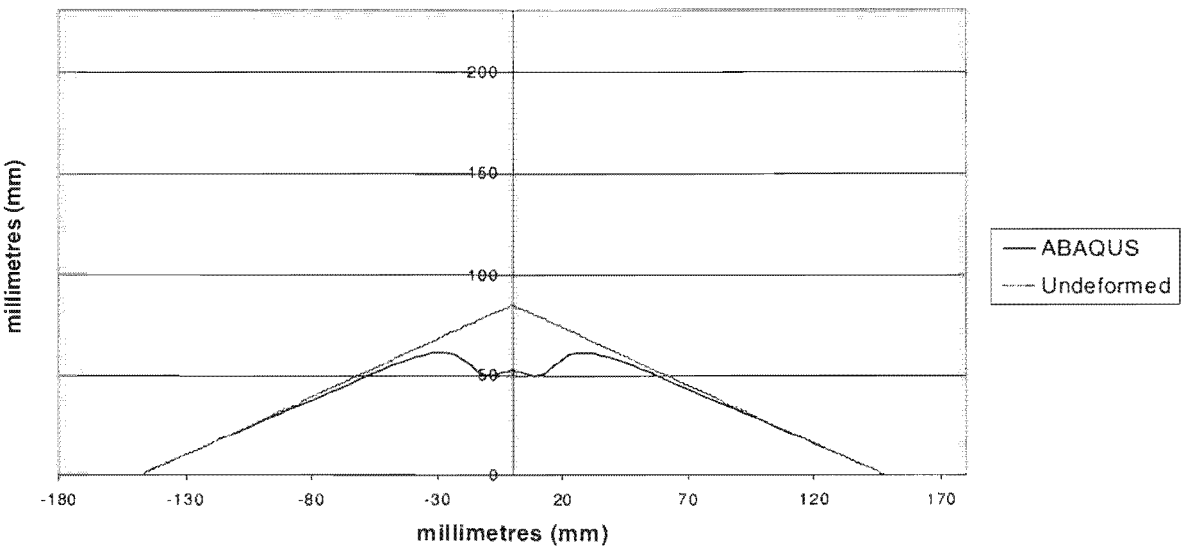

Figure 6.32: The Deformed Profile of a V-Plate (120 degrees) Exploded by a PE4 Disc (6g) As Predicted By ABAQUS Using the JWL Equation of State

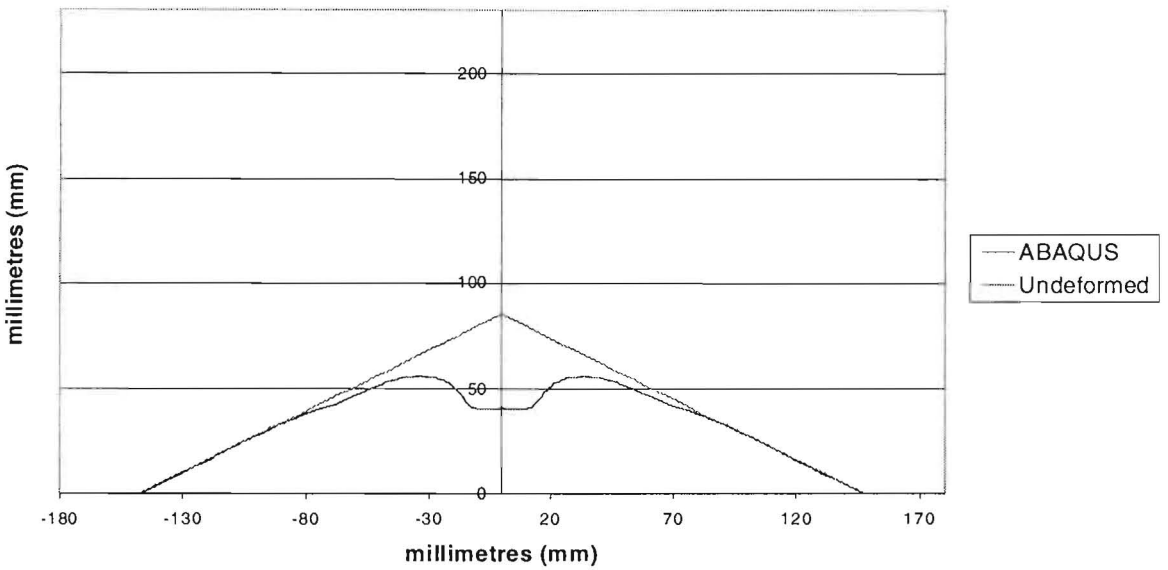

Figure 6.33: The Deformed Profile of a V-Plate (120 degrees) Exploded by a PE4 Disc (8g) As Predicted By ABAQUS Using the JWL Equation of State

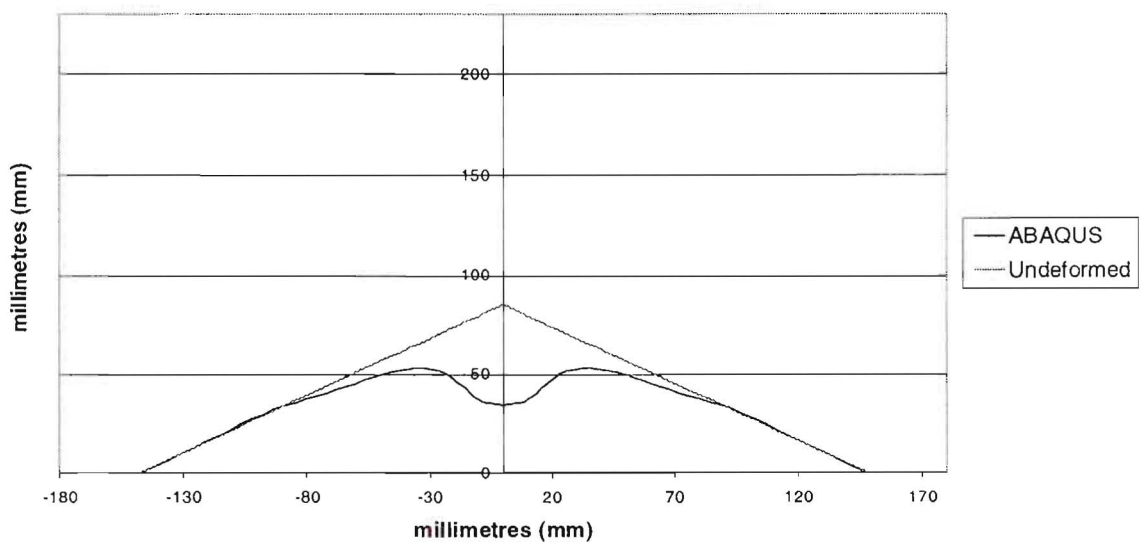

Figure 6.34: The Deformed Profile of a V-Plate (120 degrees) Exploded by a PE4 Disc (10g) As Predicted By ABAQUS Using the JWL Equation of State

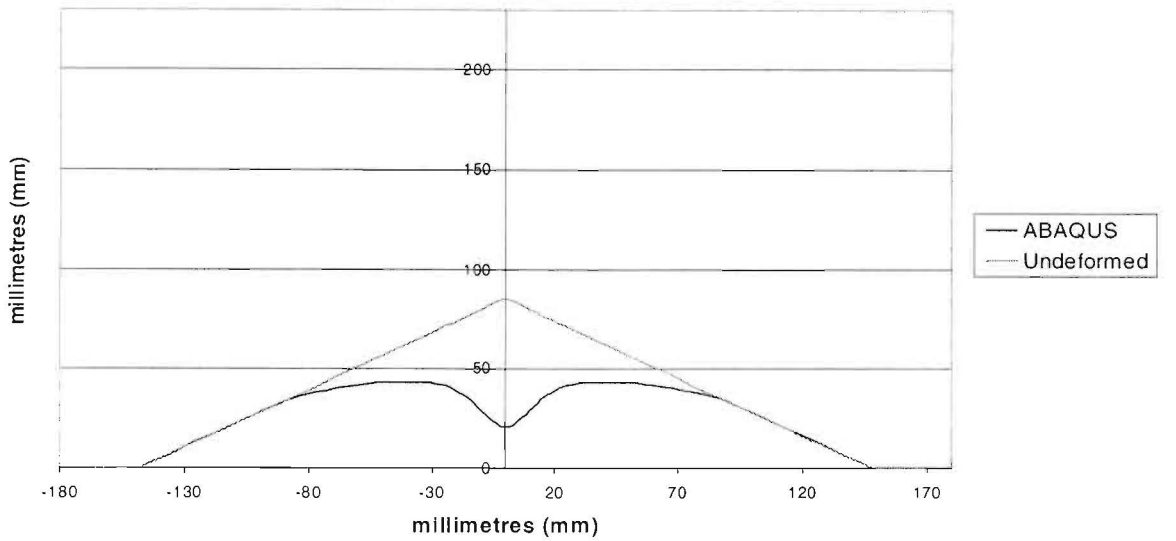

Figure 6.35: The Deformed Profile of a V-Plate (120 degrees) Exploded by a PE4 Disc (12g) As Predicted By ABAQUS Using the JWL Equation of State

As expected the degree of V-plate profile deformation generally increases with an increase in explosive disc mass for all the models. This can be seen in the series in Figure 6.31 to Figure 6.35. The degree of profile deformation increases and the shape of the profile changes with an increase in V-plate angle. The series of 60^0 V-plates exploded by varying explosive masses yield profiles where the V-plate tips have had their sides pinched in. The series of 90^0 V-plates exploded by varying explosive masses yield profiles where the V-plate shapes appear to be a combination of the tips being pinched and the tips being inverted. In Figure 6.31 to Figure 6.35 it can be seen that a clear progression from a slightly pinched V-plate profile to a high level of inversion occurs as the explosive mass increases. For the series of 150^0 V-plates exploded by varying explosive masses the V-plate profiles are all inverted and as the explosive mass increases so the degree of inversion increases.

6.2.3.2.2 Predictions of the V-Plate Profiles for the Systems with the Explosive Discs Horizontally Offset

The effect on the V-plate profile, of horizontally offsetting the explosive disc, was examined. Figure 6.36 to Figure 6.40 show the V-plate profiles resulting from the explosive disc being offset to varying distances. All the V-plates had an angle of 90^0 and all the explosive discs were 8g.

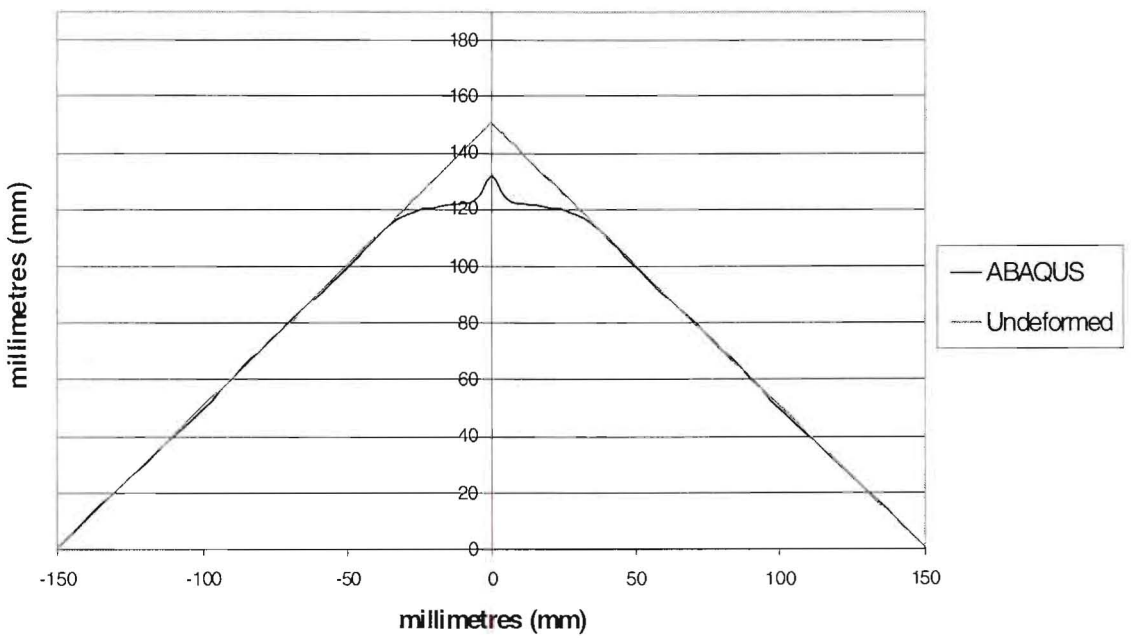

Figure 6.36: The Deformed Profile of a V-Plate (90 degrees) Exploded by a PE4 Disc (8g) As Predicted By ABAQUS Using the JWL Equation of State

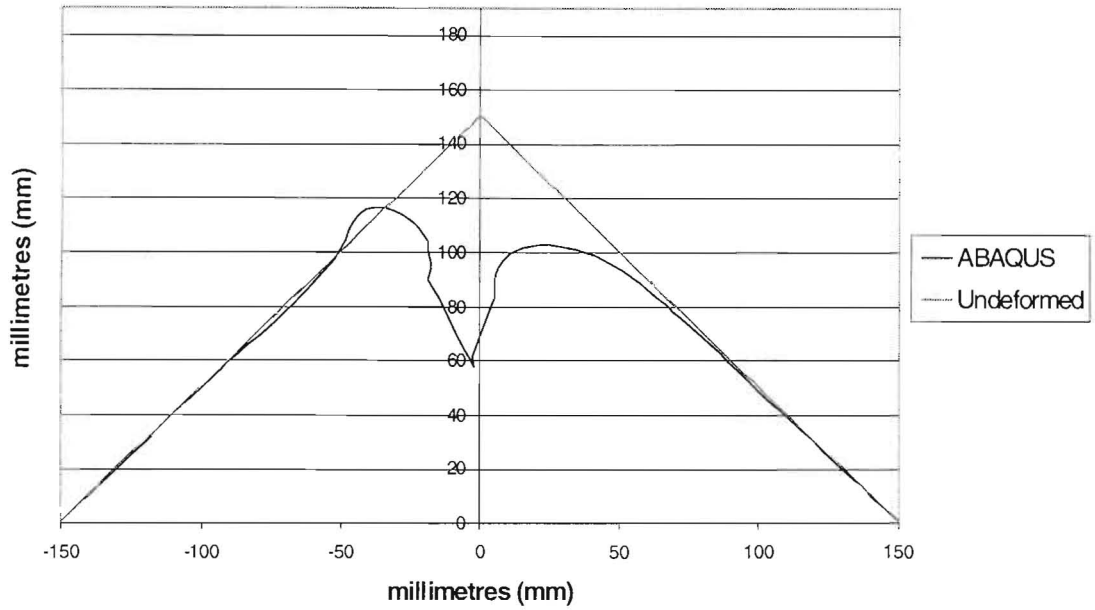

Figure 6.37: The Deformed Profile of a V-Plate (90 degrees) Exploded by a PE4 Disc (8g; 5mm Offset) As Predicted By ABAQUS Using the JWL Equation of State

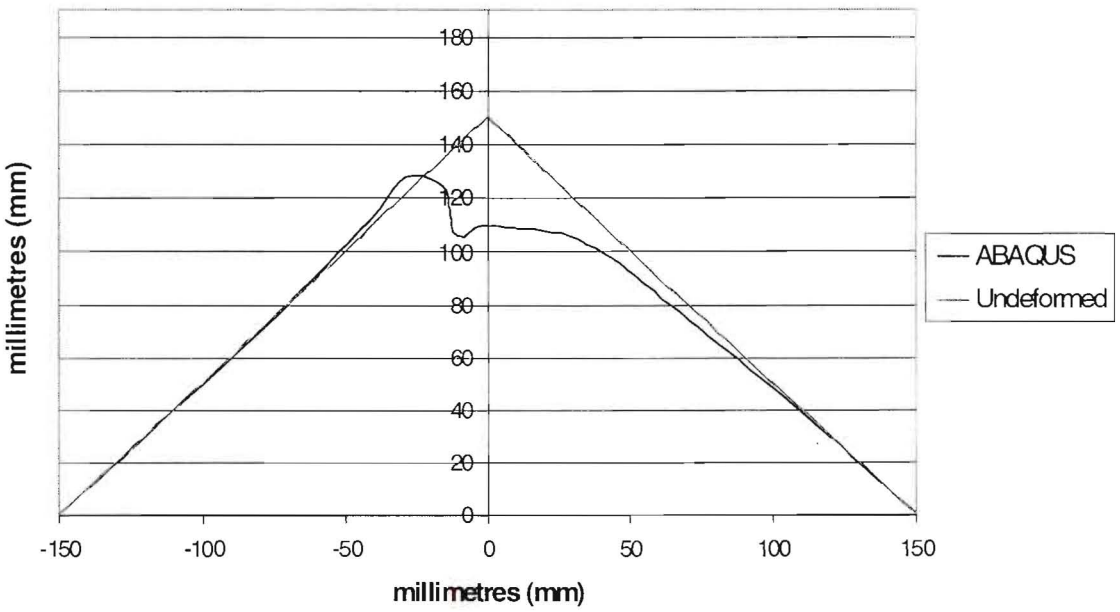

Figure 6.38: The Deformed Profile of a V-Plate (90 degrees) Exploded by a PE4 Disc (8g; 10mm Offset) As Predicted By ABAQUS Using the JWL Equation of State

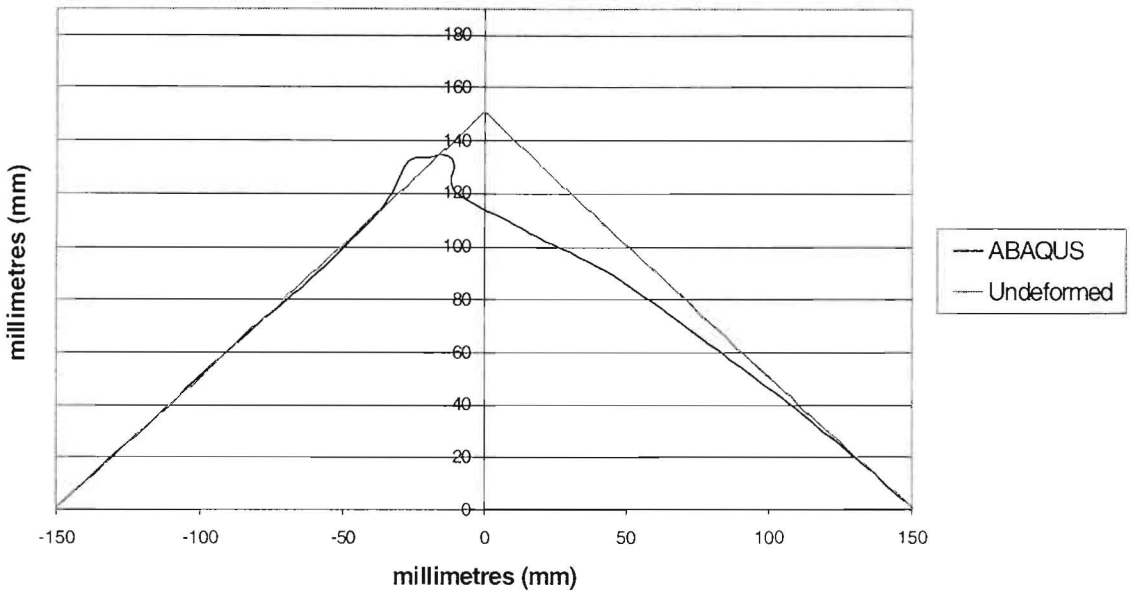

Figure 6.39: The Deformed Profile of a V-Plate (90 degrees) Exploded by a PE4 Disc (8g; 15mm Offset) As Predicted By ABAQUS Using the JWL Equation of State

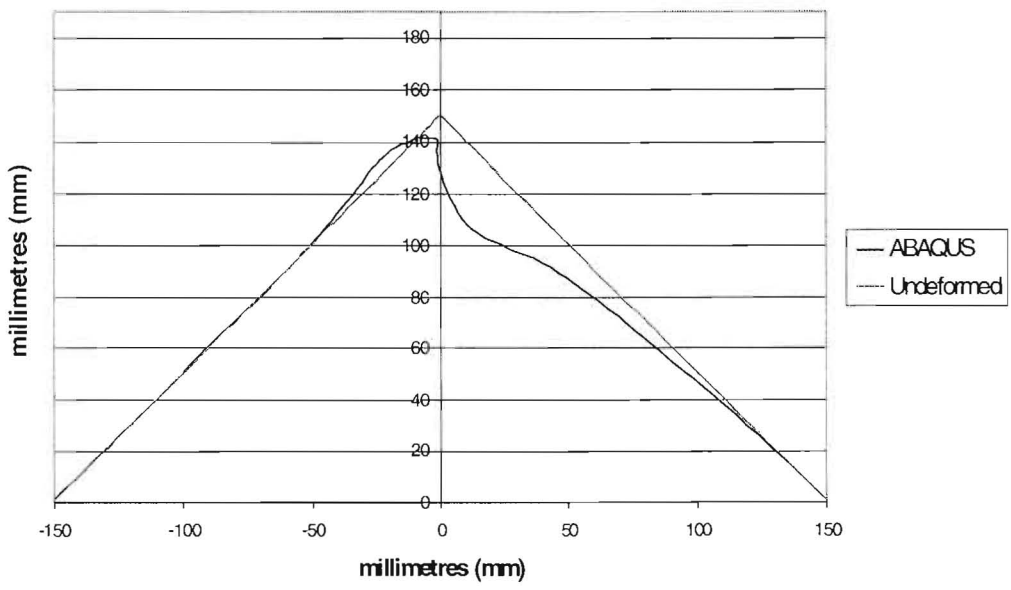

Figure 6.40: The Deformed Profile of a V-Plate (90 degrees) Exploded by a PE4 Disc (8g; 20mm Offset) As Predicted By ABAQUS Using the JWL Equation of State

Previously, the displacement of the V-plate mid-point was used as a measure of the V-plate deformation as the explosive was always vertically above the V-plate ridge. But because the explosive disc is horizontally offset at varying distances in this series, mid-point displacement will not be a reliable method of deformation measurement. Instead, the shapes and degree of deformation of the V-plate profiles will be examined.

The series of V-plate profiles resulting from offset explosive discs, exhibit definite trends with the exception of the V-plate profile resulting from no horizontal disc offset. As the offset of the disc increases from 5mm where the profile deformation is relatively large, the degree of V-plate deformation decreases. This is because the more the explosive disc is offset, the greater the distance is between the disc and the V-plate. It is known that the distance between an explosive and the object it is exploding greatly influences the amount of impulse that is transferred to the object as energy is irreversibly absorbed by the medium between the explosive and the object [6]. So as the distance increases, the transferred impulse decreases.

The V-plate profile resulting from the model with no disc offset, does not follow the trend of the degree of deformation being large for small disc offsets. This V-plate profile has a relatively small degree of deformation and the V-plate tip has not even been inverted and has barely been deformed, as has happened in the other V-plate profiles. The reason for the degree of deformation of this V-plate profile being so small, is thought to be because of the rigidity that the V-plate would possess owing to symmetry. This rigidity would occur to a degree in reality, but would be exaggerated in the numerical model owing to the mathematically perfect symmetry. This rigidity was discussed in the "Attempts to Determine What Causes the Inaccuracies in the Models Containing Rod Explosives and How to Improve the Results" section in this chapter.

A clear indent in the V-plate profiles can be seen where the expanding explosives are thought to make initial contact, except for the V-plate profile

resulting from no disc offset. The V-plate profile resulting from the 5mm disc offset appears to exhibit tearing at the ridge as the model predicts that the ridge elements experience strains of around 300% and temperatures of 1000^0C. These exceed the tearing rule of thumb of 200% strain and 600^0C [40].

The indents of the V-plate profiles thought to be situated where the expanding explosives initially made impact with the V-plates, roughly indicate the direction from which the explosive came. This applies to all the V-plate profiles except the profile resulting from no disc offset. The 'sharpness' of the indents decrease as the disc is offset further away and the impulse transfer decreases. The indent of the profile resulting from the 5mm disc offset has a pointy tip while the indent of the profile resulting from the 20mm disc offset is flat and rounded.

6.2.3.2.3 Tearing of the V-Plates

As previously mentioned, an ABAQUS tearing model has not been incorporated into the JWL EOS models as the tearing models have not yielded accurate results in the past [30]. The rule of thumb of 200% strain and 600^0C temperature [40] is once again used to predict tearing of the V-plates from the results of the models. The system which is most likely to experience tearing is the system containing the V-plate with the largest angle and the explosive with the largest mass. The model results of the system with a 150^0 V-plate and a 12g explosive disc were therefore examined. Figure 6.41 shows the temperature distribution for the deformed V-plate predicted by the model. The area of the V-plate which experienced the greatest strain and the highest temperature is midway along the V-Plate ridge directly beneath the initial position of the explosive. This is the region where the V-plates exploded by the rod explosives tore and is the region where tearing is expected to occur. The strain in this region in the JWL EOS model reached approximately 40% and the temperature reached about 500^0C. This indicates that this region has not torn. According to the ABAQUS results, tearing does not occur in any of the disc explosive models.

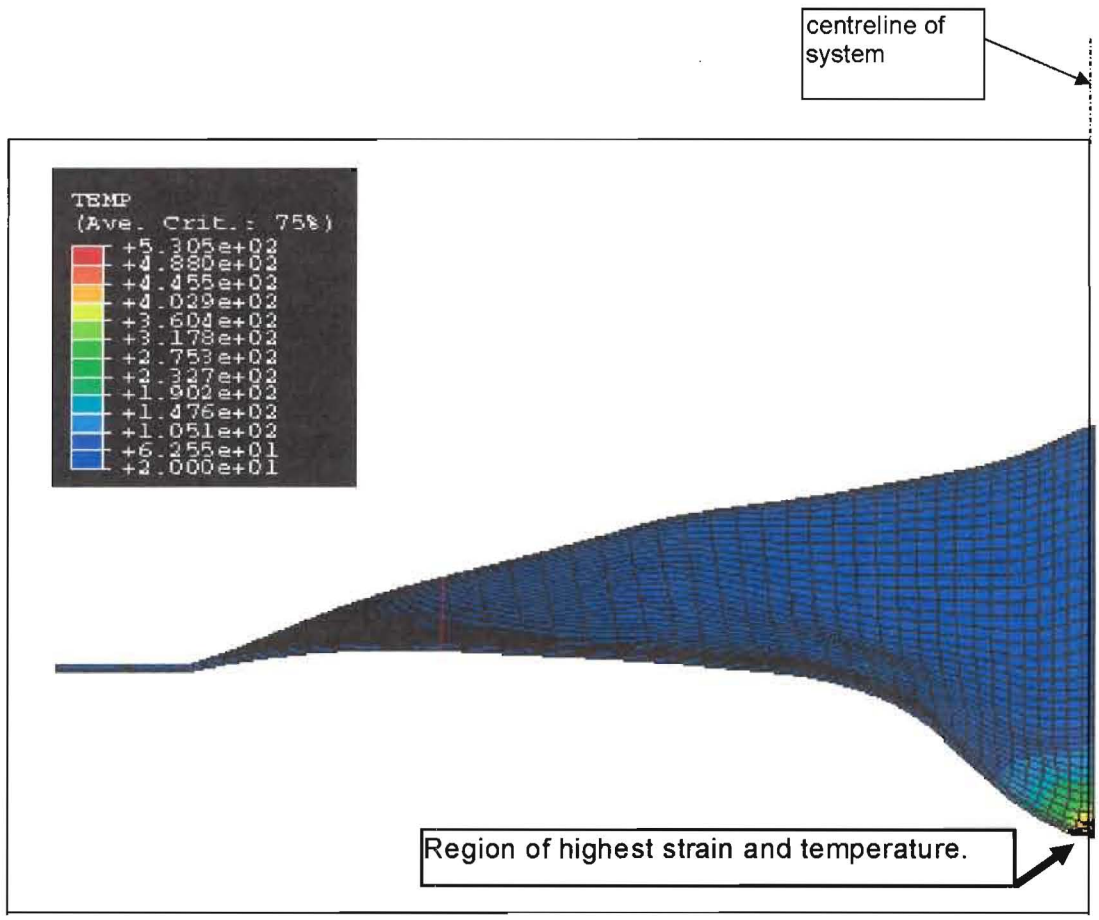

Figure 6.41: The temperature distribution of a deformed 150^0 V-plate as predicted by the model containing a 12g explosive disc

6.2.4 Comparison of the Results of the Models Containing Rod Explosives and the Models Containing Disc Explosives

The results of the models containing rod explosives and the results of the models containing disc explosives are not, strictly speaking, comparable. Because the shapes of the explosives in the two different versions of the models are completely different they will generate shock waves of different shapes which will interact differently with the V-plates. However, it is believed

that the mass of the explosive is the over-riding factor and if a V-plate is exploded by a rod of a certain mass and an identical V-plate is exploded by a disc of a similar mass to the rod, the degree of the V-plate deformations should be similar.

Figure 6.42 Shows a comparison between the V-plate profiles of an experiment containing a rod explosive, the corresponding JWL EOS model containing a rod explosive, and the JWL EOS model containing a disc explosive of a mass similar to the rod explosives. The V-plate has a 150^0 angle and the mass of the explosive rods are both 9g while the mass of the explosive disc is 8g (the closest disc mass to 9g).

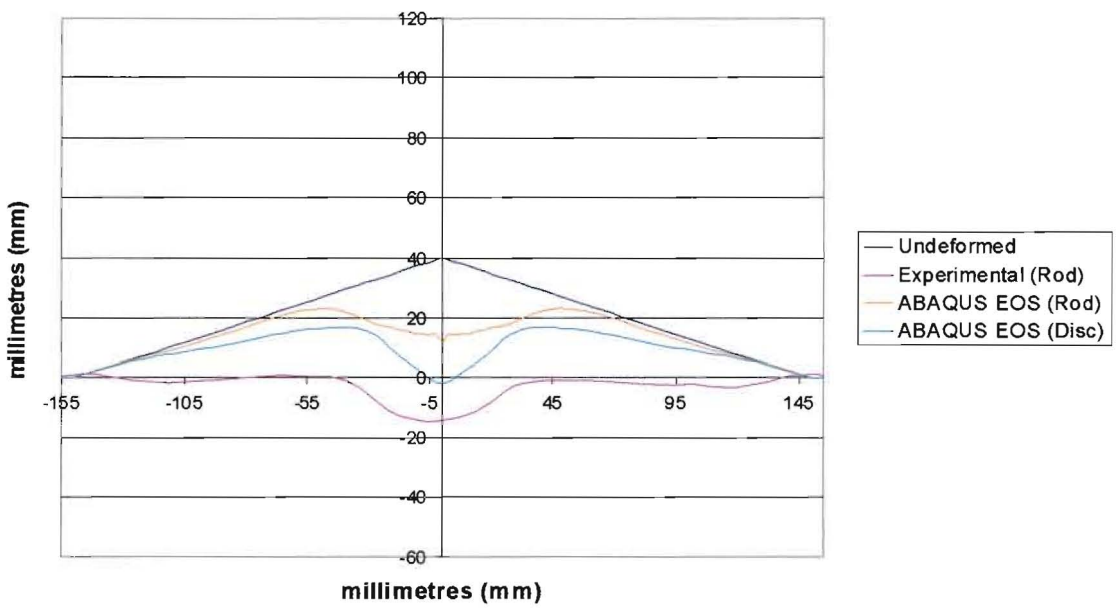

Figure 6.42: Comparison Between the 150 Degree V-Plate Profiles of an Experiment Containing a 9g Explosive Rod, the JWL EOS Model Containing a 9g Explosive Rod, and the JWL EOS Model Containing an 8g Explosive Disc.

From Figure 6.42 it can be seen that the shape of the displacement profiles from the model containing a rod explosive and from the model containing a disc explosive are similar in form. The central bulge or indent of the disc

explosive model profile is slightly narrower with a sharper point though. However, the shapes of the rod explosive model profile and the disc model explosive profile are thought to be similar enough so that a comparison of their mid-point displacements will represent a comparison of the degree of deformation of the two predicted profiles. From Figure 6.42 It can be seen that the degree of deformation of the disc explosive model profile is significantly greater than the rod explosive model profile deformation and closer to the experimental displacement. The mid-point displacements of these profiles also reflect this observation. Comparing the mid-point displacements of the rod explosive model profiles and the corresponding disc explosive model profiles was the method used to compare the degree of deformation of these two systems for all the V-plates.

Figure 6.43 shows a comparison between the V-plate mid-point displacement versus explosive mass relationships of the disc and rod explosive models, and the experiments, for 150^0 V-plates.

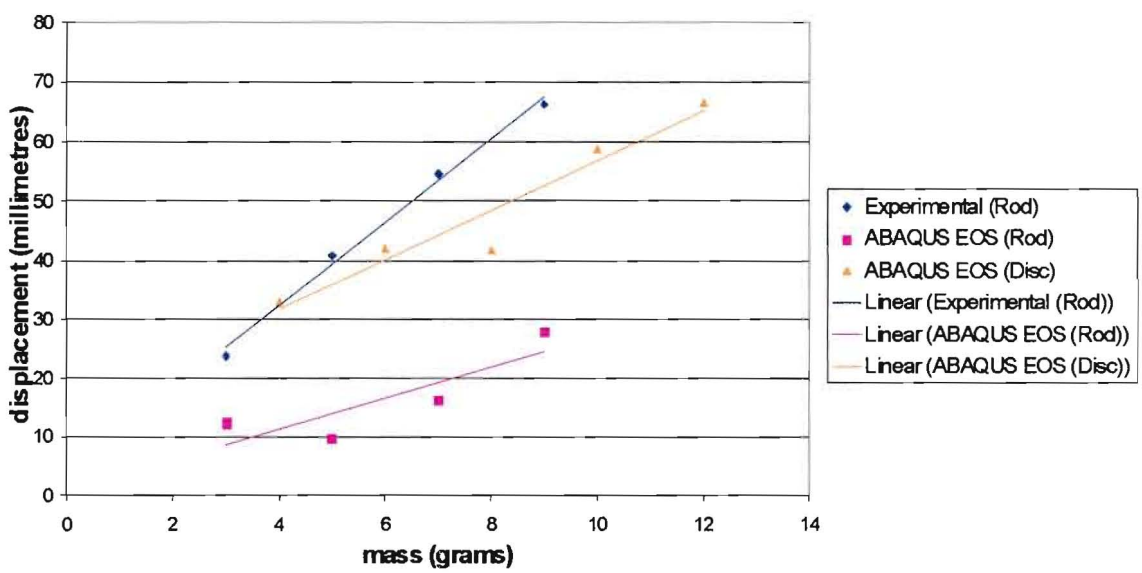

Figure 6.43: Comparison Between the 150 Degree V-Plate Mid-Point Displacement Versus Explosive Mass Relationships of the Rod Explosive Experiments, the Models Containing Rod Explosives, and the Models Containing Disc Explosives

It can be clearly seen in Figure 6.43 that the magnitudes of the displacements of the disc models are far higher than the corresponding displacements of the rod models. The displacements of the disc models are far closer to the experimental displacements of the rod systems. The slopes of the linear trend-lines in Figure 6.43, indicating the sensitivity of the relationships to mass, were also compared. The slope of the rod explosive experimental trend-line is $7mm.g^{-1}$, the slope of the disc explosive model trend-line is $4.1mm.g^{-1}$, and the slope of the rod explosive model trend-line is $2.8mm.g^{-1}$. This means that the sensitivity of the disc explosive models to explosive mass is greater than the sensitivity of the rod explosive models and is closer to the sensitivity of the rod explosive experiments. From these results it appears that the disc explosive models produce more accurate results although they still under-predict the rod experimental results. The comparisons conducted on the 150^0 V-plate series above were conducted on all the other V-plates of different angles, and similar results were found.

Figure 6.44 shows a comparison between the V-plate mid-point displacement versus V-plate angle relationships of the disc and rod explosive models, and the experiments, for 9g explosive rods and an 8g explosive disc.

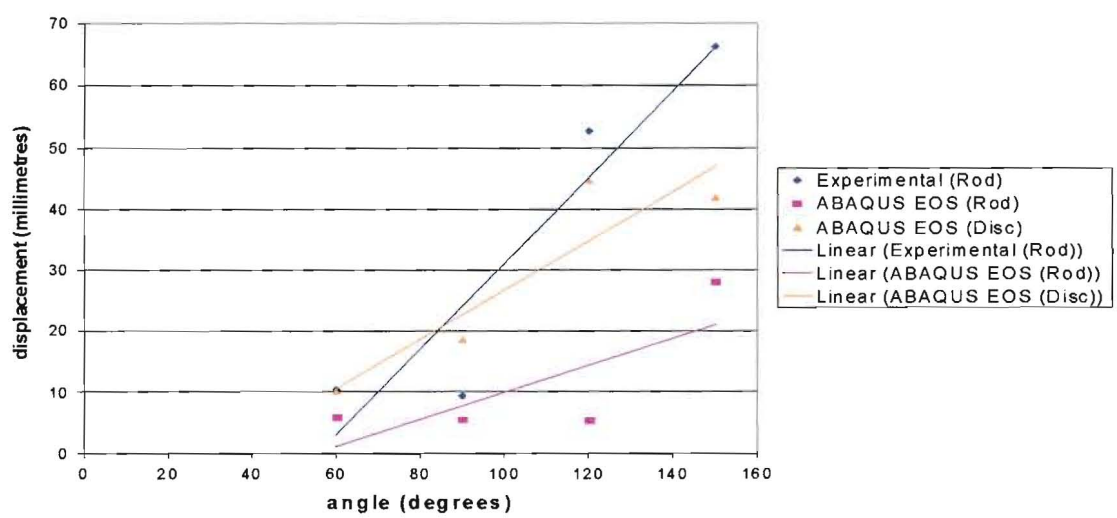

Figure 6.44: Comparison Between the 150 Degree V-Plate Mid-Point Displacement Versus V-Plate Angle Relationships of the 9g Rod Explosive Experiments, the Models Containing 9g Rod Explosives, and the Models Containing 8g Disc Explosives

It can be clearly seen in Figure 6.44 that the magnitudes of the displacements of the disc models are far higher than the corresponding displacements of the rod models. The displacements of the disc models are far closer to the experimental displacements of the rod systems. The slopes of the linear trend-lines in Figure 6.44, indicating the sensitivity of the relationships to V-plate angle, were also compared. The slope of the rod explosive experimental trend-line is $0.71 mm.degree^{-1}$, the slope of the disc explosive model trend-line is $0.4 mm.g^{-1}$, and the slope of the rod explosive model trend-line is $0.22 mm.g^{-1}$. This means that the sensitivity of the disc explosive models to the V-plate angle is greater than the sensitivity of the rod explosive models and is closer to the sensitivity of the rod explosive experiments. From these results it appears that the disc explosive models produce more accurate results although they still under-predict the rod experimental results. The comparisons conducted on the 150^0 V-plate series above were conducted on all the other V-plates of different angles, and similar results were found.

Another comparison conducted between the explosive disc model results and the explosive rod experimental results, was for tearing. It was found that tearing did not occur for any of the disc explosive models which is surprising as tearing occurs in a number of the rod explosive experiments. The V-plates in the disc explosive models are closer to tearing than the V-plates in the rod explosive models. It is thought that because the disc explosive models under-predict the deformation of the V-plates, the V-plates in these models did not reach the point of tearing.

From comparing the results of the rod explosive models and the disc explosive models to the rod explosive experimental results, it appears that the disc explosive models yield more realistic results than the rod explosive models by far. This is because the degree of deformation of the disc explosive model profiles is greater than the degree of deformation of the corresponding rod explosive model profiles. This means that the disc explosive model profiles are therefore closer to the rod explosive

experimental profiles. The rod explosives are actually 1g heavier than the disc explosives yet the rod explosive models yield profiles with far less deformation than the corresponding models with disc explosives.

In conclusion, it is thought that the disc explosive models will yield far more accurate results than the rod explosive models have. This is because the disc explosive models have yielded results which are similar to the experimental results of similar systems, while the rod explosive models yielded poor results for these systems. To prove the superior accuracy of the disc explosive models, experiments of the systems containing disc explosives need to be conducted to verify the results of the models.

7. Conclusions

From reviewing the literature review, all the aspects of the numerical models used in this study, and most importantly, the results of this study, many conclusions can be drawn. These conclusions are presented here.

7.1 The Finite Element Modelling Technique

If the models can successfully predict the deformation of V-plates being exploded by PE4 rods and discs, the need for expensive and time-consuming experiments can be eliminated. But it must be kept in mind that even if a numerical model appears to predict successful results, these predictions must not be blindly accepted. This is because the predictions are obtained from a mathematical model which tries to emulate reality. The mathematical model makes assumptions and cannot incorporate all the factors that occur in reality and therefore may not always produce accurate predictions.

The performance of many of the aspects of the numerical models in this study were examined and conclusions drawn. These aspects include element selection, mesh selection, boundary conditions (which involve symmetry and simulation of clamping), and contact interaction.

7.1.1 Element Selection

Element selection is important as it can influence the model predictions significantly. This was clearly seen in the comparison conducted by Grobbelaar [35] discussed in "The Finite Element Model" chapter in "The V-Plate". The same system was modelled using 2-noded axisymmetric elements and then 4-noded axisymmetric elements and a large difference was seen in the displacement results. It was found that the 4-noded axisymmetric elements produced more accurate results. In this study it was shown that modelling this same system with three-dimensional 8-noded hexahedral elements produced superior results to the 4-noded axisymmetric elements. These comparisons lead to the conclusion that three-dimensional 8-noded hexahedral elements are the best choice for this study and that it is

unlikely that these elements will be responsible for any inaccurate model predictions.

Three-dimensional tetrahedral elements were also incorporated in some of the models in this study and resulted in hybrid meshes. It was shown that using only hexahedral elements to model a system, and then incorporating a hybrid mesh with tetrahedral elements to model the same system, did not significantly alter the model results. This indicates that it is unlikely that these elements or the resulting hybrid mesh, will be responsible for any inaccurate model predictions.

7.1.2 Mesh Selection

It is a mathematical fact that the finer the mesh in a numerical model, the more the results will improve. This improvement occurs until a sufficiently fine mesh is reached where the results will no longer significantly change, no matter how much finer the mesh is made. This indicates that the results have converged to the most accurate solution that that specific model can produce.

In comparison to similar previous studies which were successful, the mesh densities used in this study were more than suitable for the models (in other words, fine enough) and it is unlikely that the mesh density will be the reason for any inaccurate predictions.

As already mentioned, the hybrid mesh used to model the rod explosives is also considered suitable and it is unlikely that it will be the reason for any inaccurate predictions.

7.1.3 Boundary Conditions

Boundary conditions were used for two reasons in the models in this study:

One, to allow a quarter model of a system to produce identical results to those that would be produced by a whole model owing to planes of symmetry.

It is far quicker to analyse a quarter model than it is to analyse a whole model so the computational time was greatly reduced as a result of these symmetry boundary conditions.

The second reason boundary conditions were used in the models, was to simulate the clamping of the V-plates. This was done by fixing all the degrees of freedom of the nodes on the top and bottom surfaces of the V-plate flanges.

Boundary conditions have been used in the same way for the same reasons in many similar previous studies which were successful such as the study conducted by Grobbelaar [35]. This indicates that it is unlikely that these boundary conditions will be responsible for any inaccurate model predictions.

7.1.4 Contact Interaction

The contact interaction model used by ABAQUS/Explicit is suitable for the dynamic interaction of surfaces. However, it must be noted that the systems which are being modelled in this study will place the contact algorithm under extreme conditions as the explosive will impact with the V-plate at high velocities of up to 4500m.s^{-1}.

There are many choices that can be made which will affect the contact interaction between the explosive and the V-plate. Choices can be made between:

- the kinematic and penalty stiffness contact algorithms
- hard and soft contact (and the choice of function used for soft contact)
- pure master-slave and weighted contact surfaces

It was found that the different choices did affect the predictions of the models to a small degree, but not to the degree required. This will be discussed later. When comparing the displacement profiles of a model predicted using hard

contact and then soft contact, it was seen that a difference in the displacement of the V-plate ridge of a few millimetres would occur.

According to Dr. Izak Snyman [41] using the penalty contact algorithm for models of V-plates being exploded by disc explosives greatly improves the results by increasing the displacement profiles. Unfortunately the penalty contact algorithm could not be implemented in this study.

The choice of kinematic, hard contact between pure master-slave surfaces was made for this study. These choices were made based on the advice of the ABAQUS/Explicit manual [38], on what the version of ABAQUS/Explicit being used would allow, and what had been successfully used in similar previous studies.

It is thought that the choices made will probably not be responsible for any inaccurate predictions as the selections were informed decisions and the different choices did not affect the results significantly. It is a possibility, though, that all the different choices could produce similarly inaccurate results, and that using the penalty contact algorithm would be the crucial choice which would produce accurate results. This was the view of Dr Izak Snyman [41] but, as mentioned, this theory could not be tested. Grobbelaar [35] also mentioned that the penalty stiffness algorithm helped alleviate discontinuities to obtain a reasonable surface profile.

7.2 Results of the Models

The results obtained from the models in this study allowed conclusions to be drawn about the JWL EOS approach to modelling V-plates that are exploded by PE4 rods and discs.

7.2.1 Results of the Models Containing Explosive Rods

The systems containing rod explosives were modelled because experimental results were available of V-plates exploded by PE4 rods. If the JWL EOS models could predict displacement profiles and absorbed impulses of the V-plates which were similar to the experimental profiles and imjpulses, for all the parametric variations of the model, then the numerical models will be verified. This will then mean that there can be a reasonably high level of confidence in the model predictions of similar systems, such as those with the V-plates that are exploded by PE4 discs.

The results of the JWL EOS models which were compared to the experimental results were:

- the displacements of the mid-points (ridges) of the V-plate profiles
- the profiles of the V-plates
- the impulses absorbed by the V-plates

The results of models of these systems that used the pressure profile approach, which were modelled by Nannucci [44], were also compared to the results of the experiments and JWL EOS models.

7.2.1.1 Comparison Between the JWL Equation of State Model Predictions of the V-Plate Mid-point Displacements, the Pressure Profile Model Displacements, and the Experimental Displacements

As expected, the JWL EOS models predicted increasing V-plate deformation as the explosive mass increased. The models also predicted increasing V-plate deformation as the angle of the V-plate increased, which was expected. The pressure profile models also exhibited these trends.

7.2.1.1.1 Comparison of the V-Plate Mid-Point Displacements Versus the Explosive Rod Masses

The relationships between the mid-point displacements of the V-plate profiles and the explosive rod masses, predicted by the JWL EOS models, appear to be linear for all the V-plate angles. The experimental results and the predictions of the pressure profile models also show this relationship to be linear. It was found that, generally, the JWL EOS models greatly under-predicted the mid-point displacements of the V-plate profiles and that the mid-point displacements were not sufficiently sensitive to the explosive masses.

The pressure profile models predicted the mid-point displacements of the V-plate profiles far more accurately than the JWL EOS models. The sensitivity of the mid-point displacements to the explosive masses was also far more accurately predicted by the pressure profile models.

7.2.1.1.2 Comparison of the V-Plate Mid-Point Displacements Versus the V-Plate Angles

The relationships between the mid-point displacements of the V-plate profiles and the V-plate angles, predicted by the JWL EOS models, appear to be linear for all the explosive rod masses. The experimental results and the predictions of the pressure profile models also show this relationship to be linear. It was found that, generally, the JWL EOS models again greatly under-predicted the mid-point displacements of the V-plate profiles and that the mid-point displacements were not sufficiently sensitive to the V-plate angles.

The pressure profile models once again predicted the mid-point displacements of the V-plate profiles far more accurately than the JWL EOS models. The sensitivity of the mid-point displacements to the V-plate angles was also far more accurately predicted by the pressure profile models.

7.2.1.2 Comparison Between the JWL Equation of State Model Predictions of the V-Plate Profiles, the Pressure Profile Model Profiles, and the Experimental Profiles

For low V-plate angles such as the 60^0 and 90^0 V-plates, the experimental results exhibit significantly asymmetric profiles. The experimental profiles are more symmetric for the 120^0 and 150^0 V-plate. The JWL EOS models cannot model asymmetric behaviour and therefore the profile predictions of the V-plates with lower angles, are not similar to the experimental profiles. For the V-plates with larger angles, the JWL EOS models greatly under-predict the degree to which the V-plate profiles are deformed. The profile predictions of the lower angle plates which are exploded by the larger explosive masses are also significantly under-predicted. So whenever a large degree of deformation is expected according to the experimental V-plate profiles, the JWL EOS models greatly under-predict the profiles. It is speculated though, that if the problem involving the insufficient impulse transfer is corrected, the profiles predicted will be reasonably similar to the corresponding experimental profiles for the 120^0 and 150^0 V-plates. This will not necessarily be the case for the 60^0 and 90^0 V-plates as asymmetry is the main reason for the differences between the predicted profiles and the corresponding experimental profiles.

The under-predictions of the V-plate profiles are so significant for the V-plates with larger angles that the general shapes of the predicted profiles are not even similar to the experimental profiles for the series of 120^0 V-plates. This is because the V-plate tips have inverted in the experiments while in the predicted profiles they have not. The JWL EOS models manage to predict the inversion for the 150^0 V-plate series so the shapes of the predicted profiles are similar to the experimental profiles but the degree of deformation is still greatly under-predicted.

The pressure profile models also have difficulty modelling asymmetric behaviour so they do not accurately predict the profiles for the V-plates with the lower angles (60^0 and 90^0). The more symmetric V-plate profiles of the V-plates with larger angles are far more accurately predicted by the pressure profile models than by the JWL EOS models. This is because the pressure profile models predict higher, and therefore more accurate, degrees of deformation of the V-plate profiles. Because of this, the shapes of these predicted profiles are more similar to the experimental profile shapes.

7.2.1.3 Comparison Between the Effectiveness of the V-Plates Determined by the JWL Equation of State Model, the Pressure Profile Model, and the Experiments

A method to determine the effectiveness of the different V-plates as protection from explosive blasts, is required, so that the optimum V-plate can be identified. The characteristics of this optimum V-plate can then be applied to the under-carriage of mine-protected vehicles.

The method of determining the effectiveness of a V-plate involves extracting the impulse that the V-plate absorbed from the explosive blast, from the results of the JWL EOS models. This impulse can then be used to determine what percentage of the entire explosive impulse the V-plate managed to deflect. The blast deflection percentages of the models containing rod explosives could be compared to the corresponding percentages obtained from the rod explosive experiments to determine the accuracy of the model predictions.

Unfortunately it was found that the impulses absorbed by the V-plates as predicted by the models were greatly under-predicted. This problem was also encountered by Wiehahn [34]. The under-predictions of the impulses absorbed by the V-plates were expected as the degree of deformation of the V-plate profiles was greatly under-predicted. Because of the great under-

predictions of the models, reliable predictions of the effectiveness of the V-plates could not be determined.

7.2.1.4 Attempts to Determine What Causes the Inaccuracies in the Models Containing Rod Explosives and How to Improve the Results

Because the JWL EOS models produced large unacceptable errors and the models were therefore not verified, attempts were made to determine what causes these inaccuracies and to improve the results.

Possible reasons for the model inaccuracies were investigated such as human error in creating the model, unrealistic mathematical rigidity of the V-plates, and incorrect transfer of impulse from the explosive to the V-plate. All these possibilities were found to be unlikely reasons for the inaccuracies of the model predictions except for incorrect impulse transfer. This theory is supported by the fact that the model predicted impulses absorbed by the V-plates were greatly under-predicted.

Possible reasons for an incorrect impulse transfer from the rod explosives to the V-plates were the complex shape of the rod, the hybrid mesh resulting from having to model the complex shape of the explosive, and the oblique impact of the explosive nodes with the V-plates. On investigation it was found that these possibilities were unlikely reasons for the poor transfer of impulse from the rod explosives to the V-plates. Therefore the factor responsible for the inaccurate predictions of the models containing rod explosives remains unknown.

7.2.1.5 Tearing of the V-Plates

An ABAQUS tearing model was not incorporated into the JWL EOS models as the tearing models have not yielded accurate results in the past [30]. The rule of thumb of 200% strain and 600^0C temperature [40] is used to predict tearing of the V-plates from the results of the models.

Tearing of the experimental V-plates generally occurred for the V-plates with the larger angles and for the V-plates which were exploded by the larger explosive masses. The tearing appears to initially occur along the ridge of the V-plate and for the more extreme cases of tearing, the sides of the V-plates are then pealed away into strips.

Using the mentioned rule of thumb, it was found that none of the predicted V-plate profiles from the models containing rod explosives would experience tearing. This was expected because the V-plate profiles are greatly under-predicted by the JWL EOS models so it is unlikely that the predicted profiles would reach the conditions of tearing.

7.2.2 Results of the Models Containing Explosive Discs

The models containing V-plates exploded by PE4 discs are the models of greatest interest in this study as they simulate the detonation of a landmine under the V-shaped undercarriage of a mine-protected vehicle. There are no experimental results for these systems so the accuracy of the predictions of the JWL EOS models for these systems could not be determined. Instead, certain characteristics of the models were examined for trends to determine the dependency of the displacements and profiles of the V-plates on parametric variations. The characteristics examined were:

- the displacements of the mid-points (ridges) of the V-plate profiles
- the profiles of the V-plates

7.2.2.1 Model Predictions of the V-Plate Mid-Point Displacements

The relationships that the V-plate mid-point displacements have with the explosive rod masses and the V-plate angles were investigated. As expected the JWL EOS models predicted increasing V-plate deformation as the

explosive mass increased. The models also predicted increasing V-plate deformation as the angle of the V-plate increased which was expected.

7.2.2.1.1 V-Plate Mid-Point Displacements Versus the Explosive Disc Masses

It was found that the relationship between the mid-point displacement of the V-plate profiles and the explosive mass was linear. The sensitivity of the mid-point displacement to the explosive mass varies for V-plates of different angles. The sensitivity of the displacements to explosive mass is similar for the 60^0 and 150^0 V-plates. The sensitivity of the displacements to explosive mass are also similar for the 90^0 and 120^0 V-plates, but these V-plates are far more sensitive than the 60^0 and 150^0 V-plates.

7.2.2.1.2 V-Plate Mid-Point Displacements Versus the V-Plate Angles

The relationship between the mid-point displacement of the V-plate profiles and the V-plate angles was found to be linear. The model predictions showed that the mid-point displacements have similar sensitivity to the V-plate angle for all the explosive masses. The sensitivity of the mid-point displacement for all the explosive masses is significant meaning that an increase in the angle of the V-plate caused the V-plate mid-point displacements to increase significantly.

7.2.2.2 Model Predictions of the V-Plate Profiles

As expected the degree of the predicted V-plate profile deformations increased with an increase in the explosive mass and an increase in the V-plate angle. As the V-plate angles increase the shape of the profiles change. The series of 60^0 V-plates exploded by different masses yield profiles where the V-plate tips have had their sides pinched in. The results of the models of the 90^0 V-plate series yield profiles which appear to be a combination of pinched tips and the tips being inverted. The 120^0 V-plate series shows a clear progression from a slightly pinched profile to a high level of inversion as

the explosive mass increases. The profiles of the 150^0 V-plate series are all inverted with the degree of inversion increasing with an increase in explosive mass.

Models of a slightly different system of a V-plate being exploded by a horizontally offset explosive disc, were also analysed. The disc was offset to different distances in the different models and the results were best examined through the predicted V-plate profiles than through the mid-point displacements of the V-plate profiles.

The general trend of the degree of deformation of the profiles was that the deformation decreases as the offset distance of the disc increases. This was expected as some of the explosive energy is absorbed by the air inbetween the explosive and the V-plate. The model with a disc which had zero offset *did not follow* this trend though as the predicted profile exhibited relatively small deformation. This is thought to be because of the rigidity of a totally symmetric system.

All the predicted profiles, except the profile resulting from the disc with no offset, had indents where it is thought that the expanding explosives initially made contact with the V-plates. These indents roughly indicate the direction from which the blast came from.

7.2.2.3 Tearing of the V-Plates

Using the rule of thumb of 200% strain and 600 ^{0}C temperature [40], it was found that none of the predicted profiles from the JWL EOS models containing disc explosives would experience tearing. The models containing disc explosives of larger masses and containing V-plates with larger angles, though, came much closer to the conditions of tearing along the V-plate ridge than similar models containing rod explosives.

7.2.3 Comparison of the Results of the Models Containing Rod Explosives and the Models Containing Disc Explosives

The results of the models containing rod explosives and the results of the models containing disc explosives are not, strictly speaking, comparable as the shapes of the explosives are very different and the masses of the explosives are slightly different as well. However it is believed that the mass of the explosive is the over-riding factor determining the degree of the V-plate deformation. This means that if a V-plate is exploded by a rod of a certain mass, and an identical V-plate is exploded by a disc of similar mass to the rod, then the degree of the V-plate deformations should be similar.

Comparing the results of the models containing rod explosives to the results of the models containing disc explosives of similar masses to the rod explosives, it was seen that the degree of deformation of the profiles resulting from the disc explosives were significantly and consistently higher. These profiles produced by the disc explosives were far closer to the results obtained from the rod explosive experiment than the actual rod explosive models. This indicates, but does not prove, that the models containing disc explosives may produce more accurate results than the models containing rod explosives were able to. To prove this theory, though, experiments containing explosive discs will have to be conducted.

7.3 Concluding Remarks

The JWL EOS models were unacceptably inaccurate with their predictions and were therefore not verified. The reason for inaccuracies is thought to be because of an incorrect transfer of impulse from the explosives to the V-plates. The reason for this incorrect impulse transfer is not known. There is a possibility which could not be tested, that the penalty stiffness contact algorithm would improve the impulse transfer. The results of the models containing disc explosives appear promising but they will have to be verified with experiments.

There appears to be a problem with the contact interaction of a JWL EOS governed object impacting at high velocities with another object in ABAQUS/Explicit. This must be investigated. It is believed that if this problem is solved, models involving explosives governed by the JWL EOS such as those in this study, may produce greatly improved results.

Because of the problems encountered in this study, certain objectives of this study could not be achieved. The models containing rod explosives that were meant to verify that ABAQUS/Explicit was capable of modelling systems such as those in this study, could not be verified. This means that the results of the models containing disc explosives are not reliable. Therefore any conclusions drawn with respect to what V-plate geometry would be optimum for the undercarriage of a mine-protected vehicle would also be unreliable.

8. Recommendations

From all the aspects of this study the following recommendations can be made:

8.1 The Finite Element Model

When modelling systems such as those in this study, the following must be considered:

- The effect that different boundary conditions have on the predictions of the models should be investigated and the appropriate boundary conditions chosen.
- The element type selected for the models can significantly affect the model predictions and therefore the different element options should be investigated to determine the most appropriate element type.
- The mesh densities in a model can affect the model predictions and therefore these effects should be investigated so that a suitable mesh can be selected.
- A tearing model was not included in the models in this study. A tearing model that successfully predicts tearing is highly desirable in a study such as this so that reliable conclusions can be made. This is because, from the literature review, it was found that if the undercarriage of a mine-protected vehicle tore in anyway, the occupants of the vehicle would most likely be injured. So, because resistance to tearing is such an important requirement of the undercarriage of these vehicles, it is necessary that the models are capable of accurately predicting tearing of the V-plates.
- The contact interaction of surfaces needs to be thoroughly understood and investigated so that informed choices are made when selecting the contact interaction model. This is important because the interaction of the explosives with the V-plates is where the impulse gets transferred to the V-plates and this impulse is what determines the degree of deformation of the V-plate profiles.

8.2 The Results of the Models

- The problems causing the inaccuracies in this study must be investigated and solved.
- Systems such as those in this study which involve the high velocity impact of a JWL EOS governed body with another body should not be modelled in ABAQUS/Explicit until the problems encountered are solved. Instead, the pressure profile method should be used to model problems involving explosive loading in the meantime.
- Experiments must be conducted on the systems containing explosive discs which were modelled in this study. Comparing the experimental results to the numerical predictions presented here will help to isolate the problems causing the inaccuracies. If the numerical predictions are reasonably accurate, the problem will appear to be related to the shape of the explosive. But if the numerical predictions display the same type of inaccuracies as the predictions for the rod explosive systems encountered in this study, then the problem will appear to be a more general contact interaction problem.

9. Appendices

9.1 Appendix A: Photographs of Experimentally Deformed V-Plates Exploded by PE4 Rod Explosives

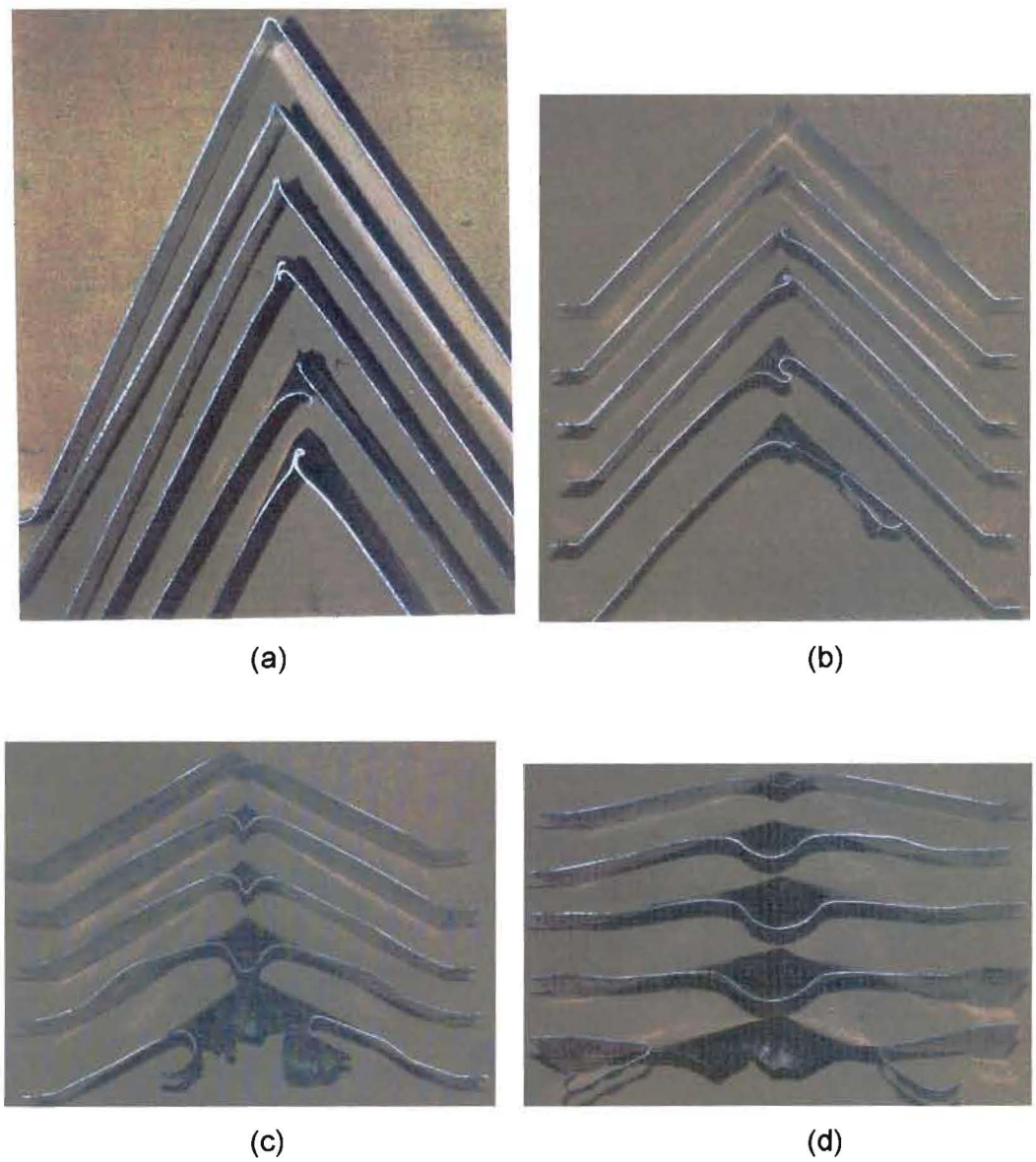

(a) (b)

(c) (d)

Figure A.1: Photographs of Lockley's [43] experimentally deformed V-plates exploded by PE4 rod explosives with the V-plates grouped together according to the V-plate angles of; (a) 60^0; (b) 90^0; (c) 120^0; (d) 150^0.

9.2 Appendix B: Pictures of Pressure Profile Method Numerically Predicted Deformed V-Plates Exploded by PE4 Rod Explosives

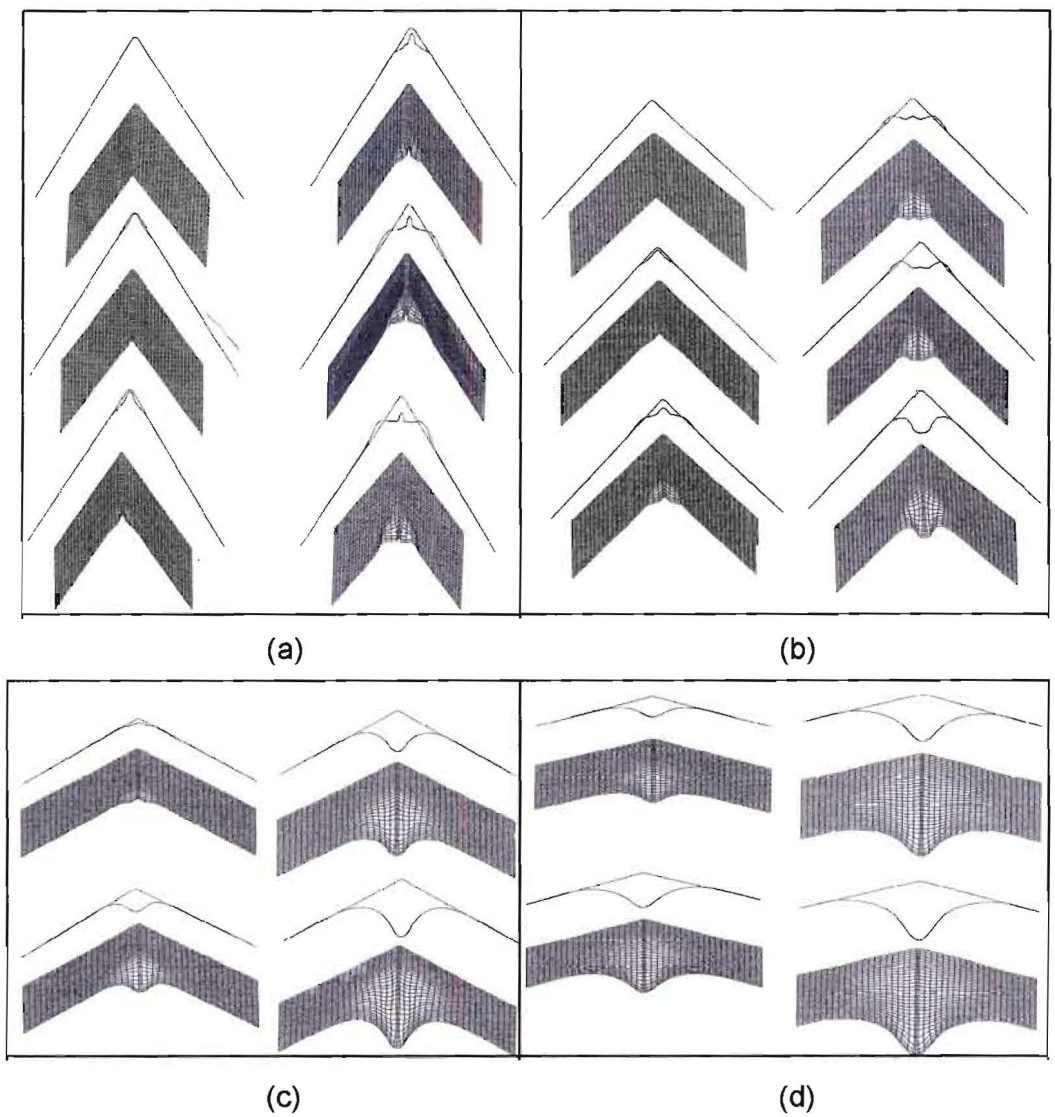

Figure B.1: Pictures of Nannucci's [44] pressure profile method numerically predicted deformed V-plates exploded by PE4 rod explosives with the V-plates grouped together according to the V-plate angles of; (a) 60^0; (b) 90^0; (c) 120^0; (d) 150^0.

9.3 Appendix C: Graphs of JWL Equation of State Method Numerically Predicted Deformed V-Plate Profiles Exploded by PE4 Rod Explosives, Compared with the Corresponding Experimental and Pressure Profile Method Numerically Predicted V-Plate Profiles

9.3.1 Comparison of the Experimental and Numerically Predicted Deformed V-Plate Profiles for the 60^0 V-Plates

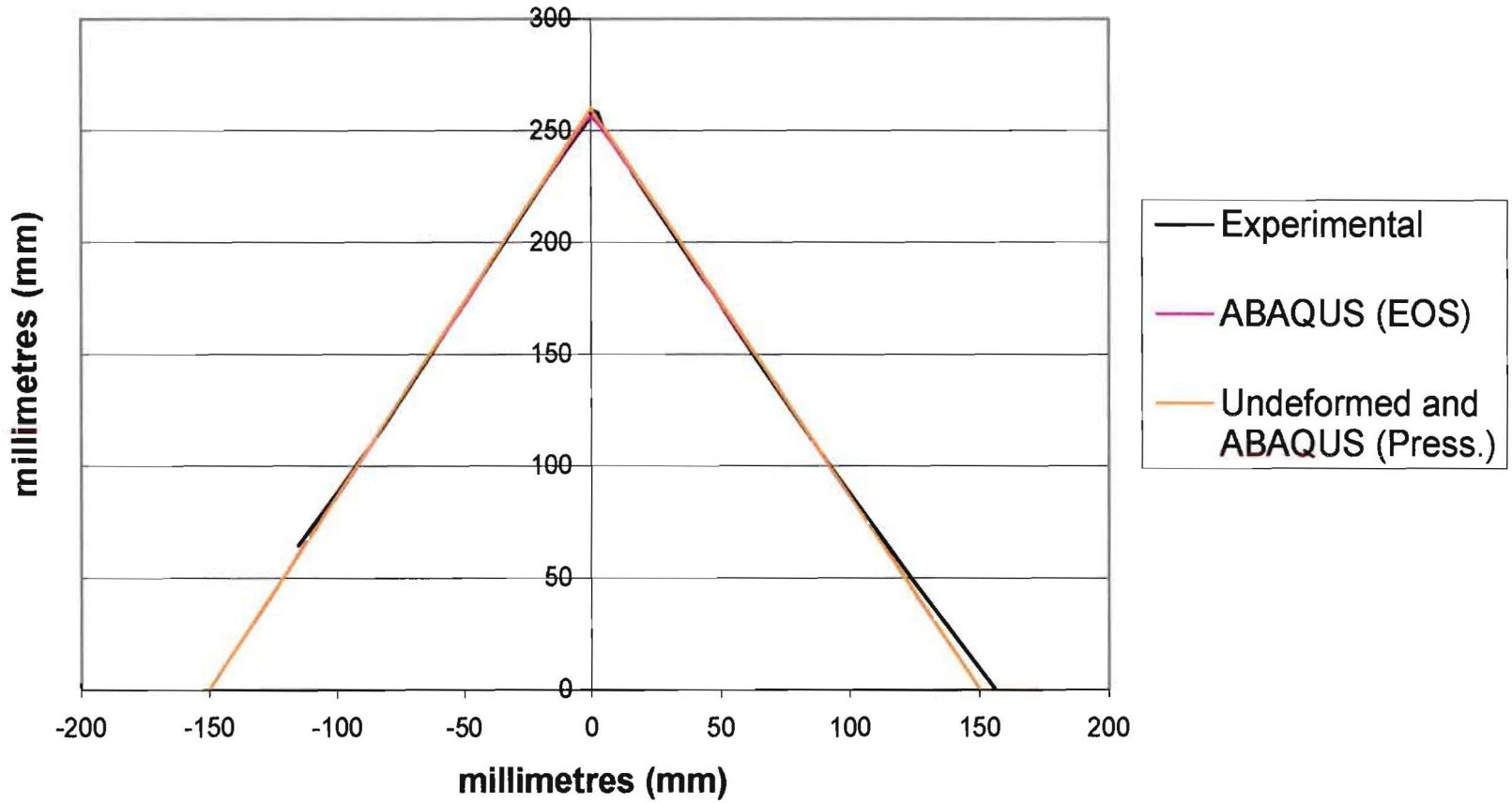

Figure C.1: Comparison of the Experimental Deformed Profile of a V-Plate (60 degrees) Exploded by a PE4 Rod (5g), With the ABAQUS Deformed Profile Obtained Using a Pressure Profile, and With the ABAQUS Deformed Profile Obtained Using the EOS

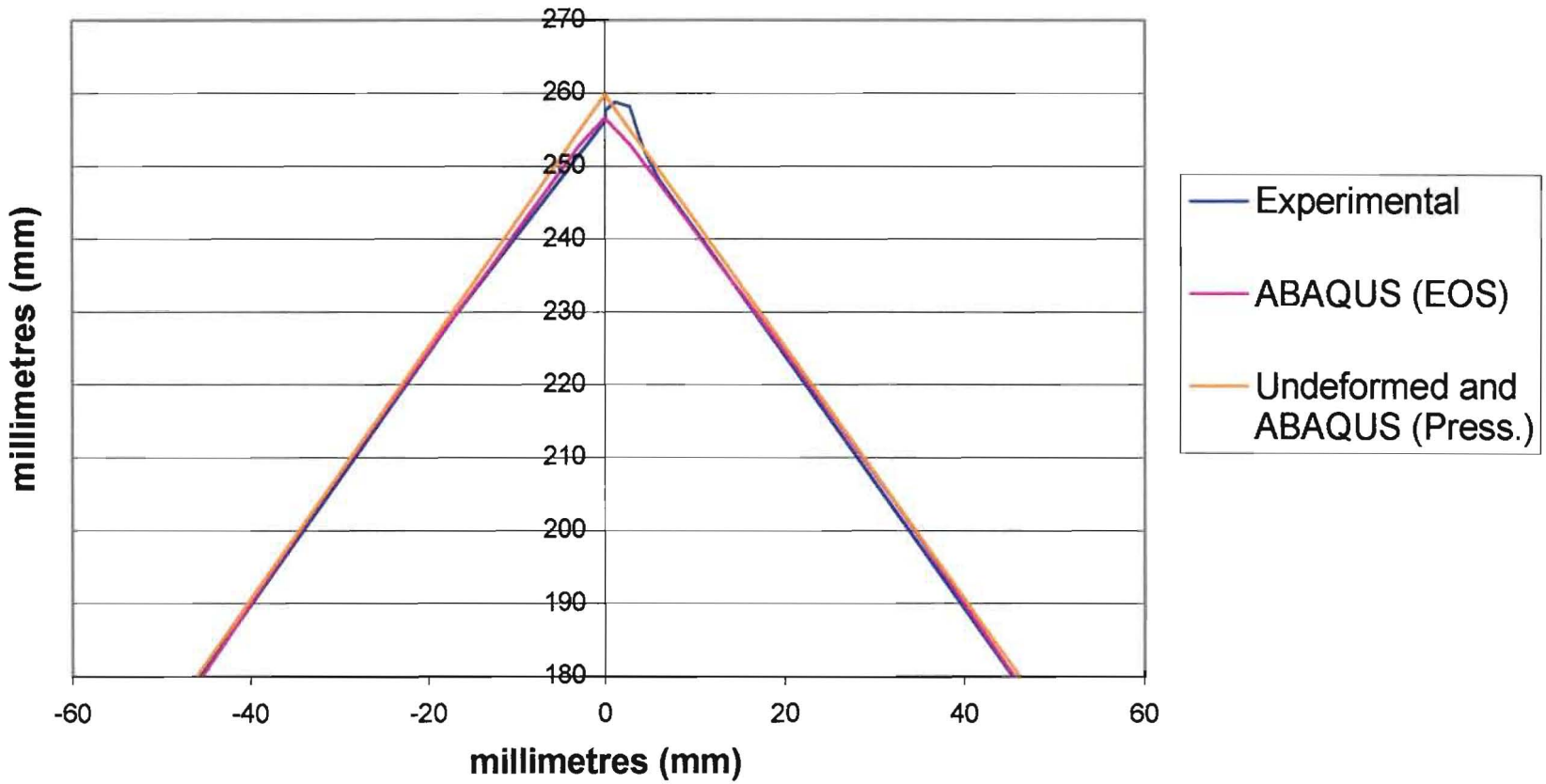

Figure C.2: Comparison of a Magnified Section of the Experimental Deformed Profile of a V-Plate (60 degrees) Exploded by an PE4 Rod (5g), With the ABAQUS Deformed Profile Obtained Using a Pressure Profile, and With the ABAQUS Deformed Profile Obtained Using the EOS

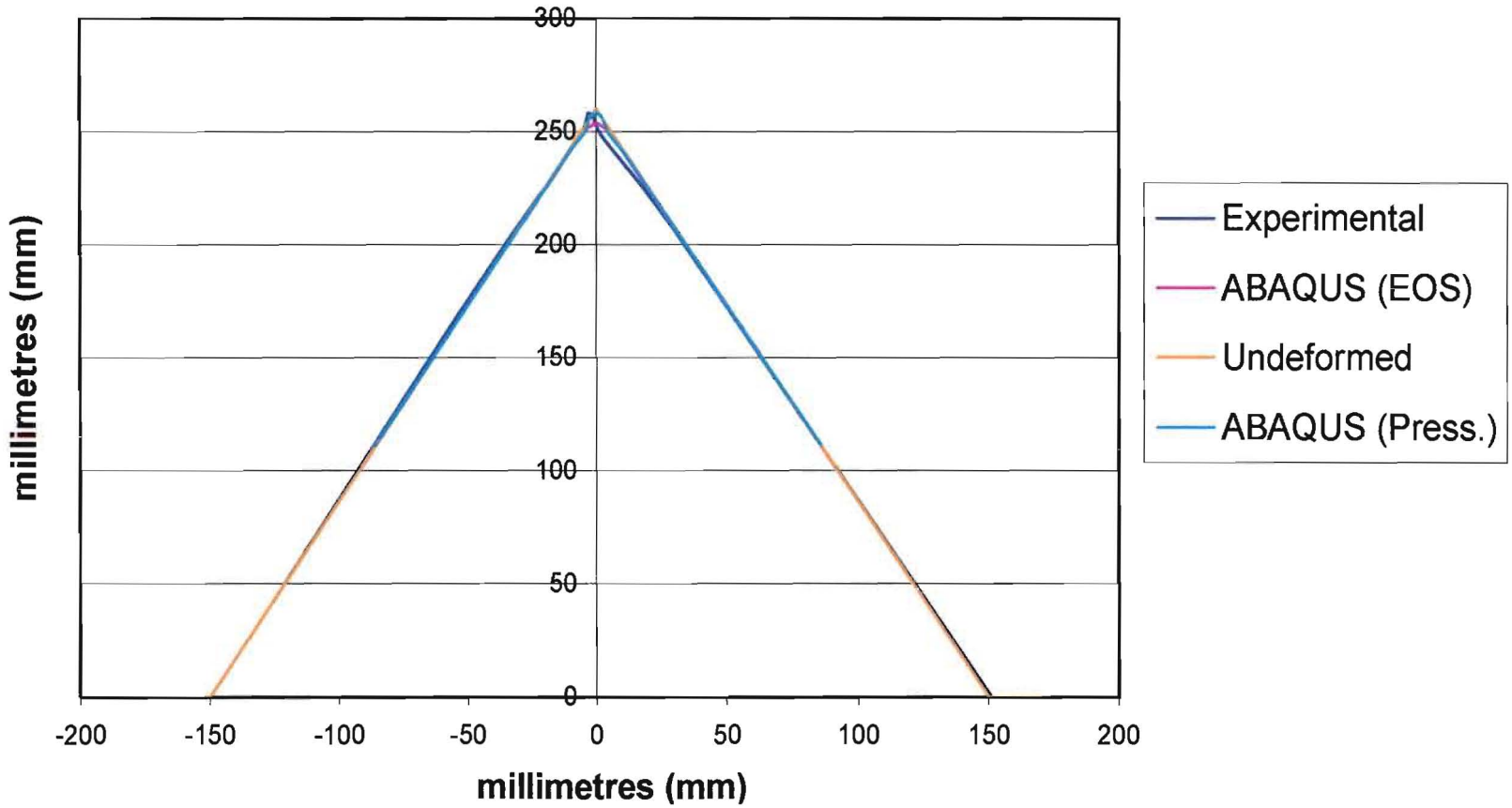

Figure C.3: Comparison of the Experimental Deformed Profile of a V-Plate (60 degrees) Exploded by a PE4 Rod (7g), With the ABAQUS Deformed Profile Obtained Using a Pressure Profile, and With the ABAQUS Deformed Profile Obtained Using the EOS

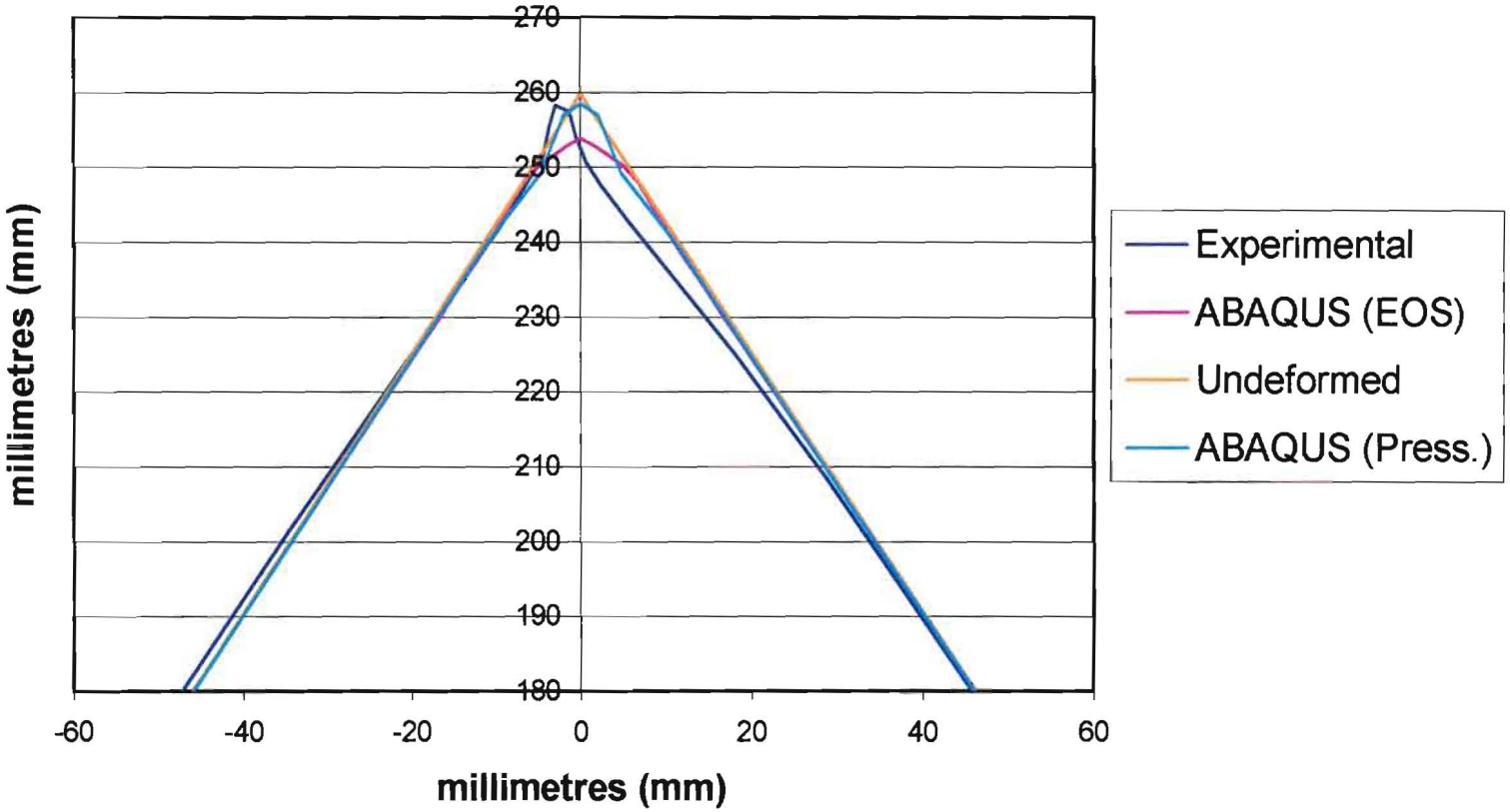

Figure C.4: Comparison of a Magnified Section of the Experimental Deformed Profile of a V-Plate (60 degrees) Exploded by an PE4 Rod (7g), With the ABAQUS Deformed Profile Obtained Using a Pressure Profile, and With the ABAQUS Deformed Profile Obtained Using the EOS

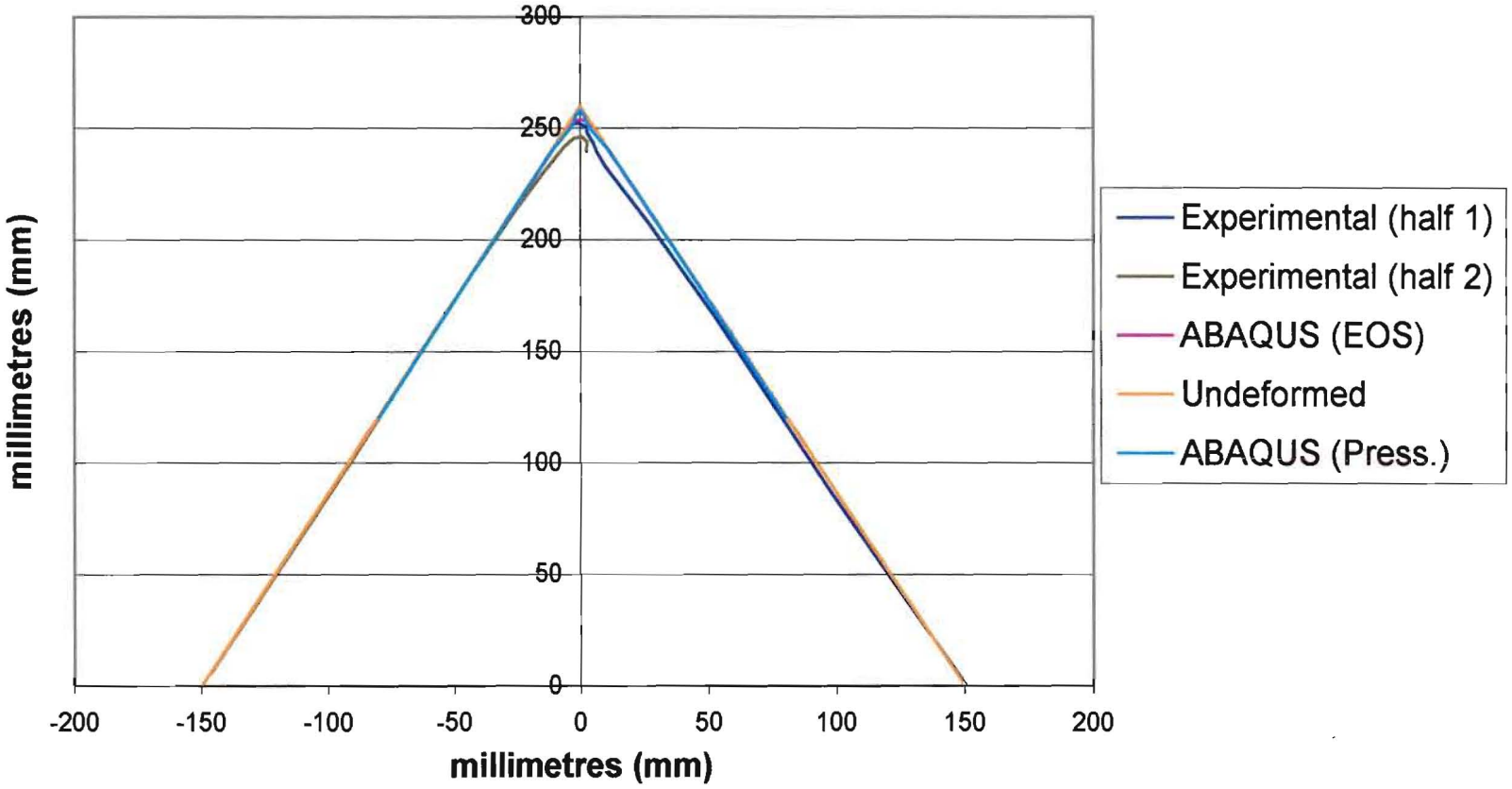

Figure C.5: Comparison of the Experimental Deformed Profile of a V-Plate (60 degrees) Exploded by a PE4 Rod (9g), With the ABAQUS Deformed Profile Obtained Using a Pressure Profile, and With the ABAQUS Deformed Profile Obtained Using the EOS

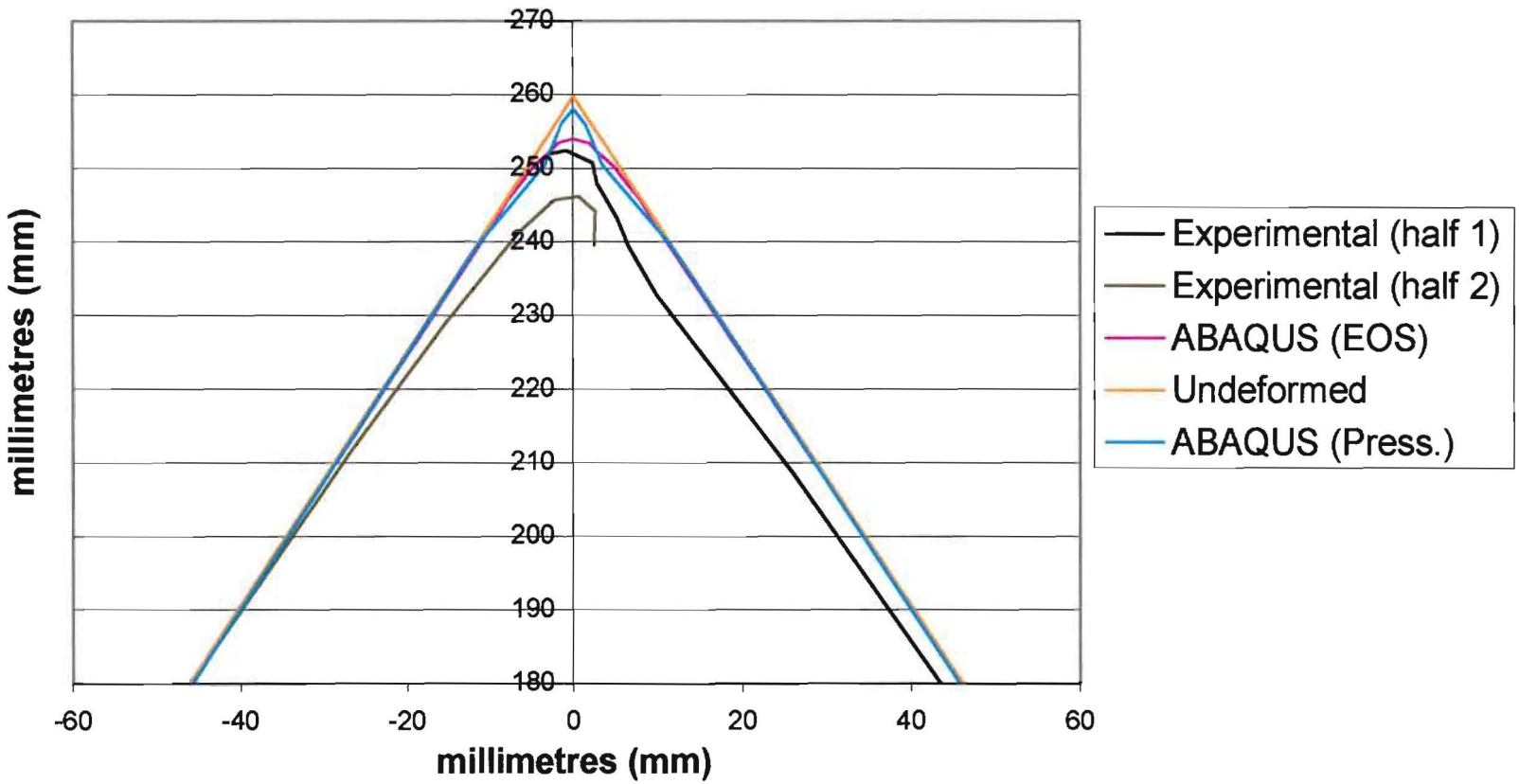

Figure C.6: Comparison of a Magnified Section of the Experimental Deformed Profile of a V-Plate (60 degrees) Exploded by an PE4 Rod (9g), With the ABAQUS Deformed Profile Obtained Using a Pressure Profile, and With the ABAQUS Deformed Profile Obtained Using the EOS

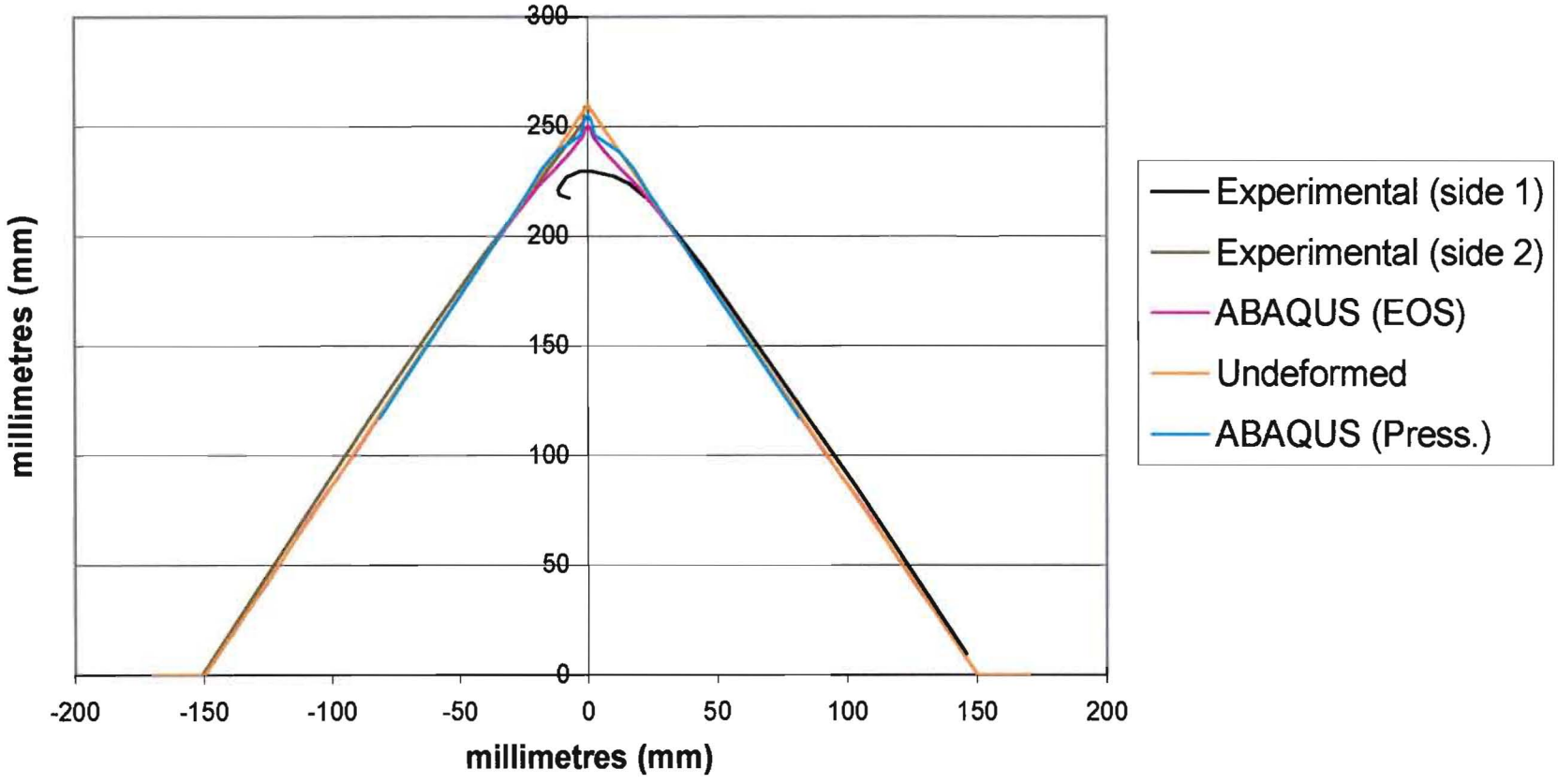

Figure C.7: Comparison of the Experimental Deformed Profile of a V-Plate (60 degrees) Exploded by a PE4 Rod (11g), With the ABAQUS Deformed Profile Obtained Using a Pressure Profile, and With the ABAQUS Deformed Profile Obtained Using the EOS

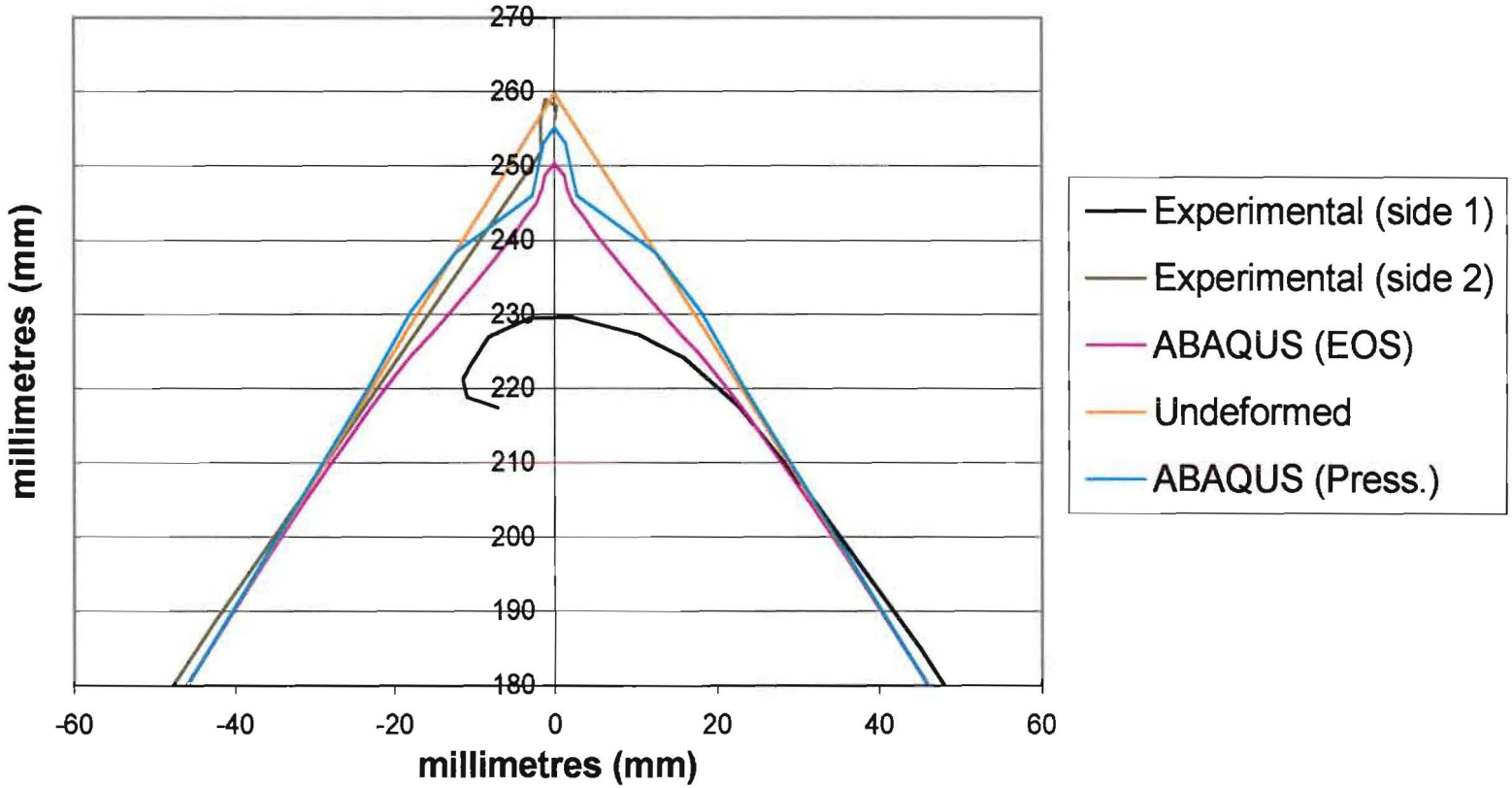

Figure C.8: Comparison of a Magnified Section of the Experimental Deformed Profile of a V-Plate (60 degrees) Exploded by a PE4 Rod (11g), With the ABAQUS Deformed Profile Obtained Using a Pressure Profile, and With the ABAQUS Deformed Profile Obtained Using the EOS

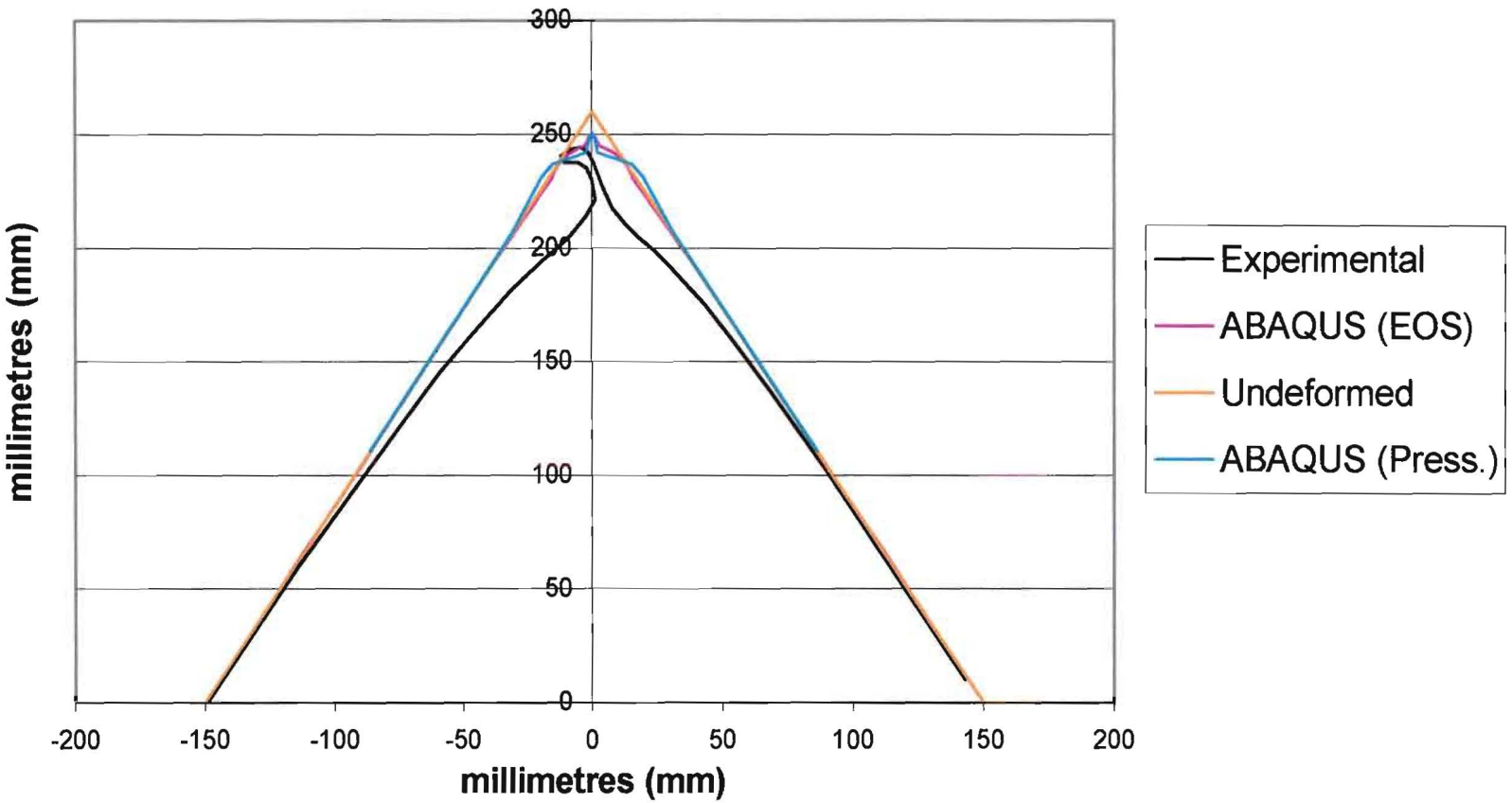

Figure C.9: Comparison of the Experimental Deformed Profile of a V-Plate (60 degrees) Exploded by a PE4 Rod (13g), With the ABAQUS Deformed Profile Obtained Using a Pressure Profile, and With the ABAQUS Deformed Profile Obtained Using the EOS

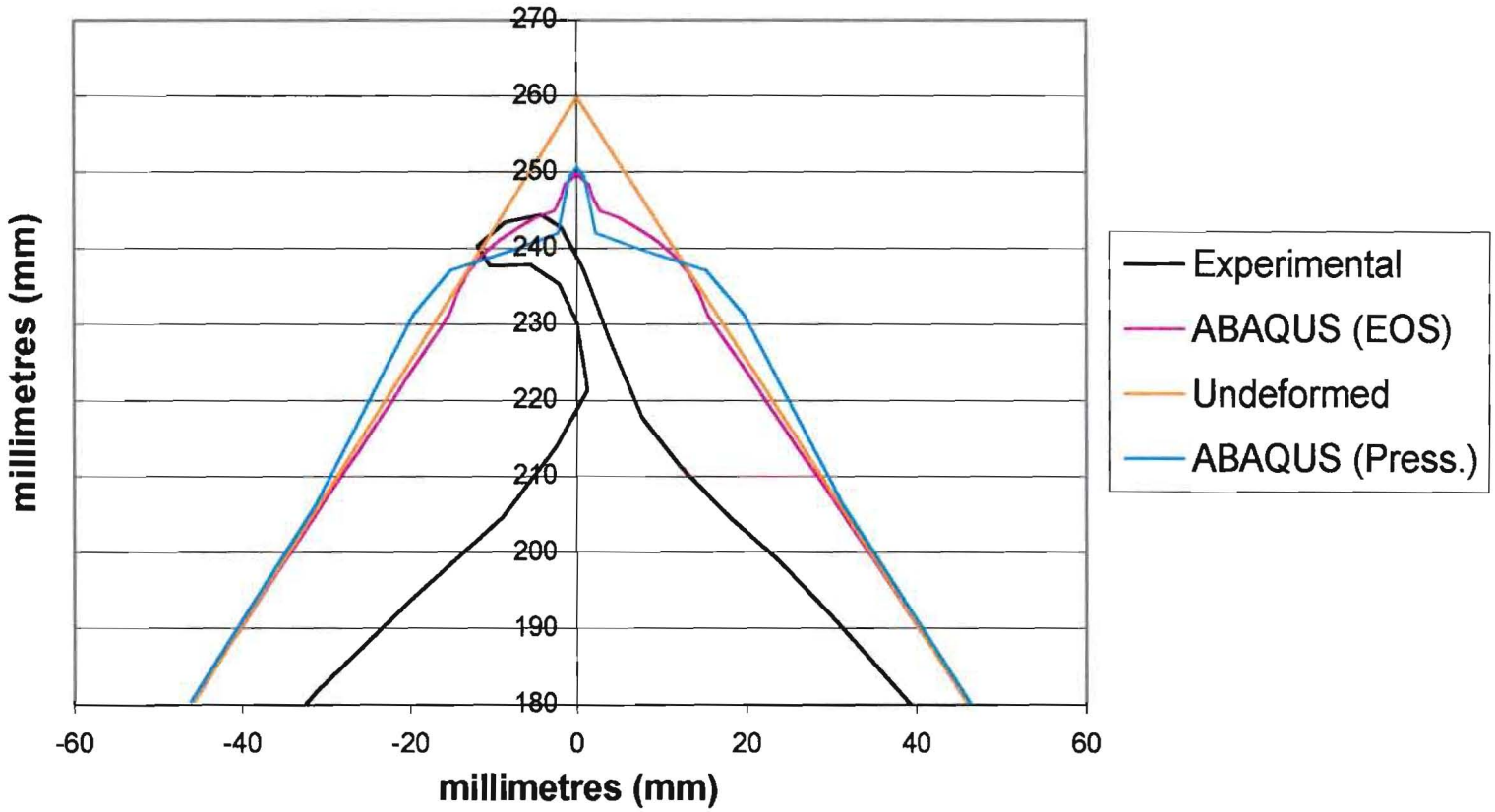

Figure C.10: Comparison of a Magnified Section of the Experimental Deformed Profile of a V-Plate (60 degrees) Exploded by a PE4 Rod (13g), With the ABAQUS Deformed Profile Obtained Using a Pressure Profile, and With the ABAQUS Deformed Profile Obtained Using the EOS

9.3.2 Comparison of the Experimental and Numerically Predicted Deformed V-Plate Profiles for the 90^0 V-Plates

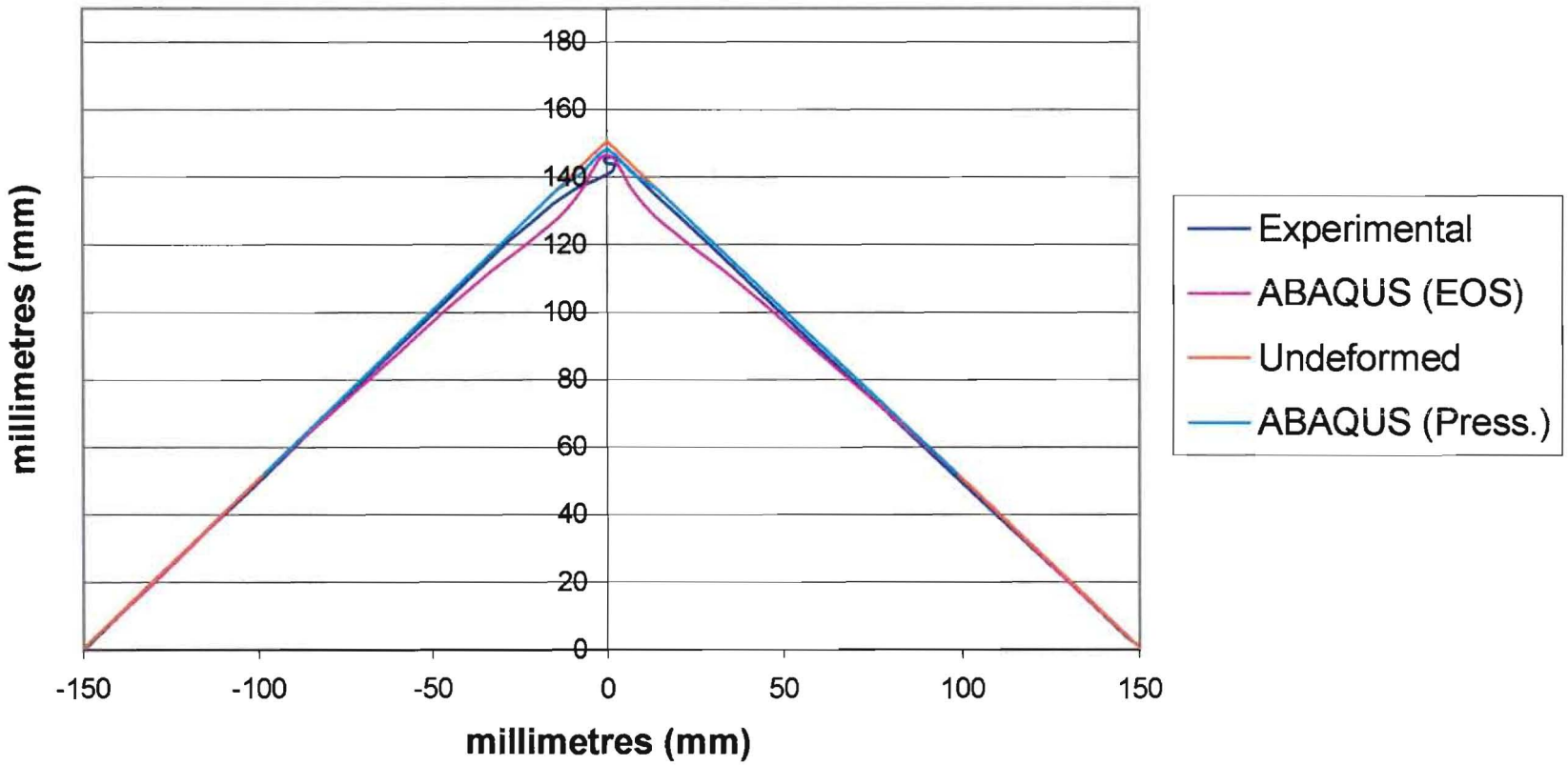

Figure C.11: Comparison of the Experimental Deformed Profile of a V-Plate (90 degrees) Exploded by a PE4 Rod (5g), With the ABAQUS Deformed Profile Obtained Using a Pressure Profile, and With the ABAQUS Deformed Profile Obtained Using the EOS

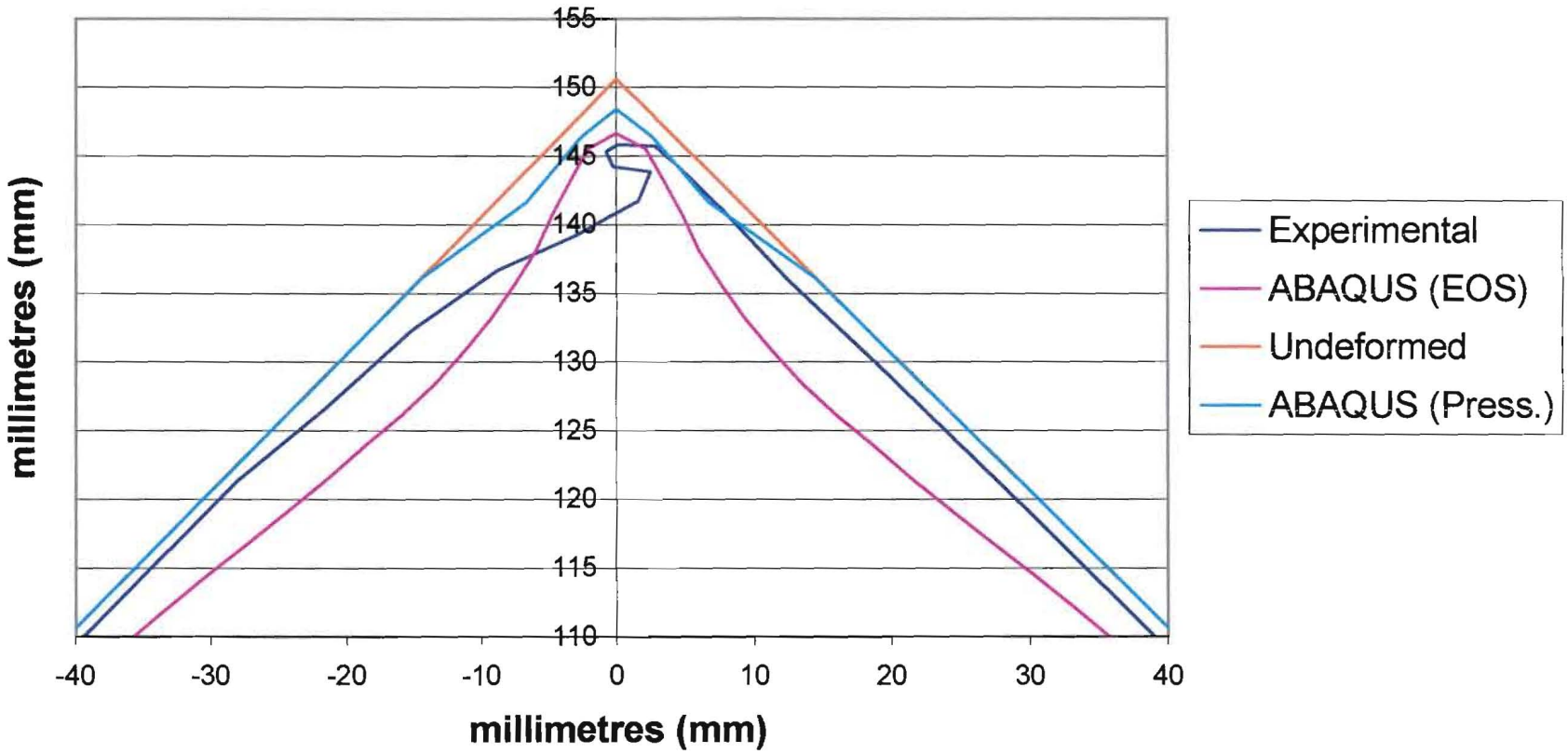

Figure C.12: Comparison of a Magnified Section of the Experimental Deformed Profile of a V-Plate (90 degrees) Exploded by a PE4 Rod (5g), With the ABAQUS Deformed Profile Obtained Using a Pressure Profile, and With the ABAQUS Deformed Profile Obtained Using the EOS

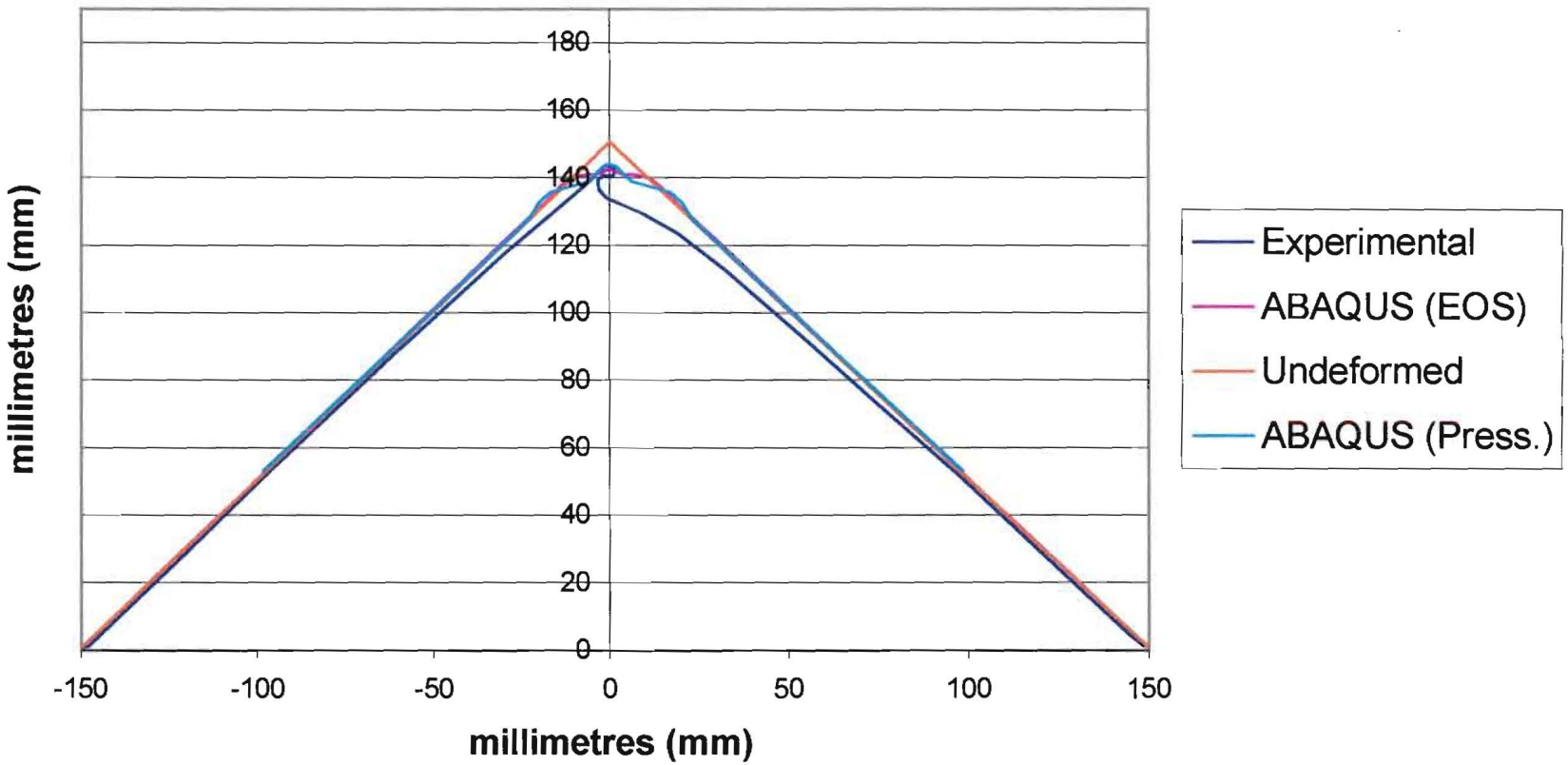

Figure C.13: Comparison of the Experimental Deformed Profile of a V-Plate (90 degrees) Exploded by a PE4 Rod (7g), With the ABAQUS Deformed Profile Obtained Using a Pressure Profile, and With the ABAQUS Deformed Profile Obtained Using the EOS

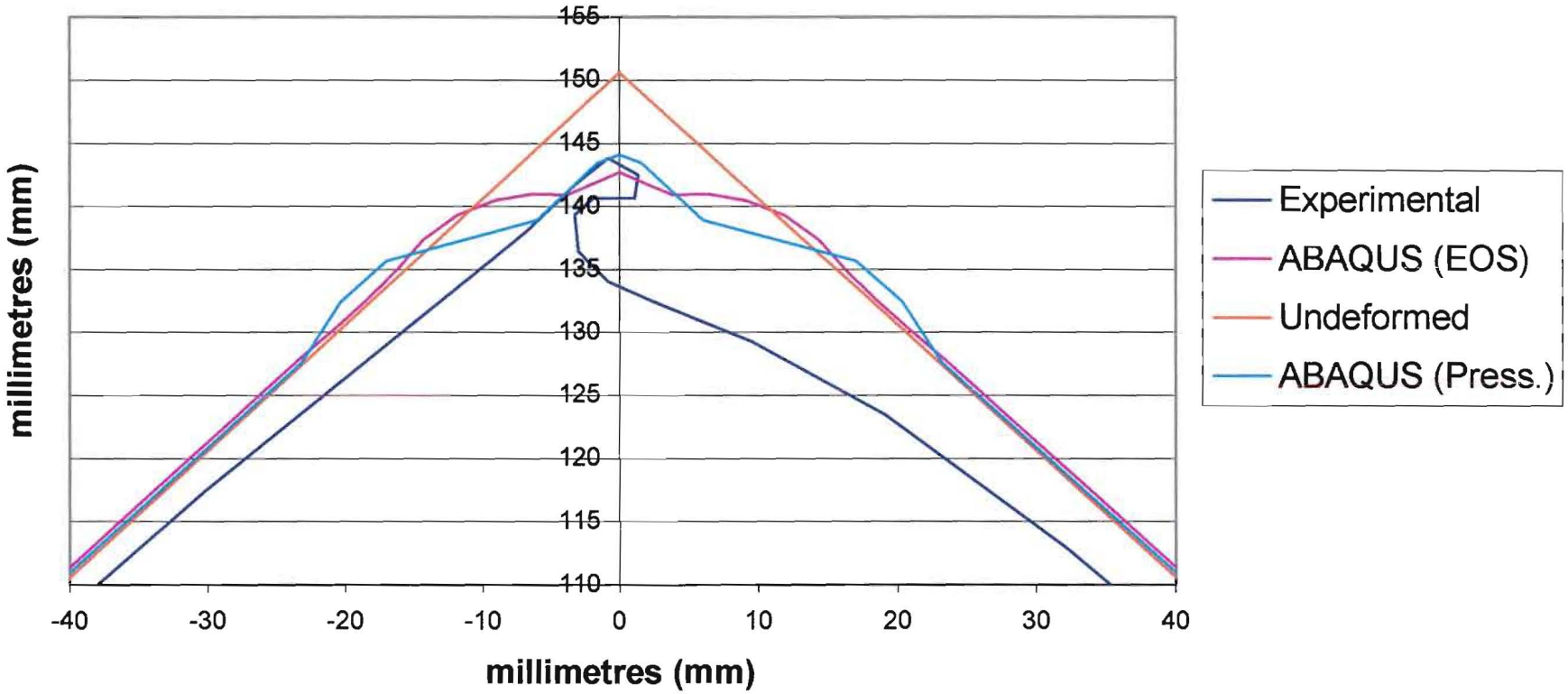

Figure C.14: Comparison of a Magnified Section of the Experimental Deformed Profile of a V-Plate (90 degrees) Exploded by a PE4 Rod (7g), With the ABAQUS Deformed Profile Obtained Using a Pressure Profile, and With the ABAQUS Deformed Profile Obtained Using the EOS

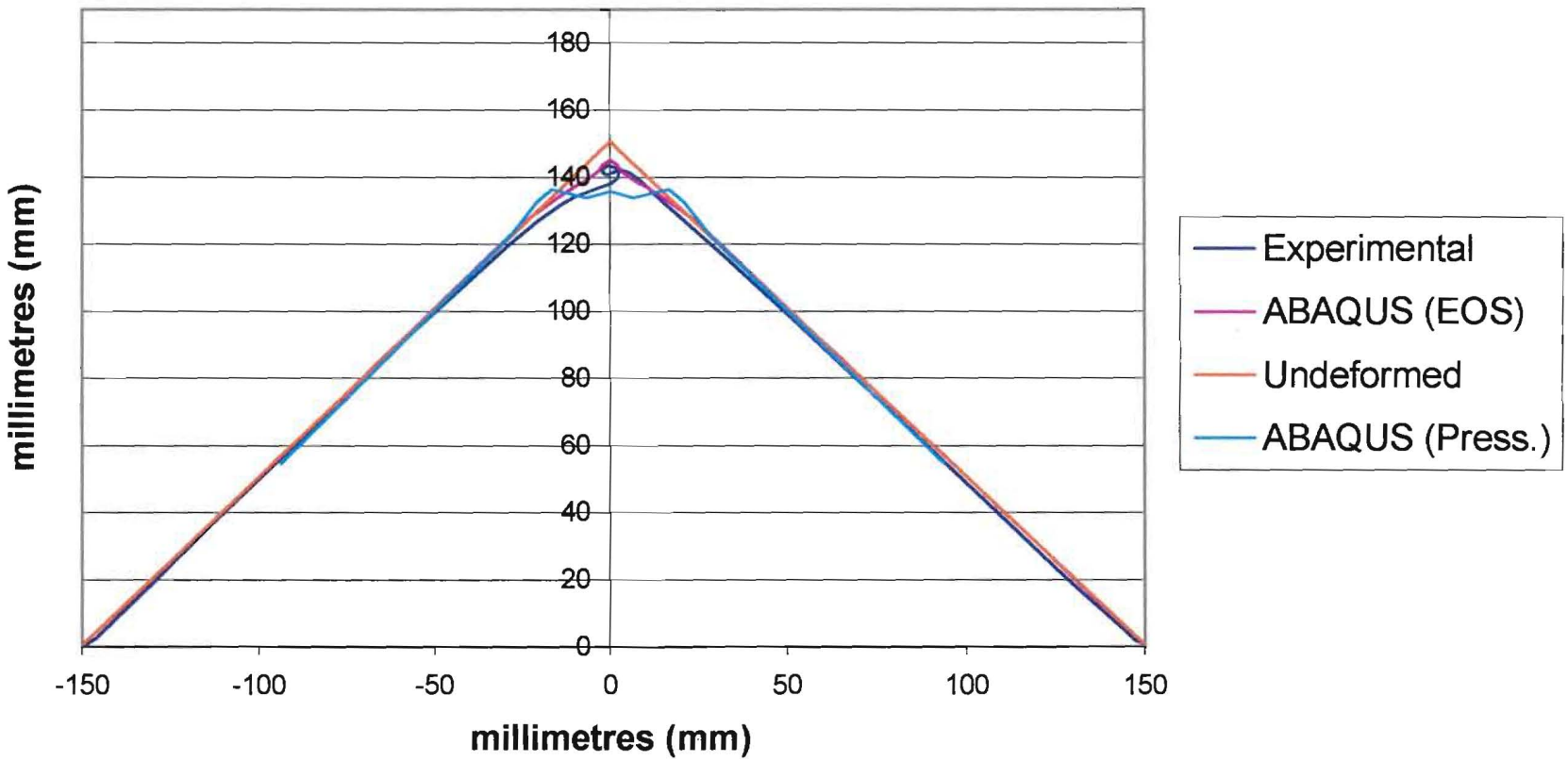

Figure C.15: Comparison of the Experimental Deformed Profile of a V-Plate (90 degrees) Exploded by a PE4 Rod (9g), With the ABAQUS Deformed Profile Obtained Using a Pressure Profile, and With the ABAQUS Deformed Profile Obtained Using the EOS

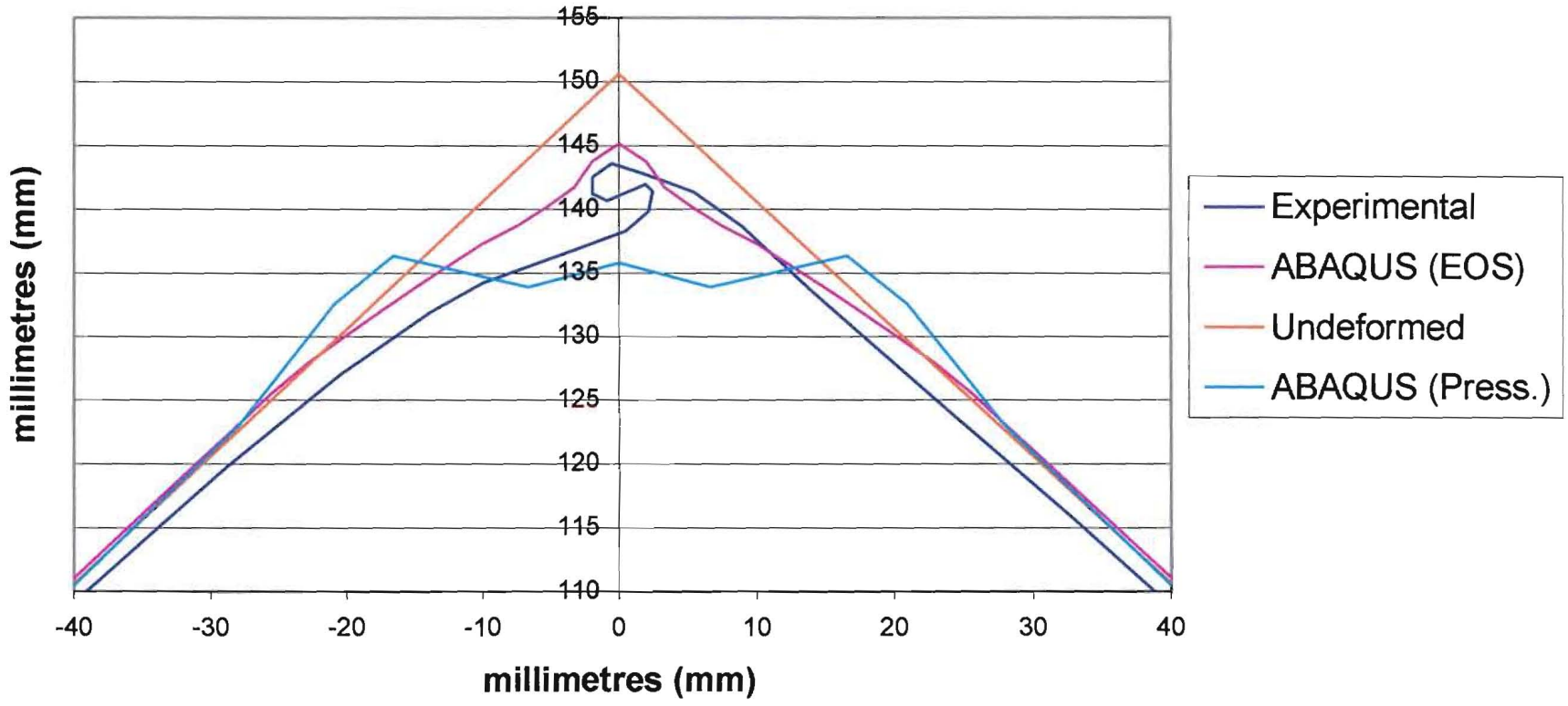

Figure C.16: Comparison of a Magnified Section of the Experimental Deformed Profile of a V-Plate (90 degrees) Exploded by a PE4 Rod (9g), With the ABAQUS Deformed Profile Obtained Using a Pressure Profile, and With the ABAQUS Deformed Profile Obtained Using the EOS

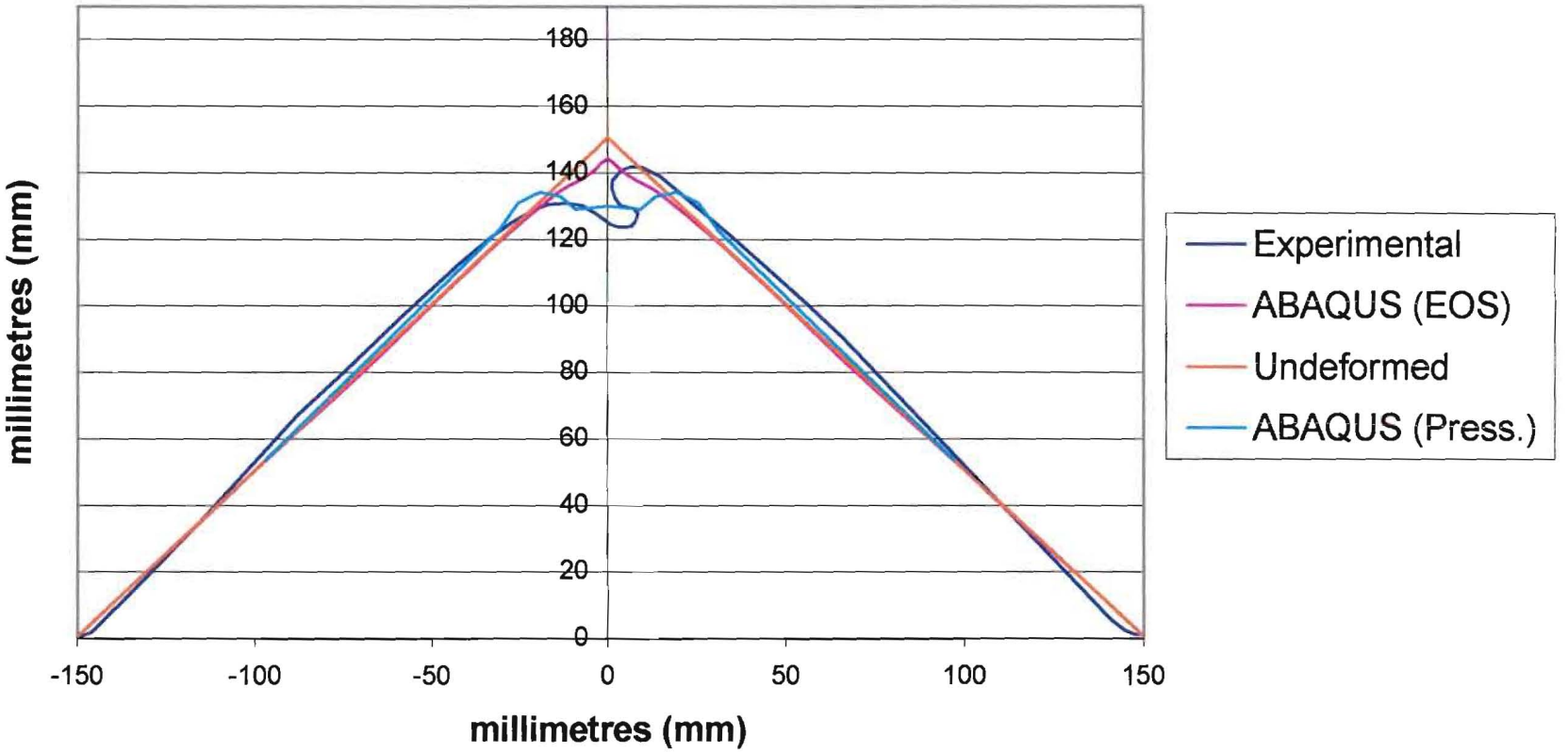

Figure C.17: Comparison of the Experimental Deformed Profile of a V-Plate (90 degrees) Exploded by a PE4 Rod (11g), With the ABAQUS Deformed Profile Obtained Using a Pressure Profile, and With the ABAQUS Deformed Profile Obtained Using the EOS

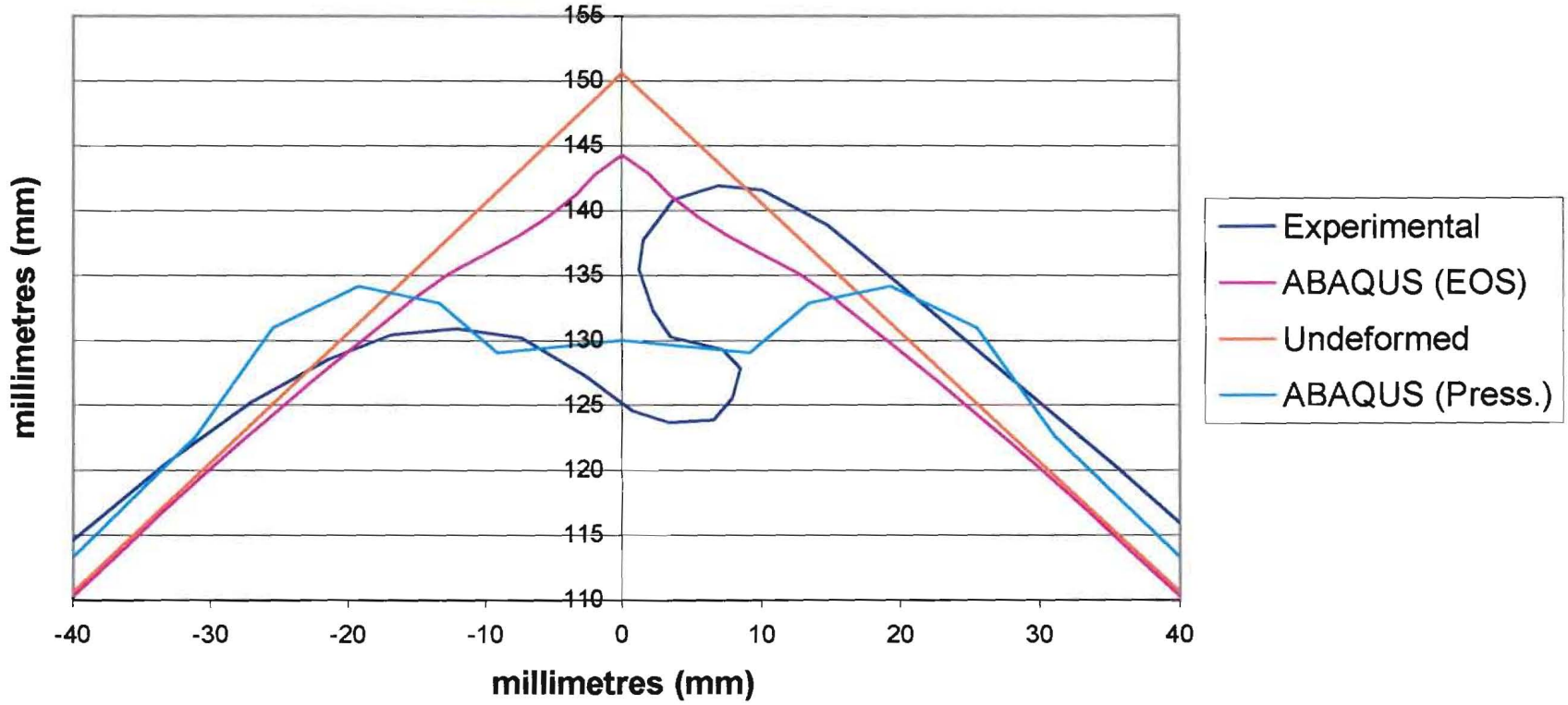

Figure C.18: Comparison of a Magnified Section of the Experimental Deformed Profile of a V-Plate (90 degrees) Exploded by a PE4 Rod (11g), With the ABAQUS Deformed Profile Obtained Using a Pressure Profile, and With the ABAQUS Deformed Profile Obtained Using the EOS

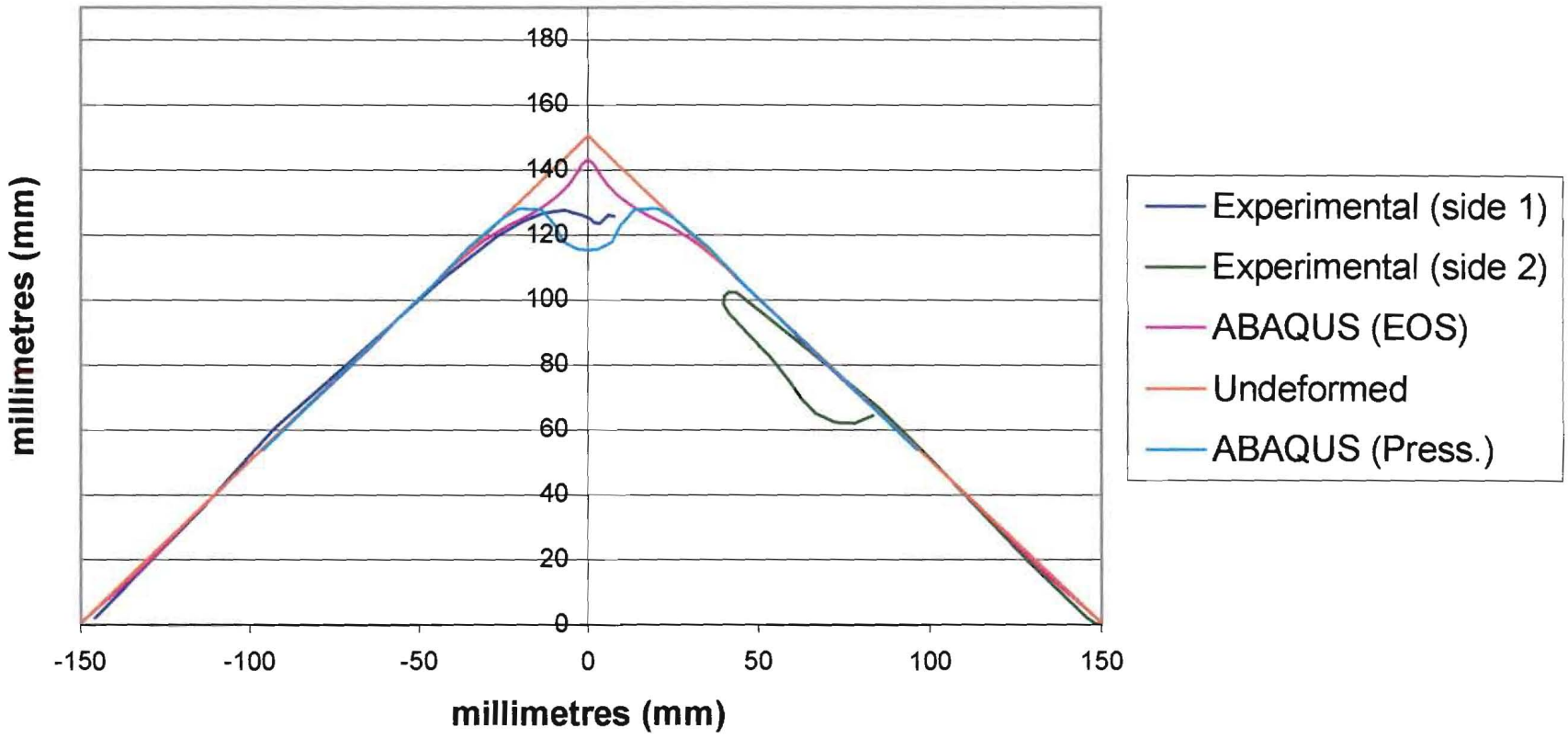

Figure C.19: Comparison of the Experimental Deformed Profile of a V-Plate (90 degrees) Exploded by a PE4 Rod (13g), With the ABAQUS Deformed Profile Obtained Using a Pressure Profile, and With the ABAQUS Deformed Profile Obtained Using the EOS

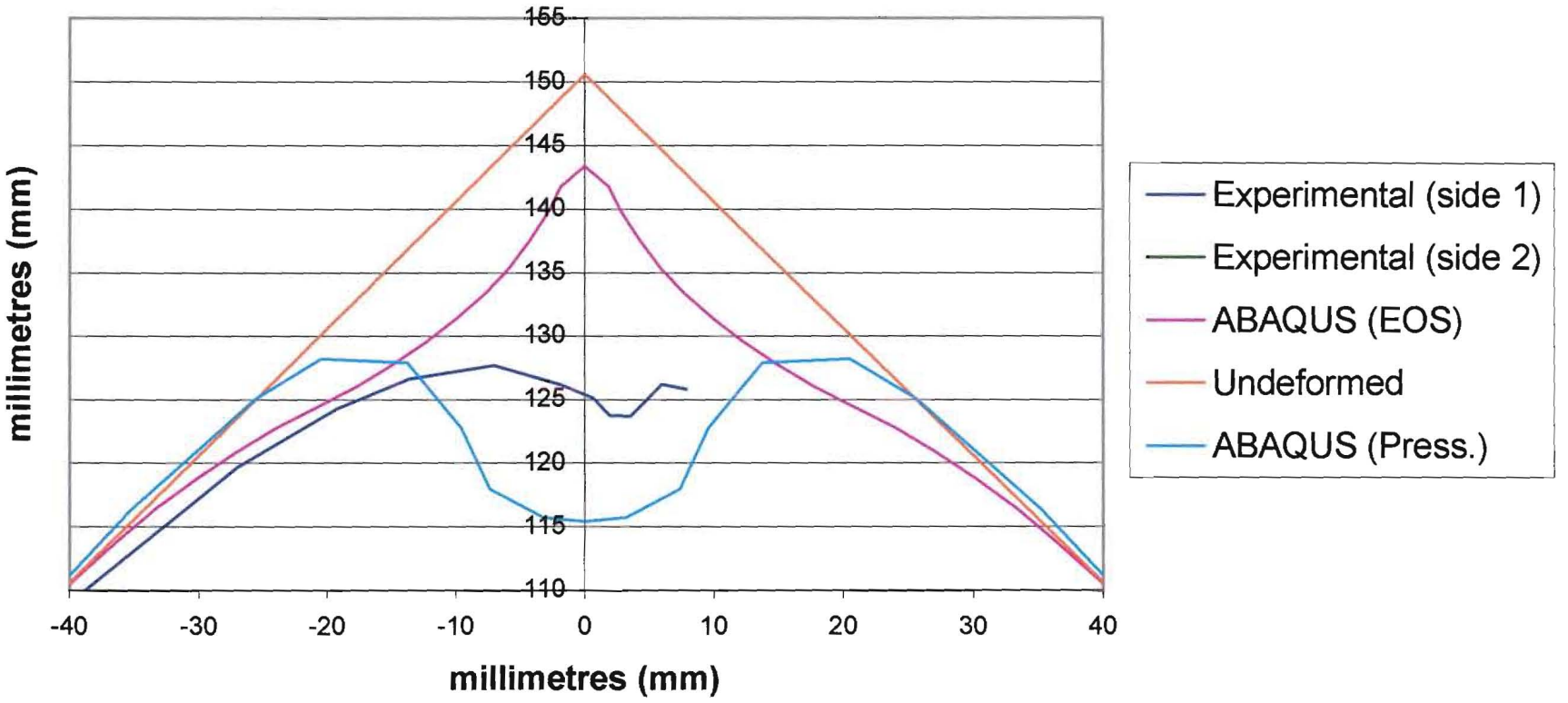

Figure C.20: Comparison of a Magnified Section of the Experimental Deformed Profile of a V-Plate (90 degrees) Exploded by a PE4 Rod (13g), With the ABAQUS Deformed Profile Obtained Using a Pressure Profile, and With the ABAQUS Deformed Profile Obtained Using the EOS

9.3.3 Comparison of the Experimental and Numerically Predicted Deformed V-Plate Profiles for the 120^0 V-Plates

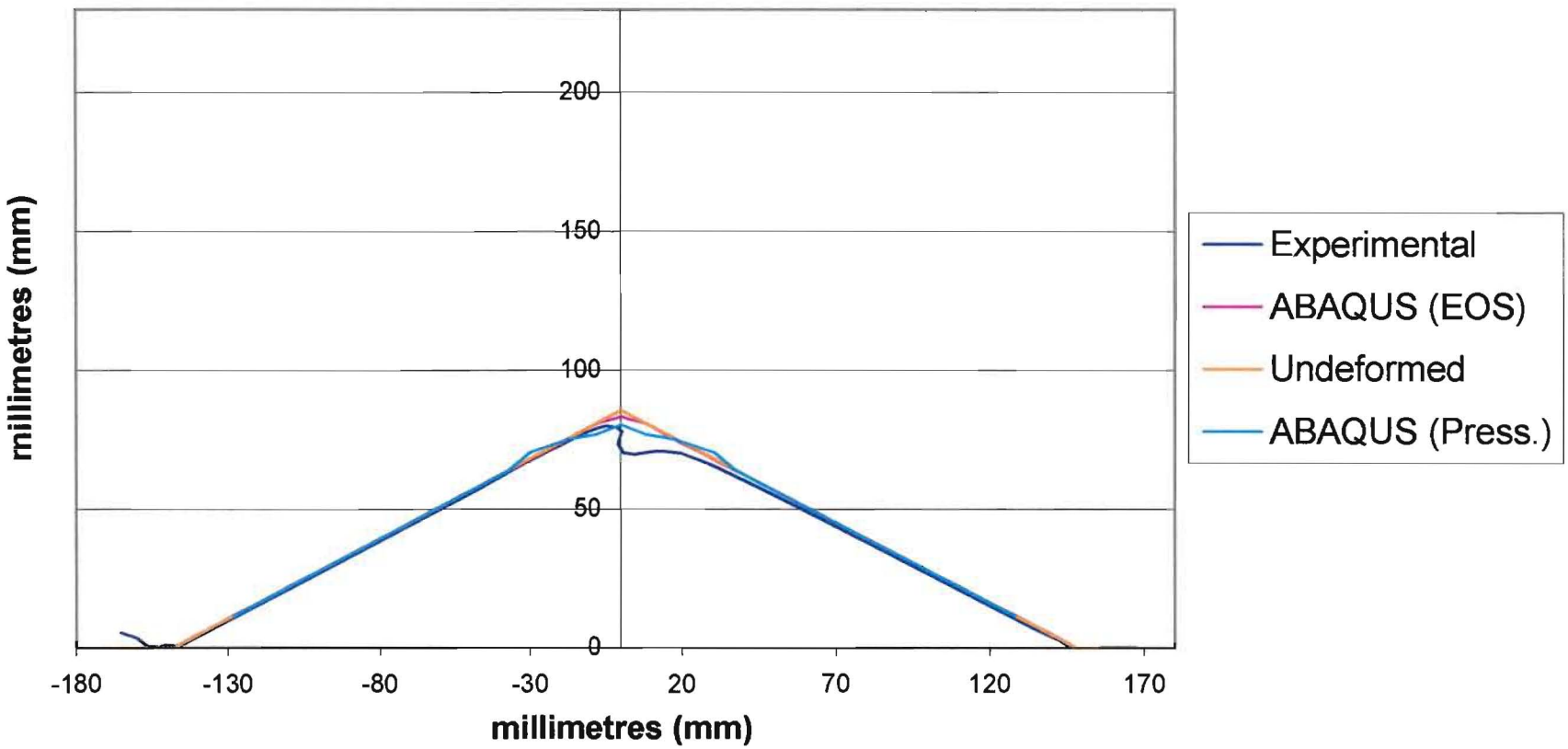

Figure C.21: Comparison of the Experimental Deformed Profile of a V-Plate (120 degrees) Exploded by a PE4 Rod (3g), With the ABAQUS Deformed Profile Obtained Using a Pressure Profile, and With the ABAQUS Deformed Profile Obtained Using the EOS

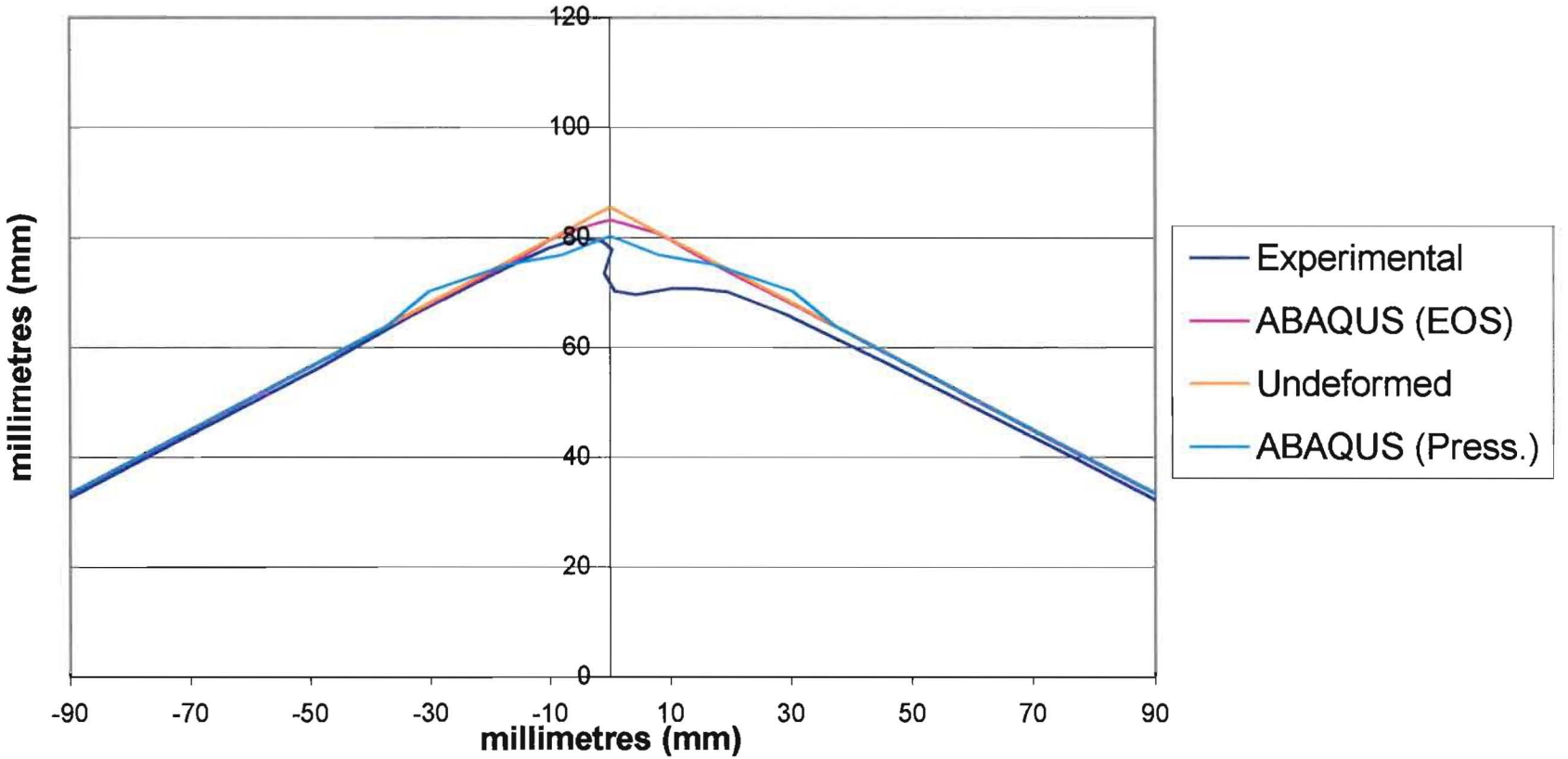

Figure C.22: Comparison of a Magnified Section of the Experimental Deformed Profile of a V-Plate (120 degrees) Exploded by a PE4 Rod (3g), With the ABAQUS Deformed Profile Obtained Using a Pressure Profile, and With the ABAQUS Deformed Profile Obtained Using the EOS

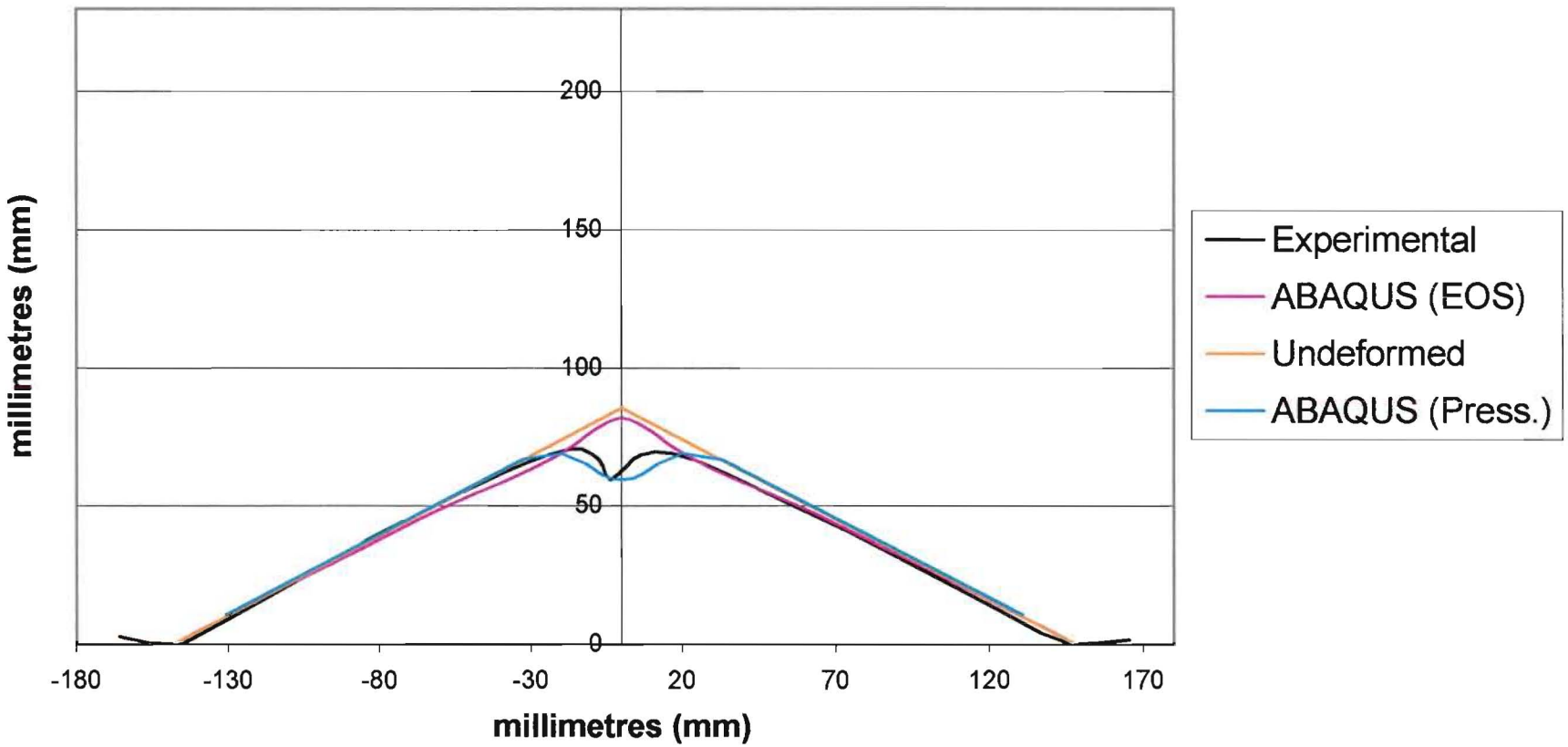

Figure C.23: Comparison of the Experimental Deformed Profile of a V-Plate (120 degrees) Exploded by a PE4 Rod (5g), With the ABAQUS Deformed Profile Obtained Using a Pressure Profile, and With the ABAQUS Deformed Profile Obtained Using the EOS

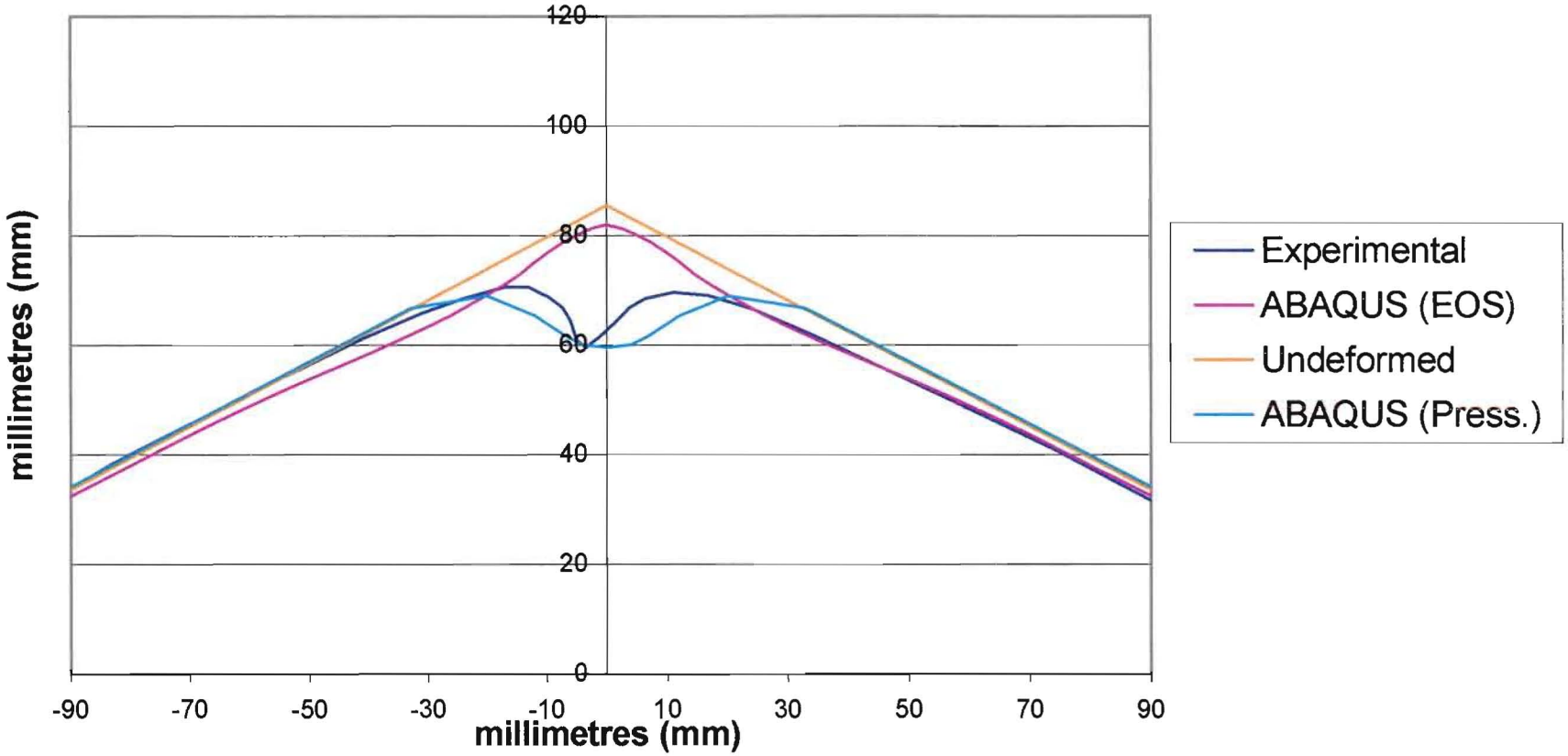

Figure C.24: Comparison of a Magnified Section of the Experimental Deformed Profile of a V-Plate (120 degrees) Exploded by a PE4 Rod (5g), With the ABAQUS Deformed Profile Obtained Using a Pressure Profile, and With the ABAQUS Deformed Profile Obtained Using the EOS

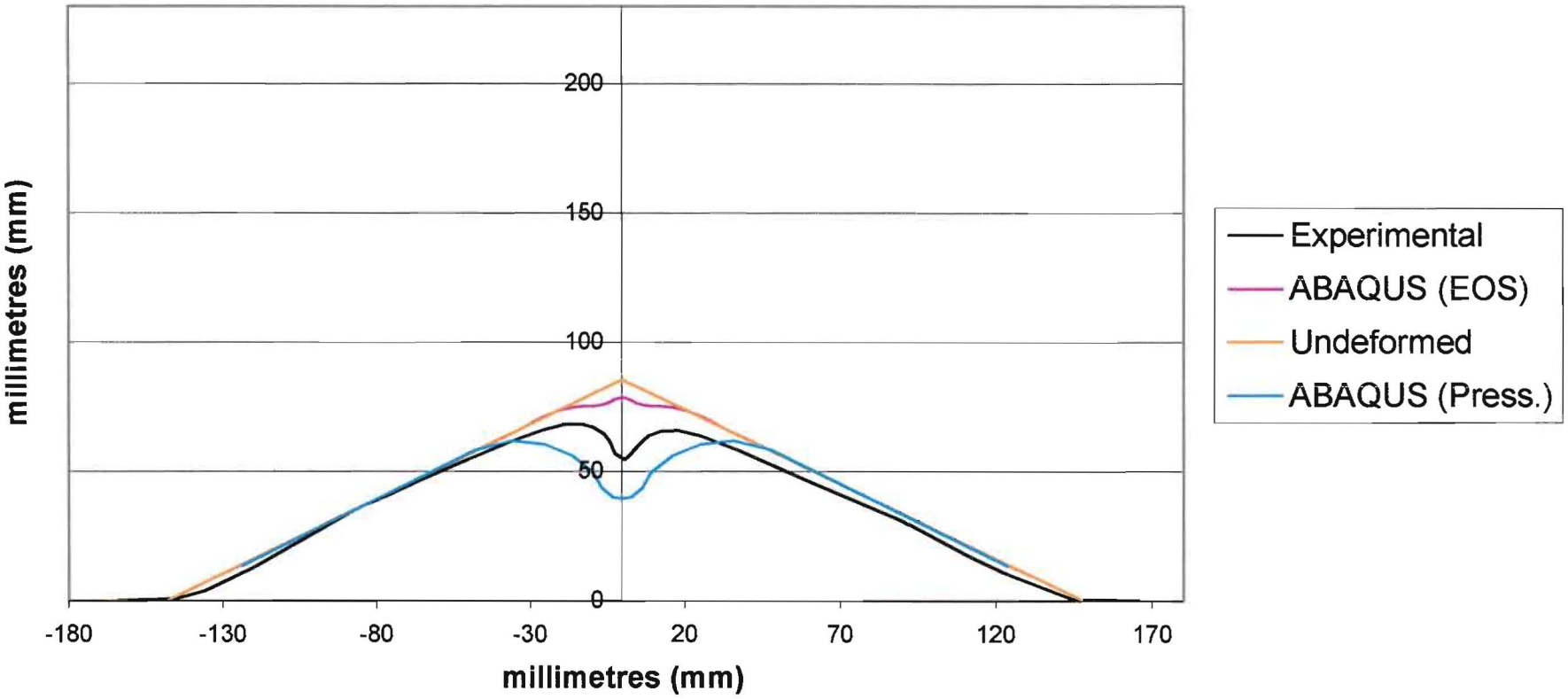

Figure C.25: Comparison of the Experimental Deformed Profile of a V-Plate (120 degrees) Exploded by a PE4 Rod (7g), With the ABAQUS Deformed Profile Obtained Using a Pressure Profile, and With the ABAQUS Deformed Profile Obtained Using the EOS

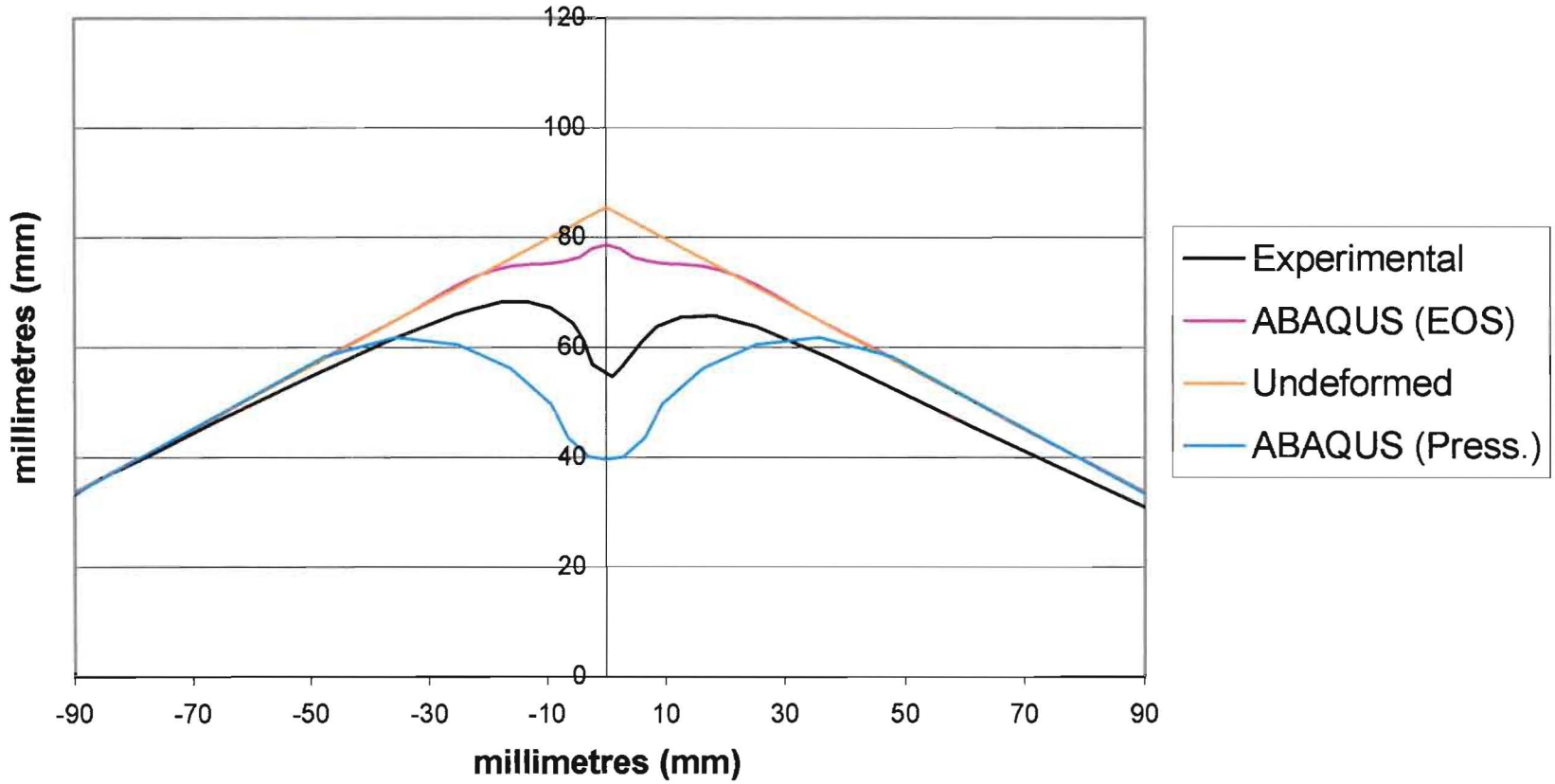

Figure C.26: Comparison of a Magnified Section of the Experimental Deformed Profile of a V-Plate (120 degrees) Exploded by a PE4 Rod (7g), With the ABAQUS Deformed Profile Obtained Using a Pressure Profile, and With the ABAQUS Deformed Profile Obtained Using the EOS

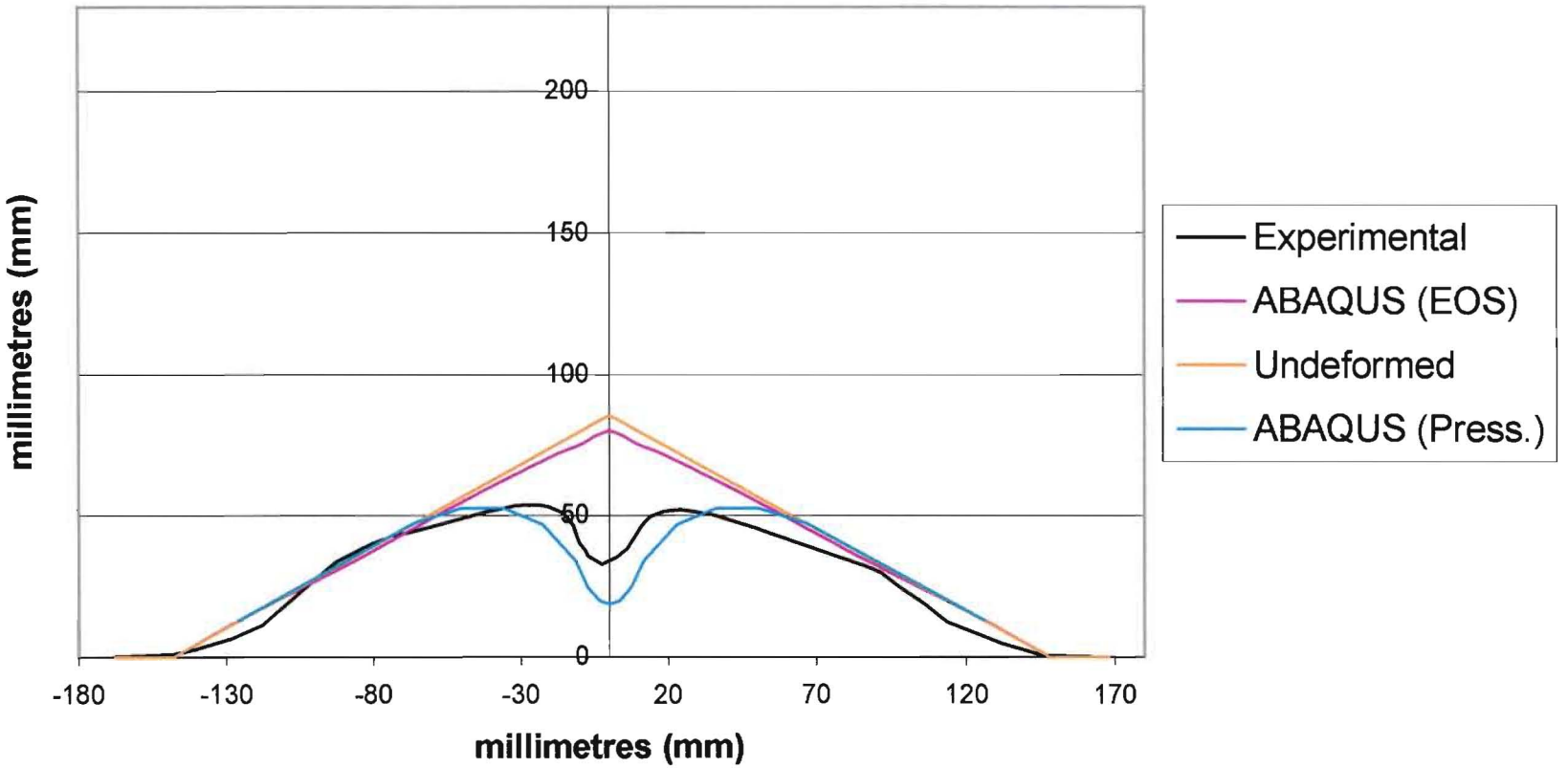

Figure C.27: Comparison of the Experimental Deformed Profile of a V-Plate (120 degrees) Exploded by a PE4 Rod (9g), With the ABAQUS Deformed Profile Obtained Using a Pressure Profile, and With the ABAQUS Deformed Profile Obtained Using the EOS

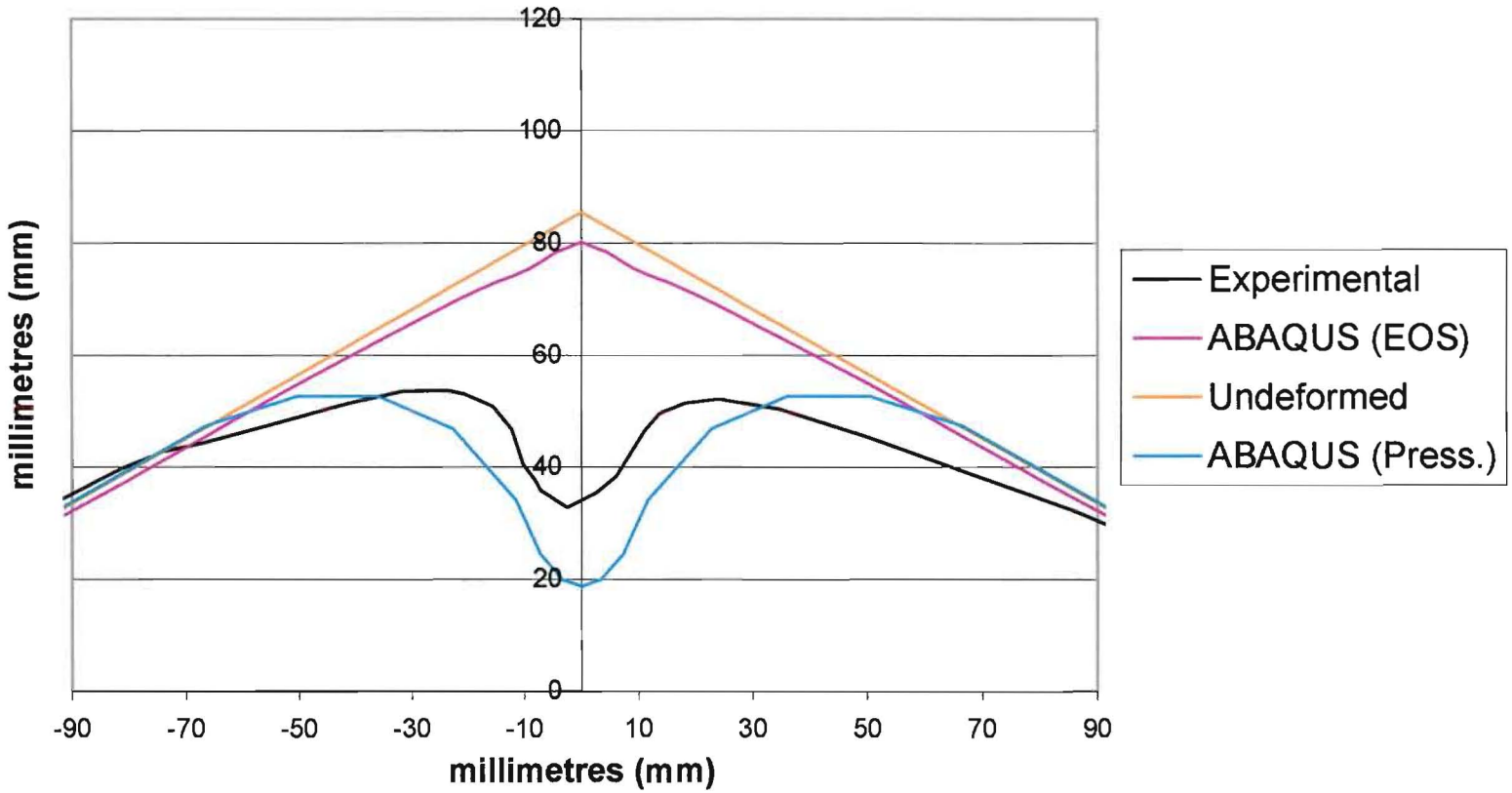

Figure C.28: Comparison of a Magnified Section of the Experimental Deformed Profile of a V-Plate (120 degrees) Exploded by a PE4 Rod (9g), With the ABAQUS Deformed Profile Obtained Using a Pressure Profile, and With the ABAQUS Deformed Profile Obtained Using the EOS

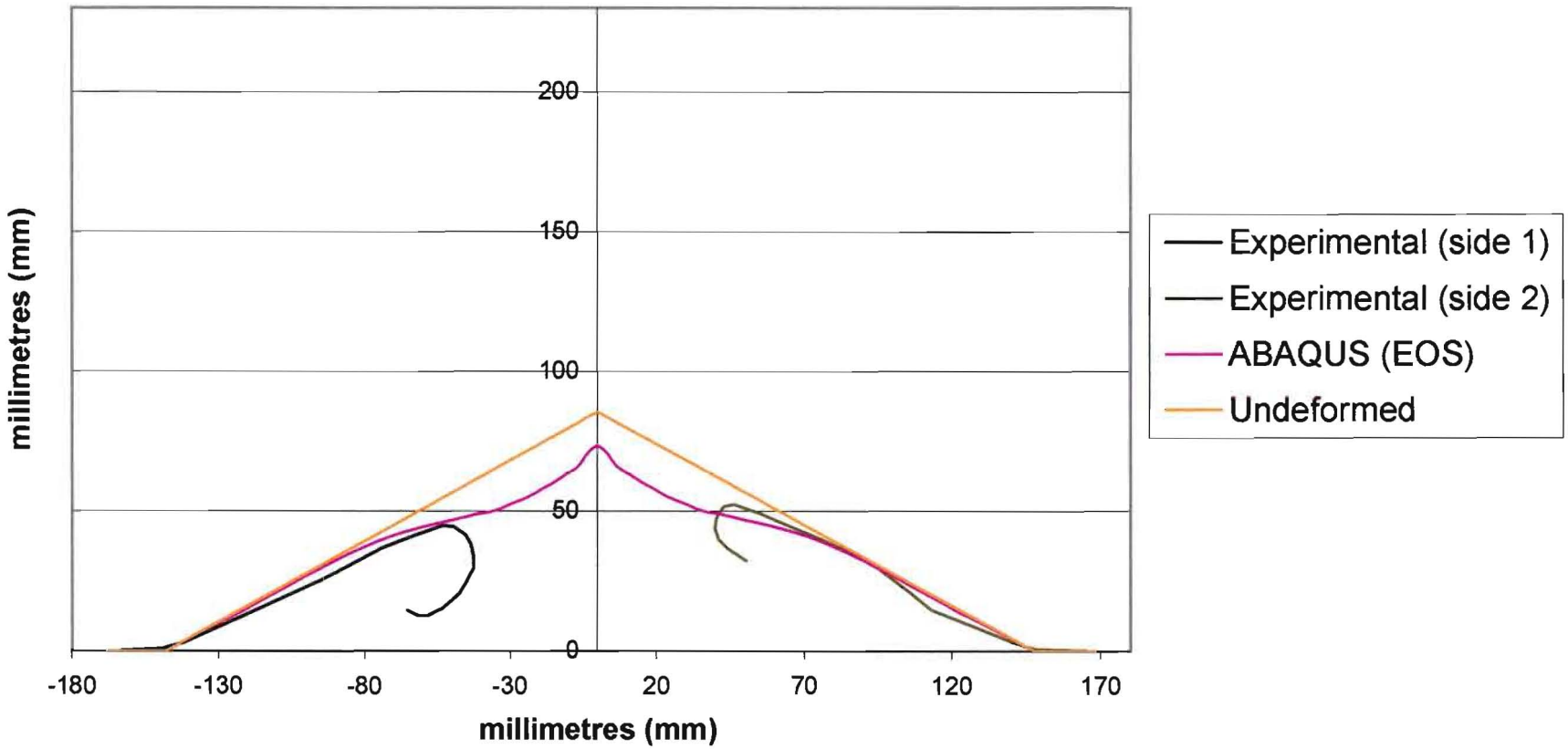

Figure C.29: Comparison of the Experimental Deformed Profile of a V-Plate (120 degrees) Exploded by a PE4 Rod (11g), with the ABAQUS Deformed Profile

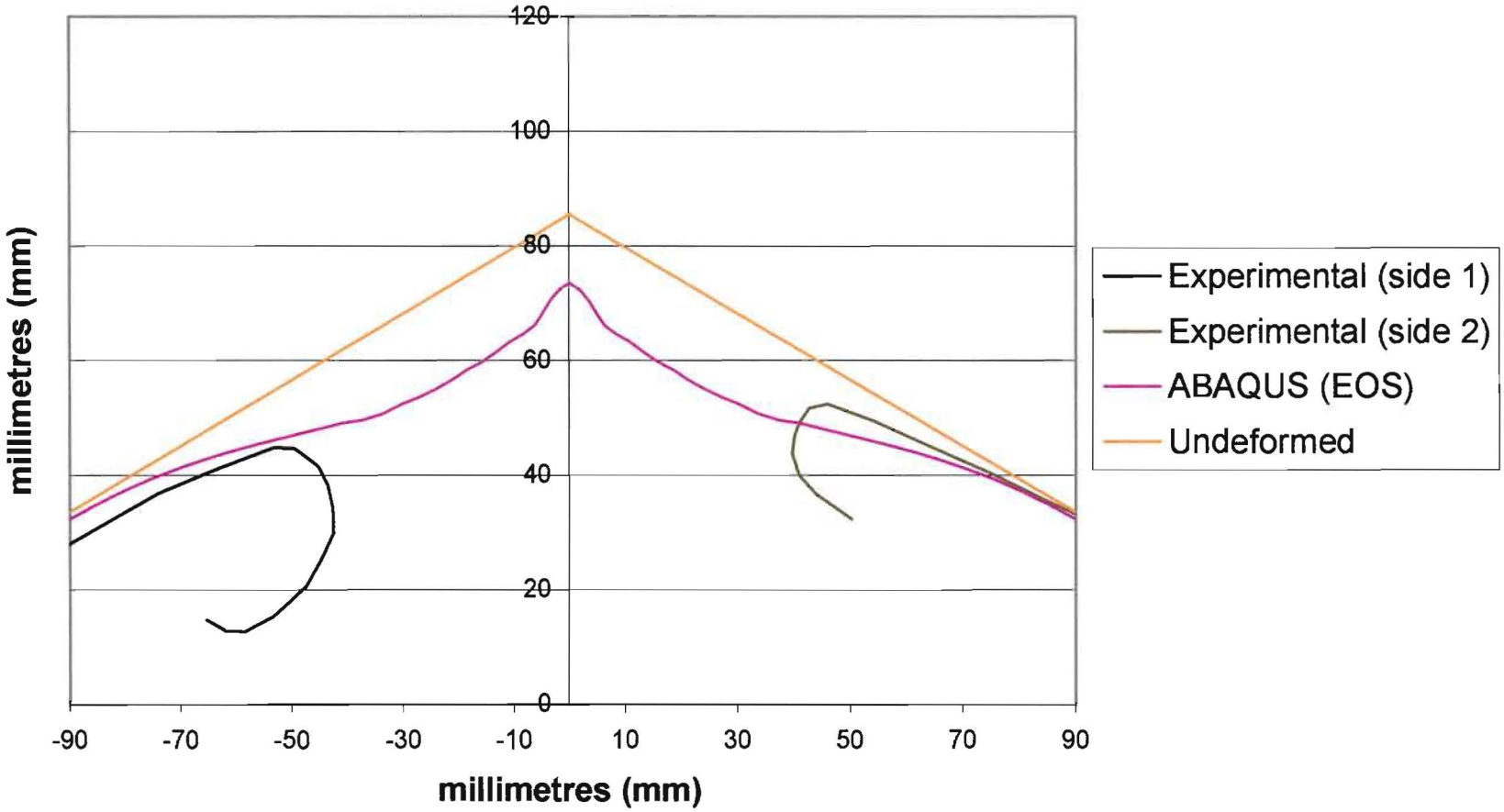

Figure C.30: Comparison of a Magnified Section of the Experimental Deformed Profile of a V-Plate (120 degrees) Exploded by a PE4 Rod (11g), with the ABAQUS Deformed Profile

9.3.4 Comparison of the Experimental and Numerically Predicted Deformed V-Plate Profiles for the 150^0 V-Plates

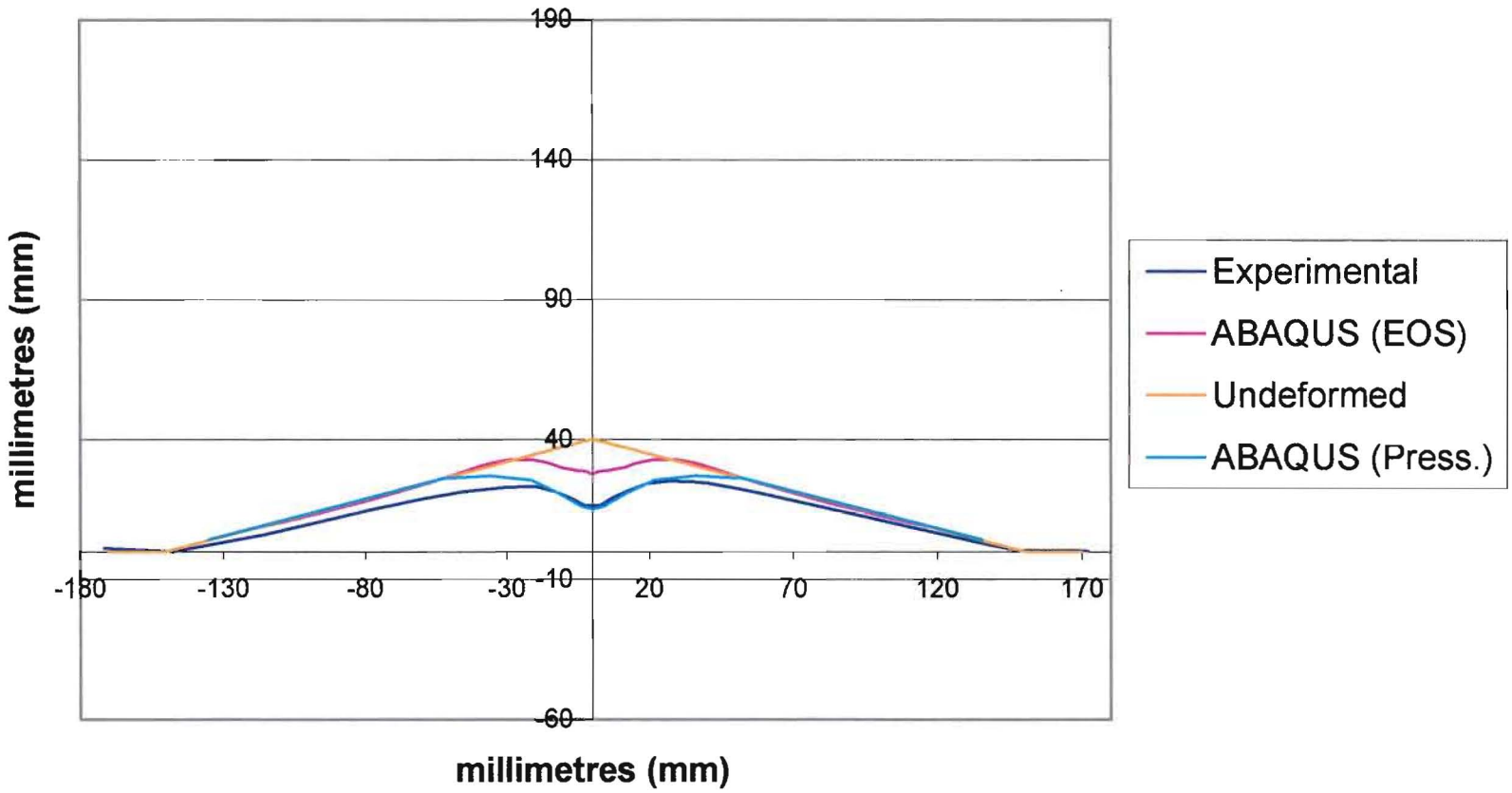

Figure C.31: Comparison of the Experimental Deformed Profile of a V-Plate (150 degrees) Exploded by a PE4 Rod (3g), With an ABAQUS Deformed Profile Obtained Using a Pressure Profile, and With an ABAQUS Deformed Profile Obtained Using the EOS

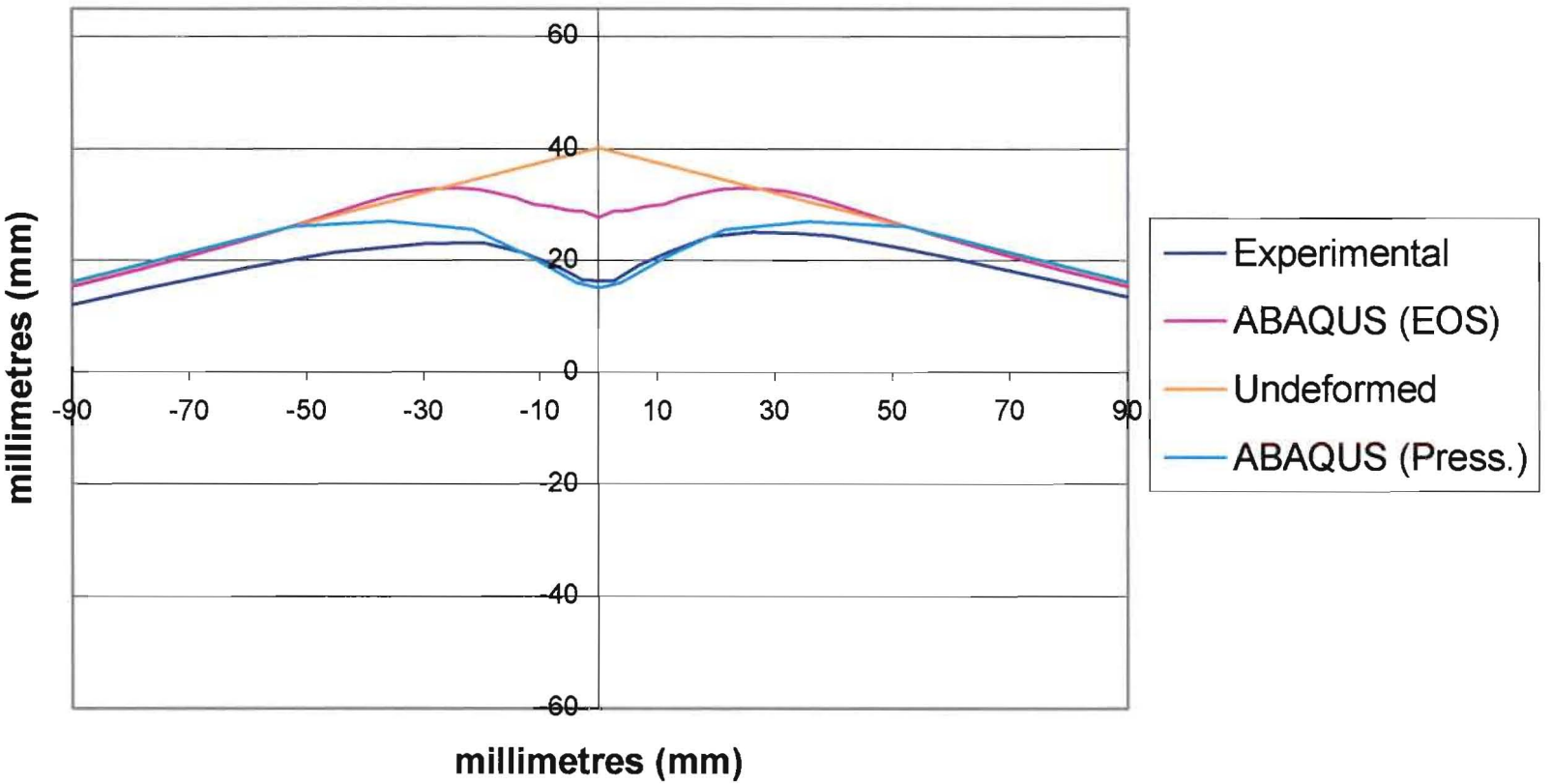

Figure C.32: Comparison of a Magnified Section of the Experimental Deformed Profile of a V-Plate (150 degrees) Exploded by a PE4 Rod (3g), With an ABAQUS Deformed Profile Obtained Using a Pressure Profile, and With an ABAQUS Deformed Profile Obtained Using the EOS

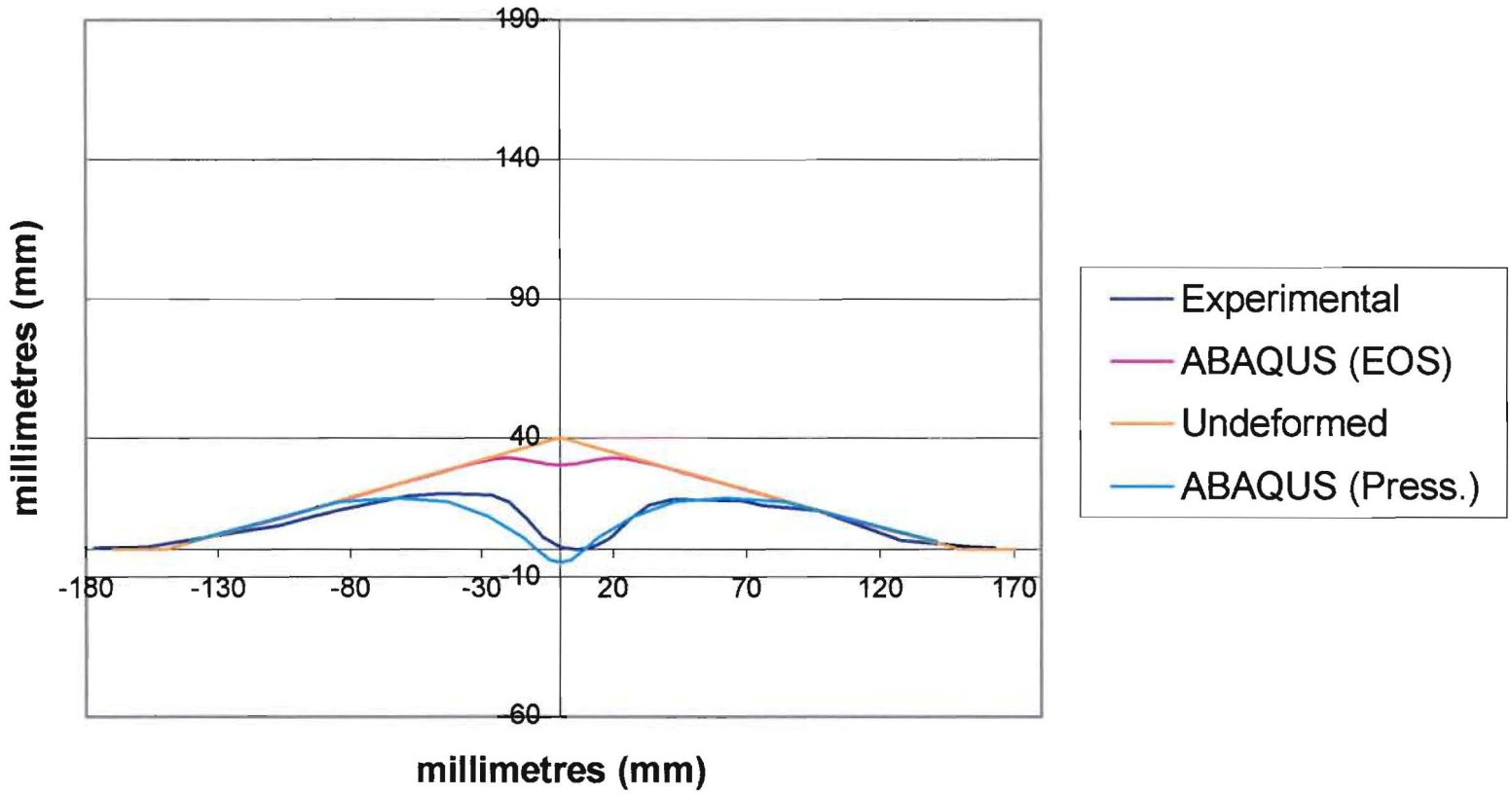

Figure C.33: Comparison of the Experimental Deformed Profile of a V-Plate (150 degrees) Exploded by a PE4 Rod (5g), With an ABAQUS Deformed Profile Obtained Using a Pressure Profile, and With an ABAQUS Deformed Profile Obtained Using the EOS

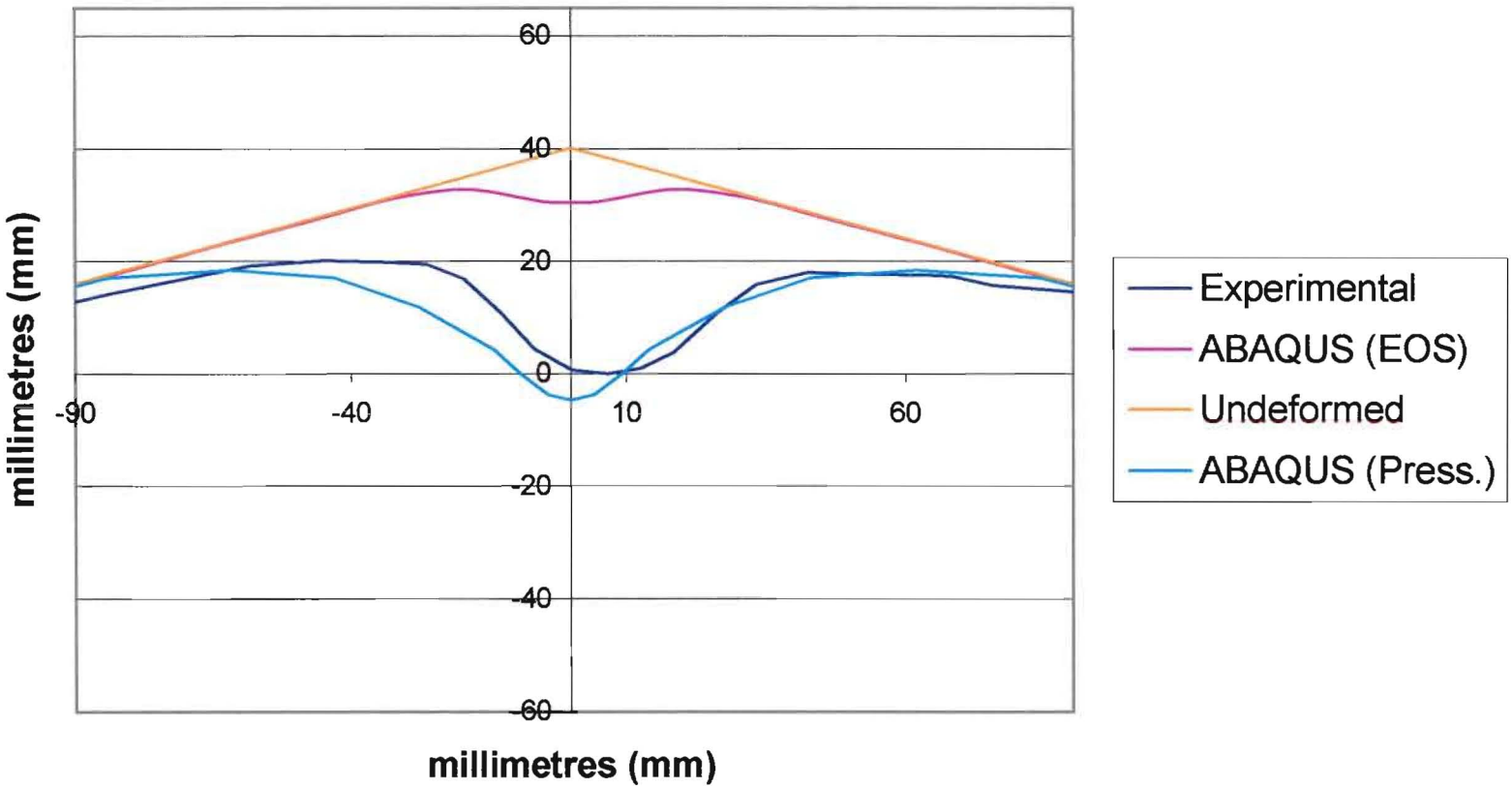

Figure C.34: Comparison of a Magnified Section of the Experimental Deformed Profile of a V-Plate (150 degrees) Exploded by a PE4 Rod (5g), With an ABAQUS Deformed Profile Obtained Using a Pressure Profile, and With an ABAQUS Deformed Profile Obtained Using the EOS

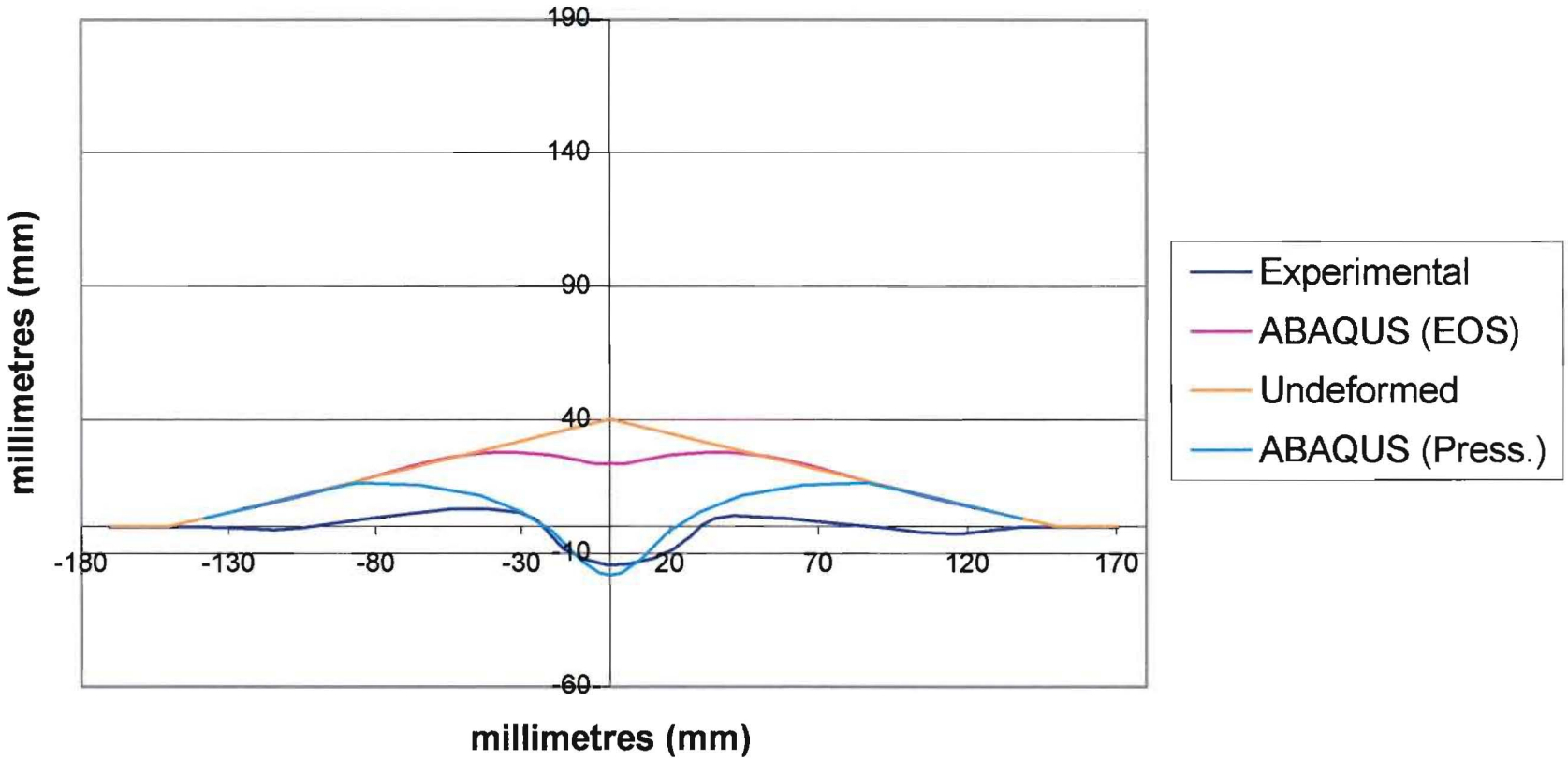

Figure C.35: Comparison of the Experimental Deformed Profile of a V-Plate (150 degrees) Exploded by a PE4 Rod (7g), With the ABAQUS Deformed Profile Obtained Using a Pressure Profile, and With the ABAQUS Deformed Profile Obtained Using the EOS

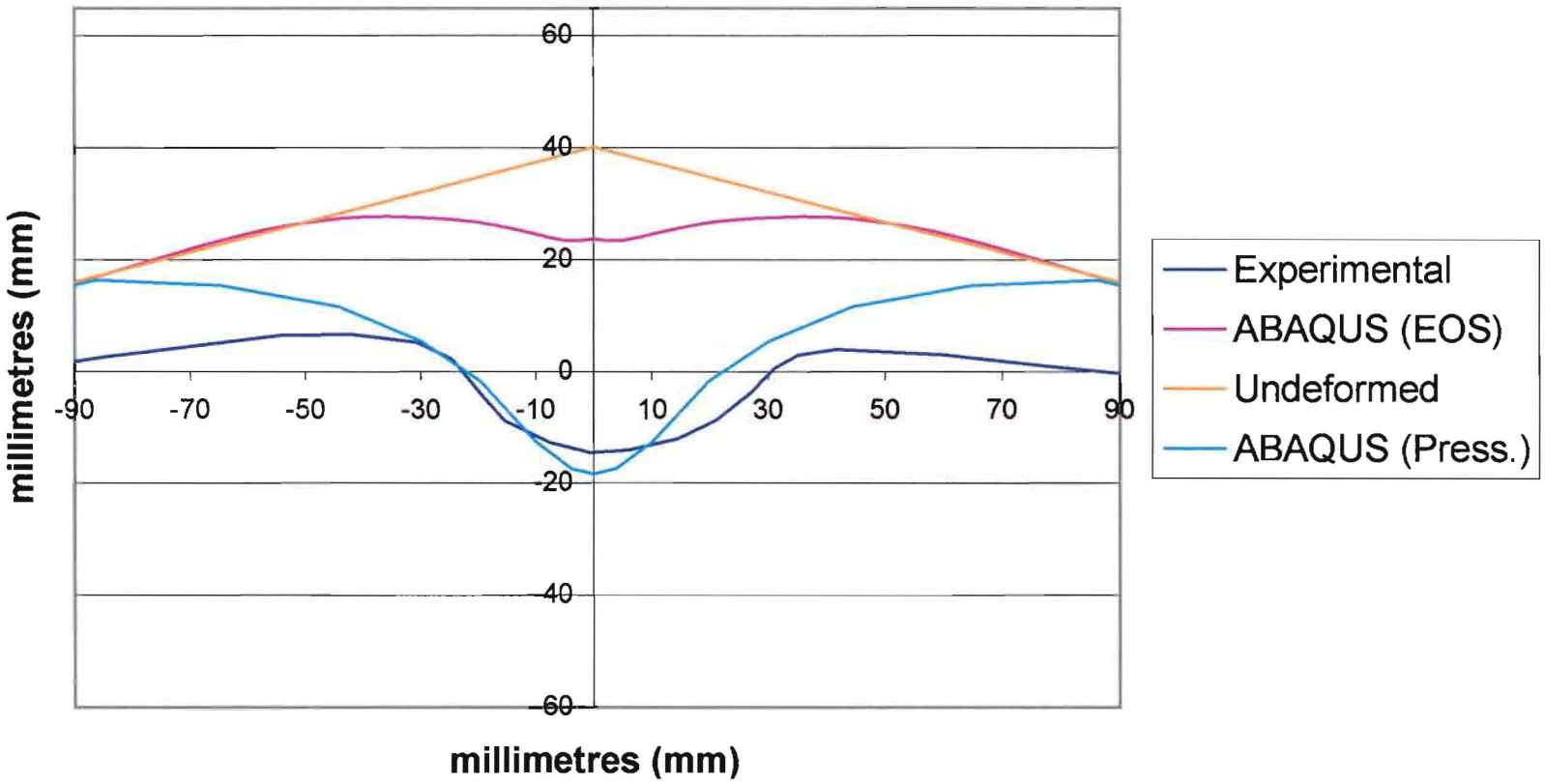

Figure C.36: Comparison of a Magnified Section of the Experimental Deformed Profile of a V-Plate (150 degrees) Exploded by a PE4 Rod (7g), With the ABAQUS Deformed Profile Obtained Using a Pressure Profile, and With the ABAQUS Deformed Profile Obtained Using the EOS

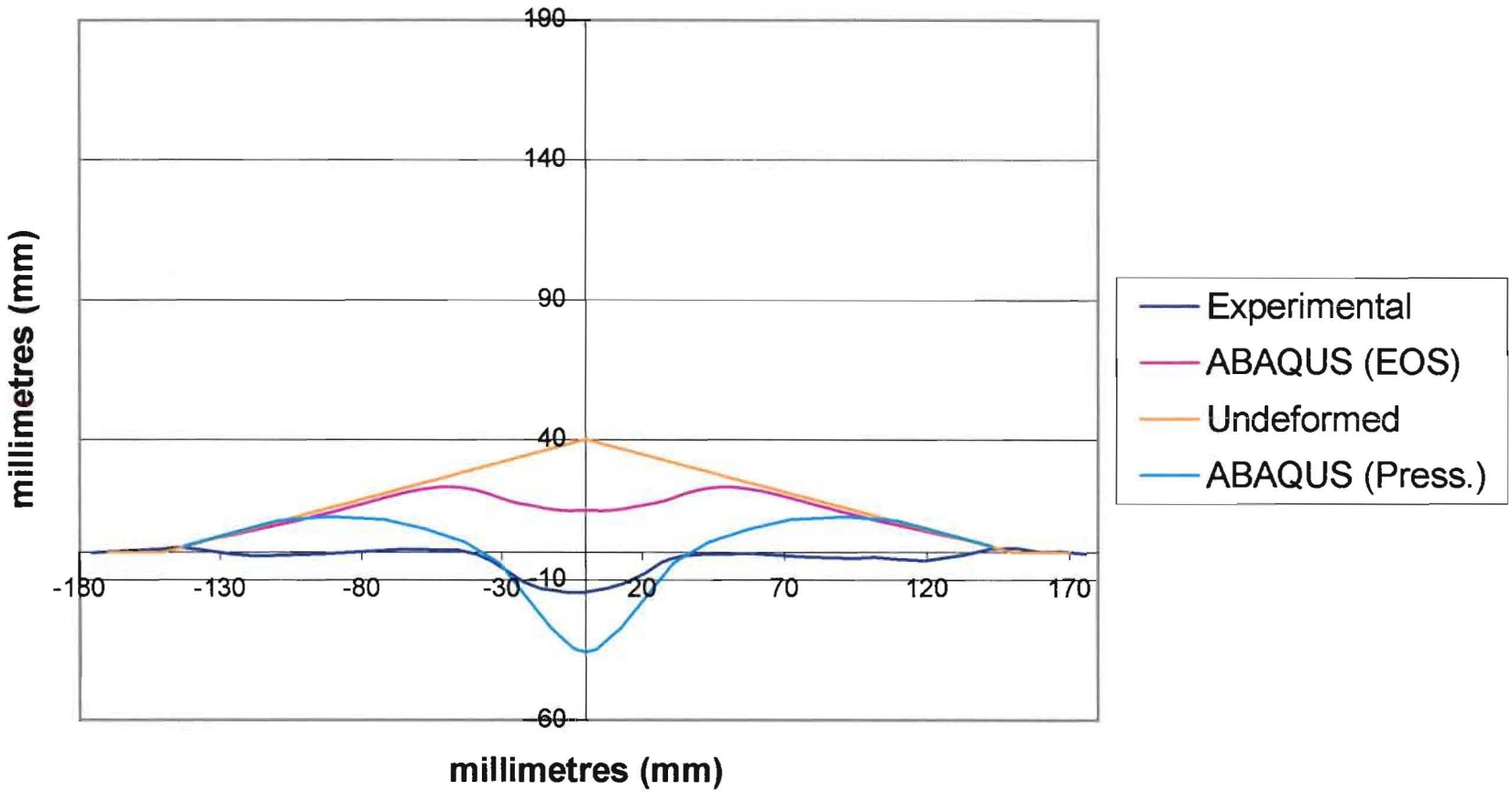

Figure C.37: Comparison of the Experimental Deformed Profile of a V-Plate (150 degrees) Exploded by a PE4 Rod (9g), With the ABAQUS Deformed Profile Obtained Using a Pressure Profile, and With the ABAQUS Deformed Profile Obtained Using the EOS

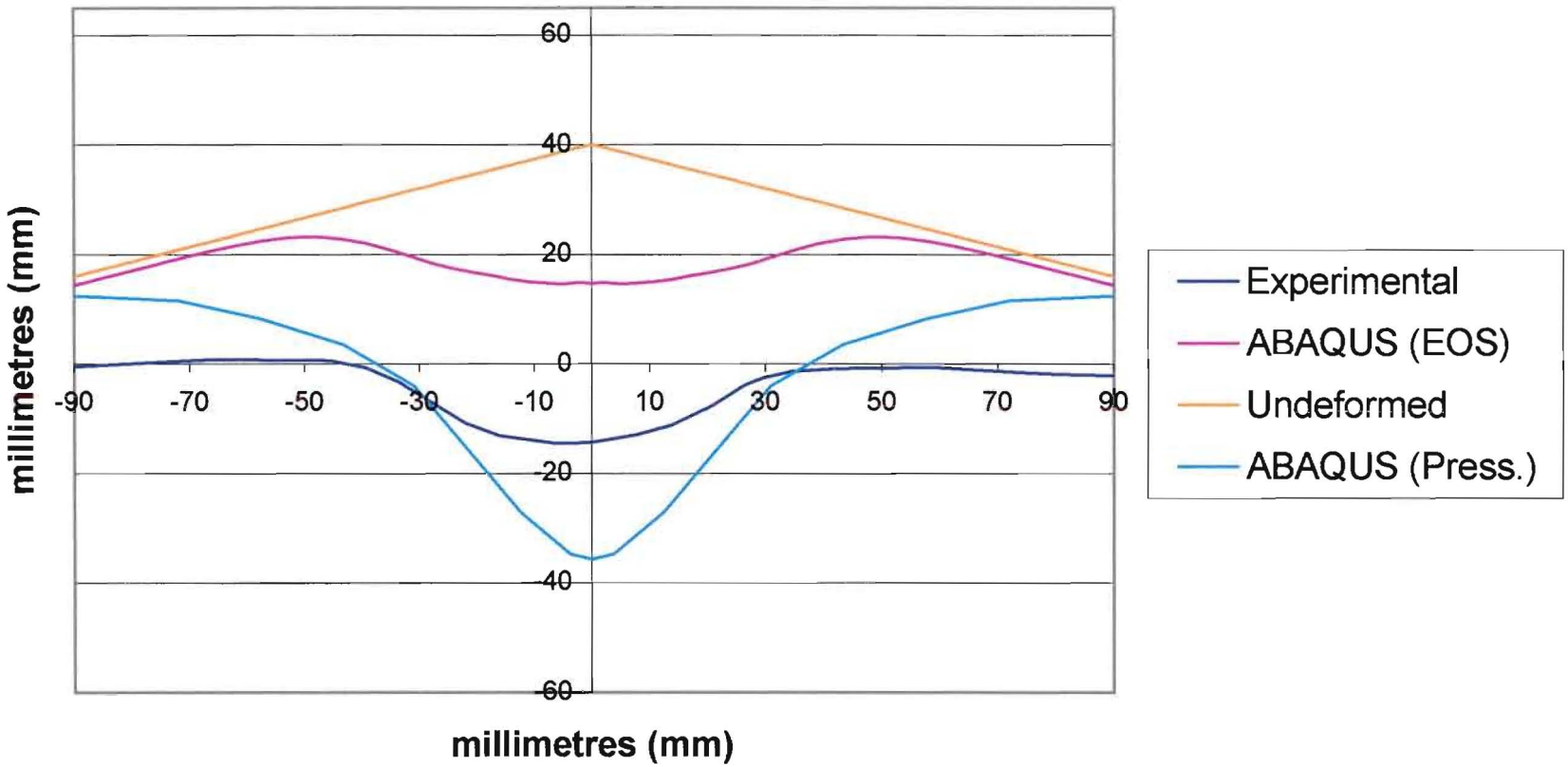

Figure C.38: Comparison of a Magnified Section of the Experimental Deformed Profile of a V-Plate (150 degrees) Exploded by a PE4 Rod (9g), With the ABAQUS Deformed Profile Obtained Using a Pressure Profile, and With the ABAQUS Deformed Profile Obtained Using the EOS

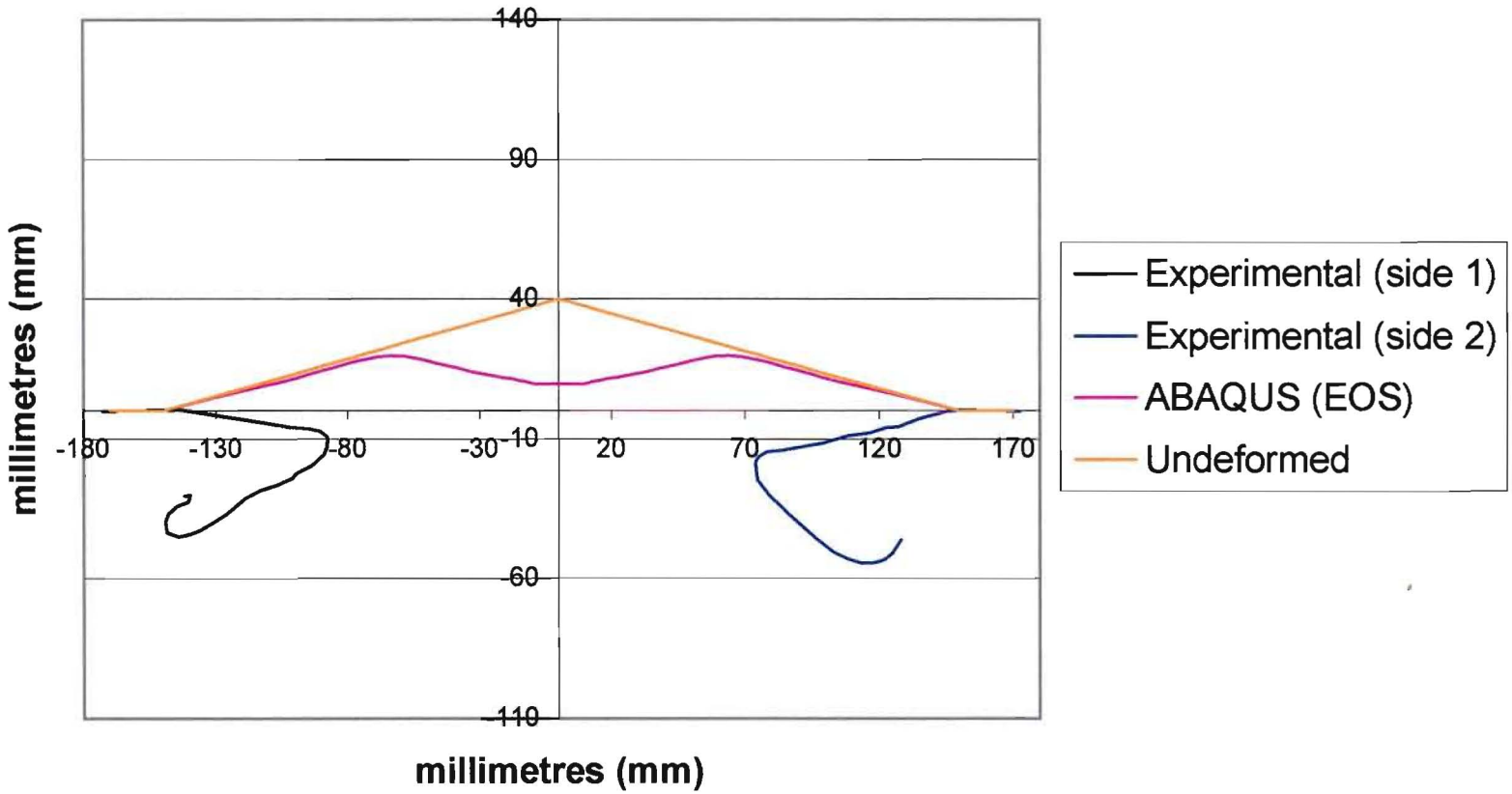

Figure C.39: Comparison of the Experimental Deformed Profile of a V-Plate (150 degrees) Exploded by a PE4 Rod (11g), with the ABAQUS Deformed Profile

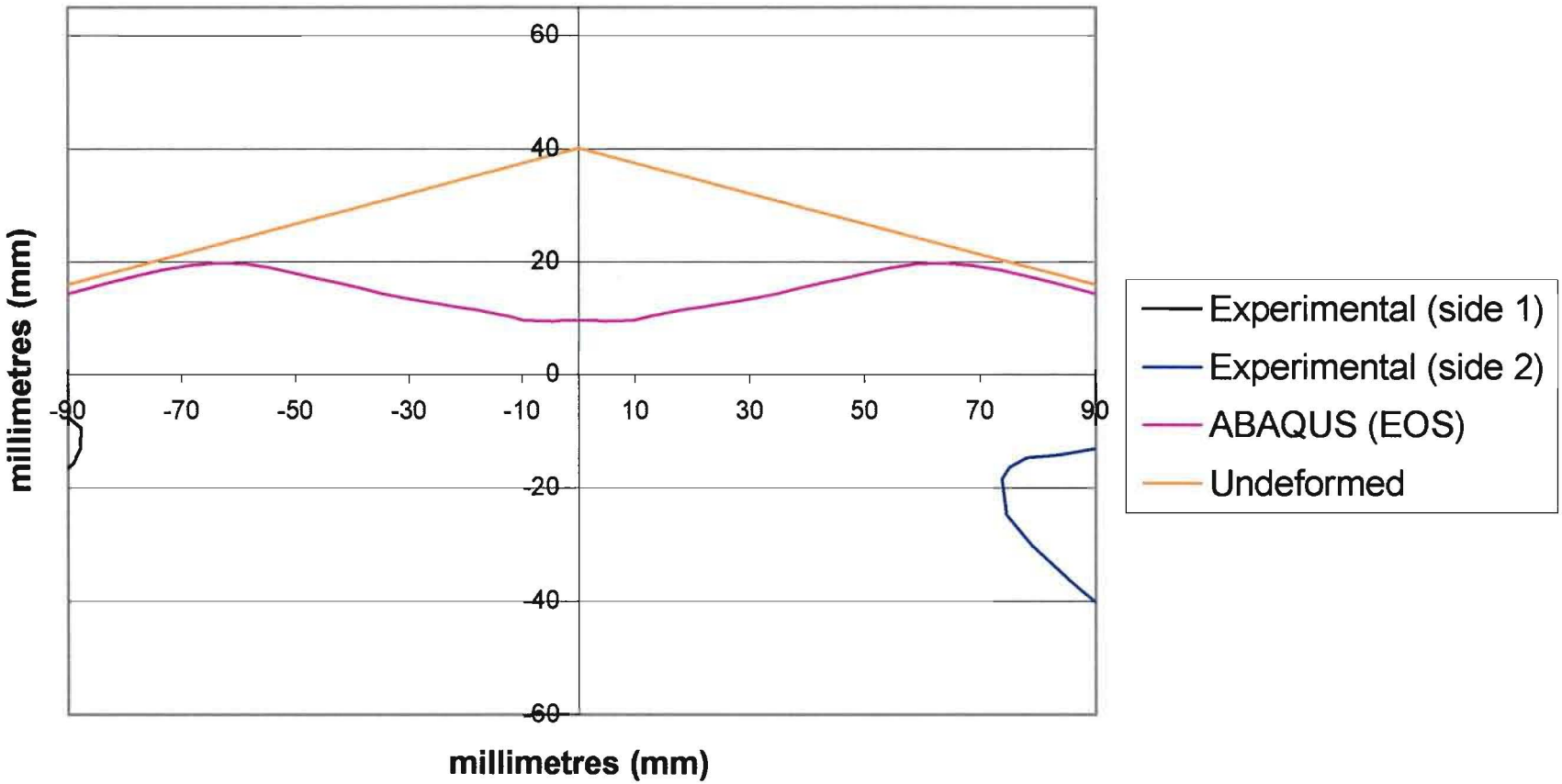

Figure C.40: Comparison of a Magnified Section of the Experimental Deformed Profile of a V-Plate (150 degrees) Exploded by a PE4 Rod (11g), with the ABAQUS Deformed Profile

9.4 Appendix D: Graphs of JWL Equation of State Method Numerically Predicted Deformed V-Plate Profiles Exploded by PE4 Disc Explosives

9.4.1 JWL Equation of State Method Numerically Predicted Deformed V-Plate Profiles for the 60^0 V-Plates

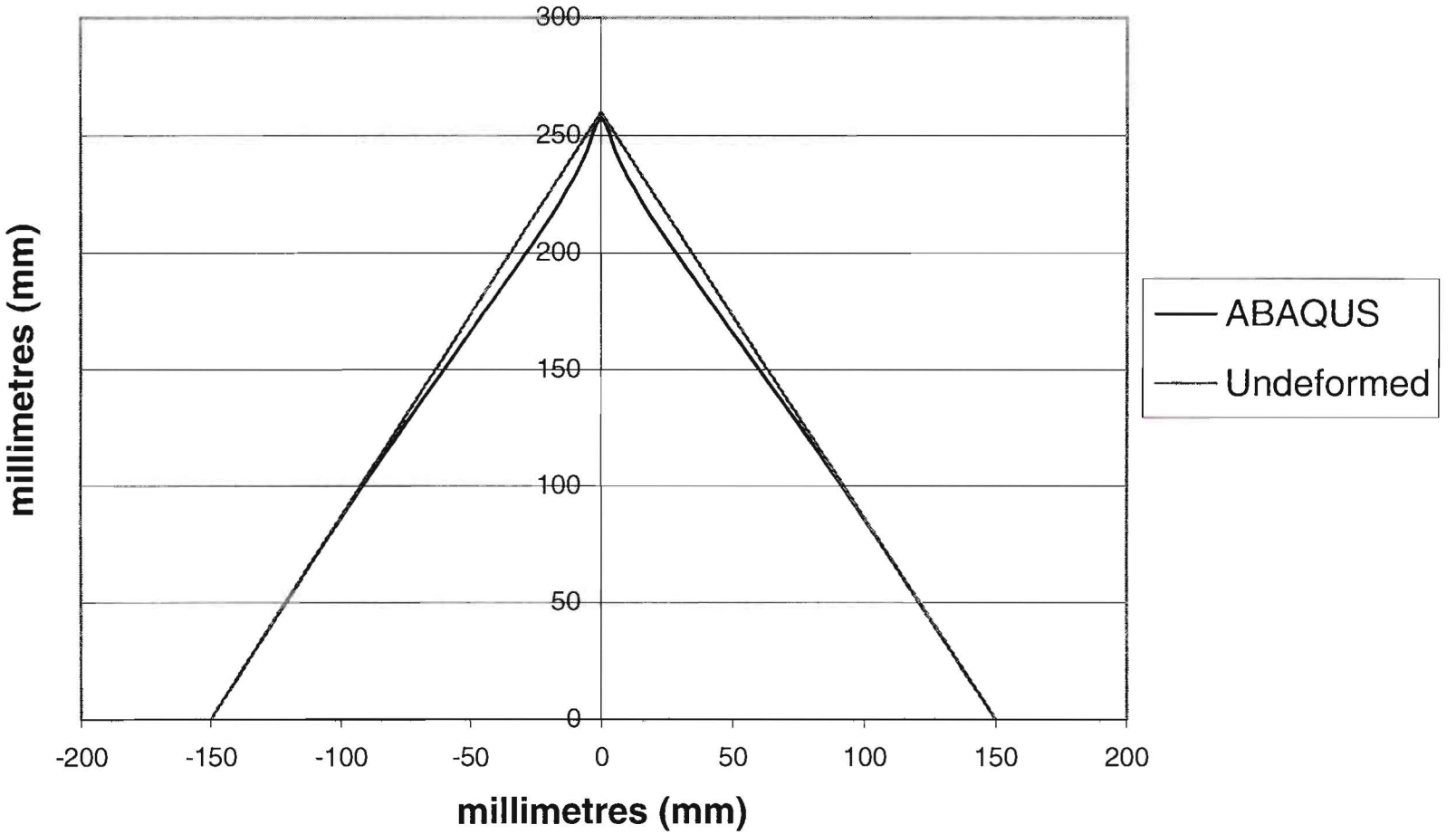

Figure D.1: The Deformed Profile of a V-Plate (60 degrees) Exploded by a PE4 Disc (4g) As Predicted By ABAQUS Using the JWL Equation of State

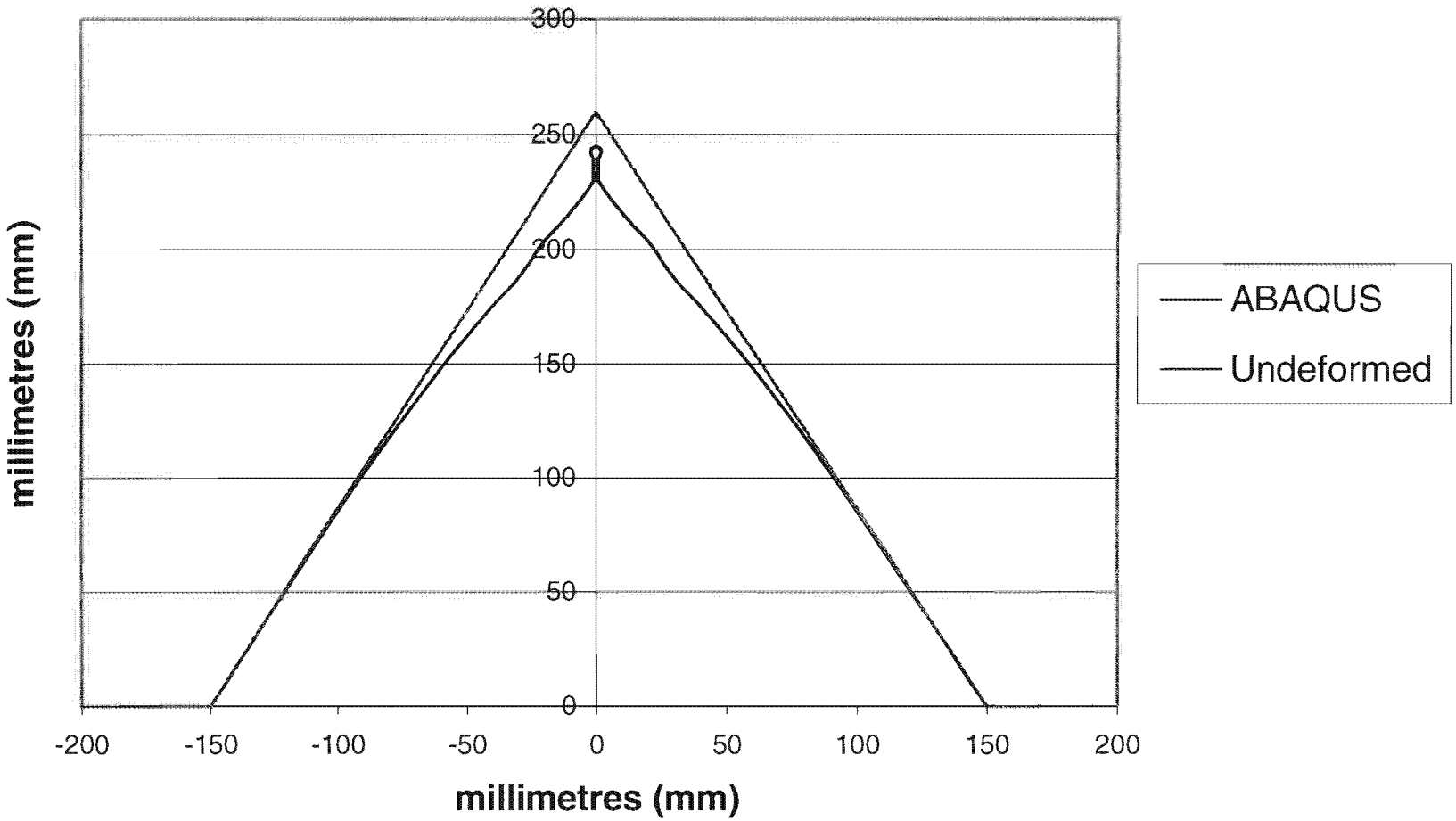

Figure D.2: The Deformed Profile of a V-Plate (60 degrees) Exploded by a PE4 Disc (6g) As Predicted By ABAQUS Using the JWL Equation of State

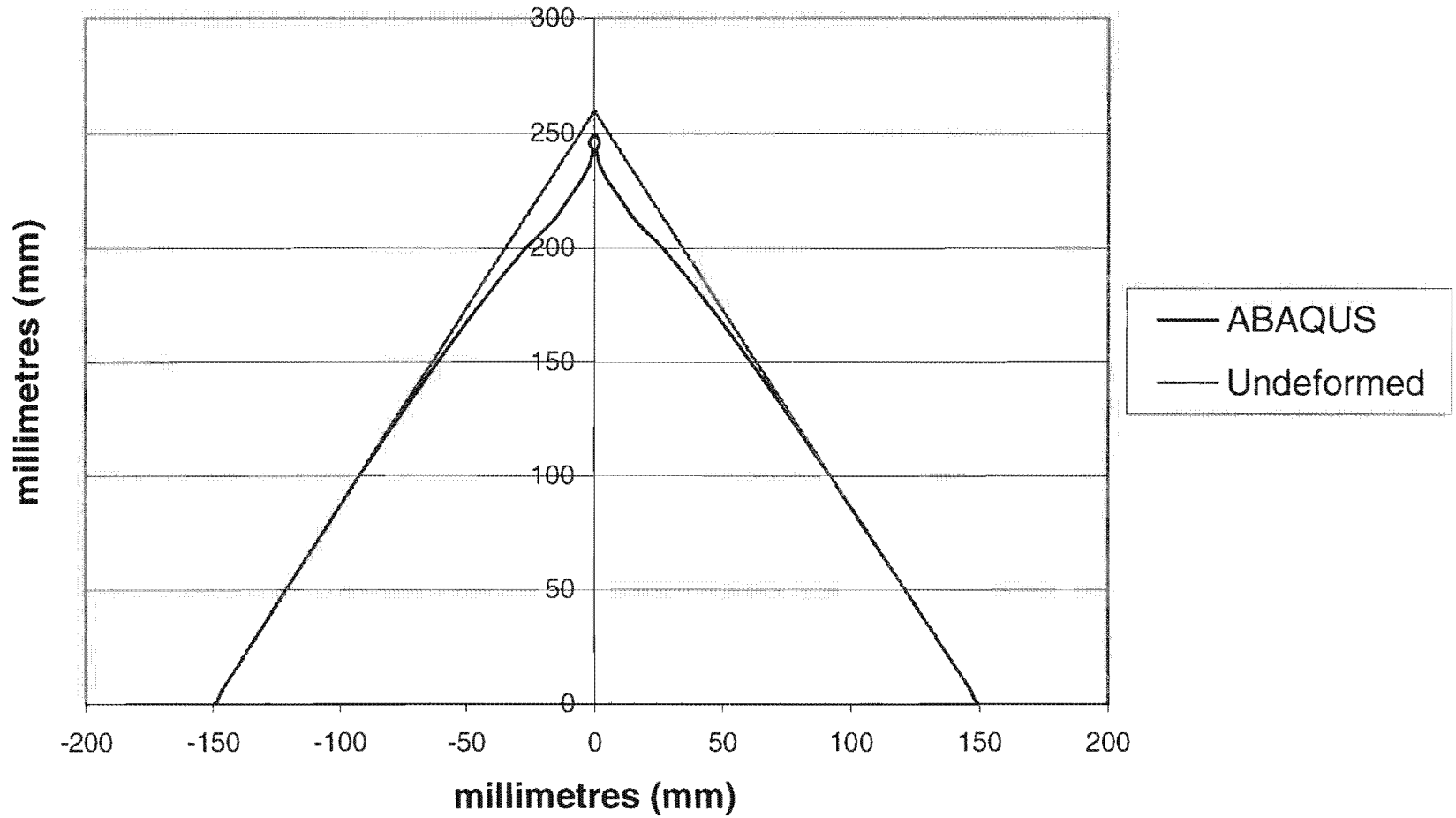

Figure D.3: The Deformed Profile of a V-Plate (60 degrees) Exploded by a PE4 Disc (8g) As Predicted By ABAQUS Using the JWL Equation of State

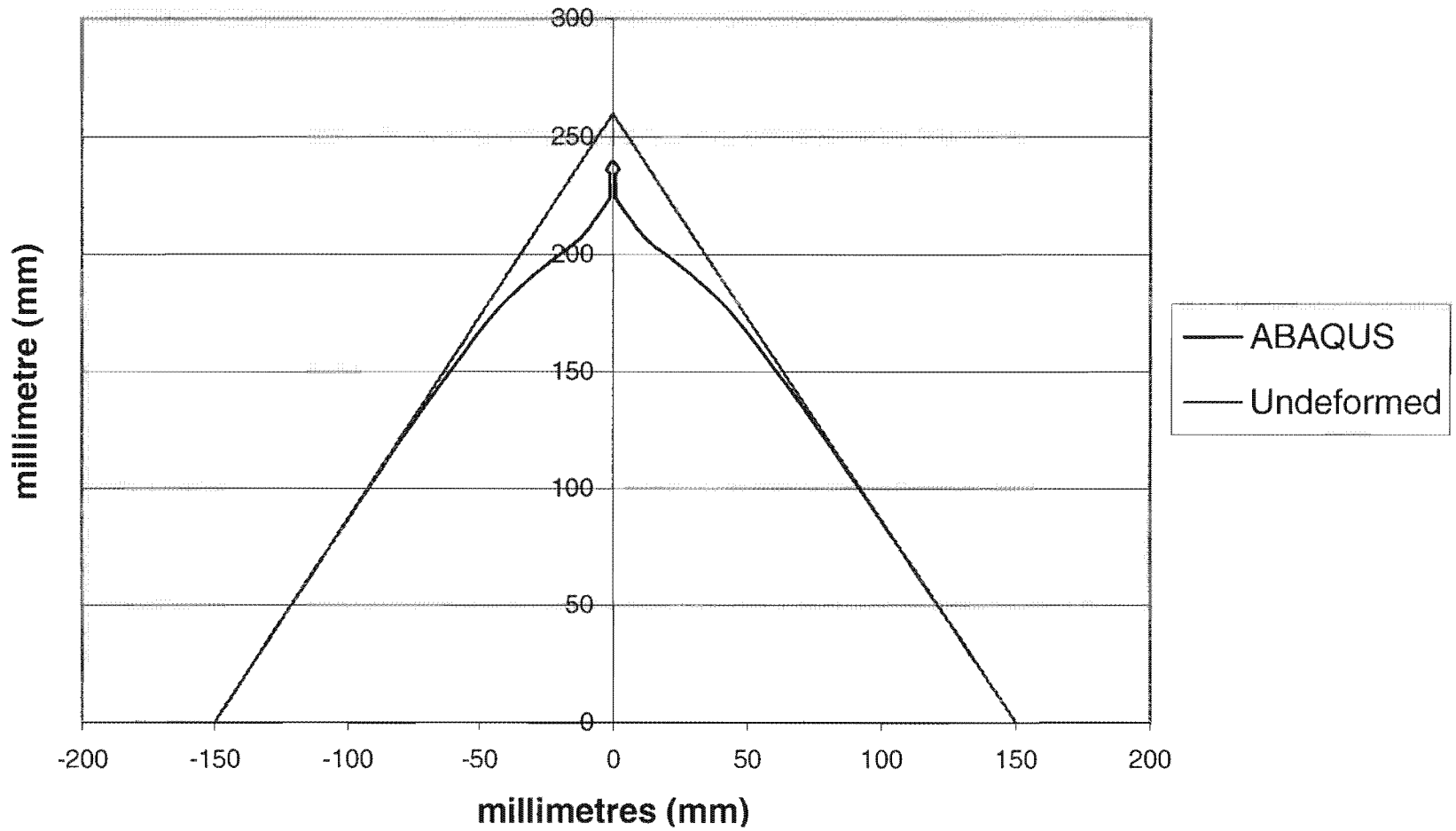

Figure D.4: The Deformed Profile of a V-Plate (60 degrees) Exploded by a PE4 Disc (10g) As Predicted By ABAQUS Using the JWL Equation of State

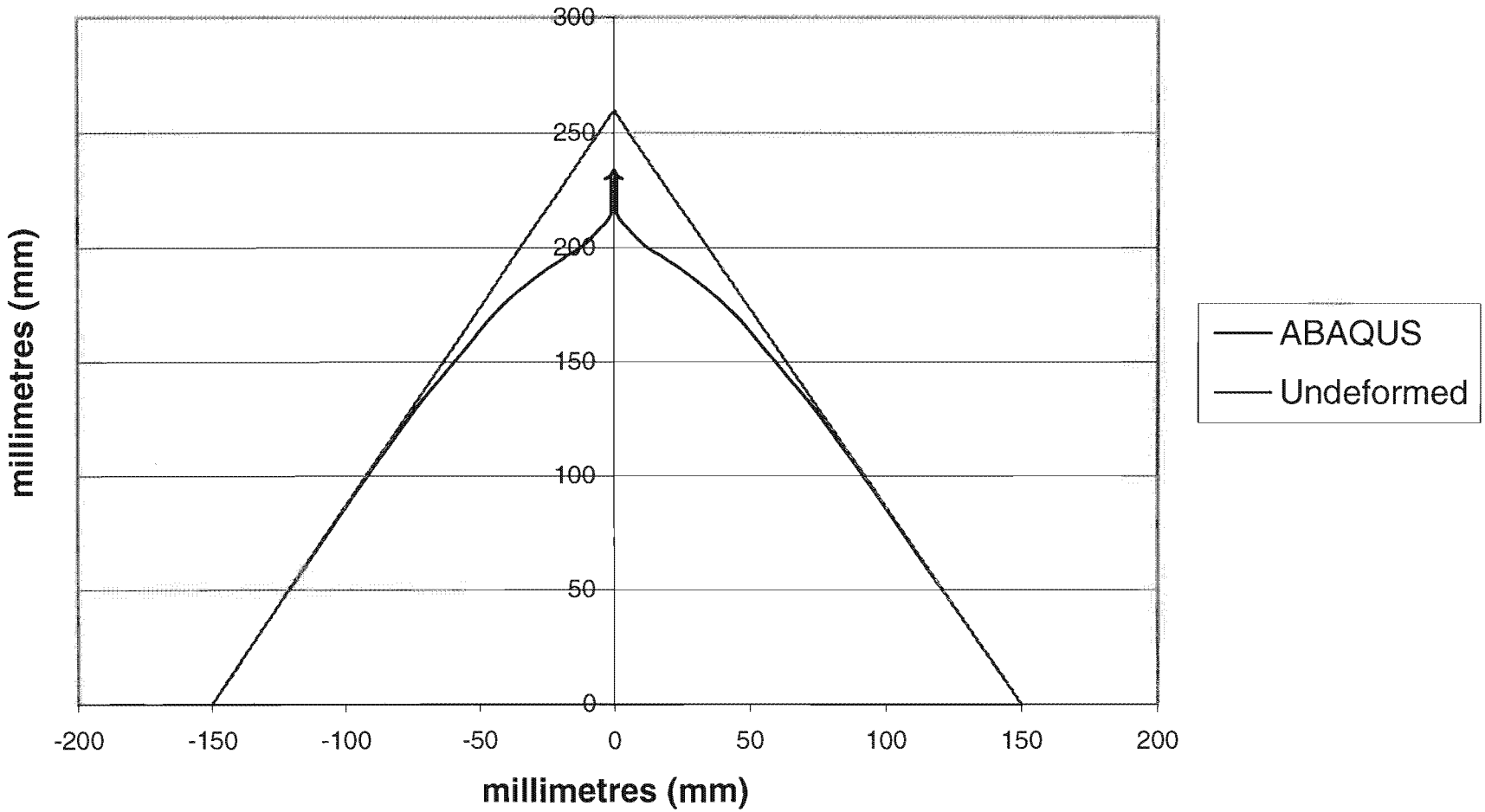

Figure D.5: The Deformed Profile of a V-Plate (60 degrees) Exploded by a PE4 Disc (12g) As Predicted By ABAQUS Using the JWL Equation of State

9.4.2 JWL Equation of State Method Numerically Predicted Deformed V-Plate Profiles for the 90^0 V-Plates

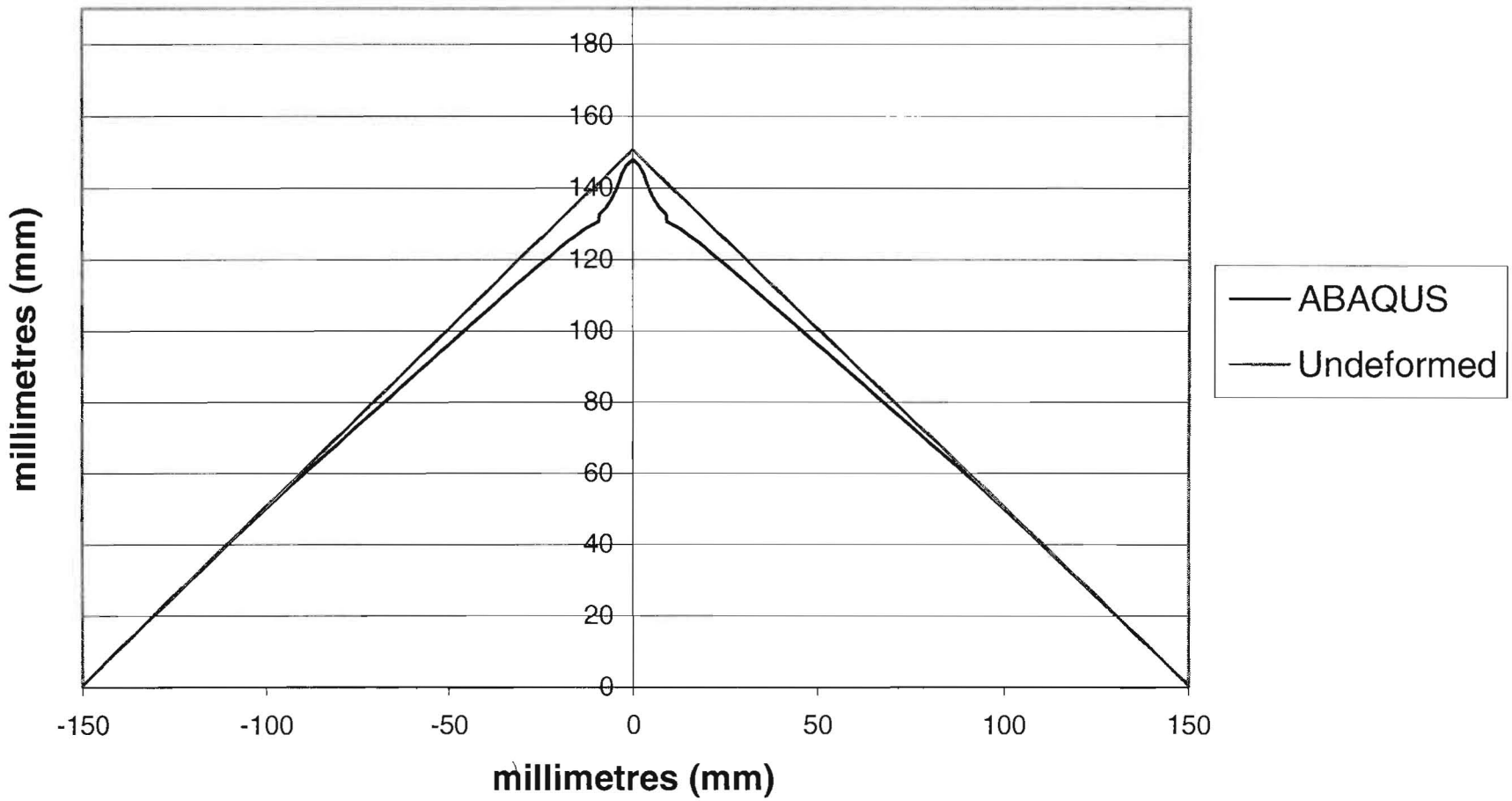

Figure D.6: The Deformed Profile of a V-Plate (90 degrees) Exploded by a PE4 Disc (4g) As Predicted By ABAQUS Using the JWL Equation of State

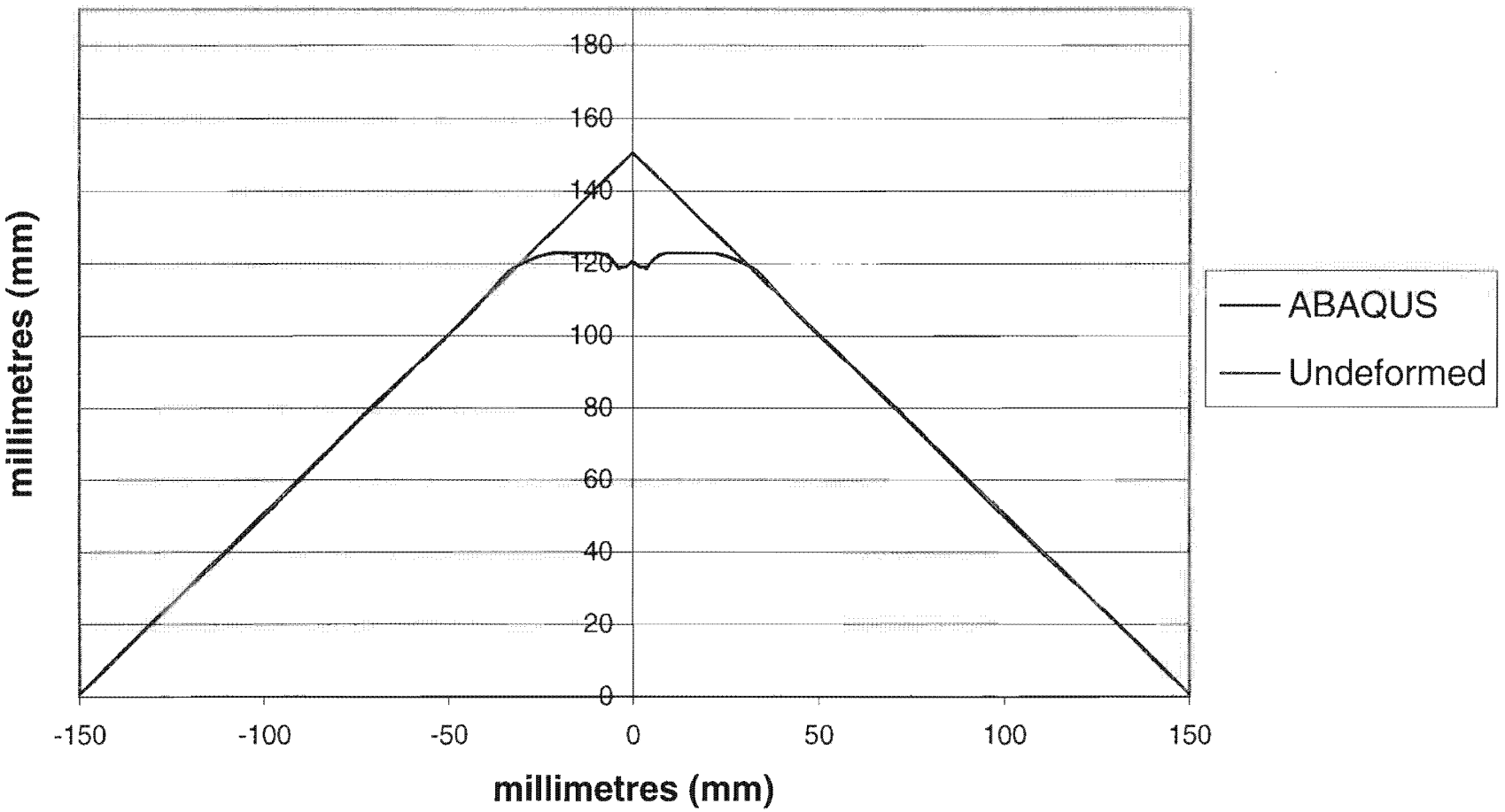

Figure D.7: The Deformed Profile of a V-Plate (90 degrees) Exploded by a PE4 Disc (6g) As Predicted By ABAQUS Using the JWL Equation of State

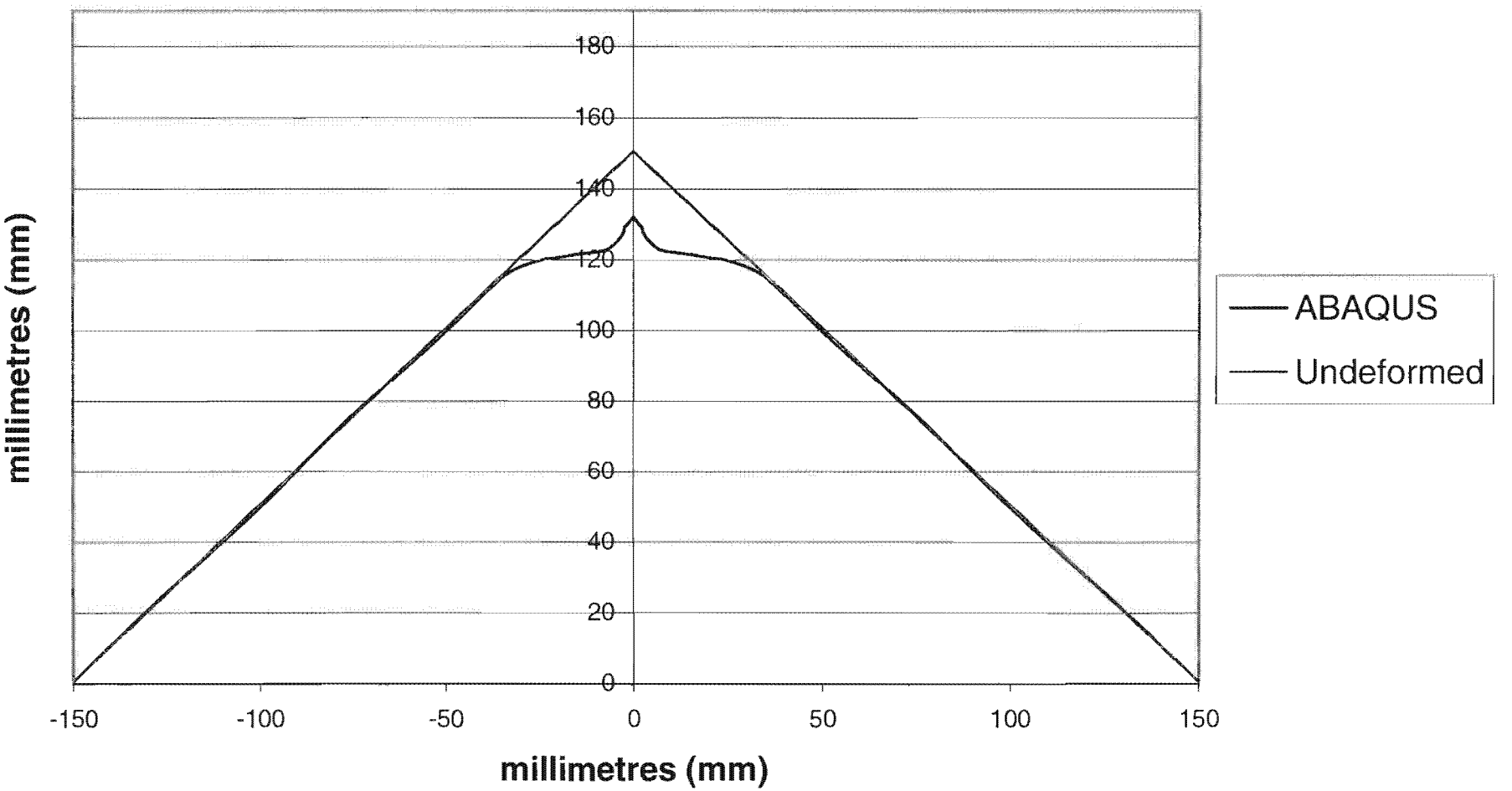

Figure D.8: The Deformed Profile of a V-Plate (90 degrees) Exploded by a PE4 Disc (8g) As Predicted By ABAQUS Using the JWL Equation of State

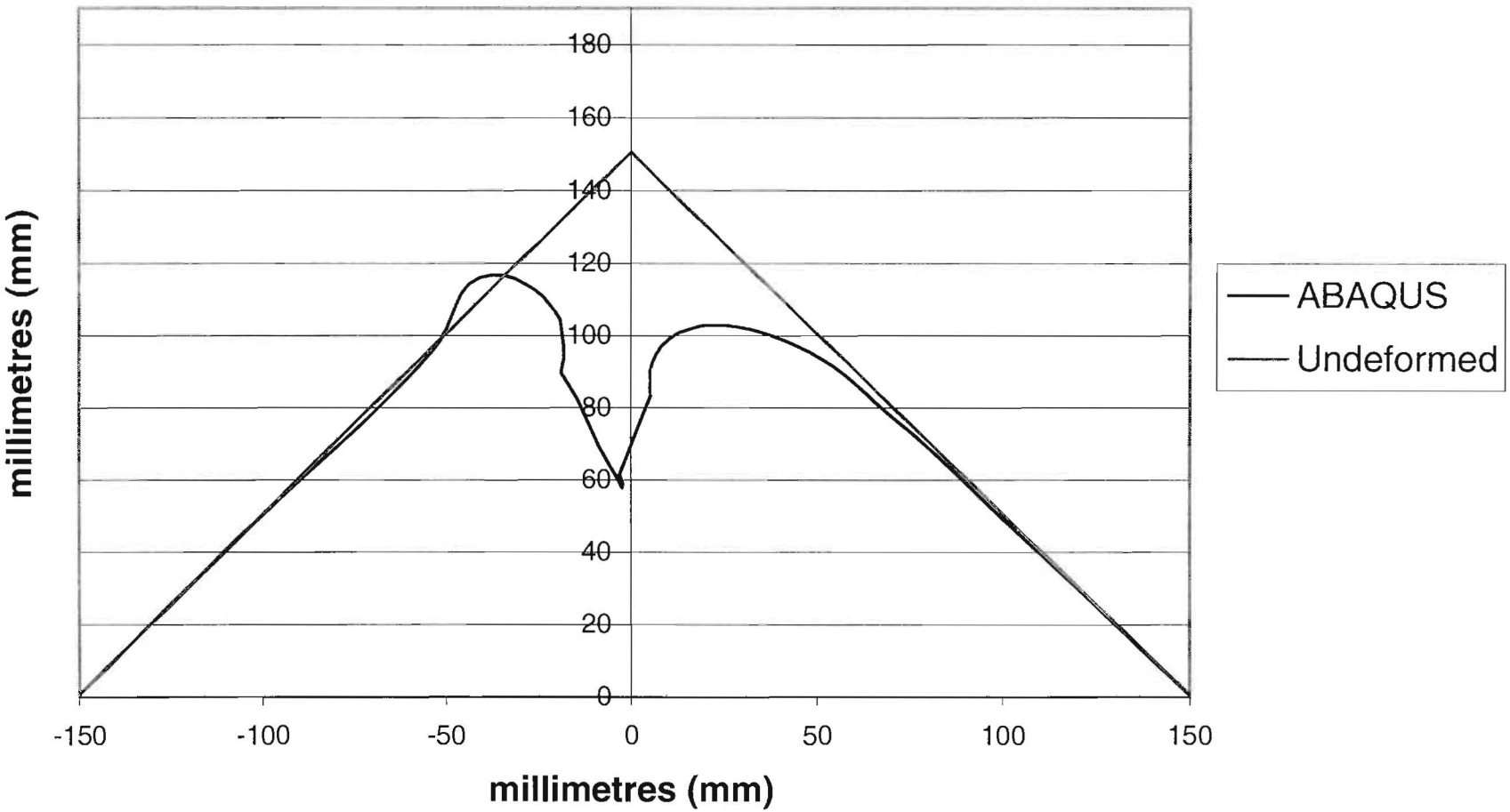

Figure D.9: The Deformed Profile of a V-Plate (90 degrees) Exploded by a PE4 Disc (8g; 5mm Offset) As Predicted By ABAQUS Using the JWL Equation of State

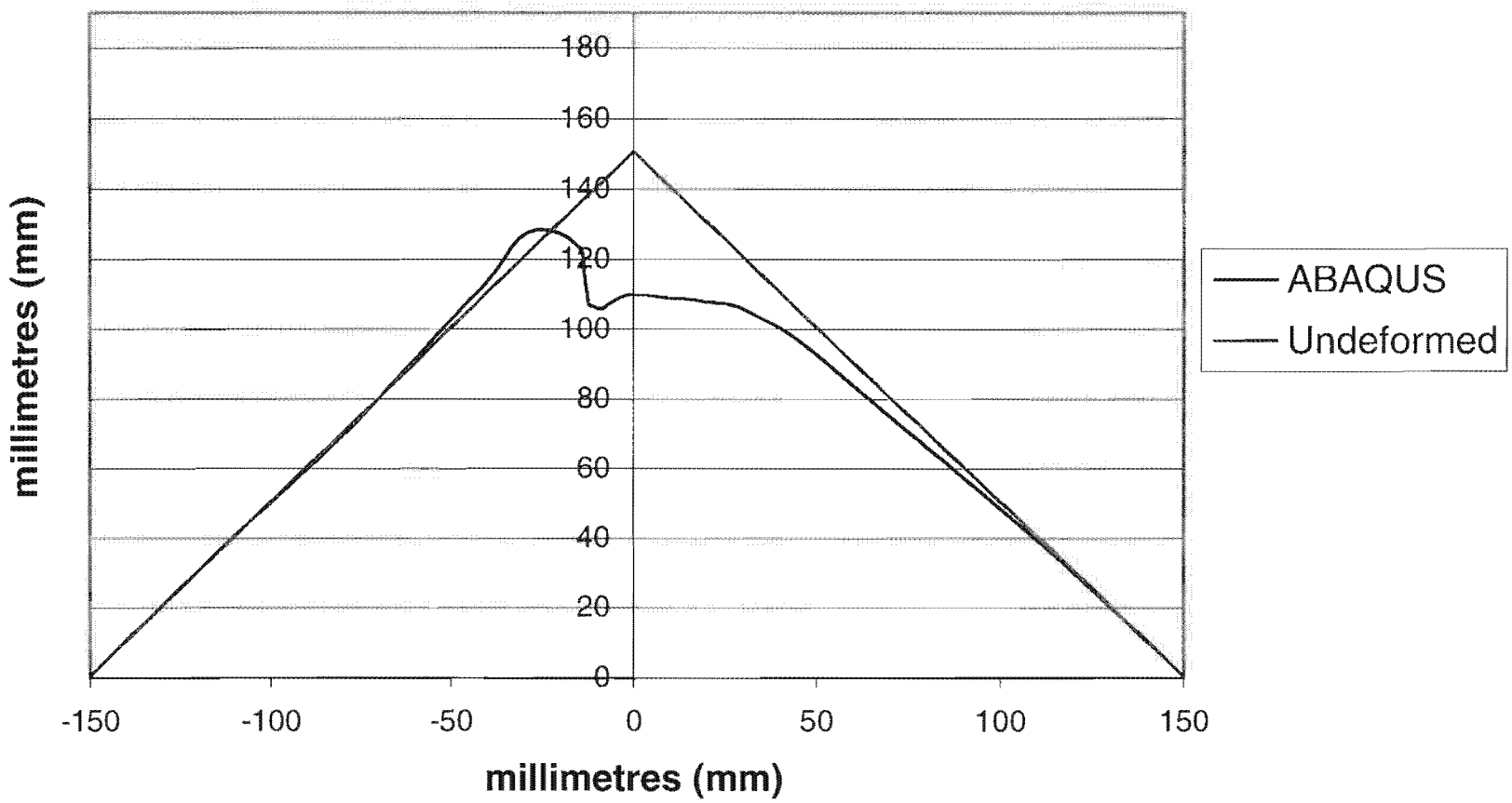

Figure D.10: The Deformed Profile of a V-Plate (90 degrees) Exploded by a PE4 Disc (8g; 10mm Offset) As Predicted By ABAQUS Using the JWL Equation of State

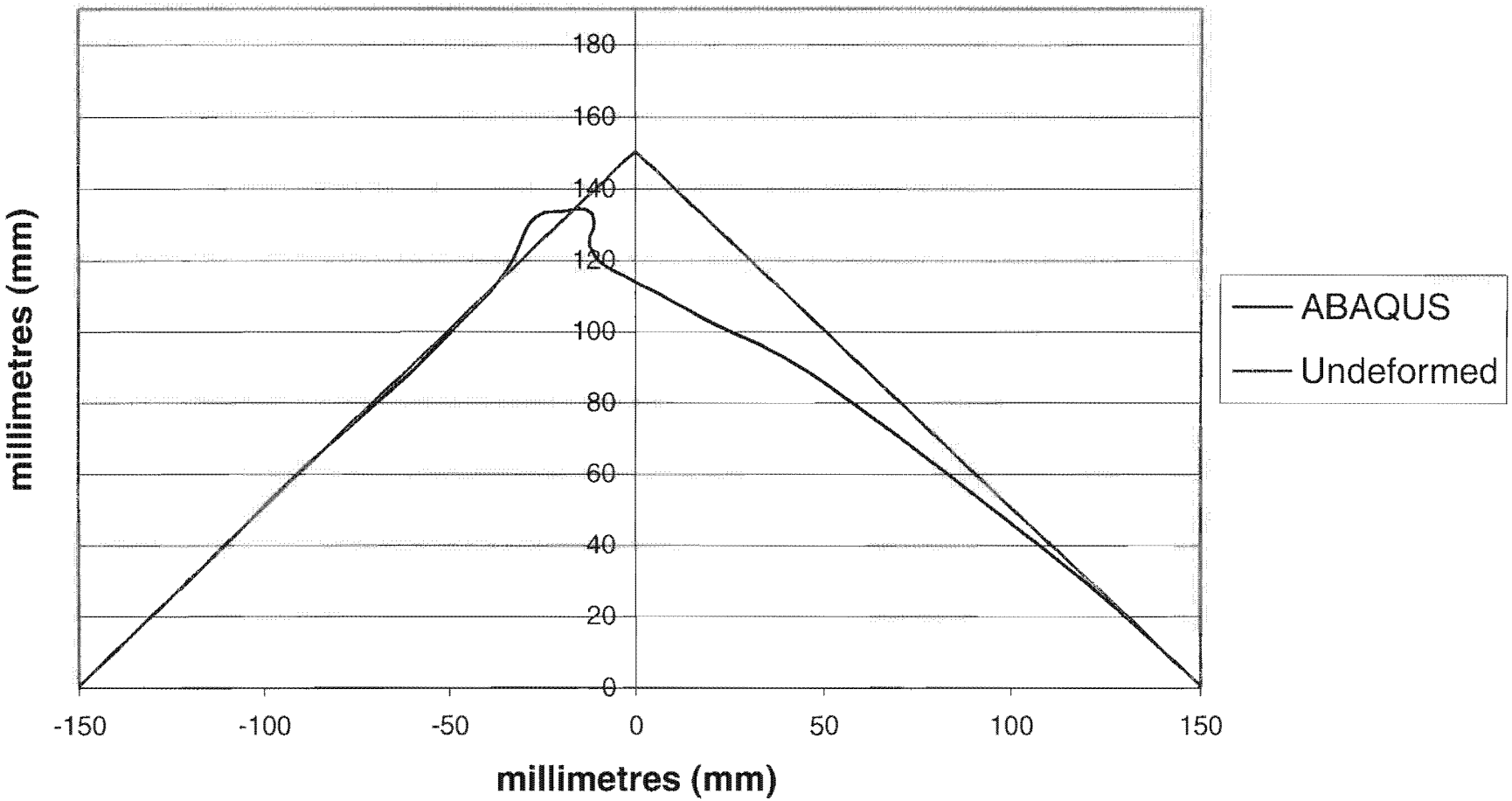

Figure D.11: The Deformed Profile of a V-Plate (90 degrees) Exploded by a PE4 Disc (8g; 15mm Offset) As Predicted By ABAQUS Using the JWL Equation of State

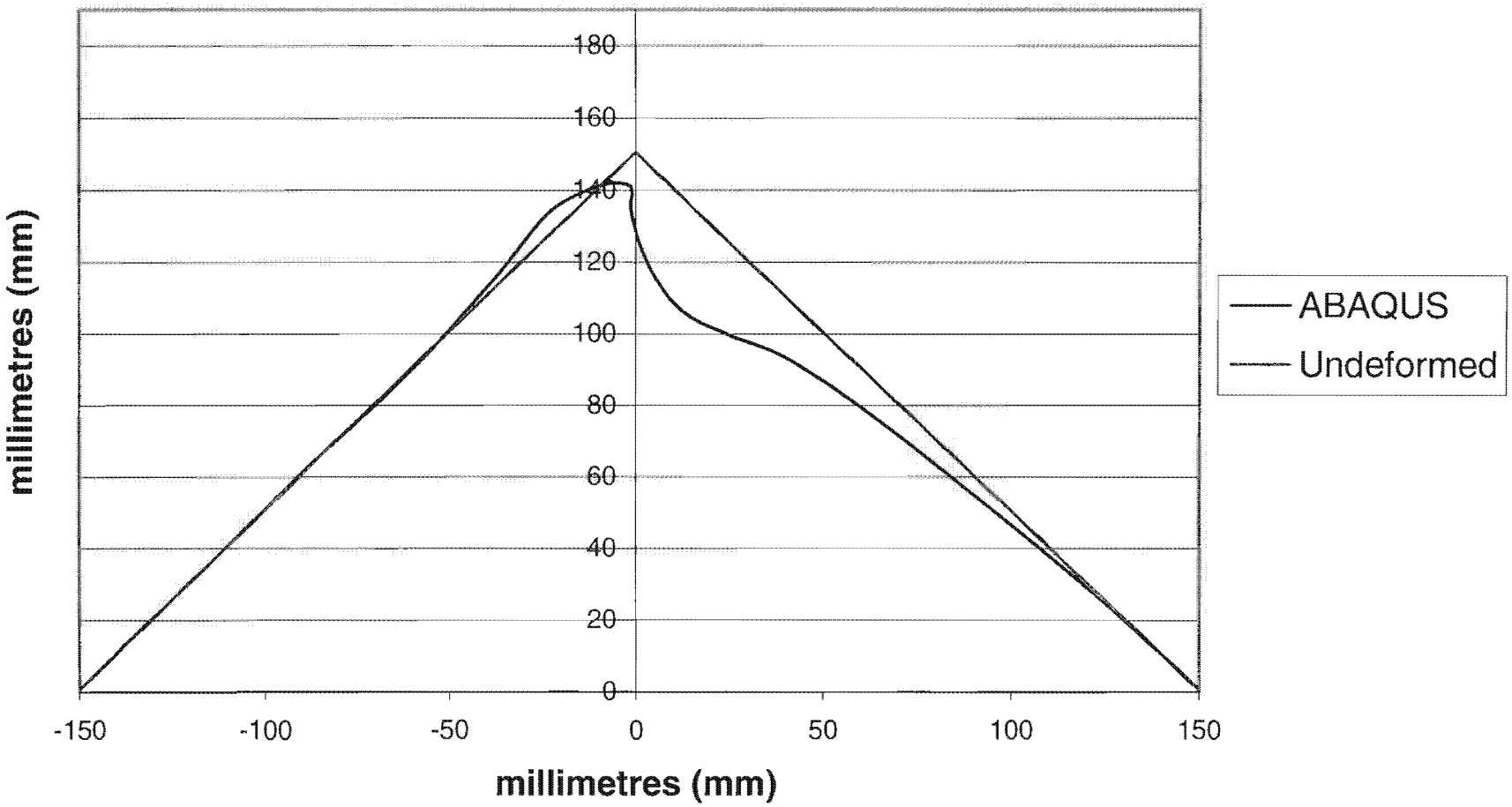

Figure D.12: The Deformed Profile of a V-Plate (90 degrees) Exploded by a PE4 Disc (8g; 20mm Offset) As Predicted By ABAQUS Using the JWL Equation of State

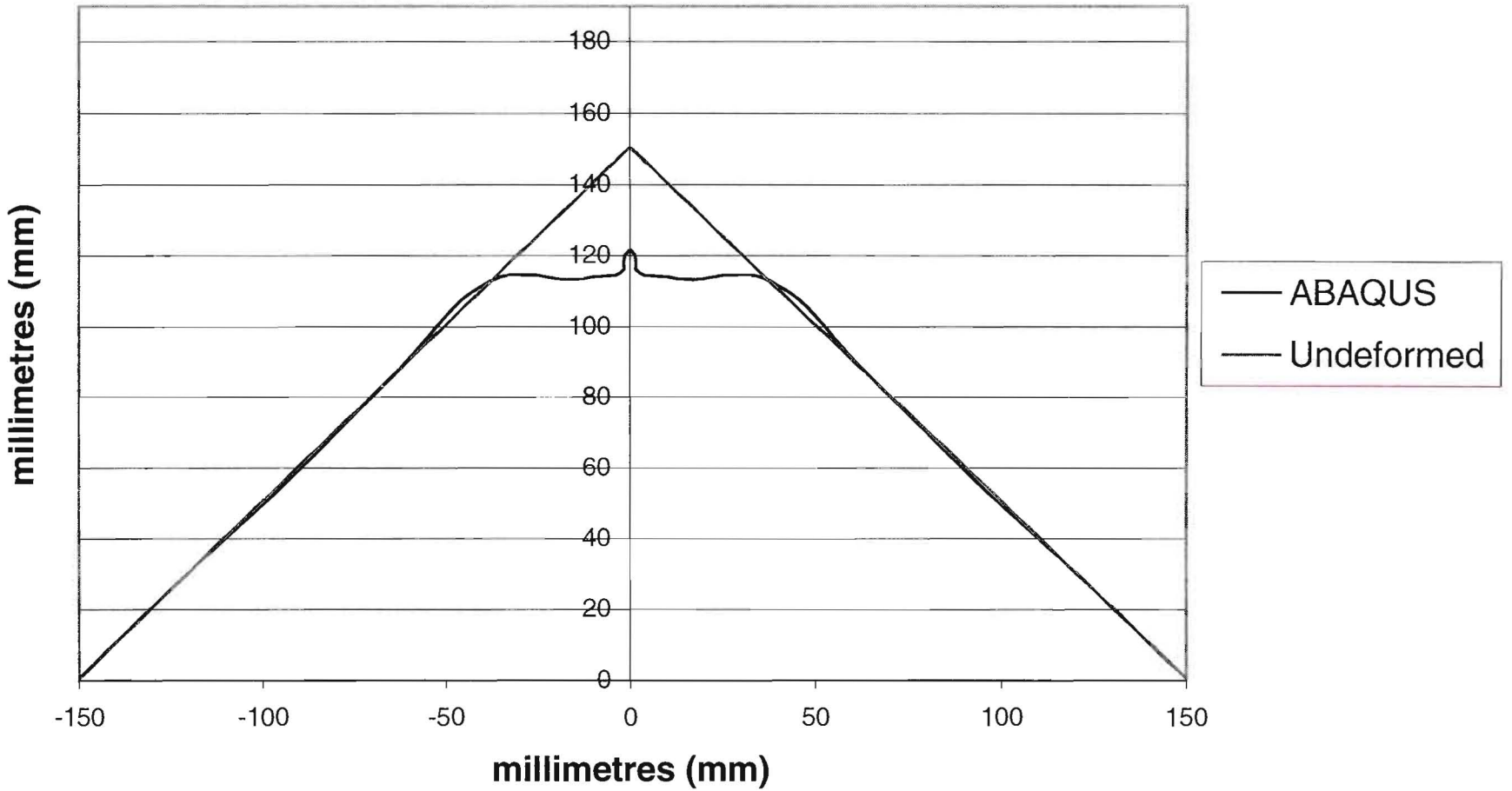

Figure D.13: The Deformed Profile of a V-Plate (90 degrees) Exploded by a PE4 Disc (10g) As Predicted By ABAQUS Using the JWL Equation of State

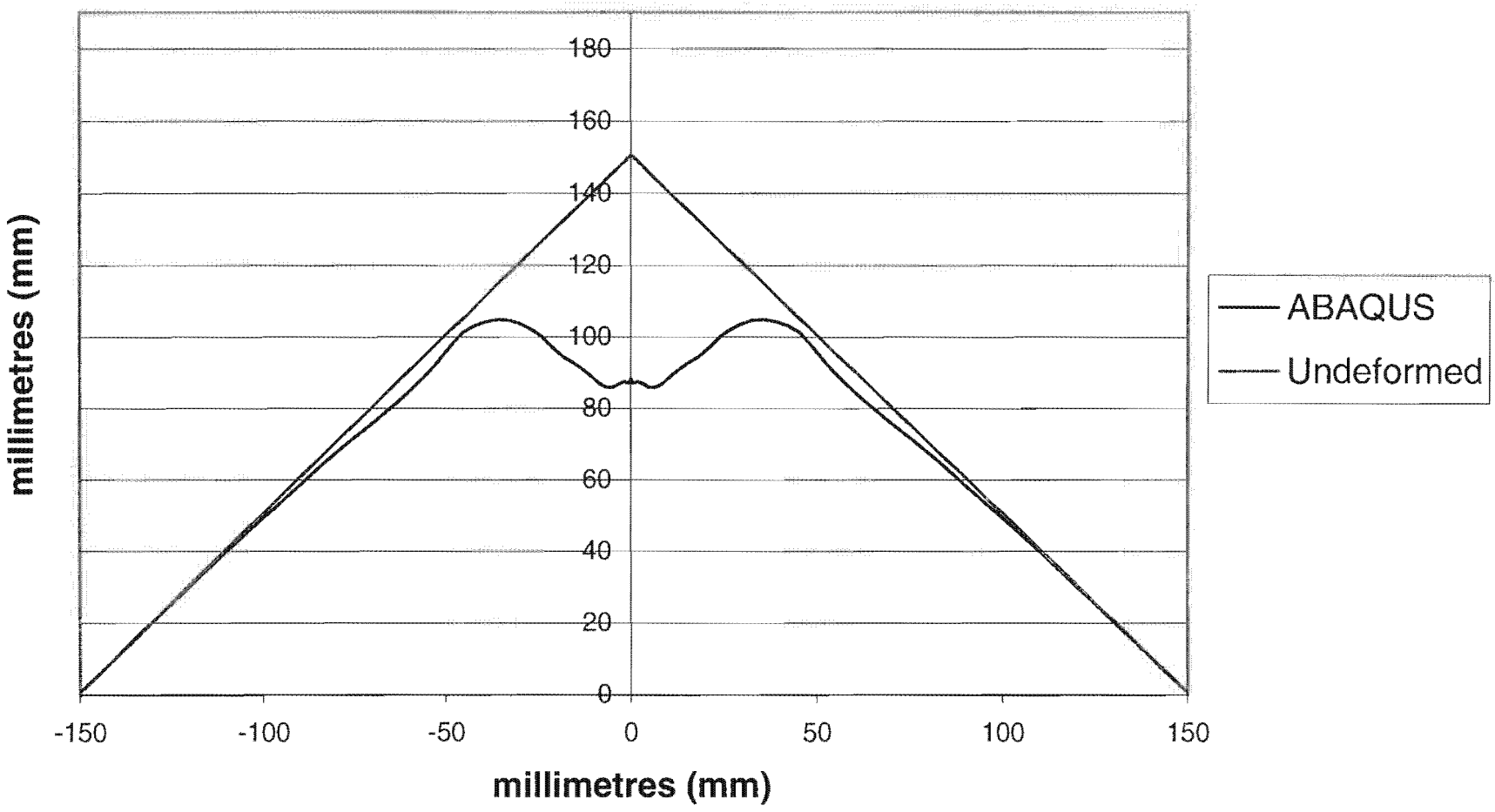

Figure D.14: The Deformed Profile of a V-Plate (90 degrees) Exploded by a PE4 Disc (12g) As Predicted By ABAQUS Using the JWL Equation of State

9.4.3 JWL Equation of State Method Numerically Predicted Deformed V-Plate Profiles for the 120^0 V-Plates

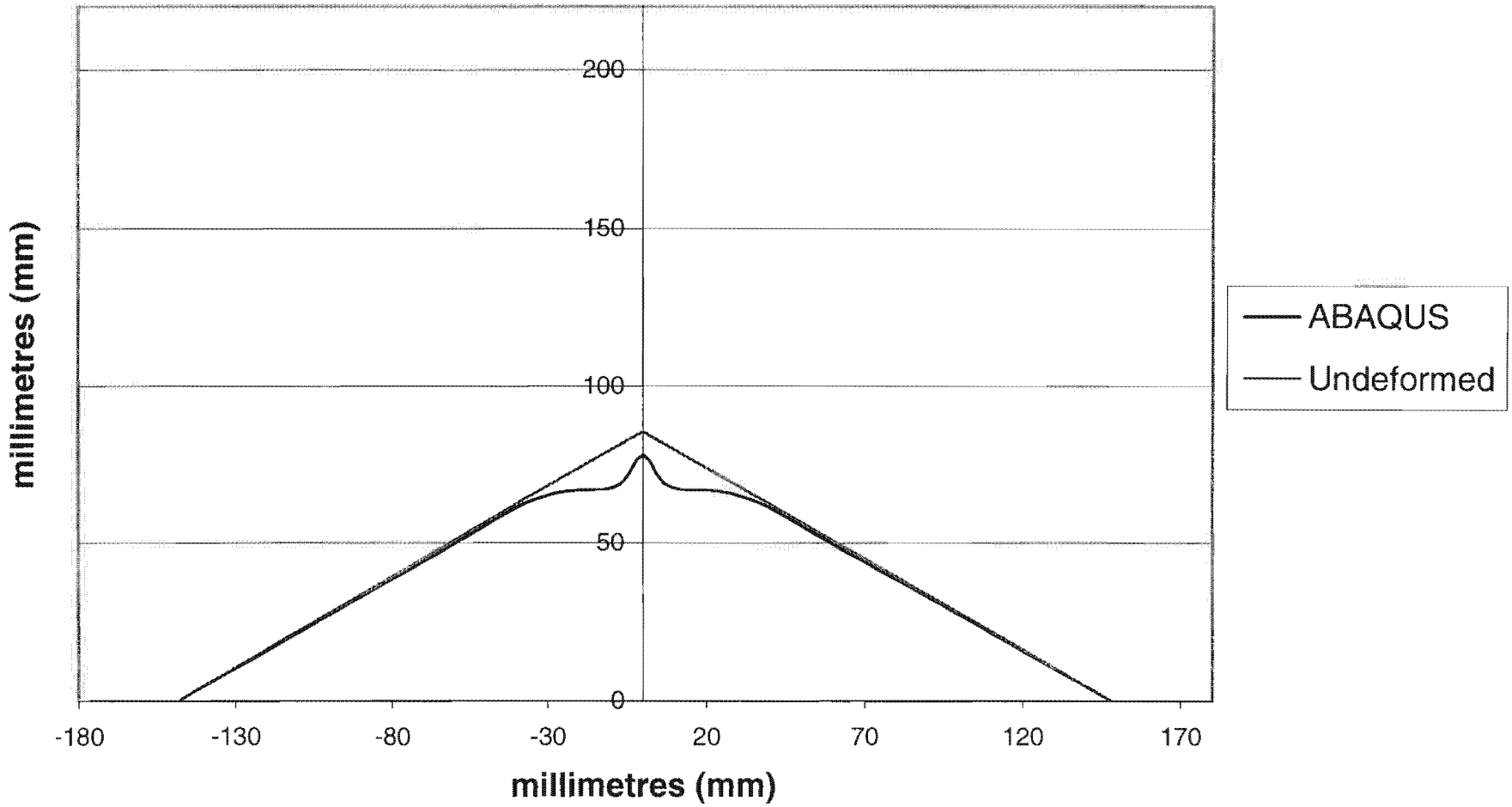

Figure D.15: The Deformed Profile of a V-Plate (120 degrees) Exploded by a PE4 Disc (4g) As Predicted By ABAQUS Using the JWL Equation of State

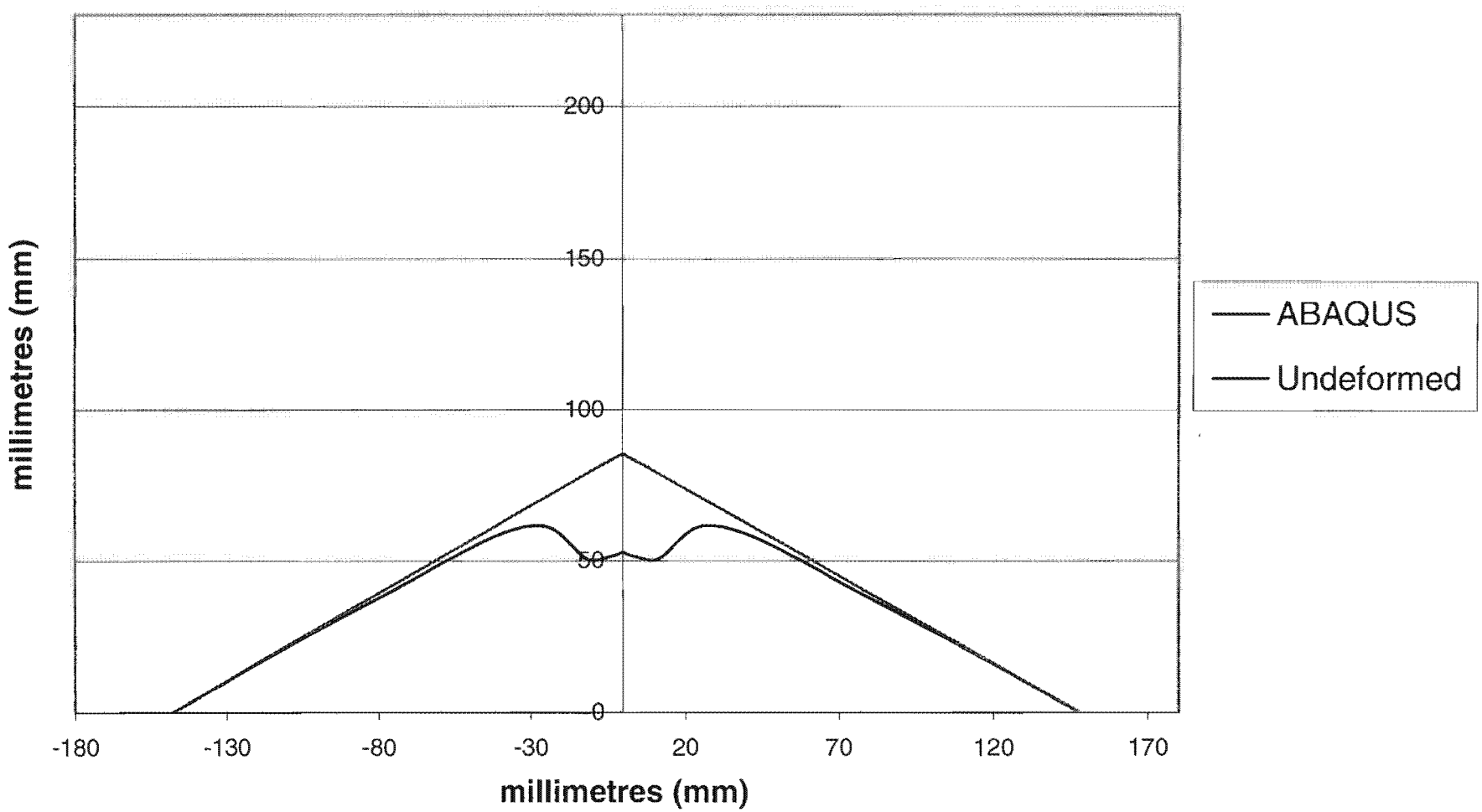

Figure D.16: The Deformed Profile of a V-Plate (120 degrees) Exploded by a PE4 Disc (6g) As Predicted By ABAQUS Using the JWL Equation of State

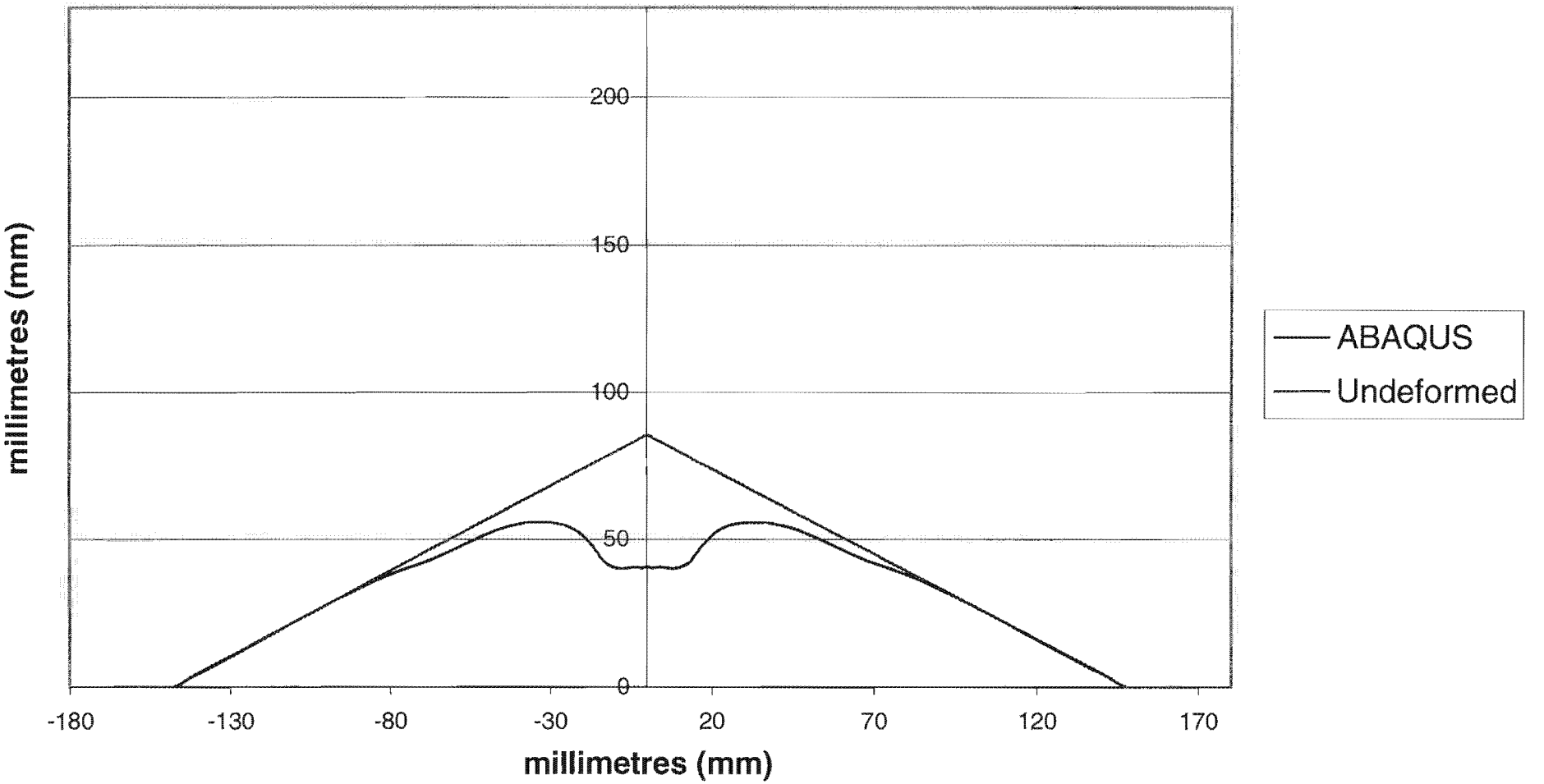

Figure D.17: The Deformed Profile of a V-Plate (120 degrees) Exploded by a PE4 Disc (8g) As Predicted By ABAQUS Using the JWL Equation of State

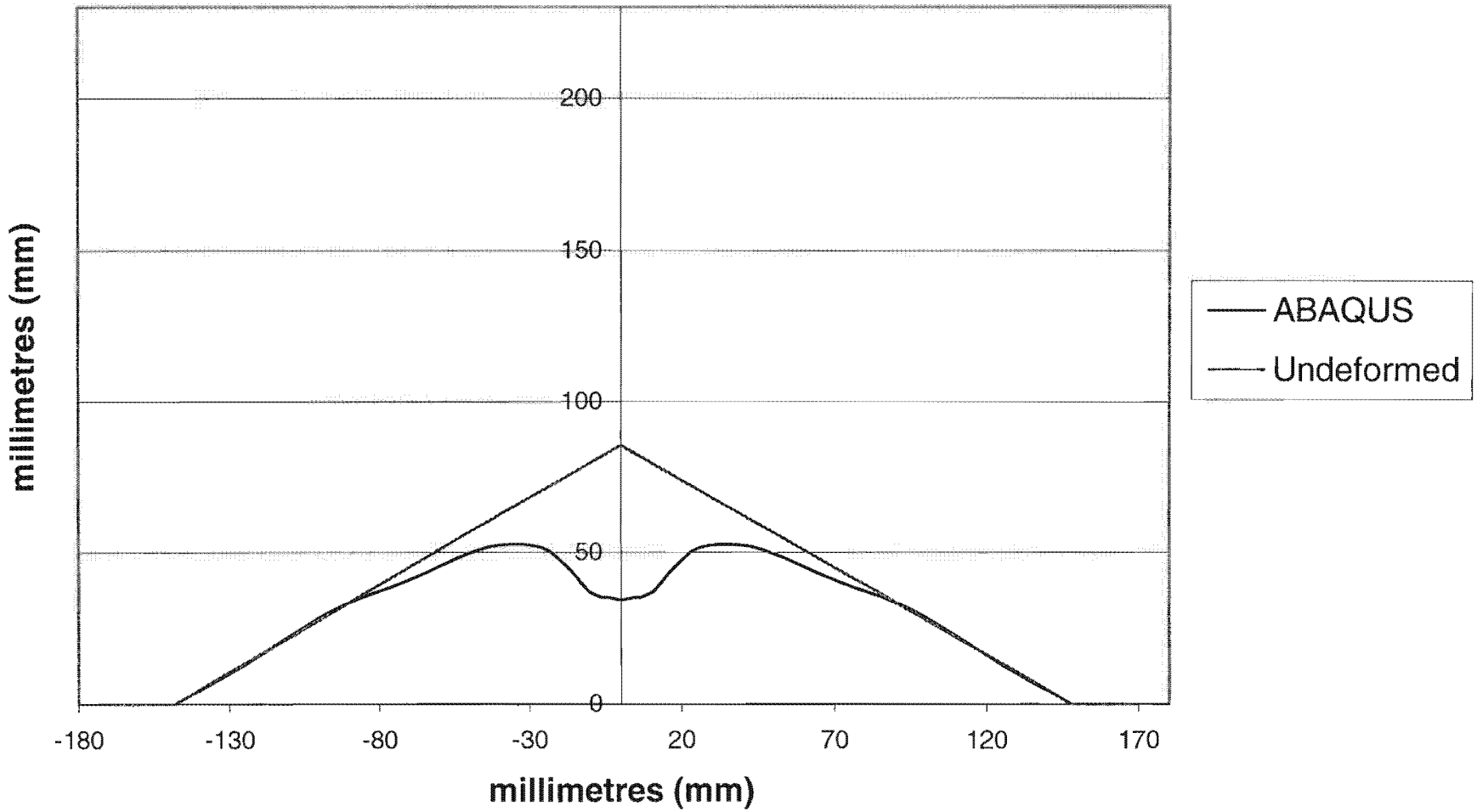

Figure D.18: The Deformed Profile of a V-Plate (120 degrees) Exploded by a PE4 Disc (10g) As Predicted By ABAQUS Using the JWL Equation of State

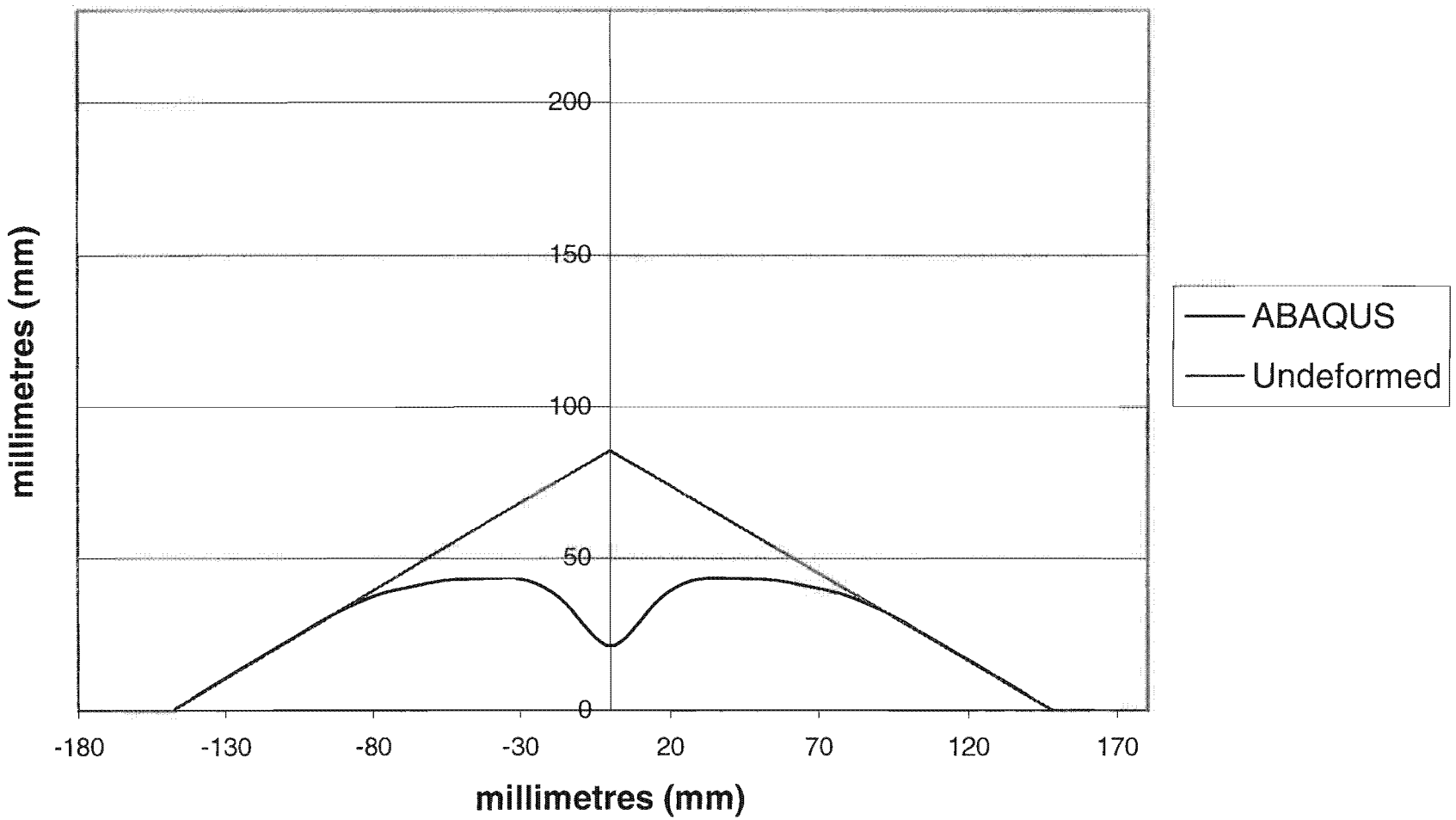

Figure D.19: The Deformed Profile of a V-Plate (120 degrees) Exploded by a PE4 Disc (12g) As Predicted By ABAQUS Using the JWL Equation of State

9.4.4 JWL Equation of State Method Numerically Predicted Deformed V-Plate Profiles for the 150^0 V-Plates

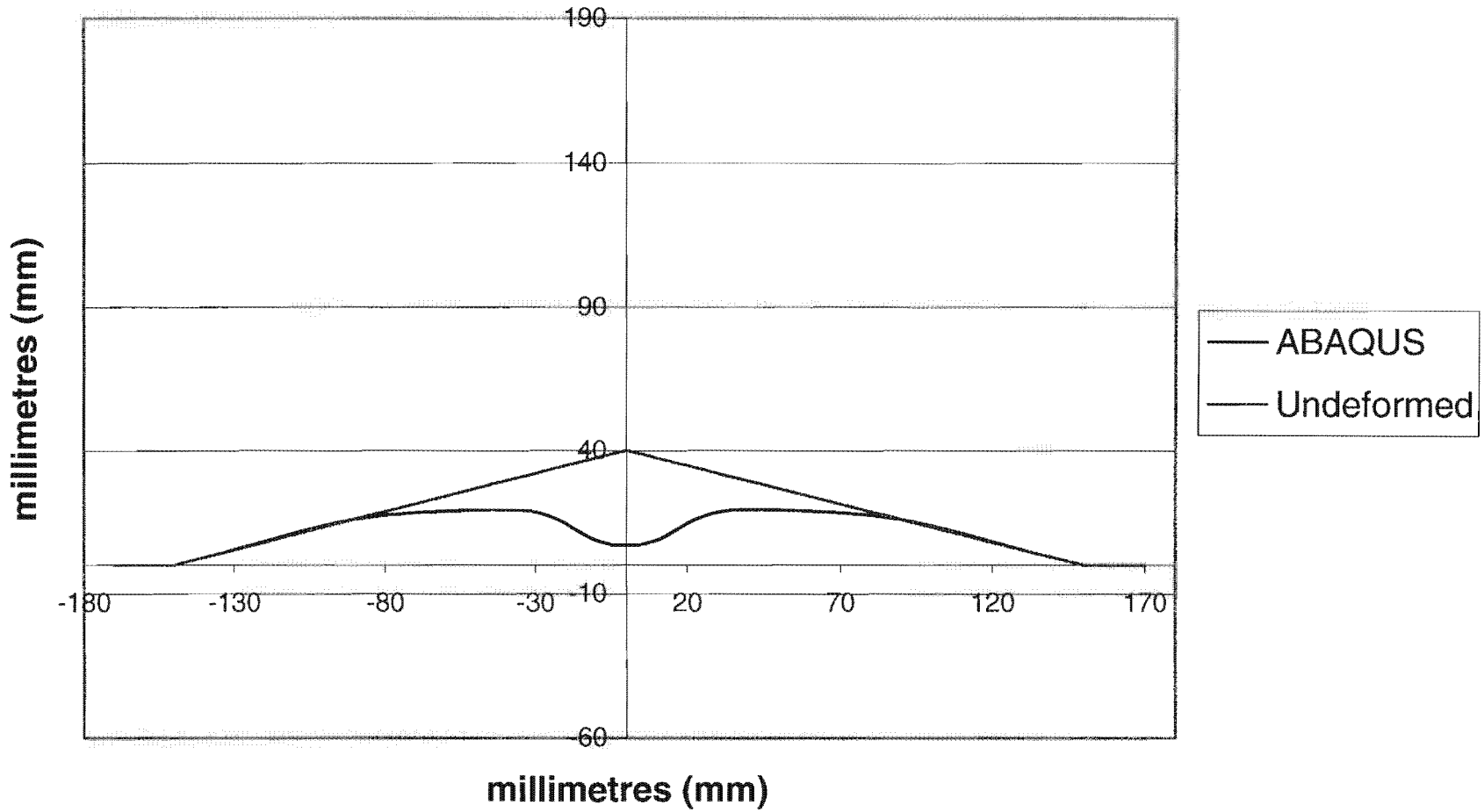

Figure D.20: The Deformed Profile of a V-Plate (150 degrees) Exploded by a PE4 Disc (4g) As Predicted By ABAQUS Using the JWL Equation of State

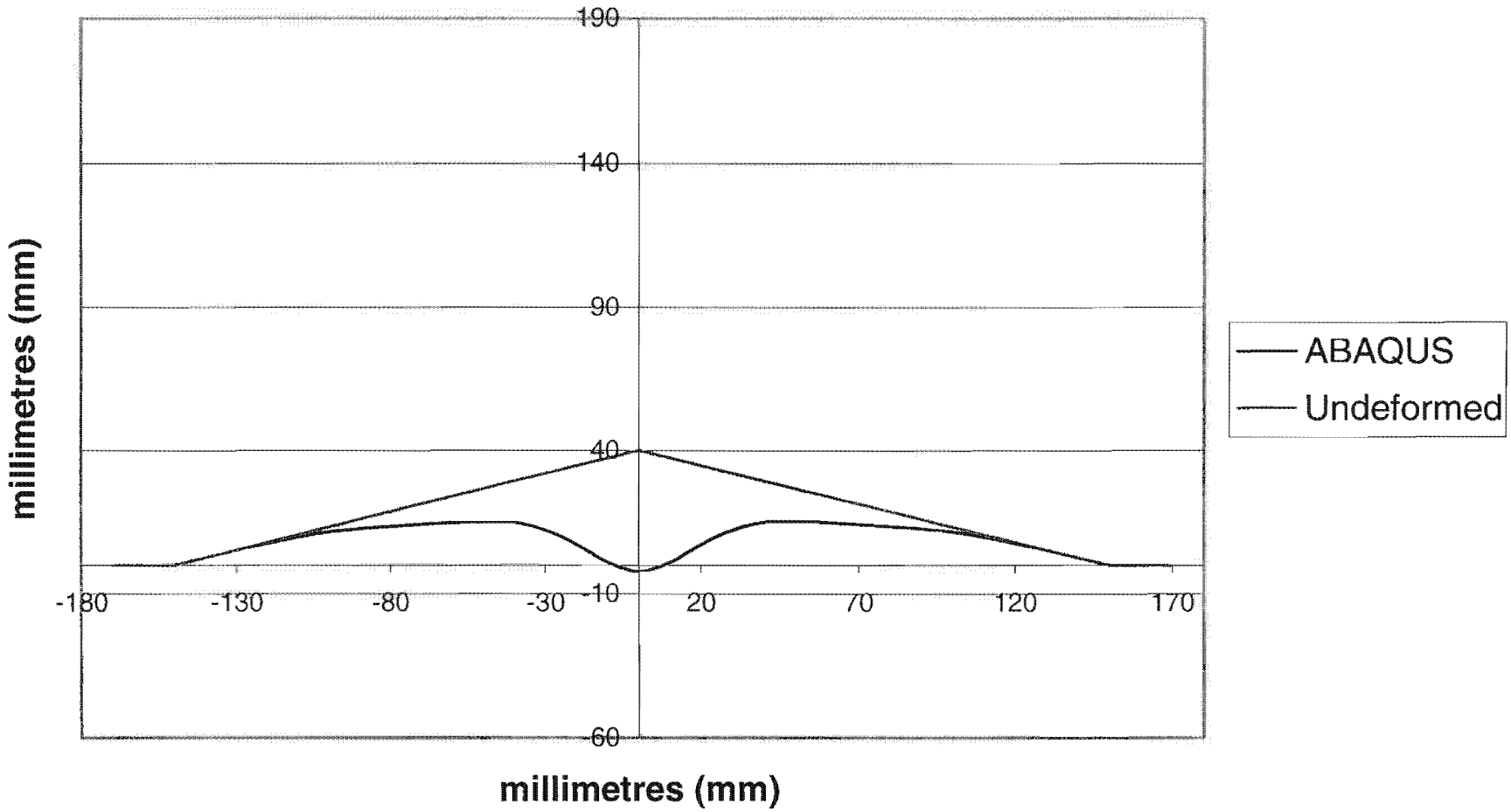

Figure D.21: The Deformed Profile of a V-Plate (150 degrees) Exploded by a PE4 Disc (6g) As Predicted By ABAQUS Using the JWL Equation of State

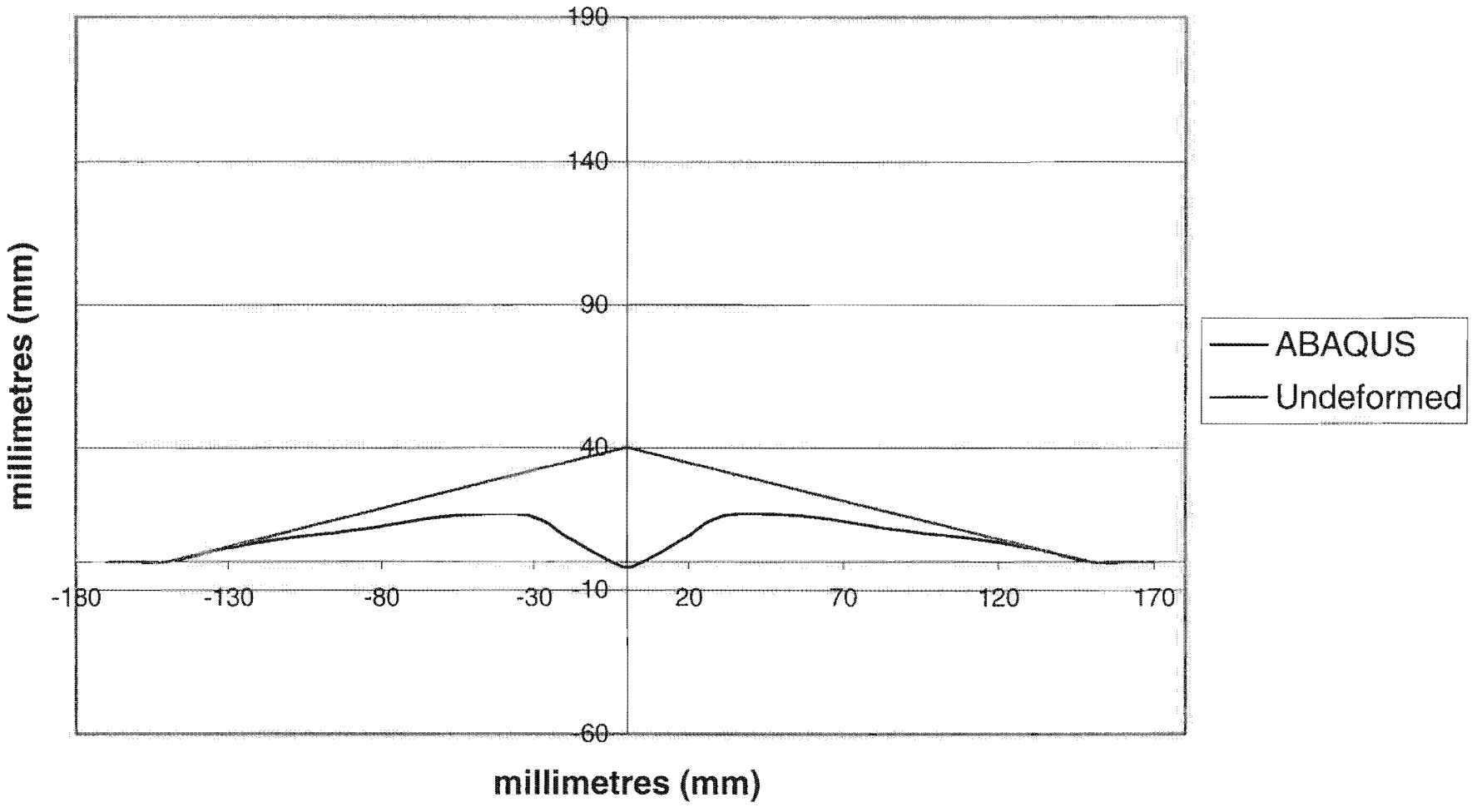

Figure D.22: The Deformed Profile of a V-Plate (150 degrees) Exploded by a PE4 Disc (8g) As Predicted By ABAQUS Using the JWL Equation of State

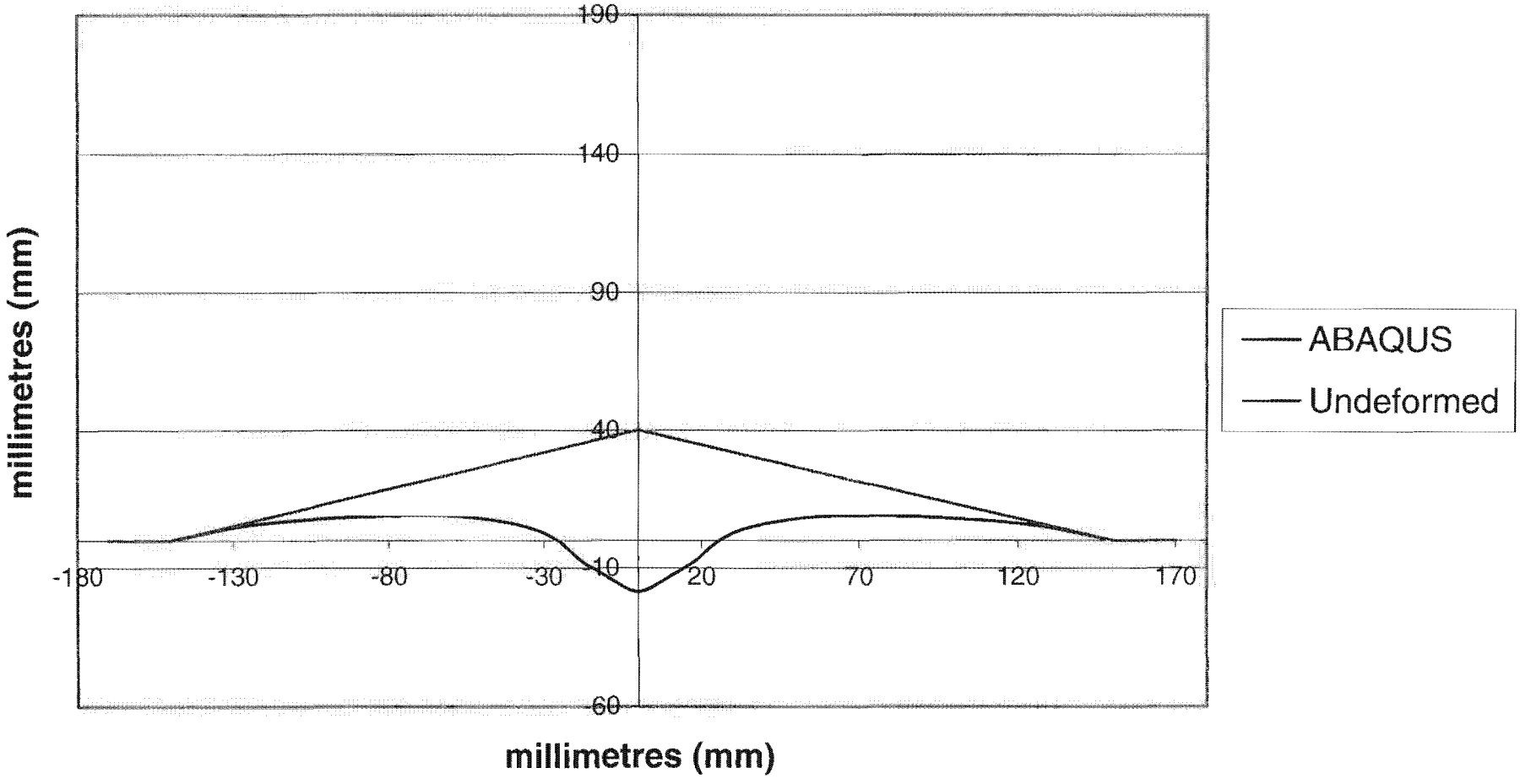

Figure D.23: The Deformed Profile of a V-Plate (150 degrees) Exploded by a PE4 Disc (10g) As Predicted By ABAQUS Using the JWL Equation of State

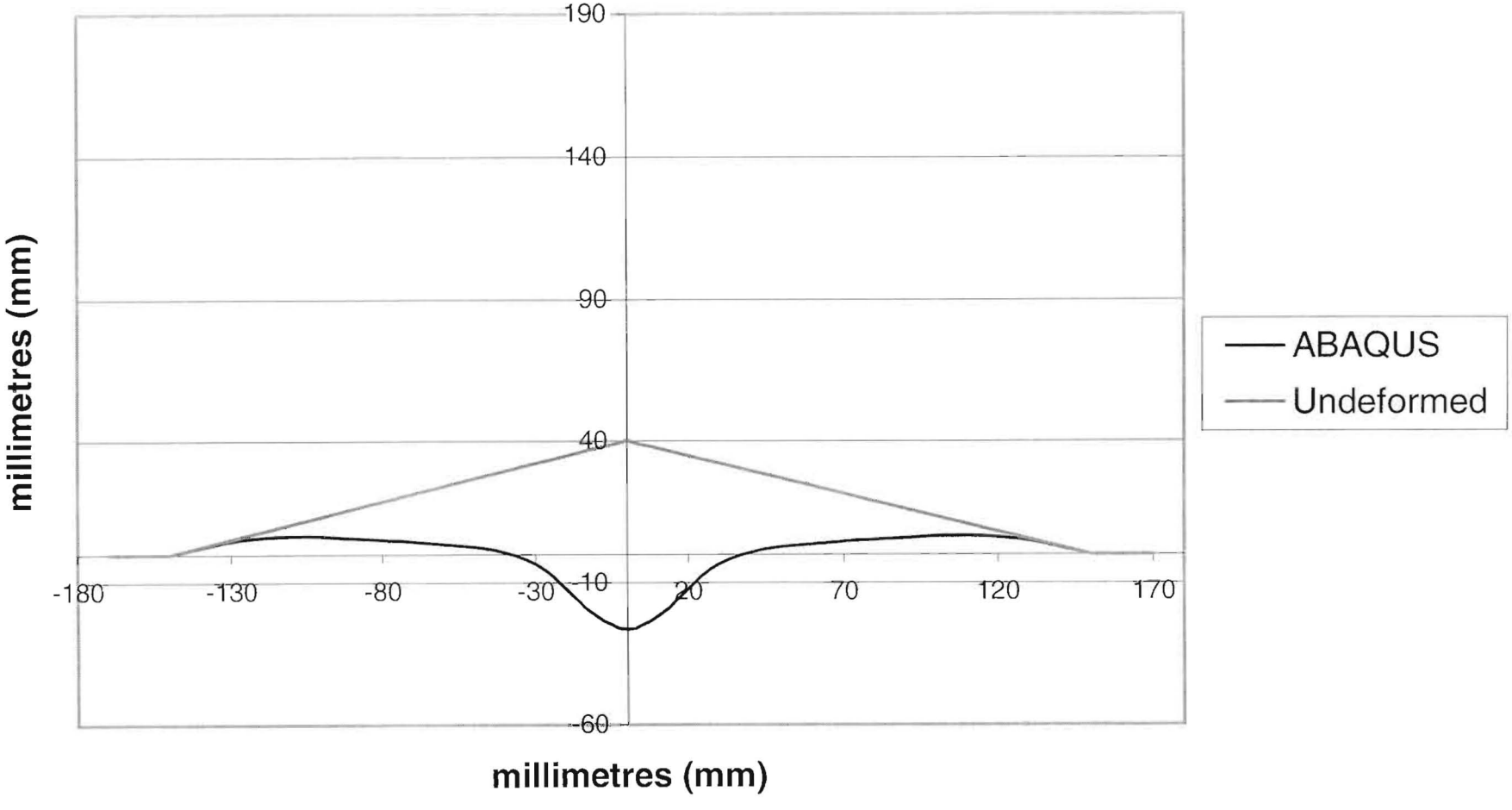

Figure D.24: The Deformed Profile of a V-Plate (150 degrees) Exploded by a PE4 Disc (12g) As Predicted By ABAQUS Using the JWL Equation of State

9.5 Appendix E: Co-Ordinates of the Deformed V-Plate Profiles Exploded by PE4 Rod Explosives for the Experimental and Numerically Predicted Profiles (Both the JWL Equation of State Method and Pressure Profile Method)

9.5.1 Co-Ordinates of the Deformed V-Plate Profiles for the 60^0 V-Plates

Table E.1: Co-Ordinates of the Deformed V-Plate Profiles for the 60^0 V-Plates and 3g rod explosive

3g Explosive Rod					
Experimental		ABAQUS (Press.)		ABAQUS (EOS)	
X-Coord (mm)	Y-Coord (mm)	X-Coord (mm)	Y-Coord (mm)	X-Coord (mm)	Y-Coord (mm)
161.281265	0	170	0	170	0
158.0809458	0.183018558	160	0	160	0
155.7387891	0.897345993	150	0	150	0
153.7069641	2.44636158	145.817	7.245	145.817	7.245
150.6176481	7.229827956	141.713	14.353	141.713	14.353
145.5173405	16.51744417	137.686	21.328	137.686	21.328
126.9242708	49.6469243	133.735	28.172	133.735	28.172
102.4369014	93.66921066	129.858	34.888	129.858	34.888
83.27000133	127.5932594	126.053	41.478	126.053	41.478
71.33923033	148.7159329	122.32	47.944	122.32	47.944
71.34405149	148.4775179	118.657	54.288	118.657	54.288
41.97003827	201.099601	115.062	60.514	115.062	60.514
21.73868629	235.8780161	111.535	66.623	111.535	66.623
14.22559961	248.0513676	108.075	72.617	108.075	72.617
11.79852857	252.0442755	104.679	78.499	104.679	78.499
9.824371753	255.8525837	101.347	84.271	101.347	84.271
8.788545141	258.6777096	98.077	89.934	98.077	89.934
7.629174413	259.6508615	94.8687	95.491	94.8687	95.491
6.281264954	260	91.7207	100.943	91.7207	100.943
5.197726548	259.5405272	88.6317	106.293	88.6317	106.293
4.135856756	258.6717317	85.6006	111.543	85.6006	111.543
2.917943326	256.5649434	82.6265	116.695	82.6265	116.695
-1.565791007	249.1811551	79.7081	121.749	79.7081	121.749
-18.43885628	220.5147955	76.8445	126.709	76.8445	126.709
-35.85588025	189.5670783	74.0347	131.576	74.0347	131.576
-47.60375598	168.723919	71.2775	136.352	71.2775	136.352
-54.08123398	157.1466149	68.5721	141.038	68.5721	141.038
-54.0704008	156.9419545	65.9174	145.636	65.9174	145.636
-75.52907591	118.63051	63.3126	150.147	63.3126	150.147
-102.8671066	69.99981683	60.7566	154.574	60.7566	154.574
-105.281265	65.37691954	58.2486	158.918	58.2486	158.918
		55.7877	163.1809	55.7877	163.1809
		53.3729	167.3634	53.3729	167.3634
		51.0034	171.4675	51.0034	171.4675
		48.6784	175.4945	48.6784	175.4945
		46.3971	179.4459	46.3971	179.4459
		44.1585	183.3233	44.1585	183.3233
		41.9619	187.1278	41.9619	187.1278
		39.8066	190.861	39.8066	190.861
		37.6916	194.5242	37.6916	194.5242
		contd.	contd.	contd.	contd.

35.6164	198.1186	35.6164	198.1186
33.5801	201.6455	33.5801	201.6455
31.582	205.1063	31.582	205.1063
29.6214	208.5022	29.6214	208.5022
27.6976	211.8343	27.6976	211.8343
25.8099	215.1039	25.8099	215.1039
23.9576	218.3122	23.9576	218.3122
22.1401	221.4602	22.1401	221.4602
20.3567	224.5492	20.3567	224.5492
18.6067	227.5803	18.6067	227.5803
16.8896	230.5544	16.8896	230.5544
15.2046	233.4728	15.2046	233.4728
13.5513	236.3364	13.5513	236.3364
11.9291	239.1463	11.9291	239.1463
10.3372	241.9034	10.3372	241.9034
8.77525	244.6088	8.77525	244.6088
7.24259	247.2635	7.24259	247.2635
5.73869	249.86831	5.73869	249.86831
4.263	252.42427	4.263	252.42427
2.815	254.93228	2.815	254.93228
1.39417	257.39323	1.39417	257.39323
0	259.808	0	259.808
-1.39417	257.39323	-1.39417	257.39323
-2.815	254.93228	-2.815	254.93228
-4.263	252.42427	-4.263	252.42427
-5.73869	249.86831	-5.73869	249.86831
-7.24259	247.2635	-7.24259	247.2635
-8.77525	244.6088	-8.77525	244.6088
-10.3372	241.9034	-10.3372	241.9034
-11.9291	239.1463	-11.9291	239.1463
-13.5513	236.3364	-13.5513	236.3364
-15.2046	233.4728	-15.2046	233.4728
-16.8896	230.5544	-16.8896	230.5544
-18.6067	227.5803	-18.6067	227.5803
-20.3567	224.5492	-20.3567	224.5492
-22.1401	221.4602	-22.1401	221.4602
-23.9576	218.3122	-23.9576	218.3122
-25.8099	215.1039	-25.8099	215.1039
-27.6976	211.8343	-27.6976	211.8343
-29.6214	208.5022	-29.6214	208.5022
-31.582	205.1063	-31.582	205.1063
-33.5801	201.6455	-33.5801	201.6455
-35.6164	198.1186	-35.6164	198.1186
-37.6916	194.5242	-37.6916	194.5242
-39.8066	190.861	-39.8066	190.861
-41.9619	187.1278	-41.9619	187.1278
-44.1585	183.3233	-44.1585	183.3233
-46.3971	179.4459	-46.3971	179.4459
-48.6784	175.4945	-48.6784	175.4945
-51.0034	171.4675	-51.0034	171.4675
-53.3729	167.3634	-53.3729	167.3634
-55.7877	163.1809	-55.7877	163.1809
-58.2486	158.918	-58.2486	158.918

contd. contd. contd. contd.

-60.7566	154.574	-60.7566	154.574
-63.3126	150.147	-63.3126	150.147
-65.9174	145.636	-65.9174	145.636
-68.5721	141.038	-68.5721	141.038
-71.2775	136.352	-71.2775	136.352
-74.0347	131.576	-74.0347	131.576
-76.8445	126.709	-76.8445	126.709
-79.7081	121.749	-79.7081	121.749
-82.6265	116.695	-82.6265	116.695
-85.6006	111.543	-85.6006	111.543
-88.6317	106.293	-88.6317	106.293
-91.7207	100.943	-91.7207	100.943
-94.8687	95.491	-94.8687	95.491
-98.077	89.934	-98.077	89.934
-101.347	84.271	-101.347	84.271
-104.679	78.499	-104.679	78.499
-108.075	72.617	-108.075	72.617
-111.535	66.623	-111.535	66.623
-115.062	60.514	-115.062	60.514
-118.657	54.288	-118.657	54.288
-122.32	47.944	-122.32	47.944
-126.053	41.478	-126.053	41.478
-129.858	34.888	-129.858	34.888
-133.735	28.172	-133.735	28.172
-137.686	21.328	-137.686	21.328
-141.713	14.353	-141.713	14.353
-145.817	7.245	-145.817	7.245
-150	0	-150	0
-160	0	-160	0
-170	0	-170	0

Table E.2: Co-Ordinates of the Deformed V-Plate Profiles for the 60^0 V-Plates and 5g rod explosive

5g Explosive Rod					
Experimental		ABAQUS (Press.)		ABAQUS (EOS)	
X-Coord (mm)	Y-Coord (mm)	X-Coord (mm)	Y-Coord (mm)	X-Coord (mm)	Y-Coord (mm)
156.1669689	0	170	0	170	0
124.39496	48.86439018	160	0	160	0
91.83866178	100.9670805	150	0	150	0
63.76129608	147.9819041	145.817	7.245	145.815	7.242
32.01691617	203.151739	141.713	14.353	141.717	14.35
32.01691617	203.151739	137.686	21.328	137.694	21.324
11.33559497	239.0759767	133.735	28.172	133.738	28.158
6.051741155	248.0537475	129.858	34.888	129.854	34.858
4.324878767	252.3517443	126.053	41.478	126.041	41.435
3.292912749	256.2350701	122.32	47.944	122.311	47.902
2.776929707	258.1767341	118.657	54.288	118.66	54.265
1.166968886	258.7822916	115.062	60.514	115.089	60.523
0.066116705	257.6633893	111.535	66.623	111.578	66.661
0.107376101	256.3601748	108.075	72.617	108.114	72.663
-0.972848636	254.5896663	104.679	78.499	104.702	78.521
-17.21058174	229.1180262	101.347	84.271	101.35	84.245
-80.77185331	119.2278809	98.077	89.934	98.0735	89.855
-98.05542838	90.89972195	94.8687	95.491	94.8761	95.373
-98.05542838	90.89972195	91.7207	100.943	91.7384	100.81
-115.1669689	64.3157579	88.6317	106.293	88.6533	106.166
		85.6006	111.543	85.6181	111.433
		82.6265	116.695	82.6188	116.604
		79.7081	121.749	79.6803	121.676
		76.8445	126.709	76.8102	126.651
		74.0347	131.576	74.0185	131.531
		71.2775	136.352	71.301	136.316
		68.5721	141.038	68.642	141.001
		65.9174	145.636	66.0289	145.582
		63.3126	150.147	63.4535	150.056
		60.7566	154.574	60.9096	154.426
		58.2486	158.918	58.3935	158.701
		55.7877	163.1809	55.9172	162.8957
		53.3729	167.3634	53.4827	167.0223
		51.0034	171.4675	51.0987	171.0901
		48.6784	175.4945	48.7593	175.0992
		46.3971	179.4459	46.4635	179.0549
		44.1585	183.3233	44.2171	182.9481
		41.9619	187.1278	42.0147	186.7771
		39.8066	190.861	39.8551	190.5305
		37.6916	194.5242	37.7389	194.2159
		35.6164	198.1186	35.6639	197.8232
		33.5801	201.6455	33.6285	201.345
		31.582	205.1063	31.6259	204.7663
		29.6214	208.5022	29.6425	208.0737
		27.6976	211.8343	27.7185	211.3446
		25.8099	215.1039	25.8202	214.562
		23.9576	218.3122	23.9605	217.7027
		22.1401	221.4602	22.1553	220.7769
		20.3567	224.5492	20.356	223.8098
		18.6067	227.5803	18.5798	226.7802
		16.8896	230.5544	16.8529	229.6913

contd. contd. contd. contd.

15.2046	233.4728	15.2244	232.519
13.5513	236.3364	13.6179	235.2702
11.9291	239.1463	12.0071	237.9844
10.3372	241.9034	10.5324	240.6414
8.77525	244.6088	9.18014	243.2338
7.24259	247.2635	7.96826	245.7431
5.73869	249.86831	6.70893	248.1841
4.263	252.42427	4.95221	250.5969
2.815	254.93228	3.06142	252.84608
1.39417	257.39323	1.64221	254.67972
0	259.808	-1.43051E-05	256.58704
-1.39417	257.39323	-1.64221	254.67972
-2.815	254.93228	-3.06142	252.84608
-4.263	252.42427	-4.95221	250.5969
-5.73869	249.86831	-6.70893	248.1841
-7.24259	247.2635	-7.96826	245.7431
-8.77525	244.6088	-9.18014	243.2338
-10.3372	241.9034	-10.5324	240.6414
-11.9291	239.1463	-12.0071	237.9844
-13.5513	236.3364	-13.6179	235.2702
-15.2046	233.4728	-15.2244	232.519
-16.8896	230.5544	-16.8529	229.6913
-18.6067	227.5803	-18.5798	226.7802
-20.3567	224.5492	-20.356	223.8098
-22.1401	221.4602	-22.1553	220.7769
-23.9576	218.3122	-23.9605	217.7027
-25.8099	215.1039	-25.8202	214.562
-27.6976	211.8343	-27.7185	211.3446
-29.6214	208.5022	-29.6425	208.0737
-31.582	205.1063	-31.6259	204.7663
-33.5801	201.6455	-33.6285	201.345
-35.6164	198.1186	-35.6639	197.8232
-37.6916	194.5242	-37.7389	194.2159
-39.8066	190.861	-39.8551	190.5305
-41.9619	187.1278	-42.0147	186.7771
-44.1585	183.3233	-44.2171	182.9481
-46.3971	179.4459	-46.4635	179.0549
-48.6784	175.4945	-48.7593	175.0992
-51.0034	171.4675	-51.0987	171.0901
-53.3729	167.3634	-53.4827	167.0223
-55.7877	163.1809	-55.9172	162.8957
-58.2486	158.918	-58.3935	158.701
-60.7566	154.574	-60.9096	154.426
-63.3126	150.147	-63.4535	150.056
-65.9174	145.636	-66.0289	145.582
-68.5721	141.038	-68.642	141.001
-71.2775	136.352	-71.301	136.316
-74.0347	131.576	-74.0185	131.531
-76.8445	126.709	-76.8102	126.651
-79.7081	121.749	-79.6803	121.676
-82.6265	116.695	-82.6188	116.604
-85.6006	111.543	-85.6181	111.433
-88.6317	106.293	-88.6533	106.166
-91.7207	100.943	-91.7384	100.81

contd. contd. contd. contd.

-94.8687	95.491	-94.8761	95.373
-98.077	89.934	-98.0735	89.855
-101.347	84.271	-101.35	84.245
-104.679	78.499	-104.702	78.521
-108.075	72.617	-108.114	72.663
-111.535	66.623	-111.578	66.661
-115.062	60.514	-115.089	60.523
-118.657	54.288	-118.66	54.265
-122.32	47.944	-122.311	47.902
-126.053	41.478	-126.041	41.435
-129.858	34.888	-129.854	34.858
-133.735	28.172	-133.738	28.158
-137.686	21.328	-137.694	21.324
-141.713	14.353	-141.717	14.35
-145.817	7.245	-145.815	7.242
-150	0	-150	0
-160	0	-160	0
-170	0	-170	0

Table E.3: Co-Ordinates of the Deformed V-Plate Profiles for the 60^0 V-Plates and 7g rod explosive

7g Explosive Rod					
Experimental		ABAQUS (Press.)		ABAQUS (EOS)	
X-Coord (mm)	Y-Coord (mm)	X-Coord (mm)	Y-Coord (mm)	X-Coord (mm)	Y-Coord (mm)
151.0178368	0	-85.95505618	111.3148327	170	0
86.61682206	109.7008073	-10.93973442	240.1088541	160	0
46.94520722	177.8570884	-4.68845761	249.308427	150	0
28.9298763	208.0961894	-2.031664964	256.9747378	145.815	7.243
18.07023256	225.0128096	0	258.508	141.717	14.351
5.57942488	242.7179675	2.031664964	256.9747378	137.694	21.327
2.434186197	247.5074118	4.68845761	249.308427	133.738	28.169
0.658787055	250.6201395	10.93973442	240.1088541	129.854	34.878
-0.503813756	254.0566058	85.95505618	111.3148327	126.041	41.46
-1.350996797	257.5096766			122.311	47.924
-2.982163213	258.2982141			118.66	54.273
-3.748114739	255.3431575			115.089	60.509
-4.459978121	251.5165305			111.578	66.626
-9.28115878	242.5185058			108.114	72.618
-34.5857196	201.5459024			104.702	78.489
-55.20422083	166.649478			101.35	84.246
-97.97312881	90.94651593			98.0735	89.901
-125.6178368	42.17965517			94.8761	95.458
				91.7384	100.915
				88.6533	106.266
				85.6181	111.508
				82.6188	116.645
				79.6803	121.683
				76.8102	126.634
				74.0185	131.505
				71.301	136.298
				68.642	141.007
				66.0289	145.628
				63.4535	150.154
				60.9096	154.585
				58.3935	158.922
				55.9172	163.1718
				53.4827	167.338
				51.0987	171.4259
				48.7593	175.4344
				46.4635	179.3694
				44.2171	183.2272
				42.0147	187.0122
				39.8551	190.7175
				37.7389	194.3499
				35.6639	197.9022
				33.6285	201.3737
				31.6259	204.7476
				29.6425	208.0391
				27.7185	211.3368
				25.8202	214.5472
				23.9605	217.683
				22.1553	220.7735
				20.356	223.8259
				18.5798	226.8027
				16.8529	229.7065

contd. contd.

15.2244	232.5614
13.6179	235.3383
12.0071	238.0307
10.5324	240.6193
9.18014	243.1244
7.96826	245.6239
6.70893	248.0262
4.95221	250.2367
3.06142	251.68967
1.64221	252.86363
-1.43051E-05	253.86991
-1.64221	252.86363
-3.06142	251.68967
-4.95221	250.2367
-6.70893	248.0262
-7.96826	245.6239
-9.18014	243.1244
-10.5324	240.6193
-12.0071	238.0307
-13.6179	235.3383
-15.2244	232.5614
-16.8529	229.7065
-18.5798	226.8027
-20.356	223.8259
-22.1553	220.7735
-23.9605	217.683
-25.8202	214.5472
-27.7185	211.3368
-29.6425	208.0391
-31.6259	204.7476
-33.6285	201.3737
-35.6639	197.9022
-37.7389	194.3499
-39.8551	190.7175
-42.0147	187.0122
-44.2171	183.2272
-46.4635	179.3694
-48.7593	175.4344
-51.0987	171.4259
-53.4827	167.338
-55.9172	163.1718
-58.3935	158.922
-60.9096	154.585
-63.4535	150.154
-66.0289	145.628
-68.642	141.007
-71.301	136.298
-74.0185	131.505
-76.8102	126.634
-79.6803	121.683
-82.6188	116.645
-85.6181	111.508
-88.6533	106.266
-91.7384	100.915

contd. contd.

-94.8761	95.458
-98.0735	89.901
-101.35	84.246
-104.702	78.489
-108.114	72.618
-111.578	66.626
-115.089	60.509
-118.66	54.273
-122.311	47.924
-126.041	41.46
-129.854	34.878
-133.738	28.169
-137.694	21.327
-141.717	14.351
-145.815	7.243
-150	0
-160	0
-170	0

Table E.4: Co-Ordinates of the Deformed V-Plate Profiles for the 60^0 V-Plates and 9g rod explosive

9g Explosive Rod					
Experimental		ABAQUS (Press.)		ABAQUS (EOS)	
X-Coord (mm)	Y-Coord (mm)	X-Coord (mm)	Y-Coord (mm)	X-Coord (mm)	Y-Coord (mm)
150.6222375	0	-80.05617978	120.1642945	170	0
98.32057433	86.16945526	-11.49897855	239.7155059	160	0
52.72991117	164.9030776	-3.493360572	250.4444608	150	0
25.98598056	208.6644777	-1.455566905	255.962209	145.813	7.242
9.883991902	232.8870316	0	258.108	141.715	14.349
6.585887485	239.4100765	1.455566905	255.962209	137.696	21.328
5.286364896	243.2112873	3.493360572	250.4444608	133.747	28.172
2.81683603	248.0161461	11.49897855	239.7155059	129.857	34.881
2.313511472	250.7985596	80.05617978	120.1642945	126.039	41.46
-0.757950174	252.4258805			122.307	47.923
-2.984650307	251.9853181			118.662	54.272
2.457737959	239.5931845			115.093	60.51
2.621098171	244.1543611			111.583	66.628
0.654890812	246.1768089			108.119	72.62
-2.319438019	245.7059581			104.702	78.487
-6.610947884	241.3278924			101.345	84.24
-15.40589703	229.0596675			98.0672	89.893
-26.59090385	211.7897093			94.8734	95.453
-46.42516378	179.104274			91.7508	100.916
-67.21897609	142.8764597			88.6774	106.273
-89.71997815	103.075975			85.6412	111.518
-146.6222375	5.475373176			82.6398	116.653
				79.6898	121.685
				76.8116	126.629
				74.0094	131.493
				71.284	136.28
				68.6236	140.986
				66.0071	145.603
				63.4304	150.125
				60.881	154.551
				58.3659	158.884
				55.8919	163.1302
				53.4653	167.2959
				51.0898	171.3824
				48.7584	175.3911
				46.4776	179.3202
				44.2471	183.1748
				42.0692	186.9491
				39.9359	190.6425
				37.836	194.2387
				35.7621	197.7513
				33.7007	201.2494
				31.6665	204.6822
				29.6692	208.0543
				27.7192	211.3513
				25.8357	214.591
				23.9964	217.7616
				22.2104	220.8806
				20.4351	223.9269
				18.6595	226.891
				17.0141	229.8032

contd. contd.

15.3864	232.6644
13.7534	235.4412
12.1766	238.1107
10.6647	240.7256
9.24058	243.221
7.94866	245.7021
6.35971	247.9492
4.86186	250.22938
3.08661	252.00894
1.86211	253.47895
-6.67572E-05	253.99601
-1.86211	253.47895
-3.08661	252.00894
-4.86186	250.22938
-6.35971	247.9492
-7.94866	245.7021
-9.24058	243.221
-10.6647	240.7256
-12.1766	238.1107
-13.7534	235.4412
-15.3864	232.6644
-17.0141	229.8032
-18.6595	226.891
-20.4351	223.9269
-22.2104	220.8806
-23.9964	217.7616
-25.8357	214.591
-27.7192	211.3513
-29.6692	208.0543
-31.6665	204.6822
-33.7007	201.2494
-35.7621	197.7513
-37.836	194.2387
-39.9359	190.6425
-42.0692	186.9491
-44.2471	183.1748
-46.4776	179.3202
-48.7584	175.3911
-51.0898	171.3824
-53.4653	167.2959
-55.8919	163.1302
-58.3659	158.884
-60.881	154.551
-63.4304	150.125
-66.0071	145.603
-68.6236	140.986
-71.284	136.28
-74.0094	131.493
-76.8116	126.629
-79.6898	121.685
-82.6398	116.653
-85.6412	111.518
-88.6774	106.273
-91.7508	100.916

contd. contd.

-94.8734	95.453
-98.0672	89.893
-101.345	84.24
-104.702	78.487
-108.119	72.62
-111.583	66.628
-115.093	60.51
-118.662	54.272
-122.307	47.923
-126.039	41.46
-129.857	34.881
-133.747	28.172
-137.696	21.328
-141.715	14.349
-145.813	7.242
-150	0
-160	0
-170	0

Table E.5: Co-Ordinates of the Deformed V-Plate Profiles for the 60^0 V-Plates and 11g rod explosive

11g Explosive Rod					
Experimental		ABAQUS (Press.)		ABAQUS (EOS)	
X-Coord (mm)	Y-Coord (mm)	X-Coord (mm)	Y-Coord (mm)	X-Coord (mm)	Y-Coord (mm)
145.801143	9.606878107	-81.44171779	117.1748269	170	0
103.7051145	85.26862047	-23.46625767	219.9328558	160	0
45.07218019	184.9902296	-18	230.3620288	150	0
31.43629835	205.7593616	-12.42331288	238.3372788	145.776	7.233
22.69871718	217.5418098	-2.760736196	246.0057885	141.698	14.331
15.94978338	224.105878	-1.380368098	253.0608173	137.672	21.312
10.20810961	227.3444096	0	255.208	133.714	28.154
2.116478042	229.5843109	1.380368098	253.0608173	129.765	34.847
-3.091380399	229.4886053	2.760736196	246.0057885	125.901	41.402
-8.256108022	227.0050897	12.42331288	238.3372788	122.19	47.855
-10.55430959	223.1410876	18	230.3620288	118.604	54.228
-11.46669354	221.2134348	23.46625767	219.9328558	115.106	60.517
-10.95012172	218.8343254	81.44171779	117.1748269	111.687	66.686
-7.136717358	217.4712397			108.264	72.709
0.062832939	256.2320609			104.84	78.576
0.332715012	258.0714688			101.418	84.297
-1.198857023	258.960547			98.0586	89.894
-1.749661764	255.8930135			94.7488	95.391
-1.677898166	251.9196933			91.541	100.803
-42.36610544	188.800716			88.4729	106.137
-64.43989962	152.3175793			85.4622	111.39
-86.20517349	115.5343697			82.5524	116.55
-103.2438524	85.56433284			79.6867	121.61
-103.2438524	85.56433284			76.8334	126.568
-150.801143	0			74.0377	131.425
				71.285	136.187
				68.5715	140.856
				65.9158	145.436
				63.3122	149.923
				60.7625	154.316
				58.219	158.614
				55.7423	162.833
				53.3106	166.9776
				51.0049	171.0516
				48.7252	175.0507
				46.5164	178.9715
				44.337	182.8055
				42.1744	186.5402
				40.0946	190.176
				38.0284	193.7077
				36.0204	197.1425
				33.9769	200.4638
				31.9651	203.8032
				29.9009	206.9636
				27.8641	210.1232
				25.8097	213.2002
				23.8847	216.164
				21.872	219.1058
				19.8833	221.893
				17.8336	224.6021
				15.6802	227.0452
				contd.	contd.

13.6761	229.4858
11.8289	231.9051
9.97567	234.2368
8.26444	236.4197
6.62919	238.6234
5.1156	240.7438
3.72582	242.9432
2.22468	245.0481
1.55729	246.8357
1.23469	248.7248
-3.33786E-05	250.30446
-1.23469	248.7248
-1.55729	246.8357
-2.22468	245.0481
-3.72582	242.9432
-5.1156	240.7438
-6.62919	238.6234
-8.26444	236.4197
-9.97567	234.2368
-11.8289	231.9051
-13.6761	229.4858
-15.6802	227.0452
-17.8336	224.6021
-19.8833	221.893
-21.872	219.1058
-23.8847	216.164
-25.8097	213.2002
-27.8641	210.1232
-29.9009	206.9636
-31.9651	203.8032
-33.9769	200.4638
-36.0204	197.1425
-38.0284	193.7077
-40.0946	190.176
-42.1744	186.5402
-44.337	182.8055
-46.5164	178.9715
-48.7252	175.0507
-51.0049	171.0516
-53.3106	166.9776
-55.7423	162.833
-58.219	158.614
-60.7625	154.316
-63.3122	149.923
-65.9158	145.436
-68.5715	140.856
-71.285	136.187
-74.0377	131.425
-76.8334	126.568
-79.6867	121.61
-82.5524	116.55
-85.4622	111.39
-88.4729	106.137
-91.541	100.803

contd. contd.

-94.7488	95.391
-98.0586	89.894
-101.418	84.297
-104.84	78.576
-108.264	72.709
-111.687	66.686
-115.106	60.517
-118.604	54.228
-122.19	47.855
-125.901	41.402
-129.765	34.847
-133.714	28.154
-137.672	21.312
-141.698	14.331
-145.776	7.233
-150	0
-160	0
-170	0

Table E.6: Co-Ordinates of the Deformed V-Plate Profiles for the 60^0 V-Plates and 13g rod explosive

13g Explosive Rod					
Experimental		ABAQUS (Press.)		ABAQUS (EOS)	
X-Coord (mm)	Y-Coord (mm)	X-Coord (mm)	Y-Coord (mm)	X-Coord (mm)	Y-Coord (mm)
143.2307735	10.01733583	-86.28834356	110.7337674	170	0
89.92484911	101.9864602	-31.24233129	206.4371897	160	0
68.4675286	136.7666955	-19.63803681	231.2832705	150	0
53.1777964	160.3657512	-15.17484663	237.1113635	145.84	7.236
43.00618092	175.3728043	-8.331288344	239.5652974	141.694	14.335
30.37888289	191.192751	-2.231595092	242.0192313	137.628	21.304
23.82871071	198.8792404	-0.892638037	249.381033	133.666	28.134
17.81619673	204.8357509	0	250.608	129.774	34.83
12.27672908	211.2392292	0.892638037	249.381033	125.98	41.412
7.709192813	217.6658677	2.231595092	242.0192313	122.257	47.894
4.010209459	227.5987633	8.331288344	239.5652974	118.707	54.279
0.810117091	237.1078512	15.17484663	237.1113635	115.215	60.557
-1.787705202	242.7100133	19.63803681	231.2832705	111.74	66.702
-4.269226473	244.3936826	31.24233129	206.4371897	108.228	72.69
-8.617088573	243.41871	86.28834356	110.7337674	104.774	78.525
-11.92839539	240.2899456			101.348	84.23
-10.39296099	237.7123459			98.0016	89.84
-5.533291444	237.8281203			94.8083	95.371
-2.053993985	235.2968302			91.665	100.822
0.044943263	230.1184759			88.5944	106.181
1.275321811	221.4338591			85.6459	111.438
-2.392730153	213.9396288			82.6813	116.589
-8.924899292	204.6343826			79.7379	121.633
-19.79199624	193.9187737			76.9431	126.581
-31.10629487	181.8854213			74.0567	131.439
-46.10157381	162.7932289			71.3489	136.211
-59.20466727	145.4889028			68.668	140.9
-75.0168095	121.1488915			66.0434	145.501
-114.0418159	59.65736044			63.4698	150.013
-149.2307735	0			60.8817	154.433
				58.4352	158.762
				55.9889	163.0006
				53.5379	167.1526
				51.1116	171.2231
				48.8396	175.2137
				46.5756	179.1269
				44.3779	182.9664
				42.2217	186.7233
				40.036	190.3774
				37.9846	193.934
				35.9056	197.4075
				33.8707	200.7857
				31.8704	204.0521
				29.9147	207.3068
				27.9324	210.559
				25.9503	213.6934
				24.1077	216.7991
				22.2645	219.8461
				20.5326	222.8496
				18.7361	225.7611
				16.9549	228.527
				contd.	contd.

15.394	231.1875
14.3928	233.9905
13.1223	236.8011
11.3209	239.1706
9.23521	241.1455
6.94022	242.7513
4.93073	244.0232
2.73059	244.9194
1.83266	246.7956
1.41489	248.283
2.86102E-05	249.7573
-1.41489	248.283
-1.83266	246.7956
-2.73059	244.9194
-4.93073	244.0232
-6.94022	242.7513
-9.23521	241.1455
-11.3209	239.1706
-13.1223	236.8011
-14.3928	233.9905
-15.394	231.1875
-16.9549	228.527
-18.7361	225.7611
-20.5326	222.8496
-22.2645	219.8461
-24.1077	216.7991
-25.9503	213.6934
-27.9324	210.559
-29.9147	207.3068
-31.8704	204.0521
-33.8707	200.7857
-35.9056	197.4075
-37.9846	193.934
-40.036	190.3774
-42.2217	186.7233
-44.3779	182.9664
-46.5756	179.1269
-48.8396	175.2137
-51.1116	171.2231
-53.5379	167.1526
-55.9889	163.0006
-58.4352	158.762
-60.8817	154.433
-63.4698	150.013
-66.0434	145.501
-68.668	140.9
-71.3489	136.211
-74.0567	131.439
-76.9431	126.581
-79.7379	121.633
-82.6813	116.589
-85.6459	111.438
-88.5944	106.181
-91.665	100.822

contd. contd.

-94.8083	95.371
-98.0016	89.84
-101.348	84.23
-104.774	78.525
-108.228	72.69
-111.74	66.702
-115.215	60.557
-118.707	54.279
-122.257	47.894
-125.98	41.412
-129.774	34.83
-133.666	28.134
-137.628	21.304
-141.694	14.335
-145.84	7.236
-150	0
-160	0
-170	0

9.5.2 Co-Ordinates of the Deformed V-Plate Profiles for the 90^0 V-Plates

Table E.7: Co-Ordinates of the Deformed V-Plate Profiles for the 90^0 V-Plates and 3g rod explosive

3g Explosive Rod					
Experimental		ABAQUS (Press.)		ABAQUS (EOS)	
X-Coord (mm)	Y-Coord (mm)	X-Coord (mm)	Y-Coord (mm)	X-Coord (mm)	Y-Coord (mm)
-171.6103319	0.63803506	170.614	0	170.614	0
-150.0058509	0.561882448	160.614	0	160.614	0
-146.2055035	3.649696682	150.614	0	150.614	0
-133.5734416	17.00608377	144.718	5.896	144.718	5.896
-99.97068576	52.30189711	138.979	11.635	138.979	11.635
-82.56889449	70.90827323	133.391	17.223	133.391	17.223
-66.36792637	87.59771039	127.951	22.663	127.951	22.663
-46.59805215	107.6201939	122.655	27.959	122.655	27.959
-30.17235836	123.5808427	117.499	33.115	117.499	33.115
-9.476729953	142.6223941	112.479	38.135	112.479	38.135
-1.389668067	150	107.592	43.022	107.592	43.022
22.01250394	127.1656533	102.834	47.78	102.834	47.78
49.36255776	101.1294476	98.2023	52.4117	98.2023	52.4117
49.36255776	101.1294476	93.6928	56.9212	93.6928	56.9212
122.306068	26.78227312	89.3024	61.3116	89.3024	61.3116
142.4479627	5.930525341	85.0281	65.5859	85.0281	65.5859
148.7102354	0.276337886	80.8669	69.7471	80.8669	69.7471
151.0548264	0	76.8156	73.7984	76.8156	73.7984
169.6103319	0.210548947	72.8715	77.7425	72.8715	77.7425
		69.0317	81.5823	69.0317	81.5823
		65.2934	85.3206	65.2934	85.3206
		61.6539	88.9601	61.6539	88.9601
		58.1106	92.5034	58.1106	92.5034
		54.661	95.953	54.661	95.953
		51.3027	99.3113	51.3027	99.3113
		48.0331	102.5809	48.0331	102.5809
		44.85	105.764	44.85	105.764
		41.751	108.863	41.751	108.863
		38.734	111.88	38.734	111.88
		35.7967	114.8173	35.7967	114.8173
		32.9371	117.6769	32.9371	117.6769
		30.1531	120.4609	30.1531	120.4609
		27.4427	123.1713	27.4427	123.1713
		24.804	125.81	24.804	125.81
		22.2351	128.3789	22.2351	128.3789
		19.734	130.88	19.734	130.88
		17.2991	133.3149	17.2991	133.3149
		14.9286	135.6854	14.9286	135.6854
		12.6207	137.9933	12.6207	137.9933
		10.3739	140.2401	10.3739	140.2401
		8.18647	142.42753	8.18647	142.42753
		6.05687	144.55713	6.05687	144.55713
		3.98358	146.63042	3.98358	146.63042
		1.96511	148.64889	1.96511	148.64889
		0	150.614	0	150.614
		-1.96511	148.64889	-1.96511	148.64889
		-3.98358	146.63042	-3.98358	146.63042
		-6.05687	144.55713	-6.05687	144.55713
		-8.18647	142.42753	-8.18647	142.42753
		-10.3739	140.2401	-10.3739	140.2401
		-12.6207	137.9933	-12.6207	137.9933

contd. contd. contd. contd.

-14.9286	135.6854	-14.9286	135.6854
-17.2991	133.3149	-17.2991	133.3149
-19.734	130.88	-19.734	130.88
-22.2351	128.3789	-22.2351	128.3789
-24.804	125.81	-24.804	125.81
-27.4427	123.1713	-27.4427	123.1713
-30.1531	120.4609	-30.1531	120.4609
-32.9371	117.6769	-32.9371	117.6769
-35.7967	114.8173	-35.7967	114.8173
-38.734	111.88	-38.734	111.88
-41.751	108.863	-41.751	108.863
-44.85	105.764	-44.85	105.764
-48.0331	102.5809	-48.0331	102.5809
-51.3027	99.3113	-51.3027	99.3113
-54.661	95.953	-54.661	95.953
-58.1106	92.5034	-58.1106	92.5034
-61.6539	88.9601	-61.6539	88.9601
-65.2934	85.3206	-65.2934	85.3206
-69.0317	81.5823	-69.0317	81.5823
-72.8715	77.7425	-72.8715	77.7425
-76.8156	73.7984	-76.8156	73.7984
-80.8669	69.7471	-80.8669	69.7471
-85.0281	65.5859	-85.0281	65.5859
-89.3024	61.3116	-89.3024	61.3116
-93.6928	56.9212	-93.6928	56.9212
-98.2023	52.4117	-98.2023	52.4117
-102.834	47.78	-102.834	47.78
-107.592	43.022	-107.592	43.022
-112.479	38.135	-112.479	38.135
-117.499	33.115	-117.499	33.115
-122.655	27.959	-122.655	27.959
-127.951	22.663	-127.951	22.663
-133.391	17.223	-133.391	17.223
-138.979	11.635	-138.979	11.635
-144.718	5.896	-144.718	5.896
-150.614	0	-150.614	0
-160.614	0	-160.614	0
-170.614	0	-170.614	0

Table E.8: Co-Ordinates of the Deformed V-Plate Profiles for the 90^0 V-Plates and 5g rod explosive

5g Explosive Rod					
Experimental		ABAQUS (Press.)		ABAQUS (EOS)	
X-Coord (mm)	Y-Coord (mm)	X-Coord (mm)	Y-Coord (mm)	X-Coord (mm)	Y-Coord (mm)
-171.5914873	0.382473683	-98.42561081	52.26753913	170.614	0
-151.8933617	0	-14.44633965	136.153713	160.614	0
-148.8818159	1.249831948	-6.667541377	141.6385783	150.614	0
-115.9205884	34.43740677	-2.540015763	146.4781652	144.579	5.778
-101.1431557	48.52340847	0	148.414	138.686	11.347
-81.30532572	68.64986043	2.540015763	146.4781652	133.036	16.859
-60.3707654	89.27981909	6.667541377	141.6385783	127.615	22.307
-44.46085484	104.9478067	14.44633965	136.153713	122.369	27.651
-27.98471088	121.4067838	98.42561081	52.26753913	117.272	32.863
-21.60254666	126.5937115			112.312	37.94
-15.20251402	132.3198807			107.481	42.879
-8.847157608	136.6979534			102.762	47.673
-3.093785806	139.2065575			98.1268	52.3016
1.580727586	141.7508928			93.5549	56.7551
2.461361002	143.8810494			89.0475	61.0307
-0.226852747	144.2399945			84.62	65.148
-0.730537993	145.3363394			80.285	69.1275
0.096479545	145.8487789			76.062	72.9948
2.793625568	145.759451			71.9494	76.7571
4.36723695	144.3577577			67.9605	80.4286
7.766300585	141.0062005			64.0841	84.01
12.46031954	135.9922623			60.3217	87.5081
19.2673792	129.5587688			56.6788	90.92
28.9430092	120.0612008			53.1465	94.2493
57.16968957	91.86491608			49.7052	97.4692
102.3916771	46.91084221			46.328	100.6055
126.1940512	23.71955936			43.0089	103.6422
126.1940512	23.71955936			39.7407	106.5287
146.3276453	3.888766523			36.5278	109.3064
150.0053577	0.797897358			33.367	111.9517
152.1452062	0.187197071			30.2512	114.4831
171.5914873	0.352894089			27.1714	116.8928
				24.2123	119.2442
				21.3713	121.5667
				18.6651	123.9129
				15.9752	126.1131
				13.4746	128.4127
				11.3023	130.7813
				9.29433	133.2194
				7.5173	135.7193
				5.9578	138.1462
				4.80846	140.6801
				3.46284	143.14767
				2.12614	145.54353
				-4.76837E-06	146.67217
				-2.12614	145.54353
				-3.46284	143.14767
				-4.80846	140.6801
				-5.9578	138.1462
				-7.5173	135.7193
				-9.29433	133.2194

contd. contd.

-11.3023	130.7813
-13.4746	128.4127
-15.9752	126.1131
-18.6651	123.9129
-21.3713	121.5667
-24.2123	119.2442
-27.1714	116.8928
-30.2512	114.4831
-33.367	111.9517
-36.5278	109.3064
-39.7407	106.5287
-43.0089	103.6422
-46.328	100.6055
-49.7052	97.4692
-53.1465	94.2493
-56.6788	90.92
-60.3217	87.5081
-64.0841	84.01
-67.9605	80.4286
-71.9494	76.7571
-76.062	72.9948
-80.285	69.1275
-84.62	65.148
-89.0475	61.0307
-93.5549	56.7551
-98.1268	52.3016
-102.762	47.673
-107.481	42.879
-112.312	37.94
-117.272	32.863
-122.369	27.651
-127.615	22.307
-133.036	16.859
-138.686	11.347
-144.579	5.778
-150.614	0
-160.614	0
-170.614	0

Table E.9: Co-Ordinates of the Deformed V-Plate Profiles for the 90^0 V-Plates and 7g rod explosive

7g Explosive Rod					
Experimental		ABAQUS (Press.)		ABAQUS (EOS)	
X-Coord (mm)	Y-Coord (mm)	X-Coord (mm)	Y-Coord (mm)	X-Coord (mm)	Y-Coord (mm)
-170.3524691	0	-98.502827	53.1116764	170.614	0
-151.5455497	0.263809928	-23.195827	127.597564	160.614	0
-148.0021887	1.056980185	-20.33606751	132.4553393	150.614	0
-139.8249841	9.254012389	-16.99968143	135.6938562	144.708	5.89
-122.1077096	26.97017675	-6.037270042	138.932373	138.965	11.623
-95.66806576	53.94107474	-1.588755274	143.4662966	133.397	17.237
-61.32382375	87.78686558	0	144.114	127.99	22.717
-30.25049907	117.4019007	1.588755274	143.4662966	122.709	28.034
-12.80587155	132.7382134	6.037270042	138.932373	117.535	33.18
-6.809279134	138.0265987	16.99968143	135.6938562	112.492	38.179
-3.265820126	141.7284876	20.33606751	132.4553393	107.599	43.057
-0.812671847	143.8438421	23.195827	127.597564	102.862	47.832
1.367796032	142.5216255	98.502827	53.1116764	98.2722	52.4945
1.095167488	140.6706282			93.8024	57.0343
-1.903038061	140.6707269			89.4407	61.4475
-3.265903353	139.3486269			85.1944	65.7406
-2.993441265	136.4398994			81.0693	69.9266
-0.813014005	134.0599634			77.0615	74.0094
2.45769987	132.473282			73.1565	77.9835
9.544251613	129.2999012			69.3551	81.8449
19.08378518	123.4821465			65.6478	85.591
32.16648546	112.9045538			62.0438	89.2291
55.06111304	91.7494727			58.5368	92.7629
75.23017087	72.445484			55.1291	96.2004
97.30712914	51.81929121			51.8198	99.5301
132.1940908	16.91350224			48.6039	102.7575
132.1940908	16.91350224			45.5002	105.9067
144.7315987	4.484924806			42.4686	108.8847
148.5473811	1.311648138			39.5281	111.8601
151.5455681	0.782691527			36.6179	114.7628
170.3524691	0.51764353			33.7819	117.612
				31.0018	120.3537
				28.3189	122.9822
				25.738	125.5644
				23.2066	128.0528
				20.6901	130.4117
				18.3639	132.688
				16.2426	134.9851
				14.3427	137.3458
				11.9053	139.3076
				9.13018	140.4654
				6.4053	141.00133
				3.82174	140.92416
				1.99428	141.76963
				5.72205E-05	142.7122
				-1.99428	141.76963
				-3.82174	140.92416
				-6.4053	141.00133
				-9.13018	140.4654
				-11.9053	139.3076
				-14.3427	137.3458

contd. contd.

-16.2426	134.9851
-18.3639	132.688
-20.6901	130.4117
-23.2066	128.0528
-25.738	125.5644
-28.3189	122.9822
-31.0018	120.3537
-33.7819	117.612
-36.6179	114.7628
-39.5281	111.8601
-42.4686	108.8847
-45.5002	105.9067
-48.6039	102.7575
-51.8198	99.5301
-55.1291	96.2004
-58.5368	92.7629
-62.0438	89.2291
-65.6478	85.591
-69.3551	81.8449
-73.1565	77.9835
-77.0615	74.0094
-81.0693	69.9266
-85.1944	65.7406
-89.4407	61.4475
-93.8024	57.0343
-98.2722	52.4945
-102.862	47.832
-107.599	43.057
-112.492	38.179
-117.535	33.18
-122.709	28.034
-127.99	22.717
-133.397	17.237
-138.965	11.623
-144.708	5.89
-150.614	0
-160.614	0
-170.614	0

Table E.10: Co-Ordinates of the Deformed V-Plate Profiles for the 90^0 V-Plates and 9g rod explosive

9g Explosive Rod					
Experimental		ABAQUS (Press.)		ABAQUS (EOS)	
X-Coord (mm)	Y-Coord (mm)	X-Coord (mm)	Y-Coord (mm)	X-Coord (mm)	Y-Coord (mm)
-171.5781442	0.160488343	-93.73318085	54.58245863	170.614	0
-149.9848182	0.049914873	-27.97574936	122.9710686	160.614	0
-146.1099538	2.625116346	-20.90970957	132.6032671	150.614	0
-128.8334616	20.29398	-16.58356277	136.3598246	144.653	5.849
-114.6120281	35.37340837	-6.633425106	133.8875603	138.85	11.517
-54.17375691	95.62945647	0	135.814	133.256	17.096
-28.8497296	119.7647846	6.633425106	133.8875603	127.857	22.578
-20.51419866	127.0189922	16.58356277	136.3598246	122.609	27.924
-13.86245717	131.9242114	20.90970957	132.6032671	117.462	33.106
-9.992499832	134.2352519	27.97574936	122.9710686	112.452	38.128
-3.384921923	136.7630186	93.73318085	54.58245863	107.568	43.016
0.470317882	138.281576			102.832	47.782
2.139386216	139.8380847			98.2232	52.4225
2.442099549	141.4183073			93.721	56.93
1.90537169	141.9561162			89.324	61.2965
0.802473625	141.4467681			85.029	65.5337
-0.851877109	140.682746			80.8632	69.6721
-1.935146943	141.2300419			76.848	73.7392
-1.910611655	142.5508469			72.9651	77.7241
-0.524628488	143.5837736			69.1765	81.5998
1.920092863	142.7485993			65.4602	85.3382
5.448080409	141.3661291			61.8238	88.9468
8.951536241	138.6628503			58.2863	92.4476
14.0504509	133.5536652			54.8793	95.8687
24.52646549	123.5947088			51.6023	99.2216
32.855565	115.7869884			48.421	102.4956
51.9192252	97.22308161			45.3375	105.657
81.43927176	67.64357447			42.3228	108.6825
97.80457156	50.97623301			39.3555	111.6848
128.3931668	20.05694695			36.46	114.6162
128.3931668	20.05694695			33.6323	117.4513
143.973003	5.252962961			30.87	120.2065
147.4617377	1.757204655			28.176	122.8736
150.1748194	0.653125902			25.6499	125.4731
172.5781442	0			22.9333	127.8922
				20.2313	129.9722
				17.5772	131.9471
				14.9914	133.8672
				12.4077	135.6611
				9.97981	137.3359
				7.49052	138.6772
				5.27134	140.2084
				3.29368	141.71038
				1.96323	143.74218
				-8.58307E-05	145.13451
				-1.963315831	143.74218
				-3.293765831	141.71038
				-5.271425831	140.2084
				-7.490605831	138.6772
				-9.979895831	137.3359
				-12.40778583	135.6611

contd. contd.

-14.99148583	133.8672
-17.57728583	131.9471
-20.23138583	129.9722
-22.93338583	127.8922
-25.64998583	125.4731
-28.17608583	122.8736
-30.87008583	120.2065
-33.63238583	117.4513
-36.46008583	114.6162
-39.35558583	111.6848
-42.32288583	108.6825
-45.33758583	105.657
-48.42108583	102.4956
-51.60238583	99.2216
-54.87938583	95.8687
-58.28638583	92.4476
-61.82388583	88.9468
-65.46028583	85.3382
-69.17658583	81.5998
-72.96518583	77.7241
-76.84808583	73.7392
-80.86328583	69.6721
-85.02908583	65.5337
-89.32408583	61.2965
-93.72108583	56.93
-98.22328583	52.4225
-102.8320858	47.782
-107.5680858	43.016
-112.4520858	38.128
-117.4620858	33.106
-122.6090858	27.924
-127.8570858	22.578
-133.2560858	17.096
-138.8500858	11.517
-144.6530858	5.849
-150.6140858	0
-160.6140858	0
-170.6140858	0

Table E.11: Co-Ordinates of the Deformed V-Plate Profiles for the 90^0 V-Plates and 11g rod explosive

11g Explosive Rod					
Experimental		ABAQUS (Press.)		ABAQUS (EOS)	
X-Coord (mm)	Y-Coord (mm)	X-Coord (mm)	Y-Coord (mm)	X-Coord (mm)	Y-Coord (mm)
-166.877022	1.132996967	-97.07873438	53.70491985	-170.614	0
-148.3219828	0.990079596	-31.05212043	122.6395931	-160.614	0
-146.1850379	1.801007808	-25.49542519	130.9758792	-150.614	0
-133.187504	15.5535037	-19.28500111	134.182143	-144.736	5.926
-115.3010065	35.21570414	-13.40144145	132.8996375	-139.035	11.686
-87.89022313	67.27680785	-9.152203915	129.0521208	-133.405	17.237
-75.45103498	79.60820375	0	130.014	-127.876	22.597
-57.8635652	97.55649234	9.152203915	129.0521208	-122.533	27.824
-41.91709561	112.9615298	13.40144145	132.8996375	-117.388	32.959
-33.28422024	120.5053686	19.28500111	134.182143	-112.385	38.008
-27.09299036	125.2376886	25.49542519	130.9758792	-107.525	42.939
-21.46010613	128.5489125	31.05212043	122.6395931	-102.768	47.714
-16.91554928	130.4513066	97.07873438	53.70491985	-98.1985	52.3266
-12.13436928	130.9141898			-93.673	56.7907
-7.375877047	130.2303736			-89.1901	61.1149
-2.662770941	127.253159			-84.909	65.3053
0.731057455	124.5933004			-80.6701	69.3682
3.363946955	123.6719057			-76.5658	73.3256
6.549512873	123.8849361			-72.605	77.194
7.908503806	125.5742998			-68.7451	80.9959
8.48386807	127.8554281			-65.079	84.7261
7.187278206	129.3194873			-61.5287	88.3772
3.494421991	130.2654302			-58.1084	91.9386
2.209177775	132.302839			-54.7604	95.3959
1.21161573	135.4808138			-51.5234	98.7183
1.521989122	137.7680753			-48.3736	101.9084
3.704316568	140.872402			-45.2613	105.0593
6.90690096	141.9454568			-42.1654	108.1393
10.0811177	141.5851377			-39.1427	111.1175
14.79990016	138.8945978			-36.2262	114.0367
19.74963294	134.4778721			-33.4211	116.8594
35.37679211	120.3492517			-30.6377	119.5353
55.67167832	100.9500181			-27.9069	122.1065
66.0670919	90.38423609			-25.199	124.5352
87.33117603	66.3736536			-22.6301	126.892
110.4048131	40.02671343			-20.06	129.113
110.4048131	40.02671343			-17.542	131.2695
141.0043478	5.474900832			-15.1459	133.3279
141.0043478	5.474900832			-12.6727	135.1838
144.6574942	2.52223425			-9.98557	136.6834
147.2847109	1.314164727			-7.60062	138.0672
166.877022	0			-5.43664	139.5401
				-3.40849	141.22604
				-1.92396	142.87199
				0.000100136	144.31233
				1.92396	142.87199
				3.40849	141.22604
				5.43664	139.5401
				7.60062	138.0672
				9.98557	136.6834
				12.6727	135.1838

contd. contd.

15.1459	133.3279
17.542	131.2695
20.06	129.113
22.6301	126.892
25.199	124.5352
27.9069	122.1065
30.6377	119.5353
33.4211	116.8594
36.2262	114.0367
39.1427	111.1175
42.1654	108.1393
45.2613	105.0593
48.3736	101.9084
51.5234	98.7183
54.7604	95.3959
58.1084	91.9386
61.5287	88.3772
65.079	84.7261
68.7451	80.9959
72.605	77.194
76.5658	73.3256
80.6701	69.3682
84.909	65.3053
89.1901	61.1149
93.673	56.7907
98.1985	52.3266
102.768	47.714
107.525	42.939
112.385	38.008
117.388	32.959
122.533	27.824
127.876	22.597
133.405	17.237
139.035	11.686
144.736	5.926
150.614	0
160.614	0
170.614	0

Table E.12: Co-Ordinates of the Deformed V-Plate Profiles for the 90^0 V-Plates and 13g rod explosive

13g Explosive Rod					
Experimental		ABAQUS (Press.)		ABAQUS (EOS)	
X-Coord (mm)	Y-Coord (mm)	X-Coord (mm)	Y-Coord (mm)	X-Coord (mm)	Y-Coord (mm)
-145.8225583	2.100499894	-96.13659574	53.85986667	170.614	0
-114.4004696	35.65823699	-46.14556596	104.5137889	160.614	0
-98.29241082	54.20941872	-35.25008511	116.3757833	150.614	0
-92.47044577	60.80893572	-25.63642553	125.0318333	144.599	5.712
-72.44235638	79.207635	-20.50914043	128.2377778	138.495	11.149
-42.89662241	106.6624692	-13.77957872	127.9171833	132.742	16.603
-27.00599156	119.6963139	-9.613659574	122.7876722	127.386	22.085
-19.30074873	124.2722926	-7.37047234	117.9787556	122.385	27.515
-13.6450521	126.6526693	-3.204553191	115.7345944	117.349	32.839
-7.060508212	127.6967286	0	115.414	112.45	38.005
-1.884960208	126.1952219	3.204553191	115.7345944	107.609	42.982
0.690023953	125.1199203	7.37047234	117.9787556	102.911	47.77
1.945541327	123.770896	9.613659574	122.7876722	98.2087	52.3751
3.578888319	123.7073616	13.77957872	127.9171833	93.6458	56.8311
5.967890963	126.2148071	20.50914043	128.2377778	89.2426	61.129
7.91511816	125.8140157	25.63642553	125.0318333	85.0543	65.3071
169.8225583	0.22394471	35.25008511	116.3757833	80.7333	69.3727
150.5107019	0	46.14556596	104.5137889	76.6488	73.3513
148.2368046	0.413498285	96.13659574	53.85986667	72.7193	77.2416
145.6874003	2.137900091			68.9406	81.0596
128.6995444	19.37608252			65.1476	84.7981
99.54713079	51.71454742			61.6097	88.4557
85.72364991	66.22926755			58.4239	91.9969
64.84133952	84.26902918			55.1004	95.4118
50.91553963	96.1873558			51.6555	98.7108
43.63236274	102.3215011			48.4928	101.9386
41.3456791	102.4104492			45.3152	105.1183
39.98784272	101.1630799			42.324	108.1714
39.88552357	98.56668286			39.4211	111.0631
41.41655156	95.90675495			36.3392	113.8487
46.11195094	90.5233649			33.268	116.4822
53.94614547	81.76741239			30.0909	118.842
59.54481601	74.39860826			26.9924	120.9608
62.61966176	69.40329897			23.93	122.8357
66.7000905	65.0189694			20.6844	124.506
72.47781923	62.19385214			17.6324	126.0895
78.03119685	61.97783528			14.8959	127.8053
83.36022336	64.37091885			12.3332	129.554
				9.94832	131.3981
				7.73995	133.3693
				5.91963	135.3329
				4.29151	137.5733
				2.84184	139.7745
				1.87292	141.79055
				-1.43051E-05	143.39572
				-1.87292	141.79055
				-2.84184	139.7745
				-4.29151	137.5733
				-5.91963	135.3329
				-7.73995	133.3693
				-9.94832	131.3981

contd. contd.

-12.3332	129.554
-14.8959	127.8053
-17.6324	126.0895
-20.6844	124.506
-23.93	122.8357
-26.9924	120.9608
-30.0909	118.842
-33.268	116.4822
-36.3392	113.8487
-39.4211	111.0631
-42.324	108.1714
-45.3152	105.1183
-48.4928	101.9386
-51.6555	98.7108
-55.1004	95.4118
-58.4239	91.9969
-61.6097	88.4557
-65.1476	84.7981
-68.9406	81.0596
-72.7193	77.2416
-76.6488	73.3513
-80.7333	69.3727
-85.0543	65.3071
-89.2426	61.129
-93.6458	56.8311
-98.2087	52.3751
-102.911	47.77
-107.609	42.982
-112.45	38.005
-117.349	32.839
-122.385	27.515
-127.386	22.085
-132.742	16.603
-138.495	11.149
-144.599	5.712
-150.614	0
-160.614	0
-170.614	0

9.5.3 Co-Ordinates of the Deformed V-Plate Profiles for the 120^0 V-Plates

Table E.13: Co-Ordinates of the Deformed V-Plate Profiles for the 120^0 V-Plates and 3g rod explosive

3g Explosive Rod					
Experimental		ABAQUS (Press.)		ABAQUS (EOS)	
X-Coord (mm)	Y-Coord (mm)	X-Coord (mm)	Y-Coord (mm)	X-Coord (mm)	Y-Coord (mm)
-165.2187288	5.369835147	-128.1950368	11.42160695	168.09	0
-160.0934529	3.498928772	-37.49100132	63.73431053	158.09	0
-156.5777115	0.467655057	-30.23467849	70.27339848	148.09	0
-152.7534214	0.339950902	-17.334549	75.06872964	140.951	4.1515
-150.7079014	1.000112603	-8.06258093	76.81248643	134.048	8.1826
-146.215701	0.607281571	0	80.3	127.356	12.065
-109.1315949	21.70863037	8.06258093	76.81248643	120.881	15.8038
-72.72932871	42.58992705	17.334549	75.06872964	114.613	19.4113
-48.46579454	56.34906162	30.23467849	70.27339848	108.541	22.8882
-32.87606155	66.0270316	37.49100132	63.73431053	102.646	26.2234
-20.29437803	72.8915762	128.1950368	11.42160695	96.9322	29.422
-14.34793926	76.09252704			91.4105	32.5127
-10.23599621	78.14062265			86.0826	35.5286
-7.733592546	79.02835109			80.9488	38.4744
-4.781271242	79.90105547			75.987	41.3394
-1.195872116	79.29568176			71.186	44.1081
0.337038585	77.7875583			66.5496	46.7864
-0.407495642	75.38419172			62.0663	49.3784
-0.913138972	73.45849469			57.7359	51.8941
0.795968345	70.24472633			53.5585	54.3306
4.381367548	69.63935528			49.5258	56.688
10.04015322	70.6645037			45.6233	58.9529
13.87140928	70.77939033			41.8292	61.1518
19.48143291	70.10641119			38.1698	63.2773
28.82518819	66.15205294			34.6222	65.3291
45.90316193	57.08297184			31.1755	67.3114
77.37354069	39.52013806			27.8375	69.196
77.37354069	39.52013806			24.6056	71.0015
118.7998545	15.79709822			21.4574	72.7077
135.6389374	6.250347566			18.4537	74.417
142.740078	2.613702805			15.5783	76.08638
145.3838482	0.582837706			12.9024	77.74129
148.2943734	0			10.3271	79.42316
167.2187288	0.339351755			7.6655	80.8609
				4.89579	81.74052
				2.37752	82.49852
				9.53674E-06	83.25666
				-2.37752	82.49852
				-4.89579	81.74052
				-7.6655	80.8609
				-10.3271	79.42316
				-12.9024	77.74129
				-15.5783	76.08638
				-18.4537	74.417
				-21.4574	72.7077
				-24.6056	71.0015
				-27.8375	69.196
				-31.1755	67.3114
				-34.6222	65.3291
				-38.1698	63.2773
				-41.8292	61.1518

contd. contd.

-45.6233	58.9529
-49.5258	56.688
-53.5585	54.3306
-57.7359	51.8941
-62.0663	49.3784
-66.5496	46.7864
-71.186	44.1081
-75.987	41.3394
-80.9488	38.4744
-86.0826	35.5286
-91.4105	32.5127
-96.9322	29.422
-102.646	26.2234
-108.541	22.8882
-114.613	19.4113
-120.881	15.8038
-127.356	12.065
-134.048	8.1826
-140.951	4.1515
-148.09	0
-158.09	0
-168.09	0

Table E.14: Co-Ordinates of the Deformed V-Plate Profiles for the 120^0 V-Plates and 5g rod explosive

5g Explosive Rod					
Experimental		ABAQUS (Press.)		ABAQUS (EOS)	
X-Coord (mm)	Y-Coord (mm)	X-Coord (mm)	Y-Coord (mm)	X-Coord (mm)	Y-Coord (mm)
-165.6395332	2.868652394	-130.8012931	10.79158527	168.09	0
-155.7537793	0.450898734	-33.00217241	66.76453794	158.09	0
-145.0921173	0.20225419	-20.12327586	69.00345605	148.09	0
-131.5858053	8.087636769	-12.07396552	65.42118708	140.933	4.1332
-108.9899973	21.95261671	-6.841913793	61.6150263	133.99	8.1136
-82.75901854	38.53455705	-4.024655172	60.04778362	127.27	11.932
-61.71920597	50.22879425	0	59.6	120.754	15.6051
-41.19787967	61.10914047	4.024655172	60.04778362	114.441	19.142
-31.32569482	65.73569442	6.841913793	61.6150263	108.323	22.5356
-24.31016369	68.45972265	12.07396552	65.42118708	102.384	25.7794
-17.0335582	70.64242376	20.12327586	69.00345605	96.622	28.8829
-13.13314124	70.65057895	33.00217241	66.76453794	91.0479	31.876
-9.749128306	68.76110153	130.8012931	10.79158527	85.6723	34.8016
-7.405226076	66.86945197			80.5048	37.6774
-6.100390957	64.43375688			75.5126	40.4893
-5.053494485	60.91377651			70.6838	43.1957
-3.490720713	59.56236414			65.99	45.7685
-1.154121106	61.46380251			61.4165	48.1849
2.219455978	64.99302286			56.9634	50.4453
3.775970709	66.89283019			52.6221	52.5624
6.373117931	68.52387683			48.3908	54.5606
11.05153013	69.6174021			44.2945	56.4679
16.77318626	69.08749224			40.3203	58.3221
24.05865974	66.66430178			36.5071	60.1403
34.20913562	61.80867831			32.8511	61.956
74.29411826	40.75948211			29.3401	63.7469
122.9741032	12.41298687			25.9932	65.5312
122.9741032	12.41298687			22.8773	67.4215
137.0317793	4.043363505			19.8809	69.2915
143.5376922	1.347606606			17.0571	71.1329
146.920664	0			14.4384	73.0824
155.760565	0.560355907			12.0801	75.179
165.6395332	1.664754763			9.57308	77.13424
				7.28838	78.7872
				4.70175	80.25235
				2.43013	81.31883
				-1.90735E-05	81.97091
				-2.43013	81.31883
				-4.70175	80.25235
				-7.28838	78.7872
				-9.57308	77.13424
				-12.0801	75.179
				-14.4384	73.0824
				-17.0571	71.1329
				-19.8809	69.2915
				-22.8773	67.4215
				-25.9932	65.5312
				-29.3401	63.7469
				-32.8511	61.956
				-36.5071	60.1403
				-40.3203	58.3221

contd. contd.

-44.2945	56.4679
-48.3908	54.5606
-52.6221	52.5624
-56.9634	50.4453
-61.4165	48.1849
-65.99	45.7685
-70.6838	43.1957
-75.5126	40.4893
-80.5048	37.6774
-85.6723	34.8016
-91.0479	31.876
-96.622	28.8829
-102.384	25.7794
-108.323	22.5356
-114.441	19.142
-120.754	15.6051
-127.27	11.932
-133.99	8.1136
-140.933	4.1332
-148.09	0
-158.09	0
-168.09	0

Table E.15: Co-Ordinates of the Deformed V-Plate Profiles for the 120^0 V-Plates and 7g rod explosive

7g Explosive Rod					
Experimental		ABAQUS (Press.)		ABAQUS (EOS)	
X-Coord (mm)	Y-Coord (mm)	X-Coord (mm)	Y-Coord (mm)	X-Coord (mm)	Y-Coord (mm)
-166.2129236	0	-123.655368	13.44124188	168.09	0
-145.3084712	0.698889268	-47.84043744	58.34710999	158.09	0
-135.8005186	3.797243939	-35.67761437	61.8349444	148.09	0
-119.9784913	12.72696117	-25.13650103	60.5270065	140.929	4.1193
-97.84418624	27.7635901	-16.21709744	56.16721348	133.993	8.0946
-86.25130736	35.83673682	-9.324831027	49.62752395	127.271	11.9228
-77.28165831	40.30908008	-6.486838976	43.52381372	120.788	15.6165
-65.6780004	46.72895252	-2.837992052	40.0359793	114.52	19.2063
-50.37810192	54.55274696	0	39.6	108.489	22.7168
-36.13145055	61.54241833	2.837992052	40.0359793	102.667	26.1455
-25.57384715	66.02598662	6.486838976	43.52381372	97.0782	29.4791
-21.87581213	67.15436203	9.324831027	49.62752395	91.6483	32.6846
-17.91311764	68.28460828	16.21709744	56.16721348	86.3705	35.7385
-13.41391653	68.31641252	25.13650103	60.5270065	81.2532	38.6549
-9.43684668	67.24229138	35.67761437	61.8349444	76.2934	41.4481
-5.713654782	64.51302257	47.84043744	58.34710999	71.5104	44.1601
-3.841277328	61.4951139	123.655368	13.44124188	66.9101	46.8077
-2.222777839	56.82206014			62.5115	49.4087
0.967503742	54.64014279			58.2711	51.9417
2.544676587	56.30464208			54.1443	54.3809
6.217554756	61.29065915			50.1109	56.7218
8.583312771	63.78741065			46.2284	58.9414
12.54241344	65.46874747			42.4588	61.1001
18.09845056	65.78358161			38.814	63.161
24.99215792	63.90340254			35.2471	65.158
37.20419919	58.20299858			31.9222	67.1446
61.37260686	45.42258696			28.7594	69.209
90.84856445	30.47522725			25.5853	71.1487
112.1111161	16.8475993			22.4375	72.7561
123.2681158	10.58861885			19.2655	73.9968
123.2681158	10.58861885			15.9755	74.8117
144.771967	0.544959397			12.7953	75.162
166.2129236	0.145404062			9.70822	75.2797
				7.0503	75.69394
				4.47193	76.44347
				2.38621	77.95051
				-0.000038147	78.74197
				-2.38621	77.95051
				-4.47193	76.44347
				-7.0503	75.69394
				-9.70822	75.2797
				-12.7953	75.162
				-15.9755	74.8117
				-19.2655	73.9968
				-22.4375	72.7561
				-25.5853	71.1487
				-28.7594	69.209
				-31.9222	67.1446
				-35.2471	65.158
				-38.814	63.161
				-42.4588	61.1001

contd. contd.

-46.2284	58.9414
-50.1109	56.7218
-54.1443	54.3809
-58.2711	51.9417
-62.5115	49.4087
-66.9101	46.8077
-71.5104	44.1601
-76.2934	41.4481
-81.2532	38.6549
-86.3705	35.7385
-91.6483	32.6846
-97.0782	29.4791
-102.667	26.1455
-108.489	22.7168
-114.52	19.2063
-120.788	15.6165
-127.271	11.9228
-133.993	8.0946
-140.929	4.1193
-148.09	0
-158.09	0
-168.09	0

Table E.16: Co-Ordinates of the Deformed V-Plate Profiles for the 120^0 V-Plates and 9g rod explosive

9g Explosive Rod					
Experimental		ABAQUS (Press.)		ABAQUS (EOS)	
X-Coord (mm)	Y-Coord (mm)	X-Coord (mm)	Y-Coord (mm)	X-Coord (mm)	Y-Coord (mm)
-168.079081	0.163988614	-126.0237548	13.08544706	168.09	0
-147.9511969	0.944452973	-66.52401484	47.37276468	158.09	0
-140.7788732	2.730161739	-50.40950193	52.64773663	148.09	0
-128.2827988	6.599689449	-35.94775957	52.64773663	140.975	4.1809
-117.8921854	11.31204865	-22.72559513	46.93318369	134.087	8.2542
-105.556068	22.48581323	-11.56939389	34.18533483	127.394	12.1326
-92.95531101	33.65561648	-7.230871178	24.51455294	120.878	15.7953
-81.48676576	39.70403414	-3.30554111	19.89895249	114.525	19.2391
-73.76578196	42.83372393	0	18.8	108.361	22.5141
-66.86197004	44.35301273	3.30554111	19.89895249	102.393	25.6569
-56.49849662	47.17270837	7.230871178	24.51455294	96.6022	28.6879
-41.88145515	51.28092702	11.56939389	34.18533483	91.0442	31.6444
-31.52573599	53.55986273	22.72559513	46.93318369	85.7167	34.5649
-23.84740071	53.71536404	35.94775957	52.64773663	80.5836	37.4392
-20.67951633	53.12706862	50.40950193	52.64773663	75.6658	40.2688
-15.68243953	50.88875932	66.52401484	47.37276468	70.9192	43.0174
-12.30032323	46.78155422	126.0237548	13.08544706	66.3277	45.6535
-10.27240492	40.53111075			61.8689	48.2228
-8.194083832	37.7956157			57.5541	50.7091
-7.162677562	35.88710698			53.3522	53.0907
-2.441869334	32.84161781			49.2858	55.3638
2.624995885	35.47015803			45.3321	57.5173
6.107920169	38.3928472			41.4828	59.5997
10.98769093	46.4329607			37.7719	61.5723
13.68058085	49.637915			34.1792	63.4651
18.2065428	51.46323661			30.7367	65.3003
24.04017712	52.1872294			27.4026	67.0696
34.60237395	50.40649549			24.138	68.7201
49.62074428	45.58423115			21.0128	70.3214
55.67636729	43.33007669			18.0024	71.7769
66.47218421	39.38233669			14.9879	73.0717
77.2680036	35.43459665			12.1041	74.1779
86.48375423	32.05138435			9.34175	75.363
91.48083103	29.81307505			7.04182	76.73897
98.28383745	24.30246954			4.59425	78.33557
106.4061501	18.50167886			2.34239	79.2288
113.4660395	12.44635212			-1.43051E-05	80.21877
113.4660395	12.44635212			-2.34239	79.2288
131.8859118	4.868786306			-4.59425	78.33557
145.8534902	0.603129589			-7.04182	76.73897
168.079081	0			-9.34175	75.363
				-12.1041	74.1779
				-14.9879	73.0717
				-18.0024	71.7769
				-21.0128	70.3214
				-24.138	68.7201
				-27.4026	67.0696
				-30.7367	65.3003
				-34.1792	63.4651
				-37.7719	61.5723
				-41.4828	59.5997
				contd.	contd.

-27.2043	53.6051
-30.3973	52.3591
-33.7201	50.6953
-37.312	49.6046
-40.9287	49.0746
-44.7383	48.1769
-48.7895	47.1768
-52.9046	46.2117
-57.3611	45.0944
-61.7996	43.8981
-66.3491	42.5571
-70.889	41.0575
-75.6391	39.2338
-80.3966	37.1426
-85.2942	34.7995
-90.0702	32.2559
-95.1968	29.5361
-100.487	26.6651
-105.593	23.6333
-111.203	20.4666
-116.859	17.2186
-122.512	13.9288
-128.742	10.6407
-135.054	7.2618
-141.458	3.7343
-148.091	0
-158.091	0
-168.091	0

9.5.4 Co-Ordinates of the Deformed V-Plate Profiles for the 150^0 V-Plates

Table E.18: Co-Ordinates of the Deformed V-Plate Profiles for the 150^0 V-Plates and 3g rod explosive

3g Explosive Rod					
Experimental		ABAQUS (Press.)		ABAQUS (EOS)	
X-Coord (mm)	Y-Coord (mm)	X-Coord (mm)	Y-Coord (mm)	X-Coord (mm)	Y-Coord (mm)
-171.7295945	1.12538176	-135.331781	4.183818868	170.059	0
-147.6253975	0	-52.69929167	26.05378113	162.536	0
-115.5500064	6.025170206	-35.83551833	27.00464906	155.654	0
-91.01661639	11.88557549	-21.501311	25.57834717	150.059	0
-77.0861517	15.09992334	-11.80464133	20.82400755	132.124	4.7165
-59.22525191	18.87031196	-3.794349	16.06966792	124.49	6.7318
-45.3064006	21.44902829	0	15.1188	117.128	8.6147
-29.29483776	23.0314527	3.794349	16.06966792	110.044	10.3813
-19.64270533	23.15336426	11.80464133	20.82400755	103.225	12.0497
-13.03989222	21.42961209	21.501311	25.57834717	96.6756	13.6624
-7.353032121	19.08859699	35.83551833	27.00464906	90.3849	15.2405
-2.576323848	16.44813482	52.69929167	26.05378113	84.35	16.8098
2.548286984	16.34406226	135.331781	4.183818868	78.5638	18.3745
6.820812559	19.11868279			73.0217	19.9439
11.99187664	21.55712177			67.7037	21.4886
18.97743223	24.27664214			62.6038	22.9945
26.22959447	25.08315768			57.7143	24.4655
33.76578606	24.9301098			53.048	25.9192
39.7889327	24.48985865			48.5584	27.3802
51.20910345	22.35034295			44.2871	28.8649
59.62060419	20.58985926			40.133	30.25367
79.44065961	16.05423131			36.084	31.46247
107.3649653	9.446425758			32.1075	32.34245
122.0778326	5.968311793			28.1968	32.82409
137.3935957	2.477953986			24.4038	32.91012
148.2108706	0.35068213			20.761	32.71762
148.2108706	0.35068213			17.2962	32.01089
171.7295945	0.190985624			14.0611	31.21864
				11.067	30.0124
				8.15218	29.6291
				5.09531	28.9173
				2.52447	28.7523
				-2.86102E-05	27.6496
				-2.52447	28.7523
				-5.09531	28.9173
				-8.15218	29.6291
				-11.067	30.0124
				-14.0611	31.21864
				-17.2962	32.01089
				-20.761	32.71762
				-24.4038	32.91012
				-28.1968	32.82409
				-32.1075	32.34245
				-36.084	31.46247
				-40.133	30.25367
				-44.2871	28.8649
				-48.5584	27.3802
				-53.048	25.9192
				-57.7143	24.4655
				-62.6038	22.9945
				-67.7037	21.4886

contd. contd.

-73.0217	19.9439
-78.5638	18.3745
-84.35	16.8098
-90.3849	15.2405
-96.6756	13.6624
-103.225	12.0497
-110.044	10.3813
-117.128	8.6147
-124.49	6.7318
-132.124	4.7165
-150.059	0
-155.654	0
-162.536	0
-170.059	0

Table E.19: Co-Ordinates of the Deformed V-Plate Profiles for the 150^0 V-Plates and 5g rod explosive

5g Explosive Rod					
Experimental		ABAQUS (Press.)		ABAQUS (EOS)	
X-Coord (mm)	Y-Coord (mm)	X-Coord (mm)	Y-Coord (mm)	X-Coord (mm)	Y-Coord (mm)
-176.91722	0.567383212	-140.9363656	2.884375758	170.059	0
-157.5375412	0.87780593	-84.09973289	17.0698303	162.536	0
-120.1283181	6.658130388	-61.91958356	18.48837576	155.654	0
-107.1220563	8.558253627	-42.97403933	17.0698303	150.059	0
-96.98058301	11.23723726	-27.72518667	11.86849697	132.107	4.6632
-84.24758911	14.10576525	-14.09363656	4.302921212	124.448	6.6114
-72.83467787	16.40331271	-9.241728889	0.047284848	117.089	8.4842
-58.49211583	19.19188276	-4.158778	-3.73550303	110.034	10.3224
-44.89067048	20.10761306	0	-4.6812	103.26	12.1269
-33.28556506	19.8494091	4.158778	-3.73550303	96.7658	13.8975
-26.20346399	19.49760692	9.241728889	0.047284848	90.5261	15.6089
-19.55678204	16.93950179	14.09363656	4.302921212	84.522	17.2588
-12.76654751	10.8732313	27.72518667	11.86849697	78.7549	18.8405
-6.642657493	4.398089042	42.97403933	17.0698303	73.2113	20.3601
0.265326196	0.637292371	61.91958356	18.48837576	67.892	21.807
6.687384464	0	84.09973289	17.0698303	62.7827	23.1808
12.54668902	0.982045038	140.9363656	2.884375758	57.8288	24.4696
18.49903398	3.785732243			53.0672	25.703
26.28228983	10.84314147			48.5087	26.8975
33.31812727	15.90432936			44.1464	28.0763
42.46142756	17.99634456			39.9268	29.2244
54.06653283	17.73813771			35.8985	30.32278
64.06206996	17.55988878			31.9557	31.24983
68.24694987	17.35200557			28.1499	31.92314
75.58610413	15.71432931			24.4968	32.46289
96.47805948	14.03997533			20.8532	32.80027
113.6019582	8.096931409			17.412	32.7232
127.8772804	3.250220257			14.1032	32.27966
127.8772804	3.250220257			10.9949	31.67783
153.5817257	1.018528946			8.07739	31.11124
162.91722	0.554789832			5.11456	30.60456
				2.55197	30.39342
				0.000038147	30.40006
				-2.55197	30.39342
				-5.11456	30.60456
				-8.07739	31.11124
				-10.9949	31.67783
				-14.1032	32.27966
				-17.412	32.7232
				-20.8532	32.80027
				-24.4968	32.46289
				-28.1499	31.92314
				-31.9557	31.24983
				-35.8985	30.32278
				-39.9268	29.2244
				-44.1464	28.0763
				-48.5087	26.8975
				-53.0672	25.703
				-57.8288	24.4696
				-62.7827	23.1808
				-67.892	21.807

contd. contd.

-73.2113	20.3601
-78.7549	18.8405
-84.522	17.2588
-90.5261	15.6089
-96.7658	13.8975
-103.26	12.1269
-110.034	10.3224
-117.089	8.4842
-124.448	6.6114
-132.107	4.6632
-150.059	0
-155.654	0
-162.536	0
-170.059	0

Table E.20: Co-Ordinates of the Deformed V-Plate Profiles for the 150^0 V-Plates and 7g rod explosive

7g Explosive Rod					
Experimental		ABAQUS (Press.)		ABAQUS (EOS)	
X-Coord (mm)	Y-Coord (mm)	X-Coord (mm)	Y-Coord (mm)	X-Coord (mm)	Y-Coord (mm)
-170.4631163	-0.054175157	-138.1495556	3.086436364	170.059	0
-141.3676812	-0.09956244	-102.4212222	12.58316364	162.536	0
-122.2794403	-0.788454689	-86.22437778	16.38185455	155.654	0
-114.6479856	-1.234970613	-64.78737778	15.43218182	150.059	0
-105.2283224	-0.579038753	-44.30313333	11.63349091	132.106	4.6479
-84.58156014	2.690077876	-30.0118	5.460618182	124.446	6.5538
-67.19182569	4.887820287	-19.76967778	-1.661927273	117.089	8.3697
-53.92760369	6.60269687	-10.00393333	-12.58316364	110.011	10.1519
-41.87687919	6.632829597	-3.811022222	-17.33152727	103.252	11.9641
-30.73948226	5.256931922	0	-18.2812	96.7973	13.8016
-24.63451522	2.277079107	3.811022222	-17.33152727	90.5968	15.6388
-19.48772669	-4.103340131	10.00393333	-12.58316364	84.6775	17.4496
-15.47754831	-8.749297875	19.76967778	-1.661927273	78.9887	19.2008
-7.629221045	-12.62124158	30.0118	5.460618182	73.524	20.8849
-0.61733108	-14.48	44.30313333	11.63349091	68.2873	22.4605
5.858286282	-14.04685435	64.78737778	15.43218182	63.233	23.8853
14.42869761	-11.94760649	86.22437778	16.38185455	58.3529	25.0811
20.96838791	-8.665116986	102.4212222	12.58316364	53.5333	26.0614
26.95899636	-3.660592823	138.1495556	3.086436364	48.8389	26.8087
30.87403534	0.532629106			44.33	27.3714
35.04439611	3.010033612			39.9301	27.6768
41.53282807	4.013048551			35.727	27.7669
59.73337329	3.057867027			31.7085	27.6277
77.61452118	0.969161724			27.856	27.4373
91.68955676	-0.468880483			24.1448	27.1472
104.5831285	-2.166999761			20.5717	26.7984
117.5023321	-2.725383112			17.2017	26.2251
127.5223381	-1.512011398			13.9509	25.5292
138.7238081	-0.038562613			10.8605	24.8135
138.7238081	-0.038562613			7.97157	24.0643
170.4631163	-0.139882281			5.1229	23.5049
				2.54157	23.4386
				-3.33786E-05	23.7004
				-2.54157	23.4386
				-5.1229	23.5049
				-7.97157	24.0643
				-10.8605	24.8135
				-13.9509	25.5292
				-17.2017	26.2251
				-20.5717	26.7984
				-24.1448	27.1472
				-27.856	27.4373
				-31.7085	27.6277
				-35.727	27.7669
				-39.9301	27.6768
				-44.33	27.3714
				-48.8389	26.8087
				-53.5333	26.0614
				-58.3529	25.0811
				-63.233	23.8853
				-68.2873	22.4605

contd. contd.

-73.524	20.8849
-78.9887	19.2008
-84.6775	17.4496
-90.5968	15.6388
-96.7973	13.8016
-103.252	11.9641
-110.011	10.1519
-117.089	8.3697
-124.446	6.5538
-132.106	4.6479
-150.059	0
-155.654	0
-162.536	0
-170.059	0

Table E.21: Co-Ordinates of the Deformed V-Plate Profiles for the 150^0 V-Plates and 9g rod explosive

9g Explosive Rod					
Experimental		ABAQUS (Press.)		ABAQUS (EOS)	
X-Coord (mm)	Y-Coord (mm)	X-Coord (mm)	Y-Coord (mm)	X-Coord (mm)	Y-Coord (mm)
-175.6466847	-0.409717188	-142.9133333	2.12669404	170.059	0
-150.2840108	0.974786946	-109.5668889	11.10606887	162.536	0
-146.35006	1.557946346	-91.46453333	12.5238649	155.654	0
-142.4310484	1.512994016	-71.93304444	11.57866755	150.059	0
-135.8187915	0.599439147	-57.64171111	8.270476821	132.091	4.5865
-126.5033288	-0.763978393	-43.35037778	3.544490066	124.367	6.3483
-119.8811115	-1.258793394	-30.96455556	-4.017088742	116.967	7.9629
-111.4401628	-1.355613804	-12.38582222	-27.17442384	109.862	9.5118
-94.23688881	-0.715230772	-3.811022222	-34.73600265	103.051	11.0625
-65.85460863	0.844066471	0	-35.6812	96.5066	12.6555
-53.79610972	0.705751591	3.811022222	-34.73600265	90.2737	14.2908
-45.65662515	0.612389073	12.38582222	-27.17442384	84.3283	15.9134
-39.35578725	-0.716451659	30.96455556	-4.017088742	78.5324	17.4758
-33.68774495	-3.294598281	43.35037778	3.544490066	73.0676	18.9312
-28.04459952	-6.919600353	57.64171111	8.270476821	67.7256	20.3053
-22.10496878	-10.75743027	71.93304444	11.57866755	62.6666	21.5204
-16.1304863	-13.1296648	91.46453333	12.5238649	57.7217	22.4729
-6.212098176	-14.5	109.5668889	11.10606887	52.7952	23.0882
-0.177869874	-14.35978558	142.9133333	2.12669404	48.0097	23.2347
7.695005055	-12.98409486			43.4987	22.833
13.76906385	-11.16891702			39.1494	22.0062
20.78734008	-7.689145542			35.0768	20.858
26.60972293	-3.776802667			31.2785	19.554
29.65422059	-2.555155956			27.6759	18.3041
34.50749195	-1.354258374			24.1473	17.4186
42.36045159	-0.816051273			20.5775	16.7436
58.95084524	-0.587492422			17.2902	16.1016
74.30551497	-1.601327503			14.0954	15.4947
80.32978562	-1.879854893			10.9818	15.0285
94.4935408	-2.251746712			8.12579	14.779
101.4371348	-1.912535951			5.14804	14.5946
108.9587602	-2.627094511			2.59041	14.9156
119.1985249	-3.163403951			-4.76837E-05	14.7349
119.1985249	-3.163403951			-2.59041	14.9156
133.1205646	-1.019387048			-5.14804	14.5946
133.1205646	-1.019387048			-8.12579	14.779
141.9127656	0.974041794			-10.9818	15.0285
145.5352919	1.141917305			-14.0954	15.4947
151.5695201	1.282129815			-17.2902	16.1016
159.9805959	-0.070914116			-20.5775	16.7436
166.6227285	0.271754505			-24.1473	17.4186
175.6466847	-0.669465245			-27.6759	18.3041
				-31.2785	19.554
				-35.0768	20.858
				-39.1494	22.0062
				-43.4987	22.833
				-48.0097	23.2347
				-52.7952	23.0882
				-57.7217	22.4729
				-62.6666	21.5204
				-67.7256	20.3053

contd. contd.

-73.0676	18.9312
-78.5324	17.4758
-84.3283	15.9134
-90.2737	14.2908
-96.5066	12.6555
-103.051	11.0625
-109.862	9.5118
-116.967	7.9629
-124.367	6.3483
-132.091	4.5865
-150.059	0
-155.654	0
-162.536	0
-170.059	0

Table E.22: Co-Ordinates of the Deformed V-Plate Profiles for the 150^0 V-Plates and 11g rod explosive

11g Explosive Rod					
Experimental		ABAQUS (Press.)		ABAQUS (EOS)	
X-Coord (mm)	Y-Coord (mm)	X-Coord (mm)	Y-Coord (mm)	X-Coord (mm)	Y-Coord (mm)
-172.5233399	-0.037586651	(not modelled)		170.059	0
-149.8943228	0.297384307	xxx	xxx	162.536	0
-143.8582742	0.45683467	xxx	xxx	155.654	0
-110.1927965	-4.470440511	xxx	xxx	150.059	0
-102.0798744	-5.780353262	xxx	xxx	132.872	4.3693
-94.85469107	-6.360363653	xxx	xxx	125.876	5.9251
-90.35024973	-7.20496517	xxx	xxx	119.083	7.3656
-87.68702521	-9.394669311	xxx	xxx	112.494	8.7781
-87.76918912	-12.90080462	xxx	xxx	106.247	10.208
-89.04048501	-15.66747926	xxx	xxx	100.182	11.6846
-93.96134911	-19.72191014	xxx	xxx	94.4937	13.1847
-99.45212864	-22.35476918	xxx	xxx	88.9499	14.6695
-101.0001686	-24.06004556	xxx	xxx	83.6253	16.0957
-106.7923387	-26.68334639	xxx	xxx	78.4446	17.4254
-113.1708597	-28.58630618	xxx	xxx	73.4602	18.5895
-118.6616393	-31.21916522	xxx	xxx	68.5464	19.4467
-126.0347176	-36.95019454	xxx	xxx	63.6786	19.854
-130.9309298	-39.95278556	xxx	xxx	58.9391	19.6803
-136.1285352	-42.94581827	xxx	xxx	54.478	18.9768
-139.7780978	-44.23357149	xxx	xxx	50.2528	18.0565
-144.0222306	-45.15159585	xxx	xxx	46.1764	17.094
-148.5102393	-43.60576983	xxx	xxx	42.2459	16.2253
-149.0226427	-39.72990255	xxx	xxx	38.4051	15.3695
-148.0527345	-36.95366978	xxx	xxx	34.7346	14.4044
-144.9730873	-34.24434472	xxx	xxx	31.2566	13.7248
-140.411134	-32.63465079	xxx	xxx	27.8304	13.0805
-139.7508355	-30.19947196	xxx	xxx	24.4443	12.5406
-141.8687937	-30.48317962	xxx	xxx	21.2931	11.9877
128.01374	-46.05964553	xxx	xxx	18.2459	11.6049
124.8847945	-50.8726505	xxx	xxx	15.2823	10.956
121.8133636	-53.23136331	xxx	xxx	12.4748	10.384
117.5610172	-54.5	xxx	xxx	9.80093	9.7257
112.7387498	-54.34706788	xxx	xxx	7.15504	9.5785
108.5439181	-53.16141242	xxx	xxx	4.61282	9.5464
102.8749938	-50.52551348	xxx	xxx	2.34855	9.7428
96.65258154	-45.76681163	xxx	xxx	0.000195503	9.7098
86.30107129	-37.01755	xxx	xxx	-2.34855	9.7428
78.92239244	-30.11693848	xxx	xxx	-4.61282	9.5464
74.52476416	-24.7143617	xxx	xxx	-7.15504	9.5785
73.76848489	-18.37464405	xxx	xxx	-9.80093	9.7257
75.02334807	-16.30919391	xxx	xxx	-12.4748	10.384
78.07834611	-14.6517088	xxx	xxx	-15.2823	10.956
83.51982725	-14.12253286	xxx	xxx	-18.2459	11.6049
98.96474576	-11.45448075	xxx	xxx	-21.2931	11.9877
108.3736157	-8.945878994	xxx	xxx	-24.4443	12.5406
116.5440552	-7.801496478	xxx	xxx	-27.8304	13.0805
122.6211857	-5.888981663	xxx	xxx	-31.2566	13.7248
127.1502762	-5.681743229	xxx	xxx	-34.7346	14.4044
134.7590113	-2.765176447	xxx	xxx	-38.4051	15.3695
144.7706649	-0.275691221	xxx	xxx	-42.2459	16.2253
149.6093651	0.272604357	xxx	xxx	-46.1764	17.094
172.5233399	-0.103210605	xxx	xxx	-50.2528	18.0565

contd. contd.

-54.478	18.9768
-58.9391	19.6803
-63.6786	19.854
-68.5464	19.4467
-73.4602	18.5895
-78.4446	17.4254
-83.6253	16.0957
-88.9499	14.6695
-94.4937	13.1847
-100.182	11.6846
-106.247	10.208
-112.494	8.7781
-119.083	7.3656
-125.876	5.9251
-132.872	4.3693
-150.059	0
-155.654	0

9.6 Appendix F: Co-Ordinates of the JWL Equation of State Method Numerically Predicted Deformed V-Plate Profiles Exploded by PE4 Disc Explosives

9.6.1 Co-Ordinates of the Deformed V-Plate Profiles for the 60^0 V-Plates

Table F.1: Co-Ordinates of the Deformed V-Plate Profiles for the 60^0 V-Plates

4g Explosive Disc		6g Explosive Disc		8g Explosive Disc		10g Explosive Disc		12g Explosive Disc	
X-Coord	Y-Coord	X-Coord	Y-Coord	X-Coord	Y-Coord	X-Coord	Y-Coord	X-Coord	Y-Coord
mm	mm	mm	mm	mm	mm	mm	mm	mm	mm
170	0	170	0	170	0	170	0	170	0
160	0	160	0	160	0	160	0	160	0
150	0	150	0	150	0	150	0	150	0
146.709	5.695	146.69	5.69	146.722	5.708	146.72	5.707	146.697	5.699
143.465	11.307	143.405	11.287	143.485	11.332	143.462	11.324	143.444	11.308
140.264	16.836	140.195	16.809	140.287	16.866	140.268	16.861	140.237	16.838
137.107	22.281	137.048	22.261	137.126	22.313	137.127	22.317	137.103	22.296
133.994	27.643	133.958	27.638	134.014	27.679	134.026	27.693	134.008	27.678
130.926	32.925	130.902	32.93	130.952	32.967	130.964	32.986	130.967	32.979
127.904	38.131	127.867	38.132	127.945	38.182	127.938	38.193	127.953	38.191
124.929	43.261	124.853	43.241	124.986	43.323	124.949	43.317	124.946	43.314
122	48.316	121.871	48.262	122.071	48.388	121.999	48.362	121.987	48.349
119.116	53.298	118.927	53.204	119.193	53.373	119.103	53.333	119.067	53.303
116.272	58.207	116.035	58.072	116.341	58.278	116.255	58.233	116.185	58.182
113.467	63.041	113.193	62.872	113.515	63.1	113.456	63.06	113.345	62.988
110.697	67.8	110.401	67.607	110.725	67.846	110.701	67.812	110.583	67.725
107.961	72.486	107.666	72.278	107.982	72.521	107.991	72.49	107.859	72.396
105.255	77.097	104.97	76.882	105.293	77.132	105.315	77.094	105.2	77.002
102.58	81.635	102.306	81.413	102.656	81.681	102.673	81.623	102.577	81.537
99.9324	86.099	99.6674	85.869	100.071	86.167	100.062	86.08	99.9779	85.999
97.3113	90.49	97.0501	90.246	97.5205	90.587	97.4937	90.467	97.4032	90.384
94.7153	94.809	94.4507	94.546	94.9983	94.938	94.9605	94.788	94.8515	94.694
92.143	99.055	91.8723	98.766	92.4993	99.214	92.4719	99.042	92.321	98.928
89.5945	103.231	89.3144	102.911	90.0158	103.416	90.0175	103.235	89.8135	103.086
87.0693	107.336	86.7824	106.984	87.5502	107.544	87.5894	107.356	87.3275	107.172
84.5702	111.373	84.2734	110.988	85.1068	111.6	85.1834	111.407	84.8681	111.187
82.0987	115.345	81.7945	114.924	82.6885	115.589	82.7907	115.385	82.4369	115.132
79.6586	119.254	79.3268	118.791	80.2942	119.512	80.4101	119.288	80.0461	119.014
77.2481	123.103	76.8832	122.588	77.9236	123.372	78.0556	123.121	77.706	122.829
74.8686	126.892	74.4563	126.319	75.5766	127.169	75.7173	126.89	75.3852	126.576
72.5195	130.622	72.06	129.984	73.2491	130.904	73.4173	130.592	73.0794	130.239
70.2035	134.295	69.6825	133.596	70.9437	134.574	71.1481	134.232	70.7589	133.806
67.917	137.912	67.3458	137.148	68.664	138.18	68.9128	137.797	68.4164	137.267
65.6585	141.472	65.0307	140.643	66.4084	141.723	66.6782	141.28	66.0349	140.622
63.4301	144.977	62.7353	144.085	64.1802	145.209	64.4833	144.687	63.6446	143.962
61.2325	148.431	60.4477	147.461	61.9874	148.639	62.287	148.013	61.2793	147.269
59.0639	151.83	58.1648	150.762	59.8367	152.011	60.1106	151.378	58.938	150.511
56.9217	155.177	55.889	154.026	57.7204	155.331	57.9569	154.667	56.6737	153.74
54.8053	158.471	53.6249	157.194	55.626	158.588	55.8525	157.935	54.48	156.923
52.7195	161.7151	51.3531	160.292	53.551	161.773	53.7906	161.146	52.3405	160.045
50.6605	164.9106	49.0958	163.318	51.5043	164.921	51.7384	164.3	50.2544	163.18
48.6301	168.0579	46.829	166.299	49.4496	168.011	49.6648	167.402	48.1274	166.181
46.6336	171.1623	44.5939	169.218	47.3923	171.052	47.587	170.415	45.9281	169.108
44.6671	174.2215	42.4089	172.068	45.3369	174.037	45.4737	173.348	43.6902	171.906

contd. contd. contd. contd. contd. contd. contd. contd. contd. contd.

42.7339	177.2382	40.2505	174.927	43.2915	176.969	43.3155	176.171	41.3668	174.574
40.842	180.2205	38.1024	177.721	41.2831	179.845	41.1088	178.914	38.9689	177.156
38.9822	183.1583	35.9392	180.427	39.3034	182.692	38.8811	181.556	36.6011	179.658
37.1565	186.0584	33.6467	182.989	37.3369	185.495	36.5852	184.044	34.2171	182.021
35.3511	188.913	31.5059	185.551	35.3946	188.238	34.2658	186.421	31.7662	184.286
33.5833	191.7269	29.5922	188.143	33.4388	190.912	31.995	188.719	29.4124	186.519
31.8579	194.505	27.8388	190.834	31.4709	193.485	29.7106	191.033	27.0788	188.702
30.155	197.2527	26.0977	193.548	29.5345	196.008	27.4397	193.179	24.5838	190.809
28.4588	199.935	24.5387	196.191	27.6733	198.528	25.0882	195.344	22.1295	192.774
26.8039	202.5903	23.0634	198.928	25.6778	201.003	22.8189	197.464	19.7269	194.639
25.1969	205.2014	21.3964	201.512	23.685	203.262	20.5702	199.424	17.1466	196.702
23.6403	207.8081	19.7298	203.984	21.7469	205.606	18.2286	201.338	14.7766	198.259
22.0926	210.3694	17.8759	206.4	19.777	207.766	15.8684	203.1	12.375	199.977
20.5529	212.8868	15.9043	208.591	17.8334	210.007	13.8699	205.063	10.3536	202.014
19.0951	215.3698	14.0337	210.706	16.0167	212.074	11.9524	207.145	8.55179	204.155
17.707	217.8673	12.3736	212.956	14.4453	214.408	10.2597	209.332	6.80102	206.335
16.3704	220.3374	10.62	215.015	13.0423	216.703	8.72097	211.558	5.12454	208.493
15.1248	222.8098	9.07004	217.303	11.6531	219.03	7.36812	213.759	3.40635	210.541
13.8802	225.2504	7.51081	219.494	10.3074	221.323	5.98104	215.979	1.9577	212.62
12.6119	227.6425	5.97453	221.602	8.95524	223.581	4.62757	218.172	1	214.902
11.3292	229.9496	4.52181	223.685	7.54503	225.667	3.28255	220.167	1	216.838
10.1465	232.2391	3.27829	225.783	6.2696	227.682	2.03887	222.206	1	218.967
9.065	234.5498	1.97708	227.824	5.06174	229.788	1	224.158	1	220.861
8.04874	236.8427	1	229.749	3.97689	231.764	1	226.047	1	222.869
7.0574	239.1003	1	231.621	3.02715	233.756	1	227.859	1	224.668
6.13561	241.349	1	233.502	2.1407	235.675	1	229.605	1	226.623
5.29216	243.5176	1	235.284	1.66491	237.591	1	231.3	1	228.323
4.61213	245.7495	1	236.874	1.18334	239.532	1	232.756	1	229.8
4.01805	247.9191	1	238.443	0.8457	241.363	1	233.751	1	231.032
3.37028	250.1324	1	239.069	0.69574	242.924	1	233.959	1	230.919
2.60397	252.1953	1	239.349	1.30322	244.155	1	234.399	1	231.043
2.04931	254.2184	2.00384	242.114	1.96285	245.918	2.39873	236.196	3.16264	230.15
1.15164	256.0453	1.88535	243.849	1.35095	247.725	1.41564	238.085	1.28651	231.449
9.5E-06	257.9766	5.2E-05	244.884	-3.3E-05	249.645	-5E-06	239.909	1.4E-05	234.19
-1.15164	256.0453	-1.88535	243.849	-1.35095	247.725	-1.4156	238.085	-1.28651	231.449
-2.04931	254.2184	-2.00384	242.114	-1.96285	245.918	-2.3987	236.196	-3.16264	230.15
-2.60397	252.1953	-1	239.349	-1.30322	244.155	-1	234.399	-1	231.043
-3.37028	250.1324	-1	239.069	-0.69574	242.924	-1	233.959	-1	230.919
-4.01805	247.9191	-1	238.443	-0.8457	241.363	-1	233.751	-1	231.032
-4.61213	245.7495	-1	236.874	-1.18334	239.532	-1	232.756	-1	229.8
-5.29216	243.5176	-1	235.284	-1.66491	237.591	-1	231.3	-1	228.323
-6.13561	241.349	-1	233.502	-2.1407	235.675	-1	229.605	-1	226.623
-7.0574	239.1003	-1	231.621	-3.02715	233.756	-1	227.859	-1	224.668
-8.04874	236.8427	-1	229.749	-3.97689	231.764	-1	226.047	-1	222.869
-9.065	234.5498	-1.97708	227.824	-5.06174	229.788	-1	224.158	-1	220.861
-10.1465	232.2391	-3.27829	225.783	-6.2696	227.682	-2.0389	222.206	-1	218.967
-11.3292	229.9496	-4.52181	223.685	-7.54503	225.667	-3.2826	220.167	-1	216.838
-12.6119	227.6425	-5.97453	221.602	-8.95524	223.581	-4.6276	218.172	-1	214.902
-13.8802	225.2504	-7.51081	219.494	-10.3074	221.323	-5.981	215.979	-1.9577	212.62
-15.1248	222.8098	-9.07004	217.303	-11.6531	219.03	-7.3681	213.759	-3.40635	210.541
-16.3704	220.3374	-10.62	215.015	-13.0423	216.703	-8.721	211.558	-5.12454	208.493
-17.707	217.8673	-12.3736	212.956	-14.4453	214.408	-10.26	209.332	-6.80102	206.335
-19.0951	215.3698	-14.0337	210.706	-16.0167	212.074	-11.952	207.145	-8.55179	204.155
-20.5529	212.8868	-15.9043	208.591	-17.8334	210.007	-13.87	205.063	-10.3536	202.014
-22.0926	210.3694	-17.8759	206.4	-19.777	207.766	-15.868	203.1	-12.375	199.977
-23.6403	207.8081	-19.7298	203.984	-21.7469	205.606	-18.229	201.338	-14.7766	198.259

contd. contd. contd. contd. contd. contd. contd. contd. contd. contd.

-25.1969	205.2014	-21.3964	201.512	-23.685	203.262	-20.57	199.424	-17.1466	196.702
-26.8039	202.5903	-23.0634	198.928	-25.6778	201.003	-22.819	197.464	-19.7269	194.639
-28.4588	199.935	-24.5387	196.191	-27.6733	198.528	-25.088	195.344	-22.1295	192.774
-30.155	197.2527	-26.0977	193.548	-29.5345	196.008	-27.44	193.179	-24.5838	190.809
-31.8579	194.505	-27.8388	190.834	-31.4709	193.485	-29.711	191.033	-27.0788	188.702
-33.5833	191.7269	-29.5922	188.143	-33.4388	190.912	-31.995	188.719	-29.4124	186.519
-35.3511	188.913	-31.5059	185.551	-35.3946	188.238	-34.266	186.421	-31.7662	184.286
-37.1565	186.0584	-33.6467	182.989	-37.3369	185.495	-36.585	184.044	-34.2171	182.021
-38.9822	183.1583	-35.9392	180.427	-39.3034	182.692	-38.881	181.556	-36.6011	179.658
-40.842	180.2205	-38.1024	177.721	-41.2831	179.845	-41.109	178.914	-38.9689	177.156
-42.7339	177.2382	-40.2505	174.927	-43.2915	176.969	-43.316	176.171	-41.3668	174.574
-44.6671	174.2215	-42.4089	172.068	-45.3369	174.037	-45.474	173.348	-43.6902	171.906
-46.6336	171.1623	-44.5939	169.218	-47.3923	171.052	-47.587	170.415	-45.9281	169.108
-48.6301	168.0579	-46.829	166.299	-49.4496	168.011	-49.665	167.402	-48.1274	166.181
-50.6605	164.9106	-49.0958	163.318	-51.5043	164.921	-51.738	164.3	-50.2544	163.18
-52.7195	161.7151	-51.3531	160.292	-53.551	161.773	-53.791	161.146	-52.3405	160.045
-54.8053	158.471	-53.6249	157.194	-55.626	158.588	-55.853	157.935	-54.48	156.923
-56.9217	155.177	-55.889	154.026	-57.7204	155.331	-57.957	154.667	-56.6737	153.74
-59.0639	151.83	-58.1648	150.762	-59.8367	152.011	-60.111	151.378	-58.938	150.511
-61.2325	148.431	-60.4477	147.461	-61.9874	148.639	-62.287	148.013	-61.2793	147.269
-63.4301	144.977	-62.7353	144.085	-64.1802	145.209	-64.483	144.687	-63.6446	143.962
-65.6585	141.472	-65.0307	140.643	-66.4084	141.723	-66.678	141.28	-66.0349	140.622
-67.917	137.912	-67.3458	137.148	-68.664	138.18	-68.913	137.797	-68.4164	137.267
-70.2035	134.295	-69.6825	133.596	-70.9437	134.574	-71.148	134.232	-70.7589	133.806
-72.5195	130.622	-72.06	129.984	-73.2491	130.904	-73.417	130.592	-73.0794	130.239
-74.8686	126.892	-74.4563	126.319	-75.5766	127.169	-75.717	126.89	-75.3852	126.576
-77.2481	123.103	-76.8832	122.588	-77.9236	123.372	-78.056	123.121	-77.706	122.829
-79.6586	119.254	-79.3268	118.791	-80.2942	119.512	-80.41	119.288	-80.0461	119.014
-82.0987	115.345	-81.7945	114.924	-82.6885	115.589	-82.791	115.385	-82.4369	115.132
-84.5702	111.373	-84.2734	110.988	-85.1068	111.6	-85.183	111.407	-84.8681	111.187
-87.0693	107.336	-86.7824	106.984	-87.5502	107.544	-87.589	107.356	-87.3275	107.172
-89.5945	103.231	-89.3144	102.911	-90.0158	103.416	-90.018	103.235	-89.8135	103.086
-92.143	99.055	-91.8723	98.766	-92.4993	99.214	-92.472	99.042	-92.321	98.928
-94.7153	94.809	-94.4507	94.546	-94.9983	94.938	-94.961	94.788	-94.8515	94.694
-97.3113	90.49	-97.0501	90.246	-97.5205	90.587	-97.494	90.467	-97.4032	90.384
-99.9324	86.099	-99.6674	85.869	-100.071	86.167	-100.06	86.08	-99.9779	85.999
-102.58	81.635	-102.306	81.413	-102.656	81.681	-102.67	81.623	-102.577	81.537
-105.255	77.097	-104.97	76.882	-105.293	77.132	-105.32	77.094	-105.2	77.002
-107.961	72.486	-107.666	72.278	-107.982	72.521	-107.99	72.49	-107.859	72.396
-110.697	67.8	-110.401	67.607	-110.725	67.846	-110.7	67.812	-110.583	67.725
-113.467	63.041	-113.193	62.872	-113.515	63.1	-113.46	63.06	-113.345	62.988
-116.272	58.207	-116.035	58.072	-116.341	58.278	-116.26	58.233	-116.185	58.182
-119.116	53.298	-118.927	53.204	-119.193	53.373	-119.1	53.333	-119.067	53.303
-122	48.316	-121.871	48.262	-122.071	48.388	-122	48.362	-121.987	48.349
-124.929	43.261	-124.853	43.241	-124.986	43.323	-124.95	43.317	-124.946	43.314
-127.904	38.131	-127.867	38.132	-127.945	38.182	-127.94	38.193	-127.953	38.191
-130.926	32.925	-130.902	32.93	-130.952	32.967	-130.96	32.986	-130.967	32.979
-133.994	27.643	-133.958	27.638	-134.014	27.679	-134.03	27.693	-134.008	27.678
-137.107	22.281	-137.048	22.261	-137.126	22.313	-137.13	22.317	-137.103	22.296
-140.264	16.836	-140.195	16.809	-140.287	16.866	-140.27	16.861	-140.237	16.838
-143.465	11.307	-143.405	11.287	-143.485	11.332	-143.46	11.324	-143.444	11.308
-146.709	5.695	-146.69	5.69	-146.722	5.708	-146.72	5.707	-146.697	5.699
-150	0	-150	0	-150	0	-150	0	-150	0
-160	0	-160	0	-160	0	-160	0	-160	0
-170	0	-170	0	-170	0	-170	0	-170	0

9.6.2 Co-Ordinates of the Deformed V-Plate Profiles for the 90^0 V-Plates

Table F.2: Co-Ordinates of the Deformed V-Plate Profiles for the 90^0 V-Plates

4g Explosive Disc		6g Explosive Disc		8g Explosive Disc		10g Explosive Disc		12g Explosive Disc	
X-Coord	Y-Coord	X-Coord	Y-Coord	X-Coord	Y-Coord	X-Coord	Y-Coord	X-Coord	Y-Coord
mm	mm	mm	mm	mm	mm	mm	mm	mm	mm
170.614	0	170.614	0	170.614	0	170.614	0	170.614	0
160.614	0	160.614	0	160.614	0	160.614	0	160.614	0
150.614	0	150.614	0	150.614	0	150.614	0	150.614	0
145.446	5.15	145.975	4.701	145.971	4.699	145.956	4.686	145.92	4.646
140.39	10.173	141.444	9.326	141.433	9.318	141.398	9.269	141.365	9.174
135.45	15.077	136.998	13.84	136.988	13.828	136.927	13.757	136.877	13.597
130.623	19.868	132.611	18.227	132.614	18.211	132.58	18.136	132.526	17.919
125.911	24.55	128.292	22.481	128.306	22.459	128.322	22.406	128.3	22.133
121.309	29.126	124.038	26.609	124.067	26.574	124.153	26.562	124.117	26.232
116.813	33.596	119.858	30.622	119.901	30.569	120.045	30.594	120.048	30.214
112.413	37.954	115.769	34.537	115.814	34.462	115.995	34.501	116.042	34.091
108.098	42.2	111.775	38.373	111.825	38.267	112.008	38.297	112.156	37.867
103.864	46.327	107.891	42.144	107.94	42.006	108.097	41.981	108.302	41.54
99.7033	50.334	104.116	45.852	104.176	45.691	104.264	45.583	104.494	45.171
95.6123	54.2222	100.455	49.499	100.523	49.337	100.515	49.117	100.673	48.695
91.594	57.995	96.9072	53.0849	96.9821	52.9543	96.8921	52.6101	96.9178	52.0314
87.6516	61.6608	93.4538	56.6188	93.5235	56.5373	93.3472	56.0917	93.2876	55.387
83.7861	65.2274	90.0983	60.0889	90.1762	60.1017	89.9351	59.5493	89.7734	58.7336
80.0024	68.7027	86.819	63.5084	86.9145	63.5673	86.6363	62.9575	86.2947	62.0052
76.3001	72.0915	83.5843	66.927	83.693	66.9723	83.4093	66.374	82.8073	65.1735
72.681	75.3989	80.401	70.2697	80.521	70.2906	80.2668	69.7114	79.3551	68.1788
69.1435	78.6301	77.2721	73.5167	77.3906	73.5113	77.1768	72.9748	75.9249	71.066
65.6907	81.7869	74.2119	76.6887	74.275	76.6372	74.1286	76.17	72.5496	73.8725
62.3185	84.8757	71.2025	79.7625	71.1729	79.6518	71.1118	79.2663	69.2441	76.629
59.0285	87.8934	68.2104	82.7546	68.1019	82.5598	68.1936	82.2811	66.0557	79.3504
55.8121	90.8461	65.2464	85.6463	65.0859	85.3832	65.315	85.227	62.9461	82.0294
52.6678	93.7253	62.3365	88.4483	62.1163	88.1244	62.5596	88.1307	60.0237	84.7261
49.5871	96.5347	59.4795	91.1864	59.204	90.8021	59.9214	91.014	57.2321	87.4418
46.5841	99.2717	56.6825	93.8421	56.3726	93.4203	57.4733	93.9262	54.6831	90.2198
43.6398	101.952	53.9558	96.4501	53.6557	96.0366	55.1162	96.8064	52.2093	93.0169
40.7433	104.538	51.305	99.0073	51.0499	98.6425	52.8253	99.6772	50.0211	95.8518
37.9201	107.063	48.7838	101.551	48.5254	101.205	50.5233	102.418	47.7286	98.6793
35.1675	109.546	46.3219	104.064	46.0933	103.719	48.2716	105.059	45.2899	101.29
32.4831	111.956	43.9212	106.517	43.7348	106.189	45.7969	107.474	42.1553	103.224
29.8375	114.305	41.5804	108.908	41.4479	108.613	43.2447	109.636	38.9795	104.319
27.261	116.571	39.3897	111.282	39.1554	110.979	40.3746	111.412	35.724	104.909
24.7228	118.776	37.3358	113.689	36.884	113.213	37.6698	113.004	32.2355	104.574
22.2378	120.926	35.2924	116.038	34.6447	115.364	34.6066	114.217	29.2328	103.495
19.8333	123.012	33.0565	118.199	31.9189	117.086	31.4512	114.696	26.4382	101.994
17.5191	125.065	30.443	119.801	29.256	118.314	28.4298	114.705	23.9898	100.235
15.0099	126.924	27.8779	121.01	26.4709	119.356	25.4276	114.553	22.0304	98.0069
12.8603	128.619	25.2406	122.082	23.6967	120.127	22.7066	114.097	19.9893	96.0763
9.18696	130.657	22.4665	122.775	20.8403	120.541	20.0511	113.578	18.0384	94.3457
8.95713	132.669	19.7024	123.012	18.2552	120.928	17.3918	113.311	15.7385	92.9697
7.11482	134.567	17.0027	122.905	15.5976	121.439	14.8118	113.355	13.6092	91.431
5.6488	137.03	14.4298	122.867	13.243	121.794	12.4878	113.574	11.945	90.0553

contd. contd. contd. contd. contd. contd. contd. contd. contd. contd.

4.63933	139.217	12.0527	122.84	10.8807	122.125	10.1229	114.095	10.0068	88.4732
3.69717	141.653	9.82986	123.021	8.70984	122.409	7.89927	114.28	8.65882	87.0889
2.88988	144.006	7.32761	122.547	6.81826	122.991	5.7916	114.347	7.22039	86.1786
1.72567	146.242	5.6511	121.25	5.38099	123.99	3.92769	114.541	5.85184	85.7799
1.4E-05	147.953	4.50916	119.765	4.1959	125.272	2.56188	115.153	4.60376	86.0314
-1.7257	146.242	3.67632	118.584	3.22486	126.63	1.60567	116.289	3.68585	86.7463
-2.8899	144.006	3.19611	119.121	2.51799	127.831	1.62969	117.195	2.43332	87.2354
-3.6972	141.653	1.84222	119.148	2.28415	129.029	1.72139	118.491	1.73307	87.4404
-4.6393	139.217	1.0485	119.916	1.38757	130.118	1.32173	120.234	0.56169	87.1665
-5.6488	137.03	-9E-05	120.686	1.9E-05	131.998	-5E-06	121.794	9.5E-06	88.4064
-7.1148	134.567	-1.0485	119.916	-1.3876	130.118	-1.3217	120.234	-0.5617	87.1665
-8.9571	132.669	-1.8422	119.148	-2.2842	129.029	-1.7214	118.491	-1.7331	87.4404
-9.187	130.657	-3.1961	119.121	-2.518	127.831	-1.6297	117.195	-2.4333	87.2354
-12.86	128.619	-3.6763	118.584	-3.2249	126.63	-1.6057	116.289	-3.6859	86.7463
-15.01	126.924	-4.5092	119.765	-4.1959	125.272	-2.5619	115.153	-4.6038	86.0314
-17.519	125.065	-5.6511	121.25	-5.381	123.99	-3.9277	114.541	-5.8518	85.7799
-19.833	123.012	-7.3276	122.547	-6.8183	122.991	-5.7916	114.347	-7.2204	86.1786
-22.238	120.926	-9.8299	123.021	-8.7098	122.409	-7.8993	114.28	-8.6588	87.0889
-24.723	118.776	-12.053	122.84	-10.881	122.125	-10.123	114.095	-10.007	88.4732
-27.261	116.571	-14.43	122.867	-13.243	121.794	-12.488	113.574	-11.945	90.0553
-29.838	114.305	-17.003	122.905	-15.598	121.439	-14.812	113.355	-13.609	91.431
-32.483	111.956	-19.702	123.012	-18.255	120.928	-17.392	113.311	-15.739	92.9697
-35.168	109.546	-22.467	122.775	-20.84	120.541	-20.051	113.578	-18.038	94.3457
-37.92	107.063	-25.241	122.082	-23.697	120.127	-22.707	114.097	-19.989	96.0763
-40.743	104.538	-27.878	121.01	-26.471	119.356	-25.428	114.553	-22.03	98.0069
-43.64	101.952	-30.443	119.801	-29.256	118.314	-28.43	114.705	-23.99	100.235
-46.584	99.2717	-33.057	118.199	-31.919	117.086	-31.451	114.696	-26.438	101.994
-49.587	96.5347	-35.292	116.038	-34.645	115.364	-34.607	114.217	-29.233	103.495
-52.668	93.7253	-37.336	113.689	-36.884	113.213	-37.67	113.004	-32.236	104.574
-55.812	90.8461	-39.39	111.282	-39.155	110.979	-40.375	111.412	-35.724	104.909
-59.029	87.8934	-41.58	108.908	-41.448	108.613	-43.245	109.636	-38.98	104.319
-62.319	84.8757	-43.921	106.517	-43.735	106.189	-45.797	107.474	-42.155	103.224
-65.691	81.7869	-46.322	104.064	-46.093	103.719	-48.272	105.059	-45.29	101.29
-69.144	78.6301	-48.784	101.551	-48.525	101.205	-50.523	102.418	-47.729	98.6793
-72.681	75.3989	-51.305	99.0073	-51.05	98.6425	-52.825	99.6772	-50.021	95.8518
-76.3	72.0915	-53.956	96.4501	-53.656	96.0366	-55.116	96.8064	-52.209	93.0169
-80.002	68.7027	-56.683	93.8421	-56.373	93.4203	-57.473	93.9262	-54.683	90.2198
-83.786	65.2274	-59.48	91.1864	-59.204	90.8021	-59.921	91.014	-57.232	87.4418
-87.652	61.6608	-62.337	88.4483	-62.116	88.1244	-62.56	88.1307	-60.024	84.7261
-91.594	57.995	-65.246	85.6463	-65.086	85.3832	-65.315	85.227	-62.946	82.0294
-95.612	54.2222	-68.21	82.7546	-68.102	82.5598	-68.194	82.2811	-66.056	79.3504
-99.703	50.334	-71.203	79.7625	-71.173	79.6518	-71.112	79.2663	-69.244	76.629
-103.86	46.327	-74.212	76.6887	-74.275	76.6372	-74.129	76.17	-72.55	73.8725
-108.1	42.2	-77.272	73.5167	-77.391	73.5113	-77.177	72.9748	-75.925	71.066
-112.41	37.954	-80.401	70.2697	-80.521	70.2906	-80.267	69.7114	-79.355	68.1788
-116.81	33.596	-83.584	66.927	-83.693	66.9723	-83.409	66.374	-82.807	65.1735
-121.31	29.126	-86.819	63.5084	-86.915	63.5673	-86.636	62.9575	-86.295	62.0052
-125.91	24.55	-90.098	60.0889	-90.176	60.1017	-89.935	59.5493	-89.773	58.7336
-130.62	19.868	-93.454	56.6188	-93.524	56.5373	-93.347	56.0917	-93.288	55.387
-135.45	15.077	-96.907	53.0849	-96.982	52.9543	-96.892	52.6101	-96.918	52.0314
-140.39	10.173	-100.46	49.499	-100.52	49.337	-100.52	49.117	-100.67	48.695
-145.45	5.15	-104.12	45.852	-104.18	45.691	-104.26	45.583	-104.49	45.171
-150.61	0	-107.89	42.144	-107.94	42.006	-108.1	41.981	-108.3	41.54
-160.61	0	-111.78	38.373	-111.83	38.267	-112.01	38.297	-112.16	37.867
-170.61	0	-115.77	34.537	-115.81	34.462	-116	34.501	-116.04	34.091

contd. contd. contd. contd. contd. contd. contd. contd.

-119.86	30.622	-119.9	30.569	-120.05	30.594	-120.05	30.214
-124.04	26.609	-124.07	26.574	-124.15	26.562	-124.12	26.232
-128.29	22.481	-128.31	22.459	-128.32	22.406	-128.3	22.133
-132.61	18.227	-132.61	18.211	-132.58	18.136	-132.53	17.919
-137	13.84	-136.99	13.828	-136.93	13.757	-136.88	13.597
-141.44	9.326	-141.43	9.318	-141.4	9.269	-141.37	9.174
-145.98	4.701	-145.97	4.699	-145.96	4.686	-145.92	4.646
-150.61	0	-150.61	0	-150.61	0	-150.61	0
-160.61	0	-160.61	0	-160.61	0	-160.61	0
-170.61	0	-170.61	0	-170.61	0	-170.61	0

9.6.3 Co-Ordinates of the Deformed V-Plate Profiles for the 90^0 V-Plates Exploded by Offset Disc Explosives

Table F.3: Co-Ordinates of the Deformed V-Plate Profiles for the 90^0 V-Plates exploded by offset disc explosives

Disc Offset 0mm		Disc Offset 5mm		Disc Offset 10mm		Disc Offset 15mm		Disc Offset 20mm	
X-Coord	Y-Coord	X-Coord	Y-Coord	X-Coord	Y-Coord	X-Coord	Y-Coord	X-Coord	Y-Coord
mm	mm	mm	mm	mm	mm	mm	mm	mm	mm
170.614	0	170.614	0	170.614	0	170.614	0	170.614	0
160.614	0	160.614	0	160.614	0	160.614	0	160.614	0
150.614	0	150.614	0	150.614	0	150.614	0	150.614	0
145.971	4.699	145.903	4.644	145.925	4.653	145.917	4.65	145.938	4.669
141.433	9.318	141.271	9.16	141.33	9.201	141.309	9.182	141.348	9.232
136.988	13.828	136.745	13.581	136.829	13.654	136.772	13.597	136.825	13.678
132.614	18.211	132.328	17.914	132.417	18.006	132.292	17.881	132.356	17.991
128.306	22.459	128.01	22.153	128.081	22.253	127.862	22.031	127.929	22.162
124.067	26.574	123.779	26.293	123.82	26.393	123.472	26.052	123.541	26.191
119.901	30.569	119.629	30.329	119.625	30.422	119.126	29.937	119.202	30.086
115.814	34.462	115.558	34.265	115.491	34.335	114.822	33.691	114.914	33.858
111.825	38.267	111.571	38.103	111.419	38.14	110.574	37.325	110.688	37.518
107.94	42.006	107.667	41.851	107.407	41.85	106.39	40.851	106.532	41.081
104.176	45.691	103.849	45.516	103.458	45.457	102.28	44.286	102.455	44.557
100.523	49.337	100.117	49.109	99.5598	48.963	98.2493	47.64	98.4601	47.958
96.9821	52.9543	96.4864	52.6476	95.7338	52.3693	94.295	50.9146	94.5437	51.2833
93.5235	56.5373	92.9624	56.1328	91.9858	55.711	90.4257	54.1121	90.7008	54.5317
90.1762	60.1017	89.5347	59.5872	88.3212	58.9835	86.6289	57.23	86.9292	57.7047
86.9145	63.5673	86.1633	62.9924	84.7138	62.1732	82.9127	60.2764	83.229	60.8054
83.693	66.9723	82.8378	66.2426	81.1647	65.272	79.2558	63.2358	79.5914	63.8302
80.521	70.2906	79.519	69.3674	77.6834	68.2947	75.6674	66.1061	76.0238	66.788
77.3906	73.5113	76.1729	72.4046	74.2781	71.2568	72.1077	68.9251	72.5035	69.6691
74.275	76.6372	72.8523	75.2533	70.9511	74.1692	68.6066	71.6871	69.0458	72.4733
71.1729	79.6518	69.6235	78.0258	67.7023	77.0295	65.1607	74.3371	65.6332	75.1982
68.1019	82.5598	66.5166	80.8073	64.5332	79.8429	61.7714	76.9446	62.2722	77.8456
65.0859	85.3832	63.5134	83.6294	61.4358	82.6053	58.4584	79.4747	58.963	80.4229
62.1163	88.1244	60.5497	86.4052	58.4035	85.3086	55.19	81.9292	55.7019	82.8999
59.204	90.8021	57.561	89.0366	55.4367	87.9595	51.9983	84.3172	52.4701	85.2794
56.3726	93.4203	54.458	91.4287	52.5199	90.5469	48.8277	86.6555	49.248	87.5408
53.6557	96.0366	51.2432	93.5337	49.641	93.0575	45.6658	88.8034	46.021	89.6754
51.0499	98.6425	47.9746	95.4117	46.7553	95.4587	42.5563	90.8889	42.8517	91.74
48.5254	101.205	44.6961	97.095	43.8758	97.7235	39.4182	92.8221	39.6233	93.62
46.0933	103.719	41.3926	98.5716	40.9259	99.789	36.2601	94.5292	36.3857	95.3393
43.7348	106.189	38.1065	99.8634	37.8722	101.592	33.0827	96.3385	33.0092	96.6369
41.4479	108.613	34.7792	100.965	34.8161	103.12	30.0184	97.8356	29.7507	97.8729
39.1554	110.979	31.5515	101.902	31.942	104.729	26.9683	99.257	26.5666	99.0392
36.884	113.213	28.1698	102.541	28.9448	106.233	23.9637	100.676	23.4978	100.42
34.6447	115.364	25.0013	102.926	25.7073	107.195	21.14	102.107	20.5229	101.744
31.9189	117.086	21.7462	102.984	22.5503	107.619	18.4252	103.63	17.5853	103.101
29.256	118.314	18.6338	102.661	19.4939	108.025	15.7541	105.154	14.8813	104.695
26.4709	119.356	15.6512	101.795	16.5439	108.496	13.1777	106.63	12.426	106.46
23.6967	120.127	12.9531	100.879	13.6073	108.811	10.7105	108.055	10.3602	108.563
20.8403	120.541	10.3817	99.2091	10.7959	108.985	8.29037	109.588	8.46091	110.81
18.2552	120.928	8.223	97.0181	8.06434	109.211	5.89652	111.019	6.86389	113.232
15.5976	121.439	6.81218	94.827	5.57681	109.543	3.4852	112.243	5.38459	115.54
13.243	121.794	5.68511	92.2924	2.99943	109.82	1.12425	113.431	3.99236	117.964

contd. contd. contd. contd. contd. contd. contd. contd. contd. contd.

10.8807	122.125	5.12384	89.9041	0.6628	110.028	-1.0601	114.679	2.92914	120.371
8.70984	122.409	5.26774	87.4471	-1.6891	109.852	-3.2025	115.811	1.85985	122.835
6.81826	122.991	5.02238	85.5118	-3.8199	109.106	-5.3073	116.955	0.99282	125.268
5.38099	123.99	5.254	83.444	-5.6783	108.03	-7.2346	118.105	0.27404	127.599
4.1959	125.272	4.14747	80.2833	-7.2418	106.927	-8.9435	119.334	-0.2813	130.006
3.22486	126.63	-3.0634	61.5932	-8.4811	105.809	-10.276	120.668	-0.8421	132.36
2.51799	127.831	-2.1301	58.9052	-9.4491	106.132	-11.275	122.26	-1.1885	134.571
2.28415	129.029	-2.2465	57.8023	-9.7903	105.882	-12.044	123.884	-1.3695	136.721
1.38757	130.118	-4.0119	61.3317	-10.313	106.336	-12.086	125.471	-0.8678	138.944
1.9E-05	131.998	-3.4459	60.2634	-11.252	106.689	-12.05	126.593	-1.1609	141.158
-1.3876	130.118	-5.3678	63.4239	-12.278	107.168	-11.611	127.774	-2.6494	141.736
-2.2842	129.029	-8.4535	69.1711	-12.607	110.184	-11.057	129.007	-4.583	142.032
-2.518	127.831	-14.486	82.4307	-12.864	111.721	-10.975	130.765	-6.7873	142.031
-3.2249	126.63	-18.75	89.7498	-13.128	113.76	-11.395	132.996	-8.8747	141.498
-4.1959	125.272	-18.471	91.8574	-13.413	115.666	-13.155	134.289	-10.933	140.8
-5.381	123.99	-18.043	93.8965	-13.633	117.968	-15.625	134.482	-12.979	139.989
-6.8183	122.991	-18.062	96.4511	-13.589	120.458	-17.621	133.993	-15.133	139.096
-8.7098	122.409	-18.357	99.0033	-14.122	122.706	-19.635	133.731	-17.254	138.01
-10.881	122.125	-18.628	101.273	-16.1	124.735	-21.863	133.651	-19.353	136.766
-13.243	121.794	-18.943	104.294	-17.91	126.314	-24.319	133.428	-21.389	135.312
-15.598	121.439	-20.343	106.641	-20.353	127.602	-26.66	132.179	-23.389	133.64
-18.255	120.928	-21.941	108.711	-23.012	128.412	-28.392	130.154	-25.225	131.683
-20.84	120.541	-23.777	110.877	-25.923	128.451	-29.612	127.823	-26.946	129.543
-23.697	120.127	-26.034	112.748	-28.802	127.629	-30.536	125.353	-28.626	127.291
-26.471	119.356	-28.477	114.335	-31.285	125.811	-31.523	122.821	-30.323	124.962
-29.256	118.314	-31.223	115.733	-33.191	123.433	-32.64	120.249	-32.071	122.6
-31.919	117.086	-34.248	116.658	-34.845	120.864	-34.011	117.813	-33.919	120.219
-34.645	115.364	-37.523	116.825	-36.521	118.292	-35.629	115.365	-35.842	117.816
-36.884	113.213	-40.771	116.072	-38.335	115.763	-37.506	112.999	-37.864	115.386
-39.155	110.979	-43.714	114.278	-40.374	113.299	-39.584	110.639	-39.958	112.904
-41.448	108.613	-45.881	111.529	-42.578	110.862	-41.778	108.258	-42.085	110.347
-43.735	106.189	-47.367	108.384	-44.911	108.4	-44.069	105.816	-44.256	107.739
-46.093	103.719	-48.6	105.119	-47.273	105.843	-46.408	103.303	-46.487	105.072
-48.525	101.205	-49.908	101.837	-49.662	103.217	-48.782	100.721	-48.777	102.363
-51.05	98.6425	-51.586	98.6687	-52.084	100.51	-51.238	98.1064	-51.156	99.621
-53.656	96.0366	-53.724	95.7136	-54.552	97.7338	-53.76	95.4361	-53.619	96.8562
-56.373	93.4203	-56.18	92.8453	-57.061	94.8925	-56.349	92.7139	-56.193	94.0709
-59.204	90.8021	-58.829	89.9985	-59.648	92.006	-59.03	89.9728	-58.859	91.2589
-62.116	88.1244	-61.534	87.1177	-62.294	89.0605	-61.811	87.2156	-61.62	88.4171
-65.086	85.3832	-64.318	84.1686	-65.008	86.0498	-64.701	84.4525	-64.469	85.5459
-68.102	82.5598	-67.181	81.2	-67.766	82.9683	-67.705	81.6484	-67.417	82.6458
-71.173	79.6518	-70.151	78.1869	-70.595	79.8337	-70.798	78.7812	-70.456	79.7111
-74.275	76.6372	-73.202	75.1854	-73.503	76.6495	-73.974	75.8512	-73.588	76.7294
-77.391	73.5113	-76.344	72.2268	-76.514	73.4375	-77.23	72.8607	-76.797	73.6923
-80.521	70.2906	-79.613	69.2137	-79.627	70.1895	-80.548	69.7998	-80.073	70.5866
-83.693	66.9723	-82.982	66.1914	-82.85	66.9067	-83.897	66.675	-83.408	67.3976
-86.915	63.5673	-86.39	63.0852	-86.179	63.5929	-87.253	63.4843	-86.792	64.1146
-90.176	60.1017	-89.865	59.8892	-89.619	60.2438	-90.621	60.1981	-90.214	60.7306
-93.524	56.5373	-93.402	56.5973	-93.161	56.8477	-94.024	56.8052	-93.681	57.2445
-96.982	52.9543	-96.994	53.2144	-96.793	53.3878	-97.478	53.3132	-97.194	53.6564
-100.52	49.337	-100.64	49.698	-100.5	49.845	-100.99	49.729	-100.76	49.976
-104.18	45.691	-104.36	46.042	-104.26	46.206	-104.59	46.058	-104.41	46.229
-107.94	42.006	-108.13	42.315	-108.08	42.463	-108.27	42.303	-108.14	42.418
-111.83	38.267	-111.94	38.483	-111.96	38.613	-112.05	38.47	-111.98	38.549

contd. contd. contd. contd. contd. contd. contd. contd. contd. contd.

-115.81	34.462	-115.84	34.558	-115.88	34.669	-115.93	34.566	-115.91	34.618
-119.9	30.569	-119.84	30.557	-119.89	30.636	-119.93	30.591	-119.94	30.619
-124.07	26.574	-123.95	26.483	-123.98	26.518	-124.03	26.538	-124.07	26.542
-128.31	22.459	-128.17	22.331	-128.17	22.313	-128.24	22.389	-128.29	22.375
-132.61	18.211	-132.5	18.086	-132.46	18.031	-132.55	18.136	-132.59	18.114
-136.99	13.828	-136.9	13.734	-136.85	13.667	-136.94	13.765	-136.96	13.745
-141.43	9.318	-141.39	9.265	-141.34	9.212	-141.41	9.278	-141.42	9.266
-145.97	4.699	-145.95	4.681	-145.93	4.66	-145.96	4.684	-145.96	4.681
-150.61	0	-150.61	0	-150.61	0	-150.61	0	-150.61	0
-160.61	0	-160.61	0	-160.61	0	-160.61	0	-160.61	0
-170.61	0	-170.61	0	-170.61	0	-170.61	0	-170.61	0

9.6.4 Co-Ordinates of the Deformed V-Plate Profiles for the 120^0 V-Plates

Table F.4: Co-Ordinates of the Deformed V-Plate Profiles for the 120^0 V-Plates

4g Explosive Disc		6g Explosive Disc		8g Explosive Disc		10g Explosive Disc		12g Explosive Disc	
X-Coord	Y-Coord	X-Coord	Y-Coord	X-Coord	Y-Coord	X-Coord	Y-Coord	X-Coord	Y-Coord
mm	mm	mm	mm	mm	mm	mm	mm	mm	mm
168.09	0	168.09	0	168.09	0	168.09	0	168.09	0
158.09	0	158.09	0	158.09	0	158.09	0	158.09	0
148.09	0	148.09	0	148.09	0	148.09	0	148.09	0
142.423	3.2565	142.418	3.2321	142.4	3.2056	142.397	3.1878	142.535	3.2882
136.884	6.4016	136.89	6.3731	136.846	6.2947	136.839	6.2564	137.171	6.4617
131.474	9.4374	131.514	9.4453	131.461	9.3324	131.44	9.2718	131.914	9.5674
126.211	12.3979	126.277	12.4446	126.248	12.3543	126.236	12.2948	126.804	12.5866
121.08	15.2857	121.17	15.3627	121.19	15.3467	121.219	15.3455	121.791	15.4817
116.095	18.1032	116.184	18.1832	116.269	18.2772	116.355	18.3714	116.883	18.2417
111.246	20.8758	111.306	20.9041	111.462	21.1187	111.65	21.3293	112.08	20.9295
106.524	23.5813	106.537	23.5195	106.769	23.8577	107.071	24.2319	107.4	23.5779
101.915	26.204	101.878	26.0452	102.173	26.4836	102.556	27.0308	102.873	26.2417
97.4177	28.7435	97.3306	28.4859	97.6923	29.0256	98.0809	29.62	98.4774	28.8648
93.0319	31.2119	92.8971	30.8498	93.3134	31.4797	93.5862	31.9257	94.0935	31.2801
88.7472	33.5994	88.5739	33.1472	89.0066	33.7979	89.0842	33.8962	89.7087	33.4519
84.5661	35.906	84.3686	35.3842	84.7476	35.9285	84.6149	35.5968	85.3724	35.4136
80.497	38.1571	80.272	37.5686	80.4949	37.8385	80.2264	37.1355	81.0588	37.139
76.5259	40.3392	76.2952	39.7	76.2859	39.5175	75.9695	38.6287	76.7118	38.5175
72.6597	42.4649	72.4332	41.8007	72.1668	41.0735	71.8678	40.1739	72.3898	39.5402
68.9123	44.5543	68.6883	43.8812	68.2219	42.66	67.9256	41.7879	68.1765	40.3409
65.281	46.6368	65.0485	45.9338	64.4603	44.3748	64.1244	43.4709	64.0982	41.1496
61.7567	48.6816	61.5083	47.941	60.8277	46.1912	60.432	45.1636	60.0828	41.9785
58.3325	50.6967	58.0404	49.8667	57.3081	48.014	56.832	46.8191	56.1132	42.6458
54.9941	52.6562	54.6429	51.7044	53.8827	49.8044	53.288	48.3791	52.2081	42.9966
51.7302	54.5414	51.3192	53.4558	50.5125	51.5076	49.7844	49.7935	48.3962	43.1696
48.5513	56.3722	48.0557	55.1346	47.1192	52.9842	46.2785	50.995	44.7107	43.2451
45.4581	58.1635	44.8508	56.6996	43.7224	54.1832	42.7931	51.9194	41.1114	43.3224
42.4199	59.8731	41.665	58.1322	40.3007	55.0918	39.3055	52.5099	37.6483	43.4098
39.4159	61.4607	38.4917	59.3561	36.8909	55.6251	35.9153	52.784	34.2238	43.4604
36.4158	62.8839	35.3324	60.3528	33.5561	55.795	32.5856	52.7099	30.8654	43.1964
33.4132	64.1074	32.2097	61.1448	30.3156	55.6473	29.393	52.3641	27.7052	42.7422
30.4126	65.092	29.0718	61.6007	27.1697	55.1559	26.3131	51.694	24.5359	41.6137
27.4414	65.8494	25.9579	61.5515	24.1904	54.1965	23.319	50.3612	21.8283	40.2508
24.4988	66.4268	22.9292	60.5882	21.5329	52.5859	21.1329	48.4278	19.2317	38.729
21.5806	66.7433	20.4689	58.8826	19.3708	50.4899	19.0103	46.341	16.8757	36.8517
18.8013	66.8902	18.4829	56.9933	17.6029	48.352	17.0701	44.4783	14.7032	34.9239
16.1012	66.9225	16.6037	55.0215	15.8926	46.1075	15.2027	42.5078	12.8965	32.8146
13.5141	67.0783	14.8216	53.1214	14.4383	43.9901	13.5828	40.4607	11.3028	30.8435
11.1164	67.2083	13.016	51.4546	13.0925	42.1011	11.9328	38.595	9.71673	29.0112
8.6691	67.8512	11.0994	50.347	11.0996	40.8263	10.4526	37.0256	8.13785	27.2648
6.73731	69.0536	9.06313	50.0834	8.99454	40.1136	8.72109	36.0496	6.78744	25.6051
5.28362	70.6899	7.04304	50.3778	7.12091	40.1387	6.74311	35.2519	5.29203	24.1092
4.07175	72.5403	5.17191	51.0457	5.10386	40.4977	5.07557	35.207	3.94254	22.9046
3.06394	74.5573	3.31168	51.5346	3.11929	40.677	3.08418	34.8104	2.59368	21.9957
1.8741	76.5354	1.73168	52.0646	1.58365	40.2817	1.44378	34.5265	1.29493	21.1392
1.9E-05	78.058	3.8E-05	52.9392	4.3E-05	40.7914	-5E-06	34.2887	0	21.2585
contd.	contd.	contd.	contd.	contd.	contd.	contd.	contd.	contd.	contd.

-1.8741	76.5354	-1.7317	52.0646	-1.5837	40.2817	-1.4438	34.5265	-1.2949	21.1392
-3.0639	74.5573	-3.3117	51.5346	-3.1193	40.677	-3.0842	34.8104	-2.5937	21.9957
-4.0718	72.5403	-5.1719	51.0457	-5.1039	40.4977	-5.0756	35.207	-3.9425	22.9046
-5.2836	70.6899	-7.043	50.3778	-7.1209	40.1387	-6.7431	35.2519	-5.292	24.1092
-6.7373	69.0536	-9.0631	50.0834	-8.9945	40.1136	-8.7211	36.0496	-6.7874	25.6051
-8.6691	67.8512	-11.099	50.347	-11.1	40.8263	-10.453	37.0256	-8.1379	27.2648
-11.116	67.2083	-13.016	51.4546	-13.093	42.1011	-11.933	38.595	-9.7167	29.0112
-13.514	67.0783	-14.822	53.1214	-14.438	43.9901	-13.583	40.4607	-11.303	30.8435
-16.101	66.9225	-16.604	55.0215	-15.893	46.1075	-15.203	42.5078	-12.897	32.8146
-18.801	66.8902	-18.483	56.9933	-17.603	48.352	-17.07	44.4783	-14.703	34.9239
-21.581	66.7433	-20.469	58.8826	-19.371	50.4899	-19.01	46.341	-16.876	36.8517
-24.499	66.4268	-22.929	60.5882	-21.533	52.5859	-21.133	48.4278	-19.232	38.729
-27.441	65.8494	-25.958	61.5515	-24.19	54.1965	-23.319	50.3612	-21.828	40.2508
-30.413	65.092	-29.072	61.6007	-27.17	55.1559	-26.313	51.694	-24.536	41.6137
-33.413	64.1074	-32.21	61.1448	-30.316	55.6473	-29.393	52.3641	-27.705	42.7422
-36.416	62.8839	-35.332	60.3528	-33.556	55.795	-32.586	52.7099	-30.865	43.1964
-39.416	61.4607	-38.492	59.3561	-36.891	55.6251	-35.915	52.784	-34.224	43.4604
-42.42	59.8731	-41.665	58.1322	-40.301	55.0918	-39.306	52.5099	-37.648	43.4098
-45.458	58.1635	-44.851	56.6996	-43.722	54.1832	-42.793	51.9194	-41.111	43.3224
-48.551	56.3722	-48.056	55.1346	-47.119	52.9842	-46.279	50.995	-44.711	43.2451
-51.73	54.5414	-51.319	53.4558	-50.513	51.5076	-49.784	49.7935	-48.396	43.1696
-54.994	52.6562	-54.643	51.7044	-53.883	49.8044	-53.288	48.3791	-52.208	42.9966
-58.333	50.6967	-58.04	49.8667	-57.308	48.014	-56.832	46.8191	-56.113	42.6458
-61.757	48.6816	-61.508	47.941	-60.828	46.1912	-60.432	45.1636	-60.083	41.9785
-65.281	46.6368	-65.049	45.9338	-64.46	44.3748	-64.124	43.4709	-64.098	41.1496
-68.912	44.5543	-68.688	43.8812	-68.222	42.66	-67.926	41.7879	-68.177	40.3409
-72.66	42.4649	-72.433	41.8007	-72.167	41.0735	-71.868	40.1739	-72.39	39.5402
-76.526	40.3392	-76.295	39.7	-76.286	39.5175	-75.97	38.6287	-76.712	38.5175
-80.497	38.1571	-80.272	37.5686	-80.495	37.8385	-80.226	37.1355	-81.059	37.139
-84.566	35.906	-84.369	35.3842	-84.748	35.9285	-84.615	35.5968	-85.372	35.4136
-88.747	33.5994	-88.574	33.1472	-89.007	33.7979	-89.084	33.8962	-89.709	33.4519
-93.032	31.2119	-92.897	30.8498	-93.313	31.4797	-93.586	31.9257	-94.094	31.2801
-97.418	28.7435	-97.331	28.4859	-97.692	29.0256	-98.081	29.62	-98.477	28.8648
-101.92	26.204	-101.88	26.0452	-102.17	26.4836	-102.56	27.0308	-102.87	26.2417
-106.52	23.5813	-106.54	23.5195	-106.77	23.8577	-107.07	24.2319	-107.4	23.5779
-111.25	20.8758	-111.31	20.9041	-111.46	21.1187	-111.65	21.3293	-112.08	20.9295
-116.1	18.1032	-116.18	18.1832	-116.27	18.2772	-116.36	18.3714	-116.88	18.2417
-121.08	15.2857	-121.17	15.3627	-121.19	15.3467	-121.22	15.3455	-121.79	15.4817
-126.21	12.3979	-126.28	12.4446	-126.25	12.3543	-126.24	12.2948	-126.8	12.5866
-131.47	9.4374	-131.51	9.4453	-131.46	9.3324	-131.44	9.2718	-131.91	9.5674
-136.88	6.4016	-136.89	6.3731	-136.85	6.2947	-136.84	6.2564	-137.17	6.4617
-142.42	3.2565	-142.42	3.2321	-142.4	3.2056	-142.4	3.1878	-142.54	3.2882
-148.09	0	-148.09	0	-148.09	0	-148.09	0	-148.09	0
-158.09	0	-158.09	0	-158.09	0	-158.09	0	-158.09	0
-168.09	0	-168.09	0	-168.09	0	-168.09	0	-168.09	0

9.6.5 Co-Ordinates of the Deformed V-Plate Profiles for the 150^0 V-Plates

Table F.5: Co-Ordinates of the Deformed V-Plate Profiles for the 150^0 V-Plates

4g Explosive Disc		6g Explosive Disc		8g Explosive Disc		10g Explosive Disc		12g Explosive Disc	
X-Coord	Y-Coord	X-Coord	Y-Coord	X-Coord	Y-Coord	X-Coord	Y-Coord	X-Coord	Y-Coord
mm	mm	mm	mm	mm	mm	mm	mm	mm	mm
170.059	0	170.059	0	170.059	0	170.059	0	170.059	0
160.059	0	160.059	0	160.059	0	160.059	0	160.059	0
150.059	0	150.059	0	150.059	0	150.059	0	150.059	0
133.682	4.314	133.66	4.2541	133.613	4.1403	133.584	4.0615	133.608	4.0422
127.519	6.0351	127.448	5.8311	127.333	5.4405	127.257	5.1871	127.299	5.0882
121.549	7.7395	121.415	7.3218	121.223	6.5626	121.091	6.0765	121.138	5.834
115.769	9.4046	115.549	8.6933	115.285	7.5521	115.095	6.7901	115.139	6.3066
110.157	11.0013	109.833	9.9078	109.505	8.3963	109.273	7.3522	109.301	6.508
104.701	12.4984	104.262	10.929	103.895	9.1062	103.624	7.7873	103.64	6.4714
99.3866	13.8653	98.8311	11.7457	98.4525	9.7676	98.1499	8.1409	98.1536	6.2238
94.205	15.0675	93.5487	12.3894	93.1796	10.4163	92.8462	8.4581	92.8354	5.8834
89.148	16.0748	88.4205	12.8846	88.081	11.0971	87.7039	8.7527	87.6784	5.5418
84.21	16.8702	83.4445	13.2785	83.1582	11.8448	82.7117	8.9892	82.6688	5.2451
79.4069	17.4807	78.625	13.6269	78.393	12.6583	77.8699	9.1617	77.7937	4.9824
74.7396	17.9532	73.9506	13.9459	73.7796	13.4954	73.1649	9.2477	73.0607	4.6812
70.2111	18.3188	69.4209	14.2444	69.3016	14.2969	68.5954	9.2523	68.4694	4.3336
65.8157	18.5974	65.031	14.5513	64.9433	15.0166	64.1508	9.1472	64.015	3.9613
61.5568	18.8072	60.7712	14.8567	60.6971	15.6229	59.8359	8.9302	59.6924	3.5051
57.4247	18.9764	56.6387	15.1103	56.5596	16.0915	55.6485	8.5605	55.5045	3.0342
53.4246	19.1421	52.614	15.2792	52.5237	16.4314	51.6073	8.0983	51.4339	2.6302
49.5322	19.304	48.7113	15.3563	48.5961	16.6081	47.6645	7.5385	47.4514	2.2139
45.765	19.4302	44.8973	15.2784	44.8007	16.7583	43.8858	6.9089	43.5857	1.5512
42.1039	19.5051	41.2181	15.0245	41.0869	16.8714	40.1879	6.1836	39.9128	0.678
38.5465	19.481	37.6499	14.523	37.4783	16.8955	36.6337	5.3132	36.3545	-0.4878
35.0943	19.3067	34.26	13.7533	33.9255	16.5741	33.214	4.1503	33.0437	-1.8274
31.7758	18.8835	31.0559	12.6577	30.5376	15.8354	30.0084	2.762	29.8401	-3.4687
28.5983	18.1749	28.0319	11.4536	27.3839	14.5813	27.0589	0.9826	27.0094	-5.3687
25.5993	17.188	25.1528	10.0999	24.5833	12.7915	24.3435	-0.9636	24.3821	-7.5703
22.7679	15.9863	22.4554	8.6172	22.1847	10.8042	22.0393	-3.3483	22.1387	-10.072
20.1438	14.5755	19.9453	7.0899	19.7852	8.9847	19.9005	-5.5606	19.9719	-12.299
17.7721	13.1476	17.5025	5.6165	17.3349	7.4742	17.7098	-7.7098	17.8715	-14.562
15.433	11.6443	15.2346	4.1951	14.9401	5.8826	15.4277	-9.318	15.7249	-16.652
13.197	10.2218	12.925	2.6559	12.6219	4.4651	13.0697	-10.936	13.7346	-18.778
11.01	9.0753	10.6809	1.305	10.4167	3.1357	10.82	-12.476	11.5537	-20.554
8.65718	8.1611	8.5252	0.2637	8.12994	1.809	8.65018	-14.011	9.40991	-22.187
6.46883	7.5434	6.28769	-0.662	6.09234	0.5439	6.52451	-15.424	7.38319	-23.742
4.17432	7.0856	4.11352	-1.4107	3.98983	-0.5222	4.44223	-16.872	5.07328	-24.862
2.03942	6.8591	1.99553	-2.0444	2.04915	-1.6009	2.53222	-18.042	2.85288	-26.055
-3E-05	6.9959	-1E-05	-2.0494	9.5E-06	-1.7707	-3E-05	-18.718	-1E-05	-26.501
-2.0394	6.8591	-1.9955	-2.0444	-2.0492	-1.6009	-2.5322	-18.042	-2.8529	-26.055
-4.1743	7.0856	-4.1135	-1.4107	-3.9898	-0.5222	-4.4422	-16.872	-5.0733	-24.862
-6.4688	7.5434	-6.2877	-0.662	-6.0923	0.5439	-6.5245	-15.424	-7.3832	-23.742
-8.6572	8.1611	-8.5252	0.2637	-8.1299	1.809	-8.6502	-14.011	-9.4099	-22.187
-11.01	9.0753	-10.681	1.305	-10.417	3.1357	-10.82	-12.476	-11.554	-20.554
-13.197	10.2218	-12.925	2.6559	-12.622	4.4651	-13.07	-10.936	-13.735	-18.778
-15.433	11.6443	-15.235	4.1951	-14.94	5.8826	-15.428	-9.318	-15.725	-16.652

contd. contd. contd. contd. contd. contd. contd. contd. contd. contd.

-17.772	13.1476	-17.503	5.6165	-17.335	7.4742	-17.71	-7.7098	-17.872	-14.562
-20.144	14.5755	-19.945	7.0899	-19.785	8.9847	-19.901	-5.5606	-19.972	-12.299
-22.768	15.9863	-22.455	8.6172	-22.185	10.8042	-22.039	-3.3483	-22.139	-10.072
-25.599	17.188	-25.153	10.0999	-24.583	12.7915	-24.344	-0.9636	-24.382	-7.5703
-28.598	18.1749	-28.032	11.4536	-27.384	14.5813	-27.059	0.9826	-27.009	-5.3687
-31.776	18.8835	-31.056	12.6577	-30.538	15.8354	-30.008	2.762	-29.84	-3.4687
-35.094	19.3067	-34.26	13.7533	-33.926	16.5741	-33.214	4.1503	-33.044	-1.8274
-38.547	19.481	-37.65	14.523	-37.478	16.8955	-36.634	5.3132	-36.355	-0.4878
-42.104	19.5051	-41.218	15.0245	-41.087	16.8714	-40.188	6.1836	-39.913	0.678
-45.765	19.4302	-44.897	15.2784	-44.801	16.7583	-43.886	6.9089	-43.586	1.5512
-49.532	19.304	-48.711	15.3563	-48.596	16.6081	-47.665	7.5385	-47.451	2.2139
-53.425	19.1421	-52.614	15.2792	-52.524	16.4314	-51.607	8.0983	-51.434	2.6302
-57.425	18.9764	-56.639	15.1103	-56.56	16.0915	-55.649	8.5605	-55.505	3.0342
-61.557	18.8072	-60.771	14.8567	-60.697	15.6229	-59.836	8.9302	-59.692	3.5051
-65.816	18.5974	-65.031	14.5513	-64.943	15.0166	-64.151	9.1472	-64.015	3.9613
-70.211	18.3188	-69.421	14.2444	-69.302	14.2969	-68.595	9.2523	-68.469	4.3336
-74.74	17.9532	-73.951	13.9459	-73.78	13.4954	-73.165	9.2477	-73.061	4.6812
-79.407	17.4807	-78.625	13.6269	-78.393	12.6583	-77.87	9.1617	-77.794	4.9824
-84.21	16.8702	-83.445	13.2785	-83.158	11.8448	-82.712	8.9892	-82.669	5.2451
-89.148	16.0748	-88.421	12.8846	-88.081	11.0971	-87.704	8.7527	-87.678	5.5418
-94.205	15.0675	-93.549	12.3894	-93.18	10.4163	-92.846	8.4581	-92.835	5.8834
-99.387	13.8653	-98.831	11.7457	-98.453	9.7676	-98.15	8.1409	-98.154	6.2238
-104.7	12.4984	-104.26	10.929	-103.9	9.1062	-103.62	7.7873	-103.64	6.4714
-110.16	11.0013	-109.83	9.9078	-109.51	8.3963	-109.27	7.3522	-109.3	6.508
-115.77	9.4046	-115.55	8.6933	-115.29	7.5521	-115.1	6.7901	-115.14	6.3066
-121.55	7.7395	-121.42	7.3218	-121.22	6.5626	-121.09	6.0765	-121.14	5.834
-127.52	6.0351	-127.45	5.8311	-127.33	5.4405	-127.26	5.1871	-127.3	5.0882
-133.68	4.314	-133.66	4.2541	-133.61	4.1403	-133.58	4.0615	-133.61	4.0422
-150.06	0	-150.06	0	-150.06	0	-150.06	0	-150.06	0
-160.06	0	-160.06	0	-160.06	0	-160.06	0	-160.06	0
-170.06	0	-170.06	0	-170.06	0	-170.06	0	-170.06	0

9.7 Appendix G: Mid-Point Displacements and their Error Percentages, of the Deformed V-Plates Exploded by PE4 Rod Explosives, Obtained from the Experiments and from the Pressure Profile Method Numerical Predictions and the JWL Equation of State Method Numerical Predictions

9.7.1 Mid-Point Displacements of the Deformed V-Plates

	Deflection (millimetres) - 60 degree V-Plates		
Mass (grams)	Experimental	ABAQUS (Press.)	ABAQUS (EOS)
3	0	0	0
5	1.025708436	0	3.22096
7	2.298323438	1.3	5.93809
9	10.5066553	1.7	5.81199
11	15.98011013	4.6	9.50354
13	19.51805436	9.2	10.0507

Table G.1: Mid-point deflection predictions of 60^0 V-plates exploded by rod explosives

	Deflection (millimetres) - 90 degree V-Plates		
Mass (grams)	Experimental	ABAQUS (Press.)	ABAQUS (EOS)
3	0	0	0
5	5.3	2.2	3.94183
7	8.1	6.5	7.9018
9	9.4	14.8	5.47949
11	21.3	20.6	6.30167
13	26.9	35.2	7.21828

Table G.2: Mid-point deflection predictions of 90^0 V-plates exploded by rod explosives

<-- Experimental values that have been changed according to pictures

<-- Unlisted torn plate so estimate

<-- Unlisted exp. values so obtained from pictures

--- <-- Totally torn - can't estimate

xxx <-- No experiments/models

	Deflection (millimetres) - 120 degree V-Plates		
Mass (grams)	Experimental	ABAQUS (Press.)	ABAQUS (EOS)
3	10.1	5.2	2.24334
5	26	25.9	3.52909
7	30.9	45.9	6.75803
9	52.7	66.7	5.28123
11	---	xxx	11.9849
13	xxx	xxx	xxx

Table G.3: Mid-point deflection predictions of 120^0 V-plates exploded by rod explosives

	Deflection (millimetres) - 150 degree V-Plates		
Mass (grams)	Experimental	ABAQUS (Press.)	ABAQUS (EOS)
3	23.8	25	12.4692
5	40.9	44.8	9.71874
7	54.6	58.4	16.4184
9	66.3	75.8	27.9739
11	---	xxx	30.409
13	xxx	xxx	xxx

Table G.4: Mid-point deflection predictions of 150^0 V-plates exploded by rod explosives

<-- Experimental values that have been changed according to pictures

<-- Unlisted torn plate so estimate

<-- Unlisted exp. values so obtained from pictures

--- <-- Totally torn - can't estimate

xxx <-- No experiments/models

9.7.2 Error Percentages of the Mid-Point Displacements of the Deformed V-Plates

	60 degree V-Plates	
Mass (grams)	ABAQUS Press. (% error)	ABAQUS EOS (% error)
3	0	0
5	100	214.0229609
7	43.43702987	158.3661595
9	83.81977945	44.68277646
11	71.2142159	40.52894552
13	52.86415422	48.50562553

Table G.5: Error Percentages of the mid-point deflection predictions of 60^0 V-plates exploded by rod explosives

	90 degree V-Plates	
Mass (grams)	ABAQUS Press. (% error)	ABAQUS EOS (% error)
3	0	0
5	58.49056604	25.62584906
7	19.75308642	2.44691358
9	57.44680851	41.70755319
11	3.286384977	70.41469484
13	30.85501859	73.16624535

Table G.6: Error Percentages of the mid-point deflection predictions of 90^0 V-plates exploded by rod explosives

	120 degree V-Plates	
Mass (grams)	ABAQUS Press. (% error)	ABAQUS EOS (% error)
3	48.51485149	77.78871287
5	0.384615385	86.42657692
7	48.54368932	78.12935275
9	26.5654649	89.9786907
11	xxx	xxx
13	xxx	xxx

Table G.7: Error percentages of the mid-point deflection predictions of 120^0 V-plates exploded by rod explosives

	150 degree V-Plates	
Mass (grams)	ABAQUS Press. (% error)	ABAQUS EOS (% error)
3	5.042016807	47.60840336
5	9.535452323	76.23779951
7	6.95970696	69.92967033
9	14.32880845	57.80708899
11	xxx	xxx
13	xxx	xxx

Table G.8: Error percentages of the mid-point deflection predictions of 150^0 V-plates exploded by rod explosives

9.8 Appendix H: Mid-Point Displacements of the Deformed V-Plates Exploded by PE4 Disc Explosives, Obtained from the JWL Equation of State Method Numerical Predictions

	grams of explosive				
	4	6	8	10	12
V-plate angle (dgrs)	ABAQUS (EOS)	ABAQUS (EOS)	ABAQUS (EOS)	ABAQUS (EOS)	ABAQUS (EOS)
60	1.83138	14.9245	10.1632	19.8989	25.6179
90	2.66053	29.9281	18.616	28.8198	62.2076
120	7.44202	32.5608	44.7086	51.2113	64.2415
150	33.1229	42.1682	41.8895	58.8371	66.6202

Table H.1: Mid-Point displacements of the deformed V-plates exploded by PE4 disc explosives, obtained from the JWL EOS method numerical predictions

9.9 Appendix I: An Example of the Input Decks Used to Model V-Plates Being Exploded by PE4 Disc Explosives

NOTE: Because the input decks were generated by the preprocessor, ABAQUS/CAE, each node and element is defined in the input deck instead of being generated by the suitable keywords when the input deck is created manually. Because of this the input decks are excessively long, so the majority of the node and element definitions have been omitted from the example input deck below.

```
*Heading
 Explosive disc is 6g. V-Plate is 90 degrees.
** Job name: f_disc2 Model name: f_disc2
**
** PARTS
**
*Part, name=V-plate_flange
*End Part
*Part, name=bomb
*End Part
**
** ASSEMBLY
**
*Assembly, name=Assembly
**
*Instance, name=V-plate-1, part=V-plate_flange
*Node
      1,     15.0614,     -15.0614,          0.
      2,          0.,          0.,          0.
      3,          0.,          0.,         15.
** Majority of node definitions have been omitted owing to extreme length
   6629,      15.8389,     -15.1155,      6.22344
   6630,      15.8389,     -15.1155,      5.83084
*Element, type=C3D8R
   1,  372, 4416, 4670, 4342,    1,   15,  494,  192
   2, 4416, 4417, 4671, 4670,   15,   16,  495,  494
```

```
  3, 4417, 4418, 4672, 4671,   16,   17,  496,  495
** Majority of element definitions have been omitted owing to extreme length
4216, 4653,  476, 4593, 6629, 4654,  477, 4592, 6628
4217, 4652,  475, 4594, 6630, 4653,  476, 4593, 6629
4218, 4651,  474, 4558, 6594, 4652,  475, 4594, 6630
** Region: (V-plate:Picked)
*Elset, elset=_I1, internal, generate
   1,  4218,    1
** Section: V-plate
*Solid Section, elset=_I1, material=steel
1.,
*End Instance
**
*Instance, name=bomb-1, part=bomb
0., 1.2, 0.
0., 1.2, 0., -1., 1.2, 0., 90.
*Node
     1,          0.,       -1.65,       0.2628
     2,          0.,       -1.65,           0.
     3,      1.1116,    -1.21936,           0.
** Majority of node definitions have been omitted owing to extreme length
  1402,     0.69844,   -0.288847,       0.3504
  1403,    0.706597,   -0.192911,       0.3504
  1404,     0.71434,  -0.0965897,       0.3504
*Element, type=C3D8R
  1,  65, 367, 922, 269,   1,  22, 241,  39
  2, 367, 368, 923, 922,  22,  23, 242, 241
  3, 368,  79, 318, 923,  23,   2,  24, 242
** Majority of element definitions have been omitted owing to extreme length
1038,  563,  562,  115,  116, 1402, 1403,  819,  818
1039,  562,  561,  114,  115, 1403, 1404,  820,  819
1040,  561,  146,   12,  114, 1404,  865,  222,  820
** Region: (bomb:Picked)
*Elset, elset=_I1, internal, generate
   1,  1040,    1
** Section: bomb
*Solid Section, elset=_I1, material=PE4
1.,
*End Instance
*Nset, nset=_G9, internal, instance=V-plate-1
```

9, 12, 13, 14, 375, 376, 377, 378, 379, 380, 381, 382, 383, 384, 385, 386
387, 388, 389, 390, 391, 392, 393, 394, 395, 396, 397, 398, 399, 400, 401, 402
403, 404, 405, 406, 407, 408, 409, 410, 411, 413, 454, 456, 457, 458, 459, 460
461, 462, 463, 464, 465, 466, 467, 468, 469, 470, 471, 472, 473, 474, 475, 476
477, 478, 479, 480, 481, 482, 483, 484, 485, 486, 487, 488, 489, 490, 491, 492
4558, 4559, 4560, 4561, 4562, 4563, 4564, 4565, 4566, 4567, 4568, 4569, 4570, 4571,
4572, 4573
4574, 4575, 4576, 4577, 4578, 4579, 4580, 4581, 4582, 4583, 4584, 4585, 4586, 4587,
4588, 4589
4590, 4591, 4592, 4593, 4594
*Elset, elset=_G9, internal, instance=V-plate-1
4029, 4030, 4031, 4032, 4033, 4034, 4035, 4036, 4037, 4038, 4039, 4040, 4041, 4042,
4043, 4044
4045, 4046, 4047, 4086, 4087, 4088, 4089, 4090, 4091, 4092, 4093, 4094, 4095, 4096,
4097, 4098
4099, 4100, 4101, 4102, 4103, 4104, 4105, 4106, 4107, 4108, 4109, 4110, 4111, 4112,
4113, 4114
4115, 4116, 4117, 4118, 4119, 4120, 4121, 4122, 4123, 4200, 4201, 4202, 4203, 4204,
4205, 4206
4207, 4208, 4209, 4210, 4211, 4212, 4213, 4214, 4215, 4216, 4217, 4218
*Nset, nset=_G180, internal, instance=bomb-1
9, 10, 11, 12, 13, 15, 19, 20, 21, 94, 95, 112, 113, 122, 123, 124
125, 126, 127, 128, 129, 130, 131, 132, 133, 134, 135, 136, 146, 163, 164, 165
166, 167, 168, 169, 201, 202, 203, 204, 205, 206, 207, 216, 217, 218, 219, 220
221, 222, 223, 224, 233, 234, 235, 236, 237, 238, 239, 240, 427, 428, 429, 430
431, 432, 433, 434, 435, 436, 437, 438, 439, 440, 625, 626, 627, 628, 629, 630
631, 821, 822, 823, 824, 825, 826, 827, 828, 829, 830, 831, 832, 833, 834, 859
860, 861, 862, 863, 864, 865
*Elset, elset=_G180, internal, instance=bomb-1
201, 210, 219, 228, 237, 246, 255, 264, 273, 282, 291, 300, 309, 318, 327, 336
345, 354, 363, 372, 381, 390, 399, 408, 409, 410, 427, 428, 445, 446, 463, 464
481, 482, 499, 500, 517, 518, 535, 536, 689, 698, 707, 716, 725, 734, 743, 752
761, 770, 779, 788, 797, 806, 815, 824, 833, 842, 851, 860, 869, 878, 887, 896
905, 914, 923, 932, 941, 950, 959, 968, 977, 986, 995, 1004, 1013, 1022, 1031, 1040
*Nset, nset=_G183, internal, instance=bomb-1
1, 2, 5, 6, 17, 18, 19, 20, 21, 22, 23, 40, 41, 65, 66, 67
68, 69, 70, 71, 79, 80, 81, 82, 83, 84, 85, 177, 185, 186, 187, 188
189, 190, 191, 192, 193, 194, 195, 196, 197, 198, 199, 200, 208, 209, 210, 211
212, 213, 214, 215, 223, 224, 225, 226, 227, 228, 229, 230, 231, 232, 233, 367
368, 369, 370, 371, 372, 373, 374, 375, 376, 377, 378, 379, 380, 653, 654, 655

656, 657, 658, 659, 835, 836, 837, 838, 839, 840, 841, 842, 843, 844, 845, 846
847, 848, 849, 850, 851, 852, 853, 854, 855, 856, 857, 858
*Elset, elset=_G183, internal, instance=bomb-1
1, 2, 3, 25, 26, 27, 49, 50, 51, 73, 74, 75, 97, 98, 99, 121
122, 123, 145, 146, 147, 169, 170, 171, 560, 568, 576, 584, 592, 600, 608, 616
624, 632, 640, 648, 656, 664, 672, 680, 681, 682, 683, 684, 685, 686, 687, 688
689, 753, 754, 755, 756, 757, 758, 759, 760, 761, 825, 826, 827, 828, 829, 830
831, 832, 833, 897, 898, 899, 900, 901, 902, 903, 904, 905, 906, 907, 908, 909
910, 911, 912, 913, 914
*Nset, nset=_G199, internal, instance=V-plate-1
1, 4, 10, 11, 156, 157, 158, 159, 160, 161, 162, 163, 164, 165, 166, 167
168, 169, 170, 171, 172, 173, 174, 175, 176, 177, 178, 179, 180, 181, 182, 183
184, 185, 186, 187, 188, 189, 190, 191, 192, 414, 415, 416, 417, 418, 419, 420
421, 422, 423, 424, 425, 426, 427, 428, 429, 430, 431, 432, 433, 434, 435, 436
437, 438, 439, 440, 441, 442, 443, 444, 445, 446, 447, 448, 449, 450, 451, 453
4595, 4596, 4597, 4598, 4599, 4600, 4601, 4602, 4603, 4604, 4605, 4606, 4607, 4608, 4609, 4610
4611, 4612, 4613, 4614, 4615, 4616, 4617, 4618, 4619, 4620, 4621, 4622, 4623, 4624, 4625, 4626
4627, 4628, 4629, 4630, 4631
*Elset, elset=_G199, internal, instance=V-plate-1
4048, 4049, 4050, 4051, 4052, 4053, 4054, 4055, 4056, 4057, 4058, 4059, 4060, 4061, 4062, 4063
4064, 4065, 4066, 4067, 4068, 4069, 4070, 4071, 4072, 4073, 4074, 4075, 4076, 4077, 4078, 4079
4080, 4081, 4082, 4083, 4084, 4085, 4143, 4144, 4145, 4146, 4147, 4148, 4149, 4150, 4151, 4152
4153, 4154, 4155, 4156, 4157, 4158, 4159, 4160, 4161, 4162, 4163, 4164, 4165, 4166, 4167, 4168
4169, 4170, 4171, 4172, 4173, 4174, 4175, 4176, 4177, 4178, 4179, 4180
*Nset, nset=_G200, internal, instance=V-plate-1
1, 2, 5, 8, 9, 10, 13, 15, 16, 17, 18, 19, 20, 21, 22, 23
24, 25, 26, 27, 28, 29, 30, 31, 32, 33, 34, 35, 36, 37, 38, 39
40, 41, 42, 43, 44, 45, 46, 47, 48, 49, 50, 51, 52, 53, 54, 55
56, 57, 58, 59, 60, 61, 62, 63, 64, 65, 66, 193, 194, 195, 196, 197
198, 199, 200, 201, 202, 203, 204, 205, 206, 207, 208, 209, 210, 211, 212, 213
214, 215, 216, 217, 218, 219, 220, 221, 222, 223, 224, 225, 226, 227, 228, 229
230, 231, 232, 233, 234, 235, 236, 237, 238, 239, 240, 241, 242, 243, 244, 372
374, 412, 413, 451, 455, 4416, 4417, 4418, 4419, 4420, 4421, 4422, 4423, 4424, 4425, 4426

```
 4427, 4428, 4429, 4430, 4431, 4432, 4433, 4434, 4435, 4436, 4437, 4438, 4439, 4440,
4441, 4442
 4443, 4444, 4445, 4446, 4447, 4448, 4449, 4450, 4451, 4452, 4453, 4454, 4455, 4456,
4457, 4458
 4459, 4460, 4461, 4462, 4463, 4464, 4465, 4466, 4467, 4557
*Elset, elset=_G200, internal, instance=V-plate-1
   1,   2,   3,   4,   5,   6,   7,   8,   9,  10,  11,  12,  13,  14,  15,  16
  17,  18,  19,  20,  21,  22,  23,  24,  25,  26,  27,  28,  29,  30,  31,  32
  33,  34,  35,  36,  37,  38,  39,  40,  41,  42,  43,  44,  45,  46,  47,  48
  49,  50,  51,  52,  53, 2015, 2016, 2017, 2018, 2019, 2020, 2021, 2022, 2023, 2024, 2025
 2026, 2027, 2028, 2029, 2030, 2031, 2032, 2033, 2034, 2035, 2036, 2037, 2038, 2039,
2040, 2041
 2042, 2043, 2044, 2045, 2046, 2047, 2048, 2049, 2050, 2051, 2052, 2053, 2054, 2055,
2056, 2057
 2058, 2059, 2060, 2061, 2062, 2063, 2064, 2065, 2066, 2067, 4047, 4048, 4105, 4124, 4143
*Nset, nset=_G201, internal, instance=V-plate-1
   2,   3,   5,   6,  67,  68,  69,  70,  71,  72,  73,  74,  75,  76,  77,  78
  79,  80,  81,  82,  83,  84,  85,  86,  87,  88,  89,  90,  91,  92,  93,  94
  95,  96,  97,  98,  99, 100, 101, 102, 103, 245, 246, 247, 248, 249, 250, 251
 252, 253, 254, 255, 256, 257, 258, 259, 260, 261, 262, 263, 264, 265, 266, 267
 268, 269, 270, 271, 272, 273, 274, 275, 276, 277, 278, 279, 280, 281, 373, 374
4379, 4380, 4381, 4382, 4383, 4384, 4385, 4386, 4387, 4388, 4389, 4390, 4391, 4392,
4393, 4394
 4395, 4396, 4397, 4398, 4399, 4400, 4401, 4402, 4403, 4404, 4405, 4406, 4407, 4408,
4409, 4410
 4411, 4412, 4413, 4414, 4415
*Elset, elset=_G201, internal, instance=V-plate-1, generate
  53, 4028,   53
*Nset, nset=b_all, instance=bomb-1, generate
   1, 1404,    1
*Elset, elset=b_all, instance=bomb-1, generate
   1, 1040,    1
*Nset, nset=point, instance=V-plate-1
 2,
*Nset, nset=profile, instance=V-plate-1
   1,   2,  10,  15,  16,  17,  18,  19,  20,  21,  22,  23,  24,  25,  26,  27
  28,  29,  30,  31,  32,  33,  34,  35,  36,  37,  38,  39,  40,  41,  42,  43
  44,  45,  46,  47,  48,  49,  50,  51,  52,  53,  54,  55,  56,  57,  58,  59
  60,  61,  62,  63,  64,  65,  66, 451
*Elset, elset=profile, instance=V-plate-1
```

```
  1,  2,  3,  4,  5,  6,  7,  8,  9, 10, 11, 12, 13, 14, 15, 16
 17, 18, 19, 20, 21, 22, 23, 24, 25, 26, 27, 28, 29, 30, 31, 32
 33, 34, 35, 36, 37, 38, 39, 40, 41, 42, 43, 44, 45, 46, 47, 48
 49, 50, 51, 52, 53, 4048, 4143
*Nset, nset=v_all, instance=V-plate-1, generate
  1, 6630,   1
*Elset, elset=v_all, instance=V-plate-1, generate
  1, 4218,   1
*Nset, nset=all, instance=V-plate-1, generate
  1, 6630,   1
*Nset, nset=all, instance=bomb-1, generate
  1, 1404,   1
*Elset, elset=all, instance=V-plate-1, generate
  1, 4218,   1
*Elset, elset=all, instance=bomb-1, generate
  1, 1040,   1
*Elset, elset=_V-surf_S4, internal, instance=V-plate-1
 4048, 4049, 4050, 4051, 4052, 4053, 4054, 4055, 4056, 4057, 4058, 4059, 4060, 4061,
4062, 4063
 4064, 4065, 4066, 4143, 4144, 4145, 4146, 4147, 4148, 4149, 4150, 4151, 4152, 4153,
4154, 4155
 4156, 4157, 4158, 4159, 4160, 4161, 4162, 4163, 4164, 4165, 4166, 4167, 4168, 4169,
4170, 4171
 4172, 4173, 4174, 4175, 4176, 4177, 4178, 4179, 4180
*Elset, elset=_V-surf_S3, internal, instance=V-plate-1, generate
 4067,  4085,   1
*Elset, elset=_V-surf_S2, internal, instance=V-plate-1, generate
  1, 2014,   1
*Surface, type=ELEMENT, name=V-surf
_V-surf_S4, S4
_V-surf_S3, S3
_V-surf_S2, S2
*Elset, elset=_b-surf_S2, internal, instance=bomb-1
  1,  2,  3,  4,  5,  6,  7,  8,  9, 10, 11, 12, 13, 14, 15, 16
 17, 18, 19, 20, 21, 22, 23, 24, 193, 194, 195, 196, 197, 198, 199, 200
201, 202, 203, 204, 205, 206, 207, 208, 209, 210, 211, 212, 213, 214, 215, 216
217, 218, 219, 409, 410, 411, 412, 413, 414, 415, 416, 417, 418, 419, 420, 421
422, 423, 424, 425, 426, 553, 554, 555, 556, 557, 558, 559, 560, 561, 562, 563
564, 565, 566, 567, 568, 681, 682, 683, 684, 685, 686, 687, 688, 689, 690, 691
692, 693, 694, 695, 696, 697, 698, 699, 700, 701, 702, 703, 704, 705, 706, 707
```

```
 708, 709, 710, 711, 712, 713, 714, 715, 716, 717, 718, 719, 720, 721, 722, 723
 724, 725, 726, 727, 728, 729, 730, 731, 732, 733, 734, 735, 736, 737, 738, 739
 740, 741, 742, 743, 744, 745, 746, 747, 748, 749, 750, 751, 752
*Elset, elset=_b-surf_S4, internal, instance=bomb-1, generate
  3, 192,   3
*Elset, elset=_b-surf_S3, internal, instance=bomb-1
 193, 194, 195, 196, 197, 198, 199, 200, 201, 220, 221, 222, 223, 224, 225, 226
 227, 228, 247, 248, 249, 250, 251, 252, 253, 254, 255, 274, 275, 276, 277, 278
 279, 280, 281, 282, 301, 302, 303, 304, 305, 306, 307, 308, 309, 328, 329, 330
 331, 332, 333, 334, 335, 336, 355, 356, 357, 358, 359, 360, 361, 362, 363, 382
 383, 384, 385, 386, 387, 388, 389, 390
*Surface, type=ELEMENT, name=b-surf
_b-surf_S2, S2
_b-surf_S4, S4
_b-surf_S3, S3
*End Assembly
**
** MATERIALS
**
*Material, name=steel
*Density
 7.85,
*Elastic
   2.,  0.3,   0.
 1.667,  0.3, 600.
 1.659,  0.3, 601.
 1.396,  0.3, 700.
  1.19,  0.3, 800.
 1.042,  0.3, 900.
 0.953,  0.3,1000.
 0.924,  0.3,1100.
*Inelastic Heat Fraction
        0.9,
*Plastic
   0.0025,      0.,      0.
 0.00264, 0.007185,      0.
 0.00314, 0.025556,      0.
 0.00372, 0.051413,      0.
 0.00432, 0.091745,      0.
 0.00458, 0.115659,      0.
```

0.00488, 0.150734, 0.
0.00505, 0.174145, 0.
0.00522, 0.204152, 0.
0.00532, 0.226766, 0.
0.00539, 0.247764, 0.
0.00529, 0.280197, 0.
0.0025, 0., 200.
0.00264, 0.007185, 200.
0.00314, 0.025556, 200.
0.00372, 0.051413, 200.
0.00432, 0.091745, 200.
0.00458, 0.115659, 200.
0.00488, 0.150734, 200.
0.00505, 0.174145, 200.
0.00522, 0.204152, 200.
0.00532, 0.226766, 200.
0.00539, 0.247764, 200.
0.00529, 0.280197, 200.
0.000279, 0., 699.
0.000296, 0.007185, 699.
0.000351, 0.025556, 699.
0.000415, 0.051413, 699.
0.000483, 0.091745, 699.
0.000513, 0.115659, 699.
0.000546, 0.150734, 699.
0.000564, 0.174145, 699.
0.000584, 0.204152, 699.
0.000595, 0.226766, 699.
0.000602, 0.247764, 699.
0.000591, 0.280197, 699.
0.000333, 0., 700.
0.000352, 0.007185, 700.
0.000417, 0.025556, 700.
0.000494, 0.051413, 700.
0.000575, 0.091745, 700.
0.00061, 0.115659, 700.
0.00065, 0.150734, 700.
0.000671, 0.174145, 700.
0.000695, 0.204152, 700.
0.000707, 0.226766, 700.

```
 0.000716, 0.247764,    700.
 0.000704, 0.280197,    700.
 4.12e-05,      0.,   1000.
 4.36e-05, 0.007185,   1000.
 5.17e-05, 0.025556,   1000.
 6.12e-05, 0.051413,   1000.
 7.13e-05, 0.091745,   1000.
 7.56e-05, 0.115659,   1000.
 8.05e-05, 0.150734,   1000.
 8.32e-05, 0.174145,   1000.
 8.61e-05, 0.204152,   1000.
 8.76e-05, 0.226766,   1000.
 8.88e-05, 0.247764,   1000.
 8.72e-05, 0.280197,   1000.
*Specific Heat
 4.52e-06,
*rate dependent
4e-05,5.
*material, name=PE4
*density
1.6
*elastic
0.00001, 0.3
*eos, type=jwl
0.819, 6.0977, 0.1295, 0.25, 4.5, 1.4
*detonation point
0.0, 1.638, 0.0
**
** BOUNDARY CONDITIONS
**
** Name: bomb_xsymm Type: Symmetry/Antisymmetry/Encastre
*Boundary
_G183, XSYMM
** Name: bomb_zsymm Type: Symmetry/Antisymmetry/Encastre
*Boundary
_G180, ZSYMM
** Name: plate_fixed Type: Symmetry/Antisymmetry/Encastre
*Boundary
_G9, ENCASTRE
** Name: plate_fixed2 Type: Symmetry/Antisymmetry/Encastre
```

```
*Boundary
_G199, ENCASTRE
** Name: plate_xsymm Type: Symmetry/Antisymmetry/Encastre
*Boundary
_G201, XSYMM
** Name: plate_zsymm Type: Symmetry/Antisymmetry/Encastre
*Boundary
_G200, ZSYMM
*initial conditions, type=specific energy
b_all, 9.0e-2
*initial conditions, type=temperature
all, 20
** ----------------------------------------------------------------
**
** STEP: Step-1
**
*Step, name=Step-1
Explosive detonation and interaction with V-plate
*Dynamic, Explicit, adiabatic
, 50.
*Bulk Viscosity
0.06, 1.2
**
** INTERACTION PROPERTIES
**
*Surface Interaction, name=bomb-plate
*Surface Behavior, pressure-overclosure=HARD
**
** INTERACTIONS
**
** Interaction: bomb-plate
*Contact Pair, interaction=bomb-plate, mechanical constraint=KINEMATIC
b-surf, V-surf
**
** OUTPUT REQUESTS
**
*Restart, write, number interval=1, time marks=NO
*Monitor, dof=2, node=point
**
** FIELD OUTPUT: F-Output-1
```

```
**
*Output, field, number intervals=50, time marks=YES
*Node Output
U, V, A, COORD
*Element Output
S, E, PE, PEEQ, LE, ENER, ELEN, TEMP, PRESS
*Contact Output
CSTRESS,
**
** HISTORY OUTPUT: H-Output-1
**
*Output, history, time interval=1.
*Node Output, nset=v_all, variable=PRESELECT
*Element Output, elset=v_all, variable=PRESELECT
*Energy Output, elset=v_all, variable=PRESELECT
*Incrementation Output, variable=PRESELECT
*file output, number interval=300
*node file, nset=profile
u,coord
*diagnostics, deformation speed check=off
**energy output, elset=v_all, instance=V-plate-1, variable=all
**energy output, elset=b_all, instance=bomb-1, variable=all
*End Step
** ----------------------------------------------------------------
**
** STEP: Step-2
**
*Step, name=Step-2
Explosive is frozen and V-plate continues deformation
*Dynamic, Explicit, adiabatic
, 550.
*Bulk Viscosity
0.06, 1.2
**
** BOUNDARY CONDITIONS
**
** Name: bomb_xsymm Type: Symmetry/Antisymmetry/Encastre
*Boundary, op=NEW
** Name: bomb_zsymm Type: Symmetry/Antisymmetry/Encastre
*Boundary, op=NEW
```

```
** Name: freeze Type: Symmetry/Antisymmetry/Encastre
*Boundary, op=NEW
b_all, ENCASTRE
** Name: plate_fixed Type: Symmetry/Antisymmetry/Encastre
*Boundary, op=NEW
_G9, ENCASTRE
** Name: plate_fixed2 Type: Symmetry/Antisymmetry/Encastre
*Boundary, op=NEW
_G199, ENCASTRE
** Name: plate_xsymm Type: Symmetry/Antisymmetry/Encastre
*Boundary, op=NEW
_G201, XSYMM
** Name: plate_zsymm Type: Symmetry/Antisymmetry/Encastre
*Boundary, op=NEW
_G200, ZSYMM
**
** OUTPUT REQUESTS
**
*Restart, write, number interval=1, time marks=NO
**
** FIELD OUTPUT: F-Output-2
**
*Output, field, number intervals=500, time marks=YES
*Node Output
U, V, A, RF, COORD
*Element Output
S, E, PE, PEEQ, LE, ENER, ELEN, TEMP, PRESS
*Contact Output
CSTRESS,
**
** HISTORY OUTPUT: H-Output-2
**
*Output, history, time interval=1.1
*Node Output, nset=v_all, variable=PRESELECT
*Element Output, elset=v_all, variable=PRESELECT
*Energy Output, elset=v_all, variable=PRESELECT
*Incrementation Output, variable=PRESELECT
**energy output, elset=v_all, instance=V-plate-1, variable=all
**energy output, elset=b_all, instance=bomb-1, variable=all
*file output, number interval=500
```

```
*node file, nset=profile
u,coord
*diagnostic, deformation speed check=off
*End Step
```

9.10 Appendix J: Experimentally Obtained Impulses Transferred to the V-Plates Exploded By Rod Explosives

	Transferred Impulses (Ns)			
	V-Plate Angle (degrees)			
Explosive Mass (grams)	**60**	**90**	**120**	**150**
3	1.5	2.83	3.7	5.16
5	3	4.77	6.77	7.88
7	4.95	6.31	9.35	10.54
9	7.16	9.35	11.93	13.89
11	7.27	10.98	18.02	19.29
13	11.5	14.99	-	-

Table J.1: Experimentally obtained impulses transferred to the V-plates exploded by rod explosives

10. References

1. S. Carpenter, Landmines Litter the Planet: One False Step Away From Death, Cape Times, 27 December, 2001

2. M. Granelli, SA Offers to Clear Landmines in Afghanistan, Cape Times, 25 January, 2002

3. Luc P. Lafrance, Mine Blast Protection System for Military Support Vehicles, PVP, Vol. 361, Structures Under Extreme Loading Conditions, pp 305-309, 1998

4. N. Jones, Structural Impact, Cambridge University Press, Cambridge, 1989

5. C. E. Gregory, Explosives for Engineers, Fourth Edition, ch. 2, 1993

6. John S. Rinehart and John Pearson, Explosive Working of Metals, ch. 2-4, 1963

7. T. Wierzbicki and A. L. Florence, A Theoretical and Experimental Investigation of Impulsively Loaded Clamped Circular Viscoplastic Plates, Int. J. Solids Struct., Vol 6, pp 553-568, 1970

8. S. R. Bodner and P. S. Symonds, Experiments on Viscoplastic Response of Circular Plates to Impulsive Loading, J. Mech. Phys. Solids, Vol. 27, pp 91-113, 1979

9. T. Wierzbicki and G. N. Nurick, Large Deformation of Thin Plates Under Localised Impulsive Loading, Int. J. Impact Engng, Vol. 18, Nos 7-8, pp. 899-918, 1996

10. S. B. Menkes and H. J. Opat, Tearing and Shear Failures In Explosively Loaded Clamped Beams, Expl. Mech., Vol 13, pp 480-486, 1973

11. G. N. Nurick and J. B. Martin, Deformation of Thin Plates Subjected to Impulsive Loading - A Review, Int. J. Impact Engng, Vol. 8, pp. 159-186, 1989

12. R. G. Teeling-Smith and G. N. Nurick, The Deformation and Tearing of Thin Circular Plates Subjected to Impulsive Loads, Int. J. Impact Engng, Vol. 11, No. 1, pp. 77-91, 1991

13. G. N. Nurick and R. G. Teeling-Smith, Predicting the Onset of Necking and Hence Rupture of Thin Plates Loaded Impulsively - An Experimental View, Structures Under Shock and Impact (Edited by P. Bulson), pp 431-445, 1992

14. G. N. Nurick and G. C. Shave, The Deformation and Tearing of Thin Square Plates Subjected to Impulsive Loads - An Experimental Study, Int. J. Impact Engng, Vol. 18, No. 1, pp. 99-116, 1996

15. G. K. Schleyer, S. S. Hsu, and M. D. White, Blast Loading of Stiffened Plates: Experimental, Analytical, and Numerical investigations, PVP, Vol. 361, Structures Under Extreme Loading Conditions, pp237- 255, 1998

16. Dr A. A. Ezra, Principles and Practice of Explosive Metalworking, ch.2, 1973

17. T. A. Duffey, The Large Deflection Dynamic Response of Clamped Circular Plates Subjected to Explosive Loading, Sandia Laboratories Research Report, SC-RR-67-532, 1967

18. H. Lippman, Kinetics of the Axisymmetric Rigid-Plastic Membrane Subject to Initial Impact, Int. J. Mech. Sci., Vol 16, pp 297-303, 1974

19. N. Jones, Plastic Failure of Ductile Beams Loaded Dynamically, Trans. ASME, J. Engng Industry, Vol 98 (B1), pp 131-136, 1976

20. P. S. Symonds and T. Wierzbicki, Membrane Mode Solutions for Impulsively Loaded Circular Plates, J. Appl. Mech., Vol 46, pp 58-64, 1979

21. J. B. Martin and P. S. Symonds, Mode Approximations for Impulsively Loaded Rigid-Plastic Structures, J. Engng Mech. Div., Proceedings of the ASCE 92 (EMS), pp 43-66, 1966

22. G. N. Nurick, N. T. Pearce, and J. B. Martin, The Deformation of Thin Plates Subjected to Impulsive Loading, Inelastic Behaviour of Plates and Shells (Edited by L. Bevilacqua), Springer, Berlin, pp 597-616, 1986

23. T. A. Duffey, Dynamic Rupture of Shells, Structural Failure, eds. T. Wierzbicki and N. Jones, New York: Wiley, 1989

24. Wei Qin Shen and Norman Jones, Dynamic Response and Failure of Fully Clamped Circular Plates Under Impulsive Loading, Int. J. Impact Engng, Vol. 13, No. 2, pp. 259-278, 1993

25. A. M. Radford, Deformation and Tearing of Clamped Circular Plates Subjected to Localised Blast Loads, MSc Thesis, Department of Mechanical Engineering, University of Cape Town, 1995

26. R. Bimha, Response of Thin Circular Plates to Blast Loading, MSc Thesis, Department of Mechanical Engineering, University of Cape Town, 1996

27. M. D. Olson, G. N. Nurick, and J. R. Fagnan, Deformation and Rupture of Blast Loaded Square Plates - Predictions and Experiments, Int. J. Impact Engng, Vol. 13, No. 2, pp. 279-291, 1993

28. N. S. Rudrapatna, R. Vaziri, and M. D. Olson, Deformation and Failure of Blast-Loaded Square Plates, Int. J. Impact Engineering, Vol. 22, No. 4, pp. 449-467, March 1999

29. G. H. Farrow, G. N. Nurick, and G. P. Mitchell, Modelling of impulsively Loaded Circular Plates Using the ABAQUS Finite Element Code, Proceedings of the 13th Symposium on Finite Element Methods in South Africa, 1995

30. M. E. Gelman, A Numerical Study of the Response of the Blast Loaded Thin Circular Plates, with Both Clamped and Integral Boundary Conditions, MSc Thesis, Department of Mechanical Engineering, University of Cape Town, 1996

31. G. N. Nurick, Large Deformations of Thin Plates Subjected to Impulsive Loading, Phd Thesis, Department of Mechanical Engineering, University of Cape Town, 1987

32. Martin N. Raftenberg, Close-In Blast Loading of a Steel Disc; Sensitivity to Steel Strength Modelling, Int. J. Impact Engng, Vol. 20, pp. 651-662, 1997

33. M. E. Tollner and G. N. Nurick, Predictions of Stiffened Circular Plates Subjected to Impulsive Loads, PVP, Vol. 394, Structures Under Extreme Loading Conditions, Fluid-Structure Interaction, and Structural Mechanics Problems in Reactor Safety, 1999

34. M. A. Wiehahn, Circular Plates Subjected to Localised Blast Loads. Some Insights into the Mechanism of Tearing and the Energy Required,

MSc Thesis, Department of Mechanical Engineering, University of Cape Town, June 2000

35. W. P. Grobbelaar, An investigation of Structures Subjected to Blast Loads Incorporating an Equation of State to Model the Material Behaviour of the Explosive, MSc Thesis, Department of Mechanical Engineering, University of Cape Town, February 1999

36. British Gas Research and Technology (MRS), Computerised Analysis Tools for Assessing the Response of Structures Subjected to Blast Loading, 1992

37. Hibbit, Karlson, and Sorenson, INC., ABAQUS/Explicit User's Manual, Version 6.2, Vol I, 2001

38. Hibbit, Karlson, and Sorenson, INC., ABAQUS/Explicit User's Manual, Version 6.2, Vol II, 2001

39. T. Masui, T. Nunokawa, and T. Hiramatsu, Shape Correction of Hot Rolled Steel Using an On-Line Leveller, Journal of Japan Society for Technology of Plasticity, No. 1, 1987

40. G. N. Nurick, Personal consultation, University of Cape Town, Cape Town, 2001

41. I. M. Snyman, Personal consultation, Armscor, Pretoria, 2001

42. Steeve Chung Kim Yuen, Deformation and Tearing of Uniformly Blast-Loaded Quadrangular Stiffened Plates, MSc Thesis, Department of Mechanical Engineering, University of Cape Town, 2000

43. J. Lockley, Title unknown as report has been lost, BSc Final Year Project, Department of Mechanical Engineering, University of Cape Town, 1996

44. P. Nannucci, Title unknown as report has been lost, MSc Course-Work Project, Department of Mechanical Engineering, University of Cape Town, 1997

45. N. S. Rudrapatna, M. D. Olson, and R. Vaziri, Deformation and Tearing of Thin Square Plates Under Explosive Loading – Numerical Simulation, Developments in Theoretical and Applied Mechanics, Vol. XVIII, pp. 251-261, 1996

46. G. N. Nurick and D. M. Lumpp, Deflection and Tearing of Clamped Stiffened Circular Plates Subjected to Uniform Impulsive Blast Loads, Structure Under Shock and Impact IV (Edited by N. Jones, C. A. Brebbia, A. J. Watson), pp. 393-402, 1996

47. D. Bergeron and S. Watkins, Land Mine Effects on 5/4 Ton Vehicles, Motion Analysis of High Speed Films for Events 1 to 5, Defense Research Establishment Suffield Research Note No. 1453, Suffield Canada, 1995

48. D. Bergeron, S. Watkins, and R. Walker, Land Mine Effects on 5/4 Ton Vehicles, Processing of Pressure and Acceleration Data for event 1 During Summer 1995, Defense Research Establishment Suffield Research Note No. 1454, Suffield, Canada, 1996

49. Hibbit, Karlson, and Sorenson, INC., ABAQUS Example Problems Manual, Version 6.2, Vol II, 2001